Analysis of cell movement coordination mechanisms in the axial mesoderm during gastrulation of the zebafish Danio rerio.

Arthur Boutillon

INSTITUT POLYTECHNIQUE DE PARIS

NNT : 2021IPPAX080

Thèse de doctorat

Analysis of cell movement coordination mechanisms in the axial mesoderm during gastrulation of the zebrafish *Danio rerio*

Thèse de doctorat de l'Institut Polytechnique de Paris
préparée à l'École Polytechnique

École doctorale n°626
Ecole Doctorale de l'Institut Polytechnique de Paris (ED IP Paris)
Spécialité de doctorat: Biologie

Thèse présentée et soutenue à Palaiseau, le 15/10/2021, par

Arthur Boutillon

Composition du Jury :

René-Marc Mège Directeur de recherche, Institut Jacques Monod (UMR7592)	Rapporteur, président
Virginie Lecaudey Professeure, Interdisciplinary Center for Neurosciences Frankfurt	Rapportrice
Marie Bréau Chargée de recherche, Institut de Biologie Paris Seine (UMR7622)	Examinatrice
Sylvie Rétaux Directrice de recherche, Institut des NeuroPSI (UMR9197)	Examinatrice
Éric Théveneau Chargé de recherche, Centre de Biologie Intégrative Toulouse (UMR5547)	Examinateur
Nicolas David Chargé de recherche, Laboratoire Optique et Biosciences (UMR7645, U1182)	Directeur de thèse

Résumé en français

Le développement embryonnaire, la cicatrisation et certains processus métastatiques impliquent la migration de groupes de cellules au sein desquels l'orientation de chaque cellule dépend d'interactions avec ses voisines, un processus appelé migration cellulaire collective. De plus, le mouvement de ces groupes de cellules doit souvent être coordonné avec d'autres mouvements cellulaires ayant lieu simultanément. Durant ce doctorat j'ai étudié comment la migration de cellules peut être orientée par les interactions cellulaires et comment différentes populations de cellules coordonnent leur mouvement durant le développement embryonnaire précoce du poisson téléostéen *Danio rerio*, aussi appelé poisson-zèbre. Durant la gastrulation du poisson-zèbre a lieu l'extension du mésoderme axial, une structure dorsale composée d'une population dense de cellules mésodermales. Cette extension est menée par le polster, qui migre vers le pôle animal de l'embryon suivi par le mésoderme axial postérieur, qui exécute un mouvement de convergence et extension. Nous avons utilisé le polster ainsi que son interaction avec le mésoderme axial postérieur afin d'étudier respectivement la migration cellulaire collective et la coordination de mouvement entre tissus.

Dans un premier temps, nous avons rapproché la migration du polster de celle d'un tissu très étudié, les crêtes neurales céphaliques du Xénope. En effet, les cellules des deux tissus présentant une morphologie et un mode de migration similaire. Nous avons donc supposé que les mécanismes orientant la migration des cellules des crêtes neurales, l'inhibition de locomotion par contact et la co-attraction, pourraient être à l'œuvre dans la migration du polster. Cependant, en reproduisant les expériences menant à leur identification chez le Xénope, je n'ai pas observé de tels comportements de la part des cellules du polster. Le mode de migration du polster est donc distinct de celui des crêtes neurales.

Dans une précédente étude du laboratoire, il a été établi que les cellules de polster s'orientent au contact les unes des autres, suggérant qu'il existe dans le tissu une information de direction qui se propage par contact cellulaire. Afin d'identifier cette information, j'ai développé une technique d'ablation laser profonde et résolue spatialement. Cela m'a permis d'isoler dans l'embryon des parties du polster du reste du mésoderme axial et d'observer si celles-ci continuent d'avoir un mouvement orienté. Contrairement à nos attentes, j'ai observé que le polster, une fois isolé, est incapable de s'orienter correctement, suggérant que l'information de direction n'est pas contenue dans le tissu. Au contraire, il semble que le polster doive se trouver au contact du mésoderme axial postérieur pour migrer de manière dirigée.

Nous nous sommes ensuite demandé comment est-ce que le mésoderme axial postérieur dirige la migration du polster. J'ai pour cela développé des approches avancées de transplantation cellulaire me permettant de découpler la migration des deux tissus et d'isoler les différents effets cellulaire- et tissulaire-autonomes. Cela m'a notamment permi d'établir que le mésoderme axial postérieur doit s'étendre pour que le mouvement du polster soit dirigé correctement. J'ai ensuite effectué d'autres

expériences de transplantation pour comprendre au niveau cellulaire d'où vient l'orientation par contact. Il s'est avèré que les cellules de polster alignent leur migration avec les cellules alentours, mais seulement si ces dernières migrent activement, formant des extensions cytoplasmiques adhésives et contractiles.

Puis nous avons cherché à identifier le mécanisme moléculaire permettant cette orientation par contact. A l'aide de transplantations cellulaires conventionnelles et d'approches de génétique fonctionnelle, j'ai identifié que l'orientation des cellules de polster repose sur la détection de signaux mécaniques à travers la voie de signalisation mécanosensible impliquant par E-Cadhérine, α-Caténine et Vinculine. Je n'ai malheureusement pas pu explorer plus loin le mécanisme moléculaire liant cette voie à l'orientation cellulaire bien que nous soupçonnons des liens avec les voies de polarité cellulaire planaire et PI3K.

Finalement, afin de comprendre comment la transmission d'orientation par contact peut orienter la migration d'un tissu, nous avons collaboré avec le groupe de Lutz Brüsch qui nous a aidés à construire des simulations numériques de ce phénomène. Nous avons notamment identifié que l'alignement d'une cellule avec la migration des cellules derrière elle est suffisant pour expliquer l'orientation d'un groupe entier et de reproduire plusieurs résultats expérimentaux. Nous avons nommé ce phénomène « guidage par les suiveuses » et montré qu'il garantit le guidage des cellules de polster, mais aussi la robustesse développementale de l'extension du mésoderme axial en assurant le contact continu entre le polster et le mésoderme axial postérieur durant la gastrulation. Ce travail a donc contribué à une meilleure compréhension de la régulation des mouvements gastruléens dans le poisson-zèbre et a permis d'identifier un nouveau mécanisme par lequel la migration collective peut s'établir. Plusieurs articles, rassemblés en annexe, ont été rédigés à partir de ces travaux.

D'autres résultats issus de recherches préliminaires sur la migration du polster sont également présentés dans cette thèse. Je me suis en particulier intéressé au confinement latéral du polster et ai exploré le rôle du mésoderme latéral. A l'aide d'ablations laser et de transplantation, j'ai commencé à montrer qu'en absence de mésoderme latéral, les cellules de polster ont tendance à dévier de leur trajectoire normale indiquant une possible limitation du mouvement latéral des cellules de polster par le mésoderme latéral. De plus, j'ai observé que les fronts de migration du polster et du mésoderme latéral restent à une distance constante, suggérant une forme de régulation commune de la migration de ces deux tissus. J'ai également commencé à explorer le rôle des voies de signalisation de polarité cellulaire planaire, PI3K et FGF dans la migration des cellules de polster. Je présente aussi des tentatives de mise en culture de ces cellules, ainsi que de mesure d'anisotropie de forme afin d'obtenir des informations sur la distribution des forces mécaniques dans le tissu. Tous ces travaux sont préliminaires et n'ont pas donné lieu à des publications.

Enfin, les résultats de plusieurs collaborations sont également rapportés dans cette thèse. J'ai ainsi contribué à l'étude du rôle de CYFIP2, sous unité du complexe WAVE, dans la migration cellulaire. Avec l'équipe d'Alexis Gautreau, nous avons montré que CYFIP2 joue le rôle d'un agoniste inverse au sein d'une balance avec la sous unité concurrente CYFIP1. CYFIP2 limitant la réactivation du complexe WAVE, la migration cellulaire diminue si la balance CYFIP1/CYFIP2 penche vers CYFIP2. J'ai également contribué à la mise au point de senseur de force intra-tissulaires sous la forme de billes de PDMS fluorescentes avec l'équipe de François Gallet. J'ai inséré de telles billes dans le polster de poissons en développement et imagé leur forme. A partir des déformations de ces billes et de leurs propriétés mécaniques, nous avons pu pour la première fois produire une mesure quantitative de la distribution des stresses anisotropiques dans le polster. Les articles résultant de ces collaborations sont également rassemblés en annexe.

Acknowledgments

Tout d'abord, je voudrais vous dire que je vous apprécie tous immensément et que cinq années ici, au Laboratoire Optique et Biosciences, sont un temps trop court à travailler parmi de si excellents collègues. Je ne connais pas la moitié d'entre vous à moitié autant que je le voudrais; et j'aime moins que la moitié d'entre vous à moitié aussi bien que vous ne le méritez. Cela étant, mon temps ici touche à sa fin. Ma thèse se termine et, d'ici six semaines, je serai déjà à marcher dans la neige puis, ensuite, j'irai continuer outre Rhin ma quête de la compréhension du développement embryonnaire. Avant cela, néanmoins, j'ai beaucoup de personnes à remercier.

Naturellement, je ne peux pas ne pas commencer par Nicolas. Nico, ces cinq année -peu ou prou- ont fait de moi un chercheur. Par ton encadrement, nos discussion, la liberté croissante que tu m'as donné et les quelques coups de ciseaux à un parterre d'idées trop florissant m'ont permis de m'approprier mon travail et de construire ma maturité scientifique. Tu as toujours été disponible pour m'écouter, me supporter, pour t'interrompre quinze fois par jour et écouter une idée à moitié formée. Tu m'as laissé te convaincre, tenter des choses que l'on pensait impossible, bref, tu m'as laissé être un chercheur. Mais surtout, tu as été bien plus qu'un « chef de thèse » : j'ai d'ailleurs bien du mal à t'appeler ainsi tant nous avons partagé, dans la science et au-delà, et que la hiérarchie s'est cantonnée à de gentils rappel sur mes retards administratifs et mes oublis de rendez-vous. En effet, outre la recherche, tu as aussi éveillé une nouvelle passion et fait de moi un grimpeur. Pour tout cela, je ne pourrais jamais assez te remercier. J'espère que les mille et une idées que nous avons plantées germeront un jour.

Sophie, je dois également te remercier pour ce temps passé ensemble. Tes conseils et tes avis ont été précieux, surtout ici, à l'X, où la biologie du développement est quelque chose de rare. Tout autant précieuse a été ton aide, aussi bien pour les manips que pour l'enseignement. Finalement, malgré les rudesses de la recherche, tu as toujours été là, avec un sourire, un maté à la main et une friandise pour remonter le moral : ta bonne humeur a éclairé ma thèse et t'avoir en voisine de paillasse est inestimable.

La relève, ensuite! Amélie, je te souhaite bonne chance et surtout bon courage! J'ai fait la partie facile du travail, il te reste ce que je n'ai su faire… Et tu risques de devoir ouvrir le grimoire qu'est mon cahier de manip, et de cela je m'excuse platement.

Finalement, je voulais te remercier tout particulièrement, Emilie, pour ton travail admirable dans l'élevage des poissons et la production de notre matériel de base pour travailler : les embryons. Tu as toujours fait au mieux pour satisfaire ma demande constante et, sans toi, je n'aurais pu accomplir tout ce que j'ai fait. De plus ta jovialité a également contribué à égayer de nombreuses journées.

Je ne peux hélas pas m'attarder à remercier un à un et une à une tous les lobsters, je m'en excuse par avance : toutes et tous vous le mériteriez. J'aimerais tout de même insister sur quelques personnes qui m'ont beaucoup aidé pendant cette aventure.

Hugo, je te remercie d'avoir été là, ma thèse aurait été beaucoup moins supportable sans toi. Que ce soit à se geler la nuit en forêt, à suffoquer l'été dans la salle de sport, à suer sur un rocher ou à hurler sur un lancer de dé malchanceux, tu m'as aidé été à rester sain, de corps comme d'esprit.

Je vous remercie particulièrement, Jùlia et Fanny, de m'avoir épaulé dans des moments particulièrement difficiles de ma vie et de m'avoir aidé à les surmonter. Je vous remercie également dans le désordre, Maëlle, pour les nos discussions, musicales ou non, Maxime et Clothilde, pour vos bonnes humeurs quotidiennes, Anaïs, pour les pauses café beaucoup trop longues, Seongbin, pour les cours d'histoire et d'art culinaires coréens, Clément, auprès duquel je m'excuse pour la nuit au bord de l'eau, Anne pour les parties de volley, Yoann pour me rappeler régulièrement la manière dont je traite les paillasses … Vous êtes fantastiques et avez été mon bol d'air

Parmi les permanents du labo, je voudrais remercier celles et ceux qui m'ont rendu la vie possible au labo. Merci à toi, Pierre, tu es le magicien des microscopes et sans toi, je n'aurais pu faire grand'chose. Merci à Laure et Christelle pour leur soutien administratif et avoir patiemment répondu pour la cinquantième fois à mes questions sur les bons de commandes, mais également à François, pour être à la tête du laboratoire et s'assurer que tout fonctionne. Merci aux joueuses et joueurs, des soirées jeux, comme Emmanuel et ses traits d'humours, Marie Claire et ton franc-parler et Jean-Louis avec qui l'on va conquérir Mars, mais aussi de musique : Karsten, pour les concerts. Merci également à Roxane, qui m'a aidé durant mes enseignements et qui a toujours été de bon conseil. Merci à toutes et tous, merci au LOB.

Je pense que je dois également un mot aux membres de mon jury, qui ont accepté d'évaluer mon travail sans se douter du pavé qui allait arriver sur leur bureau : j'espère que la lecture n'en a pas été trop indigeste. Je tenais également à vous dire, René Marc et Virginie, que vos rapports m'ont faits chaud au cœur : si seulement les referees écrivaient tous comme cela… Quoi qu'il en soit, la soutenance fut un superbe moment, je vous remercie d'être venu en cette contrée lointaine du plateau de Saclay pour que nous puissions discuter de mon travail.

Maintenant, une thèse n'est pas que faite de science, il faut également penser à manger, dormir, et surtout fuir de temps en temps le monde merveilleux de la recherche pour celui, plus calme, des gens normaux. Je voudrais d'abord dire merci à ma famille, qui m'a accompagné tout au long de ce parcours. Vous m'avez hébergé, supporté, soutenu, je ne peux pas vous remercier assez pour avoir toujours été là avec moi, même lorsque j'étais dur à vivre -ce qui a dû arriver une ou deux fois-. Shukran également à toi, Dina, qui supporte au quotidien mes sautes d'humeur, mes enthousiasmes comme mes angoisses avec toujours le même optimisme.

Ensuite, naturellement, je me tourne vers les barbu-e-s. Alex, Brieuc, Etienne, François, JL et Jeanne, je n'aurais tout simplement jamais pu y arriver sans vous. Tous ce que nous avons vécu durant ces années a été un véritable soleil qui a illuminé ma vie et m'a donné le courage de tenir quand les journées se faisaient écrasantes. Nous voir nous éloigner tous les uns des autres, vaquant à notre vie, est difficile, et moi-même ne vais pas tarder à partir, mais nous sommes toujours là les uns pour les autres et vous resterez tous toujours proches dans mon cœur.

Finalement, le dernier envoi va au club d'escrime, le Chapitre des Armes, qui est une machine à produire de la bonne humeur. Contre vents et marées, ce club a tenu et a su transformer nombre de soirée pourries -c'est le terme technique- en sourires et en sueur. Adrien, Elisa, Mathieu, merci pour votre travail acharné pour faire survivre et vivre le club. Merci également pour les amitiés qui se sont créées là-bas, merci à toutes et tous d'avoir pris et distribué les coups, les blagues, les rires et la bonne humeur, partir va être bien difficile…

Merci, finalement, à toutes et tous les autres.

List of abbreviations

AJ adherens junction
Arp actin-related protein
BMP Bone morphogenetic protein
CA constitutively active
CCC Cadherin-Catenin complex
CFC Cripto-1/FRL-1/Cryptic
CIL contact inhibition of locomotion
CoA co-attraction
DAC directional autocorrelation
DN dominant negative
ECM extracellular matrix
EGF epidermal growth factor
EGFR EGF receptor
EM embryo medium
EMT epithelium to mesenchyme transition
EVL enveloping layer
FA focal adhesion
FAK focal adhesion kinase
FGF Fibroblast growth factor
FGFR FGF receptor
FN Fibronectin
FRET Förster resonance energy transfer
GPCR G-protein coupled receptor
H2B Histone 2B
hpf hours post fertilisation
JAK Janus kinase
MBT mid-blastula transition
MCS Monte Carlo step
MET mesenchyme to epithelium transition
MLCK Myosin light chain kinase
MO morpholino
MSD mean square displacement
MZ maternal zygotic
NC neural crest
PCP planar cell polarity pathway
PDMS polydimethylsiloxane
PI3K phosphoinositide 3-kinase
PIP3 phosphatidylinositol-trisphosphate
PKB Protein kinase B
PLLp posterior lateral line primordium
PTEN Phosphatase and Tensin homolog
PVR Pvf1 receptor
ROCK Rho-associated protein kinase
RTK receptor tyrosine kinase
STAT signal transducers & activators of transcription
Tar TARAM-A receptor
Tar* constitutively active aTARAM-A
TGF Transforming growth factor
VBD Vinculin binding domain
WAVE WASP-family Verprolin-homologous protein
YSL yolk syncytial layer

Table of content

List of figures and tables.

"It is not birth, marriage, or death, but *gastrulation* which is truly the most important time in your life."
— Lewis Wolpert

“Although gastrulation may be conveniently divided into a number of particular movements for convenience of analysis, it is essentially a phenomenon of the whole. Each movement depends directly and indirectly on every other. Its cardinal feature is integration. For this reason, it is the process *par excellence* in which it will ultimately be necessary to understand each movement in relation to the others, in order to have a really meaningful comprehension of each one separately.”
— John Philip Trinkaus

Introduction

Embryonic development is the very first process an animal has to go through in order to exist as such. As a consequence, all branches of animal biology make sense only because development happened and produced an organism that moves, digests, thinks and interacts with its environment. Simply because of that, developmental biology is essential to understand the living word around us. But interest of developmental biology reaches way further. The diverse developmental defects, used by scientists to study embryos, actually occur out of a lab and affect the life of individuals and animals. Developmental biology allows us to better understand such defects and, hopefully, avoid them. In the same spirit, developmental biology gives important keys to understand a wide diversity of pathologies, the main one being cancer, which shares many characteristics and processes with embryonic development. Furthermore, development is not a phenomenon happening on isolation. The growing embryo already interacts with its environment, be it the placenta of its mother or the water in which it has been laid, and developmental biology allows us to better understand the relationship between an organism and its environment. Embryonic development is also a window open to the past as it bears the mark of ancestors and of former living forms. As such, studying and comparing the developmental processes of different species is particularly valuable to understand the phylogenetic links between animals. Finally, the mere fact of observing developing embryos, appreciating how a fertilised zygote turns into an unwrought mass of cells from which the first shapes arise and shift, how the rough outline of a living being becomes more and more complex until an animal is born, is a particularly aesthetically pleasing experience. For all these reasons, I estimate that developmental biology is one of the most important branches of biology and that it is thus worth studying (or so I believe after several years of PhD).

What is development made of? It boils down to only a few main processes: cell proliferation, in order to increase the number of cells from one to several billion; cell differentiation, diversifying the role of these billion cells into several hundreds of different cell types; and, finally, morphogenesis, the process of shaping these billions specialised cells to organise them as functioning tissues and organs. During this PhD, I mainly focused on this third aspect of the embryonic development. Morphogenesis, from the Greek *morphê*, shape, and *genesis*, creation, literally the generation of shape, involves several processes all aimed to modify the shape of tissues: cell shape change, cell death, cell proliferation and cell migration. These four ingredients are accountable for all the shapes in multicellular life. As a model for morphogenesis, I chose to look at a phase of intense cell movement, basis of all eumetazoans embryonic development, the gastrulation. In particular, I focused on understanding how cells forming the axial mesoderm coordinate their migration during the gastrulation of the teleost fish *Danio rerio*.

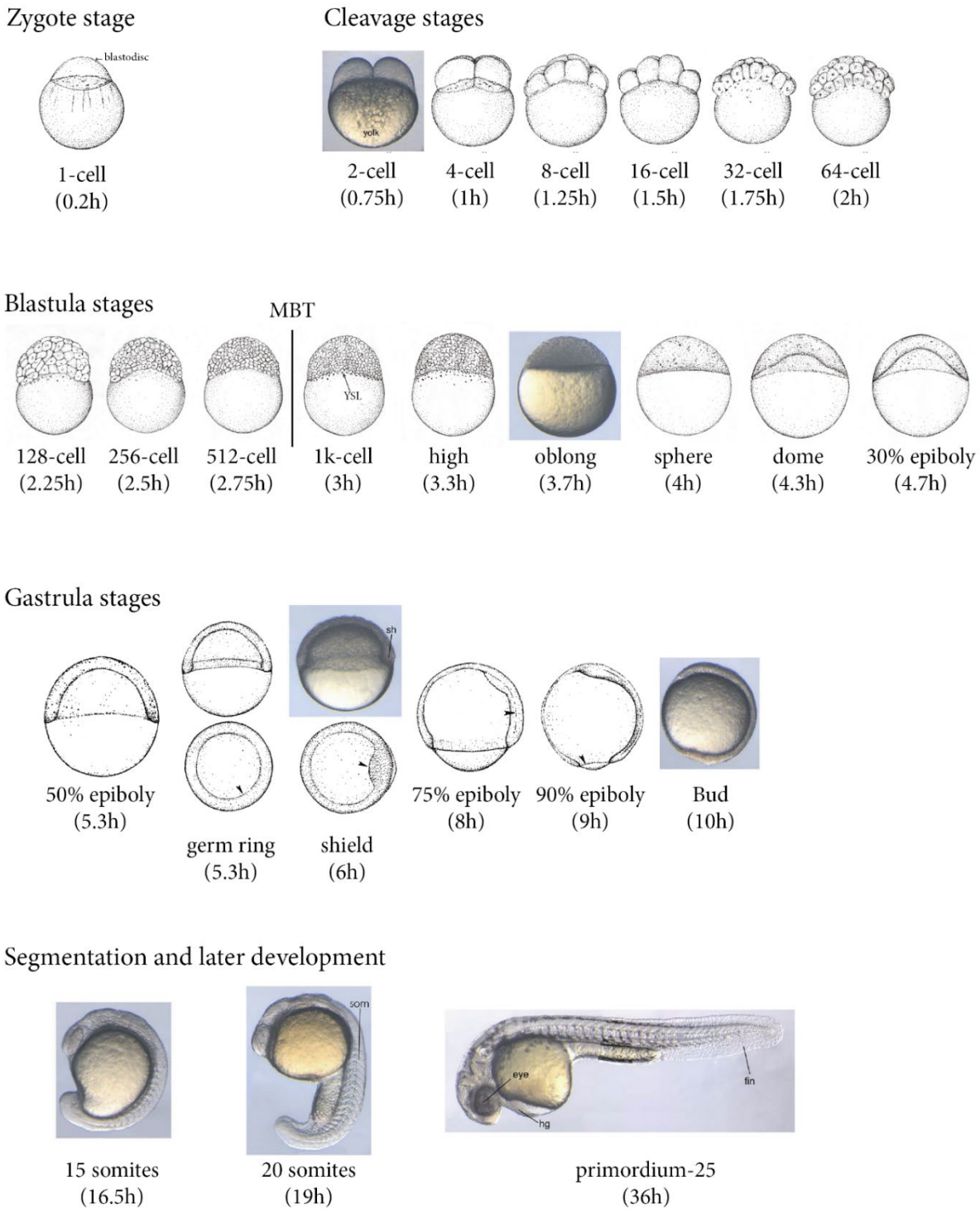

Figure 1. Zebrafish stages of early development. Modified from Kimmel et al., 1995 & Schier & Talbot, 2005. MBT: mid-blastula transition; sh: shield; som: somite; hg: hatching gland.

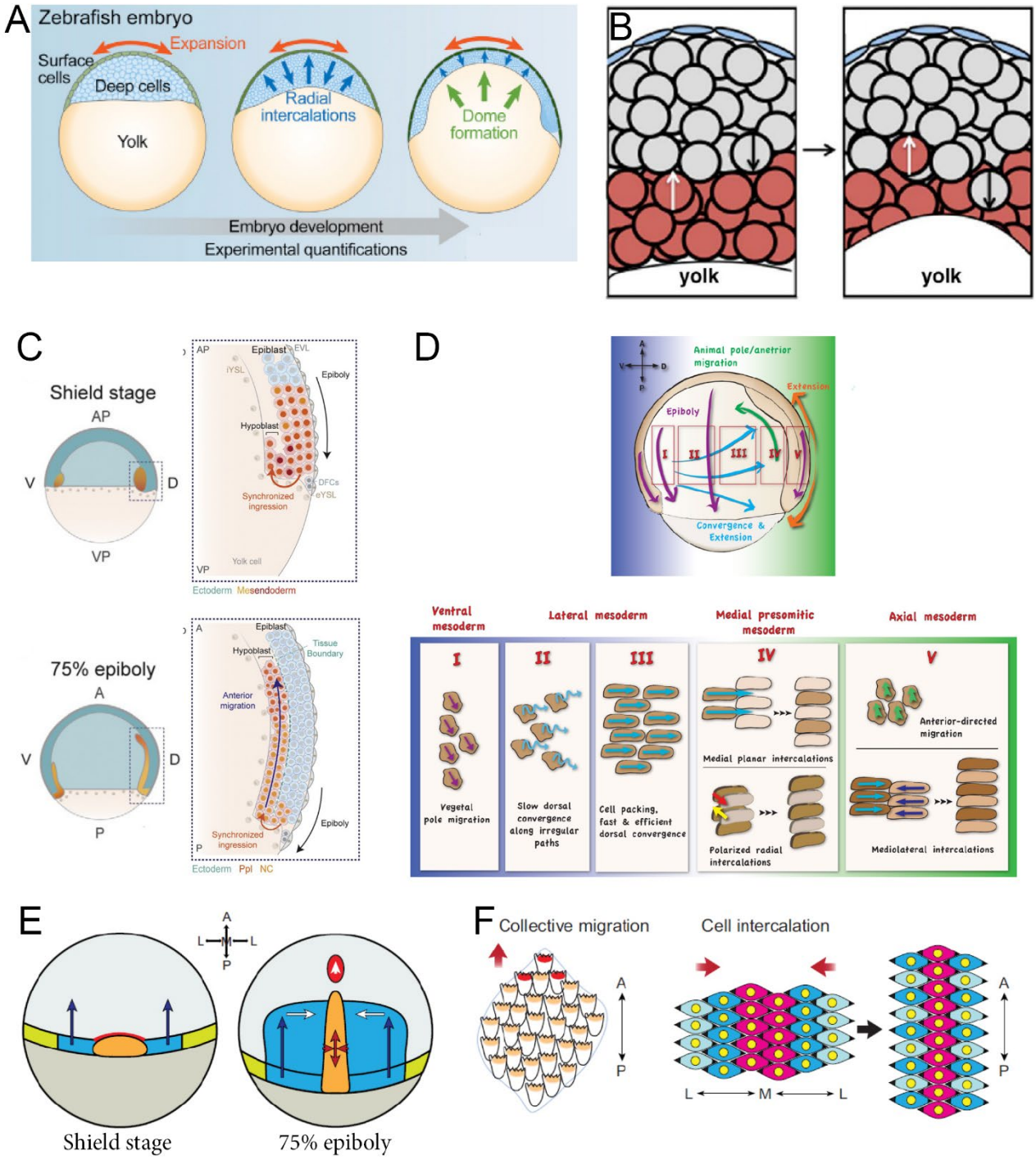

Figure 2. Cell movement of deep cells during gastrulation. A, B: radial intercalation of deep cells at the origin of doming and deep cell epiboly. Modified from Bruce, 2016 & Morita et al., 2017 respectively. **C**: Hypoblast internalisation at the embryonic margin during gastrulation. Modified from Pinheiro & Heisenberg, 2020. **D**: Epiboly movement of mesodermal cells during gastrulation. Mesoderm movements depends on dorso-ventral gastrulation and can be divided in five domains corresponding to different cell behaviours. **E**: Convergence & extension of dorsal mesoderm. Red: polster; orange: notochord; blue: adaxial mesoderm; green: lateral mesoderm. Modified from Tada & Heisenberg, 2012. **F**: Cell behaviours leading to convergence and extension in dorsal mesoderm. Lateral mesoderm and anterior dorsal mesoderm display directional cell migration while posterior mesoderm undergo mediolateral cell intercalation. Modified from Tada & Heisenberg, 2012.

1. Zebrafish early development

Danio rerio, commonly called zebrafish because of its stripped pattern, is a small fresh water Cyprinidae native of South Asia and is present in many labs throughout the world. It has been used as a model animal in biology for the last 50 years, now being the second most used vertebrate (Grunwald & Eisen, 2002). This is mainly due to easy handling and raising of the fishes as they are small (3-5 cm) and gregarious (raised at the density of 5 fishes per litre). Furthermore, mating happens synchronously, upon sunrise or activation of light in a fish facility, and a single female can lay up to several hundred eggs, allowing easy access to a large quantity of material. Finally, these embryos develop quickly, are rather big, allowing easy manipulations (injection, transplantation, ablation, etc.) as well as transparent, which makes them perfect for live imaging. All these characteristics, combined with a sequenced and largely annotated genome, many mutant and transgenic lines, and tools to interact with genetics make zebrafish a perfect vertebrate model to study disciplines ranging from toxicology to neurology and, obviously, developmental biology. I will now describe the early development of the zebrafish embryo, from fertilisation to the end of gastrulation.

a. Early stages of development

Stages of zebrafish development have been described in (C.B. Kimmel et al., 1995), and are named after characteristic features of the embryonic stage. As mentioned before, zebrafish development is fast, gastrulation ending at 10 hours post fertilisation (hpf). Embryos hatch between 24 and 48 hpf and become feeding larvae in 5 days. The optimal temperature for development, in terms of survival and absence of morphological defects, is 28.5 °C, but it is possible to accelerate development by incubating at higher temperature (usually up to 33 °C) or to slow it down at lower temperatures (down to 24 °C). After opening of the mouth, the larva will feed, first on microorganisms then on plankton. One month later, it grew to form a juvenile that will ultimately turn into a sexually mature adult three to four months after fertilisation. Early developmental stages from zygote to 36 hpf are shown in Fig. 1.

i. Zygote and cleavage stages

In zebrafish, development starts by fertilisation of an oocyte by a spermatozoid at a place marking the future animal pole (Hart et al., 1992). This place is defined by a particular structure ensuring efficient penetration of the sperm cell (personal discussion with V. Lecaudey). After fertilisation, the zygote looks like a homogeneous 600 µm diameter sphere surrounded by a transparent, rigid chorion. The first axis of the embryo quickly becomes visible as the mix of yolk and cytoplasm starts to separate (Hisaoka & Battle, 1958). The cytoplasm streams toward the animal pole forming the first embryonic cell, the blastodisc, which sits above the yolk cell, the vegetal pole of the embryo. After 35 minutes starts a fast

series of synchronous divisions, one every 15 minutes. These divisions are called meroblastic and have incomplete cytokinesis, the cytoplasms of embryonic and yolk cells staying in contact (Kimmel & Law, 1985a). Cleavage stage corresponds to the first six rounds of division, the first 2 hours of development, and happens without change of volume, cells becoming smaller over time. At the 5th cycle, cells divide orthogonally to previous plans of division forming a double-layered blastoderm with a first group of cells that are totally isolated from the yolk (Olivier et al., 2010).

ii. Blastula stage

The blastula stage encompasses the period from the moment the blastoderm looks ball-like, at 128-cell stage, to the onset of gastrulation. Cells continue to divide synchronously until the 1000-cell stage. The embryo then rounds up, and staging is made on the basis of its shape until the onset of epiboly. Then, stages are named after the percentage of yolk covered by the epiblast (Kimmel et al., 1995).

Two extraembryonic tissues are formed during the blastula stage, the enveloping layer (EVL) and the yolk syncytial layer (YSL). At the 6th cleavage, some cells are produced that are surrounded by other cells, thus defining deep and superficial cells. Cells at the surface divide asymmetrically forming one deep and one surface cell until the 11th round of division (3.3 hpf). At this stage, superficial cells start to form the EVL, an epithelial layer of cells covering the whole inner cell mass and ensuring embryo integrity, which is completely specified by 4 hpf (Betchaku & Trinkaus, 1978; Kimmel et al., 1990). Later during development, these cells give rise to the periderm (Kimmel et al., 1990), the first skin of the embryonic fish, and also, during gastrulation, form dorsal forerunner cells that will later give rise to the Kupffer's vesicle (Oteíza et al., 2008). Meanwhile, marginal blastomeres, in contact with the yolk, remain connected to it via cytoplasmic bridges (Kimmel & Law, 1985a; Lentz & Trinkaus, 1967). After the tenth round of division, these cells fuse with the yolk to form a ring of nuclei just under the interface between the yolk and the inner cell mass that propagates to form a uniform layer, the YSL (Betchaku & Trinkaus, 1978; Kimmel & Law, 1985b; Sakaguchi et al., 2002). More specifically, nuclei at the margin constitute the external YSL while those underneath blastomeres form the internal YSL. All YSL nuclei are transcriptionally active and required for multiple events of induction (Giger & David, 2017; Sakaguchi et al., 2002; Williams et al., 1996). From blastula stage to the end of gastrulation, the EVL stays tightly linked to the external YSL.

Mid blastula transition (MBT) is defined as the moment when the zygotic genome starts to be expressed. In zebrafish, MBT occurs between the 9th and 10th cycles of division (Kane & Kimmel, 1993), although a recent work observed some zygotic transcription as soon as the 64-cell stage (Heyn et al., 2014). At the 10th round of division, the cell cycle lengthens, variations in cell volume happen, and, as mitosis is controlled by the nucleocytoplasmic ratio, synchrony of divisions is lost (Kane & Kimmel, 1993). Patterns of cell divisions thus become metasynchronous, with waves of divisions travelling from

the animal pole to the margin (Kimmel et al., 1995). Longer interphases actually allow chromatin decondensation and expression of the zygotic genome (Kane & Kimmel, 1993).

Soon after the MBT, deep cells start to exhibit random motility and become softer, likely as a result of the zygotic genome expression (Morita et al., 2017). At that moment, tissue architecture changes as the average number of neighbours per cell decreases while, concomitantly, cells start to intercalate radially (Fig. 2A, B) (Morita et al., 2017; Petridou et al., 2021). These two behaviours fluidise the inner cell mass and decrease its rigidity. As a result, the YSL surface begins to dome toward the animal pole, which induces thinning and spreading of the blastoderm (Kimmel et al., 1995; Morita et al., 2017). Cells thus form an inverted cup on top of the yolk, which corresponds to the dome stage (Fig. 1 & 2A, B). After doming of the yolk, cells start covering the yolk by migrating toward the vegetal pole. This is the epiboly movement that will ultimately lead to cover the whole embryo surface (Fig. 1).

iii. Gastrula stage

Gastrulation is allegedly the most important step of embryonic development as it sets the stage for all further developmental processes. Indeed, during gastrulation the three germ layers, which will each give rise to a specific subset of tissues, are formed, as well as the three embryonic axes. The beginning of gastrulation is defined by the onset of mesoderm and endoderm internalisation, at 50% epiboly (5.3 hpf). This internalisation, happening at the margin of the embryo, induces a thickening of the margin, called the germ ring, and the appearance of the shield on the dorsal side of the embryo (Fig. 1 & 2C). Internalisation at the margin will continue as epiboly proceeds, until the whole yolk is covered, marking the tail bud stage (10 hpf) and the end of gastrulation (Kimmel et al., 1995).

Gastrulation is a key step in eumetazoan development as it corresponds to the specification of germ layers, as well as their positioning in the embryo. Deep layers, endoderm and mesoderm, go from the periphery to the inside while the ectoderm covers the embryo. Broadly, the ectoderm will give rise to the central and peripheral nervous systems, the epidermis and, in vertebrates, the neural crests. Endodermal cells will specialise in gut and associated organs, as well as lung/gills tissues. Finally, the mesoderm will give rise to a large variety of tissues, in particular haematopoietic tissues, heart, kidneys, skeletal muscle and bones (Fig. 3) (Kimmel et al., 1990; Pinheiro & Heisenberg, 2020). It is to note that neural crest cells, that colonise the embryo after neurulation, occupy territories and differentiate in cell types coming from the three germ layers, suggesting that the genetic frontier between germ layers is not definitive (Mayor & Theveneau, 2013a). Actually, some people proposed to describe neural crest cells as a fourth, vertebrate specific germ layer (Shyamala et al., 2015).

In the zebrafish embryo, cells at the margin internalise and form the deep hypoblast layer composed of mesoderm and endoderm (Fig. 2C, 3A). Above the hypoblast stands the pluristratified epiblast layer forming the ectoderm (Pinheiro & Heisenberg, 2020). Mesoderm and endoderm are

intermingled before and during internalisation, forming a mixed group of cells called mesendoderm. Separation of the two germ layers happens during gastrulation (Pézeron et al., 2008; Pinheiro & Heisenberg, 2020; Solnica-Krezel et al., 1995). Endodermal cells flatten and disperse by random walk while mesodermal cells keep a round morphology and form a loose sheet of cells all along the margin, except dorsally (Fig. 2D) (Kane & Kimmel, 1993; Pézeron et al., 2008; Lilianna Solnica-Krezel et al., 1995; Warga & Nusslein-Volhard, 1999; Yin et al., 2008). Here forms a structure which is particularly important for patterning of the embryo, constituted by a local dorsal thickening of cells happening at 6 hpf, called the embryonic shield (Fig. 1 & 2C) (Kimmel et al., 1995; Montero et al., 2005). Mesodermal cells that internalise in the shield organise in a dense and thick tissue called axial mesoderm (Fig. 2D & E) (Boutillon et al., 2021; Dumortier et al., 2012; Montero et al., 2005; Smutny et al., 2017; Ulrich et al., 2003). Depending on the timing of internalisation, cells acquire different identities, first prechordal plate progenitors then notochord progenitors (Fig. 2E) (Blanco et al., 2007; Dumortier et al., 2012; Pinheiro & Heisenberg, 2020). During gastrulation, axial mesoderm extends toward the animal pole of the embryo and acts as an inducer, patterning the overlying neurectoderm (Rembold et al., 2015; Seiliez et al., 2006; Varga et al., 1999). As such, the shield can be considered as an analogue of the Spemann organiser for the embryonic fish. I will describe structure and movement of axial mesoderm more extensively in the last part of the introduction.

At the beginning of gastrulation, it is possible to predict the future fate of cells based on their position in the embryo and to establish a fate map (Fig. 3). In zebrafish, because of cell mixing, there is no precise fate map before the onset of gastrulation (Fig. 3A) (Kimmel et al., 1990; Pinheiro & Heisenberg, 2020). Comparatively, in Xenopus, where there are way less cell rearrangements, a first fate map can be defined as soon as the 32-cell stage (Dale & Slack, 1987). Despite this difference, at the onset of gastrulation, the zebrafish and Xenopus fate maps are very similar (Kimmel et al., 1990; Lane & Sheets, 2006; Pinheiro & Heisenberg, 2020). Cells at the animal pole will give rise to ectoderm (Fig. 3B), while endoderm derives mainly from the first four cell rows of the dorsal and lateral margin, and mesoderm from the first six tiers from the margin. Since endodermal and mesodermal progenitors are largely mixed, their fate map territories largely overlap, and the separation is statistical rather than physical (Fig. 3C) (Kimmel et al., 1990; Warga & Nusslein-Volhard, 1999). Among each layer, the position of the cell along the dorso-ventral axis predicts its future fate. At more dorsal positions, ectoderm gives rise to neurectoderm, mesoderm to notochord and endoderm to pharynx while, at more ventral positions, they respectively give rise to epidermis, blood derivatives and gut (Pinheiro & Heisenberg, 2020; Schier & Talbot, 2005; R.M. Warga & Nusslein-Volhard, 1999).

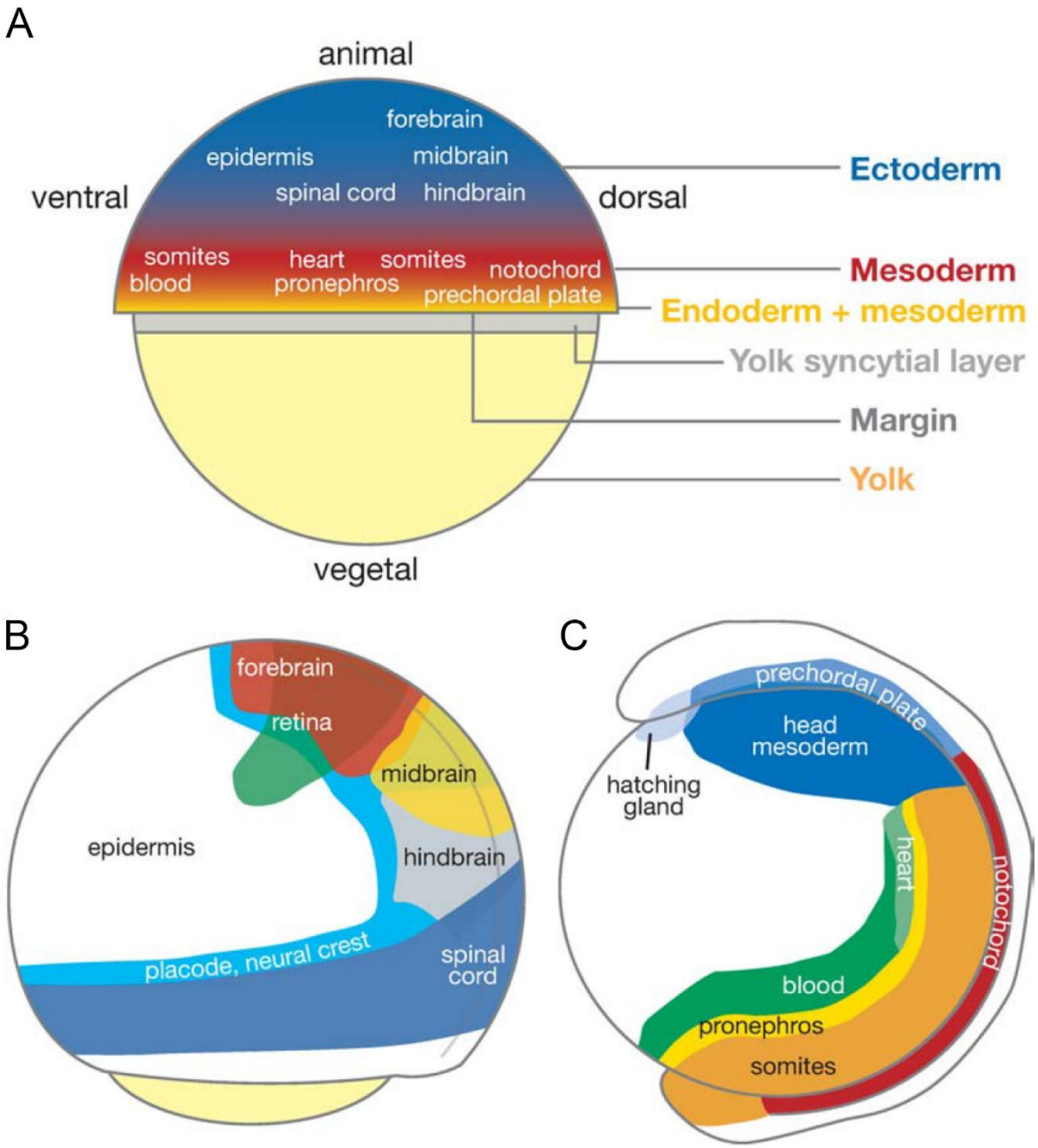

Figure 3. Embryonic fate map. Modified from Schier & Talbot, 2005. **A**: Fate map at shield stage, just before gastrulation. **B**: Ectodermal fate map at 75% epiboly, during gastrulation. **C**: Mesendodermal fate map after gastrulation.

b. Morphogenetic gastrulation movements

i. Epiboly

After doming (4.3hpf), epiboly begins and cells start moving toward the vegetal pole. The epiboly happens in two phases. There is first initiation, from doming to 30% epiboly, then vegetal progression from 30% to 100% epiboly. End of gastrulation is usually regarded as the moment when the yolk plug closes, so that the yolk cell is completely covered. During initiation, superficial blastodermal cells intercalate radially, displacing deepest cells laterally, toward external layers, contributing to spreading of the blastoderm over the yolk (Fig. 2A & B) (Heisenberg et al., 2000; Morita et al., 2017; Warga & Nusslein-Volhard, 1999; Wilson et al., 1995). By the end of initiation, cells form an upturned bowl over the yolk cell. During vegetal progression, EVL, YSL and blastoderm all undergo epiboly, in a coordinated fashion although following different processes (Fig. 4). The margin progresses at around 100 µm/h toward the vegetal pole until the whole yolk is covered, at 10 hpf. At the equator, epiboly takes a 40 min brake corresponding to the onset of internalisation and formation of the germ ring and shield (Fig. 2C) (Kane & Adams, 2002; Warga & Kimmel, 1990).

YSL nuclei are the most vegetal structure, preceding EVL by 50-100 µm. The beginning of epiboly corresponds to their mitotic arrest. External YSL nuclei form large vertical arrays of microtubules running toward the vegetal pole, just below the yolk cell membrane (Fig. 4A) (Solnica-Krezel & Driever, 1994). These cables shorten during epiboly, contributing to pulling these nuclei toward the vegetal pole (Betchaku & Trinkaus, 1986; Solnica-Krezel & Driever, 1994; Strahle et al., 1993). Indeed, their depolymerisation by injection of nocodazole in the yolk largely delays epiboly (Solnica-Krezel & Driever, 1994). Concomitantly, intense endocytosis happens in a ring-like fashion around the external YSL, contributing to epiboly by locally removing yolk cell membrane (Fig. 4B) (Bruce, 2016; Solnica-Krezel & Driever, 1994). Meanwhile, the EVL is linked to the external YSL through adherens and tight junctions, ensuring mechanical integrity and sealing. It has been described that a cortical flow of actomyosin in the YSL, just below the margin, drags the EVL vegetally by pulling on tight junctions (Fig. 4D) (Behrndt et al., 2012; Betchaku & Trinkaus, 1978; Bruce, 2016; Bruce & Heisenberg, 2020). When epiboly reaches 50%, two actin cables form, one in the YSL and one in the EVL, close to the margin. Contraction of these cables through myosin II was thought to contribute to the epiboly movement, acting as a purse string that pulls EVL cells tight and toward the vegetal pole to close the blastopore (Fig. 4D) (Cheng et al., 2004; Köppen et al., 2006). This view has, however, been challenged through experiments where embryos were deformed in a cylindrical geometry (Behrndt et al., 2012). The epiboly of these deformed embryos is normal although contraction of the actomyosin cable cannot contribute to the pulling of the EVL.

The mechanism of blastodermal cells epiboly is less well understood. It mainly relies on radial intercalation that results in thinning and spreading (Fig. 2A & B) (Bruce, 2016; Lepage & Bruce, 2010; Warga & Kimmel, 1990). The classical view is that cells from the superficial layers intercalate in the

deepest ones, but this view has been challenged by precise observations and it appears that intercalation happens in both directions (Bensch et al., 2013; Bruce, 2016). During intercalation, cells change neighbours and have to establish new junctions. This process largely relies on the junction protein E-Cadherin, variations in quantity or in junctional dynamics of E-Cadherin leading to delays in deep cells epiboly (Babb et al., 2001; Babb & Marrs, 2004; Kane et al., 2005). What triggers blastodermal intercalation is not clear. It has been proposed that it is a rearrangement due to compressive forces exerted by the bulging yolk cell and the spreading EVL (Fig. 2A & 4D) (Kimmel et al., 1995; Morita et al., 2017). However, it appears that epiboly of the blastoderm is at least partly independent from the EVL. For example, in *hab*/*e-cadherin* or in maternal zygotic (MZ) *spg*/*pou5f1* mutants, respectively deprived of E-Cadherin and with a decreased dynamic of E-Cadherin, epiboly is way more affected for deep cells than for EVL (Kane et al., 2005; Song et al., 2013).

ii. Internalisation

When the margin reaches the equator of the embryo at 5.7 hpf, it stalls for 40 min, during which the first mesodermal and endodermal cells internalise, forming the germ ring (Fig. 2C) (Kane & Adams, 2002). This process relies on an epithelium to mesenchyme transition (EMT) as perturbing EMT gene expression like Rac1 or Snail largely disrupts internalisation (Blanco et al., 2007; Giger & David, 2017; Yamashita et al., 2004). Whether cells internalise as a cohesive tissue or ingress as individual cells used to be under debate. Indeed, at the dorsal margin, at the level of the shield, it has been described that axial mesoderm internalise collectively as a large band of loosely organised tissue (Montero et al., 2005). Internalising axial mesoderm is nonetheless able to carry immotile cells or objects, showing that internalisation is at least partly non-cell-autonomous (Dumortier et al., 2012; Dumortier & David, 2015). Conversely, along the rest of the margin, observations rather suggest active, cell-autonomous ingression of single cells (Carmany-Rampey & Schier, 2001; Giger & David, 2017). Indeed, endodermal or mesodermal cells transplanted at the animal pole are capable of ingression through an active migration process (Giger & David, 2017). Furthermore, ingressing cells can be observed 3-4 rows away from the margin (Pinheiro & Heisenberg, 2020). Hence, it seems that hypoblast cell internalisation lies in between collective and individual processes, the level of collectiveness depending on the location along the margin. The term of synchronous ingression has been coined to describe this phenomenon between single cell ingression and coordinated internalisation (Adams & Kimmel, 2004; Pinheiro & Heisenberg, 2020).

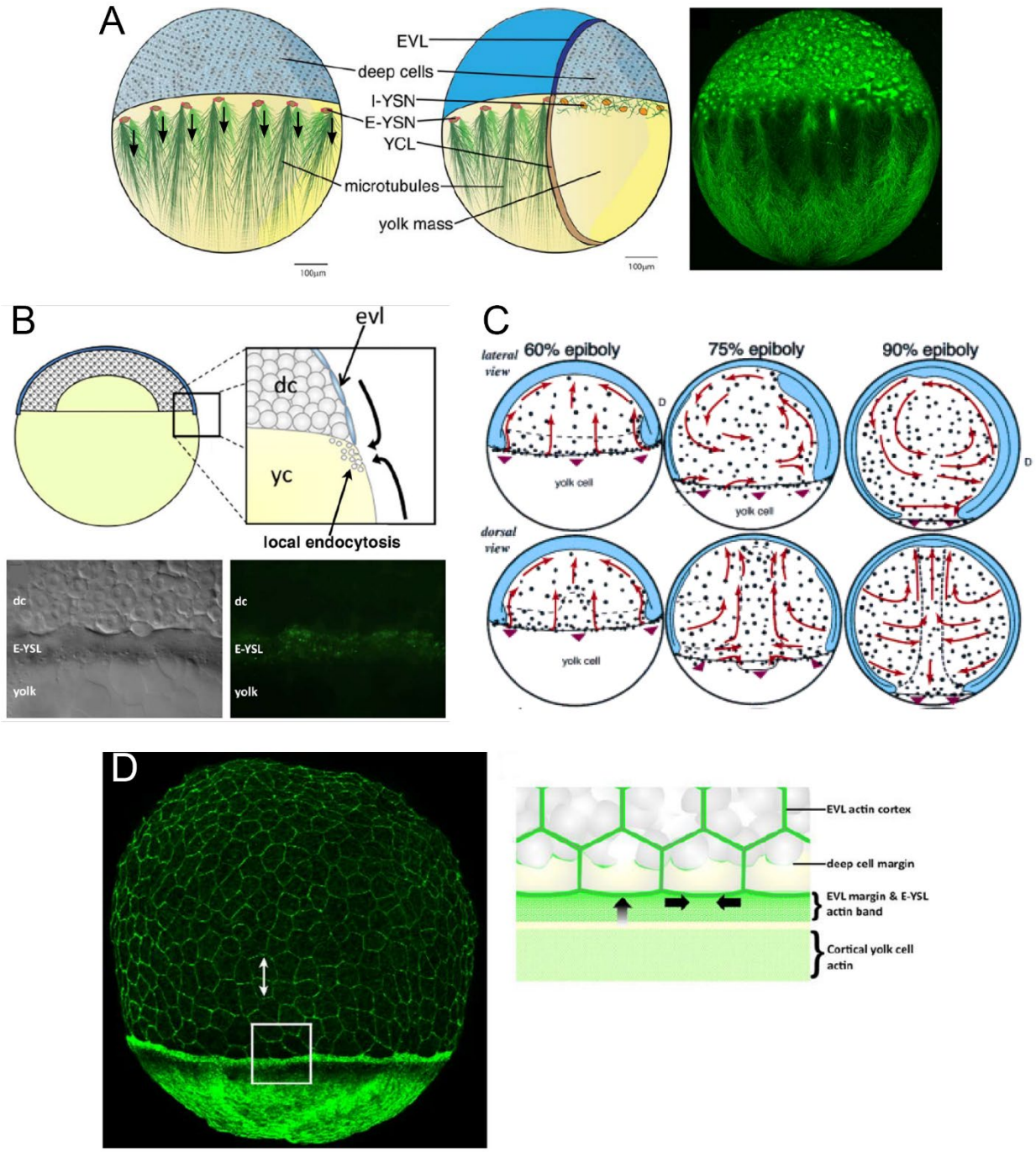

Figure 4. Cell movement of extraembryonic layers during gastrulation. A: Schematics and fluorescence image of the microtubule array involved in external YSL nuclei epiboly. Microtubules are labelled by microtubule-associated protein Dclk2 fused to GFP. Black arrows represent microtubule shortening and displacement of external YSL nuclei. EVL: enveloping layer; I-YSN: internal YSL nuclei; E-YSN: external YSL nuclei. Modified from Bruce, 2016. **B**: Schematics, bright field and fluorescence image of the endocytosis ring along the external YSL contributing to external YSL and EVL epiboly. dc: deep cells; yc: yolk cell. Modified from Bruce, 2016. **C**: YSL nuclei movements during gastrulation. Red arrows: convergence and extension; purple arrowheads: epiboly. Modified from D'Amico & Cooper, 2001. **D**: Fluorescent image and schematics of actomyosin rings during EVL epiboly. Actin is labelled by phalloidin staining at 75% epiboly. Modified from Bruce, 2016.

Once in contact with the yolk, endodermal cells flatten on the yolk and disperse by displaying random migration during the first part of gastrulation (Pézeron et al., 2008). Mesodermal cells keep a rounder morphology and migrate toward the animal pole (Dumortier et al., 2012; Montero et al., 2005; Solnica-Krezel et al., 1995). Organisation of internalised mesoderm depends on its location, dorsal mesoderm forming a dense, multi-layered structure that elongates while lateral and ventral mesoderm form a loose sheet of cells whose front also moves toward the animal pole (Fig. 2D) (Dumortier et al., 2012; Montero et al., 2005; Roszko et al., 2009; Smutny et al., 2017).

iii. Convergence and extension

Convergence and extension describes the simultaneous occurrence of two behaviours that affect cells from epiblast, hypoblast and YSL. There is first a movement of convergence that concentrates cells dorsally. Lateral cells move toward the dorsal axis and, later, ventral cells toward the tail bud (Fig. 2D & 3C). Almost concomitantly happens a bidirectional movement of dorsal cells along the antero-posterior axis that leads to the elongation of the embryo (Tada & Heisenberg, 2012). Convergence and extension slowly builds up during gastrulation, first in the dorsal margin, then in lateral and ventral regions (Fig. 2D & E) (Roszko et al., 2009). At the onset of gastrulation, cells at the dorsal margin converge and form the embryonic shield (Montero et al., 2005; Roszko et al., 2009; Warga & Nüsslein-Volhard, 1998). There, they internalise to form the axial mesoderm, constituted anteriorly of prechordal plate progenitors and posteriorly of notochord progenitors. During gastrulation, notochord progenitors exhibit medio-lateral intercalation by emitting lateral protrusions, contributing to notochord narrowing and extension (Fig. 2E & F) (Glickman et al., 2003; Keller et al., 2000; Skoglund et al., 2008). However, unlike in Xenopus, notochord extension does not rely solely on intercalation. In *ntl*/brachyury mutants, there is a loss of intercalation in the notochord but axial mesoderm still extends to some extent, suggesting the presence of other motors (Glickman et al., 2003; Odenthal et al., 1996; Schulte-Merker et al., 1994; Tada & Heisenberg, 2012). It is likely that addition of new cells at the dorsal margin is required for notochord elongation (Tada & Heisenberg, 2012). Furthermore, it has been suggested that prechordal plate, that migrate straight toward the animal pole contribute to notochord extension as in Xenopus (Pinheiro & Heisenberg, 2020; Tada & Heisenberg, 2012; Tada & Kai, 2012). Very recently, a study proposed that a population of cells at the interface between the notochord and the prechordal plate is actually contributing to notochord elongation by actively migrating (Bosze et al., 2020).

In the lateral margin, between 50 and 70 % of epiboly, cells internalise and move seemingly individually, toward the animal pole. Convergence movement of these cells only starts around 70% epiboly (Fig. 2D) (Roszko et al., 2009). The displayed convergence movement depends on the lateral position relative to the dorsal axis. Five domains of distinct mesodermal behaviour have been described depending on the longitudinal position. Dorsal cells form the axial mesoderm and exhibit convergence and extension. Cells closest to the axial mesoderm tend to intercalate radially and laterally, forming the adaxial mesoderm thickening and later, the somitic mesoderm. More lateral cells display two different

intensities of dorsal convergence. Finally, cells located in the ventral part of the embryo are essentially not converging, and follow epiboly movement toward the vegetal pole, until they join with axial cells, once the yolk is covered and the yolk plug closed (Roszko et al., 2009). Endodermal cell movement is similar to mesodermal ones, their behaviour also depending on their dorso-ventral location (Pézeron et al., 2008).

Interestingly, the ectoderm, that is mainly undergoing epiboly, is also subject to convergence and extension (Quesada-Hernández et al., 2010; Smutny et al., 2017; Williams & Solnica-Krezel, 2020). Around the same period, ectodermal cells above the axial mesoderm gradually align with it and start migrating toward the animal pole. It has first been suggested that extension of the neuroepithelium relies on oriented cell divisions, aligned with the antero-posterior axis (Quesada-Hernández et al., 2010). This view was, however, challenged by the observation that neurectoderm extends even in embryos where cell division is blocked (Smutny et al., 2017; Zhang et al., 2008). More recently, it has been proposed that ectoderm convergence and extension is due to E-Cadherin mediated friction between epiblast and hypoblast (Smutny et al., 2017). While extending, axial mesoderm literally drags the ectoderm, contributing to its elongation, which in turn creates a converging motion to fill the space left empty by animal ward moving cells. Vegetal-most cells are not subject to this friction and continue epiboly. Altogether, these behaviours recreate a convergence and extension phenomenon, apparently driven by the mesodermal axis. However, in embryos deprived of mesodermal or endodermal cells, like maternal zygotic *oep* mutants (MZ *oep*), the ectoderm still converges and extends to some extent, suggesting that other mechanisms are at work (Williams & Solnica-Krezel, 2020). In particular, oriented division and friction with underlying mesoderm are not mutually exclusive and might cooperate to ensure ectoderm extension.

Finally, surprisingly, inner YSL nuclei also exhibit dorsal convergence and antero-posterior extension (Fig. 4C) (D'Amico & Cooper, 2001). YSL convergence and extension is largely disrupted in MZ *oep* mutant embryos, suggesting that YSL motion is driven by mesodermal cells (Carvalho et al., 2009). They actually generate a cortical actin flow in the YSL, dependent on the presence of E-Cadherin, which carries YSL nuclei (Carvalho et al., 2009). However, the precise mechanism leading to YSL cortical flow remains unclear.

Now, before describing in minute details the induction and migration of axial mesoderm cells, I need to introduce how cells actually perform their migration and how they are guided, as individuals or as part of a group of cells.

2. Cell migration

a. Actin cytoskeleton

Cell migration can be defined as an at least partly autonomous displacement of a cell. There are several ways a cell can displace itself in its environment, all of them involving modification of cell shape. The shape of a cell is given by its plasma membrane and its cytoskeleton, consisting of three different kinds of protein filaments that, among numerous other functions, can push, pull and rigidify the membrane (Longley et al., 1999; Luxenburg & Zaidel-Bar, 2019; Mastrogiovanni et al., 2020; Tang & Gerlach, 2017). The most dynamic cytoskeleton filaments are actin microfilaments. Filamentous actin (F-Actin) is a homopolymer composed of globular actin (G-Actin), which has the ability to bind and hydrolyse ATP and to bind to other G actin monomers (Fig. 5) (Korn et al., 1987).

The shape of a G-Actin monomer is asymmetric, one end being barbed, the other pointed (Fig. 5A). Actin polymerisation happens much faster at the barbed end of the filament than at the pointed end, resulting in a directional assembly of filaments. Concomitantly, actin filaments disassemble as actin monomers leave at the pointed end (Korn et al., 1987). Hence a filament is not a fixed entity but a dynamically maintained equilibrium. This assembly/disassembly state is called treadmilling, as monomers are travelling from the font, the barbed end, to the back, the pointed end, before leaving the filament (Bugyi & Carlier, 2010; Campellone & Welch, 2010; Carlier & Shekhar, 2017).

During cell migration, as during many other biological processes, actin assembly and disassembly are regulated, and numerous proteins are involved in modulating monomer incorporation (Fig. 5A) (Pollard & Cooper, 2009; Ridley, 2011). Nucleators are proteins initiating growth of actin filaments. Formins for example are proteins that can start filament assembly and, sitting at the barbed end add monomers to accelerate growth rate (Pring et al., 2002; Zigmond, 2004) while the Arp2/3 complex binds to F-Actin and nucleates new filaments branched on the initial filament (Bugyi & Carlier, 2010; Campellone & Welch, 2010; Goley et al., 2010). Some proteins like Profilin, bind to G-Actin and promote their incorporation in growing filaments (Krishnan & Moens, 2009; Pernier et al., 2016). Conversely, capping proteins will bind to the barbed end of filaments, preventing their growth and stabilising their size (Edwards et al., 2014). Finally, proteins like Cofilin destabilise the pointed end of filaments, accelerating depolymerisation, thus promoting shortening and replenishment of the pool of G-Actin (Bamburg, 1999; Bamburg & Bernstein, 2010). All these interactors are tightly controlled to ensure correct shaping of the actin cytoskeleton.

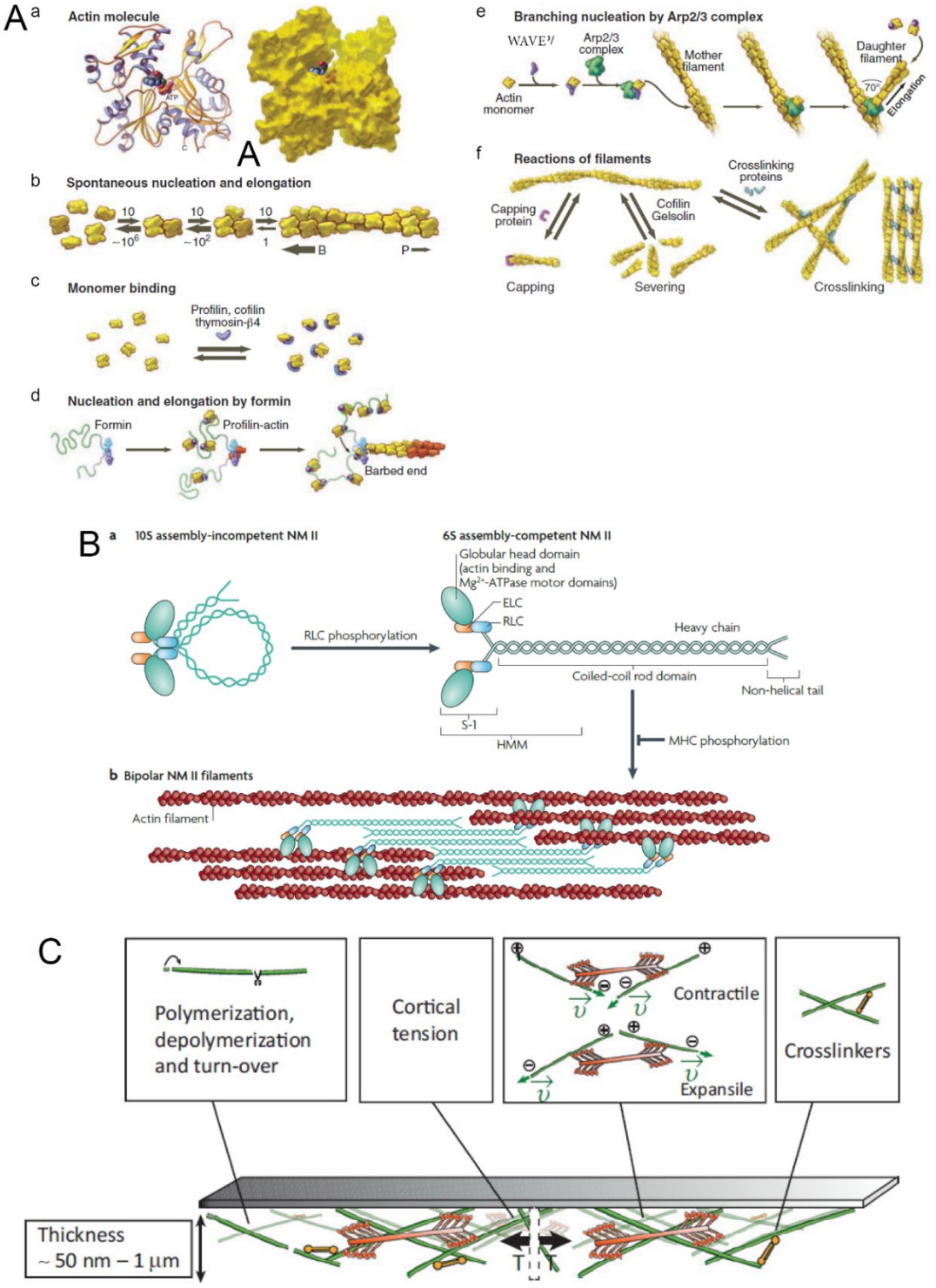

Figure 5. Structure of actomyosin cortex. A: Assembly of actin cytoskeleton. a: Structure of an actin monomer. b: Assembly of an actin filament from the barbed end. Actin dimers and trimers are less stable than monomers and filaments. B: barbed end; P: pointed end. c: Monomer binding by proteins promoting actin assembly. d: Formin nucleate filament by recruiting two monomers and continuously adding monomers by sitting at the growing barbed end. e: Arp2/3 binds to an existing microfilament and nucleates a branched daughter filament. f: Assembly and regulation of actin cytoskeleton by actin-binding proteins. Modified from Pollard & Cooper, 2009. **B**: Structure and assembly of non-muscular Myosin II (NM II). a: Activation of Myosin II unfolds the protein and allows assembly in bipolar mini-filaments. b: Myosin II assemble in mini-filaments that bind actin microfilaments. RLC: regulatory light chain; ELC: essential light chain; HMM: heavy meromyosin subunits. **C**: Actomyosin cortex is a complex network of actin microfilaments, Myosin II mini –filaments and crosslinker proteins located under the cell membrane. Cortex dynamics is ensured by Myosin II activity, which, depending on the distribution of motor protein could result in contractile or expansile stress and ultimately define cell shape. Modified from Salbreux et al., 2012.

A single actin microfilament is 8 nm wide and can be up to a dozen µm long (Yanagida et al., 1984). However, a rapid glance at order of magnitudes shows that a single actin microfilament generates pushing forces way too small (pN) to displace the plasma membrane over several µm (nN) (Ananthakrishnan & Ehrlicher, 2007; Capozza et al., 2018; Footer et al., 2007; Upadhyaya et al., 2003; Xie et al., 2015). Thus, actin filaments need to assemble to generate sufficient forces. This can be done through filament bundling and/or branching, forming different structures that interact with the plasma membrane (Fig. 5A). In particular, just beneath the membrane, lies a large dynamic network of interconnected actin filaments called the cortical actin network that gives its rigidity to the cell membrane and is accountable for membrane deformations (Mattila & Lappalainen, 2008; Mejillano et al., 2004; Svitkina et al., 2003).

Microfilaments are simple active cables, and can only apply pushing forces by growing. Organising a network of filaments able to dynamically control membrane rigidity requires filaments to slide in order to modify the mesh (Chugh & Paluch, 2018; Salbreux et al., 2012). This is mainly done by a molecular motor, the myosin. As its name suggests (*mys*, muscle), myosin was first found in muscle cells, being responsible for muscle shortening upon muscular contraction. But it turned out that there are many types of myosin (18 families have been discovered today) and that they can be found in many other places (Hartman & Spudich, 2012). In particular, associated with the cortical actin network are found non-muscular myosins of type II (Fig. 5B) (Conti et al., 2008; Vicente-Manzanares et al., 2009). They themselves form mini-filaments able to bind actin microfilaments and apply pulling forces on it. Indeed, myosins are able to hydrolyse ATP to change their shape and produce a pulling motion, hence the name molecular motor (Hartman & Spudich, 2012; Houdusse & Sweeney, 2016).

Cell shape and function are largely dependent on cortex contractility (Fig. 5C) (Chalut & Paluch, 2016; Taneja et al., 2020). Indeed, rigidity of the cortex, and, by extension, cell resistance to deformation, rely on the interplay between crosslinking proteins that connect several actin microfilaments, and myosin, that make them slide relative to each other (Bray & White, 1988; Laevsky & Knecht, 2003; Rivero et al., 1996). Increasing both crosslinking and myosin activity results in a tensed, rigid meshwork. Decreasing crosslinking and maintaining high myosin activity results in a very fluid cortex while decreasing myosin activity largely softens cells. It is thus cortex organisation that ensures the plasticity that a cell requires to evolve in a complex 3D environment.

Deformation of the cell membrane does not necessarily rely on myosin, it can also be due to the gathering of polymerising actin filaments. In particular actin can form a branched network via the Arp2/3 complex (Fig. 5A). This complex allows another actin filament to grow, branched to a previous one, forming an angle of approximately 70° (Rouiller et al., 2008). This property allows cortical actin to form a canopy-like network of filaments, pointing toward the membrane and dense enough to push and displace it (Ballestrem et al., 2000; Mejillano et al., 2004; Mogilner & Keren, 2009). Alternatively,

bundling of parallel actin microfilaments by actin-binding proteins like Fascin or α-Actinin can also form structure able to deform the cell membrane (Mattila & Lappalainen, 2008; Mejillano et al., 2004; Svitkina et al., 2003).

b. Cell adhesion

I just presented the main components ensuring cell shape and deformation. To displace itself, a cell has to interact with its environment. In an organism, in particular in a developing embryo, this environment is crowded with fellow cells and extracellular matrix. Cells interact with cells and matrix in many ways but, concerning cell migration, the most important is without contest adhesion. Structures formed by a cell to adhere to another cell or to the extracellular matrix are composed of different elements but share a common structure (Fig. 6, Fig.7) (Mui et al., 2016; Weber et al., 2011). They are composed first of transmembrane proteins called adhesion proteins, whose extracellular domain can physically attach to other proteins. The intracellular domain is usually linked to the cytoskeleton by other intermediate linker proteins (Burridge, 2017; Harris & Tepass, 2010; Huttenlocher & Horwitz, 2011; Wozniak et al., 2004). Indeed, as cell membrane rigidity is very low, it has to be attached to the cytoskeleton: pulling directly on the membrane actually forms an elongated, thin tube of lipids (Paraschiv et al., 2021; Tabdanov et al., 2009). As mentioned before, it is the cortical cytoskeleton that gives the cell its rigidity. The properties of the adhesion depend on the kind of adhesion proteins, linkers and cytoskeleton filaments that are recruited.

The most studied type of cell adhesion is the focal adhesion (FA), by which a cell adheres to the extracellular matrix (ECM) (Fig. 6) (Huttenlocher & Horwitz, 2011; Wozniak et al., 2004). It is a structure where transmembrane proteins from the integrin family bind to ECM proteins outside the cell and are linked to the cytoskeleton inside it. Two proteins in particular, Fibronectin (FN) and Laminin, are distributed in the matrix and contribute both to ECM assembly and cell adhesion (Berrier & Yamada, 2007; Lock & Debnath, 2008). This anchorage to the matrix involves two Integrins (α&β) loaded with Ca2+ ions that bind to FN or Laminin (Fig. 6A) (Bachmann et al., 2019; Campbell & Humphries, 2011). In the cytosol, linker proteins will connect FA to the actin cytoskeleton. Variations in the composition of the FA, in terms of integrins or intermediate linkers will modify the behaviour of the FA. Furthermore, these junctions are a hub for signalling and recruit important kinases like FAK or Rho small GTPase (Fig. 6B) (Giancotti, 1999; Guan, 1997; K Burridge, 1996; Turner, 2000).

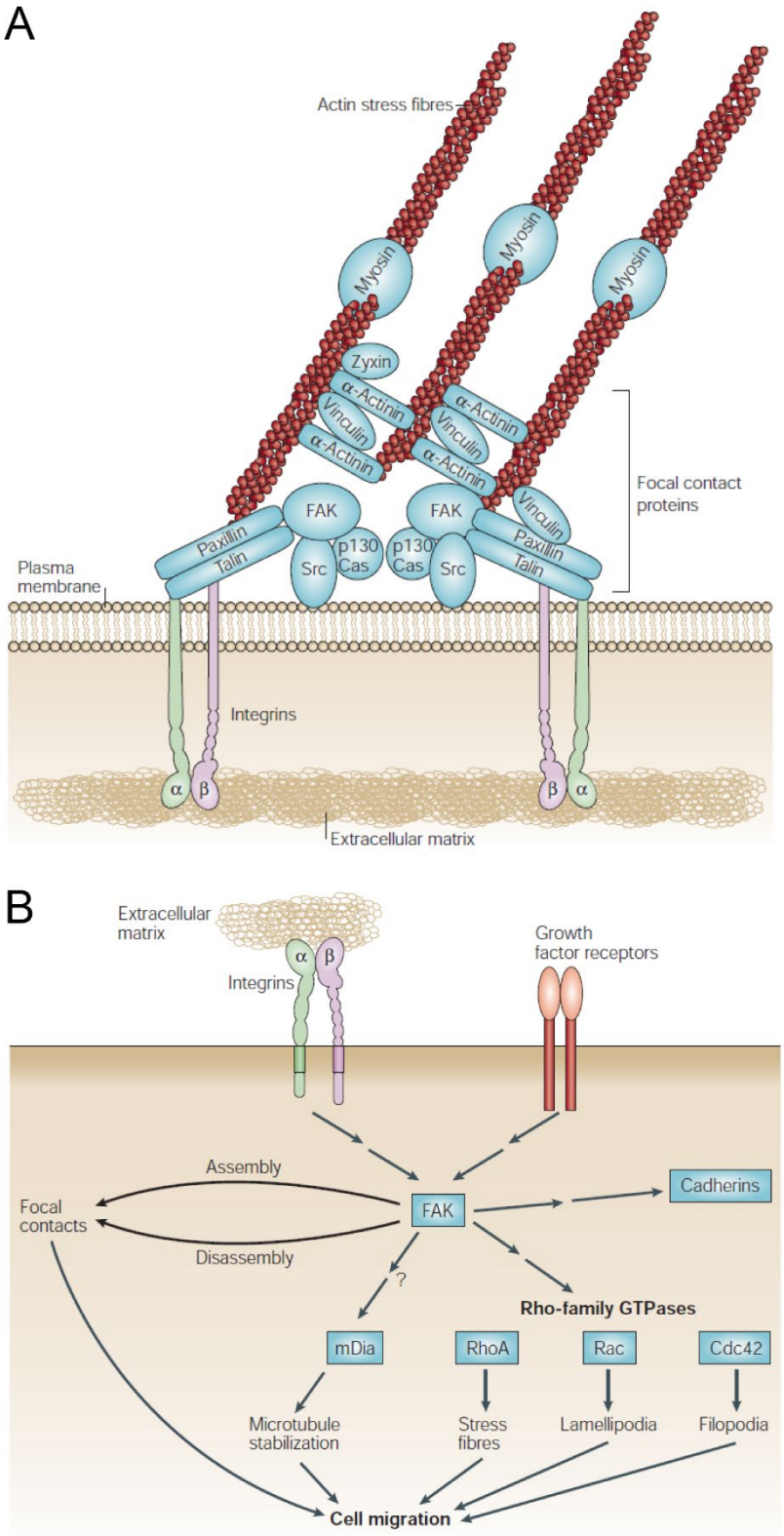

Figure 6. Focal adhesions. Modified from Mitra et al., 2005. **A**: Protein assembly at the level of focal adhesions. Binding of integrins to the extracellular matrix recruits proteins that ensure anchoring to the actin cytoskeleton and trigger its reorganisation in stress fibres. **B**: Intracellular signalling downstream of FAK, that integrates signals coming from integrin focal adhesions and growth factor signalling (RTK).

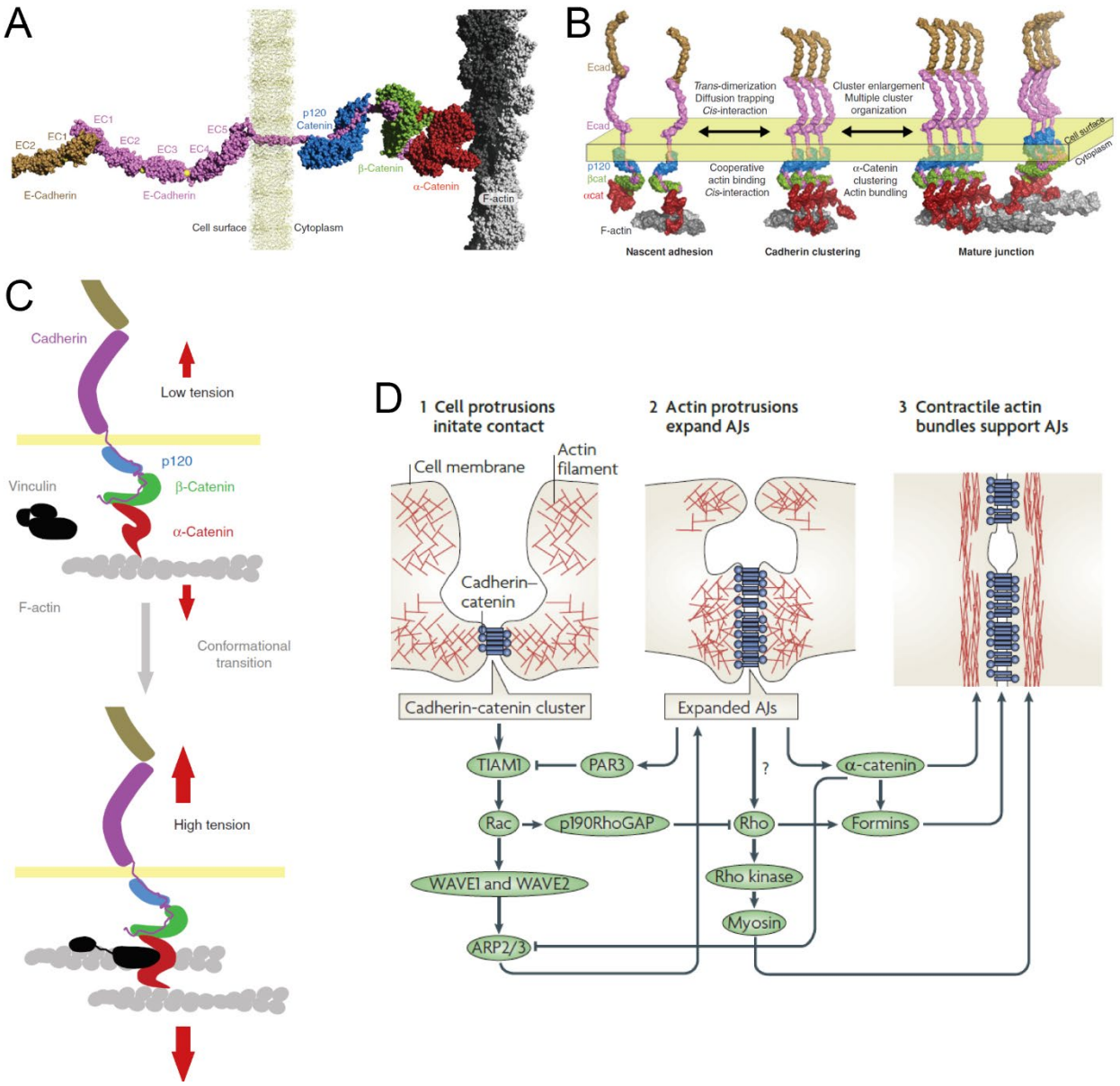

Figure 7. Adherens Junctions. A: Ultrastructure of the cadherin-catenin complex (CCC) engaged in an adherens junction. Extracellular structure of E-Cadherin is rigidified by two Ca^{2+} ions (yellow spheres) allowing the EC1 domain to bind the equivalent domain of another cadherin, located in trans. The intracellular structure of E-Cadherin is stabilised through binding to β-Catenin. Finally, the complex is linked to actin cytoskeleton by α-Catenin, which binds both actin and β-Catenin. The CCC can also recruit p120-Catenin, which is able to regulate Rho GTPases and to bind to the microtubule cytoskeleton. Modified from Mège & Ishiyama, 2017. **B-D**: Adherens junction maturation. Nascent adhesions recruit new trans-dimers of E-Cadherin through cis-interaction of extracellular domains. Concomitantly, intracellular domains gather through actin binding and α-Catenin clustering. This leads to accumulation of trans-dimers at the level of the adherens junction (B, modified from Mège & Ishiyama, 2017). Upon application of tension on the junction, α-Catenin changes conformation and recruits Vinculin, which then bundles actin, contributing to reinforcing attachment to the actin cytoskeleton (C, modified from Mège & Ishiyama, 2017). Finally, dynamics of the cortex is modified through activation of Rho GTPases and polymerisation of branched actin that pushes membranes against each other, contributing to expanding the junction. Once the junction is mature, actin cytoskeleton organises parallel to the membrane and becomes contractile, ensuring mechanical resistance of the junction (D, modified from Harris & Tepass, 2010).

There are other types of cell-cell and cell-ECM junctions in organisms but, as they are less relevant for this work, I'll only quickly present them. Tight junctions are band-like structures between cells where the two membranes are pulled so close and that are so densely packed with adhesion molecules that water cannot go through (Zihni et al., 2016). Such junctions rely on Claudin and Occludin, which are specific types of cadherins, and are used by the organism to prevent liquid flow through an epithelium, in the intestine, for example. Desmosomes are spot-like junctions between cells, where density of adhesion proteins is very high (Garrod & Chidgey, 2008). These adhesions rely on cadherin family proteins, Desmoglein and Desmocollin, connected to intermediate filaments via Desmoplakin. They ensure mechanical integrity of tissues subject to intense stretch, like cardiomyocytes. Gap junctions rely on Connexins that open small pores between cells, ensuring diffusion of molecules and ionic current, permitting a quick communication between cells (Evans & Martin, 2002). Concerning adhesion to the matrix, a structure similar to desmosomes, called hemidesmosome, gathers Integrins at high density and is connected through Plectin to keratin intermediate filaments to ensure strong linkage in tissues subject to stresses (Borradori & Sonnenberg, 1999).

Cell to cell adhesion is a prerequisite for multicellularity. Among the several structures that ensure cell-cell contacts, adherens junctions (AJ) are required to maintain integrity of epithelia and are a constitutive feature of the *Metazoa* clade (Fig. 7) (Grell & Schüller, 1991; Harris & Tepass, 2010). They are particularly dynamic and rely on the cadherin family of transmembrane proteins. There is a wide diversity of cadherin-like proteins with different shapes and functions (Harris & Tepass, 2010). In the case of adherens junctions, adhesion depends on members of the Type I family of cadherins. In particular, E-Cadherin is mostly found in epithelial cells, N-Cadherin in mesenchymal cells and in neural cells and VE-Cadherin in endothelia (Harris & Tepass, 2010; Hulpiau & van Roy, 2009; Oda et al., 2005). Type I family Cadherins display 5 extracellular (EC) domains among which the EC1 domain, that physically binds the EC1 domain of another cadherin in a homophilic manner (Fig. 7A) (Leckband & Prakasam, 2006; Pokutta & Weis, 2007; Tsukasaki et al., 2007). The role of the other EC domains is more obscure although they also contribute to adhesion. As the name suggests, cadherin adhesion depends on the presence of Ca^{2+} ions that insert between the EC domains, rigidifying the extracellular structure (Kim et al., 2011; Nagar et al., 1996).

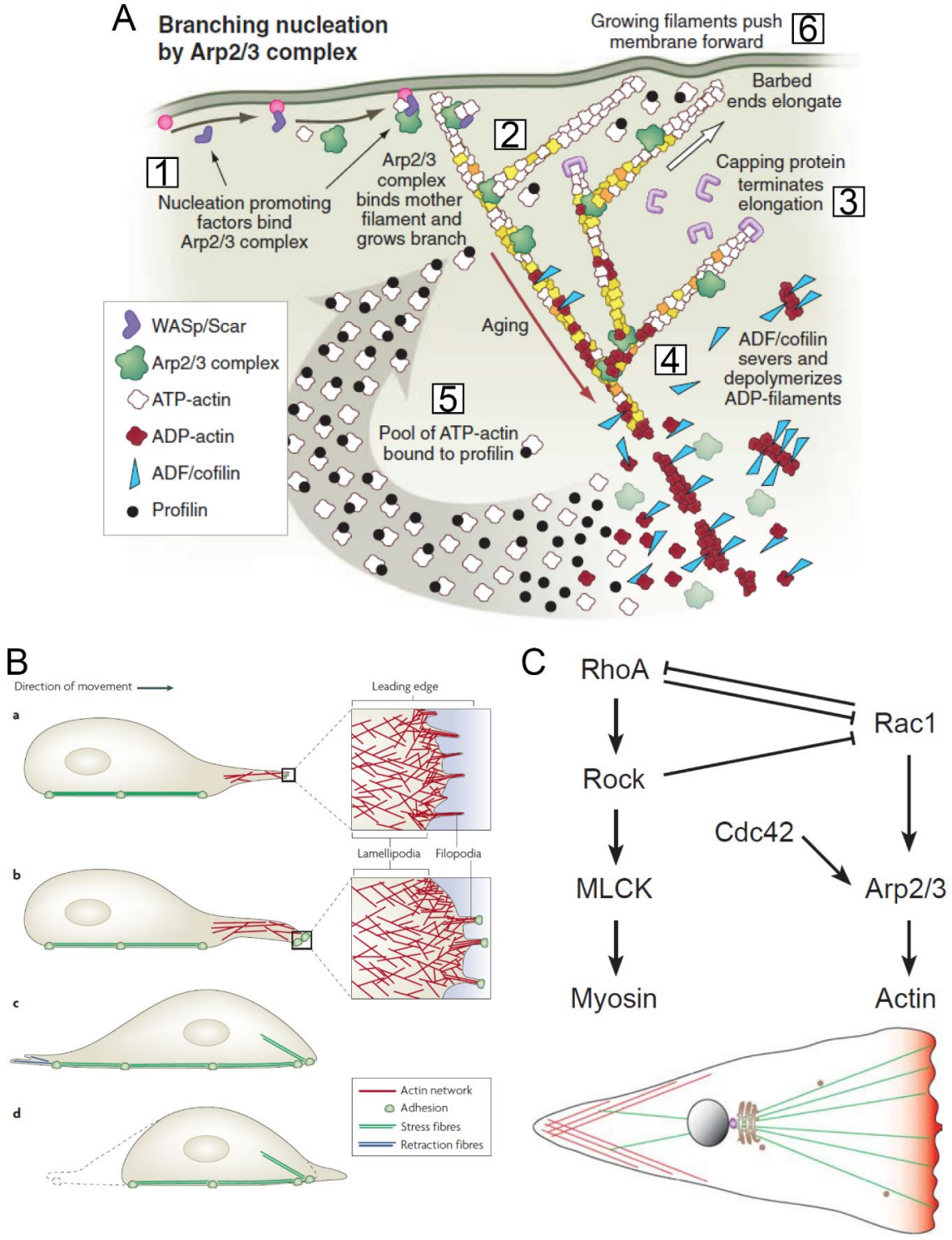

Figure 8. Lamellipodia driven cell migration. A: Regulation of actin cytoskeleton dynamics at migration front. Growing branched actin cytoskeleton pushes the membrane and forms a lamellipodium. 1: Actin regulatory complexes like WAVE and WASP activate the Arp2/3 complex. 2: Arp2/3 binds a newly formed filament and nucleates a branched daughter filament. 3: Capping proteins terminate elongation and stabilise barbed end. 4: Cofilin severs ADP-bound actin filaments and contribute to filaments depolymerisation. 5: Profilin binds to actin monomer and promotes exchange of ADP with ATP, allowing monomer recycling to form new filaments. 6: Oriented actin polymerisation pushes cell membrane to form a protrusion. Modified from Pollard & Cooper, 2009. **B**: Actin rich protrusions during migration. Formation of filopodia and lamellipodia at migration front extends cell membrane (a) and allows formation of new adhesions (b). Stress fibres extend to connect new junction to the old ones (c) then contract to retract the rear of the cell (d). Modified from Mattila & Lappalainen, 2008. **C**: Regulation of cell migration by small Rho GTPases. Rac1 and RhoA mutually inhibit, contributing to cell polarisation. At cell front, Rac1 promotes actin branching by activating WAVE and Arp2/3. At cell rear, RhoA activates Myosin II that pulls on stress fibres. Modified from Jaffe & Hall, 2005

The bond between two cadherins can bear up to around 30 pN, which is pretty low compared to forces adhering cells have to withstand (Sivasankar, 2013). Hence, AJ are constituted of a local concentration of Cadherins spanning large bands over the membrane (zonula adherens) or forming discrete spots (macula adherens) (Meng & Takeichi, 2009). Clustering of cadherin is achieved by lateral interaction of the extracellular domains of cadherins in the same membrane, also called cis dimerisation (Thompson et al., 2021), or by cytoplasmic interaction through their intracellular domains (Fig. 7B) (Kovacs et al., 2002; Meng & Takeichi, 2009; Troyanovsky, 2005).

In the textbook view of adherens junction, Cadherins are bound to the actin cytoskeleton through the cadherin-catenin complex (CCC) (Fig. 7A) (Aberle et al., 1996; Gooding et al., 2004). In the cytoplasm, β-Catenin binds the intracellular domain of Cadherin, which contributes to stabilising the structure of this domain (Huber et al., 2001). Indeed, in absence of β-Catenin, the intracellular domain of Cadherin has no rigid structure. Although it has essential functions in signalling, β-Catenin, from a junctional point of view, mainly is a linker that recruits another protein, α-Catenin (Aberle et al., 1996; Nelson, 2008; Pacquelet & Rørth, 2005). It is α-Catenin that physically links the CCC to the actin cytoskeleton (Kwiatkowski et al., 2010; Nelson, 2008; Rimm et al., 1995). This protein is crucial to ensure mechanical integrity of the junction as the complex cannot efficiently bind actin without it (Han et al., 2016; Roe et al., 1998; Vuong-Brender et al., 2018). Furthermore, α-Catenin acts as a catch bond, stabilising its binding to actin when under tension (Buckley et al., 2014; Yao et al., 2014). It then recruits proteins like Vinculin and Formins, also interacting with the actin cytoskeleton and reinforcing adhesion (Fig. 7C) (Bays & DeMali, 2017; Harris & Tepass, 2010; Kobielak et al., 2004; Seddiki et al., 2018; Yao et al., 2014).

An adherens junction is not simply a hook that connects two cells, it also acts as a signalling platform that is involved in many cellular processes, like cytoskeleton remodelling (Fig. 7D). In particular, E-Cadherin binds to proteins like Mena/VASP which then recruit Arp2/3 and promote formation of a branched actin network (Scott et al., 2006; Verma et al., 2004). AJ can also recruit RhoGEF that activates the Rac1 small GTPase, also contributing to cytoskeleton dynamics (Braga, 2002; Yamazaki et al., 2007; Yap & Kovacs, 2003). In turn, AJ are regulated by small GTPases activity. For example, branched actin network formed at the level of AJ pushes both cell membranes against each other, contributing to AJ growth (Harris & Tepass, 2010; Verma et al., 2004). AJ are also linked to other cytoskeleton fibres through recruitment by Cadherins of proteins like p120-Catenin or Plakoglobin, respectively connected to microtubules and intermediate filaments (Chen et al., 2003; Meng et al., 2008; Nieset et al., 1997; Weber et al., 2012).

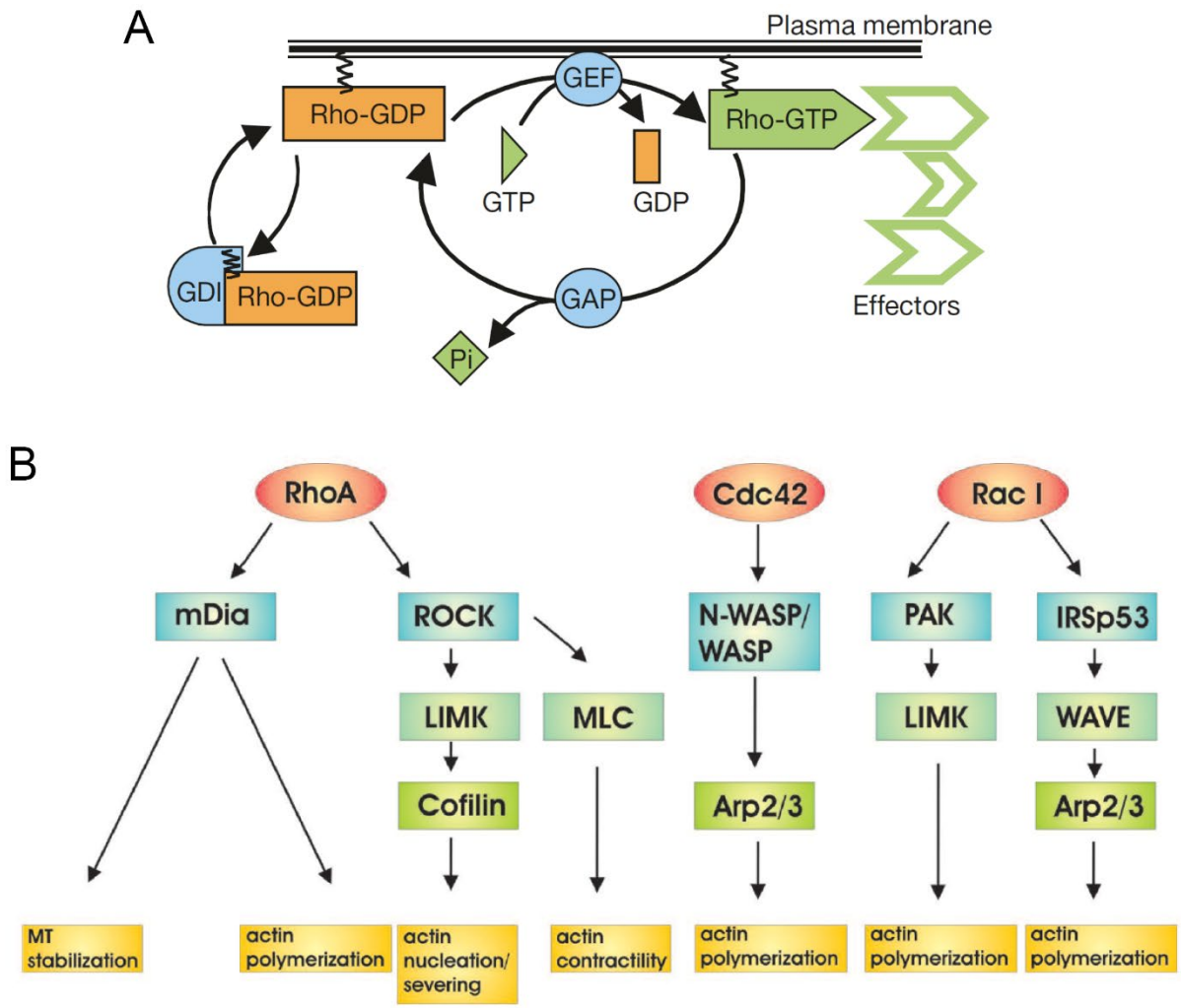

Figure 9. Small Rho GTPase family. A: The Rho GTPases cycle. Rho GTPases are bound to the membrane and cycle between active (GTP-bound) and inactive (GDP-bound) states. This cycle is tightly regulated by three classes of proteins. Guanine exchange factors (GEF) catalyse nucleotide exchange and replace GDP by GTP, mediating GTPase activation. GTPase-activating proteins (GAP) stimulate GTP hydrolysis, which leads to inactivation. Finally, GDP-bound GTPases can be sequestered by guanine nucleotide exchange inhibitors (GDI), extracting the protein from the membrane and preventing its activation. Modified from Etienne-Manneville & Hall, 2002. **B**: Principal signalling pathways downstream of the three main Rho GTPases involved in actin rich protrusion-mediated cell migration. Modified from Spiering & Hodgson, 2011.

c. Actin rich protrusions

Cells are surprisingly inventive in finding ways to displace themselves, sometimes without the need for any adhesion (Liu et al., 2015). But currently, most described instances of cell migration, both *in vivo* and *in vitro*, rely on actin rich protrusions. The textbook description of this type of migration is the following (Fig. 8A & B) (Campellone & Welch, 2010; Mattila & Lappalainen, 2008; Ridley, 2003). Cells extend their membrane using branched actin network polymerisation that generates a pushing force (Campellone & Welch, 2010; Ridley, 2011). The extension then acts as an arm that can grab a substrate for migration, be it the ECM or other cells and act as an anchor to displace the cell body (Swaminathan et al., 2016). At the same time, at the other side of the cell, actin forms thick fibres, called stress fibres, parallel to the direction of migration (Chen, 1981; Ridley & Hall, 1992). Myosin is recruited to these fibres and pull on the cables, provoking the retraction of the rear of the cell body (Chen, 1981). Cells are basically crawling by extending their front and retracting their rear. This mode of migration has largely been described using fish keratocytes in Petri dishes (Korohoda et al., 1997; Libotte et al., 2001). Such cells, migrating on a flat surface, form a nice flat and crescent-shaped structure called the lamellipodium that is typical of this actin rich protrusion dependent migration (Libotte et al., 2001). It appears that in the complex 3D environment of an organism, morphology of actin rich protrusions is completely different, looking more like an arrowhead-shaped structure, sometimes called pseudopod (Diz-Muñoz et al., 2016; Dumortier et al., 2012; Yoshida & Inoue, 2001).

At the cell front, branching of actin is mainly controlled by the Rac1 small GTPase, which is one of the main downstream effectors for cell orientation (Fig. 8C, 9A & B) (Leng et al., 1999; Nobes & Hall, 1995; Reig et al., 2014; Sit & Manser, 2011). Rac1 is first activated at the membrane by proteins of the RhoGEF family (Goicoechea et al., 2014). It then activates the WAVE complex, in turn activating Arp2/3, which nucleates branched actin filaments (Fig. 8A) (Bompard & Caron, 2004; Campellone & Welch, 2010; Swaney & Li, 2016). Structure of the meshwork is regulated by the interplay of activators and inhibitors of Arp2/3 and linear actin nucleators like Formins (Dang et al., 2013; Pollard, 2007; Swaney & Li, 2016). As mentioned before, dynamics of these filaments is controlled by other actin-binding proteins. Myosin motors then stabilise the meshwork by putting filaments under tension, forming a rigid structure that grows toward the membrane and is able to push and deform it (Morimura et al., 2011; Patel et al., 2021; Sayyad et al., 2015). Integrin is at the same time recruited in the protrusion and forms new focal adhesions when cells are migrating on ECM (Swaminathan et al., 2016).

At the cell rear, the RhoA small GTPase is controlling formation and contractility of stress fibres (Fig. 8C, 9A & B) (Nobes & Hall, 1995; Ohashi et al., 2017; Sit & Manser, 2011; Tapon & Hall, 1997). RhoA activates mDia that in turn triggers Formins that bundle actin filaments, contributing to forming the fibres that connect, through Talin, Actinin and Vinculin, nascent focal adhesions at the front to the old ones at the rear (Mitra et al., 2005; Naumannen et al., 2008; Ridley & Hall, 1992). RhoA also activates Myosin II through ROCK (Amano et al., 2010; Sit & Manser, 2011). Myosin assembles in the

stress fibres as antiparallel dimers that pull on actin cables (Fig. 5B) and, ultimately, on the cortex at the rear of the cell (Ohashi et al., 2017; Sit & Manser, 2011). This provokes the displacement of the cytoplasm, toward the front of the cell. Behind the nucleus, cell-matrix adhesions disassemble by endocytosis of Integrins, and cell rear actually moves forward (Lock & Debnath, 2008; Mitra et al., 2005; Pierini et al., 2000; Weber et al., 2011). Contrary to the assembly and disassembly of FA in cells migrating on ECM, which have been extensively described, it is not very well understood how cells use AJ to migrate on other cells. It is, however, tempting to speculate that a similar mechanism is at work, AJ assembling at the front and disassembling at the rear. It has been described that RhoA and Rac1 mutually inhibit their activities, which contribute to establishing a sharp definition of a front and a rear during migration (Fig. 8C, 9B) (Burridge & Wennerberg, 2004; Ory et al., 2000).

Other kinds of actin rich extensions exist, in particular filopodia, usually associated with environment sensing, although some studies also suggest a role in physically displacing the cell (Fig. 8A) (Mattila & Lappalainen, 2008). The main difference with the previously described protrusions is that filopodia are long and thin structures formed by extending actin bundles, perpendicular to the membrane. They form very linear structures, distinct from lamellipodia, which are large, flat and maximise the area of contact. They are also differently controlled, being activated by the CDC42 small GTPase and elongated by formins in an Arp2/3 independent context (Fig. 9B) (Etienne-Manneville, 2004; Mejillano et al., 2004; Nobes & Hall, 1995; Svitkina et al., 2003).

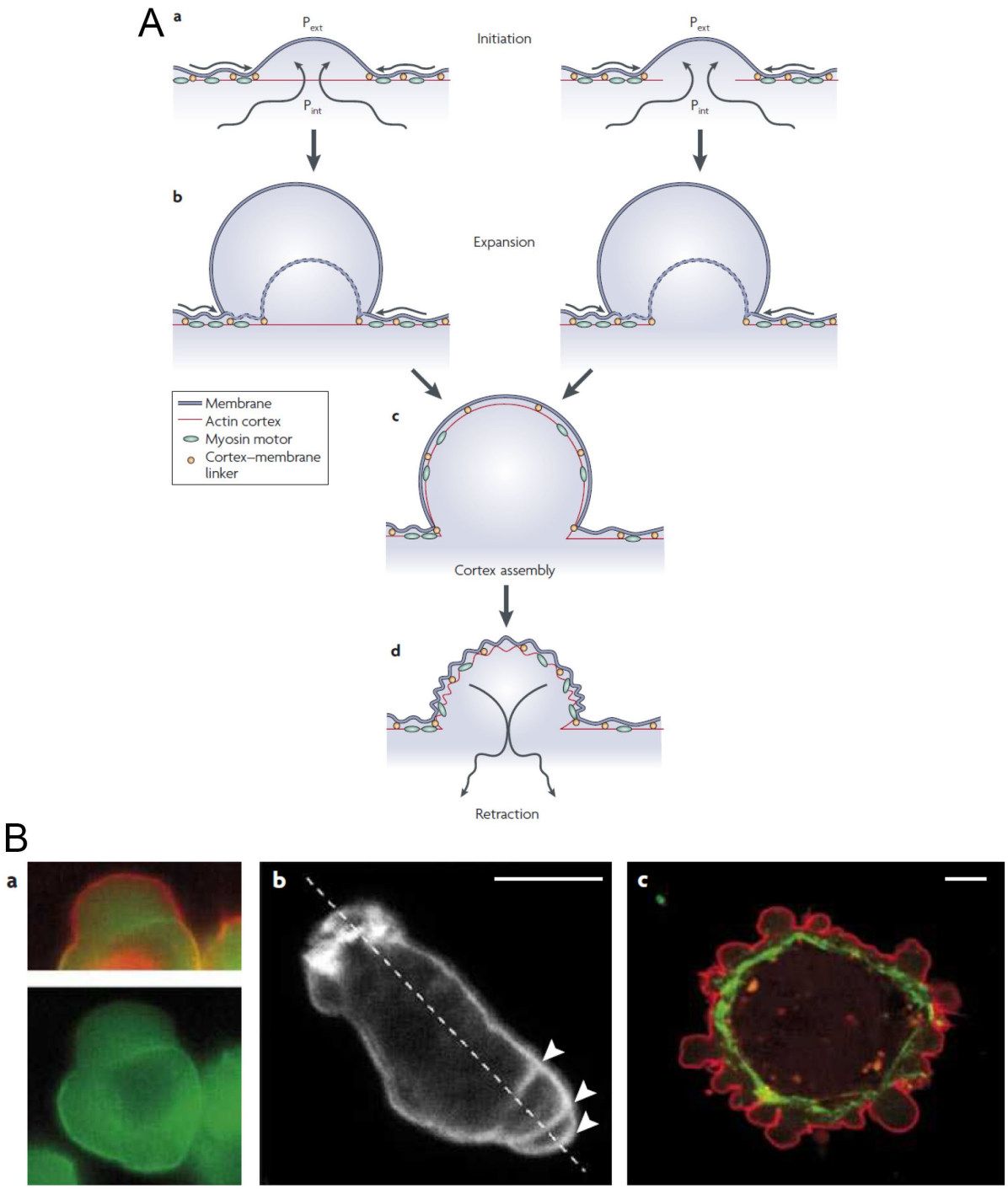

Figure 10. Bleb formation. Modified from Charras & Paluch, 2008. **A.** Schematic representation of bleb formation. Hydrostatic pressure in the bleb drives membrane extension after a break in the cortex or its local detachment from the membrane (a). Cytoplasmic fluid pushes on the free membrane, forming a spherical extension (b) in which a new cortex reassembles (c), stabilising the new shape and preventing collapse after pressure difference disappears (d). P_{int}: intracellular pressure, P_{ext}: extracellular pressure. **B**: Fluorescent images of blebbing cells. a: A bleb formed by a zebrafish primordial germ cell. Actin is labelled in green and membrane in red. Here, actin cortex is not broken and bleb must be a consequence of membrane detachment. b: Actin cortex of *Dictyostelium discoideum*. Arrowheads point to successive blebs that appeared on a previously formed bleb. c: Blebs formed by a Filamin-deficient melanoma cell. Myosin II is labelled in green and localise in puncta below the blebs. Membrane is labelled in red. Scale bars: 5 µm.

d. Blebs

First observed in Fundulus primordium germ cells (Trinkaus, 1973), blebs are spherical protrusions resulting from the loss of interaction between the cortex and the plasma membrane (Fig. 10). This can also happen upon detachment of the cortex from the membrane or directly by rupture of the cortex (Fig. 10A) (Charras & Paluch, 2008). Hence, blebs can be induced by breaking the cortex with a laser (Bergert et al., 2012). Break or detachment from the cortex frees the membrane that has no more resistance to internal cytoplasmic pressure and deforms like an inflated balloon, forming the bleb (Charras & Paluch, 2008; Diz-Muñoz et al., 2010, 2016). This pressure is essentially generated by osmotic pressure and contractility of the actomyosin cortex. For example, experimentally increasing cell contractility is sufficient to induce blebbing (Diz-Muñoz et al., 2010). After a short time, the cortex reassembles in the bleb, the shape of the membrane stabilises and new adhesions form (Charras & Paluch, 2008).

Some cells use blebs to migrate (Fig. 10B). For example, Dictyostelium migrate without ECM nor adhesion molecules simply by blebbing (Pajic-Lijakovic & Milivojevic, 2020). In some cases, blebs can play a role similar to lamellipodia, using newly formed adhesion to displace the cell body in a low-density 3D matrix. It is the case of germ cell precursors in the zebrafish embryo, known to rely solely on blebbing to migrate (Aalto et al., 2021; Yamada & Sixt, 2019).

e. Other types of migration

Some cells display very different modes of migration than those just described. In particular, amoeboid migration also relies on the actomyosin cortex but not on adhesion but rather on friction with their environment (Liu et al., 2015; Ruprecht et al., 2015). Cells adopt this mode of migration when they are confined and not excessively contractile. They then adopt a sausage-like morphology with the nucleus at the rear of the cell and actin cortex flowing from the front to the rear of the cell. This flow generates a friction force, transmitted to the ECM, that displaces the cell body (O'Neill et al., 2018). Interestingly, it appears that, at least some cells, can switch between these three actin-dependent modes of migration, depending on their level of confinement and contractility, so that a phase diagram predicting their behaviour can be built (Liu et al., 2015).

f. Cell orientation

In the three modes of migration I described, I always mentioned a front and a rear. Indeed, for a cell to move in a certain direction, it has to establish a polarity, extending at one side and retracting at the other. Describing directional migration basically boils down to "how to break symmetry and maintain polarity?" It is usually the result of the interaction of cells with their environment: they detect cues that bias their migratory behaviour through asymmetric distribution of proteins.

Polarity can spontaneously appear in migrating cells due to the feedback loops controlling activation of the small GTPases (Fig. 8C). Rac1 inhibits RhoA and reciprocally, which defines mutually exclusive front and back (Burridge & Wennerberg, 2004; Ory et al., 2000). However, this system is not particularly robust, notably due to the numerous negative regulators of actin branching (Chánez-Paredes et al., 2019; Dang et al., 2013; Henson et al., 2015). Hence, if migrating cells are on their own, they display a random motion that can be more or less persistent depending on how robust is their spontaneous polarisation. Usually, this spontaneous persistence is low, although some cell types like fish keratocytes are surprisingly persistent (Dang et al., 2013; Gorelik & Gautreau, 2014; Molinie et al., 2019; Okimura et al., 2018; Riaz et al., 2016). Hence, for a cell to display directional migration, it has to stabilise its polarity. This is usually performed by integrating external cues that bias the internal cell organisation (Fig. 11).

Perception of the environment is essentially done by receptors that change properties when they encounter a particular physical signal (Fig. 11A) (Ridley, 2003). For example, photoreceptors like opsins will react to light or chemoreceptors to a molecule by changing conformation, which elicits intracellular signalling, instructing the cell on its environment (Kojima & Fukada, 2007). There are a wide range of physical phenomena a cell detects and uses to orient its migration: light, gravity, mechanical stress, chemical concentration, electric field …

The external information has to be asymmetric to generate a polarisation in the cell and, since spontaneous cell persistence is usually low, the asymmetric external information has to be maintained over time and space. This means that cells have to detect gradients of particular properties to get a useful information of direction (Ridley, 2003; Shellard & Mayor, 2020). There are two main ways of creating a gradient in an embryo (Fig. 11A). It can be independently of migrating cells, like a concentration gradient where molecules are produced at a fixed source and degraded at a fixed sink different from migrating cells (Crick, 1970). Alternatively, gradients can be self-generated by migrating cells altering an originally uniform environment. For example, cells can act as a sink, locally degrading the molecules as they are moving (Tweedy et al., 2016). Although less well understood, this mode of migration presents the advantage of being very robust as it does not require the gradient to be pre-established. This could explain how cells travel long distances in the dynamic environment that is an embryo.

The fact that a cell migrates in a directional manner is called a taxum (the Greek for arrangement). For example, chemotaxis corresponds to the tendency for a cell to follow a gradient of chemicals. As research on cell migration goes by, more and more of these taxa were discovered, some being rather surprising (Shellard & Mayor, 2020). Cells can also integrate information coming from different sources, be it inside a taxum (e.g., different chemicals) or between them (e.g., detection of stiffness and chemicals), but how integration is made is poorly understood. I will now describe four among the most commonly studied taxa.

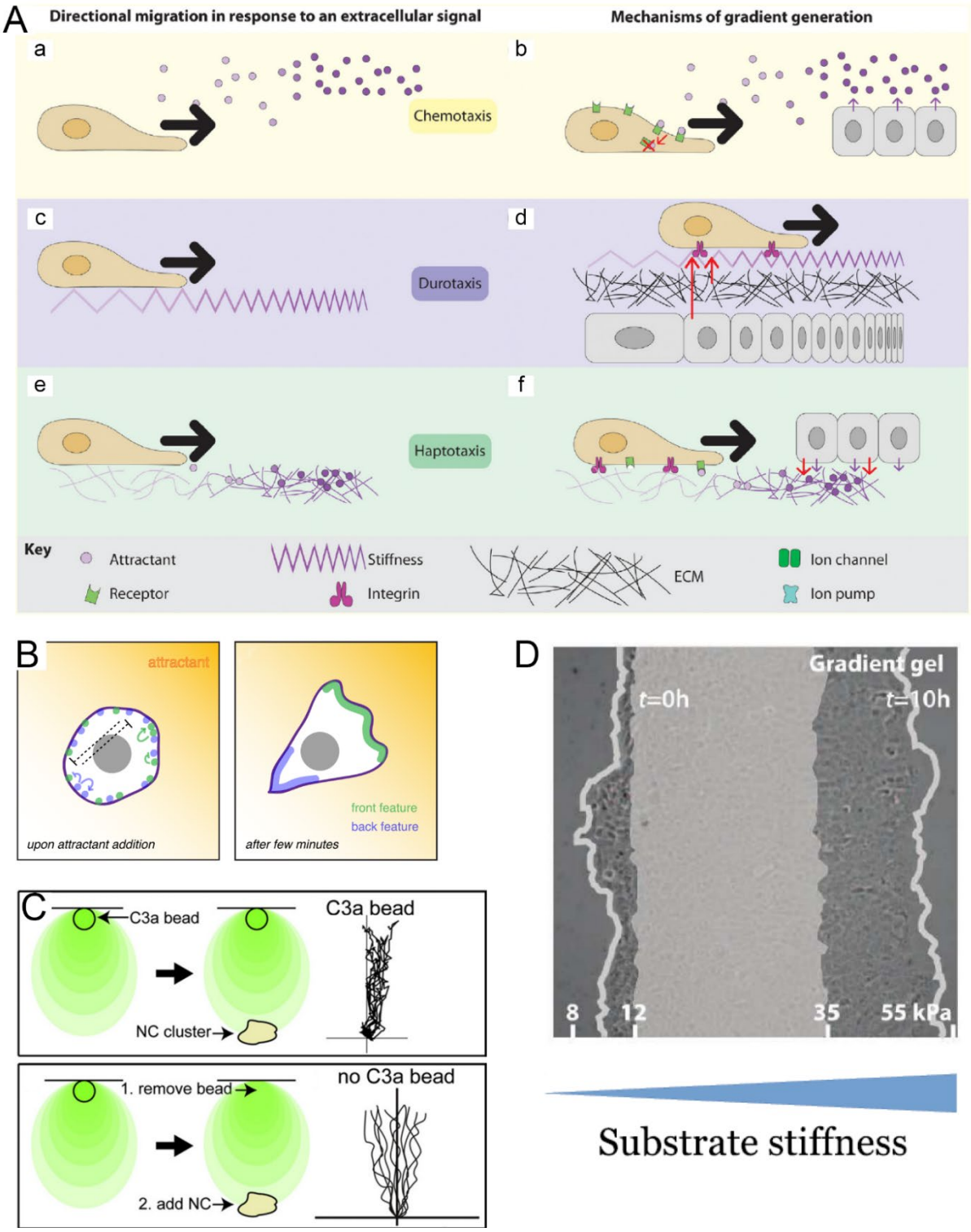

Figure 11. Cell guidance during migration. A: Main modes of cell migration guidance. Chemotaxis, durotaxis and haptotaxis respectively correspond to guidance by detection of a gradient of soluble molecules (a), substrate stiffness (c) or surface-bound molecules (e). These gradients can be pre-established (a, c & e) or self-generated (b, d & f) by the migrating cells. Modified from Shellard & Mayor, 2020. **B**: Establishment of cell polarity along a chemotactic gradient by redistribution of intracellular components. Modified from Rørth, 2011. **C**: Demonstration of hapotactic guidance. A bead soaked with C3a attracts neural crest (NC) cells, which could be considered as chemotaxis. However, even after removing the source of C3a, NC cells are still attracted, suggesting that C3a actually binds to the Fibronectin substrate and that the gradient is conserved even in absence of the source, which are hallmarks of haptotaxis. Modified from Carmona-Fontaine et al., 2011. **D**: Epithelial cells seeded on a substrate presenting a gradient of stiffness migrate preferentially toward higher values of stiffness, which is the definition of durotaxis. Light gray band indicate initial distribution of cells before migration. Modified from Camley, 2018.

i. Chemotaxis

Chemotaxis is the process by which a cell detects diffusible chemicals and uses a gradient of concentration to orient its migration (Fig. 11A & B). The cell detects more molecules at one side of its membrane than at the opposite, which constitutes a directional information. Even shallow gradients can be detected as once receptors are locally activated, more receptors get recruited, which amplifies the asymmetry (Fig. 11B). Thus, some cells can sense concentration differences of 1% along their membrane (Schneider & Haugh, 2006; Tweedy et al., 2016). Microfluidics approaches can be used to precisely establish gradients and study how cells respond to them (Samandari et al., 2021). Chemotaxis is for example used by cells during wound healing: destroyed cells secrete ATP and formylated peptides in the extracellular medium which act as chemoattractants for lymphocyte and neighbouring cells (Honda et al., 2001; Kehrl, 2006; Myrtek & Idzko, 2007).

In order to detect soluble molecules, a cell has to express receptors, which usually are transmembrane proteins that bind to the ligand in the extracellular space and elicit downstream signalling in the cytosol. Several kinds of receptors exist which share some common features. G protein-coupled receptors (GPCR) are a family of receptors that contain seven transmembrane sites corresponding each to an alpha helix (Cotton & Claing, 2009; Weis & Kobilka, 2014). GPCR are associated to three small GTPases. Upon ligand binding, a GPCR changes conformation and acts as a GEF that activates the αGTPase. This small GTPase then unbinds from β and γGTPases and affects cellular signalling (Weis & Kobilka, 2014). Despite presenting a large diversity of ligands, all GPCR can contribute to reorganising the cytoskeleton (Cotton & Claing, 2009). Receptor tyrosine kinases (RTK) are single transmembrane proteins that dimerise in the presence of a ligand, phosphorylating the other monomer, which activates the receptor and triggers intracellular response (Fig. 12) (Lemmon & Schlessinger, 2010). FGFR family of receptors are an example of RTK that can be involved in cell migration (Fig. 12A) (Turner & Grose, 2010). For instance, FGF3 and FGF10 act as chemoattractants during the migration of the posterior lateral line primordium of the Zebrafish (Breau et al., 2012). PDGF is also a ligand involved in chemotaxis (Fig. 12B). It is for example able to attract neutrophils in culture (Deuel et al., 1982). It binds to the PDGF receptor that activates the small GTPase Ras and PI3K (Klaus Okkenhaug, 2013; Tallquist & Kazlauskas, 2004). The signal is then amplified and modulated as branching of actin contributes to recruitment of RacGEF as well as translocation of PI3K on the one hand, and accumulation of the inhibitor PTEN on the other hand, triggering respectively a positive and a negative feedback loop (Sasaki et al., 2007; Sasaki & Firtel, 2006).

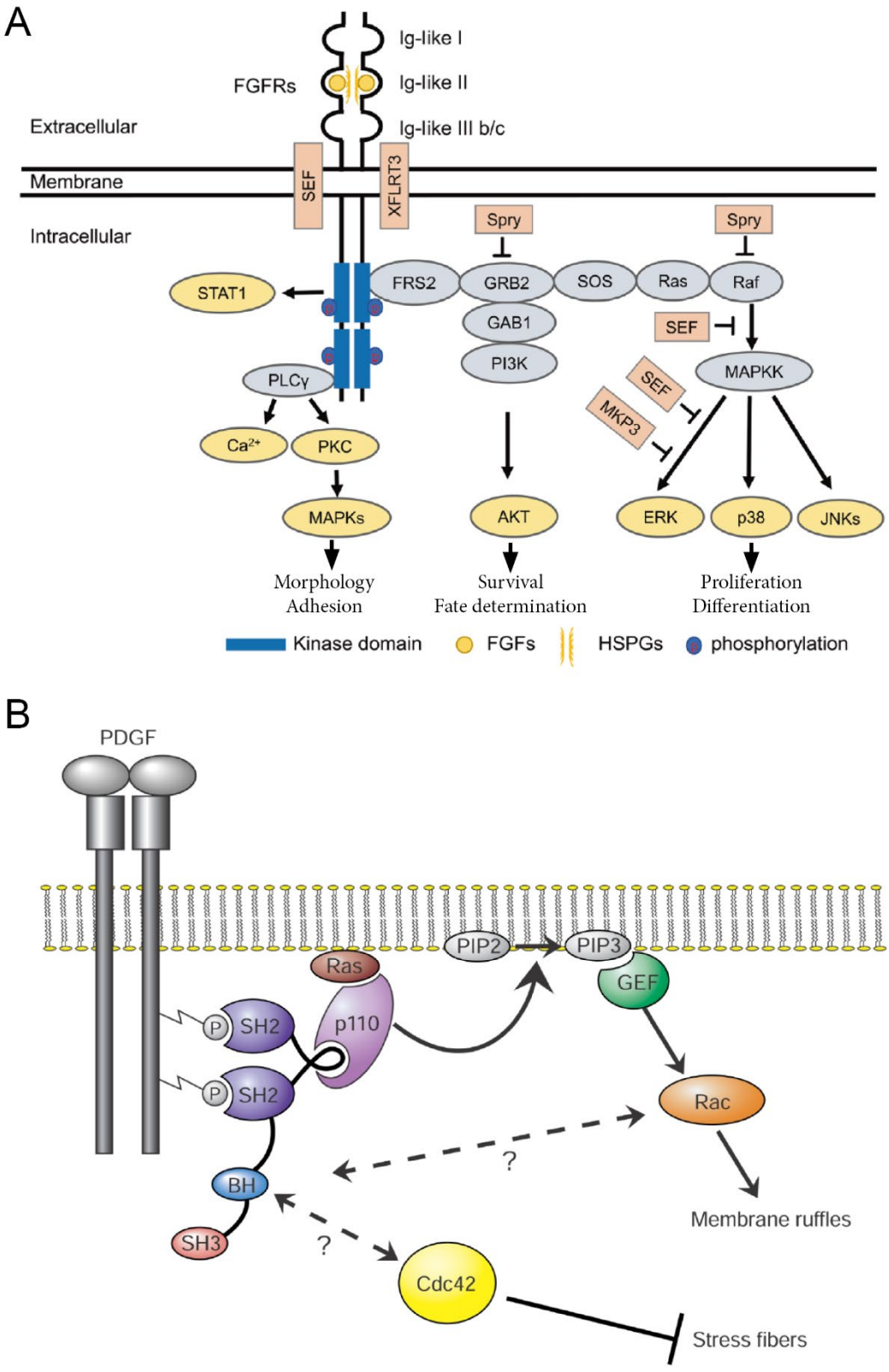

Figure 12. Receptor tyrosine kinase (RTK). A: Fibroblast growth factor (FGF) signalling. FGF receptors are homodimers that dimerise upon ligand binding and autophosphorylate, recruiting downstream effectors. This signalling pathway is in particular involved in cell migration and differentiation. Modified from Xie et al., 2020. **B**: Platelet-derived growth factor (PDGF) signalling. Similar to FGF receptors, PDFG receptors dimerise and autophosphorylate. They signal upstream of Rho GTPases and are mainly involved in cell migration. Modified from Okkenhaug & Vanhaesebroeck, 2001.

ii. Haptotaxis

Haptotaxis is conceptually close to chemotaxis but instead of detecting soluble, diffusible molecules, cells detect adhesion sites or surface bound molecules, like ECM constituents or chemicals bound to the ECM (Fig. 11A & C). Gradients of surface-bound molecules can be established like regular chemotactic gradients, molecules diffusing from a source and immobilising on the ECM (Fig. 11C). This is for example the case of CCL21 gradient produced from lymphatic endothelial cells in vivo (Weber et al., 2013), or CXCL8 gradients that guide neutrophils in zebrafish (Sarris et al., 2012). Alternatively, oriented distribution of ECM components can be detected by cells as a haptotactic cue for migration. Hence, mesodermal cells from the amphibian Ambystoma maculatum seeded on oriented fibronectin fibres display oriented migration, following these fibres (Nakatsuji & Johnson, 1983). It has been proposed that migration of the mesoderm on the blastocoel roof during amphibian gastrulation is guided by such oriented fibres of fibronectin secreted by the ectoderm (Rozario et al., 2009; Winklbauer & Keller, 1996).

iii. Durotaxis

Durotaxis is defined as orientation of cells along a gradient of stiffness (Fig. 11A & D). It has been observed that cells plated on gels presenting parts of different stiffness have a tendency to move toward the higher substrate stiffness (Fig. 11D) (DuChez et al., 2019; Isenberg et al., 2009). Variation of stiffness of a substrate can be a consequence of a change in density or nature of the constituent, or density of underlying cells (Barriga et al., 2018; DuChez et al., 2019; Isenberg et al., 2009). Cells bound to a substrate apply forces of a few nN/µm² due to their cortical contractility (Doss et al., 2020; Plotnikov et al., 2014; Schwarz & Soiné, 2015). If the ECM is too soft, it is deformed by the cell which is less able to use the pulling force to displace itself. It is conversely easier to migrate on stiffer, more resistive substrates. Hence, cells spontaneously direct their migration toward stiffer areas (Higgs, 2000; Lo et al., 2000). Furthermore, substrate stiffness can be detected by cells through focal adhesions mechanotransduction. FA adapt their morphology and composition to the substrate cells are adhering to and, via interactions with cortical actin dynamics, affect cell migration. Accordingly, the shape of cells plated on substrates of different stiffness changes dramatically (Martino et al., 2018; Yeh et al., 2017). Interestingly, it has very recently been proposed that there is an optimal stiffness for cell migration, leading sometimes to negative durotaxis (Isomursu et al., 2020).

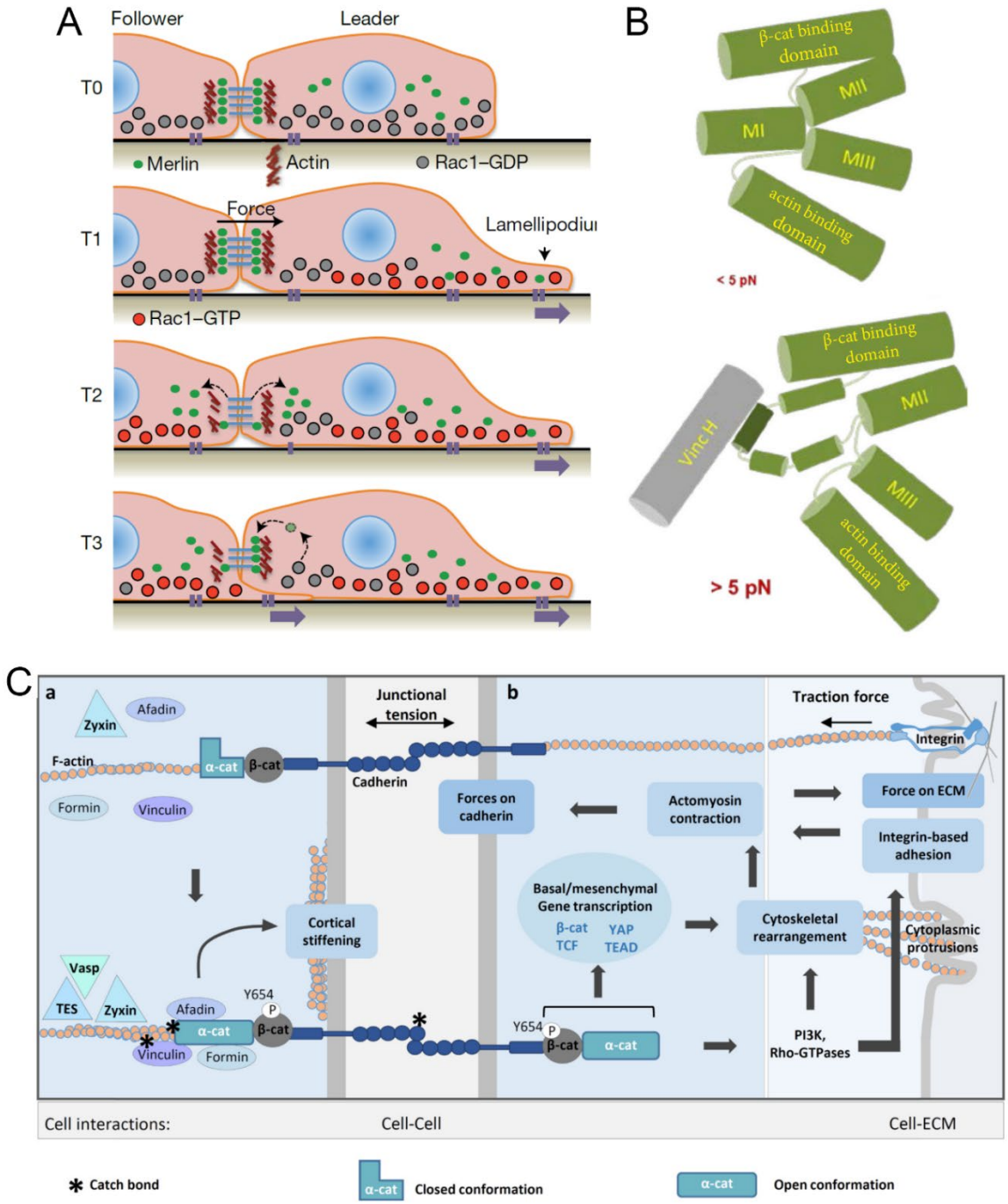

Figure 13. Adherens junction mechanotransduction. A: Merlin regulates protrusive activity in epithelial tissues. In a static monolayer, merlin localises to cell-cell contact and inhibits Rac1 activity (T0). If a cell starts moving and Rac1 activity gets polarised at one edge, it pulls on the cell immediately behind (T1). This pulling force delocalises merlin from the cortex of the follower cell (T2), triggering Rac1 activation and lamellipodium formation (T3) and thus enabling this cell to follow its moving neighbour. In addition, inactive Rac1 at the rear end of the leader cell stabilises junctional localisation of merlin (T3). Modified from Das et al., 2015. **B**: Conformation change of α-Catenin. The protein has a compact structure formed of a dimerisation and β-Catenin binding domain, three modulation domains (MI to MIII) and an actin-binding domain. The MI domain is the Vinculin Binding Domain (VDB) which, at rest, is maintained in a closed conformation by the MII and MIII auto-inhibitory domains. Upon application of forces larger than 5 pN, interactions between modulation domains are lost, which reveals the Vinculin binding site (dark green) allowing Vinculin (VincH) recruitment. Modified from Ladoux et al., 2015. **C**: Application of forces at the level of adherens junction triggers several cellular reactions. Opening of α-Catenin recruits Vinculin and other proteins that contribute to cortex rearrangement, like actin filament bundling or increased contractility. Pulling forces also activate catch bonds that strengthen the link between Cadherin doublets, and between actin and α-Catenin or Vinculin. Finally, recruitment of β-Catenin has consequences in terms of gene expression as it depletes the pool that can be used by Wnt/β-Catenin pathway. Modified from Khalil & de Rooij, 2019.

iv. Plithotaxis

While cells are able to feel the stiffness of their substrate through FA, they also experience forces exerted by neighbouring cells via their AJ. Indeed, Cadherins are able to transmit mechanical stress from one cell to another, which enable cells to react to their environment, for example in stretched epithelia (Charras & Yap, 2018). These mechanical forces can be used by cells as an orienting cue for their migration. It was in particular observed that cells in crowded environments align their movement with the axis of minimal shear stress, which is described as plithotaxis (Tambe et al., 2011).

v. Mechanical perception of the environment

The idea that cells interact with their mechanical environment in processes like morphogenesis and differentiation is rather old (D'Arcy, 1917; Trinkaus, 1970; Turing, 1952). However, due to a lack of tools to interact with cell mechanics, researchers focused for a long time on chemical signals. I already presented several instances of how chemical perception directs migration, I now would like to detail how cells perceive mechanical signals (Fig. 13). In the past two decades, many proteins involved in such perception have been identified. They perform mechanotransduction, which is the transformation of a mechanical signal in a chemical one, readable by the cell (Martino et al., 2018). For example, sensation of touch depends for a part on Piezo, an ion channels that open under tension, triggering a neuronal response in response to a contact (Dance, 2020).

Mechanical perception is involved in many developmental processes. For instance, the Hippo pathway detects cell crowding and regulates cell proliferation accordingly, which controls organ size (Zhao et al., 2011). It has recently been shown that Merlin, a mechanosensor belonging to the Hippo pathway can instruct cell migration (Fig. 13A) (Das et al., 2015). At rest, it is located at the membrane, inhibiting Rac1. However, upon application of a local tension, Merlin relocates to the nucleus, relieving inhibition at the membrane which induces lamellipodia formation. Adherens junctions are also known to be mechanosensitive and involved in local force detection (Das et al., 2015; Khalil & de Rooij, 2019; Lenne et al., 2021). When two cells are bound by an AJ, each cadherin-catenin complex experiences a direct tension of 2 to 3 pN that can increase of 1 to 2 pN when under tension (Herbomel et al., 2017; Mège & Ishiyama, 2017; Yao et al., 2014). Perception of such tensions is done locally at the level of cell-cell contacts. The most studied mechanotransduction pathway involves Vinculin. This protein, also involved in the mechanosensory response of FA, can bind to the vinculin binding domain (VBD) of α-Catenin (Fig. 13B, C) (Han et al., 2016; Mège & Ishiyama, 2017; Twiss et al., 2012). At rest, this domain is hidden by the neighbouring domains MII and MIII of α-Catenin that fold over the VBD (Fig. 13B). However, when the CCC is put under a load of 5 pN, for example due to cortical myosin activity or pulling forces applied on a tissue, α-Catenin switches conformation and unfolds, revealing the VBD and increasing 1000-fold vinculin affinity (Choi et al., 2012; Han et al., 2016; Mège & Ishiyama, 2017;

Twiss et al., 2012). Vinculin binds to actin, strengthening AJ linkage to the cortex (Fig. 13C) (Bays & DeMali, 2017; Merkel et al., 2019). It can also bundle actin filaments and recruit proteins that reorganise the cytoskeleton like Mena/VASP (Nowotarski & Peifer, 2014; Reinhard et al., 1996) or, in a less certain fashion, Arp2/3 (personal discussion with A. Gautreau). Mutation of this VBD domain in gastrulating zebrafish embryos led to convergence defects and slower migration of lateral mesodermal cells (Han et al., 2016). Beside α-Catenin and Vinculin, other proteins recruited at the level of AJ are involved in mechanotransduction. For example, pulling on Xenopus prechordal plate cells with a small bead coated with cadherin induces local recruitment of Plakoglobin at contact site, in turn recruiting keratin intermediate filaments (Weber et al., 2012). Through an unknown mechanism, this leads to protrusion orientation away from the pulling force.

g. Crosstalk between cell migration and other developmental processes

As a final note on cellular perception of the environment, I would like to mention the fact that several signals acting as migration guidance cues are also involved in other developmental processes. The most common examples are linked to chemoperception. For instance, the Wnt family of ligands binds to the Frizzled family of GPCR (Gao, 2012; Komiya & Habas, 2008). Some Wnt/Fz couples elicit a planar cell polarity response, instructing a cell on its polarity in the plane of a tissue (Gao, 2012). Conversely, other Wnt/Fz couples elicit a canonical signalling, triggering relocation of β-Catenin to the nucleus and activation of target genes controlling cell specification (Komiya & Habas, 2008). Similarly, FGF/FGFR couples can drive migration or specify populations of cells, depending on ligands, receptors and even cell types (Amaya et al., 1993; Breau et al., 2012; Dorey & Amaya, 2010; Lee, 2005). More recently, it has been shown that substrate stiffness can also influence cell differentiation as stem cells cultured in an identical medium adopt different fates depending on the stiffness of their substrate (Engler et al., 2006; Lv et al., 2015; Park et al., 2011; Smith et al., 2017). It is remarkable to observe that these cells differentiate in cells belonging to tissues whose stiffness is close to their substrate, like osteoblasts for the stiffer substrate and neurons for the softer (Engler et al., 2006). Finally, it has recently been shown that persistence of cell migration is linked to cell cycle length (Molinie et al., 2019). The branched actin network actually integrates chemical and mechanical signals perceived by the cell and Arp2/3 activity is required for the cell cycle of some cell types. However, the mechanism by which branched actin controls the cell cycle is still obscure.

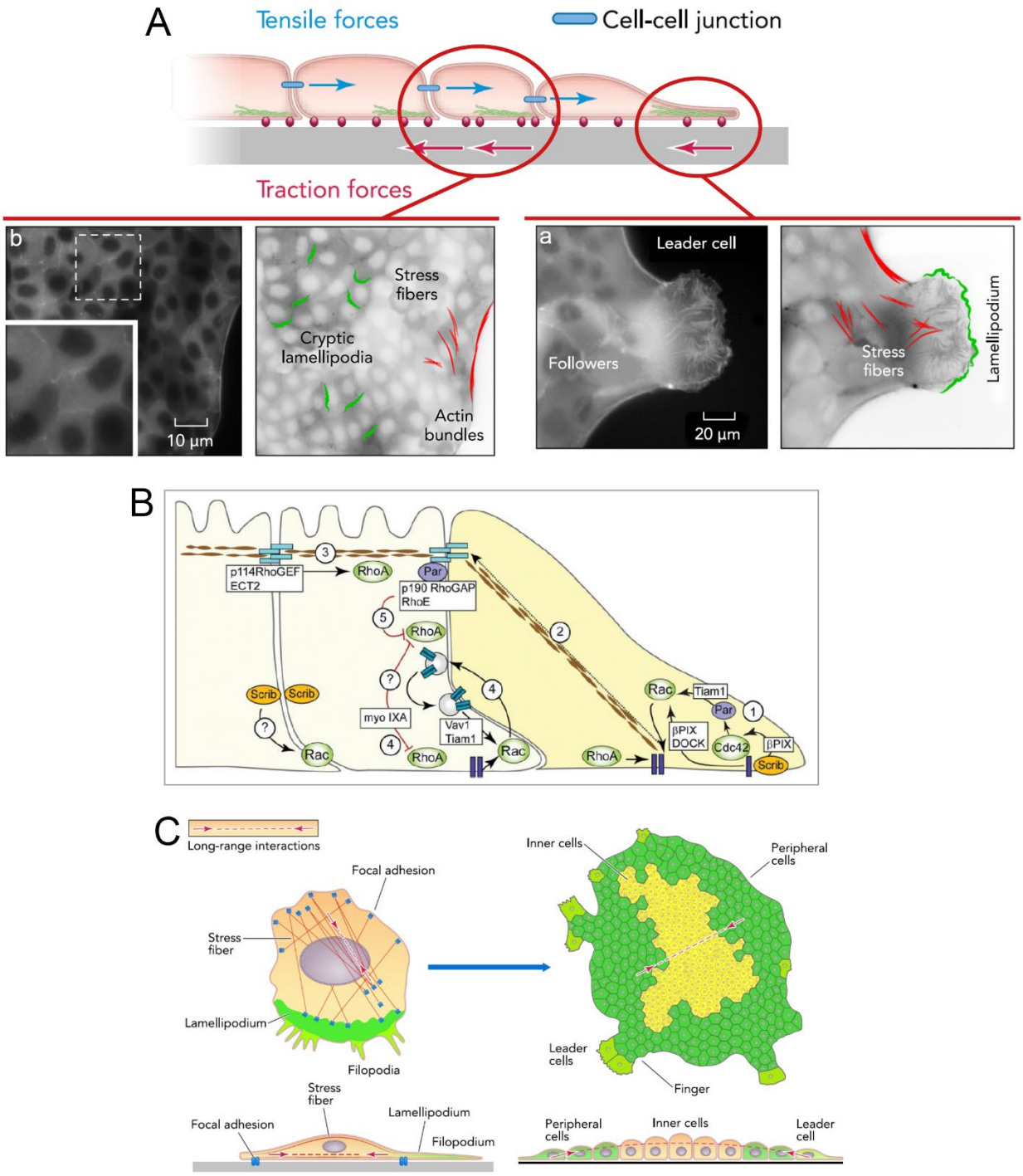

Figure 14. ***In vitro*** **collective cell migration. A**. Cell organisation during epithelial collective migration. At the leading edge, some cells become leader. They adopt a pseudo-mesenchymal morphology, forming large lamellipodia (in green) and dragging follower cells, forming finger like structures. Cells at the leading edge that are not leader cells form long supracellular actomyosin cables (in red) that coordinate cell movement, prevent formation of large lamellipodia and ensure regular spacing of leader cells (a). Concomitantly, follower cells form small, cryptic lamellipodia as well as stress fibres, also contributing to applying traction forces on the substrate and displacing the group of cells (b). Modified from Vedula et al., 2013. **B**: Signalling pathways involved in regulating actin dynamics in leader and follower cells during epithelial collective migration. 1: Rac1 activation at the front promotes protrusion formation. 2: Cells are mechanically coupled through actomyosin cables and apical junctional complexes. 3: Apical contractility is ensured by RohA. 4: Rac1 activation at the leading edge of follower cells maintained by a feedback loop leading to cryptic lamellipodia formation. 5: Rac1 and adherens junction complex inhibit RhoA at the leading edge. Modified from Zegers & Friedl, 2014. **C**: Comparison of single cell and collective migrations. In both cases, interactions between front and rear elements ensure polarisation of the migrating structure and efficient movement. In the case of single cells, front is connected to the rear through stress fibres while supracellular actin cables ensure this function in cell collectives. Modified from Vedula et al., 2013.

3. Collective cell migration

In many cases, cells will not migrate as individuals but as a group. Morphogenesis but also physiological and pathological processes, like wound healing and cancer metastasis, rely on such kind of migrations. Collective cell migration can be defined as the cooperative motion of a group of cells, an emergent property by which a group organises its migration when individual cells are unable to do so. This coordinated motion emerges from chemical, physical and/or mechanical interactions between the cells. This often implies division of labour among the group with the frequent presence of specialised cells, like leader cells. The emerging behaviour resulting from cell interactions, as well as the complex interplay of mechanical and chemical signals that ensure collectiveness, require multidisciplinary approach to study collective cell migration.

a. Epithelial cell migration

i. In vitro

As for single cell migration, most of our knowledge on collective cell migration comes from in vitro studies, mostly on mammalian epithelial cell cultures. Such cells form large epithelial monolayers that set into motion when they encounter free space, which is experimentally done by scratching the monolayer or removing a stencil that obstructed the migration path (Fig. 14) (Poujade et al., 2007; Rørth, 2009; Vedula et al., 2013). Cells lining the free space then change morphology, some of them acquiring the role of leader cells (Fig. 14A & B). Apparition of such cells relies on the Notch lateral inhibition pathway as well as on mechanical and topological cues (Khalil & de Rooij, 2019; Riahi et al., 2015). These cells acquire a pseudomesenchymal morphology, forming large lamellipodia, pulling on their neighbours, which sometimes forms multicellular finger-like structures (Fig. 14A) (Khalil & de Rooij, 2019; Vedula et al., 2013; Vishwakarma et al., 2020b). They are coupled to followers by supracellular structures, like actin cables spanning several cells, connected at the level of adherens junction (Fig. 14A & C). Such cables ensure mechanical integrity of the tissue and prevent follower cells from forming large protrusions and becoming leaders (Vishwakarma et al., 2020b). Migration of front cells pulls on follower cells and locally decreases cell density. This activates migration in follower cells, which in turn form small, cryptic lamellipodia (Fig. 14A & B) (Trepat et al., 2009; Zegers & Friedl, 2014). Movement of these followers is thus a mix of passive pulling and active cell migration. Through this specialization with a motile front and long-range interactions with followers, the whole group behaves like a supra-cell (Vedula et al., 2013), even if behaviour away from the front is often less organised (Fig. 14C).

These models of in vitro collective cell migration are of invaluable usefulness as they are great tools to test many situations, geometries, genetic alterations, but also to measure mechanical forces, chemical reactions and so on. They are also relevant to describe some physiological phenomena, like invasive carcinomas (epithelial cancers), that invade free space with leader cells at the tip of invading

strands or recruiting so-called cancer-associated fibroblasts, non-transformed cells that will play the role of leaders (Calvo et al., 2013; Erdogan et al., 2017; Friedl & Gilmour, 2009; Rørth, 2009). However, 2D cultured models are very simplified compared to physiological instances of collective cell migration. It is possible to increase complexity of in vitro substrates, for example by seeding cells on a 3D matrigel, recapitulating more features of an in vivo substrate (Anguiano et al., 2020). However, it is still not possible to reach the complexity of physiological environments. In an organism, migrating cells are surrounded by a complex mesh of ECM and cells, and receive many diffusible signals. All of these might influence cell migration. The way cells coordinate their motion in vivo is often complicated and surprising. There are, however, a few typical organisations that lead to collectiveness. I will thus present two instances of epithelial collective migration in developing embryos to illustrate my point.

ii. Primordium of the posterior lateral line

The posterior lateral line primordium (PLLp) of the Zebrafish is a 150 µm long heterogeneous group of epithelial cells that migrate from the head to the tail following the axis of the body, just under the skin, between 22 and 48 hpf (Fig. 15) (Aman & Piotrowski, 2010; Rørth, 2009; Scarpa & Mayor, 2016). It is followed by axons and deposits rosettes of cells along its migration path (Fig. 15A). Rosettes will differentiate into neuromasts, which, together with the axons, will later constitute the lateral line of the fish, a sensory organ. The primordium is regionalised along the AP axis by different levels of FGF and Wnt signalling (Fig. 15B) (Aman & Piotrowski, 2010; Knutsdottir et al., 2017). Cells at the rear are compact and have a barely motile morphology, forming local rosettes and lumens that will be deposited at regular intervals. They express FGF, which is essential to maintain their epithelial identity (Lecaudey et al., 2008; Neelathi et al., 2018). Cells at the front express Wnt signalling, display a protrusive behaviour and a less rigid organisation (Chitnis et al., 2012). Wnt signalling and FGF signalling are mutually exclusive, which creates a boundary between the leading zone and the trailing zone.

Sdf1, also called CXCL12, is a chemokine expressed by cells forming a trail that runs along the path that the primordium follows during its migration (Fig. 15A & C) (David et al., 2002; Haas & Gilmour, 2006). PLLp cells, especially in the leading zone, express CXCR4, a receptor for Sdf1 (Fig. 15B). This receptor is required for PLLp migration as CXCR4 loss of function leads to immobilisation of the tissue, suggesting that Sdf1 is the guidance cue for PLLp migration (David et al., 2002; Haas & Gilmour, 2006; Valentin et al., 2007). However, surprisingly, the trail of Sdf1 is homogeneous and no pre-patterned gradient is observable (Fig. 15A & C) (David et al., 2002; Haas & Gilmour, 2006; Venkiteswaran et al., 2013).

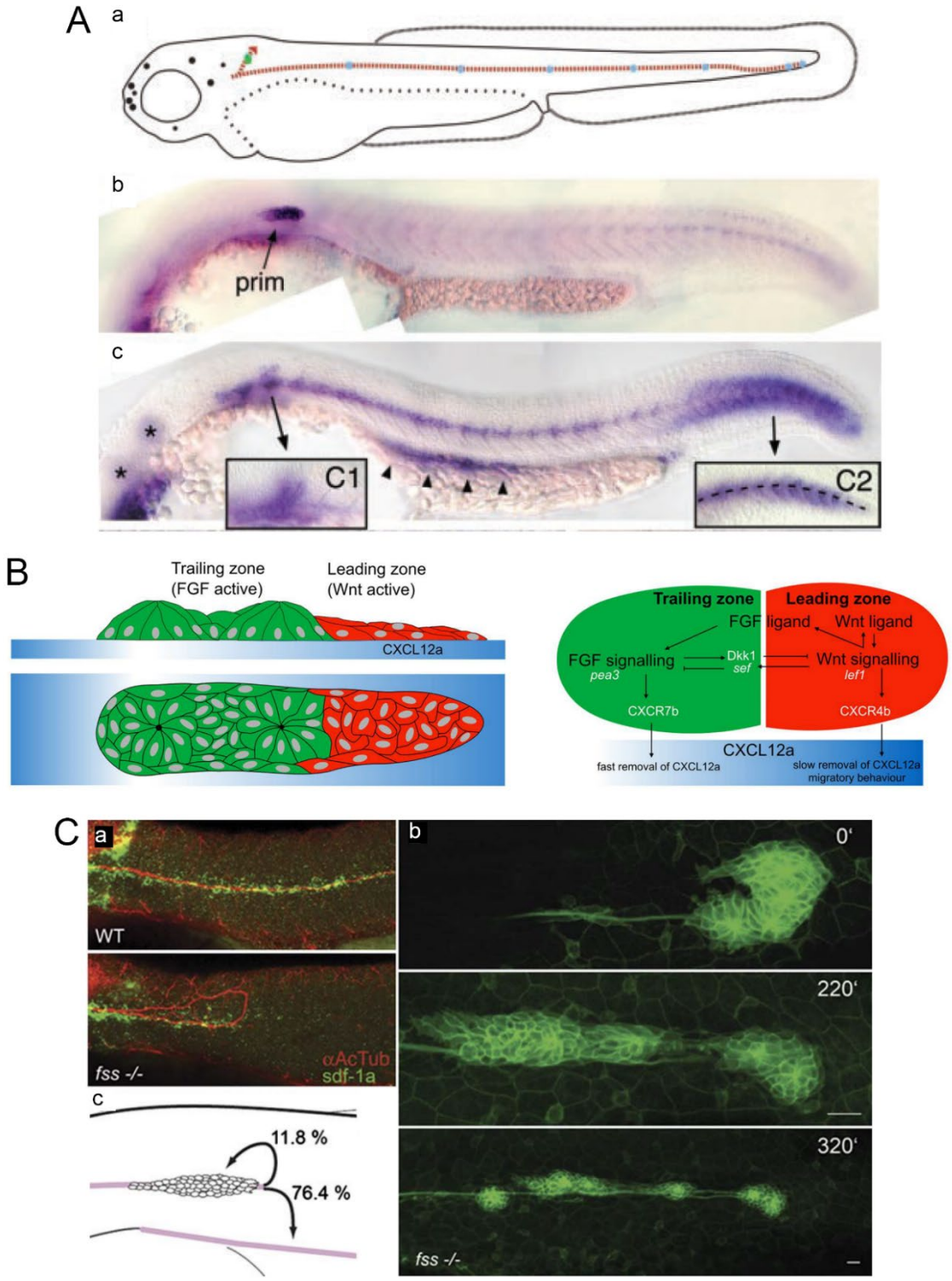

Figure 15. Migration of the posterior lateral line primordium (PLLp). A: Migration of the PLLp. a: The primordium migrate from the back of the head to the tip of the tail (red dashed line), laying neuromasts at regular intervals (blue dots). b: The primordium can be visualised by *in situ* hybridisation of *cxcr4* expression. prim: PLLp. c: *in-situ* hybridisation reveals that *sdf1* is expressed all along the migration trail. Modified from David et al., 2002. **B**: Genetic and cellular organisation of the PLLp. Cells at the leading edge are exposed to Wnt signalling and adopt a motile morphology while expressing of *cxcr4.* Cells at the rear are exposed to FGF signalling, mutually exclusive with Wnt, and adopt epithelial morphology, forming rosettes with micro lumens and expressing *cxcr7*. Cells at the rear locally remove Sdf1 *via* CXCR7 receptors, creating a dynamic Sdf1 gradient that is detected by front cells through CXCR4, leading to directional migration. Modified from Knutsdottir et al., 2017. **C**: Interruption of Sdf1 trail provokes PLLp U-turn. a: Sdf1 protein, labelled in green, normally forms a homogeneous track, which is interrupted in the $fss^{-/-}$ mutant. b, c: when encountering a gap in the trail, the PLLp stalls and sometime undergo a U-turn as a new, rearward-oriented gradient is formed by *cxcr7* expressing cells. Modified from Haas & Gilmour, 2006.

It appears that the PLLp expresses another Sdf1 receptor, CXCR7, but only in the trailing zone, at the rear (Fig. 15B). This receptor seems important for PLLp migration as loss of function also leads to immobilisation (Burns et al., 2006; Valentin et al., 2007). This was surprising as this CXCR7 receptor is not known to elicit chemotactic signalling. It rather appears that CXCR7 acts as a sink, contributing to endocytosis and degradation of Sdf1 upon binding (Boldajipour et al., 2008; Donà et al., 2013; Venkiteswaran et al., 2013). This creates a chemical gradient, Sdf1 concentration in the ECM being lower at the rear than at the front of the PLLp (Fig. 15B). This gradient is detected by leading cells, which then orient their migration and drag the whole tissue.

In this model, individual cells are unable to orient their migration as there is no gradient to follow. Even a small group of cells expressing only CXCR4 would not be able to orient its migration (Valentin et al., 2007). However, from collectiveness emerges directionality through the generation of a self-sustained gradient. Hence, surprisingly, if the trail of Sdf1 is interrupted, the leading zone of the PLLp explores the free space around and sometimes perform a U-turn and follow the track of Sdf1 in the other direction (Fig. 15C) (Haas & Gilmour, 2006). This shows that a self-generated gradient, guaranteed by the intrinsic polarity of the moving group, ensures the robustness of the system.

iii. Border cells

Border cells constitute a small cluster of about 8 cells that migrate in the Drosophila ovary during oogenesis, surrounding and carrying two polar cells (Fig. 16) (Aman & Piotrowski, 2010; Bianco et al., 2007; Rørth, 2009; Scarpa & Mayor, 2016). The ovary is composed of several egg chambers like beads on a string, each representing a stage of oogenesis. The egg chamber is polarised: at the proximal end are located nurse cells and at the distal end, the maturing oocyte (Fig. 16A) (Duhart et al., 2017). During maturation, polar and border cells delaminate from the surrounding follicular epithelium at the proximal end and cross the egg chamber toward the oocyte (Fig. 16A & B). Polar cells are non-motile, but they are surrounded by the border cells, which form long cellular extensions. Contrary to PLLp, border cells organisation is closer to a mesenchyme. Cells are looser and display frequent neighbour exchanges and rotations (Fig. 16B) (Cliffe et al., 2017; Veeman & McDonald, 2016). However, the cluster stays cohesive throughout its migration and adhesion between cells through AJ, and in particular E-Cadherin, is required for proper border cell migration and polar cell transportation (Niewiadomska et al., 1999). Migration of border cells has extensively been studied thanks to the powerful genetic tools that have been developed in Drosophila. It is thus one of the better understood models of collective cell migration.

Border cell protrusions are triggered by secretion of the Upd cytokine from polar cells, a short-range signal that activates the JAK/STAT pathway (Silver et al., 2005; Silver & Montell, 2001). Two other juxtacrine signalling pathways, Notch and Wnt/Planar cell polarity (PCP), are also required for acquisition of normal protrusion behaviour (Bastock & Strutt, 2007; Prasad & Montell, 2007). Hence,

if a border cell leaves the group, it should lose its protrusive activity. Guidance of this group of cells is ensured by chemotaxis, up a gradient of Pvf1 and EGF-family ligands (Spitz, Keren and Grk) that are secreted at the distal end by the oocyte (Fig. 16C). These chemokines are detected by border cells via the partially redundant Pvf1 receptor (PVR) and EGFR, belonging to the receptor tyrosine kinase (RTK) family (Duchek et al., 2001; McDonald et al., 2003, 2006).

At the level of individual cells, leading and trailing edges are exposed to differences of chemokine concentration in the gradient (Fig. 16C). Similarly, at the scale of the cluster, cells are also subjected to different concentrations of chemoattractant depending on their position in the cluster. Two different, but not mutually exclusive, mechanisms by which the cluster orients its migration have been proposed (Bianco et al., 2007; Rørth, 2007). The first mechanism is based on the observation that each cell is prone to form protrusions in response to chemokines. All cells receive an asymmetric signal but cells closest to the source of PVF and EGF detect more contrasted signal given their position. Hence, they activate Rac1 more stably in their protrusions than the other cells, thus driving cluster migration (Bianco et al., 2007; Rørth, 2007). In this model, cells respond individually, independent from each other and migrate toward the highest level of chemoattractant concentration. However, it appears that preventing Rac1 activation in front cells or disrupting cell-cell adhesion by removing E-Cadherin leads to increased protrusiveness in follower cells (Bianco et al., 2007; Cai et al., 2014; Inaki et al., 2012; Wang et al., 2010). This suggests that some cells become leader and inhibit followers. Notably, accumulation of myosin at the level of AJ between border cells contributes to inhibition of follower cells and definition of leaders, suggesting that inhibition relies on a mechanical signal (Cai et al., 2014). These observations led to the proposition of a second model, where border cell migration is actually described as a collective process. The one or two cells with the highest PVF and EGF signalling activate Rac1 at their leading edge, and inhibit protrusiveness in follower cells through mechanical signals, thus coordinating cluster migration (Bianco et al., 2007; Cai et al., 2014; Inaki et al., 2012; Wang et al., 2010).

In actually appear that, despite being inhibited by leader cells, followers still form small extensions that also contribute to the displacement of the cluster (Cai et al., 2016). This suggests that both models are actually correct and leader cooperate with followers for proper migration. Indeed, protrusions of follower cells are responsible for rotation of the group, changing the cells exposed to the highest chemokine concentration and thus defining new leaders. This mechanism has been proposed as a way to prevent chemical desensitisation in leader cells, ensuring long-range migration (Malet-Engra et al., 2015).

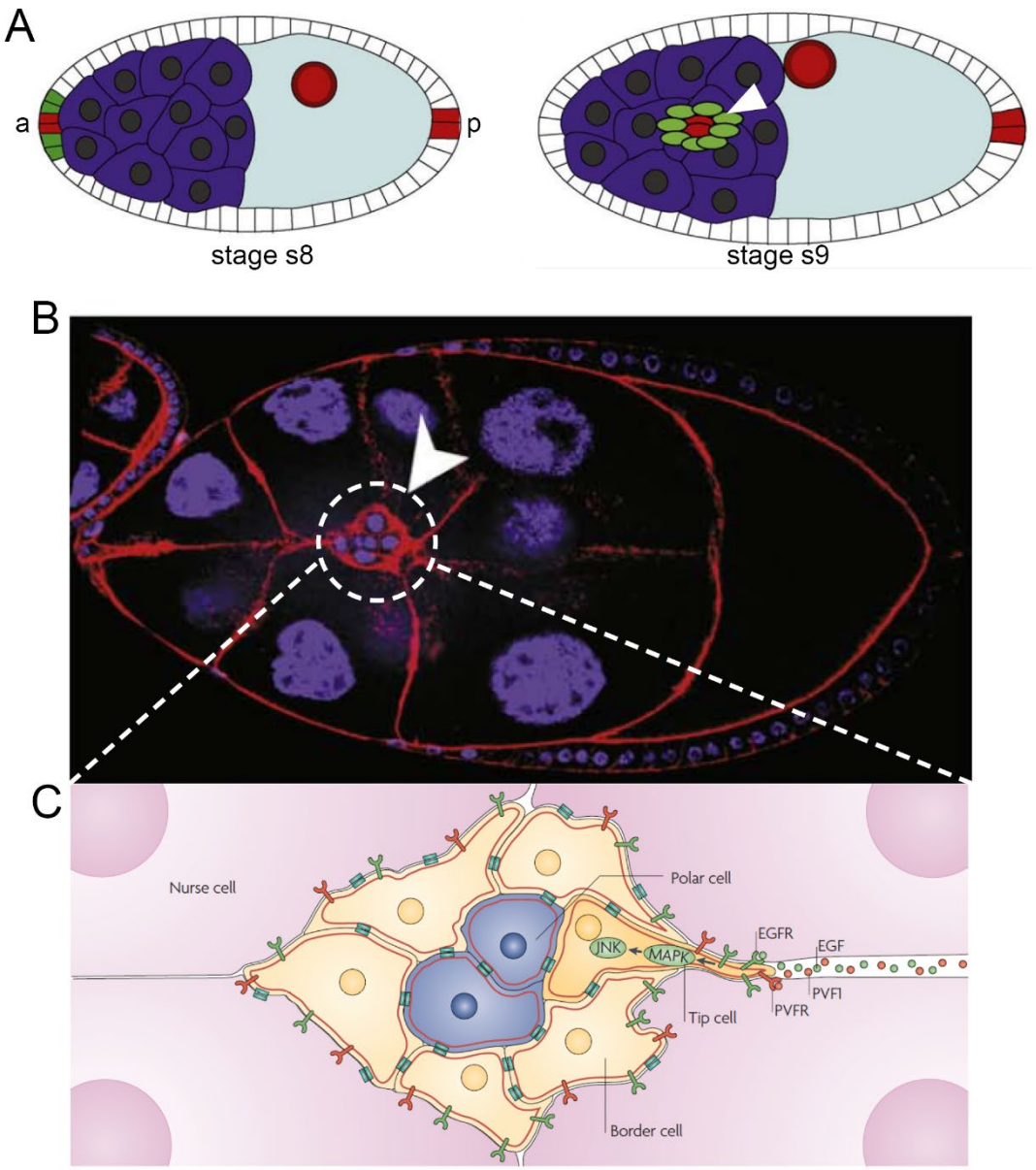

Figure 16. Migration of the border cells. A: Drosophila egg chamber at stages 8 and 9. The chamber is composed of the oocyte (turquoise) in the posterior half, of 15 nurse cells (purple) in the anterior part and is surrounded by follicular cells (white). By stage 7, two pairs of polar cells (red) are formed from follicular cells, at the anterior and the posterior poles. Border cells (green) are specified at stage 8 around the anterior pair of polar cells. They then form a mobile cluster that detach from the epithelium and migrate posteriorly toward the oocyte during stage 9. Modified from López-Schier, 2010. **B**: Image of an egg chamber at stage 9. Nuclei are labelled in purple and E-Cadherin in red, allowing visualising cell contours. Arrowhead points to the border cells cluster. Modified from López-Schier, 2010. **C**: Schematics of border cells collective migration. The cell exposed to the higher PVF/EGF signal (tip cell) develops long actin rich protrusions and inhibits protrusion formation in follower cells, thus orienting group migration. Modified from Friedl & Gilmour, 2009.

b. Mesenchymal cell migration: the case of neural crest cells

Neural crest cells are a very peculiar population of cells, specified at the interface between neural and non-neural ectoderm. These cells are multipotent, highly migratory, and colonise the embryo during development, giving rise to numerous tissues belonging to the three germ layers (Le Douarin & Teillet, 1973; Mayor & Theveneau, 2013a). From the neurectodemal epithelium sitting at the top of the neural tube, they delaminate by undergoing epithelial to mesenchymal transition, adopting a mesenchymal and migratory morphology (Fig. 17A). They then migrate as streams of loosely attached cells toward the ventral side of the embryo (Scarpa & Mayor, 2016; Theveneau & Mayor, 2012). Originally, these cells were thought to respond only to repulsive signals belonging to the Slit/Robo, Neurophilin/Semaphorin and Eph/Ephrin pathways (Jia et al., 2005; Osborne et al., 2005; Robinson et al., 1997; Theveneau & Mayor, 2011), but these cues are likely more required for delimiting a migration route (Fig. 17A). It was later discovered that Sdf1 is expressed by ectodermal cells located on the path of migration and that NC cells express CXCR4 (Fig. 17E) (Theveneau et al., 2010). Disruption of Sdf1 or CXCR4 signalling leads to defects in NC cells migration, and ectopic expression of Sdf1 attracts NC in vivo and in vitro, establishing Sdf1 as a chemoattractant for these cells.

Such a system with seemingly individual, mesenchymal cells migrating away from chemorepellents toward a source of chemoattractant could just be another model of in vivo individual cell migration. NC would then be a large group of cells that migrate independently of each other and individually perceive environmental cues. Yet, it appears that chemoattraction of neural crest cells is efficient only if they establish N-Cadherin mediated adherens junction (Theveneau et al., 2010). This suggests that NC cells behaviour is more complex than expected and that they require one another to migrate, which is the hallmark of collective cell migration.

NC cells migration has been extensively studied in the past twenty years, in particular by the laboratory of Roberto Mayor. These cells rely on several behaviours that allow emergence of an efficient collective migration. NC cells first exhibit contact inhibition of locomotion (CIL) (Fig. 17B) (Carmona-Fontaine et al., 2008). They actively inhibit protrusion formation and migration upon contact with another cell, and reorient away from this cell (Abercrombie & Heaysman, 1954; Carmona-Fontaine et al., 2008). Premigratory NC cells form a densely packed group of cells adhering through E-Cadherin (Scarpa et al., 2015). At the onset of migration, these cells undergo an EMT: they switch adhesion molecules to N-Cadherin and acquire CIL behaviour, leading to dispersion of these cells. Preventing E-Cadherin downregulation blocks EMT and N-Cadherin loss of function disrupts CIL behaviour (Scarpa et al., 2015). This shows that the cadherin switch is responsible for acquisition of CIL. It also appears that the Wnt Planar Cell Polarity (Wnt/PCP) pathway is involved in the CIL behaviour (Carmona-Fontaine et al., 2008; Matthews et al., 2008).

The Planar Cell Polarity pathway is a non-canonical type of Wnt signalling which has been identified in drosophila and contributes to polarising cells in the plane through asymmetric distribution of components (Fig. 18A & B) (Gao, 2012; Yang & Mlodzik, 2015). Many components related to this pathway have been identified. In particular, Wnt is a diffusible ligand that binds to the receptor Frizzled (Fz). In Drosophila, Fz7 is located at the distant pole of the cell and signals in the cytoplasm through Dishevelled (Dsh). At the proximal pole is located another transmembrane receptor, Vang-Gogh (Vang), which signals through Prickle (Pk). At the level of cell-cell contacts, Fz from the rear of one cell binds to Vang from the front of another cell. Concomitantly, inside a cell, Fz and Vang are mutually exclusive, which establishes a clear polarity that propagates through contact. Another receptor, Flamingo (Fmi), is present at both sides of a cell, along with Fz and Vang and binds Fmi from other cells in a homophilic manner. Once established, the Wnt/PCP pathway interacts with small GTPases, contributing to polarising cell morphology. However, even though it is established that the Wnt/PCP signalling is particularly important for vertebrate development (Carmona-Fontaine et al., 2008; Heisenberg et al., 2000; Yang & Mlodzik, 2015), its molecular mechanisms are way less clear and asymmetric distribution of its components is much less often observed than in Drosophila.

In the context of NC cell migration CIL behaviour is prevented by disruption of the Wnt/PCP pathway by removing Dsh, Wnt11 or Syndecan4, a proteoglycan receptor involved in Wnt/PCP signalling in vertebrates (Carmona-Fontaine et al., 2008; Matthews et al., 2008). Actually, upon contact, NC cells establish N-Cadherin containing adherens junction and Wnt/PCP complexes. At the contact site, Syndecan4 and N-Cadherin junction activate RhoA, while Dsh and newly activated RhoA inhibit Rac1 (Fig. 17B) (Matthews et al., 2008; Stramer & Mayor, 2016). This leads to collapse of lamellipodia and assembly of a contractile cortex around the junctions. Meanwhile, Rac1 repolarises at the other end of the cell, triggering formation of a new lamellipodium. Combination of local cortical tensions and pulling from lamellipodium puts the cell doublet under tension, ultimately leading to separation (Scarpa et al., 2015). Such CIL behaviour is commonly observed in spreading groups of cells as a way to create space between cells and better pave the environment (Stramer & Mayor, 2016). Numerical simulations, however, showed that CIL is not sufficient to account for collectiveness as, with only CIL, cells would disperse, meet less and less, and finally stop receiving orienting cues (Fig. 17D) (Szabó et al., 2016).

NC cells require another mechanism to ensure collective migration. Coattraction (CoA) has been identified in this system and consists in expressing both a diffusing chemoattractant and a receptor for this chemoattractant (Fig. 17C). Indeed, neural crest cells express both the C3a diffusible molecule and C3aR, its receptor (Carmona-Fontaine et al., 2011; Shellard & Mayor, 2016). These cells are attracted by a group of C3a expressing cells or by C3a soaked beads, which confirms the attractive role of this chemokine (Fig. 11C). A group of cells act as a source of chemoattractant so that any cell wandering away from the group will detect this chemotactic gradient and move back toward the group. This behaviour counterbalances the dispersing effect of CIL, ensuring that cells stay close to each other.

Numerical simulations established that the combination of CIL and CoA indeed allows the formation a cohesive group that migrates collectively (Fig. 17D) (Szabó et al., 2016). However, in absence of external cues that direct migration, such a group would migrate randomly.

In the Xenopus embryo, NC cells are laterally confined by Versican, an extracellular matrix protein that prevents cell migration, defining narrow tracks for neural crest cells (Fig. 17A) (Szabó et al., 2016). This ensures that cells cannot disperse laterally allowing optimal use of CIL and CoA by neural crest cells to orient their migration. Furthermore, migration is biased toward ventral regions. Indeed, in the dorsal direction, the path is blocked by neural crest cells that have not yet undergone EMT (Scarpa et al., 2015). On the other side, are located the epibranchial placodes, ectodermal structures that secrete Sdf1 (Theveneau et al., 2013). Interestingly, chemoattraction of Sdf1 does not rely on biasing protrusions but rather stabilising polarity set by cell-cell interactions, in particular CIL (Fig. 17E) (Theveneau et al., 2010). Hence, neural crest movement is prevented laterally and dorsally, and biased ventrally. Interestingly, chemoattraction by Sdf1 is maintained over time as placodal cells are repelled by contact with neural crest cells, through a CIL behaviour. Hence, they are attracting neural crest cells and fleeing them once contacted, leading to a mechanism described as a chase-and-run (Theveneau et al., 2013).

Finally, it has recently been shown that clusters of NC cells, both in vitro and in vivo, exhibit an actomyosin ring, a supracellular actin cable spanning several cells through adherens junction, which is made contractile by associating with myosin (Fig. 17F) (Shellard et al., 2018). Contractility is asymmetric in response to Sdf1-mediated chemotaxis. The cable is less contracted at the front, toward the Sdf1 source than at the rear, which contributes to directional migration. In absence of Sdf1, locally lowering or increasing cable contractility using optogenetic constructs respectively leads to collective motion toward or away from the perturbation. Conversely, increasing contraction close to the Sdf1 source or lowering it away from the source prevents migration. Hence, this actin cable potentiates the chemotactic response and coordinates cell motion.

This complex combination of behaviours, based on adhesion (CIL, confinement and actin cable) and paracrine signalling (CoA and chase-and-run), illustrates how migration collectiveness can emerge from simple cell-cell and cell-environment interactions. These interactions ensure correct guidance of neural crest cells.

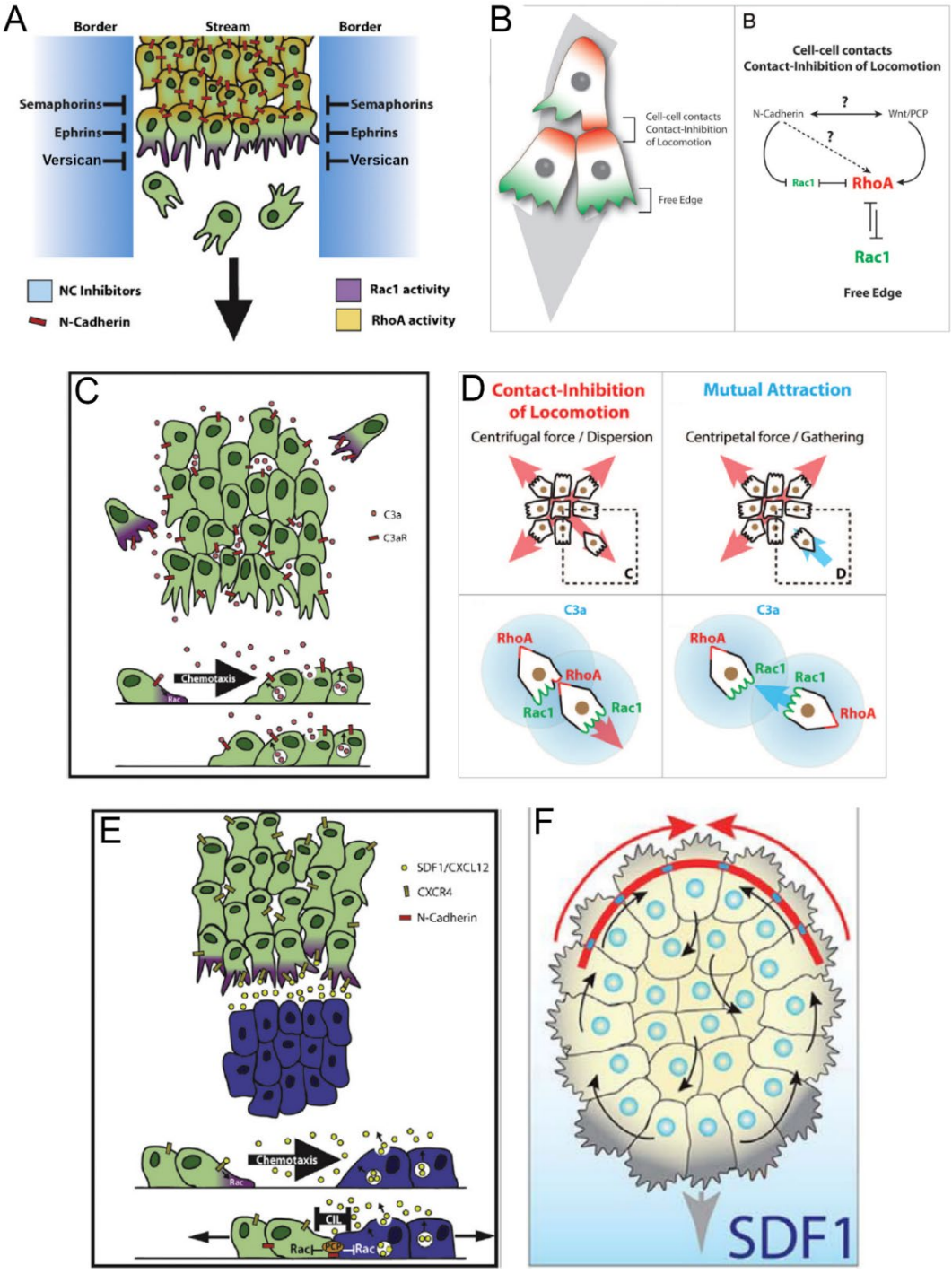

Figure 17. Migration of the Xenopus neural crest cells. A: Lateral confinement of neural crest (NC) cells by Eph/ephrin, Slit/Robo and Semaphorin signalling pathways as well as the extracellular matrix component Versican, define trails laterally confining streams of migrating NC cells. Modified from Shellard & Mayor, 2020. **B**: Contact inhibition of locomotion (CIL) upon NC cell collision. At the contact point, N-Cadherin and Wnt/PCP signalling pathways inhibit Rac1 and activate RhoA, locally preventing lamellipodia formation, while activating Rac1 at the free edge, promoting movement away from the contact point. Modified from Theveneau & Mayor, 2011. **C**: Co-attraction (CoA) behaviour exhibited by NC cells, which express both the C3a chemokine and its receptor C3aR, so that cells away from a large group of cells are attracted by this group. Modified from Shellard & Mayor, 2020. **D**: Combination of CIL, promoting cell dispersion, and CoA, ensuring contact between cells, is at the basis of NC cell collective migration along a defined track. Modified from Theveneau & Mayor, 2011. **E**: Movement of NC cells (green) is biased by chemotaxis along an Sdf1 gradient generated by placodal cells (purple). Placodal cell exhibit CIL upon contact with NC cells, prompting them to move away in a mechanism of chase-and-run. Modified from Shellard & Mayor, 2020. **F**: Chemotaxis in NC cells is enhanced by CIL and formation of a contractile supracellular actomyosin (red) cable that connects and pull cells at the rear of a cluster. Modified from Shellard et al., 2018.

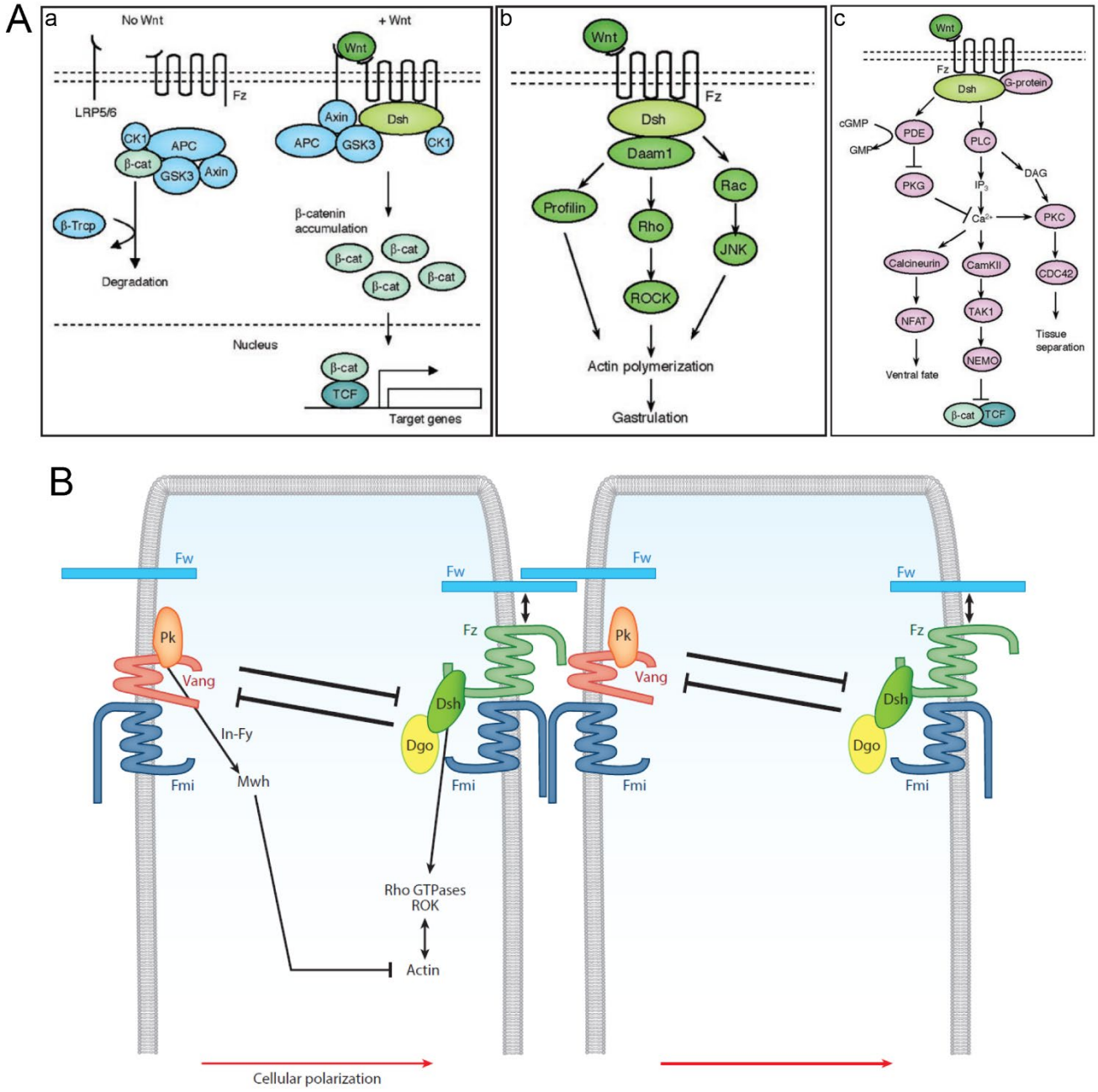

Figure 18. Wnt signalling pathways. A: The three different Wnt pathways. a: Canonical Wnt/β-Catenin signalling pathway controls TCF target genes expression. In absence of Wnt ligands, cytosolic β-Catenin is sequestered by a protein complex and degraded. Upon ligand binding, proteins from the complex are recruited by the Fz receptor and the cytoplasmic protein Dsh. This leads to accumulation of β-Catenin proteins that enter the nucleus and bind to TCF, a transcription factor. Once bound to β-Catenin, TCF is activated and promote the expression of target genes mainly involved in cell differentiation. b: Non-canonical Wnt/planar cell polarity pathway establishes a planar polarity, defining an anterior and a posterior pole in contacting cells over the scale of a whole tissue. Upon binding of Wnt ligands to Fz receptors, Dsh is recruited and activates a signalling cascade involving RhoGTPases and leading to cell polarisation and migration. c: Non-canonical Wnt/Ca^{2+} pathway is involved in multiple cellular functions among which differentiation and migration. Upon Wnt binding, a signalling cascade downstream of Fz leads to Ca^{2+} accumulation, which is detected by Ca^{2+} binding proteins. The three different signalling are related by three main components, the ligand Wnt, the receptor Fz and the cytoplasmic protein Dsh. Modified from Komiya & Habas, 2008. **B**: Wnt/PCP component distribution in a planar polarised epithelium. At the posterior side of the cell is accumulated the Fz receptor that binds Dsh and Dgo in the cytoplasm. Fz also binds the receptor Vang located at the anterior side of a contacting cell and recruiting the cytoplasmic protein Pk. This extracellular interaction is stabilised by Fmi, that is present at both side and bind Fmi from contacting cells. In a cell, Fz and Vang mutually repel and interact with Rho GTPases, ensuring planar cell polarisation. Modified from Yang & Mlodzik, 2015.

c. Other collective processes

I just described a few examples of collective cell migration, among the most extensively described in the literature, but many other instances of collective migration exist. However, morphogenesis also relies on other collective phenomena that are not collective migration. They consist in the coordination of individual cell behaviours that sum up to obtain tissue scale modification of the shape. Although not being migration *per se*, such collective behaviours are also required to shape an embryo.

Apical constriction for example, corresponds to a local increase of cortex contractility at the apical pole of epithelial cells, which can be coupled to apicobasal microtubule growth. This results in contraction of the apical surface that pulls neighbouring cells and locally forms a groove. This is for instance required for the formation of the neural tube in Xenopus and in chick (Haigo et al., 2003; Sawyer et al., 2010). Action of locally contracting cells can also be reinforced by formation of supracellular structures, like contractile actin cables contributing to pulling large groups of cells (Pasakarnis et al., 2016; Röper, 2013). In this case, the tissue has been deformed without active displacement of any cell nor change of neighbour.

Cell intercalation is also a collective process that does not rely on cell migration (Fig. 2F). Intercalation relies on the formation of junctions with new neighbours and can be performed radially or laterally. Radial intercalation corresponds to the interpenetration of superposed layers of cells. This leads to the vertical thinning and planar spreading of the tissue. Such behaviour is, for example, observed during Zebrafish epiboly, where ectodermal tissue thins and spreads over the yolk cell (Bensch et al., 2013; Bruce, 2016). Medio-lateral cell intercalation relies on the event described as T1 transition, where, in a structure of four cells, two distant cells will form a junction, breaking the junctions between the two formerly close cells (Rauzi et al., 2008; Siang et al., 2018). This elementary event leads to a local shortening on the mediolateral axis, and lengthening on the antero-posterior axis. This can happen at way larger scales, with large stripes of cells converging and intercalating along the mediolateral axis, and elongating along the anteroposterior axis (Glickman et al., 2003; Tada & Heisenberg, 2012). This behaviour has hence been called convergent-extension, and is for example displayed by mesoderm and neurectoderm during the gastrulation and neurulation of Xenopus (Keller et al., 2000; Keller & Tibbetts, 1989). Convergent-extension has to be distinguished from convergence and extension, which is an even larger scale movement involving several cell and tissue behaviours (Fig 2D-F) (Roszko et al., 2009). In particular, convergent-extension contributes to zebrafish notochord convergence and extension but does not recapitulate it completely (Heisenberg, et al., 2000; Roszko et al., 2015; Tada & Heisenberg, 2012; Ulrich et al., 2003).

Now that I have described early zebrafish development, as well as the mechanisms by which cell migrate, as individuals and collectively, I will describe in detail what is known about induction and

migration of the axial mesoderm, and in particular the polster, which is the group of cells that I have mainly studied during this PhD.

4. Axial mesoderm during gastrulation

In the zebrafish embryo, the axial mesoderm is a dorsal structure composed of the prechordal plate and the notochord. During this PhD thesis, I studied the extension of the axis during gastrulation. In particular, I tried to understand how progenitor cells from the polster, the anterior-most part of the prechordal plate, orient their migration, and how they maintain contact with the following notochord progenitors. During gastrulation, the different populations of cells that constitute these three tissues are deemed progenitors, as polster, prechordal plate and notochord are defined as tissues only by the end of gastrulation. For the sake of convenience, I will discard the use of the term "progenitor" and refer to gastrulation tissues as polster, prechordal plate and notochord.

a. Genetic control of mesendoderm formation

i. Prechordal plate

The prechordal plate is the anterior-most part of the axial mesoderm (Fig. 19A & B). It is a large group of cells located in front of the notochord, as its name suggests. During gastrulation, as axial mesoderm extends, prechordal plate progenitors cells move toward the animal pole (Fig. 19A & 20A) (Dumortier et al., 2012; Kai et al., 2008; Montero et al., 2003; Smutny et al., 2017). By the end of gastrulation, prechordal plate lies under the future head and will later contribute to the formation of the hatching gland and to some head mesenchyme (Kane et al., 1996; Muraina et al., 2020; Shimizu et al., 2005). These cells have a patterning role as their migration under the neural plate is required for separation of the eye field (England et al., 2006; Varga et al., 1999). Accordingly, defects of prechordal plate cell migration or identity lead to cyclopia and craniofacial defects as exemplified by the holoprosencephaly congenital disease (Fig. 21F) (Heisenberg et al., 2000; Seiliez et al., 2006; Varga et al., 1999). Specification of prechordal plate identity mainly depends on the nodal signalling.

1. Nodal signalling

The nodal signalling pathway relates to the TGFβ signalling pathway, largely involved in cell proliferation and differentiation (Schier, 2003). Nodal ligands bind to TGFβ receptors that are cell surface complexes made of two Type I and two Type II receptors, as well as EGF-CFC co-receptors (Nagaso et al., 1999; Renucci et al., 1996; Schier, 2003). The type I receptor is responsible for ligand specificity, is able to phosphorylate serine and threonine, and assembles with a Type II receptor and a co-receptor upon ligand binding (Pinheiro & Heisenberg, 2020). This leads to phosphorylation of the

transcription factors Smad 2 and Smad 3 (Dick et al., 2000). They accumulate in the nucleus where they form a complex along with Smad4, and cooperate with nuclear cofactors to activate nodal target genes (Dick et al., 2000; Whitman & Mercola, 2001). These factors are involved in mesendoderm and neurectoderm patterning, as well as dorso-ventral and left-right axis during development (Dick et al., 2000; Pinheiro & Heisenberg, 2020; Whitman & Mercola, 2001).

In Zebrafish, dorsal maternal determinants located in the YSL activate the canonical Wnt/β-Catenin signalling pathway, which triggers expression of Boz in the dorsal-most cells, in turn triggering expression of the two nodal ligands that pattern mesendoderm, Cyc and Sqt (Fig. 21 A & B) (Fekany et al., 1999; Shimizu et al., 2000). They form homo- or heterodimers that are detected by complexes made of the Type I receptor Taram-A (Tar) and the Type II receptor Actr2a or Actr2b (Nagaso et al., 1999; Renucci et al., 1996). Mutants for *cyc* or *sqt* exhibit reduced dorsal territory markers and prechordal plate size (Feldman et al., 1998; Rebagliati et al., 1998). The double loss of function leads to near complete loss of dorsal markers and of axial mesoderm (Dougan et al., 2003). It hence seems that there is some functional redundancy between the two ligands. Recently, a study pointed the role of another TGFβ ligand in ensuring Nodal signalling. Vg1 is ubiquitously expressed in the embryo but only secreted where Nodal signalling is active. Once secreted, Vg1 dimerises with nodal ligands and potentiates their mesendoderm inducing function (Bisgrove et al., 2017; Montague & Schier, 2017; Pinheiro & Heisenberg, 2020).

Patterning depends on the intensity of nodal signalling as exposure to high, intermediate or low levels of nodal correlates with endodermal, mesodermal and ectodermal fates, respectively (Fig. 21A) (Gritsman et al., 2000; Peyriéras et al., 1998; Pinheiro & Heisenberg, 2020). Depending on the level of signalling, phosphorylated Smad2 associate with different transcription factors. In particular, Sox32, also called Cas, is required in formation of endodermal derivatives but not of prechordal plate (Alexander et al., 1999; Aoki et al., 2002; Dickmeis et al., 2001) while FoxH1, a homeodomain transcription factor, has an opposite role (Fig. 21B) (Pogoda et al., 2000; Sirotkin et al., 2000; Slagle et al., 2011). It has first been proposed that fate was decided depending on exposition to a gradient of long range diffusing Sqt ligand. It actually appears that exposition to nodal signalling induces expression of nodal ligands (Schier & Talbot, 2005). Hence, by a mechanism of neighbour-mediated activation, nodal signalling forms a gradient extending over 6-8 cells row from the margin (Fig. 21A) (Pinheiro & Heisenberg, 2020; Schier & Talbot, 2005). In particular, it has recently been proposed that, in the shield, contact time between cells in the shield regulates nodal activity through a positive feedback loop, thus defining mesodermal or endodermal fate (Fig. 21E) (Barone et al., 2017). Yet, the precise mechanism for axial mesendoderm patterning is still not well understood.

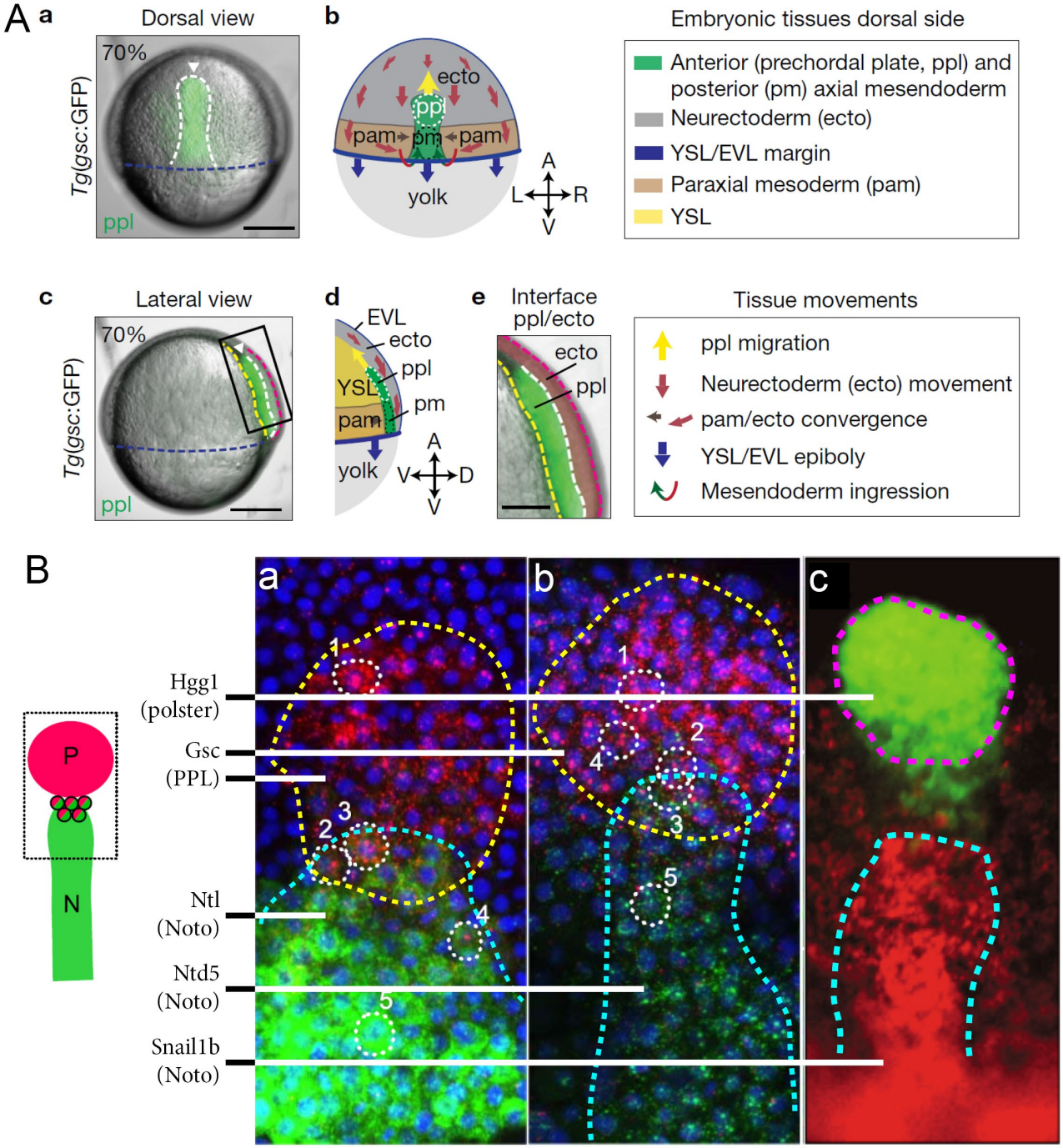

Figure 19. Anatomy and genetic expression of zebrafish axial mesoderm. A: Axial mesoderm (labelled in green) in a 70% epiboly zebrafish embryo. a: Dorsal view of a gastrulating embryo. Blue dashed line: embryonic margin. b: schematics of a 70% epiboly embryo. ecto: ectoderm; pam: lateral mesoderm; pm: notochord; ppl: prechordal plate. c-e: lateral view of a 70% epiboly embryo. Modified form Smutny et al., 2017. **B**: Genetic signature of the different tissue forming the axial mesendoderm observed by fluorescent *in situ* hybridisation. a: Axial mesoderm of a 60% epiboly embryo. Prechordal plate (yellow dashed line) is an oval tissue that expresses *gsc* while notochord (cyan dashed line) expresses *ntl*. Expression of the two markers overlaps partly at the interface between the two tissues (see schematic). Modified from Farrell et al., 2018. b: Axial mesoderm of a 75% epiboly embryo. Notochord, expressing *ntd5*, is now an elongated tissue while the prechordal plate stays oval. The intermediate population is still present. Modified from Farrell et al., 2018. c: Axial mesoderm of a 90% epiboly embryo. The polster (pink dashed line) is characterised by the expression of *hgg1* and consists in an oval group of cell located at the anterior part of the prechordal plate. Expression of *hgg1* do not overlap with *snail1b*, which is expressed by the notochord. Modified from Blanco et al., 2007.

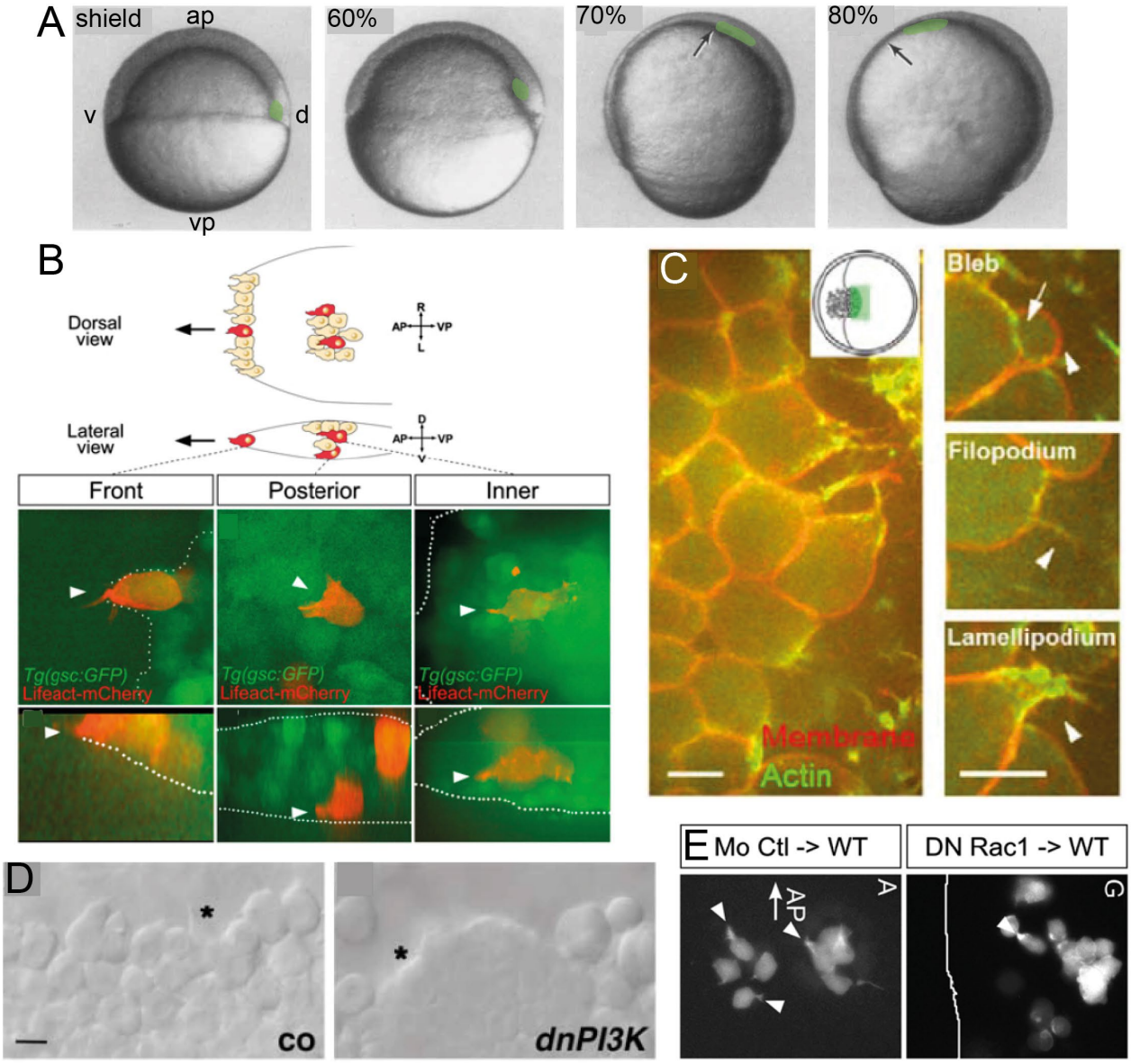

Figure 20. Prechordal plate migration during gastrulation. A: Position of the prechordal plate (green) at different stages of gastrulation. Lateral view of the embryo. ap: animal pole; d: dorsal; v: ventral; vp: vegetal pole. Modified from Kimmel et al., 1995. **B**: Actin labelled (red) prechordal plate cells transplanted in a host prechordal plate (green). Top and bottom panels show respectively dorsal and sagittal confocal views of the transplanted cells. Regardless of their position in the tissue, cells form actin rich protrusions oriented toward the animal pole, the direction of prechordal plate migration. l: left; r: right. Modified from Dumortier et al., 2012. **C**: Prechordal plate cells form three different types of protrusions: blebs, filopodia and lamellipodia, although only lamellipodia are involved in prechordal plate cell migration. Modified from Diz-Muñoz et al., 2010. **D & E**: Dorsal view of prechordal plate cells observed by bright field (D) or florescence (E) microscopy. Expression of a dominant negative form of PI3K (dnPI3K) or Rac1 (DN Rac1) prevents formation of actin rich protrusion (asterisks and arrowheads) compared to control conditions (co, Mo Ctl). Modified from Montero et al., 2003 & Dumortier et al., 2012.

Finally, in maternal zygotic mutants lacking the Oep EGF-CFC co-receptor (MZ *oep*), no mesendoderm is formed despite the presence of some nodal signals produced by the YSL, showing that this receptor is crucial for nodal signalling in the cell (Gritsman et al., 1999; Schier et al., 1997). Conversely, expression of an active form of the type I Tar receptor (referred to as Tar*) activates the nodal pathway in a cell autonomous fashion (Renucci et al., 1996). Such cells then give rise to mesodermal or endodermal derivatives, depending on the quantity of Tar* that is expressed (Dumortier et al., 2012; Peyriéras et al., 1998). Since nodal signalling induces nodal expression, Tar* expressing cells produce nodal ligands, that will activate nodal in neighbouring cells. Hence, a sufficient number of Tar* expressing cells can induce the expression of mesendodermal markers and even the formation of a secondary axis when placed at the margin of the embryo (Fig. 21C) (Aoki et al., 2002; Peyriéras et al., 1996).

2. Fibroblast Growth Factor signalling

The first fibroblast growth factors (FGF) have been identified as mitogenic factors of fibroblasts grown in culture (Fig. 12A) (Gospodarowicz & Moran, 1975). Since their discovery, FGF ligands and receptors have been implicated in many biological processes. In particular, during development, they are involved in mesoderm and neurectoderm induction and maintenance, as well as control of morphogenetic movements (Fig. 21A) (Dorey & Amaya, 2010; Turner & Grose, 2010). All extracellular FGF ligands (canonically from FGF1 to FGF23) signal through a family of tyrosine kinase receptors called FGF receptors (FGFR). In vertebrates, this family is composed of four genes, FGFR1 to FGFR4. Alternative splicing of these receptors allows a wide diversity of ligands and biological response (Zhang et al., 2006). FGF ligands dimerise and bind to the extracellular domain of FGFR, that assemble in a dimer (Turner & Grose, 2010). Receptors then cross phosphorylate themselves, leading to the activation of cytoplasmic signalling pathways such as Ras/ERK, Akt and PKC, respectively associated with differentiation, survival and cell morphology, and migration (Fig. 12A) (Dorey & Amaya, 2010; Turner & Grose, 2010).

Upon inhibition of FGF signalling by expression of a dominant negative form of FGFR (DN-FGFR), formation of posterior body structures, including all posterior mesoderm, is blocked (Amaya et al., 1991; Ota et al., 2009). Furthermore, over activation of FGF signalling by expression of constitutively active form of FGFR (CA-FGFR) leads to dorsalisation and expansion of dorsal structures (Ota et al., 2009). This shows that FGF signalling is crucial for proper dorso-ventral and antero-posterior patterning, essentially through inhibition of the ventralising BMP signalling pathway (Draper et al., 2003; Poulain et al., 2006; Schier & Talbot, 2005). Besides acting as a BMP inhibitor, FGF signalling is also involved in cell specification. Indeed, embryos mutant for FGFR1 completely loose notochord and somites (Yokoi et al., 2007). Furthermore, mutant cells transplanted in the shield of a wild type

embryo do not contribute to axial mesoderm but rather adopt neural fate (Ciruna & Rossant, 2001; Shimada et al., 2008). Accordingly, expression in cells of DN-FGFR antagonises the mesendodermal fate induction by Tar* (Poulain et al., 2006). These observations show that during zebrafish early development, FGF signalling is required for the formation of both axial and paraxial mesoderm.

Old experiments demonstrated that naïve ectodermal Xenopus cells exposed to FGF1 and FGF2 became mesodermal, suggesting a role for FGF signalling in mesoderm induction (Kimelman & Kirschner, 1987; Slack et al., 1987). Since then, many studies explored which receptors and ligands are involved and what the precise role of this pathway is. Two ligands in particular, FGF8 and FGF24, are expressed at the margin, and, for FGF8, at the basis of the elongating notochord (Draper et al., 2003). Simple or double loss of function lead, respectively, to shorter and absence of notochord, although the anterior axial mesoderm, the prechordal plate, seems unaffected. These phenotypes are similar to those induced by exposition to the SU5402 drug, which disrupts FGF signalling (Draper et al., 2003; Mathieu et al., 2004; Schier & Talbot, 2005). In such experiments, morphological structures corresponding to the shield and the notochord actually form, but the notochord does not express typical markers and disappear after gastrulation. This suggests that FGF signalling, in particular through FGF8 and FGF24, is required for maintenance of posterior axial mesoderm fate but not its acquisition (Draper et al., 2003).

3. Goosecoid

gsc is a homeodomain gene that is first expressed in the shield during its formation, then is restricted to prechordal plate cells during gastrulation (Fig. 19B, 21B &D) (Schulte-Merker et al., 1994; Stachel et al., 1993). Both zygotic mutants for FoxH1 or embryos expressing DN-FGFR1 express *gsc* in a reduced territory, showing that both FGF and Nodal signalling are involved in *gsc* expression (Germain et al., 2000; Mckendry et al., 1998; Ota et al., 2009; Whitman & Mercola, 2001). In particular, expression of Tar* or high quantities of the Cyc ligand, in absence of the endodermal factor Cas, is sufficient to induce *gsc* expression and prechordal plate fate (Dumortier et al., 2012; Montero et al., 2005; Peyriéras et al., 1996).

gsc is a key gene for dorsal patterning. Ventralisation of the embryo by lithium treatment reduces *gsc* territory while *gsc* loss of function leads to ventralisation and defects in the anterior neuroectodermal region (Stachel et al., 1993). *gsc* also has a dorsalising role as its ectopic expression is sufficient to induce complete secondary axes and inhibit BMP2b/4/7 and Wnt8 expression (Dixon Fox & Bruce, 2009; Peyrieras et al., 1996). As such, it has organising properties. It is to note that *gsc* expression has to be maintained in the shield and later in the prechordal plate as cells from these tissues transplanted elsewhere in the embryo quickly change fate and lose *gsc* expression (Carmany-Rampey & Schier, 2001; Dumortier et al., 2012; Kai et al., 2008). Interestingly, some observations on Xenopus cultured cells suggest that Gsc is also able to induce cell motility, but only when cells are in groups, thus promoting

collective cell migration (Niehrs et al., 1993). Accordingly, *gsc* is found overexpressed in some breast cancer, and is associated with poor prognosis as it promotes EMT and metastasis formation (Hartwell et al., 2006).

ii. Polster & hatching gland

During gastrulation, polster progenitor cells are the first hypoblast cells to internalise, in the embryonic shield (Fig. 19B). They form an oval tissue of roughly 200 cells that migrates toward the animal pole (Blanco et al., 2007; Kim et al., 1998; Wells et al., 2011). Around 80% of epiboly, the tissue adopts a bean shape and by 90% epiboly, it reaches the anterior neural plate and epithelializes, actually becoming the polster. Polster cells are characterised by the expression of *cstlb* (previously called *hgg1*), although they also express *gsc* (Blanco et al., 2007; Ulrich et al., 2003). They later give rise to the most anterior embryonic structure, the hatching gland that secretes the proteases responsible for chorion degradation and hatching, among which is the cathepsin Hgg1 (Muraina et al., 2020; Shih & Fraser, 1996).

Acquisition of polster identity is particularly obscure. The initial step of specification is common with the rest of the prechordal plate. Around 70% epiboly, anterior cells from the prechordal plate start to express *hgg1*, first in a salt and pepper manner, then homogeneously. Once the polster is formed, it starts to express other proteases like Ovastacin, as well as zinc transporters that ensure proper proteolysis of the chorion (Muraina et al., 2020). Old experiments performed in the Medaka teleost fish (*Latypes oryza*) suggest that treatment with retinoic acid, which disrupts anterior differentiation, leads to the absence of hatching gland, but the underlying mechanism is unknown (Inohaya et al., 1995).

iii. Notochord

The notochord is a key structure in organising the embryo and ensuring its shape. Ultimately, it consists of a rod-shaped tissue made of successive vacuolated cells that form a rigid axis around which the embryo develops (Kimmel et al., 1995; McLaren & Steventon, 2021; Saude et al., 2000). Defects in notochord structure provoke local bends giving rise to severe scoliosis phenotypes (Bagwell et al., 2020; McMillen & Holley, 2015). However, before reaching this shape, notochord progenitors during zebrafish gastrulation, are distributed all along the margin. They internalise when they reach the dorsal margin, forming an elongated rectangular tissue that extends behind the prechordal plate (Fig. 2E, 19A & B) (Bosze et al., 2020; Dumortier et al., 2012; Glickman et al., 2003; Heisenberg et al., 2000).

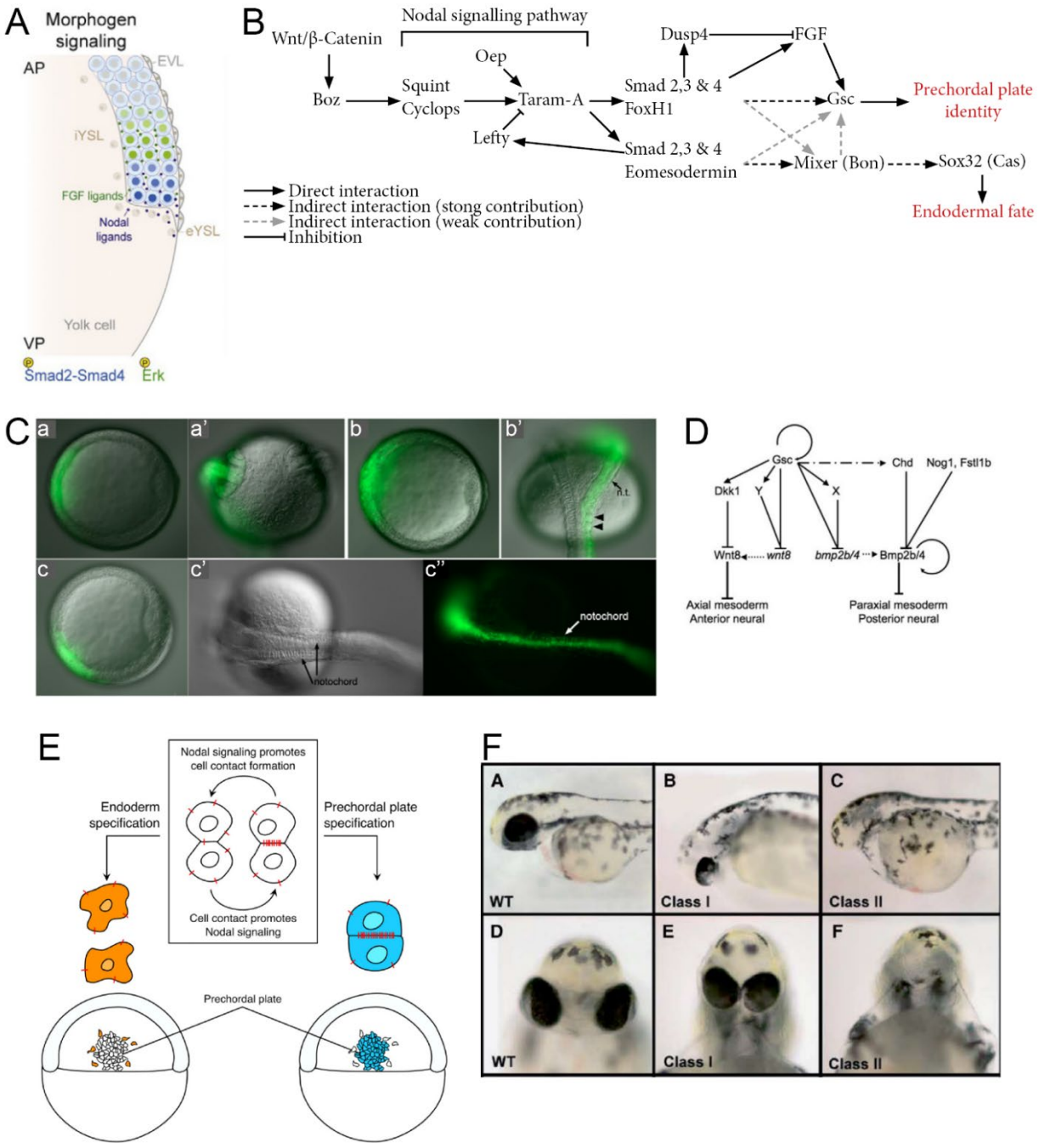

Figure 21. Nodal signalling and mesendoderm induction. **A**: Nodal and FGF ligands diffuse from the margin and trigger phosphorylation of Smad and Erk in the first 7 rows of cells. The three rows closest to the margin receive more nodal signalling and tend to adopt endodermal fate while the next four rows receive less signalling and rather adopt mesodermal fates, although the two populations are intermingled at the margin. Modified from Pinheiro & Heisenberg, 2020. **B**: Signalling pathway leading to endodermal or mesodermal fate. Wnt/β-Catenin signalling is emitted by dorsal YSL nuclei, activating Boz expression in dorsal deep cells. This triggers expression of nodal ligands that direct cells exposed to signalling toward endodermal or mesodermal fate. **C**: Transplantation of cells overexpressing *gsc* (green) at the ventral (a, b) or lateral (c) margin at the beginning of gastrulation. These cells locally induce the formation of a second axis that can be completely independent (a') or partially fused (b', c' & c'') to the endogenous axis. These ectopic axes are composed of the transplanted cells but also of endogenous cells that have been induced by ectopic nodal signalling. Modified from Dixon Fox & Bruce, 2009. **D**: Cellular signalling downstream of Gsc, preventing fates other than prechordal plate. Modified from Dixon Fox & Bruce, 2009. **E**: Positive feedback loop between cell contact and nodal signalling contribute to maintaining nodal signalling in adhesive cells, stabilising prechordal plate fate, while cells that do not form cell-cell junctions lose nodal signalling and turn endodermal. Barone et al., 2017. **F**: Loss of *gsc* expression leads to more or less severe cyclopia phenotype, showing the inductive role of prechordal plate in eye and forebrain formation. Modified from Seiliez et al., 2006.

As for all mesendodermal cells, induction of notochord cells requires nodal signalling, though at lower levels than prechordal plate ones, as a low-level expression of Tar* induces some notochordal fate (unpublished observations, Pinheiro & Heisenberg, 2020; Shimizu et al., 2000). The first gene that specifies notochordal fate is *flh*, that is expressed very early, from the sphere stage, all along the margin (Odenthal et al., 1996; Shih & Fraser, 1996). Then during early epiboly, its expression becomes restricted to the dorsal margin and the shield during its formation. Later, *flh* domain of expression extends with notochord cells. Expression of this gene is required for specification but is not sufficient to maintain notochord identity. Actually, *flh* mutants do produce notochord progenitors, but these cells change fate and the notochord disappear. Flh induces the expression of *ntl*, that is expressed at the margin all along gastrulation and in the extending notochord (Fig. 19B). *ntl* is required for maintaining notochord identity as *ntl* mutants lack all anterior notochord structures (Odenthal et al., 1996; Pinheiro & Heisenberg, 2020; Shih & Fraser, 1996).

It has recently been described that *gsc* and *ntl* expression overlaps, some cells expressing both genes (Fig. 19B) (Farrell et al., 2018). Interestingly, this domain corresponds to the posterior part of the prechordal plate, that does not express *hgg1* (Fig. 19B). Hence, axial mesoderm is divided in three genetic territories during gastrulation. The polster expresses *hgg1* and *gsc*, and corresponds to the anterior part of the prechordal plate, while the posterior prechordal plate expresses both *gsc* and *ntl*, and the notochord expresses only *ntl* (Blanco et al., 2007; Farrell et al., 2018). These three genetic territories correspond to only two morphological territories, that exhibit two different migration behaviour. I will finally describe in detail the migration of the polster during gastrulation.

b. Polster migration during gastrulation

i. Internalisation

Prior to animal migration, cells from the prechordal plate and, in particular, from the polster have to internalise. This is performed by synchronised ingression, cells individually delaminating, but in a coordinated manner so that a large flow of cells internalise at the dorsal margin (Fig. 2C) (Montero et al., 2005). This movement of internalisation requires reduction of E-Cadherin expression as cells overexpressing the adhesion protein display slower internalisation in a cell-autonomous manner (Blanco et al., 2007). Diminution of E-Cadherin expression is due to the expression of Snail1a in the margin (Blanco et al., 2007). Transcription factors from the *snail* family are involved in EMT and are in particular known to reduce cell-cell adhesion (Cano et al., 2000). EMT in the shield is controlled by the Wnt/β-Catenin signalling that activates the transcription factor Stat3 which in turn induces nuclear localisation of Snail1a by the intermediate of the zinc transporter Liv1 (Yamashita et al., 2002, 2004).

Guidance of internalising cells toward the yolk is not well understood. It has been proposed that segregation of germ layers is a passive consequence of cell sorting, due to differential adhesion or

surface tension (Maître et al., 2012; Townes & Holtfreter, 1955). However, although differences in tissue surface tension are enough to segregate cells *in vitro*, it is not critical *in vivo* (Pinheiro & Heisenberg, 2020). Instead, active migration of mesendoderm progenitors seems required. Accordingly, prechordal plate cells display extensive protrusive activity during internalisation and blocking Rac1 or Arp2/3 impairs mesendoderm internalisation (Dang et al., 2013; Giger & David, 2017). However, no directional cue has clearly been identified. Nodal signalling or the soluble ligand Dkk1 has been proposed as modulating cell contact and might bias cell migration toward the yolk (Caneparo et al., 2007; Pinheiro & Heisenberg, 2020).

ii. Animal migration

Upon internalisation, prechordal plate and polster cells start migrating toward the animal pole of the embryo. Despite a large literature on polster cell migration, a comprehensive view is still missing. I will here summarise what is known by focusing on cell-cell adhesion and cell protrusions during this migration.

1. Adhesion in prechordal plate cells

Cell-cell adhesion is crucial for prechordal plate migration and regulation of the AJ component E-Cadherin level of expression and cortical dynamics are finely tuned during migration (Babb et al., 2001; Babb & Marrs, 2004; Blanco et al., 2007; Caneparo et al., 2007; Johansson et al., 2019; Kane et al., 2005; Shimizu et al., 2005). E-Cadherin mutations like in *hab* and *rk3* mutants, as well as knock down using morpholinos, largely disrupt animal movement of the plate (Kane et al., 2005; Shimizu et al., 2005). Similarly, E-Cadherin overexpression limits cell internalisation and animal migration, in a cell-autonomous fashion (Blanco et al., 2007). Once in the hypoblast, prechordal plate cells stop expressing Snail1a and re-express E-Cadherin, which is a hallmark of mesenchymal to epithelial transition (MET) (Blanco et al., 2007; Yamashita et al., 2004). This is triggered by Dkk1, that acts as a switch for the Wnt signalling (Blanco et al., 2007; Caneparo et al., 2007; Yamashita et al., 2004). It inhibits the Wnt/β-Catenin pathway, and thus Snail1a, in the prechordal plate while activating the non-canonical Wnt/PCP pathway by binding to the PCP component Kny. However, it appears that prechordal plate cells keep a mesenchymal morphology, suggesting that MET is incomplete (Dumortier et al., 2012).

The zebrafish *slb*/Wnt11 mutant displays severe defects of convergence and extension as well as of anterior migration of the prechordal plate (Heisenberg et al., 2000; Ulrich et al., 2003, 2005; Witzel et al., 2006). At 24 hpf, *slb* embryos present a severely shortened embryonic axis and cyclopia, which are associated with defects in notochord elongation and prechordal plate migration. Ubiquitous expression of Wnt11 in *slb* mutants largely rescues gastrulation phenotypes (Ulrich et al., 2003). The

Wnt11 ligand belongs to the non-canonical Wnt/PCP pathway and signal through the Fz7 receptor (Witzel et al., 2006). Actually, *slb* and MZ *fz7a/b* mutants present similar defects (Čapek et al., 2019; Ulrich et al., 2003). Localisation of components of the pathways have been observed using tagged fluorescent versions of Wnt11, Fz7, Dsh and Fmi. It has been shown that Wnt11 accumulates at the level of cell-cell contacts and recruits Fz7, which in turn recruits Fmi and Dsh (Witzel et al., 2006). This accumulation of Wnt/PCP components increases cell-cell contact time and adhesion, suggesting that this pathway interacts with AJ. Surprisingly, knock-down of Rab5c, a small GTPase involved in endocytosis, phenocopies the effect of *slb* mutation and prevent anterior migration of the prechordal plate (Ulrich et al., 2005). Conversely, expression of a constitutively active form of Rab5c rescues *slb* phenotype, suggesting that Rab5c is involved downstream of Wnt11. Immunostaining experiments showed that E-Cadherin colocalizes with Rab5c positive endosomes. All these observations point to a role of Wnt/PCP in regulating E-Cadherin dynamics in the prechordal plate during gastrulation by controlling endocytosis and recycling. This ensures cohesion of cells and proper tissue migration.

Besides being involved in the switch in Wnt signalling, Dkk1 also regulates cell adhesion independently from the Wnt/PCP pathway. This diffusible ligand is expressed at the margin and all around the axial mesoderm (Johansson et al., 2019). Overexpression of Dkk1 reduces the anterior migration of prechordal plate and convergence and extension of the notochord (Caneparo et al., 2007; Johansson et al., 2019). Overexpression also decreases the amount of adhesion molecules at the level of AJ, both E-Cadherin and β-Catenin being more diffuse around the junction. Conversely, knocking down Dkk1 result in increased adhesion, in the prechordal plate and in cells around. Surprisingly, a mild decrease of Dkk1 leads to faster axis elongation but later leads to head formation defects (Caneparo et al., 2007). Using fluorescently tagged Dkk1, it has been observed that it localises to adhesion complexes of axial mesodermal cells, at regions where actomyosin is concentrated, and contributes to the sequestration of β-Catenin just below the plasma membrane (Johansson et al., 2019). Since AJ require β-Catenin to link E-Cadherin to actin, Dkk1 thus tends to decrease cell-cell adhesion. The fact that modulation of Dkk1 can both increase and decrease axis elongation speed suggests that its endogenous concentration is fine-tuned to ensure optimal anterior migration of the prechordal plate.

Finally, another cell adhesion protein has been described as in anterior migration of the axial mesoderm. Protocadherins do not belong to the classic cadherin family but possess a similar structure, with an intracellular, a transmembrane and an extracellular domain, the latter containing 6 cadherin repeats (Pancho et al., 2020). Pcdh18a is expressed in axial mesoderm during zebrafish gastrulation and knock-down of Pcdh18a leads to shorter and wider axis, and less anterior migration of the prechordal plate (Aamar & Dawid, 2008; Bosze et al., 2020). Experiments on zebrafish embryo explants showed faster cell dissociation when Pcdh18a is knocked down, suggesting that adhesion is reduced (Aamar & Dawid, 2008). A recent paper described that Pcdh18a is specifically expressed in the posterior part of the prechordal plate, not overlapping with the prospective polster (Bosze et al., 2020). In this work,

authors proposed that this population of cells act as a motor and contribute to elongation of axial mesoderm. Transplanting Pdh18a expressing cells in front of the embryonic axis of an embryo injected with a morpholino against Pcdh18a rescues partly the defect in elongation. In the posterior prechordal plate, Pcdh18a colocalizes with E-Cadherin in cytoplasmic endosomes. These E-Cadherin containing endosomes also colocalise with Rab5a and Rab11, respectively involved in endocytosis and recycling. Furthermore, FRAP experiments showed that Pcdh18a increases E-Cadherin dynamics at the membrane. These experiments suggest that, in the posterior prechordal plate, Pcdh18a contributes to E-Cadherin recycling, which is required for proper cell migration and axis extension. Interestingly, it appears that overexpression of Pcdh18a also disrupts axis extension, which is consistent with the idea that E-Cadherin dynamics has to be finely tuned for proper prechordal plate migration.

2. Substrate for prechordal plate migration

Little is known about the substrate on which prechordal cells migrate. This tissue is in contact with the ectoderm and the YSL and E-Cadherin is accumulated all along the contact area between the prechordal plate and the two other tissues (Fig. 19A, 22C, D) (Montero et al., 2005; Smutny et al., 2017). In particular, E-Cadherin signal between prechordal plate and the ectoderm is especially strong and electron microscopy observation showed that prechordal plate cells form protrusions toward the overlying ectoderm (Fig. 22C-E) (Montero et al., 2005). Authors of this study thus proposed that the ectoderm is the substrate for prechordal plate migration. This is actually similar to the situation in Xenopus (Huang & Winklbauer, 2018). During gastrulation, the Xenopus embryo forms a cavity, the blastocoel, delimited animally by the ectoderm and vegetally by the endoderm. The mesoderm, induced at the interface between the two, internalises and migrates toward the animal pole like in zebrafish. This animal migration happens on ECM secreted by the ectoderm that constitutes the blastocoel roof (Winklbauer & Keller, 1996). However, contrary to Xenopus, no extracellular matrix is detected at the interface between the two tissues in Zebrafish until late gastrulation (Fig. 22A) (Latimer & Jessen, 2010; Smutny et al., 2017). Furthermore, inhibition of integrin adhesion does not prevent prechordal plate migration (Fig. 22B) (Nair & Schilling, 2008), suggesting that polster cells use E-Cadherin adhesion to adhere to their substrate of migration.

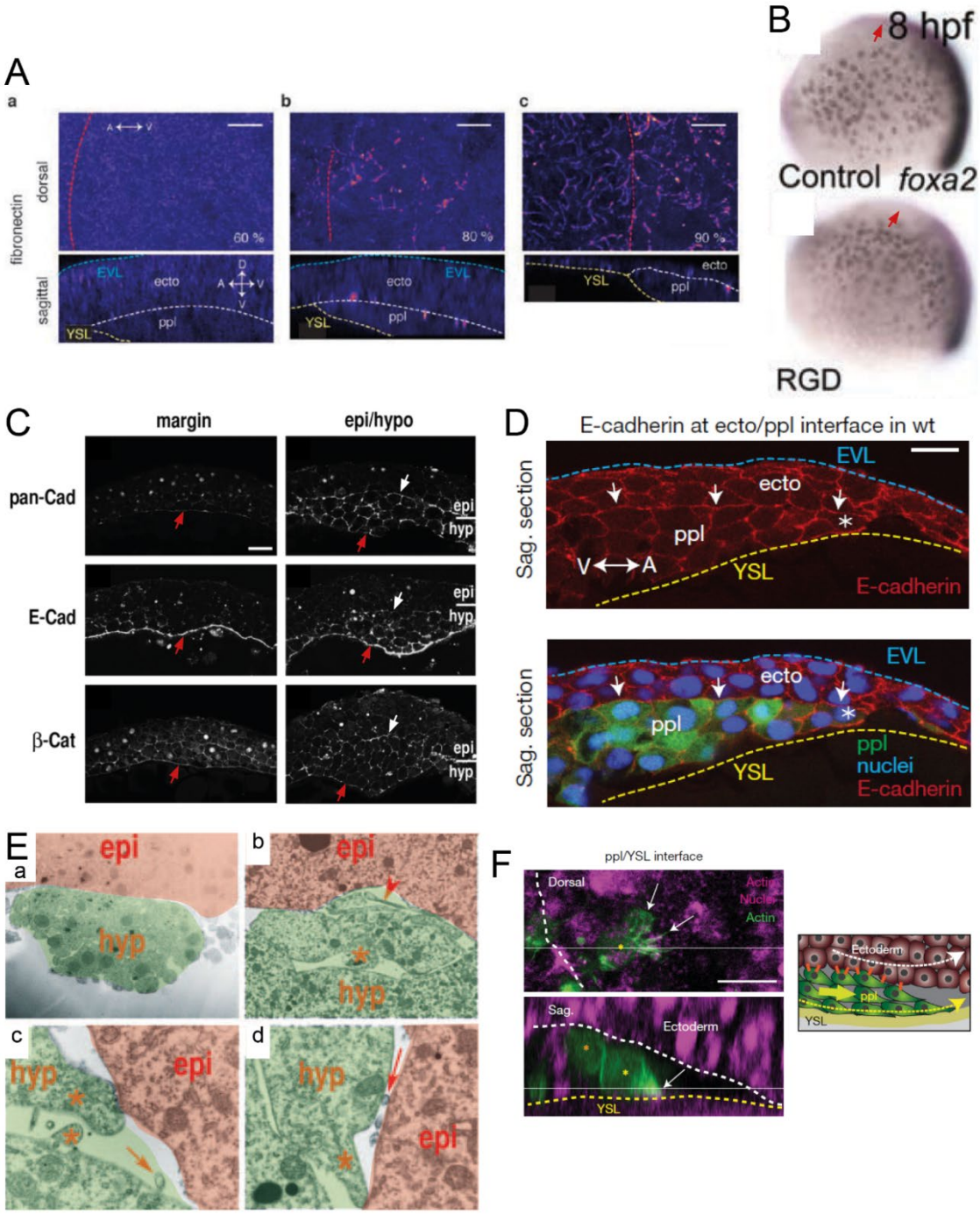

Figure 22. Substrate for prechordal plate migration. A. Immunostaining for Fibronectin during gastrulation. Fibronectin starts to accumulate at the interface between ectoderm (ecto) and prechordal plate (ppl) only at late gastrulation. Modified from Smutny et al., 2017. **B**: Inhibition of Fibronectine-Intergrin interaction using RGD peptide does not affect prechordal plate migration. Red arrows: prechordal plate front at 80% gastrulation. Modified from Nair & Schilling, 2008. **C-D**: Distribution of adherens junction proteins in embryonic shield observed by immunostaining for Cadherin (pan-Cad, E-Cad, E-cadherin) and β-Catenin (β-Cat). C: Frontal view of the margin and the prechordal plate (epi/hypo). D: Sagittal view of the region around prechordal plate front. White and red arrows respectively mark the epiblast (epi)/hypoblast (hypo) and the hypoblast/YSL contacts. Cadherin is located between cells and accumulated at both interfaces. Modified from Montero et al., 2005 & Smutny et al., 2017. **E**: Electron microscope view of the interface between epiblast (red) and hypoblast (green). Cellular protrusions oriented toward the epiblast are formed by hypoblast cells (asterisks & arrowhead: lamellipodia; arrow: filopodia). a: low magnification view. b-d: high magnification views. Modified from Montero et al., 2005. **F**: Dorsal and sagittal confocal views of actin labelled prechordal plate cells (green) transplanted near the front of a host prechordal plate (white dashed line). A transplanted cell (yellow asterisk) forms actin rich protrusions oriented toward the YSL (yellow dashed line). The schematic proposes that cell migration uses YSL as a substrate for migration. Orange bars in the schematic: E-Cadherin accumulation between polster and ectodermal cells. Modified from Smutny et al., 2017.

In a single study, it has been reported that ephrin signalling is required for proper prechordal plate migration (Chan et al., 2001). During gastrulation, the receptor ephrin B is expressed in the axial mesoderm and expression of a dominant negative form of this receptor leads to morphological defects, in particular to decreased anterior migration of the prechordal plate. Surprisingly, some polster cells were found at abnormal locations by the end of gastrulation in embryos expressing this dominant negative. The role of ephrin B during gastrulation in the zebrafish is however unclear. In Xenopus, it has been described that Eph/ephrin signalling is involved in separating germ layers (Rohani et al., 2011). Thus, ephrin B might be required to maintain the boundary between the axial mesoderm and the ectoderm.

During early gastrulation, the ectoderm is performing epiboly toward the vegetal pole while the prechordal plate migrates toward the animal pole (Myers et al., 2002; Smutny et al., 2017; Williams & Solnica-Krezel, 2020). Later during gastrulation, the ectoderm undergoes convergence and extension, following the axial mesoderm movement (Smutny et al., 2017; Williams & Solnica-Krezel, 2020). Surprisingly, disruption of the animalward motion of the prechordal plate in *slb* mutants decreases the correlation between the prechordal plate and the ectoderm, which continues to migrate vegetally (Smutny et al., 2017). Conversely, slowing down epiboly increases the animalward movement of the prechordal plate and the correlation between the two tissues. This suggests that opposite migrations of the ectoderm and prechordal plate create frictions at the interface between the two tissues. Injection of a morpholino against E-Cadherin also decreases correlation of the two tissues and animalward movement of the ectoderm suggesting that this friction is mediated by E-Cadherin (Smutny et al., 2017). This was confirmed by the observation that dragging beads coated with E-Cadherin on ectodermal explants is sufficient to generate a flow that correlates with the bead motion. However, it is not clear how prechordal plate cells can simultaneously migrate on the ectoderm while exerting friction forces that align the ectoderm with the plate, suggesting that polster cells might use the YSL as a substrate for migration, or a combination of both. This is supported by the observation that prechordal plate cells at the front of the tissue tend to form protrusions oriented toward the YSL (Fig. 22F).

During gastrulation, the ectoderm is attached to the YSL. Regardless of its substrate of migration, progression of the prechordal plate requires a detachment of the adhesion between YSL and the ectoderm. It has been hypothesised that this is performed by compression of interstitial fluid in front of the polster (personal discussion with S. Grigolon & C. P. Heisenberg). The pressure generated by the animal-ward movement of the polster would detach ectoderm from YSL (unpublished observations from C.P. Heisenberg lab). Interestingly, despite not being expressed in the polster, Snail1a controls its anterior migration. After prechordal plate cells internalised, its expression profile changes and it is expressed in the YSL, in front of the polster (Blanco et al., 2007). Loss of Snail1a expression prevents anterior migration of the polster. Since progression of the polster might require the detachment of ectoderm and YSL, and since Snail is known to decrease cell adhesion, it is tempting to hypothesise that

Snail1a reduce E-Cadherin expression in front of the polster, helping in the detachment. Alternatively, Snail1a could simply regulate polster adhesion to the YSL if the latter is a substrate for migration.

The question of the substrate for prechordal plate cell migration became even more complex with the observation that prechordal plate cells located in the middle of the tissue, completely surrounded by other prechordal plate cells, also form protrusions (Fig. 20B) (Dumortier et al., 2012). This suggests that these cells might adhere to each other and use each other as a substrate for migration, and thus change neighbours. However, it is not possible to propel a group of cells without it being attached to an exterior substrate, suggesting that protruding inner prechordal plate cells might not much contribute to the actual displacement of the group.

3. Motility of prechordal plate cells

Internalisation and migration of prechordal plate cells rely on the formation of actin rich protrusions (Fig. 20B, C). Disruption of these protrusions, for example by preventing membrane to cortex attachment leads to blebbing and loss of cell motility (Diz-Muñoz et al., 2010). Expression of a dominant negative form of Rac1 (Fig. 20E) and knock down of *arpin*, an Arp2/3 inhibitor, respectively reduce and increase the number of protrusions, suggesting that protrusion formation is triggered by the classical Rac1-WAVE-Arp2/3 signalling pathway (Dang et al., 2013; Dumortier et al., 2012).

Wnt/PCP, on top of being involved in cell adhesion, is also required for formation of actin rich protrusions (Fig. 23B). In *slb* and MZ *fz7a/b* mutants, as well as embryos expressing Dsh-DEP$^{+,}$ a dominant negative form of Dsh blocking the Wnt/PCP pathway, prechordal plate cells displayed a reduced protrusive activity (Čapek et al., 2019; Dumortier et al., 2012; Ulrich et al., 2003). In the case of the MZ *fz7a/b* mutant, this reduction in actin rich, lamellipodia-like protrusions results in increased blebbing (Čapek et al., 2019). E-Cadherin expression is also required for proper protrusion formation as morphant cells are less protrusive (Dumortier et al., 2012). The mechanisms by which Wnt/PCP and E-Cadherin regulate protrusion formation are, however, still obscure.

The last and more extensively described pathway involved in protrusion formation is the PI3K signalling pathway. PI3K is a kinase that phosphorylates a membrane phospholipid, phosphatidyl inositol bi-phosphate (PIP2), into PIP3, which acts as a secondary messenger (Kölsch et al., 2008). PIP3 is bound by the protein kinase PKB/Akt that in turn regulates myosin contractility and the Rac1 small GTPase. Loss of PI3K signalling results in a decrease of speed and orientation in migrating Dictyostellium or mammal and Zebrafish neutrophils (Funamoto et al., 2001; Sasaki et al., 2000; Yoo et al., 2010). Accordingly, expression of a dominant negative form of PI3K (DN-PI3K) in prechordal plate cells results in a dramatic decrease of protrusion formation (Fig. 20D) (Dumortier et al., 2012; Montero et al., 2003). Since PKB localises at protrusion sites and its accumulation is disrupted in cells expressing DN-PI3K, it has been proposed that it PKB mediates PI3K signalling. Another study

identified Sin1, a component of the mTORC2 complex, as a downstream effector for PI3K. Knock-down of Sin1 completely prevents protrusion formation (Dumortier & David, 2015). This phenotype is rescued by expression of a constitutively active form of Rac1 but not of PI3K, suggesting that Sin1 signals downstream of PI3K and upstream of Rac1. Finally, cell protrusiveness is activated by the chemokine PDGF (Montero et al., 2003). In culture, mesendodermal cells form more protrusions and display strong membrane accumulations of PKB in presence of PDGF and this effect on protrusiveness is blocked if PI3K signalling is inhibited. Accordingly, blocking the PDGF receptor during gastrulation also leads to a decrease of protrusion formation (Montero et al., 2003). These experiments show that PDGF signalling is able to activate PI3K and protrusion formation, likely through the receptor PDGFR. As PDGF acts as a chemoattractant in many systems, it has been proposed that PDGF is the cue for directional migration of the prechordal plate *in vivo*.

4. Orientation of prechordal plate cells

Up to now, I only presented the mechanisms leading to formation of actin rich protrusions. As mentioned earlier, every cell of the prechordal plate is forming protrusions and, interestingly, these protrusions are oriented toward the animal pole, regardless of the cell position in the tissue (Fig. 20B) (Dumortier et al., 2012). This suggests that every cell in the prechordal plate receives an information of direction that polarises the cell and biases protrusion formation. It has been proposed that Wnt11 could be the guidance cue for prechordal plate migration (Ulrich et al., 2003). Indeed, protrusion orientation in *slb* mutants is largely disrupted. Furthermore, Wnt11 is expressed first at the margin, then in paraxial mesoderm, behind the prechordal plate (Heisenberg et al., 2000). This could be compatible with a repellent role for Wnt11 that drives the plate away from the margin first, then from paraxial mesoderm. However, two observations weakened this hypothesis. First, prechordal plate migration and notochord extension are still observed in *slb* mutants, deprived of Wnt11, suggesting that Wnt11 is likely not the only guidance cue (Heisenberg et al., 2000). Second, ubiquitous expression of Wnt11 actually rescues protrusion orientation and migration phenotypes (Ulrich et al., 2003). This last experiment rather points toward a permissive role for Wnt11, rather than instructive. However, the idea that the Wnt/PCP could play an instructive role survived for some years. In particular, it has been shown that expression of Dsh-DEP^{+}, besides reducing protrusion number, also disrupted protrusion orientation (Fig. 23C) (Dumortier et al., 2012). Perhaps asymmetric accumulation of Wnt/PCP components at the membrane could polarise cells. This idea has been supported by asymmetric accumulations of Vangl and Pk in the notochord by late gastrulation (Roszko et al., 2015; Yin et al., 2008). However, in a recent paper, it has been described that the orientation of the few protrusion formed by MZ *fz7a/b* mutant cells are still oriented (Čapek et al., 2019). Furthermore, in the same study, a photoactivable version of the receptor Fz7 has been built. This construct, upon activation, rescues the protrusion defects observed in cultured MZ *fz7a/b* mutant cells, consistent with the role of Fz7 in actin rich protrusion formation. Strikingly, non-specific

activation of the optogenetic receptor rescued the migration defects observed in MZ *fz7a/b* embryos (Čapek et al., 2019), strongly suggesting that Fz7 signalling is not instructive but, like Wnt11, simply permissive.

PDGF actually looked like a promising candidate as it signals upstream of PI3K and PI3K signalling is involved in protrusion orientation (Montero et al., 2003). Indeed, expression of DN-PI3K also disrupts protrusion orientation. Furthermore, asymmetric activation of PI3K in migrating prechordal plate cells has been observed, although this has not been well characterised (Dumortier et al., 2012). However, no localised expression of PDGF ligand has been identified in the gastrulating embryo (Liu et al., 2002). Furthermore, inhibition of PDGFR only decreases the number of protrusions while their orientation is not affected (Montero et al., 2003). These observations suggest that, like Wnt/PCP, PDGF signalling only plays a permissive role in protrusion formation and that PI3K activity is oriented by something else.

Up to date, no chemoattractant that could drive prechordal plate migration has been identified in the embryo. However, as presented before, oriented migration can emerge from interaction between migrating cells. Whether prechordal plate cells migrate in a collective fashion or not has been debated over the last decades. The fact that cells form a cohesive group where cells migrate together first suggested a collective process. However, in a study, it has been shown that knock-down of *mil*/*edg5*, a sphingosine-1-phosphate (S1P) receptor, resulted in increased animalward migration of the polster (Kai et al., 2008). This receptor antagonises PDGF and PI3K signalling, preventing recruitment of PKB to the membrane in presence of PDGF ligand. Strikingly, in embryos knocked down for *edg5*, some cells at the front of the polster left the tissue, moving faster toward the animal pole for a dozen minutes, these cells stopped migrating. This individual migration has been interpreted by the author as evidence against collective cell migration. Prechordal plate cells, since they can leave the tissue and migrate individually, do not seem to require their neighbours to migrate and the tissue might simply be a group of cells that migrate individually, independent from each other. The fact that leaving cells stop after some time might then be due to a loss of identity (Carmany-Rampey & Schier, 2001). It has already been described in zebrafish that tissue identity is fluid during gastrulation and ectopic prechordal plate cells might simply change fate.

A few years later, a set of experiments challenging this view has been performed in our team. As mentioned earlier, expression of Tar* and knock down of Cas force zebrafish cells to adopt a prechordal plate fate in a cell autonomous manner (Dumortier et al., 2012). Irrespective of its position in the embryo, such a cell continues to express *gsc* (Dumortier et al., 2012; Peyriéras et al., 1996). Individual or small groups of induced cells have been transplanted in front of the polster, separated by a few dozen micrometres (Fig. 23D) (Dumortier et al., 2012). At this location, transplanted cells should perceive any chemical gradient detected by the prechordal plate. However, although being motile, neither individual

nor small groups of cells displayed oriented migration. Neither protrusions nor trajectories of these cells were oriented toward the animal pole. However, upon extension of the axis, polster front reached transplanted cells. Upon contact with prechordal plate cells that migrate directionally, transplanted cells retrieved their orientation and animalward migration (Dumortier et al., 2012). This experiment shows that individual prechordal plate cells can indeed migrate out of the tissue, but they orient only when they are in contact with neighbours. Thus it is particularly unlikely that cell migration is instructed by information extrinsic from the prechordal plate, like a chemotactic gradient detectable by individual cells or oriented migration substrate. On the contrary, this suggests that the orienting information is brought by and thus contained in the group, and that this information is transmitted from cell to cell through contact (Fig. 23E). The nature of this information is, however, still obscure. It has been shown that decrease in cadherin expression also leads to randomisation of cell protrusions, suggesting that cells need proper adhesion to orient correctly and pointing to a role for AJ in mediating this information of direction (Fig. 23C) (Dumortier et al., 2012).

This last result is particularly interesting as it has been proposed, in Xenopus, that orientation of prechordal plate cells could be due to a gradient of mechanical tension (Fig. 23F) (Behrndt & Heisenberg, 2012; Weber et al., 2012). Based on the *in vitro* observation that cells can detect traction forces and align their migration away from the force, authors hypothesised that if cells are subject to a gradient of tension, they might orient toward the lowest tension (Weber et al., 2012). Since it is thought in Xenopus that the notochord is passively dragged by the prechordal plate (Hara et al., 2013), such a gradient could establish and orient the whole tissue, only based on cell adhesion. This mechanism, close to plithotaxis, is, however, only hypothetical.

5. How is the polster oriented during gastrulation?

I will now quickly summarise the results I presented concerning prechordal plate migration. Many molecular actors have been described as affecting prechordal plate migration (Fig. 23B) (Dumortier et al., 2012; Dumortier & David, 2015; Kai et al., 2008; Montero et al., 2003; Shimada et al., 2008). Relationships between these actors are, however, largely obscure, even if a few signalling pathways have been identified. Finally, no guidance cue has yet been found. Migration of prechordal plate cells is a collective process, and guidance is achieved, at least partly, through an information that is transmitted from cell to cell through contact (Fig. 23E) (Dumortier et al., 2012).

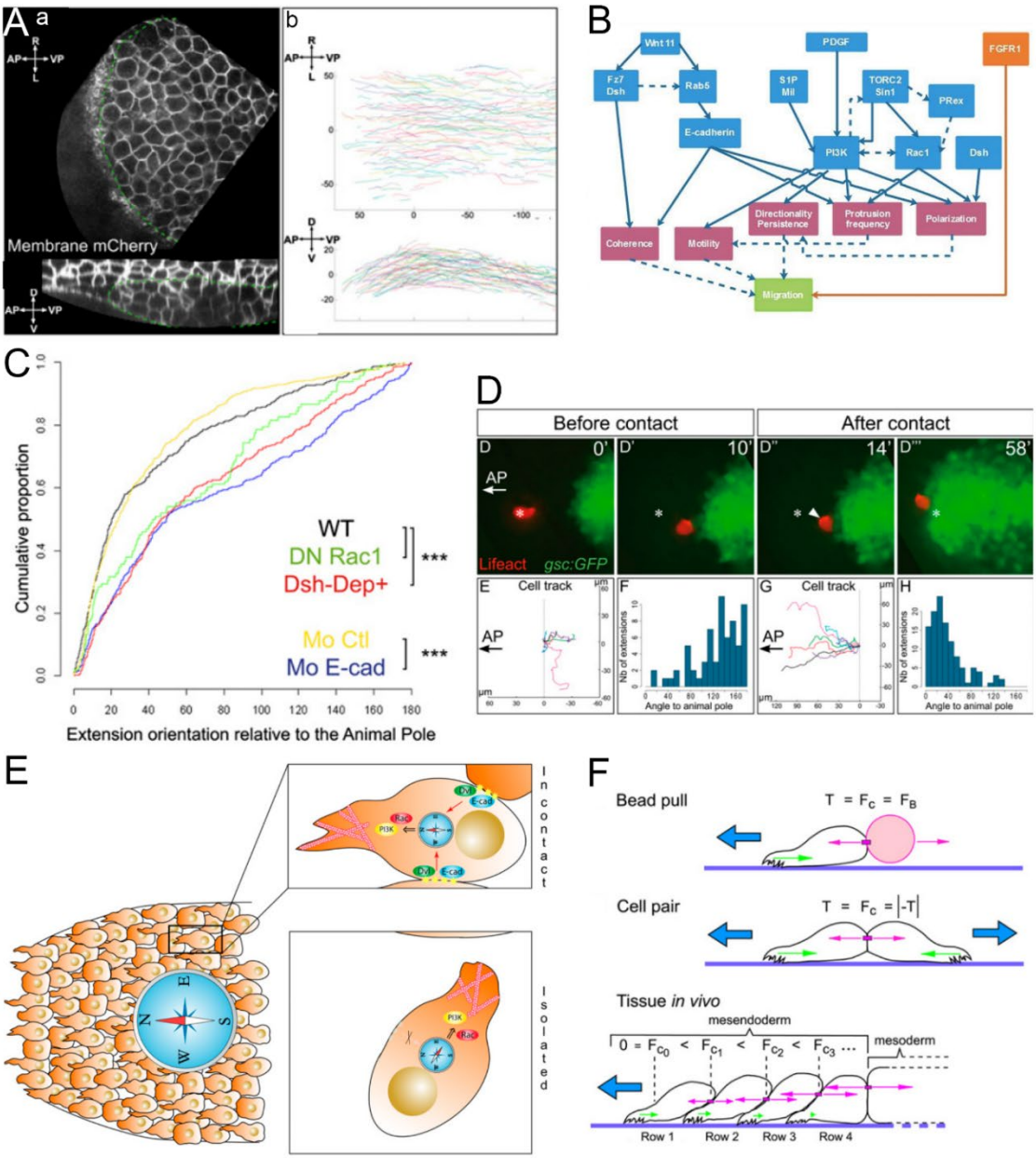

Figure 23. Orientation of prechordal plate migration. **A**: Trajectories of membrane labelled prechordal plate cells. Dorsal (top) and sagittal (bottom) views of cell contour (a) and trajectories (b) of prechordal plate cells during migration. Cell trajectories are oriented toward the animal pole, largely parallel and follow the curvature of the yolk. Dashed green line: prechordal plate front. Modified from Dumortier et al., 2012. **B**: Simplified summary of the different signalling pathways involved in prechordal plate migration. **C**: Protrusion orientation of control cells (WT, Mo Ctl) and cells with disrupted Rac1 (DN Rac1) or Wnt/PCP (Dsh-Dep+) signalling pathways, or knocked down for *e-cadherin* (Mo E-cad). Altering Rac1 or Wnt/PCP signalling, or *e-cadherin* expression actually disrupts orientation of protrusions formed by prechordal plate cells. Here, protrusion orientation is plotted using the cumulative proportion (see Methods). **D**: Images of a single actin labelled prechordal plate cell (red) transplanted in front of a host prechordal plate (green). Trajectories and protrusion orientation of such isolated cells are plotted before and after contact. Cells before contact are mobile and protrusive but are not oriented. Upon contact, they recover cell orientation, suggesting they received an information of direction. White asterisk: initial cell position; white arrowhead: contact between transplanted cell and endogenous polster. Modified from Dumortier et al., 2012. **E**: Current model for polster cell migration: an information of direction, of unknown nature, is contained in the prechordal plate and transmitted from cell to cell through cell-cell contact via E-Cadherin, Wnt/PCP, PI3K and Rac1 signalling pathways. Upon isolation, this information of direction is lost and cells are no more oriented. Modified from Dumortier et al., 2012. **F**: *In vitro*, Xenopus polster cells polarise away from a pulling force applied by an E-Cadherin coated bead or another cell. It has been hypothesised that this property could polarise a whole prechordal plate (mesendoderm), as dragging a passive notochord (mesoderm) would generate a gradient of tension (F_{c0}-F_{c3}). Modified from Weber et al., 2012.

What is the nature of this information of direction? The chemokines involved in prechordal plate migration only seem to be permissive, required for protrusion formation, but not instructive (Čapek et al., 2019; Montero et al., 2003). No localised source of chemokine at the animal pole that could establish a chemotactic gradient has been described. Furthermore, cells from the prechordal plate have to migrate a long way to reach their target destination, in an environment that is subject to large-scale cellular movements like epiboly and convergence and extension. Establishing a gradient of chemokines in these conditions might be difficult. Still, it could be possible that the tissue generates its own gradient, like in the PLLp, by locally degrading a permissive cue, which would bias cell migratory activity (Fig. 15B) (Donà et al., 2013; Venkiteswaran et al., 2013). Alternatively, cells might polarise by paracrine or juxtacrine signalling, like in the Drosophila Wnt/PCP pathway (Fig. 18B) (Yang & Mlodzik, 2015). Asymmetric accumulation of different receptors coupled to intracellular mutual inhibition could lead to propagation of cell orientation. However, components of the Wnt/PCP pathway that have been tested are not oriented and only seem to be permissive (Čapek et al., 2019). Finally, although cell morphology, tissue geometry and substrates are different in Xenopus, the idea that mechanical forces could orient the whole tissue is appealing (Fig. 23F).

Where is this information of direction located? Depending on the nature of the orienting cue, the answer to this question might vary a lot. In the case of a gradient, potentially self-generated, of chemoattractant or chemorepellent, one would expect a localised expression of the chemokine, at the animal pole or at the margin respectively. In the case of paracrine signalling, the chemokine might be expressed by the notochord or by YSL nuclei just in front of the prehcordal plate. For planar polarity as well as for propagation of a tension gradient, contact with an instructive tissue is likely required.

During my PhD, I sought to answer these two questions: what is the nature of this information of direction and where is it located? I chose to focus only on the migration of cells in the polster, the anterior-most part of the prechordal plate, as this tissue is easily recognisable on morphological criteria in live imaging. I first mapped the directional information that guides polster cell migration. Using precise 3D laser ablations and cell transplants, I identified that follower cells are actually instructing migration: it is their anteriorward movement that provides the propagating information that orients the migration of polster cells. Cell-autonomous and non-cell-autonomous inhibition revealed that a mechanical information propagates from cell to cell through their active migration. I then looked at the underlying molecular pathway and identified that the mechanosensitive domain of α-Catenin is required for cell orientation. This led us to propose a model for axial mesoderm extension in which the anteriormost tissue, the polster, is guided by more posterior, follower cells. Based on numerical simulations of axial mesoderm extension, we propose that this mechanical “guidance by followers” ensures the long-range coordination of the different cell populations forming the axis and provides a basis for its developmental robustness.

Results

Mechanisms regulating neural crest and polster collective migration are different

In the classical depiction of collective cell migration, cells are epithelial, strongly attached to each other and depending on their position in the group, cells acquire different identities, leader or follower (Fig. 14) (Vedula et al., 2013). Leader cells appear at the front of migration, adopt a pseudomesenchymal morphology and form large lamellipodia while follower cells from cryptic lamellipodia and the whole tissue is migrating. Collective migration of mesenchymal cells is fundamentally different (Fig. 17) (Theveneau & Mayor, 2011). Indeed, cells establish only transient contacts, eventually changing position relative to the others. How is collectiveness established in such a situation? To date, the most extensively described model of mesenchymal collective migration is the migration of neural crest cells (Mayor & Theveneau, 2013b). As mentioned in the introduction, two behaviours ensure guidance of collective migration in this tissue, CIL and CoA (Fig. 17B & C) (Carmona-Fontaine et al., 2008, 2011).

Cells displaying CIL tend to move away from each other upon contact, which contributes to the dispersion of dense groups of cells (Fig. 17D). CIL alone would thus lead to group disruption and loss of collectiveness. CoA corrects this by attracting cells back together, resulting in a coherent group that migrates (Szabó et al., 2016).

Polster and neural crest cells share many features (Fig. 17 & 20). They both display a mesenchymal migration, relying on actin rich protrusions, both rely on cell-cell contact and Wnt/PCP signalling for proper migration of the collective (Dumortier et al., 2012; Theveneau et al., 2010). All these similarities might suggest that polster cell migration is regulated like neural crest cell migration, relying on CIL and CoA. In order to test that hypothesis, I wanted to replicate, in the polster, the seminal experiments that led to the identification of CIL and CoA in neural crest cells.

Difficulties in cultivating polster cells

Collectiveness during migration arises from cell-cell interaction and it is easier to study such interaction *in vitro*, where one can set migration substrate, number of neighbours, chemokines in solution, *etc*., having a better control on the cell environment. I thus sought to cultivate polster cells. Protocol for culture of mesendodermal cells on a Fibronectin substrate already existed (Čapek et al., 2019; Krens et al., 2017). However, only a small fraction of cells adhere and it is not sure that polster cells attach to Fibronectin. With the help of Joseph d'Alessandro, from René Marc-Mège lab, we tried to reproduce similar culture conditions with polster cells.

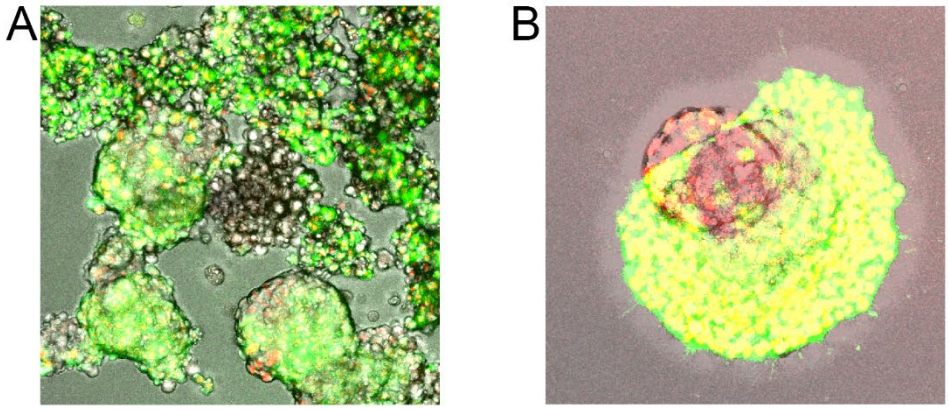

Figure 24. Attempts at cultivating polster cells. A: Z-projection of a cluster of non-protrusive, non-adhesive polster cells in culture. All cell nuclei are labelled in red, polster cells are also labelled in green. **B**: Instance of an adhesive cluster formed of a mix of polster cells and non-polster cells. Although polster cells are protrusive and asymmetrically distributed around the group on non-polster cells, the cluster is immobile.

The transgenic *Tg(Gsc:GFP)* fish line expresses GFP in cells of the axial mesoderm. I injected these fishes with a mix of Tar* and a morpholino against *cas* (MO *cas*) to force cells to adopt polster identity and, at shield stage, I dissected the GFP-expressing clone, composed of polster cells. I then dissociated the clone in Ringer's solution without calcium. This formed a mix of individual, small and large clusters of cells that I used to test culture conditions (Fig. 24A).

With Joseph, we tested different conditions and obtained some results by cultivating cells on a Fibronectin-coated plate, in a mix of 80% L15 medium at 0.65x and 20% EM. A few cells indeed adhered and formed small protrusions, and cells survived in culture for at least 24h. Furthermore, we once observed a large mix of labelled polster cells and unlabelled ones, which seemed to adhere to the slide, forming a ring of polster cells that were protruding toward the outside (Fig. 24B). This suggested that a mix of polster and non-polster cells might adhere but, though very exciting, we never observed a second instance of this phenomenon. Most cells were not adhesive, and protruding cells were immobile, so these culture conditions fail to reproduce polster cell migratory behaviour (Fig. 24A). Before we had time to explore new culture conditions like culture on E-Cadherin, COVID lockdown abruptly halted our collaboration.

As a way to observe interactions between individual cells and dissect the mechanisms leading to collectiveness, I used the animal pole of gastrulating embryos as a substitute for cell culture (Fig. 25A, B & D). This region is devoid of hypoblast cells until late gastrulation. Induced polster cells transplanted at the animal pole internalise and form a flat and loose monolayered tissue that spreads rather isotropically. Cells then migrate randomly, colliding and forming clusters, allowing me to quantify individual collisions events.

Polster cells do not exhibit contact inhibition of locomotion

I first tested the presence of CIL in polster cells by performing mixing assays (Carmona-Fontaine et al., 2008). Two groups of differently labelled polster cells were transplanted next to each other at the animal pole of an early gastrula embryo (Fig. 25A). In neural crest cells, such groups form a sharp boundary, which was not the case in our system, the two groups largely interpenetrating after 90 minutes. As a control, we numerically simulated the interpenetration of two adjacent groups of polster cells in presence or absence of CIL (see Fig. 37 & Fig. 38A). We observed that in presence of CIL, simulated groups indeed formed a sharp boundary while absence of CIL gave results similar to experiments. This suggests absence of CIL behaviour in polster cells.

While doing simulations, we observed that final interpenetration depends for a large part on the initial overlap. Even with CIL, simulated groups that initially overlap may largely mix by the end of the simulation. It is experimentally hard to avoid initial overlap when transplanting cells at the animal pole, especially since they disperse a bit while internalising. Furthermore, varying the initial number of cells

in simulations revealed that, even with CIL, the two tissues can overlap quite extensively if the initial cell number, and thus the final density is too low. Collision between cells then become rare so that cells do not often change direction due to cell-cell contacts.

We thus needed another approach to confirm the absence of CIL. The definition of this behaviour is a modification of cell trajectory upon collision (Carmona-Fontaine et al., 2008). I thus transplanted polster cells expressing H2B-mCherry at the animal pole of a host embryo, tracked their movements, and measured their change in direction upon collision with another polster cell (Fig. 25B). I collected 41 instances of cell collisions, corresponding to 82 changes of direction. The deflection I measured corresponds to the angle between the displacement vector over 9 minutes before collision and 9 minutes after collision. I observed very little change in trajectories upon contact, especially compared to what has been described in neural crest cells. As a control, I compared collision deflection to the natural tendency of these cells to change direction in absence of collision. I generated 100 bootstrapped datasets made of 80 randomly selected, contact-less time points. I then computed the "deflection" angle for each of these points, which represents the innate propensity of these cells to change direction while migrating unperturbed. I finally compared each of these bootstrapped datasets to the actual dataset corresponding to collisions. Out of 100, only one is significantly different from the real collision dataset, which is less than what is expected by chance with an α risk of 5%. This again argues against any CIL behaviour as cell trajectories do not seem particularly affected upon contact with other cells. On the contrary, in 63% of the contacts, cells adhere and migrate together.

Polster cells do not exhibit co-attraction

I then assessed whether polster cells exhibit a co-attraction behaviour by reproducing results obtained with Xenopus neural crest cells (Carmona-Fontaine et al., 2011). In these experiments, authors transplanted neural crest cells near the endogenous stream of cells, which biased migration of transplanted cells toward endogenous ones. In a similar fashion, I thus transplanted a single, actin labelled polster cell in front of the polster of unlabelled hosts (Fig. 25C). I tracked the motion of these isolated cells, as well as quantified protrusion orientation. Before contact, 65% of cells (11/17) have a net motion toward the polster. This movement is however limited, weakly persistent and orientation of protrusions is almost randomised. It is thus not clear whether the polster-oriented movement of transplanted cells is due to attraction. This movement could be due to a drag applied by overlying ectoderm that undergoes epiboly, moving toward the vegetal pole (Smutny et al., 2017). I indeed observed that motion of cells transplanted at the animal pole (like in Fig 25A,B & D) correlates with movement of the overlying ectoderm, although weakly ($r=0.23$). Comparatively, once transplanted cells were contacted by the polster, they adopt a very persistent trajectory and oriented protrusions. It thus not possible to conclude from this experiment alone.

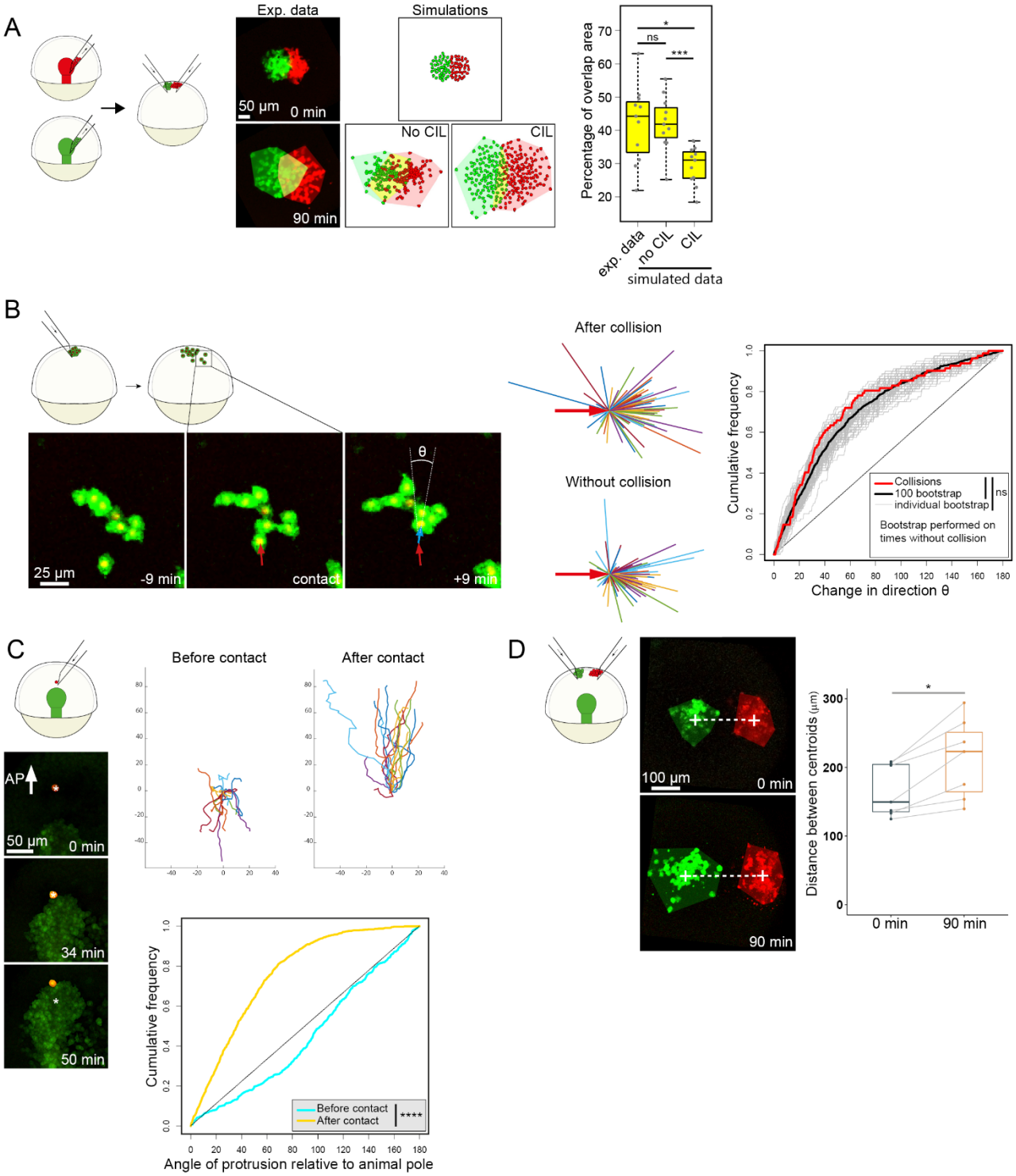

Figure 25: Polster cells do not exhibit CIL nor CoA. A: Group mixing assay: transplantation of two adjacent, differently labelled groups of polster cells (red and green). Simulated cells display migration characteristics similar to polster cells (see also Figure S4), with or without CIL behaviour. Overlap, highlighted in yellow, is measured at 90 min for experimental (n=11 embryos) and simulated data. **B**: Collisions of polster cells transplanted at the animal pole. Change in direction (θ) is measured as the angle between the displacement vector before (red arrow) and after (other colours) a given time step, upon collision or not. Cumulative frequency of angle θ is displayed. Red: change in direction upon collision (n=82 cells); grey: 100 bootstrapped datasets of change in direction in absence of collision; black: combination of all 100 bootstrapped datasets. **C**: Unique cells transplanted 58±25 µm ahead of the polster (n=19 cells). Cell trajectories and orientation of actin-rich protrusions (angle between the direction of the protrusion and the direction of the animal pole) are displayed before and after contact with the polster. Asterisks mark the initial position of the transplanted cell; white arrow indicates direction of the Animal Pole (AP). In all following figures, animal pole is located at the top. **D**: Group attraction assay: transplantation of two differently labelled groups of polster cells (n=7 embryos), initially 166±38 µm apart. White crosses mark group centroids; dashed lines mark the distance between centroids, which is plotted at 0 and 90 min. In this and following figures, ns: p.value ≥0.05; *: p<0.05; **: p<0.01; ***: $p<10^{-3}$; ****: $p<10^{-4}$.

To clarify the situation, I reproduced a last experiment by transplanting two groups of differently labelled polster cells at the animal pole, separated by some distance (Fig. 25D) (Carmona-Fontaine et al., 2011). In vitro, Xenopus neural crest cell groups in such a configuration attract each other and ultimately enter in contact. After 90 min, the distance between the centroids of polster cell groups had increased by 47±28 µm, arguing against any co-attraction. Furthermore, I observed that groups of cells at the animal pole spread as small clusters or isolated cells, they did not remain compact as would be expected in case of co-attraction.

Despite the fact that I reproduced all seminal experiments that established CIL and CoA behaviours in Xenopus neural crest cells, I could not detect any sign of them in polster cells and thus had to discard the hypothesis of a similar mechanism between the two types of cells. These experiments were exciting as they suggested that polster collective migration is ensured by a different, unknown mechanism that I had to explore. In particular, the model proposed in Dumortier et al. (2012) suggested that the information of direction is somehow contained in the polster.

Polster guidance is ensured by contact with the elongating posterior axial mesoderm

Development of deep spatially resolved 3D laser ablations

How is the polster oriented? Previously published observations that individual or small groups of cells transplanted ahead of the polster do not display oriented motion suggested that orientation is likely not the result of a pre-patterned gradient of chemoattractant (Dumortier et al., 2012). It rather seems that this information is transmitted through cell-cell contact as cells touching polster front became oriented. This result might suggest that a particular subset of cells has an instructive role in the polster, or that given its size, the polster might act as a sink, locally generating its own gradient. These two possibilities are not mutually exclusive as a particular population of cells in the polster could act as a sink, generating the gradient, much like in the PLLp (Donà et al., 2013; Venkiteswaran et al., 2013). Indeed, despite seemingly uniform in terms of cell shape and behaviour (Fig. 19B, 20B, 23A, 26A), a few genes are known to be expressed only in specific parts of the polster. *dkk1*, for example, is expressed by a line of cells all along the border of the tissue (Johansson et al., 2019), while Pcdh18a is expressed by a subpopulation of prechordal plate cells, just behind the polster (Bosze et al., 2020). I thus sought to map the origin of this directional information by finding the smallest unit able to migrate on its own. One simple way to find out if a domain is required for orientation is to remove it and look for potential effects on directionality. This can be achieved using several approaches, like microsurgery (Shih & Fraser, 1996) or induced cell death by localised activation of a photosensitizer like KillerRed (Bulina et al., 2005). These two approaches are, however, either too slow or too inaccurate and invasive to give exploitable results. I thus chose laser ablation, which is a good way to rapidly and accurately kill groups of cells in an embryo (Volpe et al., 2020).

The polster is a deep tissue, located under several layers of epiblast cells, and above the fragile yolk cell (Fig. 26A, B). Precise ablation of polster cells thus requires high power, low scattering, and good axial resolution. Standard ablation protocols use UV lasers, for their high energy but such light is strongly scattered by biological samples and can only be used for ablation of superficial structures (Volpe et al., 2020). I thus turned toward non-linear optics (so-called two-photon microscopy) that uses non-linear properties of light to excite a fluorophore with two photons of approximately half-energy, in the infrared domain (Smith et al., 2009). The use of femtosecond pulsed infrared lasers allows reaching deep structures and destroy tissues by plasma generation only in the focal volume (Rauzi & Lenne, 2011). Thus, two-photon laser ablations can be used to precisely target deep cells without affecting the environment. I took advantage of the experience of my laboratory in non-linear optics and the presence of a microscope equipped with pulsed infrared lasers (later referred to as 2-photon microscope) to develop a protocol for ablating deep polster cells.

I chose for ablation a wavelength of 820 nm as it is, on our system, the wavelength providing the highest peak energies, due to laser and optics properties. In agreement with the literature, I observed that it is better to apply several treatments at a moderately high energy than to use high laser power. I also observed that deeper cells required more power or treatment repetitions to be ablated. I thus set the exit power to 300 mW and calibrated for each depth the number of successive treatments required to ablate tissue. Intense treatment resulted in the presence of autofluorescent debris that seem to interfere with the migration of neighbouring cells. I selected the number of treatment for each depth to minimise their presence in the ablated area. I thus obtained a reproducible protocol that allowed me to ablate cells as deep as 120 µm while generating a reasonable amount of debris. Finally, 3D-ness was obtained by ablating several successive planes at different depths in the embryo, starting from the bottom of the polster, just above the yolk cell, up to the interface with the ectoderm.

I used this protocol to remove a two cell diameter wide stripe at the rear of the polster (Fig. 26B & D). Embryos were then unmounted and placed back in the incubator. At 24 hpf, 42 out of 44 embryos had survived and developed correctly, showing that the laser treatment is not harmful for development in the long-term (Fig 26C). Using this protocol, which has been published (see Appendix) (Boutillon et al., 2021), I could probe the polster and find where the information of direction is located.

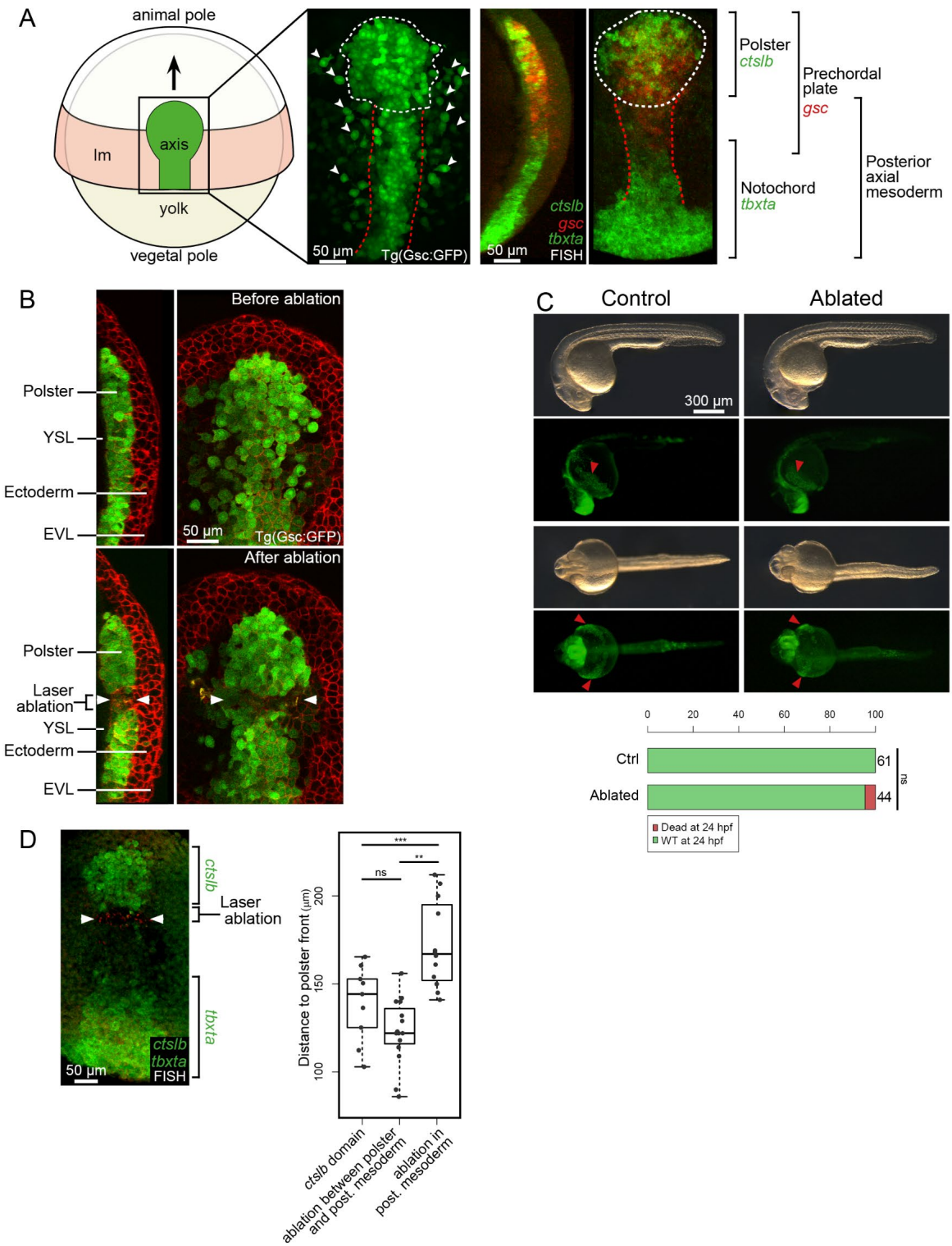

Figure 26. Polster and laser ablations. A: Scheme of a gastrulating embryo at 70% epiboly in dorsal view; lm: lateral mesoderm; black arrow marks the direction of polster migration. Close-ups on the forming embryonic axis in *Tg(gsc:GFP)* embryo where axis is labelled in green, along with some endodermal cells (white line delineates the polster; red lines mark the posterior axial mesoderm; arrowheads point to some endodermal cells), and in a fluorescent in situ hybridisation (FISH) for different antero-posterior markers of the axis (sagittal and dorsal views). Polster precursors expressing ctslb and notochord precursors expressing tbxta appear in green, prechordal plate progenitors expressing gsc appear in red. **B**: Representative *Tg(gsc:GFP)* embryo before and after laser ablation, here between the polster and the following mesoderm. Sagittal and dorsal views. Membranes are labelled in red by expression of mCherry-CAAX. Ablation is located between white arrowheads. YSL: yolk syncytial layer; EVL: enveloping layer. **C**: Morphology and survival of control and ablated *Tg(gsc:GFP)* embryos at 24 hpf. Polster derivative, the hatching gland, is indicated by red arrowheads. **D**: Fluorescent in situ hybridisation for ctslb and tbxta on a representative embryo ablated at the interface between the polster and the posterior axial mesoderm. Position of the ablation is visible through red autofluorescent debris. Distance between the front of the polster and either the posterior edge of the ctslb domain, the position of ablations between the polster and following mesoderm, and of ablations within the following mesoderm.

Directional information guiding the polster is not contained within the polster.

As described in the introduction, collective migration often relies on a specific subgroup of cells at the front of the migrating tissue called leader cells (Fig. 14) (Haeger et al., 2015; Vishwakarma et al., 2020b). These cells adopt a particular morphology, usually forming large protrusions, and drag following cells that in turn form smaller, cryptic lamellipodia. I thus tested if leader cells guide polster migration by removing the first row of cells (Fig. 27A). Individual cell migration was recorded in experiments where nuclei were labelled by H2B-mCherry and tracked over time (Fig. 27B, 28) while protrusion orientation was quantified on actin labelled cells transplanted in unlabelled hosts (Fig. 27C) (see Methods, Fig. 49 & Appendix) (Boutillon et al., 2018).

I quantified cell migration before and after removal of the most animal row of cells and measured for each cell both instantaneous speed, referred to as absolute speed, and its axial component, in the direction of the animal pole, referred to as axial speed (Fig. 27A, 28B). Ablation of front cells did not affect absolute nor axial speed of follower polster cells, suggesting that front cells are not particularly required to drive migration. Accordingly, ablation of front cells had no significant effect either on protrusion orientation of follower cells, confirming that front cells are not required to guide them (Fig. 27C). This result is consistent with the observation that front and follower polster cells have no obvious difference in terms of morphology, migration behaviour or protrusion orientation, shape and dynamics (Fig. 20B). It is to note though that cells at the front of the polster are slightly more oriented than follower cells, which could be explained by the fact that these cells have free space in front of them and forming protrusion might be easier in that direction.

To identify the source of directional information, I then performed ablations at different antero-posterior positions (Fig. 27A). I first wondered whether the anterior half of the tissue might orient its migration. Indeed, isolated, non-oriented cells acquired orientation upon contact with polster front. Hence, a specific group of cell might drive migration as is the case in PLLp migration. I thus isolated the anterior half from the posterior part by removing two transversal rows of cells in the middle of the polster.

Interestingly, once isolated, anterior cells were still migrating, as absolute speed was not affected by ablation (Fig. 28B). However, axial speed dramatically decreased, suggesting that polster cells lose directionality (Fig. 27B). I therefore checked orientation of anterior cells before and after ablation and accordingly observed that isolation led to an almost complete loss of cell orientation (Fig. 27C). Hence, the anterior half of the polster seems unable to orient its migration upon isolation. This is consistent with the observation that small groups placed ahead of the polster are motile but not oriented.

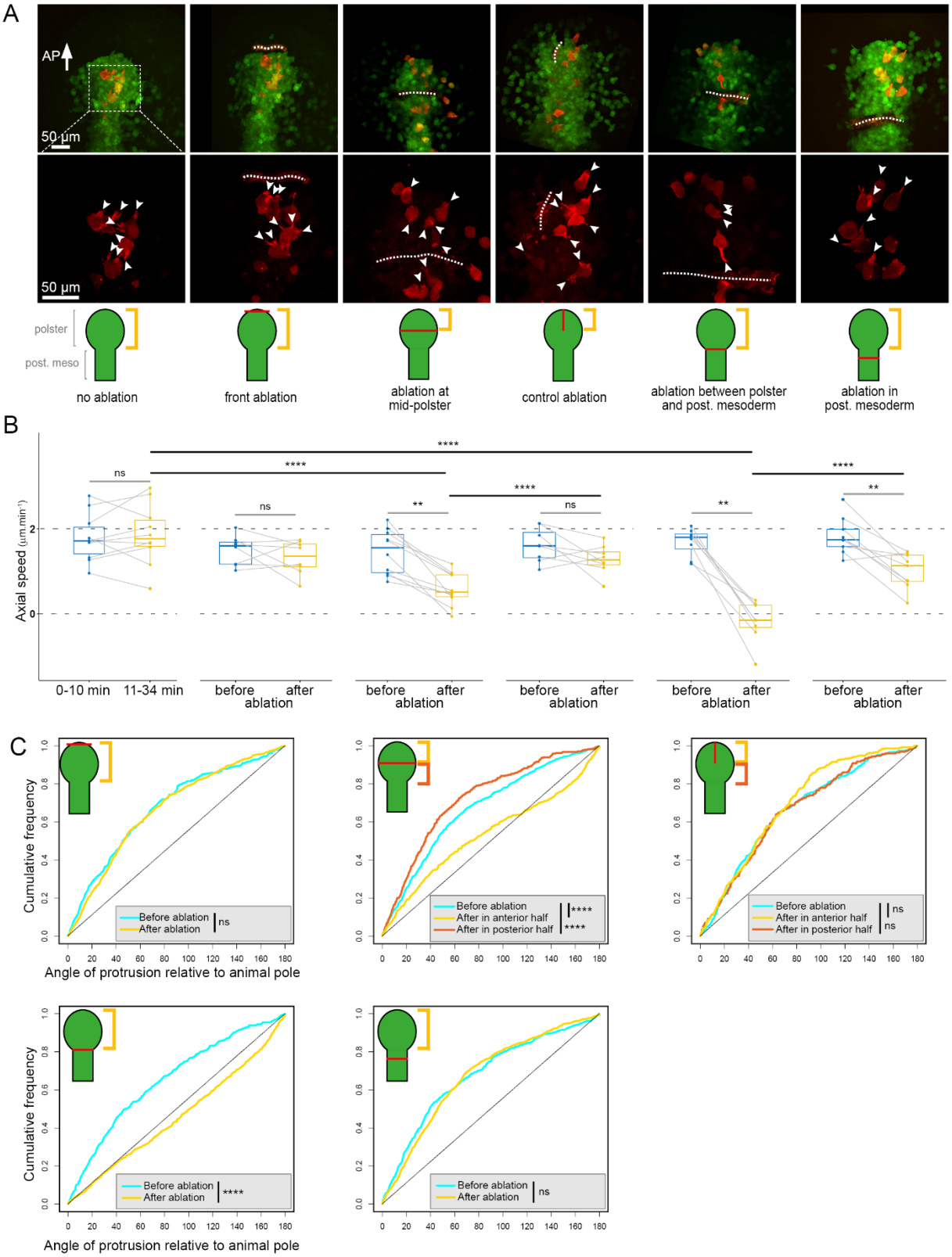

Figure 27. Directional information is not contained in the polster. A: Laser ablations at varying antero-posterior positions and/or orientations. Representative images of ablations, taken from experiments in which a few Lifeact-mCherry expressing cells were transplanted in the polster, to quantify protrusion orientation. Position of the ablation is indicated by a white dashed line on experimental images, and a red line on schematics; arrowheads mark actin rich protrusions; white arrow indicates direction of the Animal Pole (AP). **B**: Axial speed of polster cells, tracked by H2B-mCherry labelling of their nucleus, n=8 to 10 embryos, 149±11 quantified cells per embryos. Gray bars indicate paired statistical tests on embryos before and after ablation. **C**: Orientation of actin rich protrusions in Lifeact-mCherry labelled cells. Numbers of quantified cells were respectively 27 in 4 embryos; 24 in 4 embryos; 17 in 3 embryos; 34 in 5 embryos; 24 in 3 embryos. (B-C) Schematics indicate the position of ablation; yellow and orange brackets indicate the region of the polster quantified after ablation.

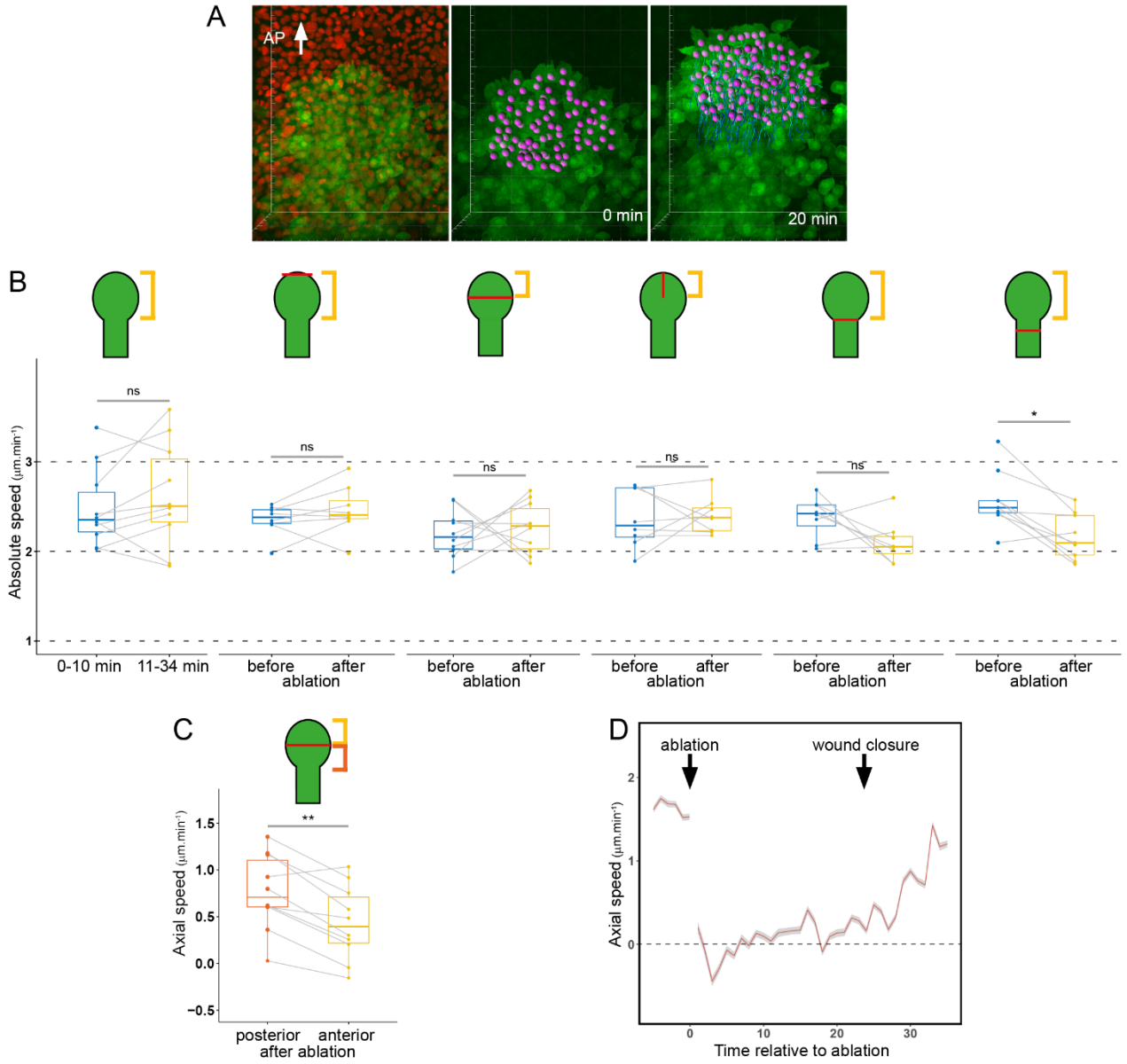

Figure 28. Migration speed of polster cells after laser ablations. A: 3D views of polster and axial mesoderm (green) migration, in a *Tg(gsc:GFP)* embryo expressing H2B-mCherry (red). Nuclei belonging to the polster are highlighted in magenta and tracked over time. AP: animal pole. **B**: Absolute speed of polster cells in control and ablated embryos, corresponding to the axial speeds presented in Figure 2. **C**: Axial speed of the anterior and posterior parts of the polster after ablation in its middle. (B-C) Schematics indicate the position of ablation; yellow and orange brackets indicate the region of the polster quantified after ablation. Gray bars indicate paired statistical tests on embryos before and after ablation. **D**: Axial speed of polster cells in embryos ablated between the polster and the posterior mesoderm, as a function of time (n=6 embryos). Black arrows indicate the moment of the ablation and the average moment of wound healing.

Laser ablations are known to generate cellular debris and release cytoplasmic components that may locally perturb signalling (Rock & Kono, 2008). We thus wondered whether this effect was artefactual, due to a large number of destroyed cells. As a control for non-specific effects induced by laser ablation, I performed sagittal ablations, parallel to the direction of migration, separating the left and right anterior polster, but leaving each side in contact with the posterior polster (Fig. 27A). This experiment leads to some cell destruction without cell isolation. In such ablations, cells around the wound slightly deviate to fill the wound but neither the absolute speed, nor the axial speed, nor the cell orientation were affected, suggesting that laser ablation in itself is not the cause for stalling of the isolated group (Fig. 27B & C, Fig. 28B). Hence, information of direction is not located in the anterior half.

I observed, doing such experiments that the posterior group of cells was still migrating forward, though at a slower pace, and that these cells were still oriented (Fig. 27C, Fig. 28C). This suggests that these cells still receive direction information and, consequently, that this information might simply be contained in the posterior part. Aiming to see whether rear of the polster is able to drive migration of the tissue, I performed ablations at the interface between the polster and the posterior axial mesoderm (Fig. 27A). The precise position of this ablation was based on morphological criteria, the polster forming an oval-shaped tissue, the posterior axial mesoderm a narrower rectangle. This location has been confirmed by in situ hybridisation against *ctslb/hgg1*, labelling the polster, on embryos fixed just after ablation (Fig. 26D). Strikingly, isolation of the polster led to complete disruption of oriented motion (Fig. 27B). Once again, absolute speed remained constant, suggesting no inhibition of cell motion, but average axial speed was almost null, and cell orientation random (Fig. 27C, Fig. 28B). Interestingly, I observed a tendency for cells at the front to move and protrude forward, cells at the rear backward, and cells in the middle randomly. This is very similar to groups of polster cells transplanted at the animal pole, which spreads isotropically as if deprived of an orienting cue (Fig. 25A, D). This surprising result led us to conclude that the hypothesis we had proposed in (Dumortier et al., 2012), knowingly that information of direction is contained in the polster, is incorrect. At this point, we were struck by the fact that polster cells were oriented as long as they were connected to the posterior axial mesoderm. Perhaps the source of directionality is not in the polster itself, but behind?

Contact with the following axial mesoderm is required for polster oriented migration

To directly test if the following axial mesoderm is actually instructing polster migration, I performed more posterior laser ablations, leaving some axial mesoderm in contact with the polster (3.7±1 rows of cells) (Fig. 26D, Fig. 27A). I observed that keeping some axial mesoderm cells in contact largely restored polster migration compared to ablations at the interface (Fig. 27B). Cell orientation was also restored compared to ablation at the interface, which is consistent with higher axial speed (Fig.

27C). These results show that contact between polster and axial mesoderm is necessary for proper orientation and migration of polster cells. Two observations are nonetheless surprising. First, absolute speed of polster cells is slightly decreased after ablation, while it stayed constant for all other ablations (Fig. 28B). Second, after ablation, axial speed was slightly decreased despite an orientation that is completely unaffected (Fig. 27B & C). Actually, lower axial speed might simply be due to the decrease of absolute speed, but the reason for this decrease is unclear. The fact that polster orientation relies on contact with posterior mesoderm is coherent with the observation that the wound created by separating the polster in two halves quickly closes (24±2 min, n=14 embryos) (Fig. 28D). Furthermore, when a group of cells is isolated by ablation, migration resumes in a few minutes after contact with posterior cells, leading to normal development at 24 hpf (Fig. 26C).

Ablation in the posterior mesoderm led to other interesting observations. First, posterior mesoderm continued to extend despite being isolated from the polster, suggesting that axial mesoderm is able to extend without the help of the polster. Second, in case of ablation is the posterior mesoderm, the few rows of cells kept behind the polster continued to exhibit some convergence and extension behaviour. This is consistent with the observation of Bosze et al. (2020) that a small piece of posterior axial mesoderm is able to autonomously reproduce to some extent the behaviour of the whole tissue.

As they completely challenge the classical views explaining polster migration, these results were unexpected and we still wondered whether they could be due to local laser perturbation. One could imagine that somehow, isolation by ablation locally inhibits orientation and that, in the last condition, the ablation being far from polster cells, they could freely migrate. We thus sought a way to confirm these results with a second, independent approach. As mentioned before, despite being less precise than laser ablation, microsurgery is a reliable way to perform cell or tissue removal. I thus reproduced the experiment of ablation at polster-posterior mesoderm interface using microsurgery and transplantation. First, using large glass pipettes, I removed the endogenous polster from *Tg(gsc:GFP)* embryos. Strikingly, in such embryos, axial mesoderm continues elongating, though slightly slower, which supports the idea that axis extension does not require the polster (Fig. 29A & B).

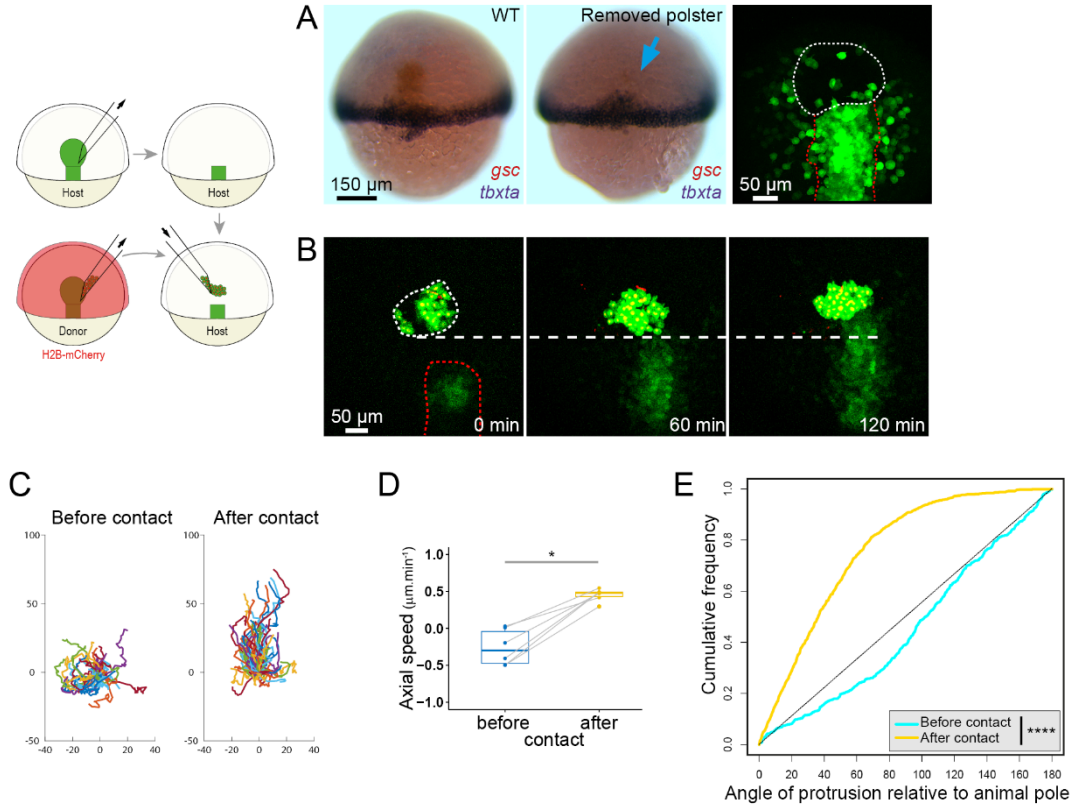

Figure 29. Polster oriented migration requires contact with posterior axial mesoderm. A: Removal of the polster revealed by in situ hybridisation for *gsc* (red) and *tbxta/ntl* (blue) or fluorescence in the *Tg(gsc:GFP)* line. The blue arrow and thin white line mark the former polster position; red lines mark posterior axial mesoderm. **B**: Transplantation of 59±51 polster cells, 106±43 µm ahead of the axis. The thin white line delineates transplanted cells; horizontal line marks the initial position of the rear of the transplanted group. **C-E**: Trajectories (C), axial speed (D) (average of all transplanted cells in each embryo, n=6 embryos) and actin rich protrusion orientations (E) (n=15 Lifeact-mCherry labelled cells in 5 embryos) of transplanted cells. Gray bars indicate paired statistical tests.

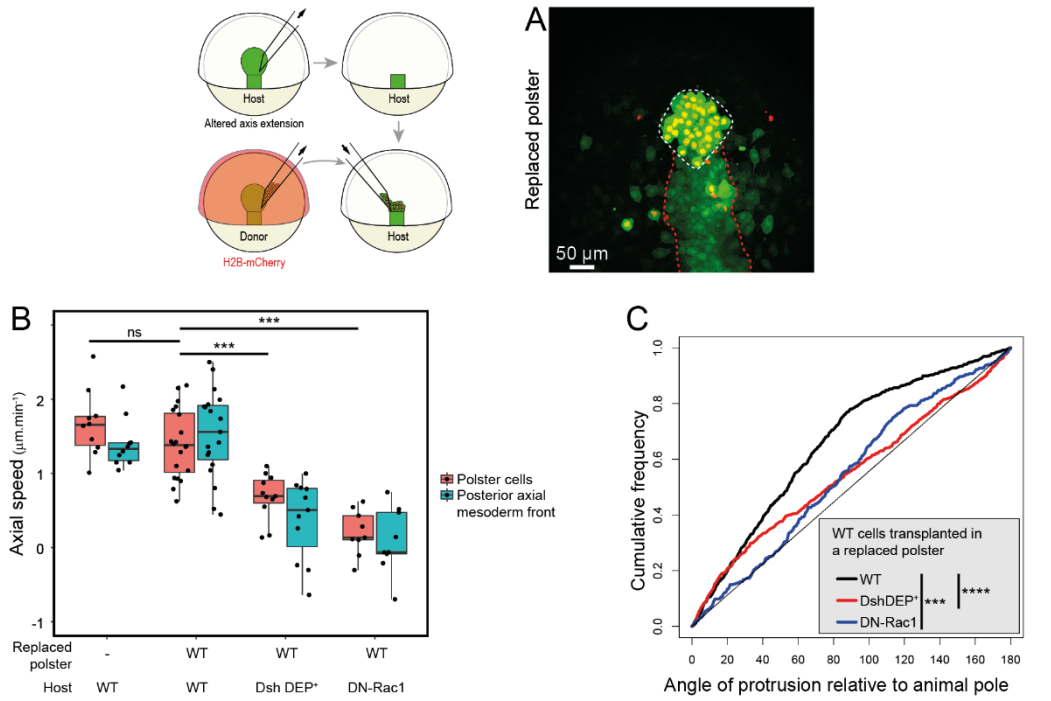

Figure 30. Orientation of polster cells requires active migration of the following axial mesoderm. A: Wild type polster replacement. The polster of an unlabelled host was removed (see Fig. 29) and induced polster cells (red nuclei) were transplanted at the place formerly occupied by the polster. White line marks transplanted polster cells and red line marks following axial mesoderm. **B**: Axial speed of polster cells (red boxes) and front of posterior axial mesoderm (blue boxes). Polster cells either belong to the endogenous polster of a wild type embryo (-) or are wild type (WT) cells transplanted in a host. In DshDEP+ and DN-Rac1 host conditions, axis extension is genetically slowed down. **C**: Protrusion orientation of wild type polster cells transplanted in a host embryo.

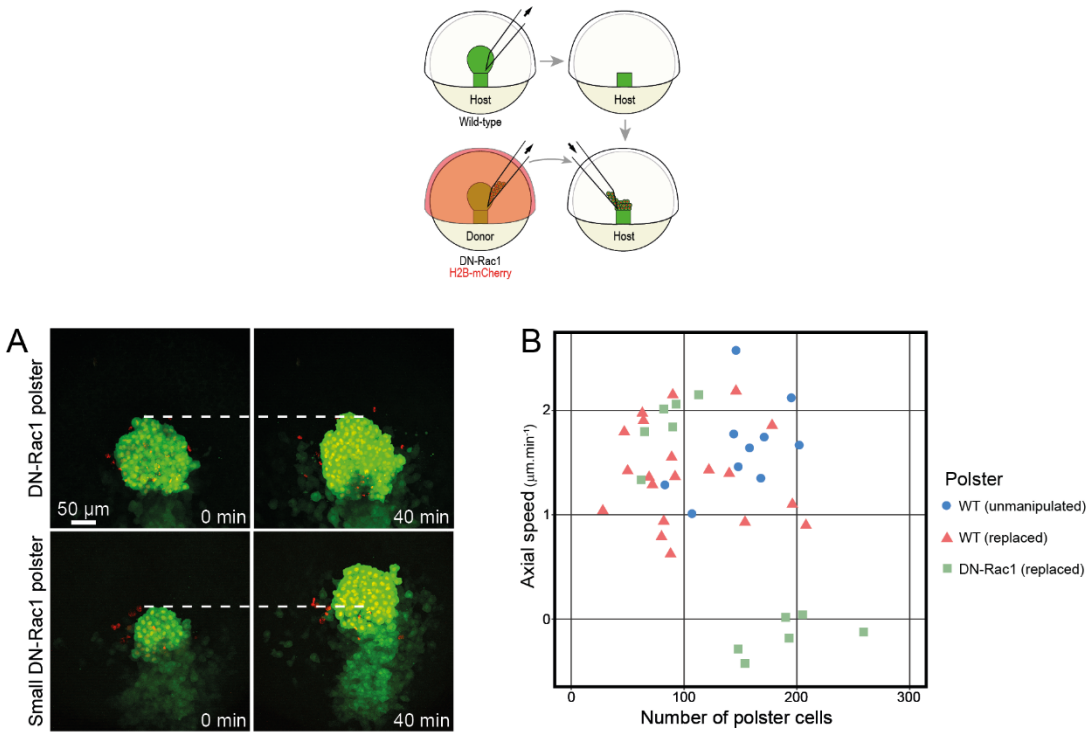

Figure 31. Active migration of polster cells is required for axis elongation. A: Replacement of the polster by a WT polster or a DN-Rac1 expressing polster, of varying size (red nuclei). Lines mark the initial position of the polster front. **B**: Axial speed of transplanted polster cells as a function of group size. Unmanipulated WT embryos have been quantified for comparison (blue circle).

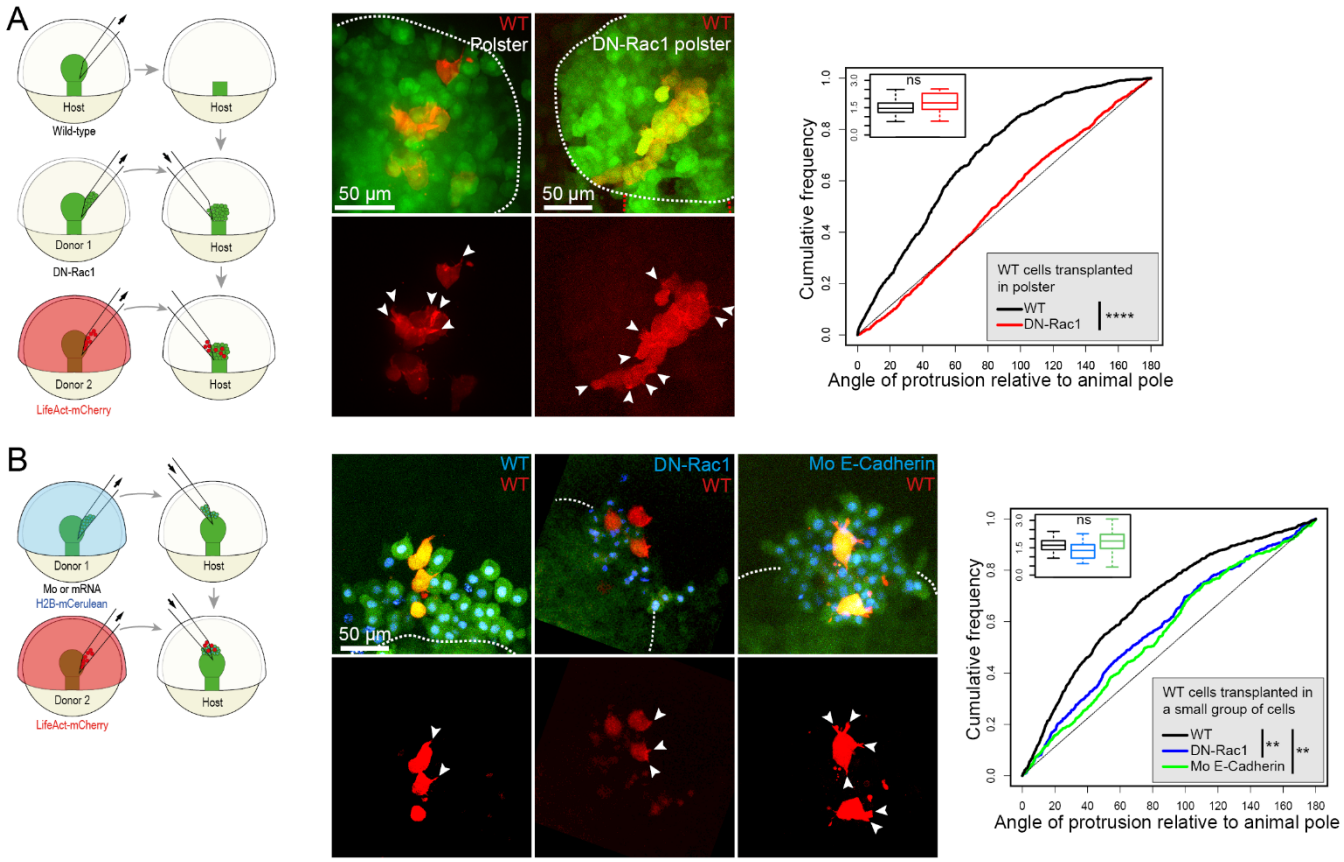

Figure 32. Polster cell orientation requires actively migrating neighbours. A: Protrusion orientation of actin labelled WT cells (red) transplanted in WT pollsters (33 cells in 7 embryos) and DN-Rac1 transplanted polsters (see Fig. 31A) (33 cells in 7 embryos and 29 cells in 4 embryos, respectively). Inlay indicates the average number of protrusions per frame for each condition. **B**: Protrusion orientation of actin labelled WT cells (red) transplanted among a small group of WT, DN-Rac1 or Mo E-Cadherin cells labelled with H2B-mCerulean (blue nuclei), in front of a WT polster (25 red cells in 6 embryos, 19 cells in 7 embryos and 11 cells in 6 embryos respectively). Inlay indicates the average number of protrusions per frame for each condition. White lines mark the endogenous polster of host embryos.

After removing the polster in host embryos, I transplanted a group of polster cells, with H2B-mCherry labelled nuclei, ahead of the polster-less axial mesoderm (Fig. 29B). While isolated, these cells spread isotropically, migrating without any preferred direction. This, again, is consistent with the observation that polster cells alone tend to disperse. In contrast, after contact with the axial mesoderm, polster cells displayed oriented migration toward the animal pole (Fig. 29C & D). Repeating this experiment with some Lifeact-mCherry-labelled cells among the transplanted polster cells, I observed that cell protrusion orientation was randomly distributed before contact but became oriented toward the animal pole once the transplanted group was contacted by the axial mesoderm (Fig. 29E). These experiments, laser ablations and microsurgery, demonstrate that the polster requires contact with the following axial mesoderm to orient its migration toward the animal pole.

Extension of the axial mesoderm is required for polster migration orientation

We then wanted to understand how the posterior axial mesoderm drives polster migration. In particular, do posterior axial cells just need to be there or do they have to be active in some way? We thus wondered whether polster cells simply required contact with the axial mesoderm, or if they required the animalward movement of the axis undergoing convergence and extension (Myers et al., 2002).

Addressing this question is trickier than it seems. Indeed, the simplest way to test whether posterior mesoderm extension is required is to slow it down and observe whether this affects polster migration. Many signalling pathways involved in convergence and extension have been described and several tools to perturb these pathways already exist (Heisenberg et al., 2000; Johansson et al., 2019; Krens et al., 2017; Montero et al., 2003). It is thus easy to disrupt extension of axial mesoderm. The point is that most of these pathways are also required for polster cell migration, sometimes in a cell-autonomous manner (Fig. 23B & C) (Dumortier et al., 2012). I thus had to find a way to decouple effects on the two tissues. Using microsurgery, I was able to remove the polster of a host embryo and replace it by polster cells from another embryo (Fig. 30). I could thus affect independently cell-autonomous signalling in host and donor.

In order to make sure that polster replacement does not perturb development, I performed control experiments, transplanting wild type, Histone2B-mCherry labelled polster cells in an unlabelled host (Fig. 30A). At first sight, transplanted cells behave like a regular polster, migrating straight toward the animal pole with the posterior mesoderm extending behind. I tracked cell nuclei and observed that axial speed of transplanted cells, as well as of posterior mesoderm front is similar to wild type, unmanipulated embryos (Fig. 30B). At 24 hpf, the eye field of transplanted embryo is separated and labelled cells are located in the hatching gland, suggesting that the replaced polster behaves normally and that transplantation has no particular effect on development.

As mentioned in the introduction, the non-canonical Wnt-PCP pathway is involved in axis extension, required for the convergence component of the convergence and extension behaviour (Čapek et al., 2019; Heisenberg et al., 2000; Ulrich et al., 2005). Indeed, the well-described *slb*/*wnt11* mutant displays a shorter and wider axis, along with cyclopia, indicating that the polster does not migrate far enough to separate the eye field (Heisenberg et al., 2000). However, Wnt11 is a diffusible ligand, also expressed by polster cells. Hence, transplanting a wild type replaced polster might restore Wnt11 function and axis extension. In order to target the non-canonical Wnt/PCP pathway in a cell-autonomous manner, I used expression of Dsh-DEP+, a dominant negative form of Dsh, specifically inhibiting this pathway (Tada & Smith, 2000). Accordingly, this resulted in strongly slowed axial mesoderm extension and wider and shorter axis, as observed in the *slb* mutant (Fig. 30B). Importantly, in Dsh-DEP+ expressing embryos, a transplanted, wild-type polster showed a similar reduction in speed, as well as in protrusion orientation (Fig. 30B & C). The observation that a wild type polster in contact with a slowly elongating axis does not migrate properly suggests that polster cells do not receive proper direction information.

In order to confirm this observation, I used expression of Rac1 N17, a dominant negative form of the Rac1 small GTPase (DN-Rac1) (Tahinci & Symes, 2003) that dramatically slows down axial mesoderm extension. I replaced the polster of embryos expressing DN-Rac1 with wild-type cells and observed that their animalward movement was essentially abrogated (Fig. 30B & C). These results demonstrate that extension of axial mesoderm is required for the migration of the polster.

Mechanism underlying polster cell orientation

Active migration of polster cells is required for axis elongation

What is the mechanism ensuring guidance of polster migration by elongation of posterior axial mesoderm? The observation that axial mesoderm extends without polster cells, and that this extension is required for polster migration raises the possibility that the polster is simply passively pushed toward the animal pole by the independently-extending axis. To test whether individual migration of polster cells is required for polster movement, I used DN-Rac1 to inhibit their migration (Dumortier et al., 2012), and then replaced the polster of a wild type embryo by these non-motile cells (Fig. 31). DN-Rac1 expressing cells indeed adopt a very round morphology and a strong tendency to bleb while forming almost no protrusions. Once transplanted, they form a compact cluster, that do not internalise well, as is expected since Rac1 is required for cell ingression. I thus had to take extra care to transplant them directly in the hypoblast, in contact with the yolk.

Strikingly, a DN-Rac1-expressing polster replacing that of a wild-type embryo did not move toward the animal pole and blocked the elongation of the axial mesoderm (Fig. 31A & B). Axial cells accumulated behind the immobile polster and, in some cases, the axis buckled as extension carried on.

This result establishes that polster is not passively pushed and that active migration of its cells is required for proper axis elongation. During some replications of the experiment, I happened to transplant groups of DN-Rac1 expressing cells smaller than a regular polster (Fig. 31A & B). In such cases I noticed that, these cells, while non-motile, were efficiently displaced toward the animal pole by the extending axis, demonstrating that extension of the axis does generate pushing forces, though not sufficient to displace an entire polster. Still, we have not yet explained how the posterior mesoderm orients this polster migration, required for axial mesoderm extension.

Polster cells can be oriented by another migrating tissue

Up to this point, it is still not clear how posterior axial mesoderm extension is orienting polster migration. One hypothesis would be that there is some orienting or repelling cue that is expressed by the axis. For example, a planar polarity signal transmitted from the axis to the polster seems a good candidate. In this case, axis extension would be required to maintain contact and hence transmission of the chemical cue between the two tissues. Alternatively, axis elongation itself could provide a mechanical information detected by polster and used as an orienting cue. This second hypothesis is appealing, in particular since the Wnt/PCP pathway is not described as instructive for polster migration. To distinguish between mechanical and chemical signals, I had to find a way to abolish one but not the other. I thus transplanted actin-labelled wild-type cells into a polster expressing DN-Rac1 (Fig. 32A). Such a polster remains in contact with the axis, so any chemical signal should propagate normally, but is immobile (Fig. 31) so its internal mechanical environment is likely to be perturbed. In this context, wild-type cells formed protrusions, at the same frequency as in a wild-type replaced polster. Strikingly, however, protrusion orientation of labelled cells was randomised. It thus seems that displacement of neighbouring cells is required for polster cell orientation, suggesting that it is movement itself of the neighbours that directs polster cells. Interestingly, this experiment indicates that, besides its well-characterised cell-autonomous role in cell migration, Rac1 has a non-cell-autonomous role in orienting polster cell protrusions.

If these cells become oriented by the movement of more posterior cells rather than a chemical signal emitted by these cells, they may not specifically require interactions with axial mesoderm, but could simply be oriented by other migrating cells. To test this idea, I transplanted polster cells ahead of the lateral mesoderm (Fig. 33). Lateral mesoderm cells, visible in the *Tg(tbx16:GFP)* line, internalise at the embryonic margin, forming a loose monolayer of hypoblast cells that migrate toward the animal pole (Solnica-Krezel et al., 1995). Before contact, polster cells internalised then moved and extended protrusions without preferred orientation, like when transplanted at the animal pole (Fig. 33A-D). Upon contact with the lateral mesoderm, however, they aligned both migration and protrusions with the movement of the lateral mesoderm. It shows that guidance of polster migration is not specific to

posterior axial mesoderm, but can be triggered by contact with another migrating tissue. This again argues against a transmitted chemical signal and rather points toward mechanics as direction information.

Polster cells are oriented by actively migrating and adhering neighbours

What is actually detected by polster cells as an orienting cue? Given the previous results, this signal is likely of mechanical origin. Intuitively, given that posterior axial mesoderm elongates and is able to push small groups of cells, one might think that cells are actually able to sense pushing forces. That would be a surprising result as mechanical pushing has never been described as an orienting cue. At most, is has been described that confinement can trigger changes in modes of migration. On the contrary, mechanoperception is generally linked with detection of traction forces (Charras & Yap, 2018). Nonetheless, pushing an object generates friction with surrounding objects, which might be detected as traction. Alternatively, the detected mechanical signal might be more local and result from tension at contact between cells. Indeed, in epithelia, cell junctions are usually under tension because of cell contractility (Das et al., 2015). It might also be due to protrusion formation in migrating neighbours as Rac1 seems required surrounding cells.

In order to check whether simple pushing forces can orient polster cell migration, I transplanted a few wild-type cells within a small group of DN-Rac1 expressing cells at the front of the polster (Fig. 32B). Transplanted cells are thus still displaced by extension of the axis, the small DN-Rac1 cell cluster being pushed (Fig. 31), but are only in contact with non-motile DN-Rac1 cells. Strikingly, protrusions of wild-type cells without actively migrating neighbours were less oriented than those of wild-type cells in a similar small group of other wild-type cells (Fig. 32B). This suggests that it is not the mere fact of being pushed that orient polster cells, but rather the fact of having actively protruding, motile neighbours. This, furthermore, confirms the non-cell-autonomous role for Rac1 as neighbour cells have to protrude to act as an orienting cue.

How then do cells perceive protrusions from the neighbours? Adherens junctions not only ensure cell-cell adhesion but can also elicit mechanotransduction and are thus good candidates for transmission and perception of mechanical forces in the polster (Charras & Yap, 2018). If cell orientation relies on a mechanical signal, cadherin should be required both within cells to perceive forces, and in neighbouring cells, to apply forces. We previously demonstrated, and I here confirmed, that cell-autonomous *e-cadherin* knock-down by a morpholino leads to a loss of protrusion orientation (Fig. 35A & B) (Dumortier et al., 2012). I made sure that this phenotype is rescued by expression of E-cadherin-GFP, demonstrating the specificity of this morpholino. I then tested whether E-cadherin was required in neighbouring cells, by transplanting wild-type cells within a small *e-cadherin* knocked-down cell cluster (Fig. 32B). The absence of E-cadherin in neighbours also led to a loss of orientation of wild-type cells.

This demonstrates that E-Cadherin is required both within polster cells and in their migrating neighbours to orient cell protrusions, suggesting that E-cadherin transmits forces and the associated directional information.

Polster cell orientation required Myosin II contractility in neighbours

In epithelial tissues, junctional tension is established through Myosin II contractility, which tends to pull on the membrane of each cells. It is thus a good candidate for application of forces at the level of adherens junction in polster cells. We thus wondered whether Myosin II is required for polster cell orientation. I first looked at myosin distribution in polster cells using *Tg(actb2:myl12.1-EGFP)* embryos, that ubiquitously express a fluorescent form of myosin light chain 12.1, labelling non-muscular myosin II (Fig. 34A). I transplanted induced polster cells from such embryos, also expressing Lifeact-mCherry, in the polster of unlabelled embryos. Myosin is distributed all over the cell at a low level, and forms small bright and transitory accumulations, usually at the level of the membrane. I quantified localisation of these cortical spots compared to direction of migration and observed that Myosin II distribution is slightly biased rearward. In several instances, I observed that myosin accumulation was associated with contraction of the membrane, which is consistent with a role of Myosin II in dragging the rear of migrating cells. However, I also observed that Myosin II sometimes accumulates at the basis of protrusions, correlating with the retraction of the protrusion or to a contraction of the membrane at its basis. These observations, although preliminary, are exciting and suggest that these accumulations might be used to exert a pulling force on surrounding cells.

I thus wanted to observe whether non-muscular Myosin II is required for polster cell orientation. In order to perturb myosin activity, I used a dominant negative form of myosin light chain kinase (DN-MLCK) that prevents activation of myosin (Fig. 34B). In particular, its expression in cells transplanted in wild type hosts decreased the number of myosin-GFP accumulations in *Tg(actb2:myl12.1-EGFP)* cells. However, disruption of Myosin II activity in polster cells had no effect on cell orientation, suggesting no cell-autonomous role in cell orientation. This is consistent with the previous observation that the RhoA small GTPase, responsible for myosin distribution and stress fibre formation, has no cell-autonomous orienting role either, as expression of a dominant negative form of RhoA only had a small effect on protrusion (Dumortier et al., 2012). It is thus likely that myosin distribution in the cell is a consequence of a polarisation established beforehand. Still, these accumulations around protrusions were surprising and might be used to pull on neighbours. This rather pointed toward a potential non-cell-autonomous role of Myosin II.

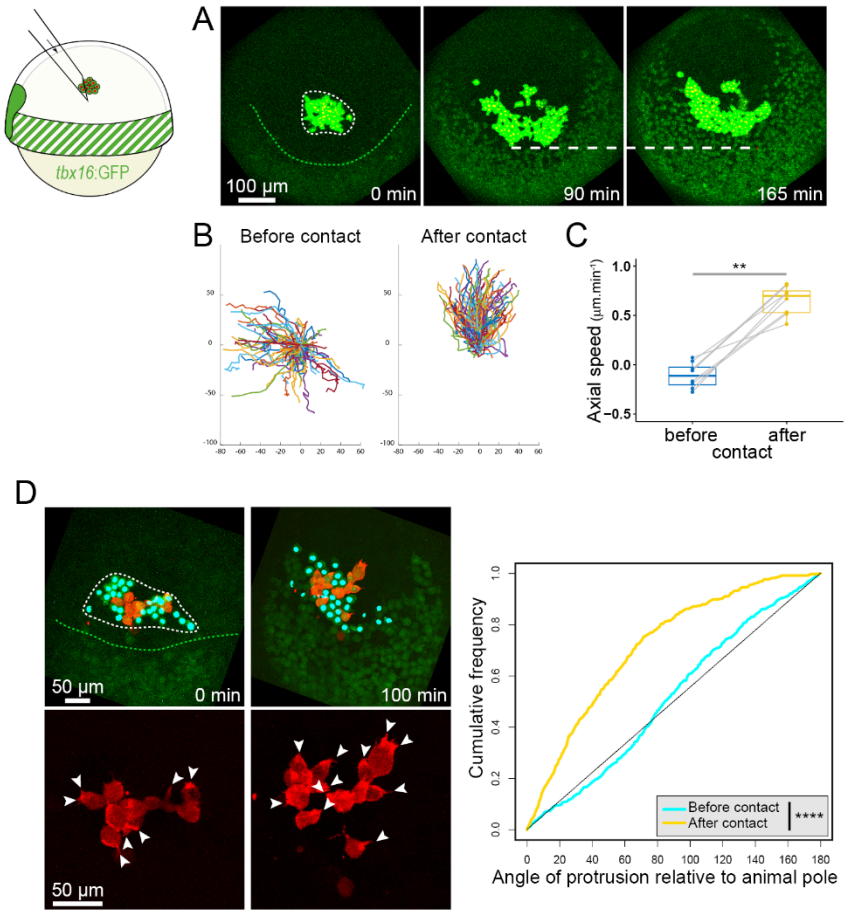

Figure 33. Lateral mesoderm can drive polster cell migration. A: H2B-mCherry expressing polster cells (strong green, red nuclei) were transplanted ahead of the lateral mesoderm (*Tg(tbx16:GFP)*; faint green). A thin white line delineates polster cells; green line marks the lateral mesoderm anterior edge; horizontal line marks the position of the rear of the polster cell group upon contact with the lateral mesoderm. **B**: Polster cell trajectories before and after contact with the lateral mesoderm of a typical experiment. **C**: Axial speed (n=8 embryos) of transplanted polster cells before and after contact with the lateral mesoderm. **D**: Protrusion orientation of Lifeact-mCherry expressing polster cells (red labelled actin) transplanted along with other polster cells expressing H2B-mCerulean (green with blue nuclei) in front of the lateral mesoderm, quantified before and after contact (22 red cells in 3 embryos).

I thus checked whether Myosin II activity was required in neighbour cells. Like before, I transplanted wild-type cells surrounded by DN-MLCK expressing cells in front of the polster of a wild type host (Fig. 34C). Surprisingly, orientation of these wild-type cells was also disrupted. This shows that Myosin II is indeed required for cell orientation but only in a non-cell autonomous manner and indeed support the idea that a mechanical signal is transmitted between cells. This is reminiscent of the process in Drosophila border cells migration, where combination of Myosin II accumulation and actomyosin contractility at the level of E-Cadherin junctions between follower and leader cells is required for maintenance of a protruding leader. We now have to understand how such a mechanical signal is detected by polster cells.

Polster cell orientation requires α-Catenin and Vinculin mediated mechanosensation

Since we established that E-Cadherin is required both cell-autonomously and non-cell-autonomously for polster cell orientation (Fig. 32B, 35A), we hypothesised that adherens junctions are involved in mechanotransduction in polster cells. However, it has been described in some cells that cadherins can influence cell migration without their cytoplasmic domain, in an adhesion and force independent process (Nguyen & Mège, 2016). I thus checked whether the cytoplasmic domain of E-cadherin is required for cell orientation. E-cadherin knocked-down cells, expressing a form of E-cadherin lacking the intracellular domain (E-cadherinΔcyto, Maître et al., 2012), were transplanted into a wild-type polster (Fig. 35A & B). Contrary to wild-type E-cadherin, expression of E-cadherinΔcyto did not rescue protrusion orientation, consistent with a potential mechanotransducer role for E-cadherin.

Looking for downstream effectors of E-cadherin, Plakoglobin was an obvious candidate. In Xenopus polster cells, it is recruited to adherens junctions upon application of tension, contributing to remodelling of intermediate filaments and, ultimately, to modification of cell orientation in response to tension (Fig. 23F) (Sonavane et al., 2017; Weber et al., 2012). We thus checked whether polster cells displayed a similar mechanism. In zebrafish, there are two paralogues of *plakoglobin* (*jupa* & *jupb*) that have never been studied in early embryonic development. A morpholino targeting jupa already existed, which induces cardiac patterning defects (Martin et al., 2009). I designed another morpholino against *jupb* and coinjected both in 1-cell stage embryos. *jupa* & *jupb* double knock-down led to cardiac oedema and embryonic death at 1 and 3 dpf, which is consistent with the phenotype described for *jupa* (Fig. 36A). I thus transplanted actin labelled cells injected the two morpholinos in the polster and measured protrusion orientation (Fig. 35A & C). It appeared that *plakoglobin* knock down did not affect protrusion orientation, excluding a role of Plakoglobin in orientation of these cells.

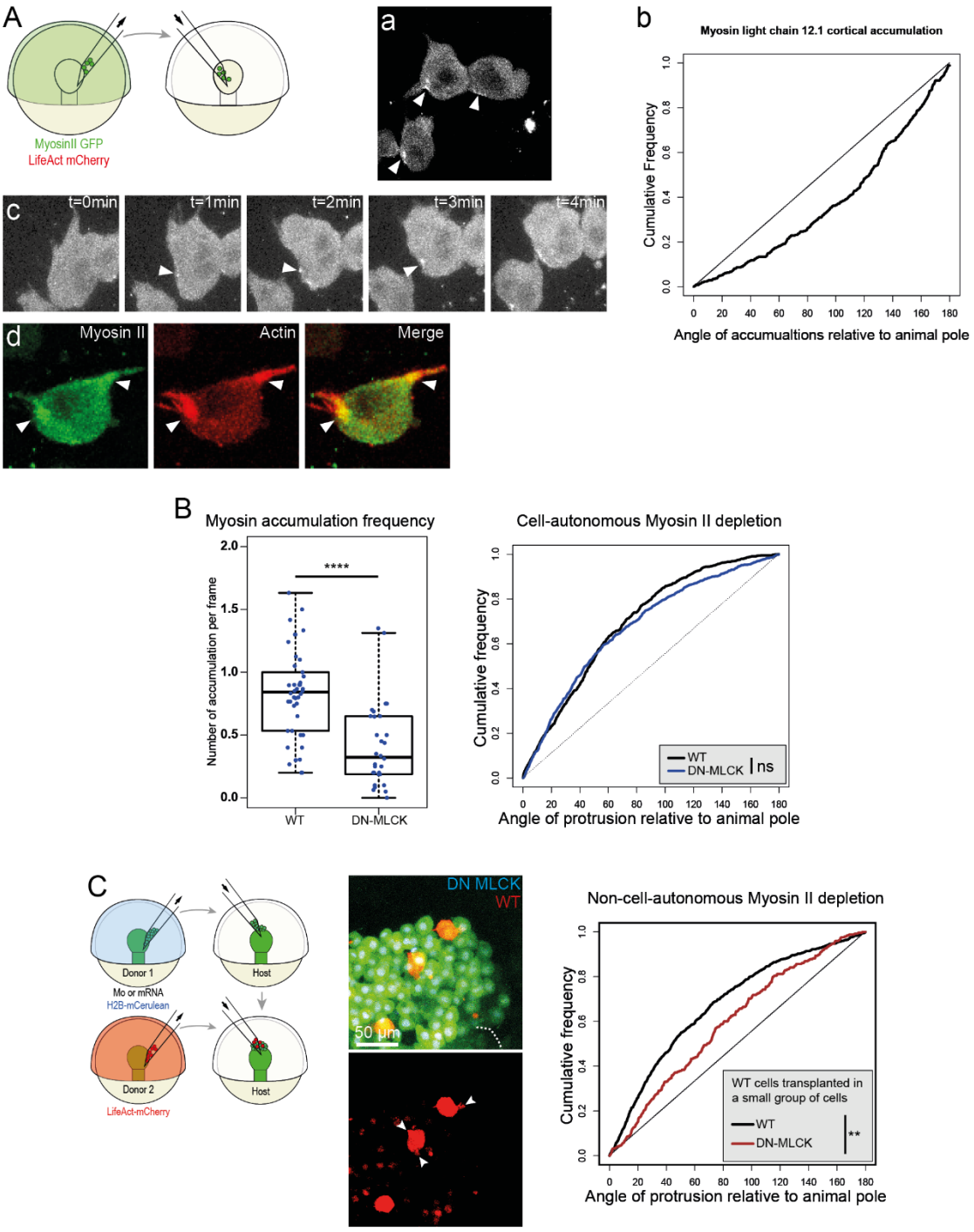

Figure 34. Non-cell-autonomous Myosin II contractility is required for polster cell orientation. A: Distribution of Myosin II accumulations in polster cells. a: Myosin II forms accumulations located at cell cortex (arrowheads). b: Angular distribution of cortical Myosin II accumulation compared to the direction of migration. c: Timelapse of membrane contraction after formation of a cortical Myosin II accumulation. (a-c) On average, myosin distribution is slightly biased toward the rear of the cell. d: Myosin II also accumulates at the basis of actin rich protrusions (42 cells in 9 embryos). **B**: Expression of DN-MLCK inhibits formation of myosin accumulations in polster cells (WT: 42 cells in 9 embryos, DN-MLCK: 29 cells in 6 embryos) but does not affect actin rich protrusion orientation (WT: 33 cells in 13 embryos, DN-MLCK: 30 cells in 8 embryos). **C**: Protrusion orientation of actin labelled WT cells (red) transplanted among a small group of WT or DN-MLCK cells labelled with H2B-mCerulean (blue nuclei), in front of a WT polster (25 red cells in 6 embryos, and 15 cells in 4 embryos respectively).

In adherens junction, E-Cadherin is connected to actin through several proteins. In particular, it is linked to β-Catenin, itself linked to α-Catenin, which ultimately directly binds actin (Fig.7A). As these proteins bear forces applied on E-Cadherin and transmitted to the actomyosin cortex, they are also good candidates for mechanotransduction. It appears that α-Catenin is a mechanosensitive protein. When under tension α-Catenin undergoes a conformational change, revealing the MI binding site for Vinculin and other proteins (Fig. 7C, Fig; 13B &C)) (Kobielak et al., 2004; Nieset et al., 1997; Pokutta et al., 2002; Yonemura et al., 2010b). This mechanosensitive property of α-Catenin is required in several instances mechanotransduction pathways. However, signalling downstream of α-Catenin is poorly known. I thus tested a potential role for α-Catenin orienting polster cells. Knock-down of α-Catenin reduced protrusion orientation, which could be rescued by co-injection of α-Catenin mRNA, first indicating that α-Catenin is indeed required for polster cell orientation (Fig. 35A & D).

Then, to determine if α-Catenin is required simply as a link between E-cadherin and the cytoskeleton or as a *bona fide* mechanosensor, I rescued the knock-down with the α-CateninΔVBS construct, which still binds actin but lacks mechanosensation (Han et al., 2016; Huveneers et al., 2012; Twiss et al., 2012). In this construct, the MI domain of α-Catenin is replaced by an equivalent and functionally similar domain from Vinculin but unable to recruit proteins that usually bind to α-Catenin. As expected, this α-CateninΔVBS construct partially rescued developmental defects induced by α-Catenin knock-down, as embryos survived the first day of development (Fig. 36B) (Han et al., 2016). Yet, it did not restore polster cell orientation establishing that this domain, involved in the mechanosensory function of α-Catenin, is required to orient polster cells (Fig. 35A & D).

Several proteins are known to bind the MI domain of α-Catenin (Fig. 13C). Among these is Vinculin, a protein that also binds actin filaments, strengthening the link between the adhesion complex and the actin cortex, but which is also suspected to interact with migration-related actors, like Arp2/3 (Fig. 13B & C). It is hence a very promising candidate to mediate adherens junction mechanosensation in polster cells. To confirm that these cells require specifically binding of Vinculin to α-Catenin, I performed similar rescue experiments with the L344P mutant form of α-Catenin, which bears a point mutation in the Vinculin binding site, specifically preventing the tension-dependent recruitment of Vinculin (Fig. 35A & D) (Seddiki et al., 2018). This mutant form did not rescue cell orientation, and effect on cell orientation is identical to the rescue with α-CateninΔVBS, suggesting that, indeed, α-Catenin mechanotransduction is mediated by Vinculin. In order to confirm this hypothesis, I directly tested the involvement of Vinculin.

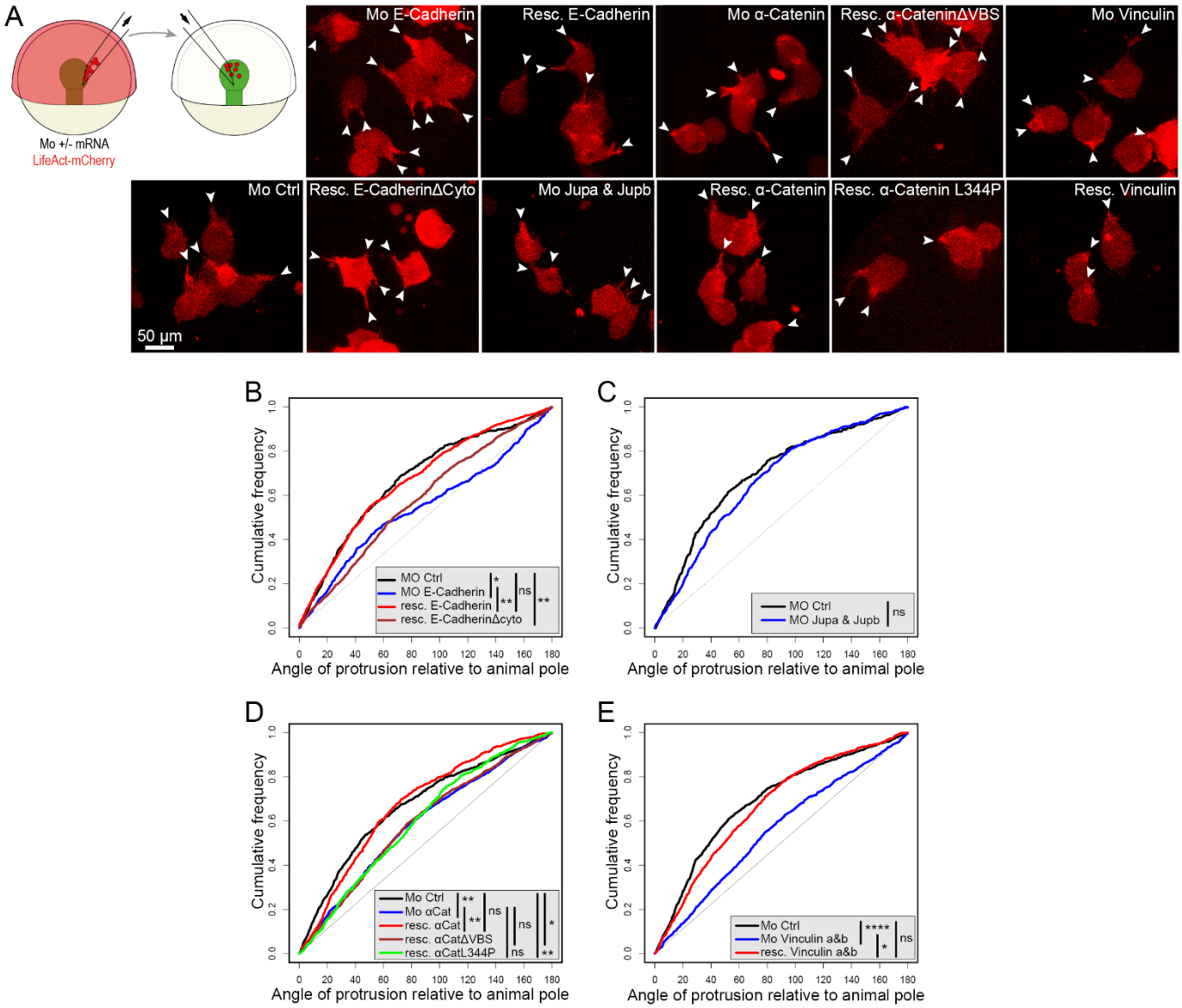

Figure 35: E-Cadherin, α-Catenin, Vinculin mechanosensation pathway is required for polster cell orientation. A: Actin rich protrusions of Lifeact-mCherry expressing cells transplanted in a WT polster. Arrowheads mark actin rich protrusions. Mo indicates that cells were injected with a morpholino against the target gene, Resc. indicates a rescue experiment where a morpholino and the mRNA coding for the corresponding gene, or a mutant form, were co-injected. Mo Ctrl: n=23 cells in 6 embryos for panel (B), n=26 cells in 9 embryos for panel (C), n=28 cells in 6 embryos for panel (D) and n=37 cells in 10 embryos for panel (E); Mo E-Cadherin: n=28 cells in 6 embryos; Resc. E-cadherin: n=22 cells in 4 embryos; Resc. E-cadherinΔcyto: n=34 cells in 8 embryos; Mo jupa & jupb (Plakoglobin a & Plakoglobin b): n=29 cells in 9 embryos; Mo α-Catenin: n=25 cells in 6 embryos; Resc. α-Catenin: n=22 cells in 4 embryos, Resc. α-CateninΔVBS: n=34 cells in 8 embryos, Resc. α-CateninL344P: n=30 cells in 8 embryos, Mo Vinculin (Vinculin a & Vinculin b): n=29 cells in 9 embryos, Resc. Vinculin: n=24 cells in 6 embryos. **B-E**: Orientation of actin rich protrusions corresponding to the different conditions presented in (A).

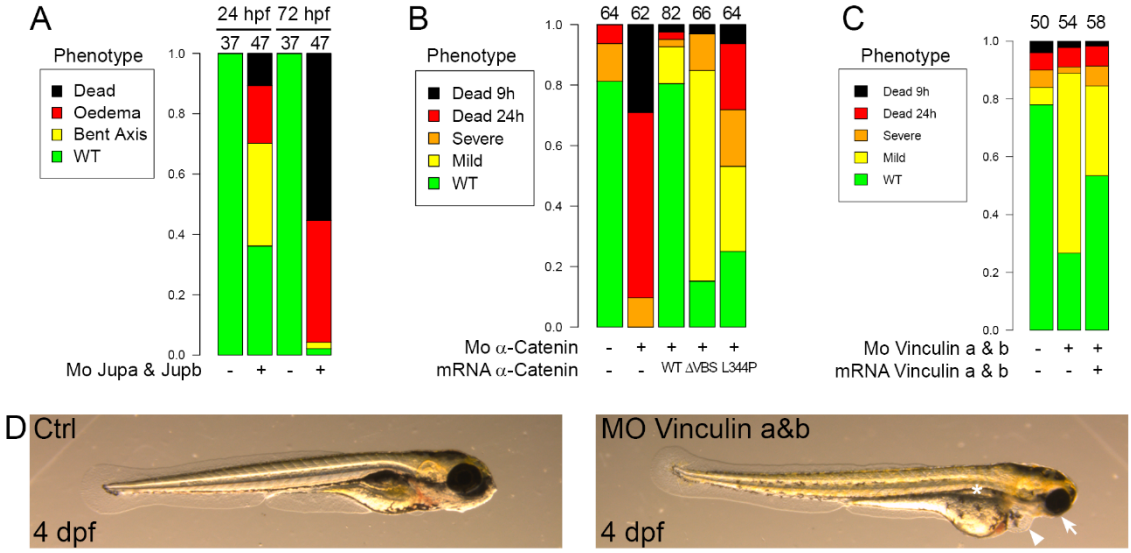

Figure 36. Developmental phenotype after morpholino injection. **A**: Phenotype at 24 and 72 hpf of control uninjected embryos (n=37) and embryos injected with jupa and jupb morpholinos (n=47). **B**: Phenotypes at 24 hpf of embryos injected with a control morpholino or Mo α-Catenin, with or without mRNAs. **C**: Phenotypes at 24 hpf of embryos injected with a control morpholino or Mo Vinculin a and Mo Vinculin b, with or without mRNAs. (A-C) Number of analysed embryos are indicated above each bar. **D**: Developmental phenotype of control and Mo Vinculin injected embryos at 4 dpf. Arrowhead: cardiac oedema; arrow: cranial malformation; asterisk: swim-bladder atrophy.

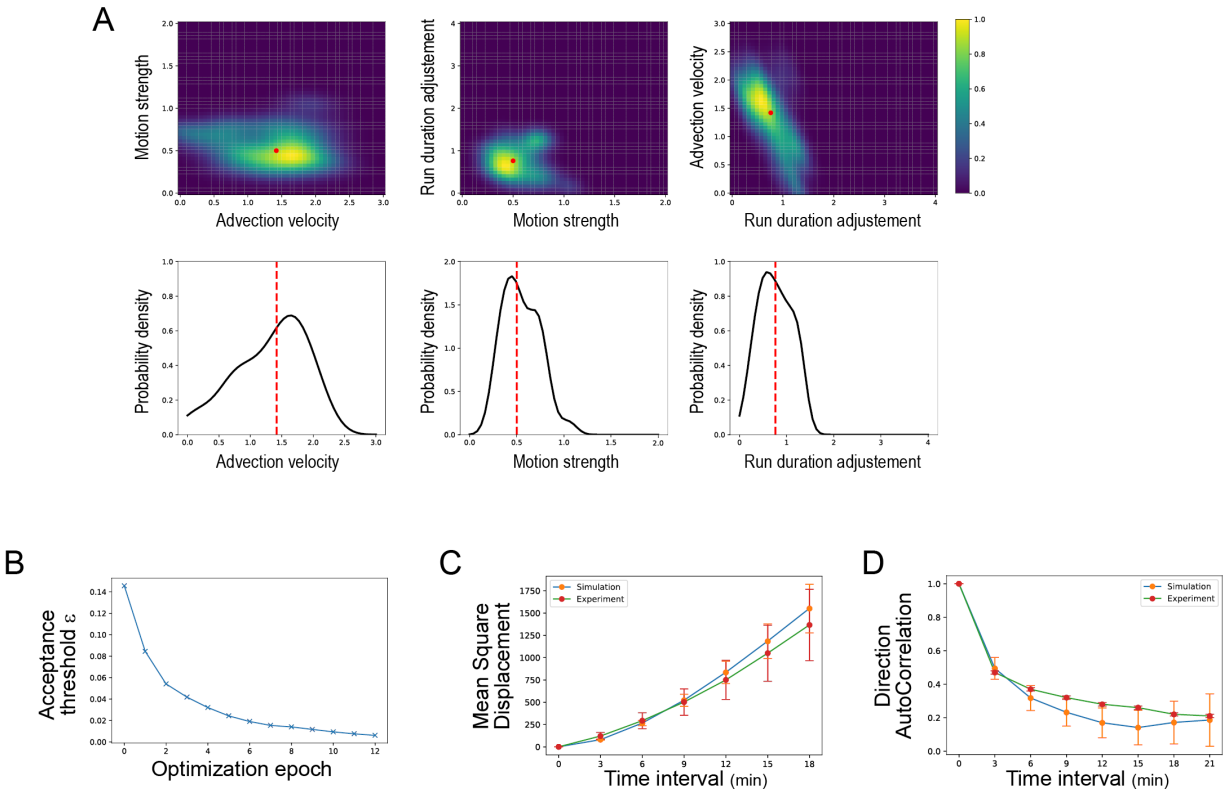

Figure 37. Parameter estimation for Cellular Potts Model simulations. **A**: Inference of model parameters from experimental data with ABC-SMC optimisation using the FitMultiCell toolbox (see Methods). Estimation results are shown as normalised two-parameter (top row) and one-parameter (bottom row) kernel density estimates of the posterior parameter distributions. The red dot (top row) and red-dashed line (bottom row) represent the weighted median (for details see Methods, Parameter estimation). **B**: Evolution of the acceptance threshold through optimisation epochs. **C-D**: Mean Square Displacement and Direction Autocorrelation of experimental and simulated data with estimated parameters. Green curve with red dots: experimental measurements; blue curve with orange dots: simulated cells.

Just like Plakoglobin, two paralogous forms of Vinculin, *vcla* and *vclb*, exist in zebrafish (Han et al., 2017). I thus knocked down both vinculin forms and observed the effect on cell orientation. Consistent with the α-Catenin results, this treatment disrupted the anteriorward protrusion bias (Fig. 35A & E). Furthermore, specificity of this phenotype was confirmed by a rescue experiment: co-injecting morpholinos targeting *vcla* and *vclb* and mRNAs coding for *vcla* and *vclb* rescued protrusion orientation. These results establish that the E-Cadherin, α-Catenin and Vinculin mechanotransduction pathway is required for polster cell orientation.

Guidance by followers ensures guidance and robustness of axial mesoderm extension

In silico simulations reveal the emergence of a robust collective behaviour

Overall, my results suggest that each polster cell is oriented by stresses exerted by actively migrating neighbours. Behind the polster extends the posterior mesoderm and cell orientation seems propagated through the whole tissue. It is not clear, though, how cells integrate information coming from neighbouring cells. In particular, we wondered whether polster cells are oriented by all neighbouring cells or only follower ones. At this point, we wondered whether such rules, guidance by neighbours, by followers, by a tissue behind and so on, could explain what we observed. To address which statistical properties can emerge from cell interactions and if this is sufficient to account for the observed collective migration of polster cells, we turned to computational modelling. We thus had to choose between analytical modelling based on equations, and rule-based numerical simulations. Analytical models are very powerful tools as they constitute an extensive and actual description of cells and tissues properties and as such might explain a phenomenon or even be used for prediction of tissue behaviours in response to a perturbation. However, such analytical models require extensive knowledge of cell behaviours and properties, which we do not have access to, or relies on strong assumptions, which diminish the interest of the model. Another approach is to go for a model as simple as possible, to test for sufficiency of our hypothesis, which is what we chose to perform using numerical simulations. In such models, the system is approximated and described by a set of rules that do not simulate precise biological events. For example, one can simulate CIL by simply implementing a repulsion upon contact without considering adhesion molecules, signalling pathways and so on. In order to test the sufficiency of our hypotheses, we wanted to build a simple model, with as little hypotheses and parameters as possible. Such simulations are thus perfectly fit for that goal and are easier to build as the full description of the tissue is not required, we just needed to reproduce an initial situation similar to simulated system and implement desired rules.

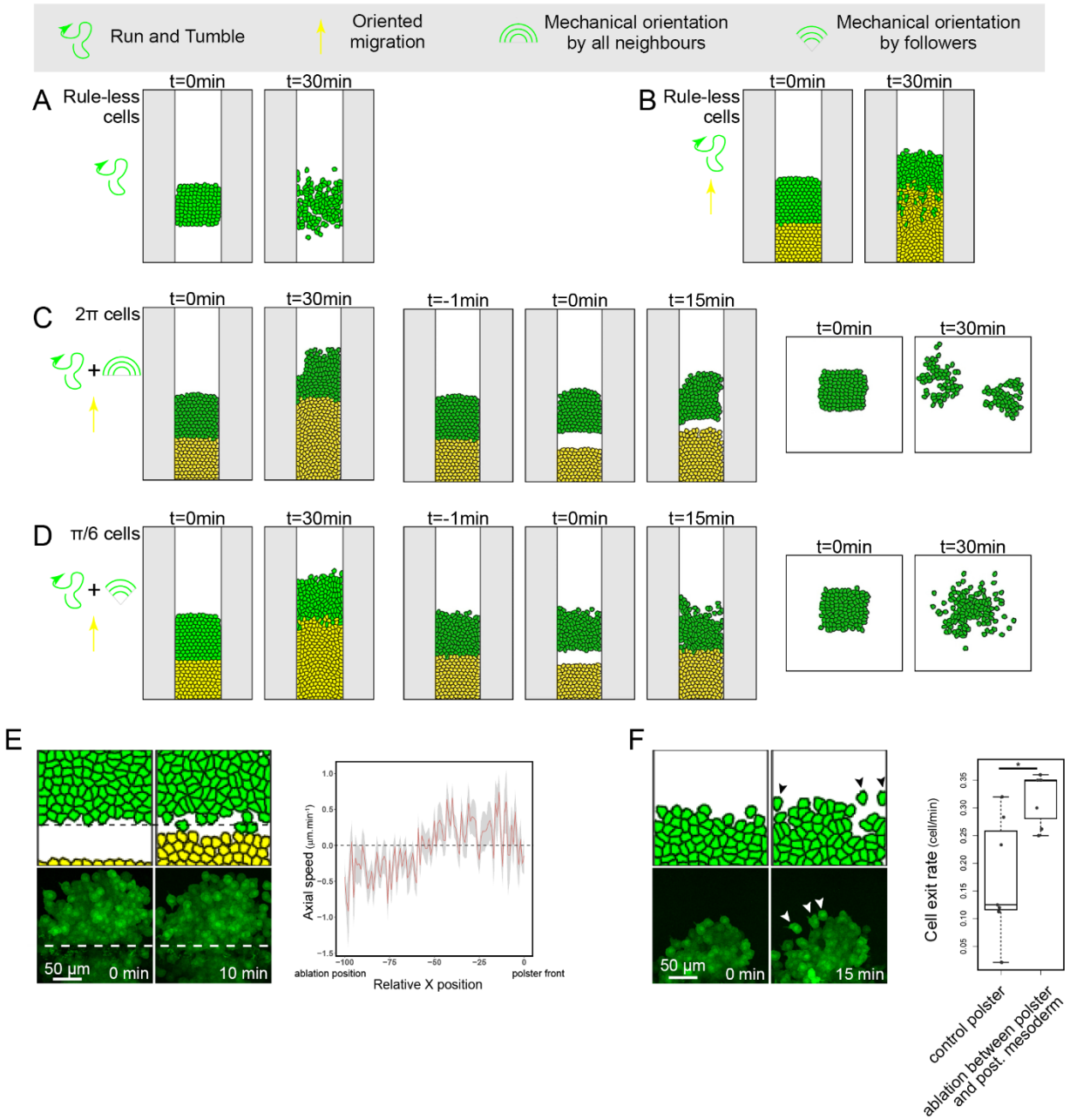

Figure 38: Simulation of guidance by followers recapitulates polster behaviour. A-D: Cellular Potts models testing different scenarios. **A**: Polster cells (green) are given a Run and Tumble behaviour (rule-less cells), fitted to observations of isolated polster cells (see Fig. 37). On their own, polster cells tend to disperse. **B**: When followed by animal-ward migrating axial mesodermal cells (yellow), rule-less cells progress toward the animal pole, but mix with axial mesoderm. **C**: Adding mechanical sensitivity to all neighbours migrating around polster cells (2π-cells) is sufficient to account for the collective oriented migration of polster cells but fails to reproduce polster halt after isolation from posterior mesoderm (see Fig. 27A & 29) and isotropic dispersion of an isolated group (see Fig. 25A & D). **D**: Adding mechanical sensitivity to neighbours migrating toward a polster cell (guidance by followers, π/6-cells) is sufficient to account for the collective oriented migration of polster cells and other experimental observations. **E-F**: Close-ups from simulated and experimental laser ablations, revealing two features we first noticed in simulations and then identified in experimental data: a backward movement of the cells at the posterior edge of the isolated group (E) and a tendency of the most anterior cells to migrate out of the group (arrowheads) (F). Both features were quantified in experimental data.

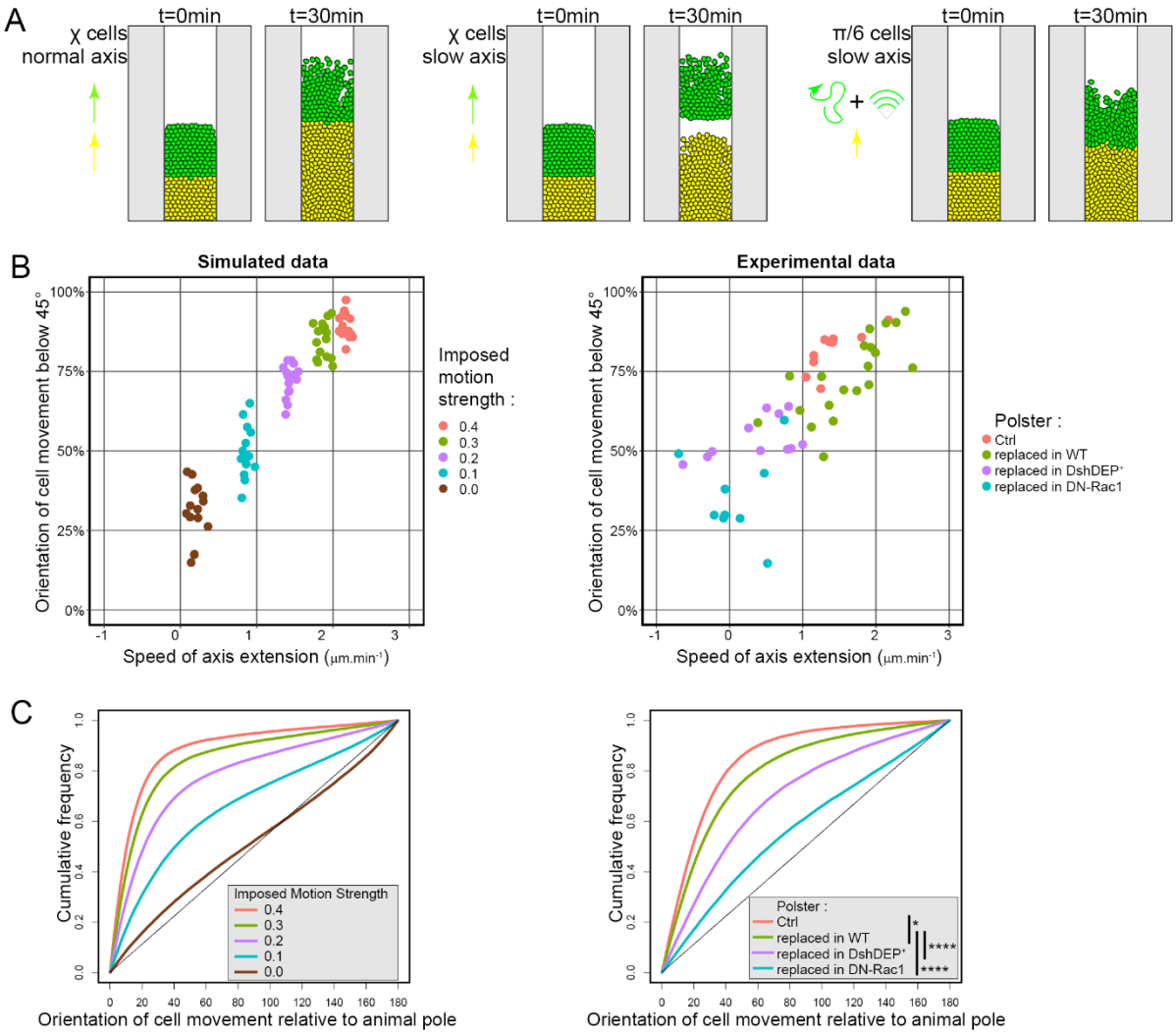

Figure 39: Guidance by followers ensures robustness of axial mesoderm elongation. A: If both polster cells and axial mesoderm are given oriented migrations toward the animal pole (χ cells), differences in their speed will induce axis disruption. On the contrary, when polster cells are oriented by followers, polster speed spontaneously adjusts to axis speed. **B-C**: Orientation of cell movements when speed of following cells (axis) varies. Simulations were performed with π/6-cells. Axial cells speed was modulated by varying the Lagrange multiplier modulating their movement (Imposed Motion Strength). Experimental data are those presented in Fig. 30, and correspond to an unmanipulated polster (Ctrl), or a wild-type polster transplanted in either a wild-type embryo, a Dsh-DEP+ injected embryo or a DN-Rac1 injected embryo. **B**: The percentage of movements oriented toward the animal pole (angle compared to animal pole lower than 45°) is plotted as a function of the measured speed of the axis. **C**: Distribution of orientations are plotted in the different situations as cumulative plots.

There are several ways to build numerical simulations of cells. They can be described as points, spheres or non-regular shapes and might have a constant or a modifiable contour. Vertex or centre-based model simulate cells with a polygonal shape, which is not the case of polster cells, that have fast changing, mesenchymal shapes. We thus chose to use the Cellular Potts Model approach, which generates cells with changing, non-geometrical shapes, to model polster cells (see Methods) (Graner & Glazier, 1992). In a nutshell, this category of models is based on a lattice where each pixel is given an identity, here, substrate or a particular cell identity. At each simulation step, random pixels are selected (a process called Monte Carlo Step, MCS) and the model checks whether they change identity. This happens according to a phenomenological "energy" described by a Hamiltonian that simulates the propensity of a particular pixel to change state. If the energy is negative, the pixel does change state and if it is positive, it has a certain probability to also change state, depending on a "temperature". This Hamiltonian is an equation where different elements, constituting the rules of the model, can be added or removed. For example, the typical Hamiltonian of a cell surrounded by medium is given by

$$H(\sigma) = H_A + H_P + H_J$$

Here, σ is the cell conformation, H_A an energetic cost for change of area, H_P an energetic cost for deviation of cell perimeter and H_J the energy associated to cell-medium interface.

In order to build the simulation, we used the Morpheus framework that provides a graphical interface that makes Potts modelling accessible for people without extensive coding skills (Starruß et al., 2014). However, during the course of model construction, we stumbled upon limitations of the software and started a collaboration with the team of Lutz Brüsch from TU Dresden, which develops and supports Morpheus. They developed new features and helped build the axial mesoderm simulation. Full details on the model are given in the Methods section and I will just briefly explain it here.

We first characterised the behaviour of isolated cells, to define their cell autonomous properties. I thus quantified migration behaviour of cells transplanted at the animal pole that migrate without being in contact with other polster cells. We set simulated cell area as the actual average polster cell area then, through an iterative process testing different combinations of migration parameters, we tried to simulate cells whose mean square discplacement (MSD) and directional autocorrelation corresponded to actual cells (Fig. 37A-D). We gave these cells a Brownian motion or run and tumble, and reached much better fit with Run and Tumble. This is actually consistent with what has been described for mesendoderm individual cell migration (Diz-Muñoz et al., 2016). We thus simulated basic polster cells with an area and a migration that correspond to actual polster cells, exhibiting no other behaviour than a run and tumble migration (Fig. 37C & D).

Simulating a group of these rule-less polster cells in a free space led to dispersion, without any particular oriented tissue motion (Fig. 38A). This is consistent with the behaviour of polster cells

transplanted at the animal pole or in front of a polster-less axial mesoderm before contact, or polster cells transplanted in the dorsal margin of mesoderm-less MZ *oep* embryos (Fig. 25A & D, Fig. 29B, Fig. 33A) (Smutny et al., 2017). We then approximated axial mesoderm as a two-dimensional tissue in a space that is 10 cell diameters wide, confined laterally and oriented vertically. We added behind polster cells a group of cells whose movement is oriented toward the top of the simulation. These cells simulate the extension of the posterior axial mesoderm. In these simulations, we observed that these simulated polster cells were inefficiently displaced and largely mixed with posterior mesoderm (Fig. 38B). In particular, we observed no coordination of migration between these rule-less polster cells. This does not correspond to what we observed during polster migration, suggesting that these cells need additional rules to align their migration.

We then tested whether adding a tendency for polster cells to align with orientation of all their neighbours fitted experimental results (Fig. 38C). This rule corresponds to what is observed in epithelial collective migrations, where cell motion correlates with the movement of cells immediately around (Poujade et al., 2007). In these simulations, polster cells average the displacement of all neighbouring cell at a given time, giving a vector that bias the run and tumble migration for the next time. I will refer to these cells as 2π polster cells. With this extra rule, simulated polster cells well aligned their migration with follower axial cells and efficiently moved upward, in front of the extending axis, as they do in the embryo. But do such simulations reproduce all experimental conditions? In particular, we simulated an ablation at the interface between the two tissues, by removing a few stripes of cells from the simulation. 2π polster cells continued to move forward once separated from posterior cells, which is a complete discrepancy with laser ablation experiments (Fig. 27A, Fig. 38C). This rule actually creates a system in which orientation is self-sustained as soon as there is an asymmetric orienting cue. Accordingly, simulating a group of these cells in an empty space led to separation of the group in two very directional subgroups (Fig. 38C). Again this is a discrepancy with the observation that polster cells transplanted at the animal pole spread and disperse isotropically, then, move randomly. The differences between experimental and simulated observations suggest that cells are not integrating migration information coming from all neighbours.

In the polster, cell orientation requires neighbours to be actively protrusive, adhesive and contractile, suggesting that the pulling force might come from the protrusions (Fig. 32B, Fig. 34C). Furthermore, in normal conditions, protrusion orientation is largely biased toward the front of migration (Fig. 35). Hence, a particular cell should be more often in contact with protrusions coming from following cells than from cells located laterally or before. It is thus possible that orientation of polster cells is more influenced by follower cells than by other neighbours. We simulated this idea by giving polster cells a tendency to align with cells migrating toward them (Fig. 38D). At each time, the angle between the displacement of a particular cell and of each of its neighbours is computed. If this angle is smaller than 30°, then this neighbour is considered as a follower. These displacement vectors from all

the followers are then averaged and the resulting vector is used to bias the cell run and tumble migration at the next time. I will refer to these cells as π/6 (30°) polster cells. When simulated in front of axial cells, a π/6 polster behaved like a 2π polster: cells display coordinated migration and efficiently align with posterior cells (Fig. 38C & D). Unlike 2π polster cells, however, π/6 polster cells stopped their directed migration upon simulation of an ablation, which is consistent with laser ablation experiment (Fig. 27A, Fig. 38C & D). Finally, π/6 polster cells simulated in an empty area dispersed, similar to the behaviour of polster cells at the animal pole (Fig. 38D). Hence, π/6 polster cells, that display run and tumble migration plus alignment with followers, recapitulated experimental observations. Furthermore we noticed, in ablation simulations, a slight backward movement of the cells at the posterior edge of the isolated group, and a tendency of the anteriormost cells to migrate out of the group (Fig. 38E). Carefully analysing laser ablation movies, I identified such characteristics, indicating that π/6 polster cells even recapitulate some complex behaviours. These simulations confirm that being oriented by followers is sufficient to create a collective behaviour able to orient polster migration from posterior axial elongation. We thus propose the expression "guidance by followers" to describe the phenomenon ensuring polster cell guidance and collective migration.

Guidance by followers ensures robustness of axial mesoderm extension

Guidance by followers through detection of mechanical forces is particularly original since it opposes classical views of collective cell migration that always relies, at least partly, on detection of a chemical gradient. We therefore considered what could be the role of such a mechanism. For that purpose, we used numerical simulations to compare guidance by followers to guidance by a gradient.

We simulated what could happen if polster cells used an external gradient, be it chemical or physical, to orient their migration (Fig. 39A). We simply simulated polster cells with noisy directional migration toward the top, just like posterior axial cells. I refer to these cells as χ polster cells. In this situation, the two tissues first stayed in contact and migrated at the same speed toward the top. Suggesting that, if the two tissues have similar migration behaviours, contact between tissues is maintained. However, because χ polster cells at the front are less constrained than following cells, they tend to move faster toward the top, leading to a progressive detachment of front cells, something that is not observed during polster migration. For χ polster cells to stay in contact over time, they would need to be slightly slower than axial cells to be pushed by the latter. We also wondered whether such a situation is robust to perturbations. In particular, we slowed down extension of simulated posterior mesoderm. Here, we observed that χ polster cells, that were still strongly biased, detached from follower cells and migrated alone. Hence, orienting migration of the two tissues using external cues is sensitive to difference in migration speed. Yet, we never observed in the literature or in our experiments a polster spontaneously detaching from the following axial mesoderm. Furthermore, the absolute speed of actual

polster cells is slightly higher than that of posterior mesoderm. This suggests that contact between tissues must be ensured by some mechanism and we wondered whether guidance by followers could account for that.

We tested this hypothesis by slowing down simulated posterior mesodermal cells and observed the effect on π/6 polster cell movement (Fig. 39B & C). Strikingly, animal ward migration of simulated polster largely decreased, even though individual π/6 polster cell properties were unchanged. This simulation actually mimics experiments in which the speed of the axial mesoderm is reduced (see Fig. 30B). Since polster cells properties are unchanged both in simulations and in experiments, reduction of the group speed likely stems from an emergent property of the interacting multicellular simulated system. In simulations, we measured the orientation coherence of π/6 polster cells and found it to be linearly dependent on the speed of posterior cells, so that when axis speed is reduced, π/6 polster cells maintain their individual speed, but are less oriented, leading to a reduction of the group speed (Fig. 39B & C). We then directly tested this model prediction by measuring cell movement orientation in the experiments where axis extension was slowed and found the same striking correlation between axis speed and polster cell orientation. Thus, the mechanical information that propagates through the tissue modulates cell orientation, and this is sufficient to modulate speed of the entire group. Guidance by followers, in which the cell-to-cell propagation of mechanical information orients cell polarity, is thus a very simple, yet very effective way of ensuring long-range coordination of cell movements and self-organized guidance (Fig. 40).

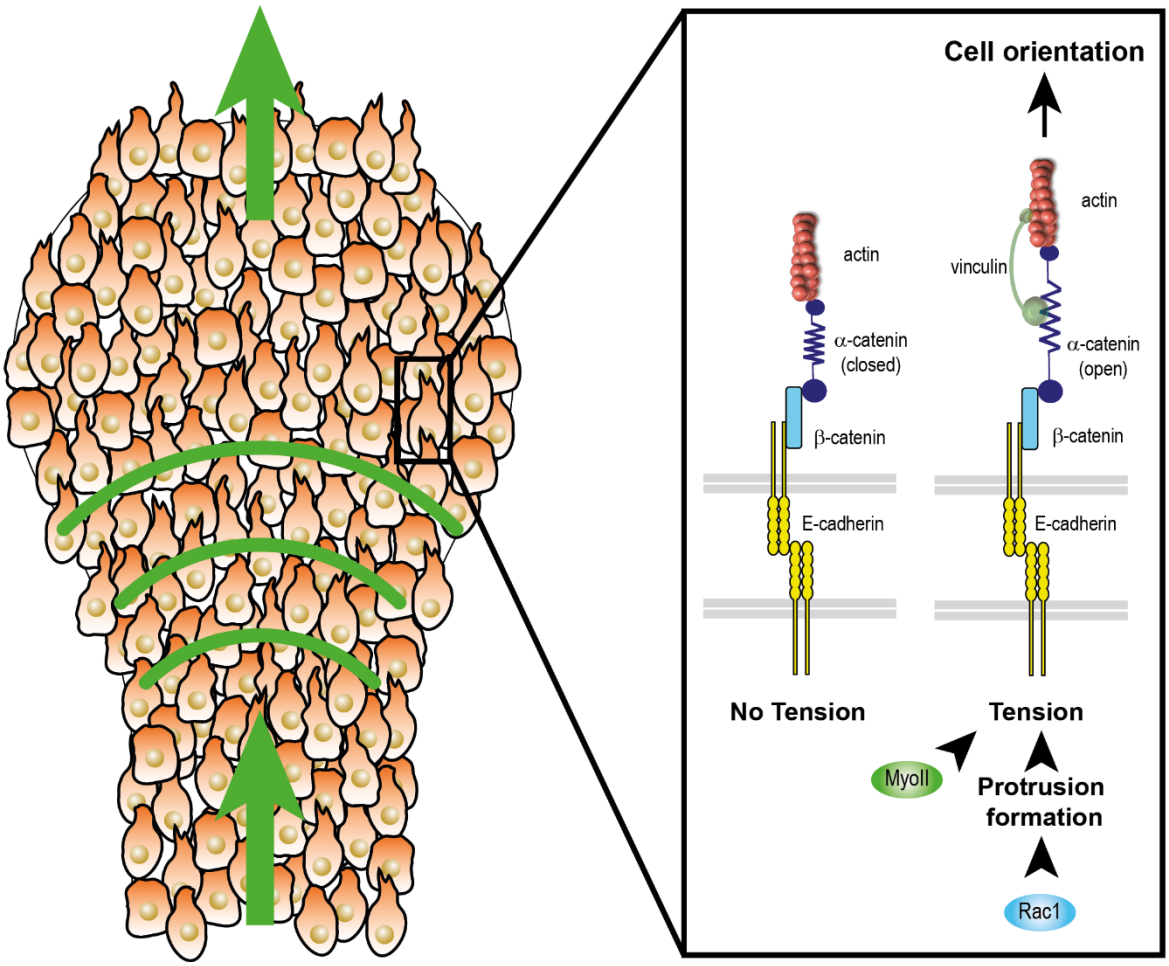

Figure 40: Guidance by followers, a model for polster collective migration. A: Model of the orientation of polster cells collective migration through guidance by followers behaviour. Cells perceive mechanical stimuli generated by the active migration of their neighbours, and orient their protrusive activity accordingly. This leads to propagation of the directional information through the entire group.

Extended results

In the previous parts, I presented my main PhD work, most of which has been published or pre-published (see Appendix) (Boutillon, et al., 2021). During the course of my PhD and the internships that preceded it, I carried several side projects and collaborations that do not directly fit in this story of guidance by followers but still relate to polster migration. Most of these projects are unfinished, although some collaborations led to publications. I will now present these extra results that occupied a significant part of my PhD.

Ensuring lateral confinement of the polster

In numerical simulations of polster migration, we imposed a lateral confinement around simulated cells (Fig. 38 & 39). Indeed, in all observations we made of wild type axial mesoderm, neither polster nor posterior cells ever migrated laterally, away from the axis. This is confirmed by *in situ* hybridisation against polster, prechordal plate or notochord markers: no cell is located out of the axis (Fig. 19B, Fig. 26A). Posterior mesodermal cells perform convergence and extension and, as such, tend to move toward the dorsal midline. However, it is not at all clear why polster cells stay grouped and do not migrate away. Indeed, groups of polster cells transplanted at the animal pole tend to disperse isotropically (Fig. 25A & D). This is also the case when such cells are transplanted in the dorsal margin of embryos devoid of mesoderm, like in MZ *oep* mutants (Smutny et al., 2017). Furthermore, contrary to neural crest cells, poster cells do not exhibit co-attraction (Fig. 25C & D), which means that cohesiveness is achieved differently. We thus tested in our simulations what would happen if we removed lateral confinement. Strikingly, polster cells largely displayed lateral migration, and ultimately dispersed, suggesting that the fact cells stay grouped in an embryo is not trivial. I thus started to explore what might laterally constrain polster movement.

The idea behind the following experiments came from an observation that entered in contradiction with the classical textbook representation of tissue distribution during gastrulation. Indeed, based on *tbx16* expression patterns obtained by in situ hybridisation, it is usually considered that the lateral mesoderm front is located far from the axial mesoderm front, roughly at the interface between polster and posterior mesoderm (Fig. 41A) (McFarland et al., 2005; Smutny et al., 2017). However, in the *Tg(tbx16:GFP)* transgenic line, labelling axial and lateral mesoderm, one can observe that, during early gastrulation, the front of the lateral mesoderm is only 40 µm behind polster front, around two cell diameters, and this distance stays remarkably constant over time (Fig. 41A). Actually, it seems that lateral mesodermal cells accumulate all along axial mesoderm suggesting that this tissue might act as a barrier that prevents lateral movement of polster cells. This hypothesis is all the more plausible that polster cells seem unable to migrate over lateral mesodermal cells when transplanted in front of them.

It seems that, out of the axis, mesodermal cells cannot move past each other, likely due to steric interactions. I thus wanted to check whether the polster is confined laterally by lateral mesoderm.

I performed preliminary ablation experiments in *Tg(tbx16:GFP)* embryos where I removed a small patch of lateral mesoderm that lines the left boundary of the polster (Fig. 41B). I tracked cells and quantified migration characteristics before and after ablation. Strikingly, polster cells that are just near the ablated area moved laterally toward it. This indeed indicated that the lateral mesoderm prevents polster cells from migrating laterally. Interestingly, I noticed a slight lateral movement of the whole polster, in particular, cells that are located at the right boundary also moved toward the hole, although less than cells from the left boundary. This shows that local perturbation can propagate through the whole width of the tissue. I also performed surgical ablation of the lateral mesoderm that nears the polster soon after it internalises, around 60% of epiboly (Fig. 41C). I observed that the polster tends to expand laterally, filling partially areas devoid of lateral mesoderm. In one case, this even led to a bend in axial mesoderm extension. This tends to confirm that the polster is confined by lateral mesoderm and that relieving this constraint leads to abnormal, lateral migration. These results are very promising but still preliminary: more replicates are required to confirm my observations and a mechanism for lateral confinement still has to be found. Exploring intracellular molecular mechanism for polster cell migration

As described in the introduction, many signalling pathways are involved in polster migration, but no comprehensive view of their relationship exists. Description of this migration is essentially a collection of observations and very few are put into perspective with the others. Interaction between pathways, precise localisation of cellular components, and epistasis are thus poorly described in the polster (Fig. 23B). Furthermore, the only output we got to measure polster cell orientation is protrusive activity. Since protrusions are the most downstream phenomenon of polarisation, it is impossible to know when polarity is lost in the signalling cascade in mutant cases. I thus explored different signalling pathways, trying to find new molecular actors involved in cell migration, interaction between pathways and new ways to measure cell polarisation.

Deciphering the tumor suppressor role of CYFIP2 in the WAVE complex

As many cell types that form actin rich protrusions, polster cells depend on actin branching to migrate and thus, on the Arp2/3 complex which nucleates branched actin filaments that power membrane protrusions. This complex is activated at the protrusive edge by the WAVE complex, which is itself activated by the Rac1 small GTPase, necessary and sufficient for lamellipodia formation (Steffen et al., 2014). The Rac1-WAVE-Arp2/3 pathway controls protrusion lifetime and migration persistence through numerous feedback and feedforward loops and has been implicated in the migration and invasion of tumour cells in various model systems (Krause & Gautreau, 2014). The WAVE complex is

composed of 5 subunits, WAVE, ABI, BRK, NCKAP and CYFIP, encoded by different paralogous genes so that the number of combinations rises up to 36 different forms of the complex (Derivery & Gautreau, 2010). Relative levels of expression of the different paralogous forms of each unit, hence different compositions of the WAVE complex, have different effects on cell migration. For example, high expression of the ABI1 subunit increases migration in tumour cells. In breast and ovary cancers where ABI1 is overexpressed, cells tend to form more metastases, which is associated with a poor prognosis (Wang et al., 2011; Zhang et al., 2015). This WAVE complex is studied by the laboratory of Alexis Gautreau at Ecole Polytechnique, working, among others, on cancer cell migration and biochemistry of the Rac1-WAVE-Arp2/3 pathway. His team made a surprising observation by looking at metastasis-free survival of breast cancer patients. They observed that high levels of NCKAP1 or CYFIP1 is associated with poor prognosis and rapidly decreasing metastasis-free survival, which is expected as these subunits are known to promote cell migration. However, they noticed that overexpression of the CYFIP2 unit, paralogous to CYFIP1 and competing for the same place in the complex, is associated with good prognosis, suggesting that this subunit of the wave complex has a tumour suppressor effect. This observation was surprising as CYFIP2 was expected to behave similarly to CYFIP1 and thus promote migration (see Appendix) (Polesskaya et al., 2020).They therefore studied the role of CYFIP2 in WAVE complex assemblies and in cell migration in cultured tumoral and normal cells. They observed that the CYFIP2 subunit is located at the edge of lamellipodia, where WAVE complex is expected to be found. Knock-down of *cyfip2* dramatically increased persistence and number of protrusions, which is the complete opposite of what is observed upon *cyfip1* or *nckap1* knockdown. This indeed suggests an inhibiting effect of CYFIP2 on WAVE complex activity and cell migration. It might, however, be that CYFIP2 is actually an activator of migration, but simply less potent than CYFIP1. In this case, CYFIP2 would compete with CYFIP1 and thus behave as an apparent inhibitor. Biochemical analyses point toward this second option. WAVE complexes containing CYFIP2 are much more stable than those containing CYFIP1, preventing normal turnover of WAVE that is required for sustained Arp2/3 activation. Hence, when the CYFIP1/CYFIP2 equilibrium shifts toward CYFIP2, more complexes contain this subunit leading to decreased migration-activating properties. All these observations have been made on cultured cells and might not be relevant in physiological contexts. In order to perform in vivo experiments, the team of Alexis Gautreau contacted us to test the role of these genes in vivo, using the polster cell migration as a model.

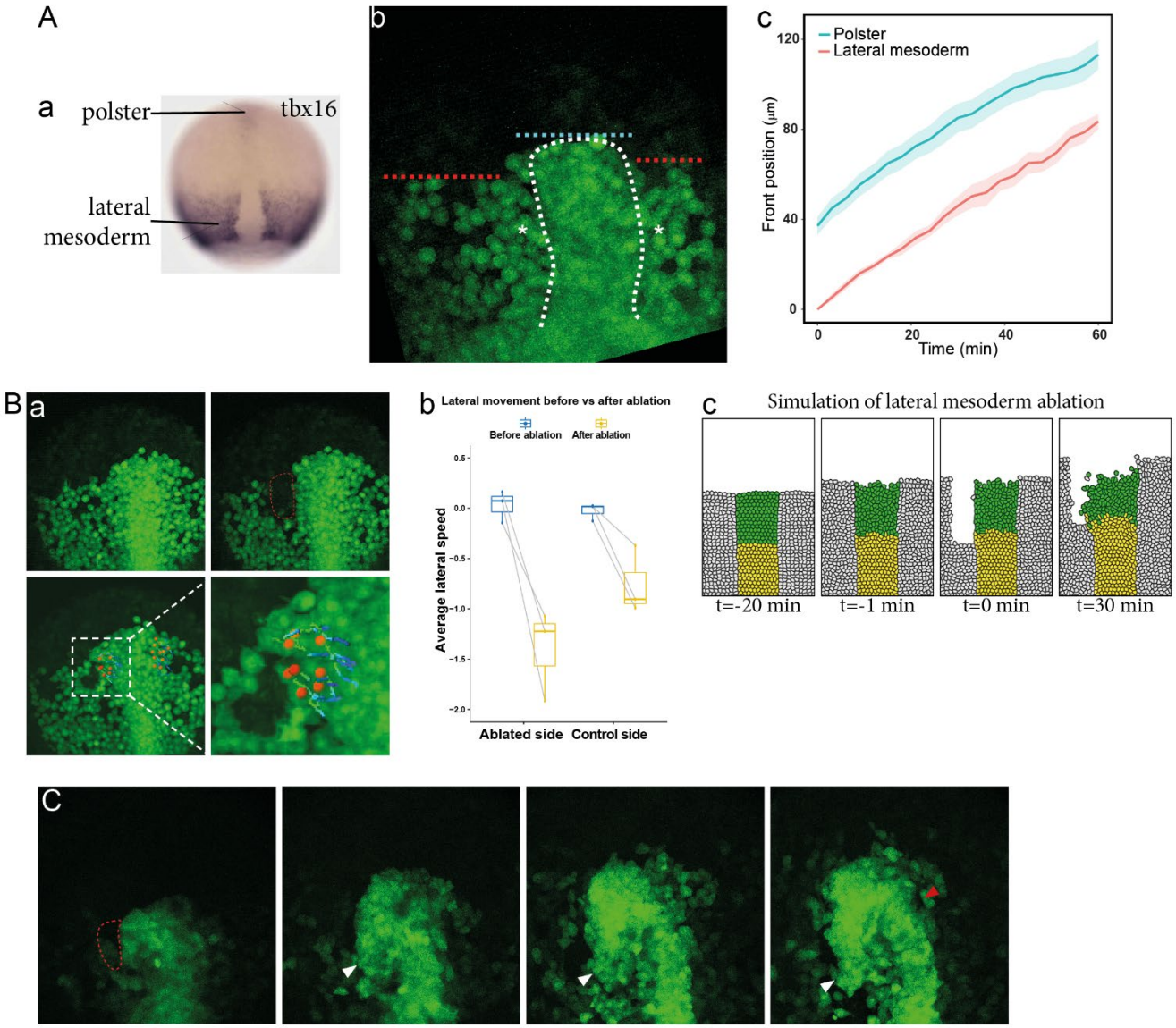

Figure 41. Lateral mesoderm confines the polster along the medio-lateral axis. A: Lateral mesoderm front is located close to polster front. a: *in situ* hybridisation labelling of *tbx16* expression at 80% epiboly, dorsal view. Note that *tbx16* expression seems limited to the vicinity of the embryonic margin and is far from the polster. Modified from Thisse et al., 2001. b: 2-photon image of polster front in a *Tg(tbx16:GFP)* embryo. Blue and red dashed lines respectively mark polster and lateral mesoderm fronts. White dashed line highlight axial mesoderm contour. Asterisks mark accumulation of lateral mesoderm along axial mesoderm. c: Position along the animal vegetal axis of polster and lateral mesoderm fronts over time (n=8 embryos). **B**: Laser ablation of lateral mesoderm near the polster (n=3 embryos). a: Images of polster region in a *Tg(tbx16:GFP)* embryo before and after ablation. Red dashed line indicate ablated area. Nuclei of cells near the ablation (white dashed square) or at the other side of the polster are tracked over time. b: Lateral displacement before and after ablation of cells near or far from the ablation site. c: Numerical simulation of lateral confinement by lateral mesodermal cells (grey) that behave similarly to axial cells, and of ablation of lateral cells on one side. **C**: Surgical removal of lateral mesoderm along one side of the polster during early gastrulation (n=5 embryos). White and red arrows respectively indicate lateral then vegetal movement of the polster, and the curvature of the embryonic axis.

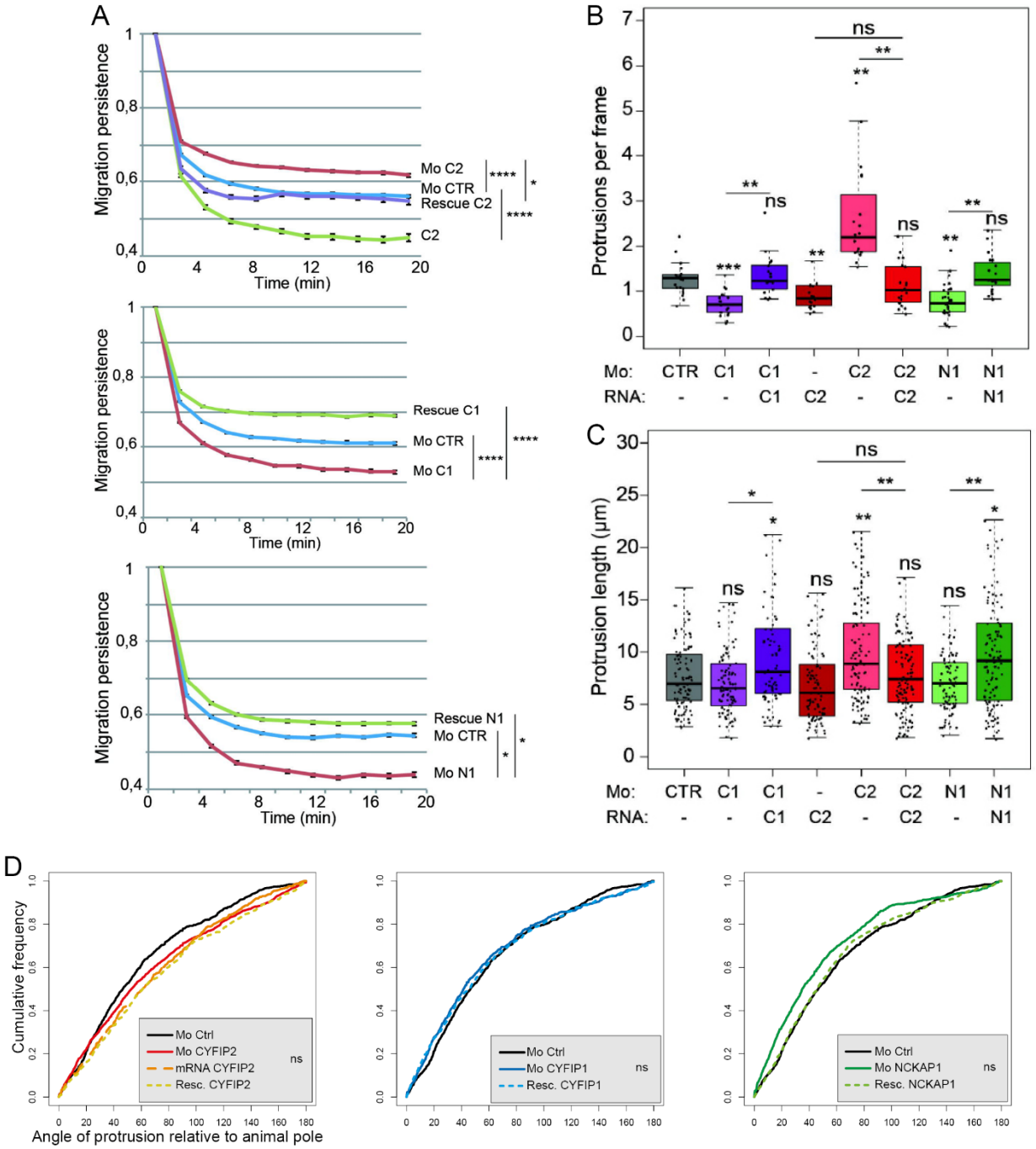

Figure 42. CYFIP2 prevents directional migration and protrusion formation. Modified from Polesskaya et al., 2020. **A**: Migration persistence, measured using directional autocorrelation, of polster cells in embryos injected with morpholino against CYFIP2 (Mo C2), CYFIP1 (Mo C1) or NCKAP1 (Mo N1), mRNA encoding for CYFIP2 (C2) or a mix of a morpholino and the corresponding mRNA (Rescue) (n=4 to 8 embryos per condition). **B-D**: Protrusion frequency (**B**), length (**C**) and orientation (**D**) in actin labelled polster cells injected with morpholino and/or mRNA transplanted in a wild type host (B, D: n=17 to 32 cells from 4 to 5 embryos per condition, C: n=95 protrusion measured per condition).

I used morpholinos targeting *cyfip1*, *cyfip2* and *nckap1* as well as mRNA encoding the human forms of these proteins to perform knockdown and rescue experiments. I first observed the effect of WAVE components on polster cell migration persistence (Fig. 42A). I imaged the migration of the polster during early gastrulation, between 60 and 70% epiboly and tracked polster cells. As a measurement of migration persistence, I used directional autocorrelation that quantifies to what extent movements of a cell stay aligned over time. I observed that knock-down of *cyfip1*, *cyfip2* or *nckap1* had the same effect on polster cells than on cultured cell migration. *cyfip1* and *nckap1* knock down decreased cell persistence while removal of CYFIP2 increased it. These phenotypes were rescued by coinjection of corresponding mRNAs, confirming their specificity. Interestingly, overexpression of CYFIP1 and NCKAP1 in rescue experiments actually increased cell persistence compared to control cells. I also performed a CYFIP2 overexpression experiment. This could not be performed on cultured cells as excess of CYFIP2 prevented cell division in the tested lines while zebrafish embryos managed to develop. This induced a large decrease of cell autocorrelation, consistent with the low-activator role of CYFIP2. However, these effects on cell migration could partly be due to non-cell-autonomous effects. Indeed, the whole embryo is affected by gain or loss of function and other cell movements might be affected, in particular axial mesoderm extension, which could in turn influence polster migration.

I thus quantified cell-autonomous role of these subunits by looking at actin-rich protrusion formation in cells transplanted in a wild type host (Fig. 42B & C). In actin labelled cells, I quantified the average number of protrusions per frame (Fig. 42B), an indication of protrusion frequency, and the length of randomly selected protrusions (Fig. 42C). *cyfip1* and *nckap1* knock down led to reduced number of protrusions, while, *cyfip2* knock down led to a large increase in number. Accordingly, overexpression of CYFIP2 reduced the frequency of protrusions, confirming its low-activating role. Cultured cells showed a similar trend in terms of protrusion frequency, and these phenotypes are consistent with the effect on migration. Co-injection with mRNA rescued the protrusion frequency phenotypes, again establishing their specificity. Surprisingly, protrusions formed upon *cyfip2* knock down were longer than in the wild-type situation, while overexpression of CYFIP1 and NCKAP1 in rescue experiments also produced longer protrusions. Thus suggests that WAVE complex stability controls both length and frequency of protrusions. These experiments in zebrafish mirrored those in cultured cells, and confirmed that CYFIP2 actually has an inhibitory effect on migration. As CYFIP2 prevents WAVE complex turnover, Arp2/3 activation and branched actin formation is decreased, leading to fewer protrusions and a less directional migration.

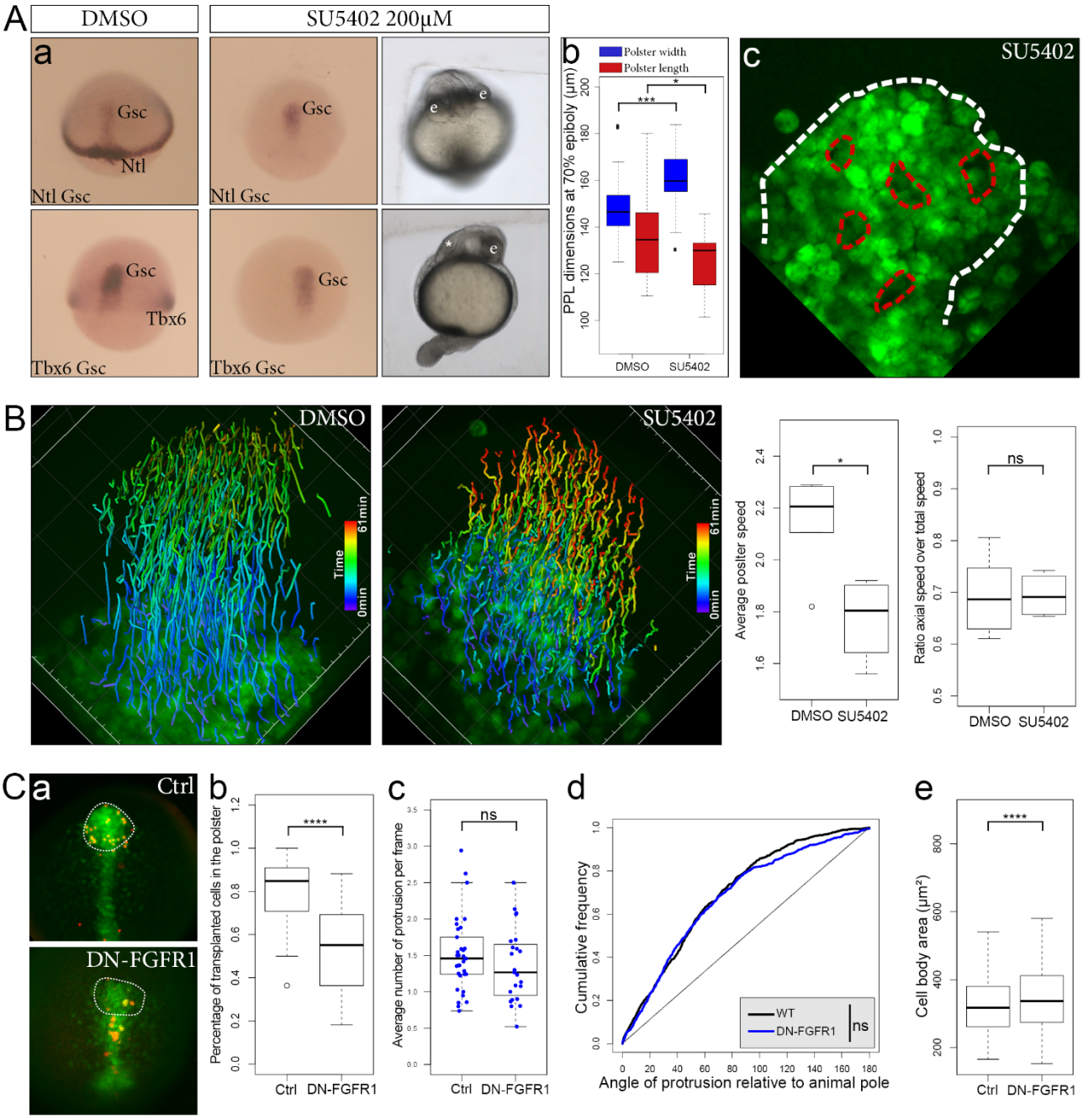

Figure 43. Disruption of FGF signalling perturb polster cells migration. A: Chemical inhibition of FGF signalling using the SU5402 drug. a: Effect on gene expression and embryonic development of SU5402 inhibition. *gsc*, *ntl* and *tbx6* expression respectively label prechordal plate, notochord and lateral mesoderm. Asterisk marks the absence of axial structure at 24 hpf, e: eye. b: Modification of polster shape upon exposition to SU5402 (DMSO: n=26 embryos, SU5402: n=23 embryos). c: Maximum projection of a polster treated with SU5402. White dashed line delineate polster contour. Red dashed line marks non-*gsc*-positive cells in the polster. **B**: Migration of polster cells upon treatment with SU5402. Trajectories of control and SU5402 treated embryos are shown colour-coded according to time (DMSO: n=6 embryos, SU5402: n=4 embryos). **C**: Cell-autonomous inhibition of FGF signalling by expression of DN-FGFR1. a: Wild type or DN-FGFR1 cells (red) transplanted in a wild type host and imaged 2 h later. White line marks the polster. b: Percentage of transplanted cells still in the polster after 2 h of migration (Ctrl: n=29 embryos, DN-FGFR1: n=30 embryos). c-e: Protrusion frequency and orientation of projected area of transplanted actin labelled cells (Ctrl: n=33 cells in 13 embryos, DN-FGFR1: n=23 cells in 3 embryos).

A role for FGF signalling in polster migration?

During the internship that preceded my PhD, we wondered whether FGF signalling could play a role in polster migration. Indeed, several pieces of evidence suggested that this might be the case. First, several FGF ligands are specifically expressed in the axial mesoderm, like FGF6 or in the prechordal plate, like FGF3, 17 and 24 (ZFIN expression patterns). Second, FGF receptors 1a and 1b are expressed in the axial mesoderm (ZFIN expression patterns, Ota et al., 2010). Third, it has been shown that FGF signalling can have a chemotactic role. For example, in the PLLp, FGF3 and 10, secreted by the primordium, attract isolated primordial cells, which express FGFR1 (Breau et al., 2012). Last, it has been shown in the Medaka fish model that FGFR1 signalling has a cell-autonomous role on prechordal plate migration (Shimada et al., 2008). The fact that polster cells both express FGF ligand and receptor prompted us to hypothesise that FGF signalling might act in a co-attraction process. It is to note that these experiments have been performed before ruling out such behaviour in polster cells. Indeed, we wondered how polster cells stay cohesive as a group and do not migrate laterally, away from the axis. Co-attraction could have been a way to ensure cohesiveness.

FGF signalling is involved in induction and maintenance of axial mesoderm identity and any effect induced by its disruption could be due to loss of mesodermal identity. I thus had to fine-tune the modulation of FGF signalling not to affect polster identity. Exposition to 200 µM of SU5402, a chemical inhibitor of FGF signalling (Shimizu et al., 2005), starting from the shield stage when mesodermal tissues are already specified leads to loss of lateral and notochord mesoderm but not of prechordal plate identity (Fig. 43A). This treatment did not prevent polster migration as axial mesoderm extends during gastrulation and the eye field is separated by 24 hpf.

Nevertheless, in these conditions, I observed that the polster was shorter and wider, a phenotype often found when polster migration is affected (Fig. 43A). It also appeared that certain areas are devoid of GFP positive cells, suggesting that either the boundary between hypoblast and epiblast has been altered so that ectodermal cells “fell” in the polster or that some axial cells might have lost their identity, something which is never observed in wild-type conditions. I then tracked polster cells in wild-type and SU5402 conditions (Fig. 42B). I observed a significant decrease of total speed suggesting migration defects of these cells, which is compatible with the delay observed in axis extension. Surprisingly, though, it appeared that the ratio between axial speed and total speed, a measure of directionality, stayed constant. Accordingly, cell persistence is only mildly affected by SU5402 treatment, suggesting that cells are still oriented but simply move slower. These results rather point toward a permissive role of FGF signalling. They are, however, obtained in embryos where FGF is completely abolished, and thus might result from non-cell-autonomous effects.

In order to study potential cell-autonomous effects, I used expression of a dominant negative form of FGFR1 (DN-FGFR1) to disrupt FGF signalling. In this construct, the intracellular domain of FGFR1

is replaced by GFP, preventing autophosphorylation upon dimerisation with a wild type receptor (Lee, 2005). I injected cells with Tar* and MOCas, to force polster identity despite FGF signalling inhibition, and Lifeact-mCherry or Histone2B-mCherry, then transplanted some in the shield of unlabelled hosts (Fig. 43C). I observed that transplanted DN-FGFR1 expressing cells are more likely to exit the polster than wild-type cells. The same experiment in Medaka fish, using transplants of FGFR1 mutant cells, gave similar results (Shimada et al., 2008). This suggests a cell-autonomous effect of FGF signalling on cell migration. As DN-FGFR1 expressing cells tend to be found in posterior axial mesoderm, despite being forced to adopt a polster identity, it might be possible that slower migration resulted in these cells trailing behind. I thus used the actin labelling to quantify protrusiveness but noticed that FGF signalling inhibition had no effect on frequency or orientation of protrusions. The fact that orientation is maintained is consistent with the absence of strong effect on cell directionality, but it is surprising that frequency is maintained while migration speed is decreased. It might be that protrusion efficiency in displacing the cell body is decreased. Accordingly, cells expressing DN-FGFR1 have a larger cell body that might be harder to displace. Still, this is surprising as even inert objects are carried by surrounding polster cells when placed among them and usually end up under the head, the destination of the polster. One possibility would be that FGF signalling modulates cell-cell adhesion. Higher amounts of E-Cadherin or changes in its dynamics might lead to stronger adhesion and this, combined to a larger cell body, might explain why these cells trail behind the polster. This constitutes an interesting lead to clearly establish the role of FGF signalling in polster cell migration.

Localizing Wnt/PCP components in polster cells

During the Master internship that preceded my PhD, I started to look for markers that could be asymmetrically distributed in polster cells and, as such, be used as a polarity readout beside protrusion formation. Wnt/PCP components were good candidates, as their distribution in polarised epithelia is well described and the Wnt/PCP signalling is required for polster cell orientation (Čapek et al., 2019; Dumortier et al., 2012; Gao, 2012; Yang & Mlodzik, 2015). At that time, the work from Čapek et al. (2019), strongly supporting a solely permissive role of the Wnt/PCP pathway was not published, so we hoped to find some of its components located in the cell. We first looked at the Dsh protein that is usually located at the rear of cells, along with the Wnt receptor Fz7 (Yang & Mlodzik, 2015). A dominant negative form of Dsh had already been used to block the Wnt/PCP pathway, resulting in loss of protrusion orientation (Dumortier et al., 2012). I thus built a mCherry tagged version of Dsh and injected it along with GFP targeted to the membrane by a CAAX tag (mb-GFP). A few injected cells were transplanted in wild type hosts for observation of Dsh-mCherry distribution (Fig. 44A).

Dsh-mCherry displays a rather homogeneous cytoplasmic distribution but it sometimes forms accumulations that appear as bright puncta. I only worked with very low doses of fluorescent Dsh, to

avoid as much as possible artefactual accumulations. Dsh is a molecule involved in several pathways but it has been described that it accumulates at the membrane when signalling in the Wnt/PCP pathway (Gao, 2012; Yang & Mlodzik, 2015). I hence quantified the localisation of cortical Dsh accumulation relative to the direction of migration (Fig. 44A). I observed that cortical Dsh accumulations were more often found at the rear of the cell. This is consistent with the localisation of Dsh in epithelia, but is surprising if we consider that the Wnt/PCP pathway only has a permissive role. Furthermore, quantification of these accumulations is very tedious as they are very rare, making it a poor maker to quantify cell orientation.

I nevertheless made some interesting observations. First, these accumulations are mobile and seem to move toward the cell centre after leaving the membrane, although I never quantified these movements. This observation is consistent with the signalling role of Dsh. Second, I observed a few cytoplasmic bridges through which cells stayed in contact despite cells bodies being away from each other. Interestingly, these cell bridges contained a stable Dsh accumulation, and were located at the rear of the cell (Fig. 44A). The role of these bridges and how they relate to Wnt/PCP signalling is, however, still obscure. They might be the result of longer adhesion, as it has been proposed that Wnt/PCP extends duration and surface of contact between cells.

Later during my PhD, I checked whether other elements of Wnt/PCP pathway could also be asymmetrically distributed. I transplanted polster cells expressing a GFP tagged version of Fz7 in the shield of an unlabelled AB embryo and observed that Fz7 is located to the membrane (Fig. 44B) but also formed numerous cytoplasmic accumulations. Strikingly, Fz7-GFP is more accumulated at the rear of the cells than at the front, again suggesting a polarised distribution of Wnt/PCP components. This observation is surprising as it contradicts published results where no polarised accumulation of Fz7 is observed.

This observation was encouraging but the asymmetry I observed is not very sharp. This prompted me to look at the distribution of other components of this pathway. Pk and Vangl2 both localise at the anterior part of the cell in planar polarised epithelia and I tried to quantify the distribution of their GFP tagged version (Gao, 2012; Yang & Mlodzik, 2015). However, despite obvious developmental effect of Pk or Vangl2 overexpression in injected embryos, suggesting a perturbed Wnt/PCP pathway, I never managed to observe signal coming from these proteins, either in injected donors or in transplanted cells. In absence of these data, I could not strongly assert asymmetric distribution of Wnt/PCP components, especially since several studies rather suggested a permissive, non-localised role. Anyway, these results are interesting and might be worth going back to in further extension of this work.

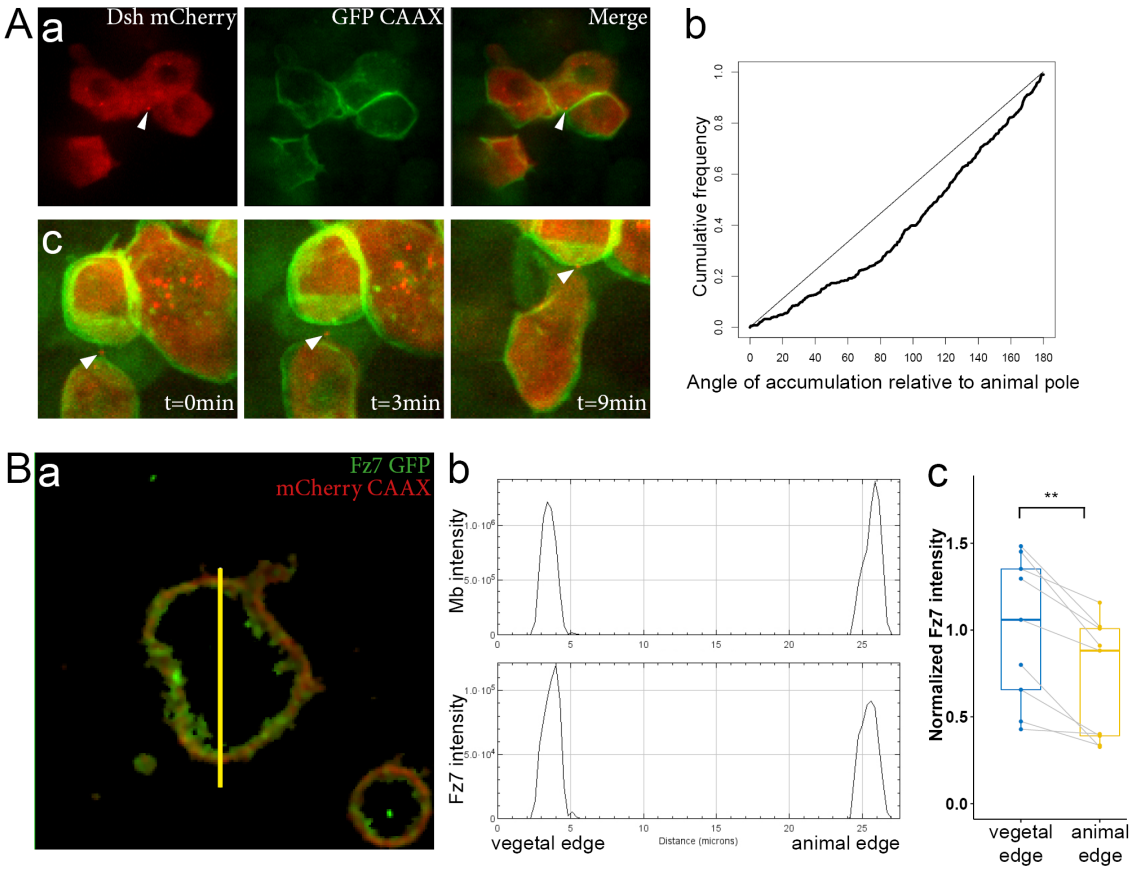

Figure 44. Distribution of Wnt/PCP components in polster cells. A: Cortical localisation of Dsh mCherry. a: Polster cells expressing Dsh mCherry and membrane-bound GFP transplanted in an unlabelled polster. Arrowhead points to a cortical Dsh accumulation. b: Angular distribution of cortical Dsh accumulation compared to the direction of migration (n=29 cells in 6 embryos). c: Timelapse of a Dsh accumulation located in a cytoplasmic bridge between to cells (arrowhead). **B**: Membrane distribution of Fz7-GFP. a: Polster cells expressing Fz7 GFP and membrane-bound mCherry transplanted in an unlabelled polster. On the presented image, most of the cytoplasmic signal has been removed by thresholding and keeping only signal at the membrane. b: Intensity profiles of Fz7 GFP and membrane mCherry along the yellow line it (a). c: Fz7 intensity normalised by membrane intensity at the animal and vegetal extremities of cells (n=9 cells in 4 embryos).

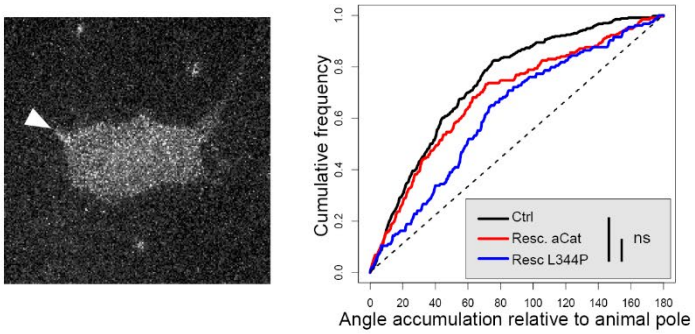

Figure 45. PIP3 distribution during polster migration visualised by Akt PH domain. Angular distribution of PH domain mCherry accumulations (arrowhead) in transplanted polster cells compared to direction of migration in different conditions (Ctrl: n=39 in 6 embryos, rescue α-Catenin: n=25 cells in 7 embryos, rescue α-CateninL344P: 26 cells in 6 embryos).

Cytoplasmic distribution of the PIP3 secondary messenger

As mentioned in the introduction, PIP3 is a phospholipid implied in intracellular signalling as a secondary messenger. It is produced by the activity of the PI3K kinase on PIP2 phospholipid contained in the membrane (Kölsch et al., 2008). This messenger in turns activates other signalling pathways implied in several cell functions including protrusion formation. Indeed, it has been described that PI3K activity is required for protrusion formation and orientation in polster cells (Dumortier et al., 2012; Dumortier & David, 2015; Montero et al., 2003). Furthermore, results from Julien Dumortier, a former PhD student in our lab, suggested that PIP3 accumulations are found more often in the anterior part of cells (Dumortier et al., 2012). I thus wondered whether we were able to reliably identify PIP3 distribution in these cells, which could be used as another marker of polarisation and be used to relate mechanotransduction with the PI3K pathway. For that purpose, I expressed in polster cells, a mCherry tagged version of the PH domain of Akt, a construct supposed to bind to PIP3 (PH-mCherry) and observed its cortical distribution (Fig. 45).

I was surprised to observe that expression of PH-mCherry is very toxic, leading to severe developmental delays in injected embryos, as other studies that used this construct never reported this. To limit toxicity, I used very low doses of PH-mCherry, but then obtained a very poor signal-to-noise ratio (Fig. 45). I counted accumulations of the protein at the membrane, and initially thought I found an animalward bias in the distribution. Encouraged by this observation I wanted to observe whether PIP3 distribution was altered upon disruption of mechanosensation by α-Catenin. In thus coinjected PH-mCherry domain with MO α-Catenin and mRNA coding either for WT *α-catenin* or for *α-cateninl344p*. I observed no difference of PIP3 accumulation distribution between these two conditions, but the data are so noisy that I strongly doubted my observations. It thus still unclear how PIP3 is distributed in polster cells during zebrafish gastrulation. Better imaging conditions or a brighter, more photostable and less toxic construct might help decipher the link between mechanosensation and PI3K signalling.

Mechanical characterisation of the polster

The conclusion that mechanical forces are responsible for guidance of polster cell migration prompted us to quantify the mechanical environment in which these cells migrate. Mechanical properties of polster cells have already been studied in individual cells, in particular cortical tension, membrane to cortex adherence, and junctional adherence (Diz-Muñoz et al., 2010; Puech et al., 2005). However, nothing is known about in vivo, tissue mechanics, except that the overlying ectoderm generates friction forces with the polster through adherens junction (Smutny et al., 2017). I thus tried to measure mechanical forces applied to polster cells and see whether they correlate with tissue motion.

Tension distribution in the polster

Measurement of living tissue mechanical properties can be performed directly in vivo using laser ablations. This technique consists in piercing a hole in a tissue and observing reaction of the tissue. If it is subject to an anisotropic tension, the tissue will retract faster along this axis (Bonnet et al., 2012; Campàs, 2016; Colombelli et al., 2007). A stress tensor can be fit from retraction speed and the size of the hole allows probing mechanics at different scales, from a single membrane to a whole tissue. Using the laser ablation protocol developed here, I performed several tests of such cuts. Upon ablation of large circles of cells, I mainly observed that cells out of the plane quickly moved in the hole, closing the wound in less than a minute (Fig. 46A). Similarly, local ablation of a single cell or a single membrane led to a collapse of neighbouring cells that fill the hole (Fig. 46B). I was hence unable to establish any clear reaction using laser ablation. At most, these tests tend to suggest that the polster is not particularly under tension.

Another non-invasive approach that allows estimation of tissue mechanics is force video microscopy (Campàs, 2016). It basically relies on simple but strong assumptions on epithelial tissue organisation. Starting from segmented epithelial cell contours, this technique compares deviation of cell geometry to a theoretical tissue at rest and makes inferences on forces applied to this tissue. I thus acquired a few movies of migrating polsters in *Tg(Gsc:GFP)* embryos expressing mb-mCherry and tried to apply force video microscopy on these. The point is that this technique relies on assumptions that are not met by polster cells, like staticity at short time scales or polygonal cell shapes, only obtained as a result of adhesion and surface tension. Hence, without surprise, my attempts at using softwares made for force inference in epithelia (CellFIT) to study mesenchymal cells resulted in absurd results (Brodland et al., 2014; Veldhuis et al., 2015). These difficulties were also amplified by the fact that it is hard to segment properly polster cell shape as the tissue is in three dimensions, cells move and deform quickly, and are deep, so that membrane signal is not particularly good.

Recently, another approach was developed to measure cell shape anisotropy without the need for segmentation (Durande et al., 2019). Starting from pictures where membranes are labelled, it relies on Fourrier transforms applied to small regions, typically 2 to 3 cell diameters, from which is extracted preferential direction of the membrane and an averaged deformation tensor. By tiling the whole image with overlapping regions of interest, and possibly by averaging over time, this method provides access to cell deformation quickly and without the need for segmentation (Fig. 46C). I performed a few tests with this approach on previously acquired movies and encountered two problems. First, Fourrier transform is very sensitive to patterned background like the low signal of a LCD screen detected by the microscope, that formed a striped pattern. I thus corrected images by removing this background noise using blurring and background removing filters. Then, the analysis routine has been written for large, mono-layered and slowly moving tissues, while the polster is rather narrow, multilayered and migrates fast. I thus selected for each movie a single plane that contains the largest slice of polster. I then

registered the movies so that polster front stays immobile during the movie. I finally ran analysis on the mb-mCherry channel and basically observed no particular pattern of cell shape anisotropy (Fig. 46C). I am, however, not certain that I did not miss something and perhaps some better image analysis could lend some interesting result.

Development of a sensor to measure stress distribution in the polster

Despite relatively unsuccessful attempts at measuring large-scale tension gradients based on cell shape anisotropy, we still wanted to measure mechanical properties of the polster. In particular, we wondered whether cells are subject to asymmetric mechanical shear stress as this could be an instructive cue for migration. One approach to do so is to use deformable sensors inserted directly in the tissue (Campàs, 2016). This has for example been done with deformable fluorocarbon oil droplets or soft hydrogel beads inserted in tissues that respectively allow measurement of normal and shear stresses (Campàs et al., 2014). During a summer school, I met Alexandre Souchaud, a student from the Matière et Système Complexe laboratory, whose PhD was supervised by François Gallet and François Graner and aimed at developing such sensors. We started a collaboration, the results of which are pre-published on bioRXiv and described in this part (see Appendix) (Souchaud et al., 2021).

The sensors Alexandre designed are made of small PDMS droplets produced by a microfluidic device. They have a size similar to cells, tuned between 20 and 40 μm in diameter (Fig. 47A). These droplets are produced in large quantity, then polymerised to form a deformable but incompressible bead. Mechanical properties of these sensors were calibrated on the gel bulk, directly on beads, and on beads inserted in cell aggregates. Composition of the PDMS mix has been optimised for the bead to deform in the range of stresses applied in biological tissues, that is around 10^2 Pa for zebrafish development (Mongera et al., 2018). In order for the sensor to interact with surrounding living tissues, it can be coated with Fibronectin through non-covalent interaction. Unfortunately, it was not possible to coat these beads with E-Cadherin as it requires complex chemical work to specifically bind this protein to the bead. Finally, PDMS is made fluorescent by covalent binding of hydrosilane to isothiocyanate-bearing Rhodamine B that fluoresces in red. Thus, by performing 3D stacks acquisition with good axial resolution (1 μm), the shape of the sensor within tissues can be precisely reconstituted.

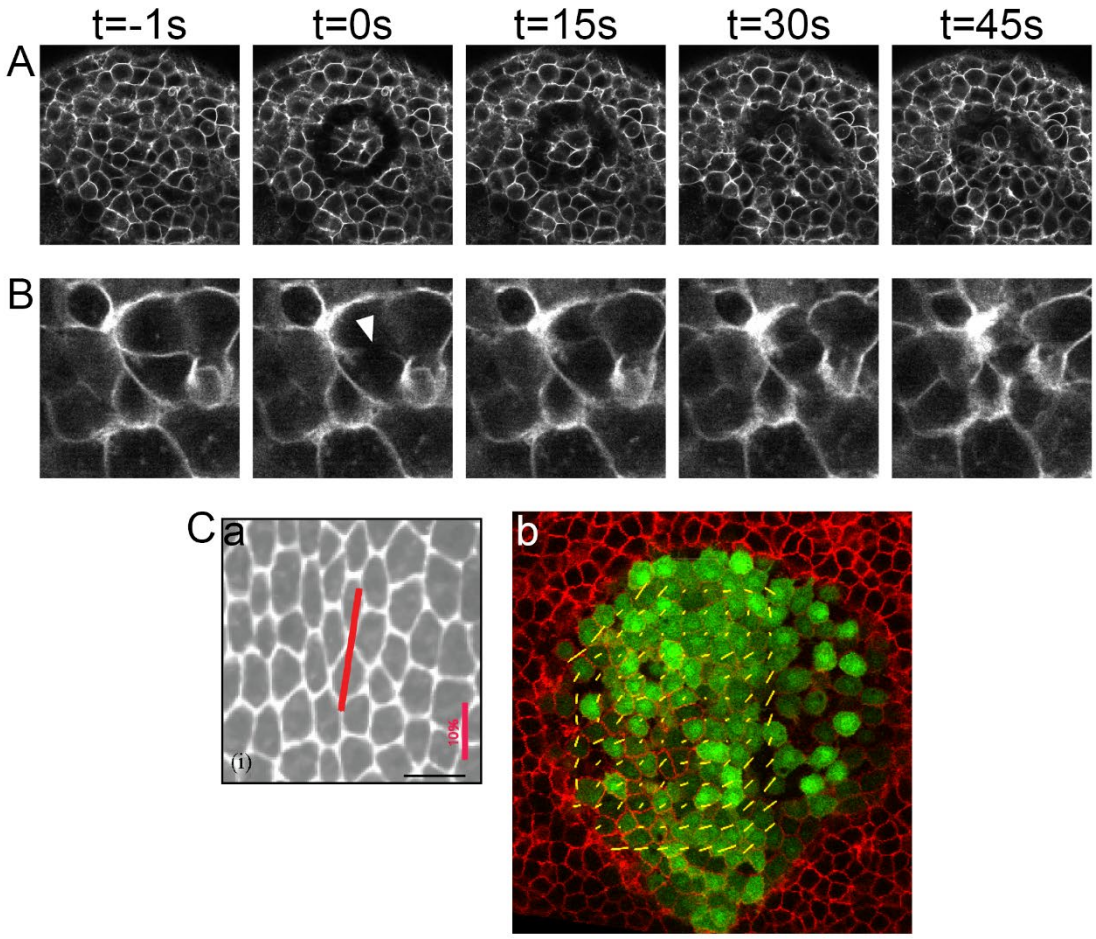

Figure 46. Attempts at measuring polster mechanical properties. A: Timelapse movie of a large ring of cells being laser ablated. No particular retraction is observed and out of plane cells quickly fill the ablated area. **B**: Timelapse movie of cell membrane local laser ablation. Again, no particular retraction happens and neighbouring cells collapse and replace the ablated cell. **C**: Local cell shape anisotropy. a: Example of cell shape anisotropy measurement on an image of Drosophila dorsal thorax. Local cell shape anisotropy pattern is determined by Fourier transform. Its magnitude is represented by the bar size, and its direction is the direction of the bar. Modified from Durande et al., 2019. b: Cell shape anisotropy measured on zebrafish polster cells labelled with membrane mCherry (Average of 7 embryos over 24 times).

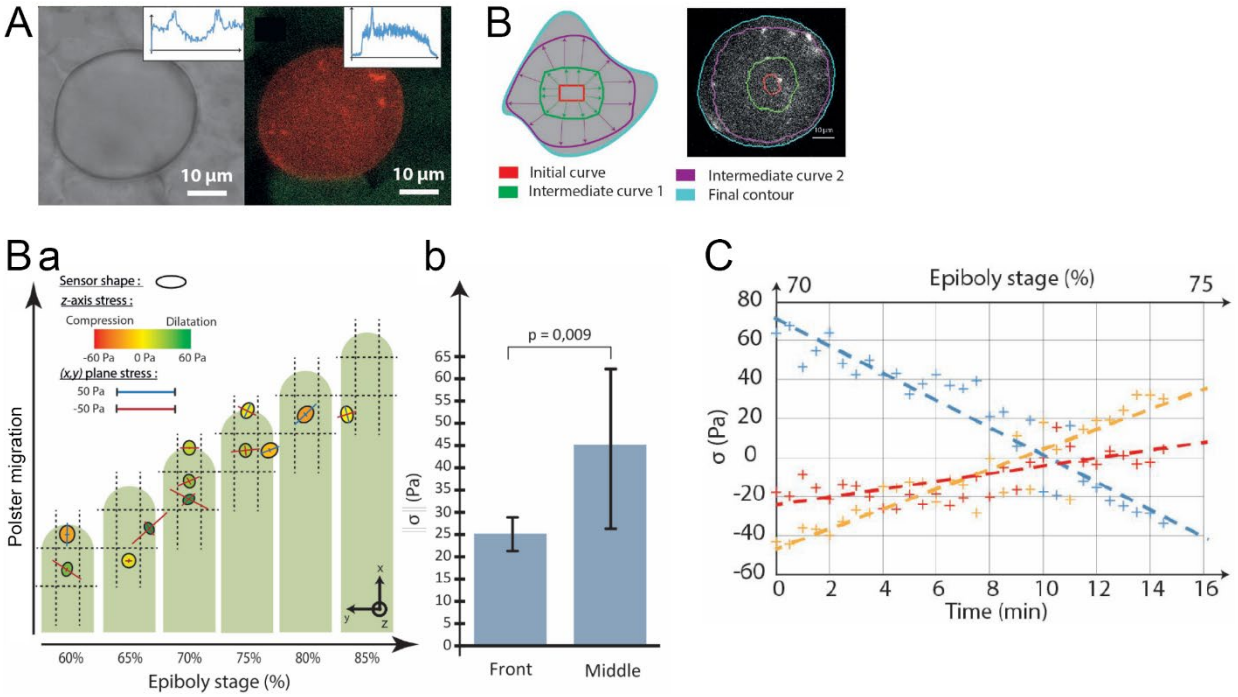

Figure 47. Deformable PDMS sensor allows measurement of shear stress in the polster. Modified from Souchaud et al., 2021. **A**: Bright field and fluorescence image of a PDMS bead transplanted in the polster of a host embryo. Insets represent intensity profile through sensor diameter. **B**: Determination of the PDMS sensor contour using active contour method: the initial seed (red) progressively swells (green, purple), until it reaches the contour of the object (cyan), which minimises its pseudo-energy. **C**: Shear stresses in the polster. a: Mapping of shear stresses in the polster at different epiboly stages (n=12 measurements on 7 different embryos). Planar projection on the (x, y) plane of the main shear stresses is drawn as an ellipse, while projection along the normal axis z is represented by a colour code. Polster is divided in nine areas, and position of sensors on the schematics corresponds to their actual position in the polster. b: Comparison of the shear stress amplitude $\|\sigma\|$, averaged at the front (n=3) and in the middle (n=7) of the polster. **C**: Time evolution of shear stress tensor main components for a sensor located in the polster central zone of one particular zebrafish embryo. Each principal axis is colour-labelled according to its nearest axis of the polster referential (x: red, y: yellow, z: red). Within 15 minutes, the stress amplitude along the z axis changes from positive (extension) to negative (compression). In the same time, the stress along y axis follows the opposite evolution, as does to a lesser extent the component along x axis.

Once acquired, the bead contours were automatically detected by a custom-made algorithm (Fig. 47B). An initial seed contour is selected in the bead which grows by iteration. At each step, an energy like function is computed corresponding to the geometrical properties of the contour. As long as the energy function decreases, the contour grows, in three dimensions, until it reaches a minimum corresponding to the edge of the bead. An ellipsoidal shape is then fitted to the generated contour and length and orientation of the three main axes are extracted and used to compute the stress applied on the bead and responsible for its deformation.

In order to quantify mechanical stress and contribute to the development of these sensors, I inserted them in the migrating polster. Using a large glass transplantation needle, I was able to insert individual PDMS sensors in the shield of embryos (Fig. 47A). This operation is somehow complex for two reasons. First because PDMS is less dense than water, beads tend to float. It is thus hard to catch them in the needle and they tend to exit the wound once inserted in the embryo. Then, these beads strongly stick to glass surfaces so that I had to be careful and prevent the bead from touching the side of the needle. Still, I was able to insert a bead in 7 different embryos and, since some of these beads were imaged several times, we ended up with 12 measurements, at different locations in the polster and at different moments during gastrulation, from 60 to 85% epiboly (Fig. 47B). We unfortunately did not have enough time to acquire enough data to precisely map stress distribution in the polster and draw robust conclusions. We nevertheless managed to make some interesting and promising observations.

To analyse the stress spatial distribution in the polster, we divided it into 9 zones (front/middle/rear and left/centre/right). We observed that all stress components lie in a range comprised between +60 and − 60 Pa, with approximately equal distribution between positive and negative values (Fig. 47B). However, we found no clear correlation between sensor location and stress orientation or amplitude. Similarly, we observed no obvious pattern of stress variation over time. However, we observed that averaged stress amplitude over the left/centre/right zones and over the different epiboly stages, was higher in the middle of the polster than at the front (Fig. 47B). This is actually the first indication that stress gradients might exist in the polster. Furthermore, we noted a general trend as beads seem to be shortened in the mediolateral axis and elongated in the animal-vegetal one, as if stretched. This is actually at odds with the idea that these cells might be pushed by the elongating axis and rather suggest that these cells are actually being being pulled along the animal vegetal axis.

For 7 sensors we were able to follow the evolution of the stress components over time, during 15 to 30 min, at different stages of epiboly. They did not show any significant changes, except for one particular event (Fig. 47C). A sensor inserted was imaged during 15 min, between 70 and 75% of epiboly and it appeared that the stress amplitude along the principal tensor axis, closest to the dorso-ventral axis, changes from positive (extension) to negative (compression). In the same time, the stress along the tensor axis closest to the medio-lateral axis follows the opposite evolution, and so does, to a lesser extent,

the component close to animal-vegetal axis. Directions of main tensor axes remain stable except for some small fluctuations. This event is a clear signature of a main change in the stress partition, which takes place within a few minutes at this stage of epiboly. This observation might correspond to the local cell rearrangement leading to a redistribution of tensions. It could also correspond to the change of orientation of the ectoderm above the polster, that starts following the convergence and extension movement of axial mesoderm around these stages of developments (Smutny et al., 2017). The short duration of this event might explain why it has been observed only once, out of 7 assays. It is, of course, impossible to draw general conclusions from one single event, but its occurrence demonstrates that PDSM bead sensors can measure the time evolution of shear stress tensor during the polster migration.

Unfortunately, we lacked time to perform more experiments and collect more data. Furthermore, E-Cadherin could have lent more interesting result as polster cells should fully adhere on it but development of the sensor was stopped after Alexandre Souchaud's PhD, defence. Still, these preliminary results, potential stress gradient and quick modification of stress distribution are particularly encouraging and suggests that understanding stress distribution in the polster might give some interesting insights in understanding tissue migration.

Discussion

Precise guidance of migrating cells is required to achieve proper development and morphogenesis. In vitro, many chemical and physical cues can orient cell migration, but it is not clear how such cues can guide cells over long distances in the dynamic environment of the developing embryo. During this PhD, I studied how is guided the collective migration of the polster and how this migration is coordinated with the migration of the following posterior axial mesoderm. Using cell transplantation, I first showed that collectiveness of polster and neural crest cell migration relies on different mechanisms. In order to locate the information of direction guiding polster migration, I developed deep and spatially restricted laser ablations and observed that contact with posterior mesodermal cells is required for polster guidance. I then confirmed this observation using surgical removal of the polster and transplantation of large groups of polster cells, showing that isolated polster cells are unable to orient their migration and tend to disperse. Using similar transplantation approaches, I showed that this guidance relies on the extension of the posterior axial mesoderm and is actually not restricted to this tissue since migrating lateral mesoderm is also able to drive polster migration. I indeed showed that polster cell orientation requires the presence of actively migrating neighbouring cells. By the means of functional genetic approaches, I established that polster cells rely on perception, at the level of adherens junction established at cell-cell contact, of a mechanical signal that is detected through the E-Cadherin/α-Catenin/Vinculin mechanotransduction pathway. I have thus shown that, rather than being attracted to its destination by long-range signals, the polster is guided by mechanical cues provided by the anteriorward movement of more posterior cells, creating a robust and self-organising system. Interestingly, the idea that a mechanical information can propagate and coordinate movements of cells at a distance was recently proposed in two other systems (Fig. 40) (Das et al., 2019; Xiong et al., 2020).

Do polster cell exhibit contact inhibition of locomotion and co-attraction?

Given the apparent similarities between polster cells and neural crest cells in terms of morphology, migration and tissue organisation, we supposed that similar mechanisms might control the migration of the two cell types (Fig. 17, Fig. 20). Since neural crest cell migration is rather well understood and largely relies on two behaviours, CIL and CoA (Carmona-Fontaine et al., 2008, 2011), we tested whether polster cells exhibited these behaviours. By reproducing the seminal experiments performed in Xenopus to establish these two behaviours in neural crest cells, we showed that polster cells do not display obvious CIL or CoA behaviour (Fig. 25). However, in these experiments, we lacked positive and negative controls to compare our results with, which might weaken our conclusions.

In the case of CIL, we used numerical simulations of polster cell where we could add or not CIL and observed that simulations without CIL were closer to experimental observations. However the CIL we implemented in the simulation might not properly recapitulate a potential CIL behaviour displayed by polster cells. This point largely depends on the definition of CIL (Fig. 48). Indeed, we implemented

our CIL rule as active movement away from a contact, which corresponds to a strict definition of the CIL (Fig. 48A). It is actually the case for neural crest cells, where a complex containing cell-cell adhesion molecules, signalling receptors and polarity regulators assembles at the level of cell-cell junctions (Carmona-Fontaine et al., 2008; Stramer & Mayor, 2016). This complex inhibits migration at the contact and promotes protrusion formation away from it. A broader definition of CIL would simply be a change of motion upon contact (Fig. 48B) (Abercrombie & Heaysman, 1954). According to this definition, CIL could be a passive phenomenon, where steric interactions force a cell to change direction upon contact with another. It seems to be the case for polster cells transplanted at the animal pole, that form a mono-layered tissue and where I never observed a cell migrating over another (Fig. 25B, Fig. 29B, Fig. 33A). Based on our observations, we could consider that, at least at the animal pole, polster cell exhibit a passive, steric CIL but not an active one like in neural crest cells.

It is to note, however, that the reaction to cell-cell contact depends on the angle of contact between the cells. In particular, active CIL happens mainly when the leading edge of two cells collide, and much less when another part of the cell is contacted (Stramer & Mayor, 2016). Actually, it has recently been proposed that a cell contacting the rear of another cell through its leading edge could lead the contacting cell to follow the contacted one, a mechanism deemed contact following of locomotion (Fig. 48C) (Li & Wang, 2018). This behaviour seems to rely on the Wnt/PCP signalling and coordinates trains of cells. This, however, does not correspond to what we observe in polster cells, since it is actually the follower cell that drives the leader one and not the opposite as in contact following of locomotion. Finally, it has also recently been proposed that cell-cell contacts could stabilise cell migration rather than provoke a change of direction, a behaviour that has been called contact enhancement of locomotion (Fig. 48D) (D'alessandro et al., 2017). It appears that reaction to cell-cell contact is much more complex than expected and is not limited to the classical version of CIL. Precise mechanisms controlling these newly identified behaviours as well as how cells preferentially adopt one particular response to contact rather than another are, however, largely unknown.

Concerning CoA, we completely lacked controls in our experiments and, although our results strongly advocate against such a behaviour, it would be more rigorous to perform such experiments. Using endodermal cells, which migrate randomly and individually, could constitute a good negative control for CoA (Pézeron et al., 2008). The experiment would thus be to transplant two groups of differently labelled endodermal cells at the animal pole. Finding a positive control is harder since, to our knowledge, the co-attraction behaviour has only been shown in neural crest cells, that are formed later during development. An approach to obtain positive control would be to force chemical attraction in polster cells. For example, the ligand/receptor couple Sdf1/CXCR4 is well known to be involved in chemoattraction (Doitsidou et al., 2002; Mizoguchi et al., 2008; Theveneau et al., 2013; Valentin et al., 2007). It could be possible express these two proteins in polster cells and observe whether they attract each other.

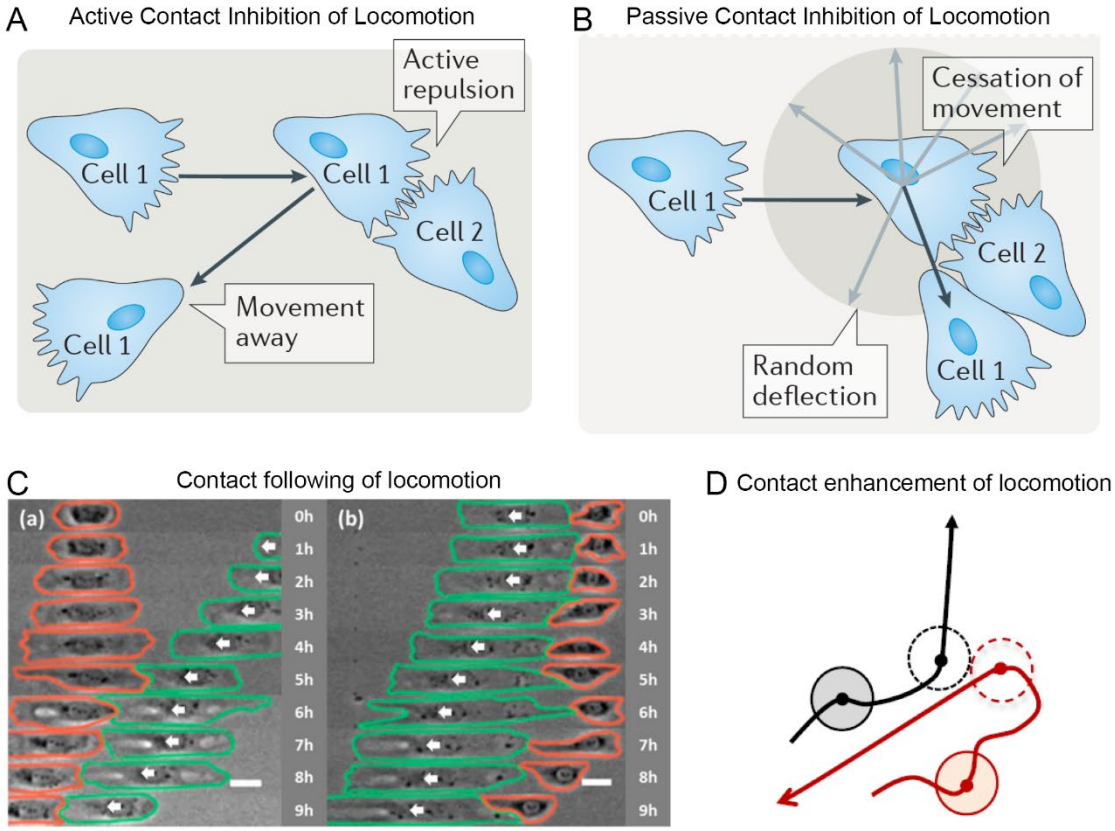

Figure 48. Different cell reactions after contact. A: Active CIL. In this situation, upon contact, colliding cells actively inhibit protrusion at the contact point and reorient away from it (see Fig. 17B). Modified from Stramer & Mayor, 2016. **B**: Passive CIL. Deflection of cell movement can occur simply out of steric interactions. If Cell 1 cannot migrate over Cell 2, it has to change direction upon contact in order to continue migrating. In this situation, Cell 2 does not actively inhibits Cell 1 but simply prevents it from migrating straight. Modified from Stramer & Mayor, 2016. **C**: Contact following of locomotion. a: The green cell collide with the rear of the orange cell. This triggers migration of the orange cell away from the green cell and resemble active CIL. However, after collision, protrusive edge of green cell do no collapse. On the contrary, green cell start to follow the orange cell, a behaviour which does not correspond to CIL. b: The green cell, in contact with the orange cell, start to migrate away from this contact. As a consequence, orange cell adopts a migratory morphology and follows the green cell, staying in contact with it. Once again, this behaviour does not correspond to CIL. The behaviour exhibited by these cells has thus been deemed Contact following of Locomotion and typically arise when the leading edge of one cell contacts the rear edge of another cell. Modified from Li & Wang, 2018. **D**: Schematic representation of Contact Enhancement of Locomotion, a behaviour where collision stabilises cell current cell trajectories rather that reorienting cell movement away from contact point. Modified from D'alessandro et al., 2017.

One surprising result we observed during the attraction assay experiment is that the centroid of transplanted groups of polster cells tended to move away from each other (Fig. 25D). Indeed, if cells exhibited co-attraction, one would expect that the two groups to get closer and, if not, that they stay still. One possible explanation is that the groups of cells are dragged away from each other by the overlying ectoderm. As a matter of fact, it has been shown that friction forces exist between the ectoderm and polster cells (Smutny et al., 2017) and I accordingly observed some correlation between animally transplanted cells migration and overlying ectoderm movement. Thus, at the animal pole, the epiboly movement of the ectoderm could tend to separate the underlying polster cell clusters. Interestingly, it is also the case in mixing assay experiments (Fig. 25A), where two groups are transplanted in contact. Although cells form the two groups actually mix at the periphery, the centroids of these groups tend to drift away. The observation that even groups that are located closely move away support the idea that polster cells do not exhibit CoA, as does the fact that these cells tend to spread after transplantation.

Does laser ablation intrinsically perturb migration?

In order to establish that contact posterior axial mesoderm is required for orientation of polster migration, I used laser ablation of polster cells. Such a technique is incredibly useful to kill groups of cells and observe reaction of surrounding tissues, but comes with a few disadvantages. Fist, killed cells are not removed and form debris that stay in the extracellular medium (Rock & Kono, 2008). Actually, when laser treatment was slightly too intense, I observed autofluorescent debris located in the ablation area, that likely are crosslinked dead material (see. Appendix) (Boutillon, et al., 2021). These debris indeed seemed to interfere with cell migration as I observed several instances of cells having to squeeze around to get past the bar of debris. However, quickly after ablation, these debris were usually evacuated from the migration path by the movement of follower cells, closing the gap and pushing them out of the wound. Presence of these debris could thus explain why, in mid-polster ablation, the posterior group of cells is slowed down although orientation of its protrusions is maintained after ablation.

Furthermore, besides generating debris that physically interact with cell migration, laser ablations release cytoplasmic content of destroyed cells, which might chemically perturb surrounding cells (Rock & Kono, 2008). A first way to rule out that our observations were due to chemical perturbations generated by cell death was to perform control, parallel ablations, that kill a similar number of cells but without isolating a group of cells (Fig. 27, Fig. 28). Such control ablation had no particular effect on migration or cell orientation, suggesting that it is not laser treatment itself that perturb migration. In order to obtain a second control for this crucial experiment and to double-check whether contact with posterior axial mesoderm is required for polster cell orientation, I used surgery to remove the endogenous polster and transplant cells in front of the polster-less axis (Fig. 29). This approach is more invasive than laser ablation since I have to introduce a needle in the embryo but no cell death is supposed

to occur during this process. Furthermore, I could put some distance between the transplanted polster and the axis, in order to make sure that the wound created by the needle properly healed before imaging the embryo. Result obtained with laser ablation and surgery are very consistent, supporting the idea that laser ablation does not particularly perturb migration of the polster in a non-specific manner.

How are mechanical forces distributed in the polster?

In this work, we showed that cells require protrusive, adhesive and contractile followers in order to be oriented (Fig. 32B, Fig. 34C). This suggests that the information of direction transmitted from cell to cell relies on these three properties. What is the nature of this transmitted information? We observed that the mechanotransduction pathway implying E-Cadherin, α-Catenin and Vinculin, and in particular, the mechanosensitive domain of α-Catenin, are required for proper cell orientation (Fig. 35). We thus hypothesised that this information was of mechanical nature and that follower cells form actin rich protrusions that establish contact with other cells and locally pull on them, which is detected by the mechanotransduction pathway. However, we did not directly observe that cells indeed apply mechanical forces on each other, nor did we measure them, which constitutes a limitation of this work.

More and more tools are developed to measure mechanical properties and force distribution at several scales (Campàs, 2016). For example, traction force microscopy, deformable force sensors and tension sensor modules respectively allow measurement of the forces applied by a tissue on its substrate, local normal and shear stresses applied on cells, and average load applied on junctional molecules. However, most of these approaches have been developed for in vitro studies and are difficult or even impossible to implement in a living organism. Furthermore, different approaches could lend different results depending on which mechanical property is measured and at which scale. For example, a traction force applied on a junction, observed for instance by laser ablation, could generate relatively high or low molecular load depending on the number of molecules that are recruited at this junction (Blanchard & Adams, 2011). One thus has to carefully choose the mechanical measurement approach depending on which property is to be probed.

During my PhD, I tested several approaches to measure mechanical properties in the polster. In particular, inspired by the hypothesis proposed in Xenopus that polster could be oriented by a gradient of tension (Weber et al., 2012), I looked for such a gradient in the zebrafish. I first tested whether cell shapes were oriented along a particular axis and observed no such thing. I, however, encountered several difficulties, in particular the fact that these cells are mesenchymal, moving and migrating over a curved surface (Fig. 46C). Better image treatments might lead to more interesting results. I also performed preliminary experiments of membrane ablations, again looking for potential differences in retraction speed depending on the orientation of the cut membrane (Fig. 46A & B). I observed no particular recoil upon ablation as the ablated membrane actually collapse and neighbouring cells fill the gap. This rather

suggests that cell membrane is not particularly under tension, and even might be under compression. Finally, I also performed preliminary experiments using deformable sensors and observed that cells rather tend to be stretched (Fig. 47) (Souchaud et al., 2021). Preliminary measurements of mechanical properties thus give contradictory measurements and a more extensive exploration is necessary to better understand the mechanical state of these cells.

How to reconcile these views that polster cells might be exposed to compression and stretched, and how does this orient cell behaviour? One first hypothesis could be that cells being pushed in a crowded environment generate friction with the neighbours and that this friction is detected by cells through mechanotransduction and is actually instructive. However, we showed that the simple fact of being pushed is not sufficient to orient cells when they are surrounded by non-motile, non-adhesive or non-contractile cells. Furthermore, it has been published that shear stress tends to weaken and disassemble adherens junction, which is not compatible with this view (Kale et al., 2018).

Another hypothesis considers the fact that these potential compressive forces are applied at the level of the tissue and of the cell, and might simply not activate mechanosensation of α-Catenin, which opens under a traction force (Hoffman & Yap, 2015). On the contrary, we hypothesised that traction applied between cells is local and applied at the level of adherens junction established by actin rich protrusions. Direct observation of this force would constitute a strong argument for this hypothesis. Inserting a FRET tension sensor module in α-Catenin or another junctional protein could constitute a good approach as we could visualise live where load is applied on these molecules (Grashoff et al., 2010; Lagendijk et al., 2017; Vuong-brender et al., 2018). Use of this sensor and analysis of the results is, however, technically challenging, in particular *in vivo*. Another approach would be to use an antibody that specifically targets the open form of α-Catenin (Yonemura et al., 2010). Such an antibody has been described and already used in zebrafish (Priya et al., 2020), it could thus be interesting to look for asymmetric distribution and test whether absence of protrusion in followers decreases binding of this antibody. By combining these different approaches, we could establish a multiscale map of mechanical tensions and stresses in the polster, which would be interesting to correlate with cell motion in wild type and mutant situations.

What is the role of myosin in polster migration?

Myosin activity is responsible for retraction of the cell body in migrating cells and for the establishment of contractility-driven junctional tension in epithelia, leading to α-Catenin opening (Hoffman & Yap, 2015). It was thus a good candidate for the application of mechanical forces by protrusions in the polster. Interestingly, Myosin II activity is not required in an autonomous manner for cell orientation (Fig. 34B), which is consistent with published observations that disruption of RhoA activity, involved in stress fibre formation and myosin activation, does not affect autonomously cell

orientation (Dumortier et al., 2012). However, downregulation of Myosin II in the neighbours actually leads to loss of orientation in wild-type cells, suggesting a non-cell-autonomous role for myosin in guiding polster migration (Fig. 34C). This observation is consistent with the hypothesis that neighbours exert traction forces required to orient cell migration. It would be particularly interesting to test whether signalling upstream of myosin is also required non-autonomously for polster cell orientation, for example using dominant negative forms of RhoA or ROCK. This would complete the mechanism by which polster cells are oriented.

Distribution of Myosin II in the cell is particularly interesting. On average, distribution of cortical myosin accumulations is biased toward the rear of the cell, as would be expected if myosin is involved in displacing the cell body (Fig. 34A). In particular, I observed that cell membrane often retract after accumulation of myosin. How could myosin-induced contractions at the rear of the cell be detected by a cell at the front? A possibility would be that stress fibres connect nascent adherens junctions in the protrusion to the cell rear and that contraction at the rear puts the fibres under tension, thus pulling on the front cell. I however never observed such cables in polster cells. It is nevertheless worth noticing that in my experiments, actin is labelled using Lifeact, which rather labels dynamically growing filaments (Belin et al., 2015). Perhaps using Utrophin, which tends to label more stable actin cables, or phalloidin staining, could reveal the presence of stress fibres in polster cells. However, I also observed that Myosin II sometime accumulates at the basis of protrusions, which seems to correlate with their retraction. It is thus tempting to hypothesise that traction could be applied through protrusions put under tension by such accumulations of myosin. To test that hypothesis, it should be possible to measure whether protrusions are under tension, for example using laser ablation, and observe whether expression of DN-MLCK changes this tension. Furthermore, it would be very interesting to understand how Myosin II activity is regulated and whether two different pools of myosin exist, potentially with different roles in the cell. For that purpose, use of photoactivable azidoblebbistatin, that could locally inhibit myosin contractility, might be useful (Képiró et al., 2012).

Do numerical simulations faithfully recapitulate polster behavior?

In order to test whether a particular series of hypotheses is sufficient to explain polster cell collective behaviour, we chose to use numerical simulations. We built a rule-based model of polster cells, first by fitting migration parameters so that the motion of simulated cells corresponds to that of individual polster cells, then by adding particular behaviours to these cells (Fig. 37, Fig. 38). We first simulated cells that do not exhibit any particular behaviour upon contact with other cells. Such basic cells failed to recapitulate polster migration, suggesting that polster cells have to exhibit particular behaviours to migrate coherently. Since contact between cells is required for proper orientation, we then tested a naïve model based on epithelial cell migration, where the movement of each individual cell is

aligned with the average displacement of neighbouring cells. Such a rule actually recapitulates guidance by posterior mesoderm but the simulated polster failed to halt after ablation as does the real tissue, ruling out this hypothesis for polster cell orientation (Poujade et al., 2007). In light of our observation that cell orientation requires neighbours that migrate toward them and pull on them, we finally simulated polster cells that tend to align only with the followers. This rule actually recapitulated both guidance and laser ablation results and was consistent with other experimental results, which prompted us to name the phenomenon orienting polster cells "guidance by followers" (Fig. 38D).

It is, however, important to note that this model is voluntarily simplistic as it simply aims at testing the sufficiency of a set of hypotheses. In particular, we have not tried to simulate mechanisms underlying the "guidance by followers" behaviour. In order to get closer to an analytical model, with which we could make educated predictions on polster behaviour, we could increase the model complexity by adding more properties to the cells. This, however, requires to collect much more information, for example on cell adhesion, intracellular signalling, and so on. Before going for a full analytical, 3D model, some simple adjustments could be performed to test new hypotheses. For example, in the basic version of the model, we arbitrarily put a rigid confinement. This corresponds to the observation that polster or posterior axial mesodermal cells never laterally leave the axis. We performed a few preliminary tests replacing this lateral confinement with other cells that simulate the lateral mesoderm (Fig. 41C). Presence of lateral cells indeed seems to confine the polster, although less well than in the embryo. Furthermore, removing locally lateral cells led to lateral migration of polster cells, similar to actual ablation of the lateral mesoderm, which is particularly encouraging. Still, in order to get more informative results, we would have to better fit the behaviour of posterior and lateral mesodermal cells.

A point in particular that could easily be improved is the biological relevance of simulated behaviour. In the current version of the model, the direction of migration itself is transmitted from one cell to another and it is hard to imagine how internal cell polarity could directly be transferred. One more biologically relevant modification could be to set cell orientation along the point where they are pulled, the contact point, and the nucleus, their centroid. Preliminary tests using this rule rather than simple transfer or orientation gave encouraging results.

Are phenotypes obtained with morpholinos reliable?

During this work, I used morpholinos to perform gene loss of function. Morpholinos are synthetic antisens oligonucleotides that are complementary to mRNA (Partridge et al., 1996). They bind to specific sequences of the mRNA, usually close to the translation start site or over a splice site, which respectively prevents translation or lead to mRNA degradation (Summerton & Weller, 1997). Morpholinos efficiently decrease protein expression and are particularly easy to design and use compared to mutant embryos. Indeed, many mutants are homozygote lethal, so that the parents have to

be kept as heterozygotes. This constitutes a first experimental difficulty as only one out of four embryos is homozygote mutant, which makes all experimental manipulation particularly tedious. This is even more problematic for studying early development because, even if the embryo is homozygote mutant, it might contain wild type maternally deposited mRNAs that ensure protein production for some time. This is, for example, the case for E-Cadherin, where the morphant has an effect even on early cleavage stages while the first mutant phenotype appears during gastrulation (Kane et al., 2005).

However, it is known that morpholinos may induce non-specific phenotypes during development. In particular, in a recent study, systematic comparison of mutant and morphant phenotypes has been performed and it appears that, in numerous cases, the morphant has a different or a stronger phenotype than the mutant (Kok et al., 2015). This study raised a lot of concerns over the use of morpholinos and the community working on zebrafish tended to shun results obtained on the basis of morpholinos alone. Solely morpholinos producing effects strictly similar to mutation were considered as valid tools (Stainier et al., 2017). However, an even more recent study on genetic compensation hinted that these observed extra phenotypes might not always be artefactual (El-Brolosy et al., 2019). This raised a controversy that is not yet finished and too long to summarise here, but prompted to be particularly cautious while using morpholinos.

Despite these reservations, we considered morpholinos as a very convenient and powerful tool to perform loss of function in zebrafish embryos. In order to confirm the specificity of the phenotype we observed using these morpholinos, I always performed a rescue experiment, where I co-injected the morpholino and an mRNA coding for the corresponding protein and insensitive to the morpholino (Fig. 35, Fig. 41). Furthermore, some of the morpholinos I used had already been shown to produce phenotypes similar to the corresponding mutant, like MO *cas*, MO *e-cadherin* and MO *α-catenin*.

In the case of *vcla* and *vclb*, I observed a discrepancy between the phenotypes of the mutant and of the morphant. Mutant lines actually exist for these two genes and one mutant line has been made where fishes are maternal-zygotic null for *vcla* and heterozygote null for *vclb* (Han et al., 2017). Authors describing this mutant line observed surprisingly few defects in double null embryos during early development. At most, these embryos display irregularities in muscle structure and cardiac defects, and die from these defects later during larval life. I tested whether morpholino mediated knock-down of *vcla* and *vclb* gave similar developmental phenotypes. At 24 hpf, more than a half of the morphant embryos presented mild and non-specific morphological defects, commonly associated with morpholino injection and around 10% already died (Fig. 36C). I kept surviving embryos until 4 dpf and observed that every embryo presented cardiac oedema and muscle defects, similar to *vinculin* mutants (Fig. 36D) (Han et al., 2017), but also, surprisingly, that they displayed cranial malformation along with atrophied swim-bladder. Hence, *vinculin* double morphant presented more phenotypes than the double mutant. Rescue of the double morphant saved these developmental phenotypes, although only partly suggesting that the

morpholinos might have non-specific effects on late development. Concerning gastrulation, absence of strong phenotype is at odds with the defect of polster cell guidance we observed in our experiments and the fact that Vinculin binding domain of α-Catenin is required for polster orientation or mesoderm convergence. Still, authors describing the mutant might have missed subtle cell orientation phenotypes or some genetic compensation or *vcla* maternal contribution might prevent occurrence of a stronger phenotype. Using morpholinos against *vcla* and *vclb*, I observed that polster cells indeed lose their orientation upon vinculin knock down (Fig. 35A & E). Furthermore, rescue of *vinculin* loss of function in polster cells completely restored cell orientation, showing that, at least in the polster, effect of this morpholino is specific.

Other tools allowing easy loss of function in embryos have been developed in the last years and could be used in zebrafish as a complementary approach to morpholino to avoid the tedious use of mutants and overcome the mRNA maternal contribution problem. Some teams tried to create F0 mutants using the CRISPR/Cas9 system, but this is not considered as very rigorous as we can't be sure that every cell is mutant and it could generate off-target effects (Kroll et al., 2021). Furthermore, such an approach cannot get rid of maternal mRNA contribution. Alternatively, it has been shown that the CRISPR/Cas13 system is able to recognise and bind mRNA and can be used to prevent translation, similar to morpholinos (Abudayyeh et al., 2017; Pickar-Oliver & Gersbach, 2019). This technique relies on expression of the Cas13 protein, and thus might be incompatible with early developmental studies. Direct injection of the purified protein along with the guide RNA could overcome this difficulty, an approach in development in our team.

How could a mechanical information orient polster cells?

During this work, I identified that cell orientation relies on mechanotransduction mediated by the E-Cadherin, α-Catenin, Vinculin pathway (Fig. 35). However, signalling downstream of this pathway and its relations to other cellular processes are still poorly known. Vinculin has first been described as a bundling protein that reinforces adherens junction attachment to the actin cytoskeleton and that helps recruit new actin filaments (Fig. 7C, Fig. 13C) (Bays & DeMali, 2017; Harris & Tepass, 2010). This simple stabilising mechanism could constitute a first answer as a more stable junction could recruit particular proteins involved in signalling, for example Wnt/PCP components. Another, non-mutually exclusive possible mechanism could be that Vinculin directly recruits signalling proteins. In particular, Vinculin has been observed directly recruiting Arp2/3 at focal adhesions and is suspected of doing so at adherens junctions (personal discussion with S. Romero, DeMali et al., 2002). Thus, AJ recruiting vinculin could locally deplete the pool of Arp2/3 and prevent protrusion formation, thus polarising the cell. Another candidate is Merlin, as in collectively migrating epithelia, it transduces mechanosensation to coordinate Rac1 activity and lamellipodium formation (Fig. 13A) (Das et al., 2015). Apart from

Merlin, very little is known on how adherens junctions regulate cytoskeleton dynamics and cell migration (Vishwakarma et al., 2020a) Nevertheless, there is accumulating evidence that mechanosensation at cell-cell contacts has a key role in coordinating many cell behaviours (Hirata et al., 2020; Vassilev et al., 2017; Vishwakarma et al., 2018).

In experiments where wild type, actin labelled cells were transplanted in front of the polster along with a small group of other cells expressing DN-Rac1, Mo E-Cadherin or DN-MCLK, I observed that cell orientation was largely lost compared to controls (Fig. 32B, Fig. 34C). However, protrusion orientation is not completely randomised. In particular, in the case of wild-type cells embedded in DN-Rac1 expressing cells, they are more oriented when located in small groups than when in a full DN-Rac1 polster (Fig. 32A & B). This might be explained by the fact that it is difficult to completely isolate a wild type cell among a small group of DN-Rac1 cells, and it is likely that protrusions from wild-type endogenous polster cell reached the transplanted wild-type cells through the DN-Rac1. Alternatively, it might be possible that being pushed also contributes to cell orientation. This pushing could then be detected through friction forces with neighbouring cells and substrate. Such friction forces have been identified between polster cells and the overlying ectoderm (Smutny et al., 2017), and the shear stress induced by neighbours was recently implicated in the collective migration of endothelial cells (Patel et al., 2020).

Two other signalling pathways are known to be involved in polster cell orientation, Wnt/PCP and PI3K (Čapek et al., 2019b; Dumortier et al., 2012; Montero et al., 2003; Ulrich et al., 2003). PI3K signalling is required for protrusion formation and orientation. In particular, accumulations of PIP3, the secondary messenger produced by PI3K, have been observed at the anterior pole of the cell (Dumortier et al., 2012). If this happens to be correct, such an asymmetric distribution could be used as a molecular readout of cell polarity. I thus tried to quantify PIP3 accumulations at the membrane but the sensor proved to be toxic and gave a very poor signal-to-noise ratio (Fig. 45). Still, I observed that the distribution of accumulations seems to be biased toward the front of the cells. I then tested for a role of α-Catenin mechanosensation in PIP3 polarisation, and I initially observed that loss of mechanosensation led to a loss of PIP3 asymmetric distribution. However, accumulations were particularly hard to quantify, which raised a doubt on this observation. Indeed, when repeating the measurements on blinded data, I did not observe any effect of α-Catenin mechanosensation on PIP3 distribution, suggesting I had been a victim of the experimenter bias, measuring what I hoped to see. So far, I thus could not link mechanosensation to polarisation of the PI3K pathway, but this may be due to the poor quality of the images obtained using this sensor. Finding a better probe and readdressing this question is still an interesting lead.

Concerning planar polarity, loss of Wnt/PCP function, in mutant for the Wnt11 ligand or the Fz7 receptor, leads to a loss of polster cell orientation and defects in polster migration. It has been shown

that ubiquitous activation of Wnt/PCP signalling rescues these phenotypes, suggesting that the Wnt/PCP signalling is rather permissive than instructive for polster migration (Čapek et al., 2019b; Ulrich et al., 2003). It has been described that the Wnt/PCP pathway regulates recycling of E-Cadherin at the level of adherens junctions and increases the contact time and strength between cells (Ulrich et al., 2005). It is thus tempting to speculate that Wnt/PCP could regulate mechanical perception at the level of adherens junctions by controlling the amount and dynamics of E-Cadherin available to establish new junctions and detect forces. Furthermore, increased cell-cell contact time could also help recruit signalling proteins downstream of the mechanotransduction pathway. Using constitutively active and dominant negative forms of Rab5c, that control E-Cadherin dynamics downstream of Wnt11 (Ulrich et al., 2005), it could be possible to dissect the role of E-Cadherin endocytosis in mechanosensation, for example by looking at the dynamics of or at the load applied on α-Catenin.

Alternatively, it has been shown that, by late gastrulation, the Wnt/PCP pathway components Vangl2 and Pk form localised accumulations in the axial mesoderm (Roszko et al., 2015; Yin et al., 2008). This distribution is similar to those of these components in Drosophila, where this pathway has an instructive role (Yang & Mlodzik, 2015), suggesting that Wnt/PCP could also be instructive in the zebrafish embryo. I spent quite a lot of time trying to locate different components of the Wnt/PCP pathway (Fig. 44). Unfortunately, I did not manage to observe the expression of Vangl2 and Pk GFP-tagged constructs, even at later stages. On the contrary, Fz7 has been described as homogeneously distributed along the cell membrane in the polster, on the basis of immunostainings (Čapek et al., 2019b). Using cell transplantation, I observed that Fz7 tends to accumulate more at the rear of the cell. The discrepancy might come from the fact that, at the level of cell-cell contacts, immunostaining labels Fz7 on both membranes, while cell transplantation allows observing distribution in a unique cell. Similarly, distribution of cortical Dsh accumulations is slightly biased toward the cell rear. These results, although preliminary, point to an instructive role of Wnt/PCP in orienting polster cell migration which is completely at odds with studies that establish Wnt/PCP as a permissive signal. It is thus tempting to speculate that Wnt/PCP actually directly contributes to cell orientation and that adherens junction mechanosensation signals upstream of Wnt/PCP pathways. Interestingly, if junctional mechanotransduction controls Wnt/PCP component distribution, it might be possible to explain why ubiquitous Wnt11 or Fz7 activation rescues loss of function. Indeed, if PCP components are asymmetrically distributed by an independent mechanism, exposition to a uniform signal might lead to a polarised response. Such hypothesis is supported by the observation that mechanical stress can indeed determine planar polarity axis in Xenopus epithelia (Chien et al., 2015). It could be tested in zebrafish provided that we possess a reliable marker for Wnt/PCP polarity. In particular, we would expect that disruption of mechanosensation lead to a randomisation of Wnt/PCP components distribution. Unfortunately, measuring the distribution of PCP components is particularly tedious and I only managed to observe Fz7 and Dsh. Finding an asymmetric distribution for other PCP components could confirm

that Wnt/PCP signalling indeed has an instructive role and finding a marker easier to quantify could help in measuring cell polarisation.

Interestingly, it appears that the Fz8 receptor is specifically expressed in the polster during gastrulation (Kim et al., 1998; Nasevicius et al., 1998). This receptor has been described as involved in axis specification in Xenopus, as a receptor for Wnt8, a ligand of the canonical Wnt/β-Catenin pathway. In particular, *fz8* ectopic expression in a Xenopus embryo creates a secondary axis (Itoh et al., 1998). However, it has recently been shown that Fz8 can bind to Wnt11 and trigger EMT in prostate cancer (Murillo-Garzón et al., 2018). It is thus possible that the Wnt/PCP signalling is mediated by different ligands and receptors than Wnt11 and Fz7. In particular, Wnt5 is known to signal through the planar polarity pathway and is required for proper notochord extension (Kilian et al., 2003). Neither *fz8* nor *wnt5* have been tested in the polster and they might have a role in orienting migration, potentially redundant with *wnt11* and *fz7*.

Finally, something in the model we proposed for guidance by followers remains obscure. If a follower cell exerts a traction on the cell ahead through a protrusion, according to Newton's second law, the cell ahead also applies a pulling force in return. How come, then, that the follower is not polarised away from the contact (Fig. 40)? In particular, it has been described that Xenopus prechordal plate cells forming a doublet indeed tend to polarise away from the contact (Fig. 23F) (Weber et al., 2012). On the contrary, I often observed doublets and small trains formed by cells transplanted at the animal pole that stick and migrate together (Fig. 25B). This could be explained by differences of membrane and cortical proteins between protrusions and the rest of the cell. For example, it could be possible that mechanosensitive response is only possible or instructive out of protruding areas of the membrane. Actually, when transplanted at the animal pole, polster cells tend to adopt a run and tumble behaviour, switching between phases of directional migration and stall. This suggests that these cells are able to spontaneously polarise but that this polarisation is short-lived. It is thus tempting to speculate that contact-mediated mechanosensation stabilises this pre-patterned polarity, thus keeping the contacted cell oriented. This is a very exciting perspective but requires a marker of polarity that is different from protrusive activity. With such a marker, we could quantify when an isolated cell is polarised and whether contact of a protrusion with the "rear" of this cell actually stabilises this polarity. A more accessible experiment could be to carefully observe cell response to collision depending on the contact location, e.g. front-front or front-rear.

Do polster cells detect other guidance cues?

Initially, it was thought that polster migration was directed by a gradient of chemoattractant (Montero et al., 2003; Ulrich et al., 2003). This view has been challenged by the observation that individual or small groups of cells transplanted in front of the polster were not attracted toward the

animal pole (Fig. 25C) (Dumortier et al., 2012). However, response to a chemotactic gradient could be a matter of group size (Camley, 2018). It is well described that groups of cells can collectively respond to a shallow gradient that individual cells are unable to detect. In this case, absence of migration of individual cells or small groups of cells placed ahead of axial mesoderm migration path would be the consequence of a too small group size. However, the observation that isolation of the whole polster by laser ablation, a group of around 150 cells, is unable to orient its migration argues against this hypothesis (Fig. 27). Alternatively, it could be possible that contact with posterior mesoderm is required for proper chemotaxis. For example, posterior mesoderm could act as a sink degrading a chemokine, creating a local gradient (Donà et al., 2013; Venkiteswaran et al., 2013). This is also unlikely as, isolated full or half polster should still detect this gradient. Furthermore, in the case of wild type polster in front of slowed down axes, one would expect that the gradient is still formed in front of the posterior mesoderm, leading to directed migration of the polster then to a halt when the poster is too far. We rather observe a continuous but slow and weakly persistent movement toward the animal pole. Thus, guidance by follower better accounts for the observed behaviours.

Since a mechanotransduction pathway is involved in the process of guidance by followers, we considered that the information transmitted from cell to cell is mechanical. Interestingly, it has been shown that filopodia can carry chemical signals to remote cells, performing contact-dependent paracrine signalling (Mattes & Scholpp, 2018). With our experiments, we cannot completely rule out that information other than mechanical could be transmitted through these protrusions. This is a point that is worth exploring, as cell orientation could also be due to a preferential exposure to a contact-mediated chemical signal. Observing accumulations in protrusions of GFP-tagged signalling protein, for example belonging to the Wnt/PCP pathway could constitute a hint that chemical signal is also transmitted through protrusions (Fig. 44A).

During this study, I pointed to a role of FGF signalling in polster migration (Fig. 43). Inhibition of FGF signalling using the SU5402 drug slowed down polster migration without largely disrupting cell movement orientation. Accordingly, cell autonomous expression of DN-FGFR1 led to migration defects but without loss of protrusion orientation. This suggests that unlike its role in PLLp migration (Breau et al., 2012), FGF signalling is not an instructive cue in polster migration. How FGF signalling prevents correct migration without disrupting cell orientation is, however, puzzling. The only morphological difference I observed upon expression of DN-FGFR1 is that the cell body is larger, which could explain the migration defect. Alternatively, it has been shown that morphant cells for *snail1a* transplanted in the polster are trailing behind the polster during migration, similar to DN-FGFR1 expressing cells (Blanco et al., 2007). Since *snail1a* is involved in EMT behaviour, in particular in reduction of cadherin expression, it could be possible that FGF signalling regulates polster cell migration by controlling *e-cadherin* expression, possibly through Snail. This is an interesting trail, since Snail1 has already been

shown as acting downstream of FGF signalling (de Frutos et al., 2007). This could easily be verified by quantitative rtPCR or western blot for *e-cadherin* in DN-FGFR1 expressing cells.

Alternatively, it is known that FGF signalling involves phosphorylation of the ERK kinase, which is then translocated in the nucleus and acts as a transcription factor (Fig. 12A) (Dorey & Amaya, 2010). Interestingly, several recent papers described that ERK signalling was involved in collective migration (Aoki et al., 2017; Hino et al., 2020; Isomursu et al., 2020). Through mechanical coupling between cells, ERK waves propagate through the tissue and contribute to orienting cell migration. Upon stretching, a cell will activate ERK, which provokes contraction of the cell and thus stretch the cell behind, transmitting the wave (Hino et al., 2020). In our system, we showed that traction applied by the neighbours is responsible for cell orientation. It could be possible that this traction activates ERK phosphorylation and that ERK waves circulate in the polster. This would, furthermore, be consistent with the observation that FGF signalling disruption cell autonomously prevents migration. Several approaches to quantify ERK activity exist that could be used to test the role for ERK signalling in polster migration, like kinase translocation reporter assay or FRET sensors (de la Cova et al., 2017; Hino et al., 2020).

In a recently published paper, it has been shown that Dkk1 accumulates at the level of cell-cell junctions in the axial mesoderm (Johansson et al., 2019). Here, it contributes to destabilising adherens junctions by promoting the localisation of β-Catenin in a sub-cortical compartment. Interestingly, overexpression of *dkk1* leads to a loss of coordination between cells. Our observations shed a new light over these results. Since adhesion is required for collective polster guidance, preventing cells from forming junctions could prevent mechanotransduction pathway, thus disrupting the collective effect coming from guidance by followers. Consistently, *e-cadherin* or *wnt11* loss of function, and *dkk1* overexpression generate similar phenotypes during polster migration, which is a wider axis and a less coordinated behaviour (Babb & Marrs, 2004; Caneparo et al., 2007; Heisenberg et al., 2000; Johansson et al., 2019; Smutny et al., 2017). In order to confirm the role of *dkk1* in polster migration, it could be interesting to measure cell orientation in an overexpression context, and perform epistasis experiments with *e-cadherin* and *wnt11*. Furthermore, authors describe that knock-down of *dkk1* leads to accumulation of cadherin at cell-cell junction and defects in axis elongation, suggesting that level of junctional E-Cadherin has to be finely tuned for correct migration (Johansson et al., 2019). This is also consistent with adherens junction mediated mechanosensation as modification of AJ composition is likely to affect mechanosensation.

In another recent study, it has been shown that Xenopus neural crest cells collective migration relies on the formation of a contractile actomyosin ring connecting cells at the periphery of the cluster through adherens junctions (Shellard et al., 2018). This supracellular cable is more contractile at the rear than at the front of migration, which is required for proper movement of the group. It is, however, unclear

how such a cable establishes between cells that are supposed to exhibit CIL and thus shun cell contact (Carmona-Fontaine et al., 2008; Szabó et al., 2016; Theveneau et al., 2010). Still, it could be possible that similar supracellular structures are formed in the context of polster cell migration. Such a structure could for example account for the absence of polster cell dispersion, during axial mesoderm extension. Furthermore, a population of cells all along the border of the axial mesoderm expresses genes that are not expressed by cells at the middle. These cells at the border might thus have a different behaviour and form a supracellular structure. I never observed actin distribution over a whole polster but, contrary to cultured clusters of neural crest cells, that form an actomyosin ring, I did not observe such a structure in actin labelled, induced polster cells transplanted at the animal pole (Fig. 25A & D). Furthermore, cell dispersion that happens in such groups argues against the presence of a cable. Still, I only took low-resolution pictures and perhaps a more careful analysis could lend some interesting results. It could be interesting to label, for example through immunostaining, Actin, Myosin and E-Cadherin and look for potential supracellular structures in the polster.

Could polster cells be cultured to study intracellular signalling?

In order to fully understand how polster cell migration is oriented, it is important to connect all the pieces of information and signalling pathways that have been identified in the literature. This requires to decipher the intricate relationships between the different pathways and establish epistatic relationships. In particular it is necessary to observe precise cellular localisation of the components of each pathways, and how disruption of each pathway affects the others. This is particularly hard in vivo as cell manipulation is complex and imaging conditions might be challenging. It is way easier to perform such cell biology in cultured cells, where imaging condition are better and interaction between cells and signalling pathways can be finely controlled. Although several zebrafish cultured cell lines exist, embryonic zebrafish cells are known to be hard to culture in vitro (Driever & Rangini, 1993). Several publications mention culture of prechordal plate cells, in suspension or seeded on Fibronectin, with relatively simple culture conditions (Čapek et al., 2019; Krens et al., 2017). This is actually surprising as prechordal plate cells are not known to adhere on Fibronectin. No Fibronectin accumulation is visible in the ECM until late gastrulation (Fig. 22A) (Latimer & Jessen, 2010; Smutny et al., 2017) and, although several integrins are expressed in the axial mesoderm (*itga3b*, *itga5*, *itga6a*, *itgb1b*), their expression is usually also observed late during gastrulation, corresponding to the moment Fibronectin starts to accumulate (ZFIN expression profiles). Finally, inhibition of the Integrin-Fibronectin interaction with RGD peptide does not affect axial mesoderm migration, again arguing against an important role for Fibronectin in prechordal plate cell adhesion (Fig. 22B) (Nair & Schilling, 2008). On the contrary, inhibition of Fibronectin adhesion is known to affect endoderm migration (Nair & Schilling, 2008). In publications that describes cultured prechordal plate cells, judging from the images, only a few are adhering to Fibronectin and migration on this substrate is very limited. In these

publications, in order to ensure that these cells keep a mesendodermal identity, their fate is induced by strong activation of nodal signalling through the expression of high quantities of Cyc ligand (Čapek et al., 2019; Krens et al., 2017). However, high levels of nodal signalling is known to induce both prechordal and endodermal fates, hence, published work might look at a mixed population (Dumortier et al., 2012; Peyriéras et al., 1998). Since mesodermal cells are not known to particularly bind Fibronectin, it could be that, in the case of these studies, only endodermal cells efficiently bind to fibronectin in culture.

During the preliminary experiments we performed to put polster cells in culture, we induced polster fate through the expression of *tar** and morpholino-mediated knock-down of *cas*, which prevents endodermal fate (Fig. 24) (Dumortier et al., 2012; Peyrieras et al., 1996). We were thus sure to look at polster cells. Individually, these cells were, for most of them, unable to adhere and the few adhesive cells only formed small protrusions and displayed no migration. The only instance of adhesion we observed was for a group of polster cells mixed with non-induced cells but in this case, adhesion to Fibronectin might be provided by these non-induced cells (Fig. 24B).

Culture conditions might be improved to ensure correct adhesion and migration of polster cells. In particular, since E-Cadherin is known to be required for polster cell migration (Babb & Marrs, 2004; Dumortier et al., 2012; Shimizu, et al., 2005), we planned to test seeding these cells on an E-Cadherin coated substrate. However, while Fibronectin forms non-specific interactions with many surfaces, including glass, it is not the case of E-Cadherin. It is thus more complex to coat surfaces with cadherin and we lacked time to try this experiment. Alternatively, it could be possible to culture these cells over feeder cells expressing E-Cadherin, but preliminary experiments by a previous PhD student weren't very promising. Finally, since the polster is sandwiched between the yolk and the ectoderm, we wondered whether vertical confinement was required for proper adhesion and migration. We thus considered the possibility of putting a roof over cultured cells and to see whether this triggers adhesion and migration.

What is the role of CYFIP2 and WAVE complex in polster migration?

During my PhD, I contributed to explore the role of the WAVE complex subunit CYFIP2. The paraloguous subunit CYFIP1 is known to strongly promote WAVE activation, which in turn activates Arp2/3 and actin branching, promoting protrusion formation and persistent migration (Derivery & Gautreau, 2010). Surprisingly, it appeared that CYFIP2 acts as an inverse agonist also activating WAVE complex but way less than CYFIP1. They then showed that both CYFIP1 and CYFIP2 compete for the same place in the WAVE complex and that the balance between the two regulates protrusion formation and migration. Thus CYFIP2, although activating WAVE complex, indeed inhibits migration when replacing CYFIP1 in WAVE complex. They also observed that NCKAP1, another WAVE complex unit, has similar a similar effect to CYFIP1, promoting protrusion formation and migration (see Appendix)

(Polesskaya et al., 2020). All these results have been obtained on cultured cells and I tested whether these subunits had a similar effect in a physiological environment using polster migration as a model.

Accordingly, I observed that knock-down of *cyfip2* led to a strong increase in protrusion formation while reduction of *cyfip1* or *nckap1* expression decreased the number of protrusions (Fig. 42B). In addition, overexpression of *cyfip2* resulted in a decreased number of protrusions. Interestingly, in rescue experiments for *cyfip1* and *nckap1,* I observed a phenotype opposed to the loss of function, suggesting that these experiments actually constitute overexpression of these two proteins. In line with these results, *cyfip2* knock down as well as *cyfip1* and *nckap1* rescues produced longer protrusions. Surprisingly, however, neither *cyfip2* overexpression, nor *cyfip1 n*or *nckap1* knock down led to shorter protrusions, as if there were a minimal size for a protrusion to form (Fig. 42C). It could be that a minimal quantity of nucleator and branched actin is required to deform the plasma membrane.

This effect on protrusiveness actually alters migration as morphant cells for *cyfip1* or *nckap1* displayed a less persistent migration, while *cyfip2* knock down gave the opposite result. Surprisingly, migration speed was not particularly affected in these experiments. Since migration of these cells relies on actin rich protrusions, one would rather expect that number and size of protrusion do influence cell speed. Furthermore, I observed that neither *cyfip1*, *cyfip2* nor *nckap1* knockdown has a strong effect on protrusion orientation (Fig. 42A). All this suggests that WAVE complex simply controls formation of protrusions downstream of an orienting pathway, and longer and more frequent protrusions increase directional migration but not speed. This hypothesis is supported by the observation of a similar phenotype with the Arp2/3 inhibitor Arpin, as *arpin* knock down increases cell persistence, but not cells speed, in cultured cells as well as in zebrafish polster cells (Dang et al., 2013).

Is there a minimal size for migration coordination?

Collective migration relies on emergent behaviours that are the result of interactions between cells (Friedl & Gilmour, 2009; Vedula et al., 2013). As such, this process requires a critical number of cells from which collectiveness can emerge. It typically occurs at the mesoscopic scale, from groups of a dozen cells but the precise number of cells required for collective behaviour has seldom been quantified (Hakim & Silberzan, 2017). What is then the critical size for emergence of collective effect in the polster? We did not directly address this question but made several observations that bring some clues. In the guidance by follower system, theoretically, as long as two cells are in contact and one is protruding toward the other, the leader cell align its migration with the follower and the doublet of cells constitute an oriented system. However as soon as the follower cell changes orientation, the doublet is expected to separate. I actually observed such doublets of cells with a rather persistent migration (Fig. 25B). They happen when two cells collide and adhere and, although I never quantified protrusions in this condition, it seemed that follower cells were indeed oriented toward the leader cell. Similarly, I observed small

trains composed of around five cells that stick together and are more oriented than isolated cells. Ultimately, these doublets and trains come to a halt and disperse or change direction. This is compatible with the run and tumble motion of polster cells since they can have relatively long runs of oriented migration before tumbling, thus orienting a doublet for some time. Hence, it seems that the critical number of cells to establish a collective behaviour is indeed only two. A systematic and detailed analysis of protrusions, adhesions and migration of these doublets and trains could give interesting details on the establishment of this guidance by follower mechanism. It, however, seems unlikely that a single oriented cell could orient a whole polster and thus, critical number of oriented cells for collectiveness might depends on the number of cells to be coordinated. This is a particularly exciting topic and could be studied using cells whose migration is controlled.

In a similar fashion, I wondered what the minimal structure able to form a coordinated, elongating axis is. It has been shown that transplantation of prechordal plate cells or a whole shield in the lateral margin of the embryo is sufficient to form an embryonic axis that elongate (Peyriéras et al., 1996; Shih & Fraser, 1996). However, prechordal plate has a patterning role and locally induces nodal signalling, which triggers formation of a new shield-like structure (Dixon Fox & Bruce, 2009; Pinheiro & Heisenberg, 2020). In an MZ *oep* mutant embryo, that cannot detect nodal signalling, similar prechordal plate cells simply disperse when transplanted at the animal pole (Smutny et al., 2017). I first tested whether transplanting a wild type shield in an MZ *oep* embryo could result in an elongating axis. I observed that such a transplanted shield rather tends to follow the epiboly movement. I, however, did not check whether these cells internalise or even keep their identity. In order to make sure that cells keep polster, prechordal plate and notochord identity, I wanted transplant cells in which fate is artificially induced. It is easy to induce polster fate through the expression of activated Tar* and knock down of *cas*. Induction of notochord fate has, however, never been published. A previous PhD student in the team observed that expression of low doses of Tar* tend to induce notochord fate, although not in all cells. I tried to reliably induce notochord fate by combining low Tar* expression, knock-down of *cas* and expression of *flh*, which is the first gene involved in specification of the notochord fate. Cells injected with such a cocktail indeed expressed *ntl* and, by 24 hpf, mostly located in the notochord, sometimes even forming secondary branches to the notochord. Unfortunately, induced notochord cells do not internalise upon transplantation, be it at the animal pole or at the margin. I thus could never test whether transplants of a mix of induced polster and notochord cells in an MZ *oep* embryo could form an axis. It is actually surprising that induced polster cells internalise even in ectopic locations while induced notochord cells are not even able to internalise at the margin. Perhaps notochord progenitors, which are distributed all along the margin receive a particular signal only in the shield that triggers internalisation. This could explain why notochord progenitors behave differently from lateral mesodermal cells that are also distributed all along the margin (except dorsally) but internalise everywhere (Roszko et al., 2009). It has recently been shown that a population of cells at the tip of the

notochord expresses *pcdh18a* and that this population acts as a motor for notochord elongation (Bosze et al., 2020). Perhaps addition of *pcdh18a* to the inducing cocktail could help cells to internalise and move animally.

Concerning polster and notochord identities, we were particularly surprised to observe that removal of the whole prechordal plate (Fig. 29A), judging by the disparition of the whole *gsc* expression territory, led to rather weak phenotypes at 24 hpf. Most embryos had a separated eye field and a small but present hatching gland. This is at odds with the mutants affecting prechordal plate migration like *slb*/*wnt11* or identity like *gsc,* which display penetrant cyclopia phenotype (Heisenberg et al., 2000; Seiliez et al., 2006). This suggests that the prechordal plate was somehow regenerated. Supporting this idea, I often observed a small bulge at the tip of the axis two hours after removing the polster, as if a new polster arose. This is particularly interesting as it suggests that cell fate is not set in the elongating axial mesoderm. Interestingly, it has actually been described that a population of cells at the interface of the prechordal plate and the notochord expresses both *ntl* and *gsc* (Carmany-Rampey & Schier, 2001). It is thus tempting to speculate that this population is responsible for the regeneration of the prechordal plate. In situ hybridisation performed on time series after prechordal plate removal as well as live FISH could help understanding the mechanism of prechordal plate regeneration (Simon et al., 2010).

How different are Xenopus prechordal plate and zebrafish polster migration?

Migration of axial mesoderm in the Xenopus has been largely described in the past thirty years and is rather well understood. Less is known about movement of the same tissues in the zebrafish. Still comparison between the two model animals is particularly interesting. The geometry of the tissue is in both cases similar at first sight: the prechordal plate/polster forms an oval-shaped tissue that migrates toward the animal pole and is located in front of the notochord/posterior axial mesoderm that elongates during gastrulation (Huang & Winklbauer, 2018; Pinheiro & Heisenberg, 2020). Although it could be tempting to consider that the mechanism ruling these movements in the two animals are similar (Behrndt & Heisenberg, 2012), systematic comparison shows many critical differences.

Xenopus prechordal plate is a quasi mono-layered epithelium where cells are assembled as shingles (Fig. 23F) (Weber et al., 2012; Winklbauer & Keller, 1996). They migrate on the blastocoel roof, on the extracellular matrix deposited by ectodermal cells through focal adhesion and are thought to be oriented by a mix of chemoattraction, oriented Fibronectin fibres and possibly mechanical forces (Huang & Winklbauer, 2018; Weber et al., 2012; Winklbauer & Keller, 1996). Indeed, these cells detect pulling forces through C-Cadherin and Plakoglobin, that recruits Keratin intermediate filaments, which orient cell protrusions and migration away from the force (Weber et al., 2012). In Xenopus, it has been shown that prechordal plate actually drags the notochord (Hara et al., 2013). It has thus been proposed

that cells are exposed to a gradient of tension established between the free edge at the front and the drag at the rear. Cell would then detect this gradient and orient their migration accordingly.

In zebrafish, the polster is a multilayered mesenchymal tissue migrating between the YSL and the ectoderm (Dumortier et al., 2012; Pinheiro & Heisenberg, 2020). The migration substrate is not clearly identified and both YSL and ectoderm have been proposed (Fig. 22) (Montero et al., 2005; Smutny et al., 2017). It is likely that polster cells adhere to both, using adherens junctions as no extracellular matrix is deposited until late gastrulation. Guidance of the polster used to be unclear, in particular, no chemotactic or haptotactic signal seemed to instruct polster cells. We showed that these cells detect mechanical forces, but through α-Catenin and Vinculin that bind to actin, rather than through Plakoglobin and intermediate filaments (Fig. 35). Furthermore the mechanical signal comes from migrating followers pulling on a leader rather than from lagging followers that are dragged by the leader. Finally, the posterior axial mesoderm does not require a polster to elongate and it is actually its elongation that drives polster migration.

It is interesting to appreciate how evolution selected such different mechanisms for the elongation of axial mesoderm from two rather similar initial situations. In particular, in both cases, mechanical information seems important but the pathway that transduces this signal is different. It could be particularly interesting to compare the mechanism we found in zebrafish with other species. For example, laser ablation experiments could be performed in the medaka *Tg(Gsc:GFP)* transgenic line, to observe whether this mechanism is conserved in Teleost fishes (Shimada et al., 2008). Alternatively, it could be possible to perform similar experiments in chick embryos, to see whether the prechordal plate of other chordates also relies on mechanical perception. Indeed, more and more instances of morphogenetic events are described through the lens of mechanical forces. In particular, it has recently been shown that extension of mesoderm in chick relies on swelling of presomitic mesoderm that squeezes notochord progenitors posteriorly, contributing to tail bud elongation without active migration, although, once again, the underlying mechanism is unclear (Xiong et al., 2020).

How is the polster interacting with other tissues?

As mentioned in the previous part, substrate for polster migration is not clearly identified. Although the tissue migrates in contact with the YSL and the ectoderm, E-Cadherin is specifically accumulated between the polster and the epiblast, and that some polster cells form protrusions oriented toward the ectoderm. Based on these observations, it has been proposed that polster cells migrate using the ectoderm as a substrate (Montero et al., 2005). However, this hypothesis is at odds with the fact that friction forces are exerted between the ectoderm and the polster, which respectively migrate toward the vegetal and animal pole. Furthermore, E-Cadherin also accumulates at the interface between the YSL and polster cells, suggesting that the YSL may be used as a substrate (Fig. 22C & D) (Smutny et al.,

2017). Finally, it has also been shown that Fibronectin is deposited at the interface between the polster and the ectoderm (Fig. 22A). I performed a few experiments aiming to identify a substrate for polster migration. In particular, I observed no particular effect on polster migration when I inhibited Fibronectin adhesion using RGD peptide, suggesting that, at least until late gastrulation, ECM is not required. I also injected a morpholino against *e-cadherin* specifically in the YSL to prevent the polster from migrating over the yolk surface. I observed that the yolk took a conical shape in these embryos, but I did not observe major effect on polster migration. Since morpholino injection happens after cells in contact with the yolk cells fused to form the YSL, absence of strong phenotype might be due to the expression of E-Cadherin in these cells before fusion, in a sufficient amount to form adherens junction with migrating cells. Actually, in wild type embryos, I observed that polster cells against the yolk tended to send protrusions toward the yolk while cells in contact with the ectoderm formed protrusions oriented toward the epiblast. This, combined with the fact that every cell in the polster form protrusions (Dumortier et al., 2012), and E-Cadherin dependant adherens junction junctions, suggests that cells actually attach to any E-Cadherin substrate they find to displace their cell bodies. Cells in contact with the yolk or the ectoderm might thus bind to a structure out of the polster and generate forces useful for the displacement of the group.

I also wondered how the polster is shaped. During early gastrulation, it has an oval shape and is multilayered. Interestingly, when transplanted elsewhere in the embryo, these cells form a shapeless monolayer that tend to disperse (Fig. 25A, B & D). Even when such polster cells are driven by lateral mesodermal cells, they do not form a multilayered tissue (Fig. 33). This suggests that, dorsally, the shape of the polster is actively maintained. During gastrulation, snail1, coding for a transcription factor, is expressed in the YSL just in front of the polster (Blanco et al., 2007). Surprisingly, *snail1a* knock down results in defects in polster migration, suggesting that Snail1a has non-cell-autonomous effect. This gene tends to inhibit E-Cadherin mediated cell-cell adhesion, suggesting that YSL to ectoderm adhesion could be weaker in front of the polster (Blanco et al., 2007; Cano et al., 2000; Yamashita et al., 2004). Interestingly, it has been proposed that the polster, while migrating, detaches the ectoderm from the YSL by locally increasing the pressure in the interstitial fluid (personal discussion with S. Grigolon & C. P. Heisenberg). If *snail1a* expression reduces adhesion between YSL and ectoderm, the two tissues might detach more easily in front of the polster. Because of this detachment, more cells could thus fit between the YSL and the ectoderm, which could explain why the tissue is multilayered. Elsewhere, *snail1a* is not expressed so we would not expect a similar phenomenon. If this hypothesis is correct, we expect the polster to be flatter in a *snail1a* knock down context, but this particular point has not been looked at.

Another, more important question is: what prevents cells from migrating laterally, away from the polster? Indeed, polster cells transplanted at the animal pole spread radially, suggesting that something in the axial mesoderm prevents lateral migration. The hypothesis that the YSL/ectoderm contact detach

preferentially in one direction could constitute a first explanation. Cells would thus migrate more easily toward the animal pole than laterally. Still, transplanted polster cells are able to migrate even without snail being expressed around, so that it is unlikely that lateral confinement is solely explained by this. During gastrulation, *dkk1* is expressed in a row of cells all along the border of the axial mesoderm (Johansson et al., 2019). This is particularly interesting as this could constitute a barrier preventing lateral migration. However, *dkk1* signalling tends to decrease cell adhesion and overexpression of this gene actually disrupts the border between notochord and paraxial mesoderm in late gastrulation (Caneparo et al., 2007; Johansson et al., 2019). Actually, knock-down of *dkk1* in the polster increases E-Cadherin accumulation in ectodermal cells immediately in front of the polster. Thus, *dkk1* might have a role similar to *snail1a* and decrease the YSL/ectoderm adhesion. Finally, in this work, we observed that lateral mesoderm seems particularly dense along axial mesoderm, almost up to polster front (Fig. 41A). Since polster cells seem unable to migrate over lateral mesodermal cells (Fig. 33), this tissue could laterally confine the polster and prevent polster cells from escaping. This hypothesis is supported by preliminary laser ablations and surgical experiments I performed, where removal of the lateral mesoderm close to the polster led to lateral migration of polster cells (Fig. 41B & C). Thus, the lateral confinement of the polster could be ensured by a mix of the presence of dense lateral mesoderm on both sides and preferential orientation of migration due to easier detachment between YSL and ectoderm at the front of the polster. Lateral confinement of the polster constitutes a whole research project in itself but most of the approaches I used during my PhD could be applied to explore confinement of the polster and thus give a full comprehensive view of polster migration.

Based on the observation that notochord is dragged by the prechordal plate in Xenopus, it has been hypothesised that polster drags posterior axial mesoderm in zebrafish (Hara et al., 2013). I, however, observed that a polster-less axial mesoderm is still able to elongate and even to displace a small group of non-motile cells placed in front of it (Fig. 29). This shows that polster is not required for axial mesoderm elongation and that, on the contrary, guidance by followers, and perhaps to some extent pushing forces, are required for proper polster orientation. These observations are completely at odds with previously proposed hypotheses for axial mesoderm extension during gastrulation. In this work, however, we did not explore what drives posterior mesoderm elongation. This elongation relies on two partially independent behaviours, convergence and extension (Fig. 2) (Roszko et al., 2009). It has recently been described that a population of cells at the tip of the notochord expresses *pcdh18a*, turning them in a fast migrating group that acts as a motor for extension, although the underlying mechanism is unclear (Bosze et al., 2020). It could be that expression of *pcdh18a* allows detection of a direction information used by these cells to drive elongation. Internalisation is also a good candidate for posterior mesoderm elongation as it continuously adds new cells that likely push those already internalised. Accordingly, mutants that affect cell internalisation also affect axis elongation (Krens et al., 2017; Shimizu et al., 2005). Finally, convergence and mediolateral intercalation could also contribute to

elongation through convergent-extension (Glickman et al., 2003). Combination of genetic approaches like *pcdh18a* knock-down and ablation located at different places in the posterior axial mesoderm could help decipher what is actually driving posterior mesoderm extension and polster orientation.

In this work, we showed that polster cells are able to orient each other and that they are oriented by contact with the elongating posterior axial mesoderm and, when transplanted ectopically, with migrating lateral mesoderm. However, strictly speaking, we only showed that guidance by followers through protrusions happens between polster cells. Thus, a question we did not directly answer is: how do lateral and posterior axial mesodermal cells orient polster cells? Both lateral and posterior axial mesodermal cells form actin rich protrusions and express *e-cadherin* during gastrulation (Diz-Muñoz et al., 2016; Han et al., 2016; Roszko et al., 2009). It could thus be that polster cells detect these protrusions the same way they detect protrusions coming from other polster cells. Furthermore, I observed that protrusion orientation of the posterior axial mesodermal cells located just behind the polster, as well as of lateral mesodermal cells, is biased toward the animal pole, which is consistent with the guidance by follower hypothesis. This could be more extensively explored using approaches similar to those I developed during my PhD.

Another question then arises: how come that protrusions of cells from lateral and posterior axial mesoderm are oriented toward the animal pole? It is tempting to hypothesise that these cells also exhibit guidance by follower behaviour. If this turns out to be correct, this mechanism would provide a unified view of animal migration of mesodermal cells during gastrulation, at least before the onset of convergence movements. It appears that there is a constant addition of new cells at the margin. If oriented migration relies on guidance by followers, cells closer to the margin will migrate away as new cells internalise, thus orienting the cells in front of them and so on until the whole mesoderm is set in motion. The difference in cell density could thus explain the difference of behaviour between the dense and straight migrating axial mesoderm, and the loose and more fuzzy-migrating lateral mesoderm (Pinheiro & Heisenberg, 2020; Roszko et al., 2009). This could be tested by modifying mesodermal cell density, for example by modulating Nodal signalling (Zhang et al., 2004), and observing the effect on migration straightness. This is a particularly strong hypothesis and mechanisms specific to the different population of cells are likely at play but still, guidance by followers is completely compatible with cell behaviour during the first half of gastrulation.

On serendipity

In order to finish this discussion, I would like to point out that, during this PhD, I realised how much serendipity is involved in scientific discoveries. Two critical points for our understanding of the process guiding polster cells were discovered unexpectedly. Experiments of ablation in the posterior axial mesoderm, which revealed that keeping contact with the posterior mesoderm rescues polster

migration, first were failed attempts at ablating at the interface between the two tissues (Fig. 27A). Similarly, the observation that polster cell migration can be driven by contact with the lateral mesoderm was first made as I used *Tg(tbx16:GFP)* embryos as host for animal transplantation of polster cells since unlabelled AB fishes had not lain that day (Fig. 29). This is an important lesson on the organic and sometime unplanned course of scientific research.

Conclusion

Previous results of the lab showed that polster migration is actually a true collective process during which an orienting information is transmitted from cell to cell through contact, at odds with previous results suggesting that the polster is a collection of individually migrating cells oriented along a chemotactic gradient (Dumortier et al., 2012). However, the nature and the origin of the polster orienting information has not been identified at that time, like for want of time and tools to precisely dissect cell-cell interactions. Soon after my arrival, the team (that is: Nicolas and I) moved from the IBENS at Ecole Normale Supérieure, to the LOB at Ecole Polytechnique, a laboratory specialised in advanced optics applied to life sciences. Thanks to the incredibly powerful microscopes of the LOB as well as to hours bent over the binoculars, I was able to develop tools allowing me to decipher precisely, and *in vivo*, the interactions between cells and tissues. Getting over the previous technical limitations using laser ablations and fine cell transplantation, I was able to identify that polster guidance is ensured by two phenomena: first, an intrinsic property of polster cells that align their migration with their followers through mechanical perception of their protrusions, a behaviour we named “guidance by followers”; second, the presence of the posterior axial mesoderm, which elongates from the margin and is located behind the polster, driving the latter’s migration toward the animal pole. This very simple system is sufficient to ensure during gastrulation the robust extension of axial mesoderm, around which the embryo later organises its development. This mechanism relies on the mechanosensation of adherens junctions, a structure formed by cells form almost every tissue. As such, guidance by followers might be a conserved process that could account for various instances of coordinated migration, from other mesodermal tissues in zebrafish gastrula to streams of metastatic cells migrating away from a tumour.

Material and methods

Note on quantification of cell polarisation

In individual cell migration, cells acquire a polarised morphology, the front corresponding to the direction of migration. In order to quantify cell-autonomous polarisation of polster cells, I used orientation of the protrusion (Fig. 49). To do so, I first labelled filamentous actin in cells by expressing Lifeact-mCherry, allowing visualisation of protrusions. I then transplanted a few polster cells, identified by their green fluorescence in *Tg(Gsc:GFP)* transgenic line in the polster of an unlabelled host. This creates a mosaic labelling allowing to easily measure orientation of each protrusion compared to the direction of migration (Fig. 49A). Indeed, if all cells were labelled, it would be very hard to identify individual protrusions as well as their cell of origin. Along with Lifeact-mCherry, I could co-inject mRNA or morpholinos that modify signalling in the cell, allowing me to observe cell-autonomous effects of these perturbations, in an unperturbed environment. Details of the transplantation protocol are accessible in the corresponding publication (see Appendix) (Boutillon et al., 2018).

Measure of orientation was done manually, by drawing a vector from the centroid of the cell to the basis of the protrusion and measuring the oriented angle formed by this vector and the direction of migration (Fig. 49A & B). I differentiate lamellipodia-like protrusions from filopodia based on morphological criteria (Diz-Muñoz et al., 2016). Is considered as lamellipodium a protrusion longer than 2µm, spearhead shaped and enriched in actin. In order to check for potential experimenter bias linked to handmade measurement, I reanalysed some movies that had been anonymized. I also asked my supervisor to analyse anonymized movies following my criteria. In most cases we found corresponding results. The only time I found obvious experimenter bias was not for protrusions but for distribution of accumulation of a reporter whose signal to nose ratio was very poor, and I discarded these data (Fig. 45). I am hence confident in the results I obtained for cell orientation.

Angles collected this way are distributed between 0 and 360° (Fig. 49C). Since polster migration happens along animal-vegetal axis and is symmetrical along this axis, I projected all angles in a space comprised between 0° (animal orientation) and 180° (vegetal orientation), 90° being a lateral orientation, right or left. This is more relevant to measure cell orientation relative to the direction of migration and allows easier data analysis, as rigorous statistical analysis of 360° angular data is very complex.

Rose plots, although very practical to provide an intuitive idea of angular distribution of something, are not easy to compare between situations (Fig. 49C). I thus chose to display angular data using cumulative frequency. It is a curve comprised between 0 and 1 that gives the percentage of occurrences smaller than a certain angle. This type of graphic representation, although being slightly less intuitive, eases comparison of angular distributions as several curves can be plotted on the same graph (Fig. 49D). Cells sending protrusions oriented toward the animal pole have more small angles and therefore a cumulative frequency that is convex. Conversely, a concave curve corresponds to a vegetally

biased distribution and a curve that is linear, following the diagonal, corresponds to a random distribution of angles.

Concerning statistical analysis, comparison of cumulative curves is classically done using a Kolmogorov Smirnov (KS) test, which compares distribution. However, this test tends to be very sensitive when there is a large number of data points, and it does not take into account the structure of the data. In these experiments, I quantify orientation several embryos, each of them containing several measured cells. Hence, observations, which are pooled before display, are not independent, and cannot be compared using the KS test. I thus used the KS test when distribution corresponded to independent observations, and used linear mixed effect models that take into account resampling of the data to compare other datasets.

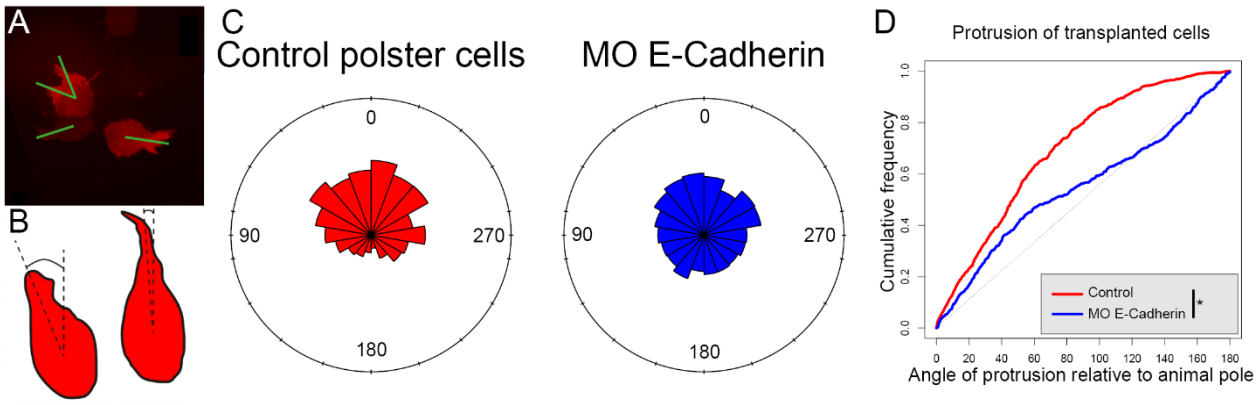

Figure 49. Quantification of cell protrusion orientation. Modified from Boutillon et al., 2018. **A**: Actin labelled cells transplanted in an unlabelled host. Green lines point to actin rich protrusions. **B**: Measurement on protrusion angle compared to animal pole. **C-D**: Roseplots and cumulative frequency plot of protrusion angular distribution for control and MO *e-cadherin* cells (data from Fig. 34B & Fig. 35B).

Experimental model

Zebrafish embryos were obtained by natural spawning of AB, *Tg(tbx16:EGFP), Tg(-1.8gsc:GFP)ml1* and *Tg(actb1:myl12.1-eGFP)* adult fishes (Behrndt et al., 2012; Doitsidou et al., 2002; Wells et al., 2011). All animal studies were approved by the Ethical Committee N°59 and the Ministère de l'Education Nationale, de l'Enseignement Supérieur et de la Recherche under the file number APAFIS#15859-2018051710341011v3.

Method details

In Situ Hybridisation

Whole-mount colour and fluorescent In Situ Hybridisation were performed following standard protocols (Hauptmann & Gerster, 1994) using *goosecoid*, *tbxta* and *ctslb* probes (Schulte-Merker, van Eeden, et al., 1994; Stachel et al., 1993; C. Thisse et al., 1994).

Embryo injection

Translation blocking morpholinos (Gene Tool LLC Philomath) and concentration used were:
Vinculin a (5′-CGTCTTGGTATGGAAAACTGGCATC-3') (0.3 mM),
Vinculin b (5′-TGGAAAACCGGCATGATGATCGCTC-3') (0.3 mM),
Jupa (Plakoglobin 1a) (5′-GAGCCTCTCCCATGTGCATTTCCAT-3') (0.4 mM) (Martin et al., 2009), Jupb (Plakoglobin 1b) (5′-CCTCACTCATTTGCAGTGACATCAC-3') (0.1 mM),
E-Cadherin (5′-TAAATCGCAGCTCTTCCTTCCAACG-3') (0.3 mM) (Babb & Marrs, 2004),
α-Catenin (5′-TAATGCTCGTCATGTTCCAAATTGC-3') (0.1 mM) (Han et al., 2016),
Sox32 (5′-CAGGGAGCATCCGGTCGAGATACAT-3') (0.3 mM) (Dickmeis et al., 2001),
zebrafish CYFIP1 (AAAAACTATCCGCTTCGACTGTTCA) (0.2 mM),
zebrafish CYFIP2 (CGACACAGGTTCACTCACAAAACAG) (0.1 mM),
zebrafish NCKAP1 (CCGAGACATGGCTCAAACGACCGTC) (0.8mM) (Biswas et al., 2014) and standard control (5′-CCTCTTACCTCAGTTACAATTTATA-3') (0.1 to 0.8 mM).

Capped sense mRNA were synthesised from pCS2+ constructs with mMessage mMachine SP6 kit (Thermo Fischer). Constructs and concentrations used were: Histone 2B mCherry (30 to 50 ng/µl), Histone2B-mCerulean (30 to 50 ng/µl), Lifeact-mCherry (30 to 50 ng/µl), Taram-A* (0.6ng/µl), Dsh-Dep^{+} (75 ng/µl), Rac1 N17 (2 or 10 nl/µl), DN-MLCK (100 ng/µl), Zf E-cadherin-GFP (60 ng/µl), Zf E-cadherin-Δcyto-GFP (60 ng/µl), Zf α-Catenin (30 ng/µl), Zf α-Catenin-ΔVBS (30 ng/µl) and Zf α-Catenin-L344P (30 ng/µl), Zf Vinculin a-GFP (25ng/µl), Zf Vinculin b-GFP (25ng/µl), human CYFIP1 (10ng/µl), human CYFIP2 (10ng/µl) or human NCKAP1 (10ng/µl). To label and/or affect the whole

embryo, 5 nl were injected at the one-cell stage. For donor embryos for cell transplantation, 1.5 nl were injected in one cell at the four-cell stage.

Cell transplantation and microsurgery

Cell transplantation was performed as described in (Boutillon et al., 2018). Cells transplanted within the polster were taken from the shield of a *Tg(gsc:GFP)* donor and transplanted to the shield of a *Tg(gsc:GFP)* host at 6 hpf. Identity of transplanted cells was then assessed by their GFP expression. Cells transplanted out of the polster (animal pole, lateral side, ahead of the polster) were taken from donor embryos injected, in one cell out of four, with Tar* mRNA and Sox32 morpholino, so as to impose a polster identity (Dumortier et al., 2012). For single cell transplant, donor embryos were dissociated at shield stage in Ringer's without calcium solution prior to transplantation. Removal of the polster was performed in *Tg(gsc:GFP)* embryos, by aspiration with a large homemade glass pipette. The polster was identified on morphological criteria, confirmed by *in situ* hybridisation against *ctslb*, a marker for polster identity, and *gsc*, a marker for prechordal plate (Fig. 26A, Fig. 29A).

Transplantation technique described in (Boutillon et al., 2018) was adapted for PDMS bead insertion in *Tg(gsc:GFP)* embryos. Beads were transplanted in the shield of a host at 6hpf. Treated embryos were incubated at 28° until reaching 60% epiboly. Success of transplant was then assessed by looking at the presence of the bead in the polster.

Embryo and cell imaging

Imaging of embryos for protrusion quantification or bead shape analysis was done on an inverted TCS SP8 confocal microscope (Leica) equipped with environmental chamber (Life Imaging Services) at 28°C using a HC PL APO 40x/1.10 W CS2 objective (Leica). Imaging of embryos for cell migration quantification was done under an upright TriM Scope II (La Vision Biotech) two-photon microscope equipped with an environmental chamber (okolab) at 28°C and a XLPLN25XWMP2 (Olympus) 25x water immersion objective or on the inverted TCS SP8 microscope (Leica) using a HCX PL Fluotar 10x/0.3 objective (Leica). Injected embryos were mounted in 0.2% agarose in embryo medium between 60% and 70% epiboly (6.5-7.5 hpf). Embryos were imaged between 30 and 60 minutes, every one to three minutes. Imaging of endothelial cells were also performed under the TriM Scope II microscope. Cells were imaged every 1.4s for 2 to 5 minutes.

Laser ablation

Laser ablation experiments were performed under the TriM Scope II microscope (La Vision Biotech) equipped with a femtosecond Mai Tai HP DeepSee laser (Spectra Physics) and an Insight DeepSee (Spectra Physics) laser.

For ablation of mesodermal cells, embryos were imaged every minute for 10 to 15 minutes prior to ablation (Boutillon et al., 2021). GFP was excited by the Mai Tai laser set to 920 nm wavelength and mCherry by the Insight laser set to 1160 nm. The ablations were performed with the Mai Tai laser at 820 nm and exit power at 0.3 W. Such an exit power allowed efficient ablation with very good axial confinement. The region to be ablated was defined as an XY ROI, and selectively illuminated using an EOM. To perform 3D ablations, laser treatment was performed on different focal planes, separated by 10 to 15 microns, starting with deeper planes. To compensate for the loss of energy in deeper planes, the number of treatment repeats was modulated with depth. Efficiency of the ablation was assessed by the absence of GFP fluorescence and the presence of cellular debris, and later confirmed by observation of locally modified cell behaviour. Embryos were imaged for 30 to 40 minutes following ablation. Polster was identified on morphological criteria and distance to the front, confirmed by *in situ* hybridisation against *ctslb*, a marker for polster identity (Figure 26A & D).

Quantification and statistical analysis

Image analysis

Mesodermal cell movements were quantified by tracking cell nuclei, labelled with H2B-mCherry, using IMARIS (Bitplane). Tracks were then processed using custom-made Matlab (Math Works) routines as described in (Dumortier et al., 2012). Axial mesoderm elongation was quantified by tracking migration of cells at its front. Actin-rich protrusions were quantified on Lifeact-mCherry expressing cells. Protrusion orientation was manually measured as the angle between protrusion axis and the animal-vegetal axis, using ImageJ (FIJI), as described in (Boutillon et al., 2018).

Statistical analysis

All statistical analyses were performed in R (R project). Cell migration absolute and axial speed were averaged over cells and embryos, and compared using Wilcoxon tests. When relevant, paired Wilcoxon tests were performed, as indicated on the corresponding boxplots. Protrusion angle distributions and frequencies were compared using linear mixed models taking into account the fact that measurements are not independent (several measurements for each cell, several cells for each embryo).

To serve as controls for collision data (Fig. 25B), 100 bootstrapped datasets were generated by randomly picking, for 80 cells, one time-step where the cell moves freely (no collision) and measuring

the angle between incident and efferent vectors (26±13 available times per cell). Each of these bootstrapped datasets, along with the combination of all, were compared to the angle of deflection upon collision using a Kolmogorov-Smirnov test. Only one bootstrapped dataset is statistically different, which is less than expected by chance with an α risk of 5%.

Migration persistence. Statistical analysis was performed using R. Persistence, measured as movement autocorrelation over time is fit for each cell by an exponential decay with plateau,

$$A = (1 - A_{min}) * e^{-\frac{t}{\tau}} + A_{min}$$

where A is the directional autocorrelation, t the time interval, A_{min} the plateau and τ the time constant of decay. The time constant τ of exponential fits were then compared using non-linear mixed-effect models for each condition.

Numerical simulations

To model cell motility and cell-cell interactions, we chose a Cellular Potts Model (CPM) since the CPM allows for arbitrary cell shapes, spatially resolved cell-cell contact interfaces and stochasticity in cell movement (Graner & Glazier, 1992). Multiple modelling and simulation frameworks for CPM exist including Chaste (Mirams et al., 2013; Pitt-Francis et al., 2009), CompuCell3D (Swat et al., 2012) and Morpheus (Starruß et al., 2014) which are free, open-source software. We have chosen Morpheus because of its user-friendly interface and its transparent separation of the solver code from the computational model description in the domain-specific language MorpheusML. The model description file was deposited in the public model repository under MorpheusModelID:M0006 (https://identifiers.org/morpheus/M0006) which renders our multicellular simulations readily reproducible and extensible following the FAIR principles.

The simulations were performed on an elongated spatial domain with 500 x1500 grid nodes of a two-dimensional hexagonal lattice with periodic boundary conditions. Left- and right-flanking static obstacles left a central channel of 200 nodes width for the cells to migrate into. These obstacles were used to mimic lateral confinement by paraxial mesoderm. The spatial unit is chosen as 1μm per grid interval and the temporal unit as 1 min per time step. Monte Carlo step duration was chosen as 0.1 min to allow thousands of potential updates per lattice node during the simulated time span. Cell shape is controlled by a target area of experimentally measured 326 μm² (average of 360 experimental measures) and a target circumference taken from the isoareal circle. Both constraints enter the Hamiltonian with equal Lagrange multipliers of 1 (Graner & Glazier, 1992). Axial mesoderm cells (yellow in simulations) are given a directed motion targeted at the animal pole, the speed of which is modulated by varying the strength parameter of the Directed Motion plugin in Morpheus (Starruß et al., 2014). Unless specified,

polster cells (green in simulations) are given a Run-and-Tumble motility with uniform reorientation probability of the target direction, a non-dimensional scaling factor "Run_duration_adjustment" of the Gamma-distributed probabilistic waiting times for reorientation events, i.e. Run_duration_adjustment * Γ(0.5,5 min) with a mean run time of Run_duration_adjustment*0.5*5 min, and a tunable Lagrange multiplier "motion_strength" that scales motion speed. The two parameter values for Run_duration_adjustment and motion_strength were estimated from experimental data of single cell trajectories (see below). In addition to the Run-and-Tumble motility, mechanical orientation of polster cells was simulated using the PyMapper plugin. At fixed time steps of 1 min, for each cell, neighbours are detected on 50 membrane points. For each neighbour, the angle between its velocity vector and the direction toward the considered cell is computed. If below a threshold "max_angle" (i.e. neighbour migrating toward the considered cell), the velocity vector of the neighbour is used as the new direction of the considered cell in the Directed Motion plugin. In case of several migrating neighbours, the direction vector is an average of their velocity vectors, weighed by the size of cell-cell contacts. In most simulations, 400 cells are initialised. An initial phase of 20 min without motility is used to equilibrate cell shapes and cell packing (not shown on the movies). Based on their antero-posterior position, cells are then given an identity, and the corresponding motility properties. Main parameters are summarised in Tab. 1.

For simulations with Contact Inhibition of Locomotion, identical parameters were used (Monte Carlo step duration, target area and circumference) and polster cells were given the same Run and Tumble behaviour. Instead of adding mechanical orientation, a CIL behaviour was added. Briefly, a membrane property is used to detect contact with neighbouring cells. The vector between the cell centre and the contact point is measured and the opposite vector is added to the current cell direction, with a tunable Lagrange multiplier "cil_strength". Simulations were performed on a square domain with 1000 x1000 grid nodes of a two-dimensional hexagonal lattice with periodic boundary conditions. Two groups of 40 cells were initialised, their centres 120 µm apart.

Parameter estimation

In order to fit the baseline cell motility parameters to experimentally observed single cell trajectory data, we define a distance function between the observed and simulated summary statistics.

$$d = \sum_i w_i^{MSD} * |MSD_i - msd_i| + \sum_{i<21min} w_i^{DAC} * |DAC_i - dac_i|$$

Here, MSD is the mean square displacement and DAC the direction autocorrelation function (Gorelik & Gautreau, 2014). Capital variables represent the experimental measurements, small letters

represent the model observables. We calculate the sum of weighted (see below) differences between the ensemble (n~200) means of MSD and DAC at the time points i ∈ {0 min, 3 min, 6 min, 9 min, 12 min, 15 min, 18 min, 21 min}. We optimise this distance function *d* employing the FitMultiCell software (https://fitmulticell.gitlab.io), which is a free, open-source Python tool embedding stochastic, multi-cellular Morpheus simulations in the highly parallel and unbiased Approximate Bayesian Computation – Sequential Monte Carlo (ABC-SMC) algorithm implemented by the computational framework pyABC (Klinger et al., 2018; Schälte & Hasenauer, 2020). FitMultiCell concurrently evaluates the model and distance measure *d* for trial parameter sets drawn from the evolving probability distribution across the search space, started from a uniform prior distribution. The distance measure *d* is then minimised over successive epochs by only accepting parameter sets with *d* below a gradually decreasing acceptance threshold ε. The pyABC meta-parameters for parameter sample number was set to 200 accepted trial parameter sets per epoch. The computations were run on the high performance computing cluster of ZIH at TU Dresden with 4 CPUs used per task, 2.5 GB/core. The approximate run time for 10 epochs was 20 hrs.

The weights w_i were chosen adaptively in pyABC to account for the different scales of MSD and DAC and two sets of optimisation epochs were concatenated. First, a uniform prior distribution in the broad interval [0.01, 10] was chosen for each fit parameter and the adaptive-weight scheme of pyABC readjusted the w_i after each of 10 epochs. To avoid convergence problems for later epochs due to fluctuating weights, we used the posterior distributions of this first set of epochs as the prior for the second set of epochs, i.e. Run_duration_adjustment: [0.05, 4], motion_strength: [0.1, 2], advection_velocity: [0.05, 3]. The weights w_i of the second set of epochs were again adaptively adjusted by pyABC but just initially and then kept fixed for the remaining 12 epochs. Convergence was judged by arriving at the plateau of the acceptance threshold ε in the ABC-SMC algorithm, see Figure S4. The following point estimate for the fitted model parameters and their confidence intervals were obtained (Fig. 37A):

Run_duration_adjustment: 0.76, CI: [0.18, 1.95]

motion_strength: 0.50, CI: [0.28, 1.00]

advection_velocity: 1.42, CI: [0.24, 2.20]

The parameter advection_velocity was used to overlay a uniform translation onto all cells, capturing potential drag forces by the overlying ectoderm. Such common translation reproduces the experimentally observed baseline of 20% in DAC (Fig. 37B-D).

Model parameter	Symbol	Value	Unit	Reference
target cell area	A_0	326	µm²	experimental measurement
target cell circumference	C_0	$\sqrt{4\pi A_0}$	µm	free choice
polster cell, motion strength	λ_1	*0,5*	-	fitted to single cell data
polster cell, mean run time	T_1	*0,76*2,5*	min	fitted to single cell data
polster cell, advection velocity	v_1	*1,42*	$\frac{\mu m}{min}$	fitted to single cell data
maximum angle	α_{max}	$\pi/6$	-	fitted to collective behaviour

Table 1. Summary of model parameter values.

Bibliographic references

Aalto, A., Olguin-Olguin, A., & Raz, E. (2021). Zebrafish Primordial Germ Cell Migration. *Frontiers in Cell and Developmental Biology*, *0*, 1477. https://doi.org/10.3389/FCELL.2021.684460

Aamar, E., & Dawid, I. B. (2008). Protocadherin-18a has a role in cell adhesion, behavior and migration in zebrafish development. *Developmental Biology*, *318*(2), 335–346. https://doi.org/10.1016/j.ydbio.2008.03.040

Abercrombie, M., & Heaysman, J. E. M. (1954). Observations on the social behaviour of cells in tissue culture: II. "Monolayering" of fibroblasts. *Experimental Cell Research*, *6*(2), 293–306. https://doi.org/10.1016/0014-4827(54)90176-7

Aberle, H., Schwartz, H., & Kemler, R. (1996). Cadherin-Catenin Complex: Protein and Their Implications for Cadherin Interactions Function. *Journal of Cellular Biochemistry*, *61*, 996. https://doi.org/10.1002/(SICI)1097-4644(19960616)61:4

Abudayyeh, O. O., Gootenberg, J. S., Essletzbichler, P., Han, S., Joung, J., Belanto, J. J., Verdine, V., Cox, D. B. T., Kellner, M. J., Regev, A., Lander, E. S., Voytas, D. F., Ting, A. Y., & Zhang, F. (2017). RNA targeting with CRISPR–Cas13. *Nature*, *550*(7675), 280–284. https://doi.org/10.1038/nature24049

Adams, R. J., & Kimmel, C. B. (2004). Morphogenetic cellular flows during zebrafish. *Gastrulation: From Cells to Embryo*, 305–316.

Alexander, J., Rothenberg, M., Henry, G. L., & Stainier, D. Y. R. (1999). casanova Plays an Early and Essential Role in Endoderm Formation in Zebrafish. *Developmental Biology*, *215*(2), 343–357. https://doi.org/10.1006/DBIO.1999.9441

Aman, A., & Piotrowski, T. (2010). Cell migration during morphogenesis. *Developmental Biology*, *341*(1), 20–33. https://doi.org/10.1016/j.ydbio.2009.11.014

Amano, M., Nakayama, M., & Kaibuchi, K. (2010). Rho-Kinase/ROCK: A Key Regulator of the Cytoskeleton and Cell Polarity. *Cytoskeleton (Hoboken, N.J.)*, *67*(9), 545. https://doi.org/10.1002/CM.20472

Amaya, E, Stein, P. a, Musci, T. J., & Kirschner, M. W. (1993). FGF signalling in the early specification of mesoderm in Xenopus. *Development*, *118*(2), 477–487. https://doi.org/10.1007/s11104-011-1034-1

Amaya, Enrique, Musci, T. J., & Kirschner, M. W. (1991). Expression of a dominant negative mutant of the FGF receptor disrupts mesoderm formation in xenopus embryos. *Cell*, *66*(2), 257–270. https://doi.org/10.1016/0092-8674(91)90616-7

Ananthakrishnan, R., & Ehrlicher, A. (2007). The forces behind cell movement. *International Journal of Biological Sciences*, *3*(5), 303–317. https://doi.org/10.7150/IJBS.3.303

Anguiano, M., Morales, X., Castilla, C., Pena, A. R., Ederra, C., Martínez, M., Ariz, M., Esparza, M., Amaveda, H., Mora, M., Movilla, N., Aznar, J. M. G., Cortés-Domínguez, I., & Ortiz-de-Solorzano, C. (2020). The use of mixed collagen-Matrigel matrices of increasing complexity recapitulates the biphasic role of cell adhesion in cancer cell migration: ECM sensing, remodeling and forces at the leading edge of cancer invasion. *PLOS ONE*, *15*(1), e0220019. https://doi.org/10.1371/JOURNAL.PONE.0220019

Aoki, K., Kondo, Y., Naoki, H., Hiratsuka, T., Itoh, R. E., & Matsuda, M. (2017). Propagating Wave of ERK Activation Orients Collective Cell Migration. *Developmental Cell*, *43*(3), 305-317.e5. https://doi.org/10.1016/J.DEVCEL.2017.10.016

Aoki, T. O., Mathieu, J., Saint-Etienne, L., Rebagliati, M. R., Peyriéras, N., & Rosa, F. M. (2002). Regulation of Nodal Signalling and Mesendoderm Formation by TARAM-A, a TGFβ-Related Type I Receptor. *Developmental Biology*, *241*(2), 273–288. https://doi.org/10.1006/DBIO.2001.0510

Babb, S. G., Barnett, J., Doedens, A. L., Cobb, N., Liu, Q., Sorkin, B. C., Yelick, P. C., Raymond, P. A., & Marrs, J. A. (2001). Zebrafish E-cadherin: Expression during early embryogenesis and regulation during brain development. *Developmental Dynamics*, *221*(2), 231–237. https://doi.org/10.1002/dvdy.1132

Babb, S. G., & Marrs, J. A. (2004). E-cadherin regulates cell movements and tissue formation in early zebrafish embryos. *Developmental Dynamics*, *230*(2), 263–277. https://doi.org/10.1002/dvdy.20057

Bachmann, M., Kukkurainen, S., Hytönen, V. P., & Wehrle-Haller, B. (2019). Cell Adhesion by Integrins. *Https://Doi.Org/10.1152/Physrev.00036.2018*, *99*(4), 1655–1699. https://doi.org/10.1152/PHYSREV.00036.2018

Bagwell, J., Norman, J., Ellis, K., Peskin, B., Hwang, J., Ge, X., Nguyen, S., McMenamin, S. K., Stainier, D. Y. R., & Bagnat, M. (2020). Notochord vacuoles absorb compressive bone growth during zebrafish spine formation. *ELife*, *9*. https://doi.org/10.7554/ELIFE.51221

Ballestrem, C., Wehrle-Haller, B., Hinz, B., & Imhof, B. A. (2000). Actin-dependent Lamellipodia Formation and Microtubule-dependent Tail Retraction Control-directed Cell Migration. *Molecular Biology of the Cell*, *11*(9), 2999. https://doi.org/10.1091/MBC.11.9.2999

Bamburg, J. R. (1999). Proteins of the ADF/Cofilin Family: Essential Regulators of Actin Dynamics. *Annual Review of Cell and Developmental Biology*, *15*(1), 185–230. https://doi.org/10.1146/annurev.cellbio.15.1.185

Bamburg, J. R., & Bernstein, B. W. (2010). Roles of ADF/cofilin in actin polymerization and beyond. *F1000 Biology Reports*, *2*(1). https://doi.org/10.3410/B2-62

Barone, V., Lang, M., Krens, S. F. G., Pradhan, S. J., Shamipour, S., Sako, K., Sikora, M., Guet, C. C., & Heisenberg, C. P. (2017). An Effective Feedback Loop between Cell-Cell Contact Duration and Morphogen Signaling Determines Cell Fate. *Developmental Cell*, *43*(2), 198–211. https://doi.org/10.1016/j.devcel.2017.09.014

Barriga, E. H., Franze, K., Charras, G., & Mayor, R. (2018). Tissue stiffening coordinates morphogenesis by triggering collective cell migration in vivo. *Nature*, *554*(7693), 523–527. https://doi.org/10.1038/nature25742

Bastock, R., & Strutt, D. (2007). The planar polarity pathway promotes coordinated cell migration during Drosophila oogenesis. *Development*, *134*(17), 3055–3064. https://doi.org/10.1242/dev.010447

Bays, J. L., & DeMali, K. A. (2017). Vinculin in cell–cell and cell–matrix adhesions. *Cellular and Molecular Life Sciences*, *74*(16), 2999–3009. https://doi.org/10.1007/s00018-017-2511-3

Behrndt, M., & Heisenberg, C. P. (2012). Spurred by Resistance: Mechanosensation in Collective Migration. *Developmental Cell*, *22*(1), 3–4. https://doi.org/10.1016/j.devcel.2011.12.018

Behrndt, M., Salbreux, G., Campinho, P., Hauschild, R., Oswald, F., Roensch, J., Grill, S. W., & Heisenberg, C. (2012). Forces Driving Epithelial Spreading in Zebrafish Gastrulation. *Science*, *338*(October), 257–260.

Belin, B. J., Goins, L. M., & Mullins, R. D. (2015). Comparative analysis of tools for live cell imaging of actin network architecture. *Ceased*, *4*(6), 189–202. https://doi.org/10.1080/19490992.2014.1047714

Bensch, R., Song, S., Ronneberger, O., & Driever, W. (2013). Non-directional radial intercalation dominates deep cell behavior during zebrafish epiboly. *Biology Open*, *2*(8), 845–854. https://doi.org/10.1242/BIO.20134614

Bergert, M., Chandradoss, S. D., Desai, R. A., & Paluch, E. (2012). Cell mechanics control rapid transitions between blebs and lamellipodia during migration. *Proceedings of the National Academy of Sciences*, *109*(36), 14434–14439. https://doi.org/10.1073/pnas.1207968109

Berrier, A. L., & Yamada, K. M. (2007). Cell–matrix adhesion. *Journal of Cellular Physiology*, *213*(3), 565–573. https://doi.org/10.1002/JCP.21237

Betchaku, T., & Trinkaus, J. P. (1978). Contact relations, surface activity, and cortical microfilaments of marginal cells of the enveloping layer and of the yolk syncytial and yolk cytoplasmic layers of Fundulus before and during epiboly. *Journal of Experimental Zoology*, *206*(3), 381–426. https://doi.org/10.1002/jez.1402060310

Betchaku, TEIICHI, & Trinkaus, J. P. (1986). Programmed Endocytosis During Epiboly of Fundulus heteroclitus. *American Zoologist*, *26*(1), 193–199. https://doi.org/10.1093/icb/26.1.193

Bianco, A., Poukkula, M., Cliffe, A., Mathieu, J., Luque, C. M., Fulga, T. A., & Rørth, P. (2007). Two distinct modes of guidance signalling during collective migration of border cells. *Nature*, *448*(7151), 362–365. https://doi.org/10.1038/nature05965

Bisgrove, B. W., Su, Y. C., & Yost, H. J. (2017). Maternal Gdf3 is an obligatory cofactor in nodal signaling for embryonic axis formation in zebrafish. *ELife*, *6*. https://doi.org/10.7554/ELIFE.28534

Biswas, S., Emond, M. R., Duy, P. Q., Hao, L. T., Beattie, C. E., & Jontes, J. D. (2014). Protocadherin-18b interacts with Nap1 to control motor axon growth and arborization in zebrafish. *Molecular Biology of the Cell*, *25*(5), 633–642. https://doi.org/10.1091/mbc.E13-08-0475

Blanchard, G. B., & Adams, R. J. (2011). Measuring the multi-scale integration of mechanical forces during morphogenesis. *Current Opinion in Genetics and Development*, *21*(5), 653–663. https://doi.org/10.1016/j.gde.2011.08.008

Blanco, M. J., Barrallo-Gimeno, A., Acloque, H., Reyes, A. E., Tada, M., Allende, M. L., Mayor, R., & Nieto, M. A. (2007). Snail1a and Snail1b cooperate in the anterior migration of the axial mesendoderm in the zebrafish embryo. *Development (Cambridge, England)*, *134*, 4073–4081. https://doi.org/10.1242/dev.006858

Boldajipour, B., Mahabaleshwar, H., Kardash, E., Reichman-Fried, M., Blaser, H., Minina, S., Wilson, D., Xu, Q., & Raz, E. (2008). Control of Chemokine-Guided Cell Migration by Ligand Sequestration. *Cell*, *132*(3), 463–473. https://doi.org/10.1016/j.cell.2007.12.034

Bompard, G., & Caron, E. (2004). Regulation of WASP/WAVE proteins: making a long story short. *The Journal of Cell Biology*, *166*(7), 957. https://doi.org/10.1083/JCB.200403127

Bonnet, I., Marcq, P., Bosveld, F., Fetler, L., Bellaiche, Y., & Graner, F. (2012). Mechanical state, material properties and continuous description of an epithelial tissue. *Journal of The Royal Society Interface*, *9*(75), 2614–2623. https://doi.org/10.1098/rsif.2012.0263

Borradori, L., & Sonnenberg, A. (1999). Structure and Function of Hemidesmosomes: More Than Simple Adhesion Complexes. *Journal of Investigative Dermatology*, *112*(4), 411–418. https://doi.org/10.1046/J.1523-1747.1999.00546.X

Bosze, B., Ono, Y., Mattes, B., Sinner, C., Gourain, V., Thumberger, T., Tlili, S., Wittbrodt, J., Saunders, T. E., Strähle, U., Schug, A., & Scholpp, S. (2020). Pcdh18a regulates endocytosis of E-cadherin during axial mesoderm development in zebrafish. *Histochemistry and Cell Biology*, *154*(5), 463–480. https://doi.org/10.1007/s00418-020-01887-5

Boutillon, A., Escot, S., & David, N. B. (2021). Deep and Spatially Controlled Volume Ablations using a Two-Photon Microscope in the Zebrafish Gastrula. *Journal of Visualized Experiments*, *173*, 1–16. https://doi.org/10.3791/62815

Boutillon, A., Giger, F. A., & David, N. B. (2018). Analysis of in vivo cell migration in mosaic zebrafish embryos. In A. Gautreau (Ed.), *Methods in Molecular Biology* (Vol. 1749, pp. 213–226). Springer New York. https://doi.org/10.1007/978-1-4939-7701-7_16

Boutillon, A., Jahn, D., Gonzalez-Tirado, S., Starruss, J., Brusch, L., & David, N. B. (2021). Guidance by followers ensures long-range coordination of cell migration through α-Catenin mechanoperception. *BioRxiv*, 2021.04.26.441407. https://doi.org/https://doi.org/10.1101/2021.04.26.441407

Braga, V. M. . (2002). Cell–cell adhesion and signalling. *Current Opinion in Cell Biology*, *14*(5), 546–556. https://doi.org/10.1016/S0955-0674(02)00373-3

Bray, D., & White, J. (1988). Cortical flow in animal cells. *Science*, *239*(4842), 883–888. https://doi.org/10.1126/science.3277283

Breau, M. A., Wilson, D., Wilkinson, D. G., & Xu, Q. (2012). Chemokine and Fgf signalling act as opposing guidance cues in formation of the lateral line primordium. *Development*, *139*(12), 2246–2253. https://doi.org/10.1242/dev.080275

Brodland, G. W., Veldhuis, J. H., Kim, S., Perrone, M., Mashburn, D., & Hutson, M. S. (2014). CellFIT: A cellular force-inference toolkit using curvilinear cell boundaries. *PLoS ONE*, *9*(6). https://doi.org/10.1371/journal.pone.0099116

Bruce, A. E. E. (2016). Zebrafish epiboly: Spreading thin over the yolk. *Developmental Dynamics*, *245*(3), 244–258. https://doi.org/10.1002/dvdy.24353

Bruce, A. E. E., & Heisenberg, C. P. (2020). Mechanisms of zebrafish epiboly: A current view. In *Current Topics in Developmental Biology* (1st ed., Vol. 136). Elsevier Inc. https://doi.org/10.1016/bs.ctdb.2019.07.001

Buckley, C. D., Tan, J., Anderson, K. L., Hanein, D., Volkmann, N., Weis, W. I., Nelson, W. J., & Dunn, A. R. (2014). The minimal cadherin-catenin complex binds to actin filaments under force. *Science*, *346*(6209), 1254211–1254211. https://doi.org/10.1126/science.1254211

Bugyi, B., & Carlier, M.-F. (2010). Control of Actin Filament Treadmilling in Cell Motility. *Http://Dx.Doi.Org/10.1146/Annurev-Biophys-051309-103849*, *39*(1), 449–470. https://doi.org/10.1146/ANNUREV-BIOPHYS-051309-103849

Bulina, M. E., Chudakov, D. M., Britanova, O. V, Yanushevich, Y. G., Staroverov, D. B., Chepurnykh, T. V, Merzlyak, E. M., Shkrob, M. A., Lukyanov, S., & Lukyanov, K. A. (2005). A genetically encoded photosensitizer. *Nature Biotechnology 2005 24:1*, *24*(1), 95–99. https://doi.org/10.1038/nbt1175

Burns, J. M., Summers, B. C., Wang, Y., Melikian, A., Berahovich, R., Miao, Z., Penfold, M. E. T., Sunshine, M. J., Littman, D. R., Kuo, C. J., Wei, K., McMaster, B. E., Wright, K., Howard, M. C., & Schall, T. J. (2006). A novel chemokine receptor for SDF-1 and I-TAC involved in cell survival, cell adhesion, and tumor development. *Journal of Experimental Medicine*, *203*(9), 2201–2213. https://doi.org/10.1084/jem.20052144

Burridge, K. (2017). Focal adhesions: a personal perspective on a half century of progress. *The FEBS Journal*, *284*(20), 3355–3361. https://doi.org/10.1111/FEBS.14195

Burridge, K., & Wennerberg, K. (2004). Rho and Rac Take Center Stage. *Cell*, *116*(2), 167–179. https://doi.org/10.1016/S0092-8674(04)00003-0

Cai, D., Chen, S. C., Prasad, M., He, L., Wang, X., Choesmel-Cadamuro, V., Sawyer, J. K., Danuser, G., & Montell, D. J. (2014). Mechanical feedback through E-cadherin promotes direction sensing during collective cell migration. *Cell*, *157*(5), 1146–1159. https://doi.org/10.1016/j.cell.2014.03.045

Cai, D., Dai, W., Prasad, M., Luo, J., Gov, N. S., & Montell, D. J. (2016). Modeling and analysis of collective cell migration in an in vivo three-dimensional environment. *Proceedings of the National Academy of Sciences*, *113*(15), E2134–E2141. https://doi.org/10.1073/PNAS.1522656113

Calvo, F., Ege, N., Grande-Garcia, A., Hooper, S., Jenkins, R. P., Chaudhry, S. I., Harrington, K., Williamson, P., Moeendarbary, E., Charras, G., & Sahai, E. (2013). Mechanotransduction and YAP-dependent matrix remodelling is required for the generation and maintenance of cancer-associated fibroblasts. *Nature Cell Biology 2013 15:6*, *15*(6), 637–646. https://doi.org/10.1038/ncb2756

Camley, B. A. (2018). Collective gradient sensing and chemotaxis: Modeling and recent developments. *Journal of Physics Condensed Matter*, *30*(22). https://doi.org/10.1088/1361-648X/aabd9f

Campàs, O. (2016). A toolbox to explore the mechanics of living embryonic tissues. *Seminars in Cell and Developmental Biology*, *55*, 119–130. https://doi.org/10.1016/j.semcdb.2016.03.011

Campàs, O., Mammoto, T., Hasso, S., Sperling, R. A., O'connell, D., Bischof, A. G., Maas, R., Weitz, D. A., Mahadevan, L., & Ingber, D. E. (2014). Quantifying cell-generated mechanical forces within living embryonic tissues. *Nature Methods*, *11*(2), 183–189. https://doi.org/10.1038/nmeth.2761

Campbell, I. D., & Humphries, M. J. (2011). Integrin Structure, Activation, and Interactions. *Cold Spring Harbor Perspectives in Biology*, *3*(3), 1–14. https://doi.org/10.1101/CSHPERSPECT.A004994

Campellone, K. G., & Welch, M. D. (2010). A nucleator arms race: cellular control of actin assembly. *Nature Reviews Molecular Cell Biology*, *11*(4), 237–251. https://doi.org/10.1038/nrm2867

Caneparo, L., Huang, Y.-L., Staudt, N., Tada, M., Ahrendt, R., Kazanskaya, O., Niehrs, C., & Houart, C. (2007). Dickkopf-1 regulates gastrulation movements by coordinated modulation of Wnt/betacatenin and Wnt/PCP activities, through interaction with the Dally-like homolog Knypek. *Genes & Development*, *21*(4), 465–480. https://doi.org/10.1101/gad.406007

Cano, A., Pérez-Moreno, M. A., Rodrigo, I., Locascio, A., Blanco, M. J., Barrio, M. G. del, Portillo, F., & Nieto, M. A. (2000). The transcription factor Snail controls epithelial–mesenchymal transitions by repressing E-cadherin expression. *Nature Cell Biology 2000 2:2*, *2*(2), 76–83. https://doi.org/10.1038/35000025

Čapek, D., Smutny, M., Tichy, A.-M., Morri, M., Janovjak, H., & Heisenberg, C.-P. (2019). Light-activated Frizzled7 reveals a permissive role of non-canonical wnt signaling in mesendoderm cell migration. *ELife*, *8*, 1–56. https://doi.org/10.7554/elife.42093

Capozza, R., Caprettini, V., Gonano, C. A., Bosca, A., Moia, F., Santoro, F., & Angelis, F. De. (2018). CellMembrane Disruption by Vertical Micro-/Nanopillars:Role of Membrane Bending and Traction Forces. *ACS Applied Materials & Interfaces*, *10*(34), 29107. https://doi.org/10.1021/ACSAMI.8B08218

Carlier, M.-F., & Shekhar, S. (2017). Global treadmilling coordinates actin turnover and controls the size of actin networks. *Nature Reviews Molecular Cell Biology 2017 18:6*, *18*(6), 389–401. https://doi.org/10.1038/nrm.2016.172

Carmany-Rampey, A., & Schier, A. F. (2001). Single-cell internalization during zebrafish gastrulation. *Current Biology*, *11*(16), 1261–1265. https://doi.org/10.1016/S0960-9822(01)00353-0

Carmona-Fontaine, C., Matthews, H. K., Kuriyama, S., Moreno, M., Dunn, G. A., Parsons, M., Stern, C. D., & Mayor, R. (2008). Contact inhibition of locomotion in vivo controls neural crest directional migration. *Nature*, *456*(7224), 957–961. https://doi.org/10.1038/nature07441

Carmona-Fontaine, C., Theveneau, E., Tzekou, A., Tada, M., Woods, M., Page, K. M., Parsons, M., Lambris, J. D., & Mayor, R. (2011). Complement Fragment C3a Controls Mutual Cell Attraction during Collective Cell Migration. *Developmental Cell*, *21*(6), 1026–1037. https://doi.org/10.1016/j.devcel.2011.10.012

Carvalho, L., Stühmer, J., Bois, J. S., Kalaidzidis, Y., Lecaudey, V., & Heisenberg, C.-P. (2009). Control of convergent yolk syncytial layer nuclear movement in zebrafish. *Development*, *136*(8), 1305–1315. https://doi.org/10.1242/DEV.026922

Chalut, K. J., & Paluch, E. K. (2016). *The Actin Cortex: A Bridge between Cell Shape and Function*. https://doi.org/10.1016/j.devcel.2016.09.011

Chan, J., Mably, J. D., Serluca, F. C., Chen, J. N., Goldstein, N. B., Thomas, M. C., Cleary, J. A., Brennan, C., Fishman, M. C., & Roberts, T. M. (2001). Morphogenesis of prechordal plate and notochord requires intact Eph/ephrin B signaling. *Developmental Biology*, *234*(2), 470–482. https://doi.org/10.1006/dbio.2001.0281

Chánez-Paredes, S., Montoya-García, A., & Schnoor, M. (2019). Cellular and pathophysiological consequences of Arp2/3 complex inhibition: role of inhibitory proteins and pharmacological compounds. *Cellular and Molecular Life Sciences 2019 76:17*, *76*(17), 3349–3361. https://doi.org/10.1007/S00018-019-03128-Y

Charras, G., & Paluch, E. (2008). Blebs lead the way: how to migrate without lamellipodia. *Nature Reviews Molecular Cell Biology*, *9*(9), 730–736. https://doi.org/10.1038/nrm2453

Charras, G., & Yap, A. S. (2018). Tensile Forces and Mechanotransduction at Cell–Cell Junctions. *Current Biology*, *28*(8), R445–R457. https://doi.org/10.1016/j.cub.2018.02.003

Chen, W. T. (1981). Mechanism of retraction of the trailing edge during fibroblast movement. *Journal of Cell Biology*, *90*(1), 187–200. https://doi.org/10.1083/jcb.90.1.187

Chen, X., Kojima, S., Borisy, G. G., & Green, K. J. (2003). p120 catenin associates with kinesin and facilitates the transport of cadherin–catenin complexes to intercellular junctions. *Journal of Cell Biology*, *163*(3), 547–557. https://doi.org/10.1083/jcb.200305137

Cheng, J. C., Miller, A. L., & Webb, S. E. (2004). Organization and function of microfilaments during late epiboly in zebrafish embryos. *Developmental Dynamics : An Official Publication of the American Association of Anatomists*, *231*(2), 313–323. https://doi.org/10.1002/DVDY.20144

Chien, Y. H., Keller, R., Kintner, C., & Shook, D. R. (2015). Mechanical strain determines the axis of planar polarity in ciliated epithelia. *Current Biology*, *25*(21), 2774–2784. https://doi.org/10.1016/j.cub.2015.09.015

Chitnis, A. B., Nogare, D. D., & Matsuda, M. (2012). Building the posterior lateral line system in zebrafish. *Developmental Neurobiology*, *72*(3), 234. https://doi.org/10.1002/DNEU.20962

Choi, H.-J., Pokutta, S., Cadwell, G. W., Bobkov, A. A., Bankston, L. A., Liddington, R. C., & Weis, W. I. (2012). αE-catenin is an autoinhibited molecule that coactivates vinculin. *Proceedings of the National Academy of Sciences*, *109*(22), 8576–8581. https://doi.org/10.1073/PNAS.1203906109

Chugh, P., & Paluch, E. K. (2018). The actin cortex at a glance. *Journal of Cell Science*, *131*(14). https://doi.org/10.1242/JCS.186254

Ciruna, B., & Rossant, J. (2001). FGF Signaling Regulates Mesoderm Cell Fate Specification and Morphogenetic Movement at the Primitive Streak. *Developmental Cell*, *1*(1), 37–49. https://doi.org/10.1016/S1534-5807(01)00017-X

Cliffe, A., Doupé, D. P., Sung, H., Lim, I. K. H., Ong, K. H., Cheng, L., & Yu, W. (2017). Quantitative 3D analysis of complex single border cell behaviors in coordinated collective cell migration. *Nature Communications*, *8*, 14905. https://doi.org/10.1038/ncomms14905

Colombelli, J., Reynaud, E. G., & Stelzer, E. H. K. (2007). Investigating Relaxation Processes in Cells and Developing

Organisms: From Cell Ablation to Cytoskeleton Nanosurgery. *Methods in Cell Biology*, *82*(06), 267–291. https://doi.org/10.1016/S0091-679X(06)82008-X

Conti, M. A., Kawamoto, S., & Adelstein, R. S. (2008). *Chapter 7 Non-Muscle Myosin Ii*. 223–264.

Cotton, M., & Claing, A. (2009). G protein-coupled receptors stimulation and the control of cell migration. *Cellular Signalling*, *21*(7), 1045–1053. https://doi.org/10.1016/j.cellsig.2009.02.008

Crick, F. (1970). Diffusion in Embryogenesis. *Nature*, *225*(5231), 420–422. https://doi.org/10.1038/225420a0

D'alessandro, J., Solon, A. P., Hayakawa, Y., Anjard, C., Detcheverry, F., Rieu, J. P., & Rivière, C. (2017). Contact enhancement of locomotion in spreading cell colonies. *Nature Physics*, *13*(10), 999–1005. https://doi.org/10.1038/nphys4180

D'Amico, L. A., & Cooper, M. S. (2001). Morphogenetic domains in the yolk syncytial layer of axiating zebrafish embryos. *Developmental Dynamics*, *222*(4), 611–624. https://doi.org/10.1002/DVDY.1216

D'Arcy, W. T. (1917). On Growth and Form. *On Growth and Form*. https://doi.org/10.1017/CBO9781107325852

Dale, L., & Slack, J. M. W. (1987). Fate map for the 32-cell stage of Xenopus laevis. *Development*, *99*, 527–551.

Dance, A. (2020). The quest to decipher how the body's cells sense touch. *Nature*, *577*(7789), 158–160. https://doi.org/10.1038/D41586-019-03955-W

Dang, I., Gorelik, R., Sousa-Blin, C., Derivery, E., Guérin, C., Linkner, J., Nemethova, M., Dumortier, J. G., Giger, F. A., Chipysheva, T. A., Ermilova, V. D., Vacher, S., Campanacci, V., Herrada, I., Planson, A. G., Fetics, S., Henriot, V., David, V., Oguievetskaia, K., … Gautreau, A. (2013). Inhibitory signalling to the Arp2/3 complex steers cell migration. *Nature*, *503*(7475), 281–284. https://doi.org/10.1038/nature12611

Das, D., Jülich, D., Schwendinger-Schreck, J., Guillon, E., Lawton, A. K., Dray, N., Emonet, T., O'Hern, C. S., Shattuck, M. D., & Holley, S. A. (2019). Organization of Embryonic Morphogenesis via Mechanical Information. *Developmental Cell*, 829–839. https://doi.org/10.1016/j.devcel.2019.05.014

Das, T., Safferling, K., Rausch, S., Grabe, N., Boehm, H., & Spatz, J. P. (2015). A molecular mechanotransduction pathway regulates collective migration of epithelial cells. *Nature Cell Biology*, *17*(3), 276–287. https://doi.org/10.1038/ncb3115

David, N. B., Sapède, D., Saint-Etienne, L., Thisse, C., Thisse, B., Dambly-Chaudière, C., Rosa, F. M., & Ghysen, A. (2002). Molecular basis of cell migration in the fish lateral line: role of the chemokine receptor CXCR4 and of its ligand, SDF1. *Proceedings of the National Academy of Sciences of the United States of America*, *99*(25), 16297–16302. https://doi.org/10.1073/pnas.252339399

de Frutos, C. A., Vega, S., Manzanares, M., Flores, J. M., Huertas, H., Martínez-Frías, M. L., & Nieto, M. A. (2007). Snail1 Is a Transcriptional Effector of FGFR3 Signaling during Chondrogenesis and Achondroplasias. *Developmental Cell*, *13*(6), 872–883. https://doi.org/10.1016/j.devcel.2007.09.016

de la Cova, C., Townley, R., Regot, S., & Greenwald, I. (2017). *A Real-Time Biosensor for ERK Activity Reveals Signaling Dynamics during C. elegans Cell Fate Specification*. https://doi.org/10.1016/j.devcel.2017.07.014

DeMali, K. A., Barlow, C. A., & Burridge, K. (2002). Recruitment of the Arp2/3 complex to vinculin: coupling membrane protrusion to matrix adhesion. *The Journal of Cell Biology*, *159*(5), 881. https://doi.org/10.1083/JCB.200206043

Derivery, E., & Gautreau, A. (2010). Generation of branched actin networks: assembly and regulation of the N-WASP and WAVE molecular machines. *BioEssays*, *32*(2), 119–131. https://doi.org/10.1002/bies.200900123

Deuel, T. F., Senior, R. M., Huang, J. S., & Griffin, G. L. (1982). Chemotaxis of monocytes and neutrophils to platelet-derived growth factor. *Journal of Clinical Investigation*, *69*(4), 1046–1049. https://doi.org/10.1172/JCI110509

Dick, A., Mayr, T., Bauer, H., Meier, A., & Hammerschmidt, M. (2000). Cloning and characterization of zebrafish smad2, smad3 and smad4. *Gene*, *246*(1–2), 69–80. https://doi.org/10.1016/S0378-1119(00)00056-1

Dickmeis, T., Mourrain, P., Saint-Etienne, L., Fischer, N., Aanstad, P., Clark, M., Str??hle, U., Rosa, F. F. M. F., Strähle, U., & Rosa, F. F. M. F. (2001). A crucial component of the endoderm formation pathway, CASANOVA, is encoded by a novel sox-related gene. *Genes & Development*, *15*(12), 1487–1492. https://doi.org/10.1101/gad.196901

Dixon Fox, M., & Bruce, A. E. E. (2009). Short- and long-range functions of Goosecoid in zebrafish axis formation are independent of Chordin, Noggin 1 and Follistatin-like 1b. *Development*, *136*(10), 1675–1685. https://doi.org/10.1242/dev.031161

Diz-Muñoz, A., Krieg, M., Bergert, M., Ibarlucea-Benitez, I., Muller, D. J., Paluch, E., & Heisenberg, C.-P. (2010). Control of Directed Cell Migration In Vivo by Membrane-to-Cortex Attachment. *PLoS Biology*, *8*(11), e1000544. https://doi.org/10.1371/journal.pbio.1000544

Diz-Muñoz, A., Romanczuk, P., Yu, W., Bergert, M., Ivanovitch, K., Salbreux, G., Heisenberg, C.-P., & Paluch, E. K. (2016). Steering cell migration by alternating blebs and actin-rich protrusions. *BMC Biology*, *14*(1), 74. https://doi.org/10.1186/s12915-016-0294-x

Doitsidou, M., Reichman-Fried, M., Stebler, J., Köprunner, M., Dörries, J., Meyer, D., Esguerra, C. V, Leung, T., & Raz, E. (2002). Guidance of primordial germ cell migration by the chemokine SDF-1. *Cell*, *111*(5), 647–659. https://doi.org/doi.org/10.1016/S0092-8674(02)01135-2

Donà, E., Barry, J. D., Valentin, G., Quirin, C., Khmelinskii, A., Kunze, A., Durdu, S., Newton, L. R., Fernandez-Minan, A., Huber, W., Knop, M., & Gilmour, D. (2013). Directional tissue migration through a self-generated chemokine gradient. *Nature*, *V*. https://doi.org/10.1038/nature12635

Dorey, K., & Amaya, E. (2010). FGF signalling: diverse roles during early vertebrate embryogenesis. *Development*, *137*(22), 3731–3742. https://doi.org/10.1242/dev.037689

Doss, B. L., Pan, M., Gupta, M., Grenci, G., Mège, R.-M., Lim, C. T., Sheetz, M. P., Voituriez, R., & Ladoux, B. (2020). Cell response to substrate rigidity is regulated by active and passive cytoskeletal stress. *Proceedings of the National Academy of Sciences*, *117*(23), 12817–12825. https://doi.org/10.1073/PNAS.1917555117

Dougan, S. T., Warga, R. M., Kane, D. A., Schier, A. F., & Talbot, W. S. (2003). The role of the zebrafish nodal -related genes squint and cyclops in patterning of mesendoderm. *Development*, *130*(9), 1837–1851. https://doi.org/10.1242/dev.00400

Draper, B. W., Stock, D. W., & Kimmel, C. B. (2003). *Zebrafish fgf24* functions with *fgf8* to promote posterior mesodermal development. *Development*, *130*(19), 4639–4654. https://doi.org/10.1242/dev.00671

Driever, W., & Rangini, Z. (1993). Characterization of a cell line derived from zebrafish (brachydanio rerio) embryos. *In Vitro Cellular & Developmental Biology - Animal*, *29*(9), 749–754. https://doi.org/10.1007/BF02631432

Duchek, P., Somogyi, K., Jékely, G., Beccari, S., & Rorth, P. (2001). Guidance of Cell Migration by the Drosophila PDGF/VEGF Receptor. *Cell*, *107*(1), 17–26. https://doi.org/10.1016/S0092-8674(01)00502-5

DuChez, B. J., Doyle, A. D., Dimitriadis, E. K., & Yamada, K. M. (2019). Durotaxis by Human Cancer Cells. *Biophysical Journal*, *116*(4), 670–683. https://doi.org/10.1016/J.BPJ.2019.01.009

Duhart, J. C., Parsons, T. T., & Raftery, L. A. (2017). The repertoire of epithelial morphogenesis on display: Progressive elaboration of Drosophila egg structure. *Mechanisms of Development*. https://doi.org/10.1016/j.mod.2017.04.002

Dumortier, J. G., Martin, S., Meyer, D., Rosa, F. M., & David, N. B. (2012). Collective mesendoderm migration relies on an intrinsic directionality signal transmitted through cell contacts. *Proceedings of the National Academy of Sciences*, *109*(42), 16945–16950. https://doi.org/10.1073/pnas.1205870109

Dumortier, Julien G., & David, N. B. (2015). The TORC2 component, sin1, controls migration of anterior mesendoderm during zebrafish gastrulation. *PLoS ONE*, *10*(2), 1–16. https://doi.org/10.1371/journal.pone.0118474

Dumortier, Julien G., Martin, S., Meyer, D., Rosa, F. M., & David, N. B. (2012). Collective mesendoderm migration relies on an intrinsic directionality signal transmitted through cell contacts. *Proceedings of the National Academy of Sciences*, *109*(42), 16945–16950. https://doi.org/10.1073/pnas.1205870109

Durande, M., Tlili, S., Homan, T., Guirao, B., Graner, F., & Delanoë-Ayari, H. (2019). Fast determination of coarse-grained cell anisotropy and size in epithelial tissue images using Fourier transform. *Physical Review E*, *99*(6), 1–10. https://doi.org/10.1103/PhysRevE.99.062401

Edwards, M., Zwolak, A., Schafer, D. A., Sept, D., Dominguez, R., & Cooper, J. A. (2014). Capping protein regulators fine-tune actin assembly dynamics. *Nature Reviews Molecular Cell Biology 2014 15:10*, *15*(10), 677–689. https://doi.org/10.1038/nrm3869

El-Brolosy, M. A., Kontarakis, Z., Rossi, A., Kuenne, C., Günther, S., Fukuda, N., Kikhi, K., Boezio, G. L. M., Takacs, C. M., Lai, S.-L., Fukuda, R., Gerri, C., Giraldez, A. J., & Stainier, D. Y. R. (2019). Genetic compensation triggered by mutant mRNA degradation. *Nature*, *568*(7751), 193–197. https://doi.org/10.1038/s41586-019-1064-z

England, S. J., Blanchard, G. B., Mahadevan, L., & Adams, R. J. (2006). A dynamic fate map of the forebrain shows how vertebrate eyes form and explains two causes of cyclopia. *Development (Cambridge, England)*, *133*(23), 4613–4617. https://doi.org/10.1242/dev.02678

Engler, A. J., Sen, S., Sweeney, H. L., & Discher, D. E. (2006). Matrix Elasticity Directs Stem Cell Lineage Specification. *Cell*, *126*(4), 677–689. https://doi.org/10.1016/J.CELL.2006.06.044

Erdogan, B., Ao, M., White, L. M., Means, A. L., Brewer, B. M., Yang, L., Washington, M. K., Shi, C., Franco, O. E., Weaver, A. M., Hayward, S. W., Li, D., & Webb, D. J. (2017). Cancer-associated fibroblasts promote directional cancer cell migration by aligning fibronectin. *The Journal of Cell Biology*, *216*(11), 3799. https://doi.org/10.1083/JCB.201704053

Etienne-Manneville, S. (2004). Cdc42 - the centre of polarity. *Journal of Cell Science*, *117*(8), 1291–1300. https://doi.org/10.1242/jcs.01115

Etienne-Manneville, Sandrine, & Hall, A. (2002). Rho GTPases in cell biology. *Nature*, *420*(6916), 629–635. https://doi.org/10.1038/nature01148

Evans, W. H., & Martin, P. E. M. (2002). Gap junctions: structure and function (Review). *Molecular Membrane Biology*, *19*(2), 121–136. https://doi.org/10.1080/09687680210139839

Farrell, J. A., Wang, Y., Riesenfeld, S. J., Shekhar, K., Regev, A., & Schier, A. F. (2018). Single-cell reconstruction of developmental trajectories during zebrafish embryogenesis. *Science*, *360*(6392). https://doi.org/10.1126/science.aar3131

Fekany, K., Yamanaka, Y., Leung, T., Sirotkin, H. I., Topczewski, J., Gates, M. A., Hibi, M., Renucci, A., Stemple, D., Radbill, A., Schier, A. F., Driever, W., Hirano, T., Talbot, W. S., & Solnica-Krezel, L. (1999). The zebrafish bozozok locus

encodes Dharma, a homeodomain protein essential for induction of gastrula organizer and dorsoanterior embryonic structures. *Development*, *126*(7), 1427–1438. https://doi.org/10.1242/DEV.126.7.1427

Feldman, B., Gates, M. A., Egan, E. S., Dougan, S. T., Rennebeck, G., Sirotkin, H. I., Schier, A. F., & Talbot, W. S. (1998). Zebrafish organizer development and germ-layer formation require nodal-related signals. *Nature*, *395*(6698), 181–185. https://doi.org/10.1038/26013

Footer, M. J., Kerssemakers, J. W. J., Theriot, J. A., & Dogterom, M. (2007). Direct measurement of force generation by actin filament polymerization using an optical trap. *Proceedings of the National Academy of Sciences*, *104*(7), 2181–2186. https://doi.org/10.1073/PNAS.0607052104

Friedl, P., & Gilmour, D. (2009). Collective cell migration in morphogenesis, regeneration and cancer. *Nature Reviews Molecular Cell Biology*, *10*(7), 445–457. https://doi.org/10.1038/nrm2720

Funamoto, S., Milan, K., Meili, R., & Firtel, R. A. (2001). Role of Phosphatidylinositol 3′ Kinase and a Downstream Pleckstrin Homology Domain–Containing Protein in Controlling Chemotaxis inDictyostelium. *Journal of Cell Biology*, *153*(4), 795–810. https://doi.org/10.1083/JCB.153.4.795

Gao, B. (2012). Wnt Regulation of Planar Cell Polarity (PCP). In *Current Topics in Developmental Biology* (1st ed., Vol. 101). Elsevier Inc. https://doi.org/10.1016/B978-0-12-394592-1.00008-9

Garrod, D., & Chidgey, M. (2008). Desmosome structure, composition and function. *Biochimica et Biophysica Acta (BBA) - Biomembranes*, *1778*(3), 572–587. https://doi.org/10.1016/J.BBAMEM.2007.07.014

Germain, S., Howell, M., Esslemont, G. M., & Hill, C. S. (2000). Homeodomain and winged-helix transcription factors recruit activated Smads to distinct promoter elements via a common Smad interaction motif. *Genes & Development*, *14*(4), 435–451. https://doi.org/10.1101/GAD.14.4.435

Giancotti, F. G. (1999). Integrin Signaling. *Science*, *285*(5430), 1028–1033. https://doi.org/10.1126/science.285.5430.1028

Giger, F. A., & David, N. B. (2017). Endodermal germ-layer formation through active actin-driven migration triggered by N-cadherin. *Proceedings of the National Academy of Sciences*, *114*(38), 201708116. https://doi.org/10.1073/pnas.1708116114

Glickman, N. S., Kimmel, C. B., Jones, M. A., & Adams, R. J. (2003). Shaping the zebrafish notochord. *Development*, *130*(5), 873–887. https://doi.org/10.1242/dev.00314

Goicoechea, S. M., Awadia, S., & Garcia-Mata, R. (2014). I'm coming to GEF you: Regulation of RhoGEFs during cell migration. *Cell Adhesion & Migration*, *8*(6), 535. https://doi.org/10.4161/CAM.28721

Goley, E. D., Rammohan, A., Znameroski, E. A., Firat-Karalar, E. N., Sept, D., & Welch, M. D. (2010). An actin-filament-binding interface on the Arp2/3 complex is critical for nucleation and branch stability. *Proceedings of the National Academy of Sciences*, *107*(18), 8159–8164. https://doi.org/10.1073/PNAS.0911668107

Gooding, J. M., Yap, K. L., & Ikura, M. (2004). The cadherin-catenin complex as a focal point of cell adhesion and signalling: new insights from three-dimensional structures. *BioEssays*, *26*(5), 497–511. https://doi.org/10.1002/bies.20033

Gorelik, R., & Gautreau, A. (2014). Quantitative and unbiased analysis of directional persistence in cell migration. *Nature Protocols*, *9*(8), 1931–1943. https://doi.org/10.1038/nprot.2014.131

Gospodarowicz, D., & Moran, J. S. (1975). Mitogenic effect of fibroblast growth factor on early passage cultures of human and murine fibroblasts. *Journal of Cell Biology*, *66*(2), 451–457. https://doi.org/10.1083/jcb.66.2.451

Graner, F., & Glazier, J. A. (1992). Simulation of biological cell sorting using a two-dimensional extended Potts model. *Phys Rev Lett*, *69*(13), 2013–2016.

Grashoff, C., Hoffman, B. D., Brenner, M. D., Zhou, R., Parsons, M., Yang, M. T., McLean, M. A., Sligar, S. G., Chen, C. S., Ha, T., & Schwartz, M. A. (2010). Measuring mechanical tension across vinculin reveals regulation of focal adhesion dynamics. *Nature*, *466*(7303), 263–266. https://doi.org/10.1038/nature09198

Grell, K. G., & Schüller, S. (1991). The ultrastructure of the plasmodial protist Leucodictyon marinum Grell. *European Journal of Protistology*, *27*(2), 168–177. https://doi.org/10.1016/S0932-4739(11)80339-1

Gritsman, K., Talbot, W. S., & Schier, A. F. (2000). Nodal signaling patterns the organizer. *Development*, *127*(5), 921–932. https://doi.org/10.1242/DEV.127.5.921

Gritsman, Kira, Zhang, J., Cheng, S., Heckscher, E., Talbot, W. S., & Schier, A. F. (1999). The EGF-CFC Protein One-Eyed Pinhead Is Essential for Nodal Signaling. *Cell*, *97*(1), 121–132. https://doi.org/10.1016/S0092-8674(00)80720-5

Grunwald, D. J., & Eisen, J. S. (2002). Headwaters of the zebrafish — emergence of a new model vertebrate. *Nature Reviews Genetics*, *3*(9), 717–724. https://doi.org/10.1038/nrg892

Guan, J.-L. (1997). Role of focal adhesion kinase in integrin signaling. *The International Journal of Biochemistry & Cell Biology*, *29*(8–9), 1085–1096. https://doi.org/10.1016/S1357-2725(97)00051-4

Haas, P., & Gilmour, D. (2006). Chemokine Signaling Mediates Self-Organizing Tissue Migration in the Zebrafish Lateral Line. *Developmental Cell*, *10*(5), 673–680. https://doi.org/10.1016/j.devcel.2006.02.019

Haeger, A., Wolf, K., Zegers, M. M., & Friedl, P. (2015). Collective cell migration: guidance principles and hierarchies. *Trends in Cell Biology*, *25*(9), 556–566. https://doi.org/10.1016/j.tcb.2015.06.003

Haigo, S. L., Hildebrand, J. D., Harland, R. M., & Wallingford, J. B. (2003). Shroom Induces Apical Constriction and Is Required for Hingepoint Formation during Neural Tube Closure. *Current Biology*, *13*(24), 2125–2137. https://doi.org/10.1016/J.CUB.2003.11.054

Hakim, V., & Silberzan, P. (2017). Collective cell migration: a physics perspective. *Reports on Progress in Physics*, *80*(7), 076601. https://doi.org/10.1088/1361-6633/aa65ef

Han, M. K. L., Hoijman, E., Nöel, E., Garric, L., Bakkers, J., & de Rooij, J. (2016). αE-catenin-dependent mechanotransduction is essential for proper convergent extension in zebrafish. *Biology Open*, *5*(10), 1461–1472. https://doi.org/10.1242/bio.021378

Han, M. K. L., Van Der Krogt, G. N. M., & De Rooij, J. (2017). Zygotic vinculin is not essential for embryonic development in zebrafish. *PLoS ONE*, *12*(8), 1–22. https://doi.org/10.1371/journal.pone.0182278

Hara, Y., Nagayama, K., Yamamoto, T. S., Matsumoto, T., Suzuki, M., & Ueno, N. (2013). Directional migration of leading-edge mesoderm generates physical forces: Implication in Xenopus notochord formation during gastrulation. *Developmental Biology*, *382*(2), 482–495. https://doi.org/10.1016/j.ydbio.2013.07.023

Harris, T. J. C., & Tepass, U. (2010). Adherens junctions: from molecules to morphogenesis. *Nature Reviews Molecular Cell Biology*, *11*(7), 502–514. https://doi.org/10.1038/nrm2927

Hart, N. H., Becker, K. A., & Wolenski, J. S. (1992). The sperm entry site during fertilization of the zebrafish egg: Localization of actin. *Molecular Reproduction and Development*, *32*(3), 217–228. https://doi.org/10.1002/mrd.1080320306

Hartman, M. A., & Spudich, J. A. (2012). The myosin superfamily at a glance. *Journal of Cell Science*, *125*(7), 1627.

https://doi.org/10.1242/JCS.094300

Hartwell, K. A., Muir, B., Reinhardt, F., Carpenter, A. E., Sgroi, D. C., & Weinberg, R. A. (2006). The Spemann organizer gene, Goosecoid, promotes tumor metastasis. *Proceedings of the National Academy of Sciences*, *103*(50), 18969–18974. https://doi.org/10.1073/pnas.0608636103

Hauptmann, G., & Gerster, T. (1994). Two-color whole-mount in situ hybridization to vertebrate and Drosophila embryos. *Trends in Genetics : TIG*, *10*(8), 266.

Heisenberg, C.-P., Tada, M., Rauch, G.-J. J., Saúde, L., Concha, M. L., Geisler, R., Stemple, D. L., Smith, J. C., Wilson, S. W., Saude, L., Concha, M. L., Geisler, R., Stemple, D. L., Smith, J. C., & Wilson, S. W. (2000). Silberblick/Wnt11 mediates convergent extension movements during zebrafish gastrulation. *Nature*, *405*(6782), 76–81. https://doi.org/10.1038/35011068

Heisenberg, C.-P., Tada, M., Rauch, G.-J., Saude, L., Concha, M. L., Geisler, R., Stemple, D. L., Smith, J. C., & Wilson, S. W. (2000). Silberblick / Wnt11 mediates convergent extension movements during zebrafish gastrulation. *Nature*, *405*(May), 76–81. https://doi.org/10.1038/35011068

Henson, J. H., Yeterian, M., Weeks, R. M., Medrano, A. E., Brown, B. L., Geist, H. L., Pais, M. D., Oldenbourg, R., & Shuster, C. B. (2015). Arp2/3 complex inhibition radically alters lamellipodial actin architecture, suspended cell shape, and the cell spreading process. *Molecular Biology of the Cell*, *26*(5), 887. https://doi.org/10.1091/MBC.E14-07-1244

Herbomel, G., Hatte, G., Roul, J., Padilla-Parra, S., Tassan, J.-P., & Tramier, M. (2017). Actomyosin-generated tension on cadherin is similar between dividing and non-dividing epithelial cells in early Xenopus laevis embryos. *Scientific Reports*, *7*(February), 45058. https://doi.org/10.1038/srep45058

Heyn, P., Kircher, M., Dahl, A., Kelso, J., Tomancak, P., Kalinka, A. T., & Neugebauer, K. M. (2014). The Earliest Transcribed Zygotic Genes Are Short, Newly Evolved, and Different across Species. *Cell Reports*, *6*(2), 285–292. https://doi.org/10.1016/J.CELREP.2013.12.030

Higgs, H. N. (2000). The harder the better: effects of substrate rigidity on cell motility. *Trends in Biochemical Sciences*, *25*(9), 427. https://doi.org/10.1016/S0968-0004(00)01653-4

Hino, N., Rossetti, L., Marín-Llauradó, A., Aoki, K., Trepat, X., Matsuda, M., & Hirashima, T. (2020). ERK-Mediated Mechanochemical Waves Direct Collective Cell Polarization. *Developmental Cell*, *53*(6), 646-660.e8. https://doi.org/10.1016/j.devcel.2020.05.011

Hirata, H., Dobrokhotov, O., & Sokabe, M. (2020). Coordination between Cell Motility and Cell Cycle Progression in Keratinocyte Sheets via Cell-Cell Adhesion and Rac1. *IScience*, *23*(11), 101729. https://doi.org/10.1016/J.ISCI.2020.101729

Hisaoka, K. K., & Battle, H. I. (1958). The normal developmental stages of the zebrafish, brachydanio rerio (hamilton-buchanan). *Journal of Morphology*, *102*(2), 311–327. https://doi.org/10.1002/jmor.1051020205

Hoffman, B. D., & Yap, A. S. (2015). Towards a Dynamic Understanding of Cadherin-Based Mechanobiology. *Trends in Cell Biology*, *25*(12), 803–814. https://doi.org/10.1016/j.tcb.2015.09.008

Honda, S., Sasaki, Y., Ohsawa, K., Imai, Y., Nakamura, Y., Inoue, K., & Kohsaka, S. (2001). Extracellular ATP or ADP Induce Chemotaxis of Cultured Microglia through Gi/o-Coupled P2Y Receptors. *Journal of Neuroscience*, *21*(6), 1975–1982. https://doi.org/10.1523/JNEUROSCI.21-06-01975.2001

Houdusse, A., & Sweeney, H. L. (2016). How Myosin Generates Force on Actin Filaments The Product-Release Steps on

Actin. *Trends in Biochemical Sciences*, *41*(12). https://doi.org/10.1016/j.tibs.2016.09.006

Huang, Y., & Winklbauer, R. (2018). Cell migration in the Xenopus gastrula. *Wiley Interdisciplinary Reviews: Developmental Biology*, *7*(6), e325. https://doi.org/10.1002/WDEV.325

Huber, A. H., Stewart, D. B., Laurents, D. V., Nelson, W. J., & Weis, W. I. (2001). The Cadherin Cytoplasmic Domain Is Unstructured in the Absence of β-Catenin: A POSSIBLE MECHANISM FOR REGULATING CADHERIN TURNOVER *. *Journal of Biological Chemistry*, *276*(15), 12301–12309. https://doi.org/10.1074/JBC.M010377200

Hulpiau, P., & van Roy, F. (2009). Molecular evolution of the cadherin superfamily. *The International Journal of Biochemistry & Cell Biology*, *41*(2), 349–369. https://doi.org/10.1016/j.biocel.2008.09.027

Huttenlocher, A., & Horwitz, A. R. (2011). Integrins in Cell Migration. *Cold Spring Harbor Perspectives in Biology*, *3*(9), a005074. https://doi.org/10.1101/CSHPERSPECT.A005074

Huveneers, S., Oldenburg, J., Spanjaard, E., van der Krogt, G., Grigoriev, I., Akhmanova, A., Rehmann, H., & de Rooij, J. (2012). Vinculin associates with endothelial VE-cadherin junctions to control force-dependent remodeling. *The Journal of Cell Biology*, *196*(5), 641–652. https://doi.org/10.1083/jcb.201108120

Inaki, M., Vishnu, S., Cliffe, A., & Rorth, P. (2012). Effective guidance of collective migration based on differences in cell states. *Proceedings of the National Academy of Sciences*, *109*(6), 2027–2032. https://doi.org/10.1073/pnas.1115260109

Inohaya, K., Yasumasu, S., Ishimaru, M., Ohyama, A., Iuchi, I., & Yamagami, K. (1995). Temporal and spatial patterns of gene expression for the hatching enzyme in the teleost embryo, Oryzias latipes. In *Developmental Biology* (Vol. 171, Issue 2, pp. 374–385). https://doi.org/10.1006/dbio.1995.1289

Isenberg, B. C., DiMilla, P. A., Walker, M., Kim, S., & Wong, J. Y. (2009). Vascular Smooth Muscle Cell Durotaxis Depends on Substrate Stiffness Gradient Strength. *Biophysical Journal*, *97*(5), 1313–1322. https://doi.org/10.1016/J.BPJ.2009.06.021

Isomursu, A., Park, K.-Y., Hou, J., Cheng, B., Shamsan, G., Fuller, B., Kasim, J., Mahmoodi, M. M., Lu, T. J., Genin, G. M., Xu, F., Lin, M., Distefano, M., Ivaska, J., & Odde, D. J. (2020). Negative durotaxis: cell movement toward softer environments. *BioRxiv*, 2020.10.27.357178. https://doi.org/10.1101/2020.10.27.357178

Itoh, K., Jacob, J., & Y. Sokol, S. (1998). A role for Xenopus Frizzled 8 in dorsal development. *Mechanisms of Development*, *74*(1–2), 145–157. https://doi.org/10.1016/S0925-4773(98)00076-8

Jaffe, A. B., & Hall, A. (2005). *Rho GTPases: Biochemistry and Biology*. https://doi.org/10.1146/annurev.cellbio.21.020604.150721

Jia, L., Cheng, L., & Raper, J. (2005). Slit/Robo signaling is necessary to confine early neural crest cells to the ventral migratory pathway in the trunk. *Developmental Biology*, *282*(2), 411–421. https://doi.org/10.1016/j.ydbio.2005.03.021

Johansson, M., Giger, F. A., Fielding, T., Houart, C., Johansson, M., Giger, F. A., Fielding, T., & Houart, C. (2019). Dkk1 Controls Cell-Cell Interaction through Regulation of Non-nuclear b -Catenin Pools. *Developmental Cell*, 1–12. https://doi.org/10.1016/j.devcel.2019.10.026

K Burridge, M. C.-W. (1996). Focal adhesions, contractility, and signaling. *Annu. Rev. Cell Dev. Biol.* , *12*, 463–518. https://doi.org/10.1146/annurev.cellbio.12.1.463

Kai, M., Heisenberg, C.-P., & Tada, M. (2008). Sphingosine-1-phosphate receptors regulate individual cell behaviours underlying the directed migration of prechordal plate progenitor cells during zebrafish gastrulation. *Development*,

135(18), 3043–3051. https://doi.org/10.1242/dev.020396

Kale, G. R., Yang, X., Philippe, J., Mani, M., Lenne, P., & Lecuit, T. (2018). Distinct contributions of tensile and shear stress on E-cadherin levels during morphogenesis. *Nature Communications*, *9*(5021). https://doi.org/10.1038/s41467-018-07448-8

Kane, D., & Adams, R. (2002). Life at the Edge: Epiboly and Involution in the Zebrafish. In *Results and problems in cell differentiation* (Vol. 40, pp. 117–135). Results Probl Cell Differ. https://doi.org/10.1007/978-3-540-46041-1_7

Kane, D.A., Hammerschmidt, M., Mullins, M. C., Maischein, H. M., Brand, M., van Eeden, F. J., Furutani-Seiki, M., Granato, M., Haffter, P., Heisenberg, C. P., Jiang, Y. J., Kelsh, R. N., Odenthal, J., Warga, R. M., & Nusslein-Volhard, C. (1996). The zebrafish epiboly mutants. *Development*, *123*(1), 47–55. https://doi.org/10.1242/dev.123.1.47

Kane, D.A., & Kimmel, C. B. (1993). The zebrafish midblastula transition. *Development*, *119*(2), 447–456. https://doi.org/10.1242/DEV.119.2.447

Kane, Donald A., McFarland, K. N., & Warga, R. M. (2005). Mutations in half baked /E-cadherin block cell behaviors that are necessary for teleost epiboly. *Development*, *132*(5), 1105–1116. https://doi.org/10.1242/dev.01668

Kehrl, J. H. (2006). Chemoattractant Receptor Signaling and the Control of Lymphocyte Migration. *Immunologic Research*, *34*(3), 211–228. https://doi.org/10.1385/IR:34:3:211

Keller, R., Davidson, L., Edlund, A., Elul, T., Ezin, M., Shook, D., & Skoglund, P. (2000). Mechanisms of convergence and extension by cell intercalation. *Philosophical Transactions of the Royal Society B: Biological Sciences*, *355*(1399), 897–922. https://doi.org/10.1098/rstb.2000.0626

Keller, Ray, & Tibbetts, P. (1989). Mediolateral cell intercalation in the dorsal, axial mesoderm of Xenopus laevis. *Developmental Biology*, *131*(2), 539–549. https://doi.org/10.1016/S0012-1606(89)80024-7

Képiró, M., Várkuti, B. H., Bodor, A., Hegyi, G., Drahos, L., Kovács, M., & Málnási-Csizmadia, A. (2012). Azidoblebbistatin, a photoreactive myosin inhibitor. *Proceedings of the National Academy of Sciences*, *109*(24), 9402–9407. https://doi.org/10.1073/PNAS.1202786109

Khalil, A. A., & de Rooij, J. (2019). Cadherin mechanotransduction in leader-follower cell specification during collective migration. *Experimental Cell Research*, *376*(1), 86–91. https://doi.org/10.1016/j.yexcr.2019.01.006

Kilian, B., Mansukoski, H., Barbosa, F. C., Ulrich, F., Tada, M., & Heisenberg, C. P. (2003). The role of Ppt/Wnt5 in regulating cell shape and movement during zebrafish gastrulation. *Mechanisms of Development*, *120*(4), 467–476. https://doi.org/10.1016/S0925-4773(03)00004-2

Kim, S. A., Tai, C.-Y., Mok, L.-P., Mosser, E. A., & Schuman, E. M. (2011). Calcium-dependent dynamics of cadherin interactions at cell–cell junctions. *Proceedings of the National Academy of Sciences*, *108*(24), 9857–9862. https://doi.org/10.1073/PNAS.1019003108

Kim, S., Park, H., Yeo, S., Hong, S., & Choi, J. (1998). *Characterization of two frizzled 8 homologues expressed in the embryonic shield and prechordal plate of zebrafish embryos 1*. *78*, 193–198.

Kimelman, D., & Kirschner, M. (1987). Synergistic induction of mesoderm by FGF and TGF-β and the identification of an mRNA coding for FGF in the early xenopus embryo. *Cell*, *51*(5), 869–877. https://doi.org/10.1016/0092-8674(87)90110-3

Kimmel, C.B., Ballard, W. W., Kimmel, S. R., Ullmann, B., & Schilling, T. F. (1995). Stages of embryonic development of

the zebrafish. *Dev.Dynam.*, *203*, 253–310. https://doi.org/10.1002/aja.1002030302

Kimmel, C.B., Warga, R. M., & Schilling, T. F. (1990). Origin and organization of the zebrafish fate map. *Development*, *108*(4), 581–594. https://doi.org/10.1242/DEV.108.4.581

Kimmel, Charles B., & Law, R. D. (1985). Cell lineage of zebrafish blastomeres I. *Developmental Biology*, *108*(1), 78–85. https://doi.org/10.1016/0012-1606(85)90010-7

Klinger, E., Rickert, D., & Hasenauer, J. (2018). pyABC: distributed, likelihood-free inference. *Bioinformatics (Oxford, England)*, *34*(20), 3591–3593. https://doi.org/10.1093/bioinformatics/bty361

Knutsdottir, H., Zmurchok, C., Bhaskar, D., Palsson, E., Dalle Nogare, D., Chitnis, A. B., & Edelstein-Keshet, L. (2017). Polarization and migration in the zebrafish posterior lateral line system. *PLoS Computational Biology*, *13*(4), 1–26. https://doi.org/10.1371/journal.pcbi.1005451

Kobielak, A., Pasolli, H. A., & Fuchs, E. (2004). Mammalian formin-1 participates in adherens junctions and polymerization of linear actin cables. *Nature Cell Biology*, *6*(1), 21–30. https://doi.org/10.1038/ncb1075

Kojima, D., & Fukada, Y. (2007). Non-Visual Photoreception by a Variety of Vertebrate Opsins. In *Novartis Foundation symposium* (Vol. 224, pp. 265–290). Novartis Found Symp. https://doi.org/10.1002/9780470515693.ch15

Kok, F. O., Shin, M., Ni, C.-W., Gupta, A., Grosse, A. S., van Impel, A., Kirchmaier, B. C., Peterson-Maduro, J., Kourkoulis, G., Male, I., DeSantis, D. F., Sheppard-Tindell, S., Ebarasi, L., Betsholtz, C., Schulte-Merker, S., Wolfe, S. A., & Lawson, N. D. (2015). Reverse Genetic Screening Reveals Poor Correlation between Morpholino-Induced and Mutant Phenotypes in Zebrafish. *Developmental Cell*, *32*(1), 97–108. https://doi.org/10.1016/j.devcel.2014.11.018

Kölsch, V., Charest, P. G., & Firtel, R. A. (2008). The regulation of cell motility and chemotaxis by phospholipid signaling. *Journal of Cell Science*, *121*(5), 551–559. https://doi.org/10.1242/JCS.023333

Komiya, Y., & Habas, R. (2008). Wnt signal transduction pathways. *Organogenesis*, *4*(2), 68–75. https://doi.org/10.4161/org.4.2.5851

Köppen, M., Fernández, B. G., Carvalho, L., Jacinto, A., & Heisenberg, C.-P. (2006). Coordinated cell-shape changes control epithelial movement in zebrafish and Drosophila. *Development*, *133*(14), 2671–2681. https://doi.org/10.1242/DEV.02439

Korn, E., Carlier, M., & Pantaloni, D. (1987). Actin polymerization and ATP hydrolysis. *Science*, *238*(4827), 638–644. https://doi.org/10.1126/science.3672117

Korohoda, W., Drukala, J., Sroka, J., & Madeja, Z. (1997). Isolation, spreading, locomotion on various substrata, and the effect of hypotonicity on locomotion of fish keratinocytes. *Biochemistry and Cell Biology*, *75*(3), 277–286. https://doi.org/10.1139/o97-048

Kovacs, E. M., Ali, R. G., McCormack, A. J., & Yap, A. S. (2002). E-cadherin Homophilic Ligation Directly Signals through Rac and Phosphatidylinositol 3-Kinase to Regulate Adhesive Contacts. *Journal of Biological Chemistry*, *277*(8), 6708–6718. https://doi.org/10.1074/jbc.M109640200

Krause, M., & Gautreau, A. (2014). Steering cell migration: lamellipodium dynamics and the regulation of directional persistence. *Nature Reviews Molecular Cell Biology 2014 15:9*, *15*(9), 577–590. https://doi.org/10.1038/nrm3861

Krens, S. F. G., Veldhuis, J. H., Barone, V., Čapek, D., Maître, J. L., Brodland, G. W., & Heisenberg, C. P. (2017). Interstitial fluid osmolarity modulates the action of differential tissue surface tension in progenitor cell segregation during

gastrulation. *Development (Cambridge)*, *144*(10), 1798–1806. https://doi.org/10.1242/dev.144964

Krishnan, K., & Moens, P. D. J. (2009). Structure and functions of profilins. *Biophysical Reviews*, *1*(2), 71. https://doi.org/10.1007/S12551-009-0010-Y

Kroll, F., Powell, G. T., Ghosh, M., Gestri, G., Antinucci, P., Hearn, T. J., Tunbak, H., Lim, S., Dennis, H. W., Fernandez, J. M., Whitmore, D., Dreosti, E., Wilson, S. W., Hoffman, E. J., & Rihel, J. (2021). A simple and effective F0 knockout method for rapid screening of behaviour and other complex phenotypes. *ELife*, *10*, 1–34. https://doi.org/10.7554/eLife.59683

Kwiatkowski, A. V, Maiden, S. L., Pokutta, S., Choi, H.-J., Benjamin, J. M., Lynch, A. M., Nelson, W. J., Weis, W. I., & Hardin, J. (2010). In vitro and in vivo reconstitution of the cadherin-catenin-actin complex from Caenorhabditis elegans. *Proceedings of the National Academy of Sciences of the United States of America*, *107*(33), 14591–14596. https://doi.org/10.1073/pnas.1007349107

Ladoux, B., Nelson, W. J., Yan, J., & Mège, R. M. M. (2015). The mechanotransduction machinery at work at adherens junctions. *Integrative Biology*, *7*(10), 1109–1119. https://doi.org/10.1039/c5ib00070j

Laevsky, G., & Knecht, D. a. (2003). Cross-linking of actin filaments by myosin II is a major contributor to cortical integrity and cell motility in restrictive environments. *Journal of Cell Science*, *116*(18), 3761–3770. https://doi.org/10.1242/jcs.00684

Lagendijk, A. K., Gomez, G. A., Baek, S., Hesselson, D., Hughes, W. E., Paterson, S., Conway, D. E., Belting, H. G., Affolter, M., Smith, K. A., Schwartz, M. A., Yap, A. S., & Hogan, B. M. (2017). Live imaging molecular changes in junctional tension upon VE-cadherin in zebrafish. *Nature Communications*, *8*(1). https://doi.org/10.1038/s41467-017-01325-6

Lane, M. C., & Sheets, M. D. (2006). Heading in a new direction: Implications of the revised fate map for understanding Xenopus laevis development. *Developmental Biology*, *296*(1), 12–28. https://doi.org/10.1016/j.ydbio.2006.04.447

Latimer, A., & Jessen, J. R. (2010). Extracellular matrix assembly and organization during zebrafish gastrulation. *Matrix Biology*, *29*(2), 89–96. https://doi.org/10.1016/J.MATBIO.2009.10.002

Le Douarin, N. M., & Teillet, M.-A. (1973). The migration of neural crest cells to the wall of the digestive tract in avian embryo. *Development*, *30*(1), 31–48. https://doi.org/10.1242/DEV.30.1.31

Lecaudey, V., Cakan-Akdogan, G., Norton, W. H. J., & Gilmour, D. (2008). Dynamic Fgf signaling couples morphogenesis and migration in the zebrafish lateral line primordium. *Development*, *135*(16), 2695–2705. https://doi.org/10.1242/dev.025981

Leckband, D., & Prakasam, A. (2006). MECHANISM AND DYNAMICS OF CADHERIN ADHESION. *Http://Dx.Doi.Org/10.1146/Annurev.Bioeng.8.061505.095753*, *8*, 259–287. https://doi.org/10.1146/ANNUREV.BIOENG.8.061505.095753

Lee, Y. (2005). Fgf signaling instructs position-dependent growth rate during zebrafish fin regeneration. *Development*, *132*(23), 5173–5183. https://doi.org/10.1242/dev.02101

Lemmon, M. A., & Schlessinger, J. (2010). Leading Edge Cell Signaling by Receptor Tyrosine Kinases. *Cell*, *141*. https://doi.org/10.1016/j.cell.2010.06.011

Leng, J., Klemke, R. L., Reddy, A. C., & Cheresh, D. A. (1999). Potentiation of cell migration by adhesion-dependent cooperative signals from the GTPase Rac and Raf kinase. *Journal of Biological Chemistry*, *274*(53), 37855–37861. https://doi.org/10.1074/jbc.274.53.37855

Lenne, P.-F., Rupprecht, J.-F., & Viasnoff, V. (2021). Perspective Cell Junction Mechanics beyond the Bounds of Adhesion and Tension. *Developmental Cell*, *56*, 1–11. https://doi.org/10.1016/j.devcel.2020.12.018

Lentz, T. L., & Trinkaus, J. P. (1967). A FINE STRUCTURAL STUDY OF CYTODIFFERENTIATION DURING CLEAVAGE, BLASTULA, AND GASTRULA STAGES OF FUNDULUS HETEROCLITUS. *Journal of Cell Biology*, *32*(1), 121–138. https://doi.org/10.1083/jcb.32.1.121

Lepage, S. E., & Bruce, A. E. E. (2010). Zebrafish epiboly: Mechanics and mechanisms. *International Journal of Developmental Biology*, *54*(8–9), 1213–1228. https://doi.org/10.1387/IJDB.093028SL

Li, D., & Wang, Y. (2018). Coordination of cell migration mediated by site-dependent cell–cell contact. *Proceedings of the National Academy of Sciences*, 201807543. https://doi.org/10.1073/pnas.1807543115

Libotte, T., Kaiser, H.-W., Alt, W., & Bretschneider, T. (2001). Polarity, Protrusion–Retraction Dynamics and Their Interplay during Keratinocyte Cell Migration. *Experimental Cell Research*, *270*(2), 129–137. https://doi.org/10.1006/excr.2001.5339

Liu, L., Korzh, V., Balasubramaniyan, N. V, Ekker, M., & Ge, R. (2002). Platelet-derived growth factor A (pdgf-a) expression during zebrafish embryonic development. *Dev Genes Evol*, *212*(6), 298–301. https://doi.org/10.1007/s00427-002-0234-3

Liu, Y.-J., Le Berre, M., Lautenschlaeger, F., Maiuri, P., Callan-Jones, A., Heuzé, M., Takaki, T., Voituriez, R., & Piel, M. (2015). Confinement and Low Adhesion Induce Fast Amoeboid Migration of Slow Mesenchymal Cells. *Cell*, *160*(4), 659–672. https://doi.org/10.1016/J.CELL.2015.01.007

Lo, C.-M., Wang, H.-B., Dembo, M., & Wang, Y. (2000). Cell Movement Is Guided by the Rigidity of the Substrate. *Biophysical Journal*, *79*(1), 144–152. https://doi.org/10.1016/S0006-3495(00)76279-5

Lock, R., & Debnath, J. (2008). Extracellular matrix regulation of autophagy. *Current Opinion in Cell Biology*, *20*(5), 583–588. https://doi.org/10.1016/j.ceb.2008.05.002

Longley, R. L., Woods, A., Fleetwood, A., Cowling, G. J., Gallagher, J. T., & Couchman, J. R. (1999). Control of morphology, cytoskeleton and migration by syndecan-4. *Journal of Cell Science*, *112*(20), 3421–3431. https://doi.org/10.1242/jcs.112.20.3421

López-Schier, H. (2010). Fly fishing for collective cell migration. *Current Opinion in Genetics and Development*, *20*(4), 428–432. https://doi.org/10.1016/j.gde.2010.04.006

Luxenburg, C., & Zaidel-Bar, R. (2019). From cell shape to cell fate via the cytoskeleton — Insights from the epidermis. *Experimental Cell Research*, *378*(2), 232–237. https://doi.org/10.1016/j.yexcr.2019.03.016

Lv, H., Li, L., Sun, M., Zhang, Y., Chen, L., Rong, Y., & Li, Y. (2015). Mechanism of regulation of stem cell differentiation by matrix stiffness. *Stem Cell Research & Therapy*, *6*(1). https://doi.org/10.1186/S13287-015-0083-4

Maître, J.-L., Berthoumieux, H., Krens, S. F. G., Salbreux, G., Jülicher, F., Paluch, E. K., & Heisenberg, C.-P. (2012). Adhesion Functions in Cell Sorting by Mechanically Coupling the Cortices of Adhering Cells. *Science*, *10*(4), 429–436. https://doi.org/10.1126/science.1225399

Malet-Engra, G., Yu, W., Oldani, A., Rey-Barroso, J., Gov, N. S., Scita, G., & Dupré, L. (2015). Collective Cell Motility Promotes Chemotactic Prowess and Resistance to Chemorepulsion. *Current Biology*, *25*(2), 242–250. https://doi.org/10.1016/j.cub.2014.11.030

Martin Pring, ‡, Marie Evangelista, §, Charles Boone, §,∥, Changsong Yang, ⊥ and, & Sally H. Zigmond*, ⊥. (2002). Mechanism of Formin-Induced Nucleation of Actin Filaments. *Biochemistry*, *42*(2), 486–496. https://doi.org/10.1021/BI026520J

Martin, E. D., Moriarty, M. A., Byrnes, L., & Grealy, M. (2009). Plakoglobin has both structural and signalling roles in zebrafish development. *Developmental Biology*, *327*(1), 83–96. https://doi.org/10.1016/j.ydbio.2008.11.036

Martino, F., Perestrelo, A. R., Vinarský, V., Pagliari, S., & Forte, G. (2018). Cellular Mechanotransduction: From Tension to Function. *Frontiers in Physiology*, *0*(JUL), 824. https://doi.org/10.3389/FPHYS.2018.00824

Mastrogiovanni, M., Juzans, M., Alcover, A., & Di Bartolo, V. (2020). Coordinating Cytoskeleton and Molecular Traffic in T Cell Migration, Activation, and Effector Functions. *Frontiers in Cell and Developmental Biology*, *8*, 1138. https://doi.org/10.3389/fcell.2020.591348

Mathieu, J., Griffin, K., Herbomel, P., Dickmeis, T., Strähle, U., Kimelman, D., Rosa, F. M., & Peyriéras, N. (2004). Nodal and Fgf pathways interact through a positive regulatory loop and synergize to maintain mesodermal cell populations. *Development*, *131*(3), 629–641. https://doi.org/10.1242/DEV.00964

Mattes, B., & Scholpp, S. (2018). Emerging role of contact-mediated cell communication in tissue development and diseases. *Histochemistry and Cell Biology*, *150*(5), 431. https://doi.org/10.1007/S00418-018-1732-3

Matthews, H. K., Marchant, L., Carmona-Fontaine, C., Kuriyama, S., Larrain, J., Holt, M. R., Parsons, M., & Mayor, R. (2008). Directional migration of neural crest cells in vivo is regulated by Syndecan-4/Rac1 and non-canonical Wnt signaling/RhoA. *Development*, *135*(10), 1771–1780. https://doi.org/10.1242/dev.017350

Mattila, P. K., & Lappalainen, P. (2008). Filopodia: molecular architecture and cellular functions. *Nature Reviews Molecular Cell Biology*, *9*(6), 446–454. https://doi.org/10.1038/nrm2406

Mayor, R., & Theveneau, E. (2013a). The neural crest. *Development*, *140*(11), 2247–2251. https://doi.org/10.1242/dev.091751

Mayor, R., & Theveneau, E. (2013b). The neural crest. *Development*, *140*(11), 2247–2251. https://doi.org/10.1242/DEV.091751

McDonald, J. A., Pinheiro, E. M., Kadlec, L., Schupbach, T., & Montell, D. J. (2006). Multiple EGFR ligands participate in guiding migrating border cells. *Developmental Biology*, *296*(1), 94–103. https://doi.org/10.1016/J.YDBIO.2006.04.438

McDonald, J. A., Pinheiro, E. M., & Montell, D. J. (2003). PVF1, a PDGF/VEGF homolog, is sufficient to guide border cells and interacts genetically with Taiman. *Development*, *130*(15), 3469–3478. https://doi.org/10.1242/dev.00574

McFarland, K. N., Warga, R. M., & Kane, D. A. (2005). Genetic locus half baked is necessary for morphogenesis of the ectoderm. *Developmental Dynamics*, *233*(2), 390–406. https://doi.org/10.1002/dvdy.20325

Mckendry, R., Harland, R. M., & Stachel, S. E. (1998). *Activin-Induced Factors Maintain goosecoid Transcription through a Paired Homeodomain Binding Site*.

McLaren, S. B. P., & Steventon, B. J. (2021). Anterior expansion and posterior addition to the notochord mechanically coordinate embryo axis elongation. *Development*. https://doi.org/10.1242/dev.199459

McMillen, P., & Holley, S. A. (2015). The tissue mechanics of vertebrate body elongation and segmentation. *Current Opinion in Genetics and Development*, *32*, 106–111. https://doi.org/10.1016/j.gde.2015.02.005

Mège, R. M., & Ishiyama, N. (2017). Integration of Cadherin Adhesion and Cytoskeleton at Adherens Junctions. *Cold Spring Harbor Perspectives in Biology*, *9*(5), a028738. https://doi.org/10.1101/cshperspect.a028738

Mejillano, M. R., Kojima, S. I., Applewhite, D. A., Gertler, F. B., Svitkina, T. M., & Borisy, G. G. (2004). Lamellipodial versus filopodial mode of the actin nanomachinery: Pivotal role of the filament barbed end. *Cell*, *118*(3), 363–373. https://doi.org/10.1016/j.cell.2004.07.019

Meng, W., Mushika, Y., Ichii, T., & Takeichi, M. (2008). Anchorage of Microtubule Minus Ends to Adherens Junctions Regulates Epithelial Cell-Cell Contacts. *Cell*, *135*(5), 948–959. https://doi.org/10.1016/J.CELL.2008.09.040

Meng, W., & Takeichi, M. (2009). Adherens Junction: Molecular Architecture and Regulation. *Cold Spring Harbor Perspectives in Biology*, *1*(6). https://doi.org/10.1101/CSHPERSPECT.A002899

Merkel, C. D., Li, Y., Raza, Q., Stolz, D. B., & Kwiatkowski, A. V. (2019). Vinculin anchors contractile actin to the cardiomyocyte adherens junction. *Molecular Biology of the Cell*, *30*(21), 2639. https://doi.org/10.1091/MBC.E19-04-0216

Mirams, G. R., Arthurs, C. J., Bernabeu, M. O., Bordas, R., Cooper, J., Corrias, A., Davit, Y., Dunn, S.-J., Fletcher, A. G., Harvey, D. G., Marsh, M. E., Osborne, J. M., Pathmanathan, P., Pitt-Francis, J., Southern, J., Zemzemi, N., & Gavaghan, D. J. (2013). Chaste: an open source C++ library for computational physiology and biology. *PLoS Computational Biology*, *9*(3), e1002970. https://doi.org/10.1371/journal.pcbi.1002970

Mitra, R., Jadhav, S., McEwen, B. S., Vyas, A., & Chattarji, S. (2005). Stress duration modulates the spatiotemporal patterns of spine formation in the basolateral amygdala. *Proceedings of the National Academy of Sciences*, *102*(26), 9371–9376. https://doi.org/10.1073/pnas.0504011102

Mitra, S. K., Hanson, D. A., & Schlaepfer, D. D. (2005). Focal adhesion kinase: In command and control of cell motility. *Nature Reviews Molecular Cell Biology*, *6*(1), 56–68. https://doi.org/10.1038/nrm1549

Mizoguchi, T., Verkade, H., Heath, J. K., Kuroiwa, A., & Kikuchi, Y. (2008). Sdf1/Cxcr4 signaling controls the dorsal migration of endodermal cells during zebrafish gastrulation. *Development*, *135*(15), 2521–2529. https://doi.org/10.1242/dev.020107

Mogilner, A., & Keren, K. (2009). The Shape of Motile Cells. *Current Biology : CB*, *19*(17), R762. https://doi.org/10.1016/J.CUB.2009.06.053

Molinie, N., Rubtsova, S. N., Fokin, A., Visweshwaran, S. P., Rocques, N., Polesskaya, A., Schnitzler, A., Vacher, S., Denisov, E. V., Tashireva, L. A., Perelmuter, V. M., Cherdyntseva, N. V., Bièche, I., & Gautreau, A. M. (2019). Cortical branched actin determines cell cycle progression. *Cell Research*, *29*(6), 432–445. https://doi.org/10.1038/s41422-019-0160-9

Mongera, A., Rowghanian, P., Gustafson, H. J., Shelton, E., Kealhofer, D. A., Carn, E. K., Serwane, F., Lucio, A. A., Giammona, J., & Campàs, O. (2018). A fluid-to-solid jamming transition underlies vertebrate body axis elongation. *Nature*, *561*(7723), 401–405. https://doi.org/10.1038/s41586-018-0479-2

Montague, T. G., & Schier, A. F. (2017). Vg1-nodal heterodimers are the endogenous inducers of mesendoderm. *ELife*, *6*. https://doi.org/10.7554/ELIFE.28183

Montero, J.-A., Carvalho, L., Wilsch-Bräuninger, M., Kilian, B., Mustafa, C., & Heisenberg, C.-P. (2005). Shield formation at the onset of zebrafish gastrulation. *Development (Cambridge, England)*, *132*(6), 1187–1198. https://doi.org/10.1242/dev.01667

Montero, J.-A., Kilian, B., Chan, J., Bayliss, P. E., & Heisenberg, C.-P. (2003). Phosphoinositide 3-Kinase Is Required for Process Outgrowth and Cell Polarization of Gastrulating Mesendodermal Cells. *Current Biology*, *13*, 1279–1289. https://doi.org/10.1016/S

Morimura, S., Suzuki, K., & Takahashi, K. (2011). Nonmuscle myosin IIA is required for lamellipodia formation through binding to WAVE2 and phosphatidylinositol 3,4,5-triphosphate. *Biochemical and Biophysical Research Communications*, *404*(3), 834–840. https://doi.org/10.1016/j.bbrc.2010.12.069

Morita, H., Grigolon, S., Bock, M., Krens, S. F. G., Salbreux, G., & Heisenberg, C. P. (2017). The Physical Basis of Coordinated Tissue Spreading in Zebrafish Gastrulation. *Developmental Cell*, *40*(4), 354-366.e4. https://doi.org/10.1016/j.devcel.2017.01.010

Mui, K. L., Chen, C. S., & Assoian, R. K. (2016). The mechanical regulation of integrin–cadherin crosstalk organizes cells, signaling and forces. *Journal of Cell Science*, *129*(6), 1093. https://doi.org/10.1242/JCS.183699

Muraina, I. A., Maret, W., Bury, N. R., & Hogstrand, C. (2020). Hatching gland development and hatching in zebrafish embryos: A role for zinc and its transporters Zip10 and Znt1a. *Biochemical and Biophysical Research Communications*, *528*(4), 698–705. https://doi.org/10.1016/j.bbrc.2020.05.131

Murillo-Garzón, V., Gorroño-Etxebarria, I., Åkerfelt, M., Puustinen, M. C., Sistonen, L., Nees, M., Carton, J., Waxman, J., & Kypta, R. M. (2018). Frizzled-8 integrates Wnt-11 and transforming growth factor-β signaling in prostate cancer. *Nature Communications 2018 9:1*, *9*(1), 1–16. https://doi.org/10.1038/s41467-018-04042-w

Myers, D. C., Sepich, D. S., & Solnica-Krezel, L. (2002). Convergence and extension in vertebrate gastrulae: Cell movements according to or in search of identity? *Trends in Genetics*, *18*(9), 447–455. https://doi.org/10.1016/S0168-9525(02)02725-7

Myrtek, D., & Idzko, M. (2007). Chemotactic activity of extracellular nucleotideson human immune cells. *Purinergic Signalling 2007 3:1*, *3*(1), 5–11. https://doi.org/10.1007/S11302-006-9032-0

Nagar, B., Overduin, M., Ikura, M., & Rini, J. (1996). Structural basis of calcium-induced E-cadherin rigidification and dimerization. *Nature*, *380*(6572), 360–364. https://doi.org/10.1038/380360a0

Nagaso, H., Suzuki, A., Tada, M., & Ueno, N. (1999). Dual specificity of activin type II receptor ActRIIb in dorso-ventral patterning during zebrafish embryogenesis. *Development, Growth & Differentiation*, *41*(2), 119–133. https://doi.org/10.1046/J.1440-169X.1999.00418.X

Nair, S., & Schilling, T. F. (2008). Chemokine Signaling Controls Endodermal Migration During Zebrafish Gastrulation. *Science*, *322*(5898), 89–92. https://doi.org/10.1126/science.1160038

Nair, Sreelaja, & Schilling, T. F. (2008). Chemokine Signaling Controls Endodermal Migration During Zebrafish Gastrulation. *Science*, *332*(October), 89–92. https://doi.org/10.1126/science.1160038

Nakatsuji, N., & Johnson, K. E. (1983). CONDITIONING OF A CULTURE SUBSTRATUM BY THE ECTODERMAL LAYER PROMOTES ATTACHMENT AND ORIENTED LOCOMOTION BY AMPHIBIAN GASTRULA MESODERMAL CELLS. *Cell Sci*, *59*, 43.

Nasevicius, a, Hyatt, T., Kim, H., Guttman, J., Walsh, E., Sumanas, S., Wang, Y., & Ekker, S. C. (1998). Evidence for a frizzled-mediated wnt pathway required for zebrafish dorsal mesoderm formation. *Development (Cambridge, England)*, *125*, 4283–4292. https://doi.org/10.1073/pnas.0702000104

Naumannen, P., Lappalainen, P., & Hotulainen, P. (2008). Mechanisms of actin stress fibre assembly. *Journal of Microscopy*, *231*(3), 446–454. https://doi.org/10.1111/j.1365-2818.2008.02057.x

Neelathi, U. M., Dalle Nogare, D., & Chitnis, A. B. (2018). Cxcl12a induces *snail1b* expression to initiate collective migration and sequential Fgf-dependent neuromast formation in the zebrafish posterior lateral line primordium. *Development*,

145(14), dev162453. https://doi.org/10.1242/dev.162453

Nelson, W. J. (2008). Regulation of cell–cell adhesion by the cadherin–catenin complex. *Biochemical Society Transactions*, *36*(Pt 2), 149. https://doi.org/10.1042/BST0360149

Nguyen, T., & Mège, R. M. (2016). N-Cadherin and Fibroblast Growth Factor Receptors crosstalk in the control of developmental and cancer cell migrations. *European Journal of Cell Biology*, *95*(11), 415–426. https://doi.org/10.1016/j.ejcb.2016.05.002

Niehrs, C., Keller, R., Cho, K. W. Y., & De Robertis, E. M. (1993). The homeobox gene goosecoid controls cell migration in Xenopus embryos. *Cell*, *72*(4), 491–503. https://doi.org/10.1016/0092-8674(93)90069-3

Nieset, J. E., Redfield, A. R., Jin, F., Knudsen, K. A., Johnson, K. R., & Wheelock, M. J. (1997). Characterization of the interactions of alpha-catenin with alpha-actinin and beta-catenin/plakoglobin. *Journal of Cell Science*, *110 (Pt 8*(8), 1013–1022.

Niewiadomska, P., Godt, D., & Tepass, U. (1999). DE-Cadherin Is Required for Intercellular Motility during Drosophila Oogenesis. *Journal of Cell Biology*, *144*(3), 533–547. https://doi.org/10.1083/jcb.144.3.533

Nobes, C. D., & Hall, A. (1995). Rho, Rac, and Cdc42 GTPases regulate the assembly of multimolecular focal complexes associated with actin stress fibers, lamellipodia, and filopodia. *Cell*, *81*(1), 53–62. https://doi.org/10.1016/0092-8674(95)90370-4

Nowotarski, S. H., & Peifer, M. (2014). Cell Biology: A Tense but Good Day for Actin at Cell-Cell Junctions. *Current Biology*, *24*, R688–R690. https://doi.org/10.1016/j.cub.2014.06.063

O'Neill, P. R., Castillo-Badillo, J. A., Meshik, X., Kalyanaraman, V., Melgarejo, K., & Gautam, N. (2018). Membrane Flow Drives an Adhesion-Independent Amoeboid Cell Migration Mode. *Developmental Cell*, *46*(1), 9-22.e4. https://doi.org/10.1016/j.devcel.2018.05.029

Oda, H., Tagawa, K., & Akiyama-Oda, Y. (2005). Diversification of epithelial adherens junctions with independent reductive changes in cadherin form: identification of potential molecular synapomorphies among bilaterians. *Evolution & Development*, *7*(5), 376–389. https://doi.org/10.1111/J.1525-142X.2005.05043.X

Odenthal, J., Haffter, P., Vogelsang, E., Brand, M., Eeden, F. J. M. Van, Granato, M., Hammerschmidt, M., Heisenberg, C., Jiang, Y., Kane, D. A., Kelsh, R. N., Mullins, M. C., Warga, R. M., Allende, M. L., Weinberg, E. S., & Nüsslein-volhard, C. (1996). Mutations affecting the formation of the notochord in the zebrafish , Danio rerio. *Development*, *123*, 153–164. https://doi.org/10.1016/j.stem.2009.10.015

Ohashi, K., Fujiwara, S., & Mizuno, K. (2017). Roles of the cytoskeleton, cell adhesion and rho signalling in mechanosensing and mechanotransduction. *Journal of Biochemistry*, *161*(3), 245–254. https://doi.org/10.1093/jb/mvw082

Okimura, C., Taniguchi, A., Nonaka, S., & Iwadate, Y. (2018). Rotation of stress fibers as a single wheel in migrating fish keratocytes. *Scientific Reports 2018 8:1*, *8*(1), 1–10. https://doi.org/10.1038/s41598-018-28875-z

Okkenhaug, K., & Vanhaesebroeck, B. (2001). New responsibilities for the PI3K regulatory subunit p85 alpha. *Science's STKE : Signal Transduction Knowledge Environment*, *2001*(65), 1–6. https://doi.org/10.1126/stke.2001.65.pe1

Okkenhaug, Klaus. (2013). Signaling by the Phosphoinositide 3-Kinase Family in Immune Cells. *Http://Dx.Doi.Org/10.1146/Annurev-Immunol-032712-095946*, *31*, 675–704. https://doi.org/10.1146/ANNUREV-IMMUNOL-032712-095946

Olivier, N., Luengo-Oroz, M. A., Duloquin, L., Faure, E., Savy, T., Veilleux, I., Solinas, X., Debarre, D., Bourgine, P., Santos, A., Peyrieras, N., & Beaurepaire, E. (2010). Cell Lineage Reconstruction of Early Zebrafish Embryos Using Label-Free Nonlinear Microscopy. *Science*, *329*(5994), 967–971. https://doi.org/10.1126/science.1189428

Ory, S., Munari-Silem, Y., Fort, P., & Jurdic, P. (2000). Rho and Rac exert antagonistic functions on spreading of macrophage-derived multinucleated cells and are not required for actin fiber formation. *Journal of Cell Science*, *113*(7), 1177–1188. https://doi.org/10.1242/JCS.113.7.1177

Osborne, N. J., Begbie, J., Chilton, J. K., Schmidt, H., & Eickholt, B. J. (2005). Semaphorin/neuropilin signaling influences the positioning of migratory neural crest cells within the hindbrain region of the chick. *Developmental Dynamics*, *232*(4), 939–949. https://doi.org/10.1002/dvdy.20258

Ota, S., Tonou-Fujimori, N., Tonou-Fujimori, N., Nakayama, Y., Ito, Y., Kawamura, A., & Yamasu, K. (2010). FGF receptor gene expression and its regulation by FGF signaling during early zebrafish development. *Genesis*, *48*(12), 707–716. https://doi.org/10.1002/dvg.20682

Ota, S., Tonou-Fujimori, N., & Yamasu, K. (2009). The roles of the FGF signal in zebrafish embryos analyzed using constitutive activation and dominant-negative suppression of different FGF receptors. *Mechanisms of Development*, *126*(1–2), 1–17. https://doi.org/10.1016/j.mod.2008.10.008

Oteíza, P., Köppen, M., Concha, M. L., & Heisenberg, C.-P. (2008). Origin and shaping of the laterality organ in zebrafish. *Development*, *135*(16), 2807–2813. https://doi.org/10.1242/dev.022228

Pacquelet, A., & Rørth, P. (2005). Regulatory mechanisms required for DE-cadherin function in cell migration and other types of adhesion. *Journal of Cell Biology*, *170*(5), 803–812. https://doi.org/10.1083/jcb.200506131

Pajic-Lijakovic, I., & Milivojevic, M. (2020). Collective cell migration and residual stress accumulation: Rheological consideration. *Journal of Biomechanics*, *108*, 109898. https://doi.org/10.1016/j.jbiomech.2020.109898

Pancho, A., Aerts, T., Mitsogiannis, M. D., & Seuntjens, E. (2020). Protocadherins at the Crossroad of Signaling Pathways. *Frontiers in Molecular Neuroscience*, *0*, 117. https://doi.org/10.3389/FNMOL.2020.00117

Paraschiv, A., Lagny, T. J., Campos, C. V., Coudrier, E., Bassereau, P., & Šarić, A. (2021). Influence of membrane-cortex linkers on the extrusion of membrane tubes. *Biophysical Journal*, *120*(4), 598–606. https://doi.org/10.1016/J.BPJ.2020.12.028

Park, J. S., Chu, J. S., Tsou, A. D., Diop, R., Tang, Z., Wang, A., & Li, S. (2011). The Effect of Matrix Stiffness on the Differentiation of Mesenchymal Stem Cells in Response to TGF-β. *Biomaterials*, *32*(16), 3921. https://doi.org/10.1016/J.BIOMATERIALS.2011.02.019

Partridge, M., Vincent, A., Matthews, P., Puma, J., Stein, D., & Summerton, J. (1996). A Simple Method for Delivering Morpholino Antisense Oligos into the Cytoplasm of Cells. *ANTISENSE & NUCLEIC ACID DRUG DEVELOPMENT*, *6*, 169–175.

Pasakarnis, L., Frei, E., Caussinus, E., Affolter, M., & Brunner, D. (2016). Amnioserosa cell constriction but not epidermal actin cable tension autonomously drives dorsal closure. *Nature Cell Biology 2016 18:11*, *18*(11), 1161–1172. https://doi.org/10.1038/ncb3420

Patel, N. G., Nguyen, A., Xu, N., Ananthasekar, S., Alvarez, D. F., Stevens, T., & Tambe, D. T. (2020). Unleashing shear: Role of intercellular traction and cellular moments in collective cell migration. *Biochemical and Biophysical Research Communications*, *522*(2), 279–285. https://doi.org/10.1016/j.bbrc.2019.11.048

Patel, S., McKeon, D., Sao, K., Yang, C., Naranjo, N. M., Svitkina, T. M., & Petrie, R. J. (2021). Myosin II and Arp2/3 cross-talk governs intracellular hydraulic pressure and lamellipodia formation. *Https://Doi.Org/10.1091/Mbc.E20-04-0227*, *32*(7), 579–589. https://doi.org/10.1091/MBC.E20-04-0227

Pernier, J., Shekhar, S., Jegou, A., Guichard, B., & Carlier, M.-F. (2016). Profilin Interaction with Actin Filament Barbed End Controls Dynamic Instability, Capping, Branching, and Motility. *Developmental Cell*, *36*(2), 201. https://doi.org/10.1016/J.DEVCEL.2015.12.024

Petridou, N. I., Corominas-Murtra, B., Heisenberg, C. P., & Hannezo, E. (2021). Rigidity percolation uncovers a structural basis for embryonic tissue phase transitions. *Cell*, *184*(7), 1914-1928.e19. https://doi.org/10.1016/j.cell.2021.02.017

Peyrieras, N., Lu, Y., Renucci, A., Lemarchandel, V., & Rosa, F. (1996). Interactions suppressives controlant l'activite de l'organisateur chez le poisson. *Comptes Rendus de l'Academie Des Sciences - Serie III*, *319*(12), 1107–1112. https://europepmc.org/article/med/9091181

Peyriéras, N., Lu, Y., Renucci, A., Lemarchandel, V., & Rosa, F. M. (1996). Inhibitory interactions controlling organizer activity in fish. *C. R. Acad. Sc. Paris*, *319*, 1107–1112.

Peyriéras, N., Strähle, U., & Rosa, F. (1998a). Conversion of zebrafish blastomeres to an endodermal fate by TGF-β-related signalling. *Current Biology*, *8*(13), 783–788. https://doi.org/10.1016/s0960-9822(98)70303-3

Peyriéras, N., Strähle, U., & Rosa, F. (1998b). Conversion of zebrafish blastomeres to an endodermal fate by TGF-β-related signalling. *Current Biology*, *8*(13), 783–788. https://doi.org/10.1016/S0960-9822(98)70303-3

Pézeron, G., Mourrain, P., Courty, S., Ghislain, J., Becker, T. S., Rosa, F. M., & David, N. B. (2008). Live Analysis of Endodermal Layer Formation Identifies Random Walk as a Novel Gastrulation Movement. *Current Biology*, *18*(4), 276–281. https://doi.org/10.1016/j.cub.2008.01.028

Pickar-Oliver, A., & Gersbach, C. A. (2019). The next generation of CRISPR–Cas technologies and applications. *Nature Reviews Molecular Cell Biology*, *20*(8), 490–507. https://doi.org/10.1038/s41580-019-0131-5

Pierini, L. M., Lawson, M. A., Eddy, R. J., Hendey, B., & Maxfield, F. R. (2000). Oriented endocytic recycling of α5β1 in motile neutrophils. *Blood*, *95*(8), 2471–2481. https://doi.org/10.1182/BLOOD.V95.8.2471

Pinheiro, D., & Heisenberg, C. P. (2020). Zebrafish gastrulation: Putting fate in motion. *Current Topics in Developmental Biology*, *136*, 343–375. https://doi.org/10.1016/bs.ctdb.2019.10.009

Pitt-Francis, J., Pathmanathan, P., Bernabeu, M. O., Bordas, R., Cooper, J., Fletcher, A. G., Mirams, G. R., Murray, P., Osborne, J. M., Walter, A., Chapman, S. J., Garny, A., van Leeuwen, I. M. M., Maini, P. K., Rodríguez, B., Waters, S. L., Whiteley, J. P., Byrne, H. M., & Gavaghan, D. J. (2009). Chaste: A test-driven approach to software development for biological modelling. *Computer Physics Communications*, *180*(12), 2452–2471. https://doi.org/10.1016/j.cpc.2009.07.019

Plotnikov, S. V., Sabass, B., Schwarz, U. S., & Waterman, C. M. (2014). High-Resolution Traction Force Microscopy. *Methods in Cell Biology*, *123*, 367. https://doi.org/10.1016/B978-0-12-420138-5.00020-3

Pogoda, H. M., Solnica-Krezel, L., Driever, W., & Meyer, D. (2000). The zebrafish forkhead transcription factor FoxH1/Fast1 is a modulator of Nodal signaling required for organizer formation. *Current Biology*, *10*(17), 1041–1049. https://doi.org/10.1016/S0960-9822(00)00669-2

Pokutta, S., Drees, F., Takai, Y., Nelson, W. J., & Weis, W. I. (2002). Biochemical and structural definition of the l-afadin- and actin-binding sites of alpha-catenin. *The Journal of Biological Chemistry*, *277*(21), 18868–18874.

https://doi.org/10.1074/jbc.M201463200

Pokutta, S., & Weis, W. I. (2007). Structure and Mechanism of Cadherins and Catenins in Cell-Cell Contacts. *Annual Review of Cell and Developmental Biology*, *23*(1), 237–261. https://doi.org/10.1146/annurev.cellbio.22.010305.104241

Polesskaya, A., Boutillon, A., Wang, Y., Lavielle, M., Vacher, S., Schnitzler, A., Molinie, N., Fokin, A., Bièche, I., David, N. B., & Gautreau, A. M. (2020). CYFIP2 containing WAVE complexes inhibit cell migration. *BioRxiv*. https://doi.org/https://doi.org/10.1101/2020.07.02.184655

Pollard, T. D. (2007). Regulation of Actin Filament Assembly by Arp2/3 Complex and Formins. *Annual Review of Biophysics and Biomolecular Structure*, *36*(1), 451–477. https://doi.org/10.1146/annurev.biophys.35.040405.101936

Pollard, T. D., & Cooper, J. A. (2009). Actin, a central player in cell shape and movement. *Science*, *326*(5957), 1208–1212. https://doi.org/10.1126/science.1175862

Poujade, M., Grasland-Mongrain, E., Hertzog, A., Jouanneau, J., Chavrier, P., Ladoux, B., Buguin, A., & Silberzan, P. (2007). *Collective migration of an epithelial monolayer in response to a model wound*.

Poulain, M., Fürthauer, M., Thisse, B., Thisse, C., & Thierry Lepage. (2006). Zebrafish endoderm formation is regulated by combinatorial Nodal, FGF and BMP signalling. *Development*, *133*(11), 2189–2200. https://doi.org/10.1242/dev.02387

Prasad, M., & Montell, D. J. (2007). Cellular and Molecular Mechanisms of Border Cell Migration Analyzed Using Time-Lapse Live-Cell Imaging. *Developmental Cell*, *12*(6), 997–1005. https://doi.org/10.1016/j.devcel.2007.03.021

Priya, R., Allanki, S., Gentile, A., Mansingh, S., Uribe, V., Maischein, H.-M., & Stainier, D. Y. R. (2020). Tension heterogeneity directs form and fate to pattern the myocardial wall. *Nature 2020 588:7836*, *588*(7836), 130–134. https://doi.org/10.1038/s41586-020-2946-9

Puech, P. H., Taubenberger, A., Ulrich, F., Krieg, M., Muller, D. J., & Heisenberg, C. P. (2005). Measuring cell adhesion forces of primary gastrulating cells from zebrafish using atomic force microscopy. *Journal of Cell Science*, *118*(18), 4199–4206. https://doi.org/10.1242/jcs.02547

Quesada-Hernández, E., Caneparo, L., Schneider, S., Winkler, S., Liebling, M., Fraser, S. E., & Heisenberg, C. P. (2010). Stereotypical Cell Division Orientation Controls Neural Rod Midline Formation in Zebrafish. *Current Biology*, *20*(21), 1966–1972. https://doi.org/10.1016/J.CUB.2010.10.009

Rauzi, M., & Lenne, P. F. (2011). Cortical Forces in Cell Shape Changes and Tissue Morphogenesis. *Current Topics in Developmental Biology*, *95*, 93–144. https://doi.org/10.1016/B978-0-12-385065-2.00004-9

Rauzi, M., Verant, P., Lecuit, T., & Lenne, P.-F. (2008). Nature and anisotropy of cortical forces orienting Drosophila tissue morphogenesis. *Nature Cell Biology 2008 10:12*, *10*(12), 1401–1410. https://doi.org/10.1038/ncb1798

Rebagliati, M. R., Toyama, R., Fricke, C., Haffter, P., & Dawid, I. B. (1998). Zebrafish Nodal-Related Genes Are Implicated in Axial Patterning and Establishing Left–Right Asymmetry. *Developmental Biology*, *199*(2), 261–272. https://doi.org/10.1006/dbio.1998.8935

Reig, G., Pulgar, E., & Concha, M. L. (2014). Cell migration: from tissue culture to embryos. *Development*, *141*(10), 1999–2013. https://doi.org/10.1242/dev.101451

Reinhard, M., Riidigerb, M., Jockuschb, B. M., & Walter, U. (1996). VASP interaction with vinculin: a recurring theme of interactions with proline-rich motifs. *FEBS 17901 FEBS Letters*, *399*, 103–107.

Rembold, M., Loosli, F., Adams, R. J., & Wittbrodt, J. (2015). *Individual the Migration for Serves Vesicle Driving Evagination*

Optic. *313*(5790), 1130–1134.

Renucci, A., Lemarchandel, V., & Rosa, F. (1996). An activated form of type I serine/threonine kinase receptor TARAM-A reveals a specific signalling pathway involved in fish head organiser formation. *Development*, *122*(12), 3735–3743. https://doi.org/10.1242/DEV.122.12.3735

Riahi, R., Sun, J., Wang, S., Long, M., Zhang, D. D., & Wong, P. K. (2015). Notch1-Dll4 signaling and mechanical force regulate leader cell formation during collective cell migration. *Nature Communications*, *6*, 6556. https://doi.org/10.1038/NCOMMS7556

Riaz, M., Versaevel, M., Mohammed, D., Glinel, K., & Gabriele, S. (2016). Persistence of fan-shaped keratocytes is a matrix-rigidity-dependent mechanism that requires α5β1 integrin engagement. *Scientific Reports*, *6*(1), 34141. https://doi.org/10.1038/srep34141

Ridley, A. J. (2003). Cell Migration: Integrating Signals from Front to Back. *Science*, *302*(5651), 1704–1709. https://doi.org/10.1126/science.1092053

Ridley, Anne J. (2011). Life at the Leading Edge. *Cell*, *145*(7), 1012–1022. https://doi.org/10.1016/J.CELL.2011.06.010

Ridley, Anne J., & Hall, A. (1992). The small GTP-binding protein rho regulates the assembly of focal adhesions and actin stress fibers in response to growth factors. *Cell*, *70*(3), 389–399. https://doi.org/10.1016/0092-8674(92)90163-7

Rimm, D. L., Koslov, E. R., Kebriaei, P., Cianci, C. D., & Morrow, J. S. (1995). Alpha 1(E)-catenin is an actin-binding and -bundling protein mediating the attachment of F-actin to the membrane adhesion complex. *Proceedings of the National Academy of Sciences*, *92*(19), 8813–8817. https://doi.org/10.1073/pnas.92.19.8813

Rivero, F., Koppel, B., Peracino, B., Bozzaro, S., Siegert, F., Weijer, C. J., Schleicher, M., Albrecht, R., & Noegel, A. A. (1996). The role of the cortical cytoskeleton: F-actin crosslinking proteins protect against osmotic stress, ensure cell size, cell shape and motility, and contribute to phagocytosis and development. *Journal of Cell Science*, *109*(11), 2679–2691. https://doi.org/10.1242/JCS.109.11.2679

Robinson, V., Smith, A., Flenniken, A. M., & Wilkinson, D. G. (1997). Roles of Eph receptors and ephrins in neural crest pathfinding. *Cell and Tissue Research*, *290*(2), 265–274. https://doi.org/10.1007/s004410050931

Rock, K. L., & Kono, H. (2008). The inflammatory response to cell death. *Annual Review of Pathology*, *3*, 99. https://doi.org/10.1146/ANNUREV.PATHMECHDIS.3.121806.151456

Roe, S., Koslov, E. R., & Rimm, D. L. (1998). A Mutation in α-Catenin Disrupts Adhesion in Clone A Cells Without Perturbing its Actin and β-Catenin Binding Activity. *Cell Adhesion and Communication*, *5*(4), 283–296. https://doi.org/10.3109/15419069809040298

Rohani, N., Canty, L., Luu, O., Fagotto, F., & Winklbauer, R. (2011). EphrinB/EphB signaling controls embryonic germ layer separation by contact-induced cell detachment. *PLoS Biology*, *9*(3), 1–18. https://doi.org/10.1371/journal.pbio.1000597

Röper, K. (2013). Supracellular actomyosin assemblies during development. *Bioarchitecture*, *3*(2), 45. https://doi.org/10.4161/BIOA.25339

Rørth, P. (2007). Collective guidance of collective cell migration. *Trends in Cell Biology*, *17*(12), 575–579. https://doi.org/10.1016/j.tcb.2007.09.007

Rørth, P. (2009). Collective Cell Migration. *Annual Review of Cell and Developmental Biology*, *25*(1), 407–429. https://doi.org/10.1146/annurev.cellbio.042308.113231

Rørth, P. (2011). Whence Directionality: Guidance Mechanisms in Solitary and Collective Cell Migration. *Developmental Cell*, *20*(1), 9–18. https://doi.org/10.1016/j.devcel.2010.12.014

Roszko, I., S. Sepich, D., Jessen, J. R., Chandrasekhar, A., & Solnica-Krezel, L. (2015). A dynamic intracellular distribution of Vangl2 accompanies cell polarization during zebrafish gastrulation. *Development*, *142*(14), 2508–2520. https://doi.org/10.1242/dev.119032

Roszko, Isabelle, Sawada, A., & Solnica-Krezel, L. (2009). Regulation of convergence and extension movements during vertebrate gastrulation by the Wnt/PCP pathway. *Seminars in Cell & Developmental Biology*, *20*(8), 986–997. https://doi.org/10.1016/j.semcdb.2009.09.004

Rouiller, I., Xu, X.-P., Amann, K. J., Egile, C., Nickell, S., Nicastro, D., Li, R., Pollard, T. D., Volkmann, N., & Hanein, D. (2008). The structural basis of actin filament branching by the Arp2/3 complex. *The Journal of Cell Biology*, *180*(5), 887. https://doi.org/10.1083/JCB.200709092

Rozario, T., Dzamba, B., Weber, G. F., Davidson, L. A., & DeSimone, D. W. (2009). The Physical State of Fibronectin Matrix Differentially Regulates Morphogenetic Movements In Vivo. *Developmental Biology*, *327*(2), 386. https://doi.org/10.1016/J.YDBIO.2008.12.025

Ruprecht, V., Wieser, S., Callan-Jones, A., Smutny, M., Morita, H., Sako, K., Barone, V., Ritsch-Marte, M., Sixt, M., Voituriez, R., & Heisenberg, C.-P. (2015). Cortical Contractility Triggers a Stochastic Switch to Fast Amoeboid Cell Motility. *Cell*, *160*(4), 673–685. https://doi.org/10.1016/j.cell.2015.01.008

Sakaguchi, T., Mizuno, T., & Takeda, H. (2002). Formation and Patterning Roles of the Yolk Syncytial Layer. In *Results and problems in cell differentiation* (Vol. 40, pp. 1–14). Results Probl Cell Differ. https://doi.org/10.1007/978-3-540-46041-1_1

Salbreux, G., Charras, G., & Paluch, E. (2012). Actin cortex mechanics and cellular morphogenesis. *Trends in Cell Biology*, *22*(10), 536–545. https://doi.org/10.1016/J.TCB.2012.07.001

Samandari, M., Rafiee, L., Alipanah, F., Sanati-Nezhad, A., & Javanmard, S. H. (2021). A simple, low cost and reusable microfluidic gradient strategy and its application in modeling cancer invasion. *Scientific Reports 2021 11:1*, *11*(1), 1–11. https://doi.org/10.1038/s41598-021-89635-0

Sarris, M., Masson, J. B., Maurin, D., Van Der Aa, L. M., Boudinot, P., Lortat-Jacob, H., & Herbomel, P. (2012). Inflammatory Chemokines Direct and Restrict Leukocyte Migration within Live Tissues as Glycan-Bound Gradients. *Current Biology*, *22*(24), 2375–2382. https://doi.org/10.1016/J.CUB.2012.11.018

Sasaki, A. T., & Firtel, R. A. (2006). Regulation of chemotaxis by the orchestrated activation of Ras, PI3K, and TOR. *European Journal of Cell Biology*, *85*(9–10), 873–895. https://doi.org/10.1016/j.ejcb.2006.04.007

Sasaki, A. T., Janetopoulos, C., Lee, S., Charest, P. G., Takeda, K., Sundheimer, L. W., Meili, R., Devreotes, P. N., & Firtel, R. A. (2007). G protein–independent Ras/PI3K/F-actin circuit regulates basic cell motility. *Journal of Cell Biology*, *178*(2), 185–191. https://doi.org/10.1083/JCB.200611138

Sasaki, T., Irie-Sasaki, J., Jones, R. G., Oliveira-Dos-Santos, A. J., Stanford, W. L., Bolon, B., Wakeham, A., Itie, A., Bouchard, D., Kozieradzki, I., Joza, N., Mak, T. W., Ohashi, P. S., Suzuki, A., & Penninger, J. M. (2000). Function of PI3Kγ in thymocyte development, T cell activation, and neutrophil migration. *Science*, *287*(5455), 1040–4046. https://doi.org/10.1126/science.287.5455.1040

Saude, L., Wooley, K., Martin, P., Driever, W., & Stemple, D. L. (2000). Axis-inducing activities and cell fates of the zebrafish

organizer. *Development*, *127*(16), 3407–3417.

Sawyer, J. M., Harrell, J. R., Shemer, G., Sullivan-Brown, J., Roh-Johnson, M., & Goldstein, B. (2010). Apical Constriction: A Cell Shape Change that Can Drive Morphogenesis. *Developmental Biology*, *341*(1), 5. https://doi.org/10.1016/J.YDBIO.2009.09.009

Sayyad, W. A., Amin, L., Fabris, P., Ercolini, E., & Torre, V. (2015). The role of myosin-II in force generation of DRG filopodia and lamellipodia. *Scientific Reports 2015 5:1*, *5*(1), 1–12. https://doi.org/10.1038/srep07842

Scarpa, E., & Mayor, R. (2016). Collective cell migration in development. *Journal of Cell Biology*, *212*(2), 143–155. https://doi.org/10.1083/jcb.201508047

Scarpa, E., Szabó, A., Bibonne, A., Theveneau, E., Parsons, M., & Mayor, R. (2015). Cadherin Switch during EMT in Neural Crest Cells Leads to Contact Inhibition of Locomotion via Repolarization of Forces. *Developmental Cell*, *34*(4), 421–434. https://doi.org/10.1016/j.devcel.2015.06.012

Schälte, Y., & Hasenauer, J. (2020). Efficient exact inference for dynamical systems with noisy measurements using sequential approximate Bayesian computation. *Bioinformatics*, *36*(Supplement_1), i551–i559. https://doi.org/10.1093/bioinformatics/btaa397

Schier, A.F., Neuhauss, S. C., Helde, K. A., Talbot, W. S., & Driever, W. (1997). The one-eyed pinhead gene functions in mesoderm and endoderm formation in zebrafish and interacts with no tail. *Development*, *124*(2), 327–342. https://doi.org/10.1242/DEV.124.2.327

Schier, Alexander F. (2003). Nodal Signaling in Vertebrate Development. *Annual Review of Cell and Developmental Biology*, *19*, 589–621. https://doi.org/10.1146/annurev.cellbio.19.041603.094522

Schier, Alexander F., & Talbot, W. S. (2005). Molecular Genetics of Axis Formation in Zebrafish. *Annual Review of Genetics*, *39*(1), 561–613. https://doi.org/10.1146/annurev.genet.37.110801.143752

Schneider, I. C., & Haugh, J. M. (2006). Mechanisms of Gradient Sensing and Chemotaxis: Conserved Pathways, Diverse Regulation. *Cell Cycle*, *5*(11), 1130–1134. https://doi.org/10.4161/cc.5.11.2770

Schulte-Merker, S., Hammerschmidt, M., Beuchle, D., Cho, K. W., De Robertis, E. M., & Nusslein-Volhard, C. (1994). Expression of zebrafish goosecoid and no tail gene products in wild-type and mutant no tail embryos. *Development*, *120*(4), 843–852. https://doi.org/10.1242/DEV.120.4.843

Schulte-Merker, S., van Eeden, F. J., Halpern, M. E., Kimmel, C. B., & Nüsslein-Volhard, C. (1994). no tail (ntl) is the zebrafish homologue of the mouse T (Brachyury) gene. *Development*, *120*(4), 1009–1015.

Schwarz, U. S., & Soiné, J. R. D. (2015). Traction force microscopy on soft elastic substrates: A guide to recent computational advances. *Biochimica et Biophysica Acta (BBA) - Molecular Cell Research*, *1853*(11), 3095–3104. https://doi.org/10.1016/J.BBAMCR.2015.05.028

Scott, J. A., Shewan, A. M., den Elzen, N. R., Loureiro, J. J., Gertler, F. B., & Yap, A. S. (2006). Ena/VASP Proteins Can Regulate Distinct Modes of Actin Organization at Cadherin-adhesive Contacts. *Molecular Biology of the Cell*, *17*(3), 1085–1095. https://doi.org/10.1091/mbc.e05-07-0644

Seddiki, R., Narayana, G. H. N. S., Strale, P. O., Balcioglu, H. E., Peyret, G., Yao, M., Le, A. P., Lim, C. T., Yan, J., Ladoux, B., & Mège, R. M. (2018). Force-dependent binding of vinculin to α-catenin regulates cell-cell contact stability and collective cell behavior. *Molecular Biology of the Cell*, *29*(4), 380–388. https://doi.org/10.1091/mbc.E17-04-0231

Seiliez, I., Thisse, B., & Thisse, C. (2006). FoxA3 and goosecoid promote anterior neural fate through inhibition of Wnt8a activity before the onset of gastrulation. *Developmental Biology*, *290*(1), 152–163. https://doi.org/10.1016/j.ydbio.2005.11.021

Shellard, A., & Mayor, R. (2016). Chemotaxis during neural crest migration. *Seminars in Cell and Developmental Biology*, *55*, 111–118. https://doi.org/10.1016/j.semcdb.2016.01.031

Shellard, A., & Mayor, R. (2020). All Roads Lead to Directional Cell Migration. *Trends in Cell Biology*, *30*(11), 852–868. https://doi.org/10.1016/j.tcb.2020.08.002

Shellard, A., Szabó, A., Trepat, X., & Mayor, R. (2018). Supracellular contraction at the rear of neural crest cell groups drives collective chemotaxis. *Science*, *362*(6412), 339–343. https://doi.org/10.1126/science.aau3301

Shih, J., & Fraser, S. E. (1996). Characterizing the zebrafish organizer: Microsurgical analysis at the early-shield stage. *Development*, *122*(4), 1313–1322.

Shimada, A., Yabusaki, M., Niwa, H., Yokoi, H., Hatta, K., Kobayashi, D., & Takeda, H. (2008). Maternal-zygotic medaka mutants for fgfr1 reveal its essential role in the migration of the axial mesoderm but not the lateral mesoderm. *Development (Cambridge, England)*, *135*(2), 281–290. https://doi.org/10.1242/dev.011494

Shimizu, T., Bae, Y. K., Muraoka, O., & Hibi, M. (2005). Interaction of Wnt and caudal-related genes in zebrafish posterior body formation. *Developmental Biology*, *279*(1), 125–141. https://doi.org/10.1016/j.ydbio.2004.12.007

Shimizu, T., Yabe, T., Muraoka, O., Yonemura, S., Aramaki, S., Hatta, K., Bae, Y. K., Nojima, H., & Hibi, M. (2005). E-cadherin is required for gastrulation cell movements in zebrafish. *Mechanisms of Development*, *122*(6), 747–763. https://doi.org/10.1016/j.mod.2005.03.008

Shimizu, T., Yamanaka, Y., Ryu, S. L., Hashimoto, H., Yabe, T., Hirata, T., Bae, Y. K., Hibi, M., & Hirano, T. (2000). Cooperative roles of Bozozok/Dharma and Nodal-related proteins in the formation of the dorsal organizer in zebrafish. *Mechanisms of Development*, *91*(1–2), 293–303. https://doi.org/10.1016/S0925-4773(99)00319-6

Shyamala, Yanduri, S., Girish, H., & Murgod, S. (2015). Neural crest: The fourth germ layer. *Journal of Oral and Maxillofacial Pathology*, *19*(2), 221. https://doi.org/10.4103/0973-029X.164536

Siang, L. C., Fernandez-Gonzalez, R., & Feng, J. J. (2018). Modeling cell intercalation during Drosophila germband extension. *Physical Biology*, *15*(6), 066008. https://doi.org/10.1088/1478-3975/AAD865

Silver, D. L., Geisbrecht, E. R., & Montell, D. J. (2005). Requirement for JAK/STAT signaling throughout border cell migration in Drosophila. *Development*, *132*(15), 3483–3492. https://doi.org/10.1242/DEV.01910

Silver, D. L., & Montell, D. J. (2001). Paracrine Signaling through the JAK/STAT Pathway Activates Invasive Behavior of Ovarian Epithelial Cells in Drosophila. *Cell*, *107*(7), 831–841. https://doi.org/10.1016/S0092-8674(01)00607-9

Simon, B., Sandhu, M., & Myhr, K. L. (2010). Live FISH: Imaging mRNA in living neurons. *Journal of Neuroscience Research*, *88*(1), 55–63. https://doi.org/10.1002/JNR.22191

Sirotkin, H. I., Gates, M. A., Kelly, P. D., Schier, A. F., & Talbot, W. S. (2000). fast1 is required for the development of dorsal axial structures in zebrafish. *Current Biology*, *10*(17), 1051–1054. https://doi.org/10.1016/S0960-9822(00)00679-5

Sit, S.-T., & Manser, E. (2011). Rho GTPases and their role in organizing the actin cytoskeleton. *Journal of Cell Science*, *124*(5), 679–683. https://doi.org/10.1242/jcs.064964

Sivasankar, S. (2013). Tuning the kinetics of cadherin adhesion. *The Journal of Investigative Dermatology*, *133*(10), 2318.

https://doi.org/10.1038/JID.2013.229

Skoglund, P., Rolo, A., Chen, X., Gumbiner, B. M., & Keller, R. (2008). Convergence and extension at gastrulation require a myosin IIB-dependent cortical actin network. *Development*, *135*(14), 2435–2444. https://doi.org/10.1242/dev.014704

Slack, J. M. W., Darlington, B. G., Heath, J. K., & Godsave, S. F. (1987). Mesoderm induction in early Xenopus embryos by heparin-binding growth factors. *Nature 1987 326:6109*, *326*(6109), 197–200. https://doi.org/10.1038/326197a0

Slagle, C. E., Aoki, T., & Burdine, R. D. (2011). Nodal-Dependent Mesendoderm Specification Requires the Combinatorial Activities of FoxH1 and Eomesodermin. *PLOS Genetics*, *7*(5), e1002072. https://doi.org/10.1371/JOURNAL.PGEN.1002072

Smith, A. M., Mancini, M. C., & Nie, S. (2009). Second window for in vivo imaging. *Nature Nanotechnology 2009 4:11*, *4*(11), 710–711. https://doi.org/10.1038/nnano.2009.326

Smith, L. R., Cho, S., & Discher, D. E. (2017). Stem Cell Differentiation is Regulated by Extracellular Matrix Mechanics. *Https://Doi.Org/10.1152/Physiol.00026.2017*, *33*(1), 16–25. https://doi.org/10.1152/PHYSIOL.00026.2017

Smutny, M., Ákos, Z., Grigolon, S., Shamipour, S., Ruprecht, V., Čapek, D., Behrndt, M., Papusheva, E., Tada, M., Hof, B., Vicsek, T., Salbreux, G., & Heisenberg, C.-P. (2017). Friction forces position the neural anlage. *Nature Cell Biology*, *19*(4), 306–317. https://doi.org/10.1038/ncb3492

Solnica-Krezel, L., & Driever, W. (1994). Microtubule arrays of the zebrafish yolk cell: organization and function during epiboly. *Development*, *120*(9), 2443–2455. https://doi.org/10.1242/DEV.120.9.2443

Solnica-Krezel, Lilianna, Stemple, D. L., & Driever, W. (1995). Transparent things: cell fates and cell movements during early embryogenesis of zebrafish. *BioEssays*, *17*(11), 931–939. https://doi.org/10.1002/bies.950171106

Sonavane, P. R., Wang, C., Dzamba, B., Weber, G. F., Periasamy, A., & DeSimone, D. W. (2017). Mechanical and signaling roles for keratin intermediate filaments in the assembly and morphogenesis of mesendoderm tissue at gastrulation. *Development*, dev.155200. https://doi.org/10.1242/dev.155200

Song, S., Eckerle, S., Onichtchouk, D., Marrs, J. A., Nitschke, R., & Driever, W. (2013). Pou5f1-Dependent EGF Expression Controls E-Cadherin Endocytosis, Cell Adhesion, and Zebrafish Epiboly Movements. *Developmental Cell*, *24*(5), 486–501. https://doi.org/10.1016/J.DEVCEL.2013.01.016

Souchaud, A., Boutillon, A., Charron, G., Asnacios, A., Noûs, C., David, N. B., Graner, F., & Gallet, F. (2021). Live 3D imaging and mapping of shear stresses within tissues using incompressible elastic beads. *BioRxiv*. https://doi.org/10.1242/dev.xxxxxx

Spiering, D., & Hodgson, L. (2011). Dynamics of the rho-family small GTPases in actin regulation and motility. *Cell Adhesion and Migration*, *5*(2), 170–180. https://doi.org/10.4161/cam.5.2.14403

Stachel, S. E., Grunwald, D. J., & Myers, P. Z. (1993). Lithium perturbation and goosecoid expression identify a dorsal specification pathway in the pregastrula zebrafish. *Development*, *117*(4), 1261–1274.

Stainier, D. Y. R., Raz, E., Lawson, N. D., Ekker, S. C., Burdine, R. D., Eisen, J. S., Ingham, P. W., Schulte-Merker, S., Yelon, D., Weinstein, B. M., Mullins, M. C., Wilson, S. W., Ramakrishnan, L., Amacher, S. L., Neuhauss, S. C. F., Meng, A., Mochizuki, N., Panula, P., & Moens, C. B. (2017). Guidelines for morpholino use in zebrafish. *PLoS Genetics*, *13*(10), 6–10. https://doi.org/10.1371/journal.pgen.1007000

Starruß, J., de Back, W., Brusch, L., & Deutsch, A. (2014). Morpheus: a user-friendly modeling environment for multiscale

and multicellular systems biology. *Bioinformatics (Oxford, England)*, *30*(9), 1331–1332. https://doi.org/10.1093/bioinformatics/btt772

Steffen, A., Koestler, S. A., & Rottner, K. (2014). Requirements for and consequences of Rac-dependent protrusion. *European Journal of Cell Biology*, *93*(5–6), 184–193. https://doi.org/10.1016/J.EJCB.2014.01.008

Strahle, U., Blader, P., Henrique, D., & Ingham, P. W. (1993). Axial, a zebrafish gene expressed along the developing body axis, shows altered expression in cyclops mutant embryos. *Genes and Development*, *7*(7 B), 1436–1446. https://doi.org/10.1101/GAD.7.7B.1436

Stramer, B., & Mayor, R. (2016). Mechanisms and in vivo functions of contact inhibition of locomotion. *Nature Reviews Molecular Cell Biology*, *18*(1), 43–55. https://doi.org/10.1038/nrm.2016.118

Summerton, J., & Weller, D. (1997). Morpholino Antisense Oligomers: Design, Preparation, and Properties. *Antisense and Nucleic Acid Drug Development*, *7*(3), 187–195. https://doi.org/10.1089/oli.1.1997.7.187

Svitkina, T. M., Bulanova, E. A., Chaga, O. Y., Vignjevic, D. M., Kojima, S. ichiro, Vasiliev, J. M., & Borisy, G. G. (2003). Mechanism of filopodia initiation by reorganization of a dendritic network. *Journal of Cell Biology*, *160*(3), 409–421. https://doi.org/10.1083/jcb.200210174

Swaminathan, V., Fischer, R. S., & Waterman, C. M. (2016). The FAK–Arp2/3 interaction promotes leading edge advance and haptosensing by coupling nascent adhesions to lamellipodia actin. *Molecular Biology of the Cell*, *27*(7), 1085–1100. https://doi.org/10.1091/mbc.E15-08-0590

Swaney, K. F., & Li, R. (2016). Function and regulation of the Arp2/3 complex during cell migration in diverse environments. *Current Opinion in Cell Biology*, *42*, 63. https://doi.org/10.1016/J.CEB.2016.04.005

Swat, M. H., Thomas, G. L., Belmonte, J. M., Shirinifard, A., Hmeljak, D., & Glazier, J. A. (2012). Multi-scale modeling of tissues using CompuCell3D. *Methods in Cell Biology*, *110*, 325–366. https://doi.org/10.1016/B978-0-12-388403-9.00013-8

Szabó, A., Melchionda, M., Nastasi, G., Woods, M. L., Campo, S., Perris, R., & Mayor, R. (2016). In vivo confinement promotes collective migration of neural crest cells. *Journal of Cell Biology*, *213*(5), 543–555. https://doi.org/10.1083/jcb.201602083

Tabdanov, E., Borghi, N., Brochard-Wyart, F., Dufour, S., & Thiery, J.-P. (2009). Role of E-Cadherin in Membrane-Cortex Interaction Probed by Nanotube Extrusion. *Biophysical Journal*, *96*(6), 2457–2465. https://doi.org/10.1016/J.BPJ.2008.11.059

Tada, M., & Heisenberg, C.-P. (2012). Convergent extension: using collective cell migration and cell intercalation to shape embryos. *Development*, *139*(21), 3897–3904. https://doi.org/10.1242/dev.073007

Tada, Masazumi, & Kai, M. (2012). Planar Cell Polarity in Coordinated and Directed Movements. In *Current Topics in Developmental Biology* (1st ed., Vol. 101). Elsevier Inc. https://doi.org/10.1016/B978-0-12-394592-1.00004-1

Tada, Masazumi, & Smith, J. C. (2000). Xwnt11 is a target of Xenopus Brachyury: regulation of gastrulation movements via Dishevelled, but not through the canonical Wnt pathway. *Development*, *127*(10), 2227–2238.

Tahinci, E., & Symes, K. (2003). Distinct functions of Rho and Rac are required for convergent extension during Xenopus gastrulation. *Developmental Biology*, *259*(2), 318–335. https://doi.org/10.1016/S0012-1606(03)00206-9

Tallquist, M., & Kazlauskas, A. (2004). PDGF signaling in cells and mice. *Cytokine & Growth Factor Reviews*, *15*(4), 205–

213. https://doi.org/10.1016/j.cytogfr.2004.03.003

Tambe, D. T., Corey Hardin, C., Angelini, T. E., Rajendran, K., Park, C. Y., Serra-Picamal, X., Zhou, E. H., Zaman, M. H., Butler, J. P., Weitz, D. A., Fredberg, J. J., & Trepat, X. (2011). Collective cell guidance by cooperative intercellular forces. *Nature Materials*, *10*(6), 469–475. https://doi.org/10.1038/nmat3025

Taneja, N., Bersi, M. R., Baillargeon, S. M., Fenix, A. M., Cooper, J. A., Ohi, R., Gama, V., Merryman, W. D., & Burnette, D. T. (2020). Precise Tuning of Cortical Contractility Regulates Cell Shape during Cytokinesis. *Cell Reports*, *31*(1), 107477. https://doi.org/10.1016/J.CELREP.2020.03.041

Tang, D. D., & Gerlach, B. D. (2017). The roles and regulation of the actin cytoskeleton, intermediate filaments and microtubules in smooth muscle cell migration. *Respiratory Research*, *18*(1), 54. https://doi.org/10.1186/s12931-017-0544-7

Tapon, N., & Hall, A. (1997). Rho, Rat and C&42 GTPases regulate the organization of the actin cytoskeleton. *Current Opinion in Cell Biology*, *9*(1), 86–92. papers3://publication/uuid/4871C8F6-C60B-4939-ABA4-856B6EB4FB7C

Theveneau, E., Marchant, L., Kuriyama, S., Gull, M., Moepps, B., Parsons, M., & Mayor, R. (2010). Collective Chemotaxis Requires Contact-Dependent Cell Polarity. *Developmental Cell*, *19*(1), 39–53. https://doi.org/10.1016/j.devcel.2010.06.012

Theveneau, E., & Mayor, R. (2011). Can mesenchymal cells undergo collective cell migration? The case of the neural crest. *Cell Adhesion and Migration*, *5*(6), 490–498. https://doi.org/10.4161/cam.5.6.18623

Theveneau, E., & Mayor, R. (2012). Neural crest migration: interplay between chemorepellents, chemoattractants, contact inhibition, epithelial–mesenchymal transition, and collective cell migration. *Wiley Interdisciplinary Reviews: Developmental Biology*, *1*(3), 435–445. https://doi.org/10.1002/WDEV.28

Theveneau, E., Steventon, B., Scarpa, E., Garcia, S., Trepat, X., Streit, A., & Mayor, R. (2013). Chase-and-run between adjacent cell populations promotes directional collective migration. *Nature Cell Biology*, *15*(7), 763–772. https://doi.org/10.1038/ncb2772

Thisse, B., Pflumio, S., Fürthauer, M., Loppin, B., Heyer, V., Degrave, A., Woehl, R., Lux, A., Steffan, T., Charbonnier, X. Q., & Thisse, C. (2001). *Expression of the zebrafish genome during embryogenesis*. ZFIN. https://zfin.org/ZDB-PUB-010810-1

Thisse, C., Thisse, B., Halpern, M. E., & Postlethwait, J. H. (1994). goosecoid Expression in neurectoderm and mesendoderm is disrupted in zebrafish cyclops gastrulas. *Developmental Biology*, *164*(2), 420–429. https://doi.org/10.1006/dbio.1994.1212

Thompson, C. J., Vu, V. H., Leckband, D. E., & Schwartz, D. K. (2021). Cadherin cis and trans interactions are mutually cooperative. *Proceedings of the National Academy of Sciences of the United States of America*, *118*(10), e2019845118. https://doi.org/10.1073/PNAS.2019845118

Townes, P. L., & Holtfreter, J. (1955). Directed movements and selective adhesion of embryonic amphibian cells. *Journal of Experimental Zoology*, *128*(1), 53–120. https://doi.org/10.1002/JEZ.1401280105

Trepat, X., Wasserman, M. R., Angelini, T. E., Millet, E., Weitz, D. A., Butler, J. P., & Fredberg, J. J. (2009). Physical forces during collective cell migration. *Nature Physics*, *5*(6), 426–430. https://doi.org/10.1038/nphys1269

Trinkaus, J. P. (1970). Cells Into Organs. The Forces That Shape the Embryo. *The Quarterly Review of Biology*, *45*(1), 76–77. https://doi.org/10.1086/406401

Trinkaus, J. P. (1973). Modes of Cell Locomotion in vivo. In *Locomotion of Tissue Cells* (pp. 233–249). John Wiley & Sons, Ltd. https://doi.org/10.1002/9780470719978.ch11

Troyanovsky, S. (2005). Cadherin dimers in cell–cell adhesion. *European Journal of Cell Biology*, *84*(2–3), 225–233. https://doi.org/10.1016/j.ejcb.2004.12.009

Tsukasaki, Y., Kitamura, K., Shimizu, K., Iwane, A. H., Takai, Y., & Yanagida, T. (2007). Role of Multiple Bonds Between the Single Cell Adhesion Molecules, Nectin and Cadherin, Revealed by High Sensitive Force Measurements. *Journal of Molecular Biology*, *367*(4), 996–1006. https://doi.org/10.1016/j.jmb.2006.12.022

Turing, A. M. (1952). The chemical basis of morphogenesis. *Bulletin of Mathematical Biology*, *52*(1–2), 153–197. https://doi.org/10.1007/BF02459572

Turner, C. E. (2000). Paxillin and focal adhesion signalling. *Nature Cell Biology*, *2*(12), E231–E236. https://doi.org/10.1038/35046659

Turner, N., & Grose, R. (2010). Fibroblast growth factor signalling: from development to cancer. *Nature Reviews Cancer*, *10*(2), 116–129. https://doi.org/10.1038/nrc2780

Tweedy, L., Susanto, O., & Insall, R. H. (2016). Self-generated chemotactic gradients—cells steering themselves. *Current Opinion in Cell Biology*, *42*, 46–51. https://doi.org/10.1016/j.ceb.2016.04.003

Twiss, F., Le Duc, Q., Van Der Horst, S., Tabdili, H., Van Der Krogt, G., Wang, N., Rehmann, H., Huveneers, S., Leckband, D. E., & De Rooij, J. (2012). Vinculin-dependent Cadherin mechanosensing regulates efficient epithelial barrier formation. *Biology Open*, *1*(11), 1128–1140. https://doi.org/10.1242/bio.20122428

Ulrich, F., Concha, M. L., Heid, P. J., Voss, E., Witzel, S., Roehl, H., Tada, M., Wilson, S. W., Adams, R. J., Soll, D. R., & Heisenberg, C.-P. (2003). Slb/Wnt11 controls hypoblast cell migration and morphogenesis at the onset of zebrafish gastrulation. *Development*, *130*(22), 5375–5384. https://doi.org/10.1242/dev.00758

Ulrich, F., Krieg, M., Schötz, E. M., Link, V., Castanon, I., Schnabel, V., Taubenberger, A., Mueller, D., Puech, P. H., & Heisenberg, C. P. (2005). Wnt11 functions in gastrulation by controlling cell cohesion through Rab5c and E-Cadherin. *Developmental Cell*, *9*(4), 555–564. https://doi.org/10.1016/j.devcel.2005.08.011

Upadhyaya, A., Chabot, J. R., Andreeva, A., Samadani, A., & Oudenaarden, A. van. (2003). Probing polymerization forces by using actin-propelled lipid vesicles. *Proceedings of the National Academy of Sciences*, *100*(8), 4521–4526. https://doi.org/10.1073/PNAS.0837027100

Valentin, G., Haas, P., & Gilmour, D. (2007). The Chemokine SDF1a Coordinates Tissue Migration through the Spatially Restricted??Activation??of Cxcr7 and Cxcr4b. *Current Biology*, *17*(12), 1026–1031. https://doi.org/10.1016/j.cub.2007.05.020

Varga, Z. M., Wegner, J., & Westerfield, M. (1999). Anterior movement of ventral diencephalic precursors separates the primordial eye field in the neural plate and requires cyclops. *Development*, *126*(24), 5533–5546.

Vassilev, V., Platek, A., Hiver, S., Enomoto, H., & Takeichi, M. (2017). Catenins Steer Cell Migration via Stabilization of Front-Rear Polarity. *Developmental Cell*, *43*(4), 463-479.e5. https://doi.org/10.1016/J.DEVCEL.2017.10.014

Vedula, S. R. K., Ravasio, A., Lim, C. T., & Ladoux, B. (2013). Collective Cell Migration: A Mechanistic Perspective. *Physiology*, *28*(6), 370–379. https://doi.org/10.1152/physiol.00033.2013

Veeman, M. T., & McDonald, J. A. (2016). Dynamics of cell polarity in tissue morphogenesis: a comparative view from

Drosophila and Ciona. *F1000Research*, *5*(0). https://doi.org/10.12688/f1000research.8011.1

Veldhuis, J. H., Mashburn, D., Hutson, M. S., & Brodland, G. W. (2015). Practical aspects of the cellular force inference toolkit (CellFIT). In *Methods in Cell Biology* (Vol. 125). Elsevier Ltd. https://doi.org/10.1016/bs.mcb.2014.10.010

Venkiteswaran, G., Lewellis, S. W., Wang, J., Reynolds, E., Nicholson, C., & Knaut, H. (2013). Generation and Dynamics of an Endogenous, Self-Generated Signaling Gradient across a Migrating Tissue. *Cell*, *155*(3), 674–687. https://doi.org/10.1016/j.cell.2013.09.046

Verma, S., Shewan, A. M., Scott, J. A., Helwani, F. M., Elzen, N. R. den, Miki, H., Takenawa, T., & Yap, A. S. (2004). Arp2/3 Activity Is Necessary for Efficient Formation of E-cadherin Adhesive Contacts. *Journal of Biological Chemistry*, *279*(32), 34062–34070. https://doi.org/10.1074/jbc.M404814200

Vicente-Manzanares, M., Ma, X., Adelstein, R. S., & Horwitz, A. R. (2009). Non-muscle myosin II takes centre stage in cell adhesion and migration. *Nature Reviews Molecular Cell Biology*, *10*(11), 778–790. https://doi.org/10.1038/nrm2786

Vishwakarma, M., Di Russo, J., Probst, D., Schwarz, U. S., Das, T., & Spatz, J. P. (2018). Mechanical interactions among followers determine the emergence of leaders in migrating epithelial cell collectives. *Nature Communications*, *9*(1). https://doi.org/10.1038/s41467-018-05927-6

Vishwakarma, M., Spatz, J. P., & Das, T. (2020a). Mechanobiology of leader–follower dynamics in epithelial cell migration. *Current Opinion in Cell Biology*, *66*, 97–103. https://doi.org/10.1016/j.ceb.2020.05.007

Vishwakarma, M., Spatz, J. P., & Das, T. (2020b). Mechanobiology of leader-follower dynamics in epithelial cell migration. *Current Opinion in Cell Biology*, *66*, 97–103. https://doi.org/10.1016/j.ceb.2020.05.007

Volpe, B. A., Fotino, T. H., & Steiner, A. B. (2020). Confocal microscope-based laser ablation and regeneration assay in Zebrafish interneuromast cells. *Journal of Visualized Experiments*, *2020*(159), 1–9. https://doi.org/10.3791/60966

Vuong-brender, T. T. K., Boutillon, A., Rodriguez, D., Lavilley, V., & Labouesse, M. (2018). HMP-1 / α -catenin promotes junctional mechanical integrity during morphogenesis. *PLoS ONE*, *13*(2), 1–21. https://doi.org/https://doi.org/10.1371/journal.pone.0193279

Wang, C., Tran-Thanh, D., Moreno, J. C., Cawthorn, T. R., Jacks, L. M., Wang, D.-Y., McCready, D. R., & Done, S. J. (2011). Expression of Abl interactor 1 and its prognostic significance in breast cancer: a tissue-array-based investigation. *Breast Cancer Research and Treatment*, *129*(2), 373–386. https://doi.org/10.1007/s10549-010-1241-0

Wang, X., He, L., Wu, Y. I., Hahn, K. M., & Montell, D. J. (2010). Light-mediated activation reveals a key role for Rac in collective guidance of cell movement in vivo. *Nature Cell Biology*, *12*(6), 591. https://doi.org/10.1038/NCB2061

Warga, R.M., & Nusslein-Volhard, C. (1999). Origin and development of the zebrafish endoderm. *Development*, *126*(4), 827–838. https://doi.org/10.1242/DEV.126.4.827

Warga, Rachel M., & Nüsslein-Volhard, C. (1998). spadetail-Dependent Cell Compaction of the Dorsal Zebrafish Blastula. *Developmental Biology*, *203*(1), 116–121. https://doi.org/10.1006/DBIO.1998.9022

Warga, Rachel M, & Kimmel, C. B. (1990). Cell movements during epiboly and gastrulation in zebrafish. *Development*, *108*, 569–580.

Weber, G. F., Bjerke, M. A., & DeSimone, D. W. (2011). Integrins and cadherins join forces to form adhesive networks. *Journal of Cell Science*, *124*(8), 1183. https://doi.org/10.1242/JCS.064618

Weber, G. F., Bjerke, M. A., & DeSimone, D. W. (2012). A Mechanoresponsive Cadherin-Keratin Complex Directs Polarized

Protrusive Behavior and Collective Cell Migration. *Developmental Cell*, *22*(1), 104–115. https://doi.org/10.1016/j.devcel.2011.10.013

Weber, M., Hauschild, R., Schwarz, J., Moussion, C., Vries, I. de, Legler, D. F., Luther, S. A., Bollenbach, T., & Sixt, M. (2013). Interstitial Dendritic Cell Guidance by Haptotactic Chemokine Gradients. *Science*, *339*(6117), 328–332. https://doi.org/10.1126/SCIENCE.1228456

Weis, W. I., & Kobilka, B. K. (2014). The Molecular Basis of G Protein–Coupled Receptor Activation. *Https://Doi.Org/10.1146/Annurev-Biochem-060614-033910*, *87*, 897–919. https://doi.org/10.1146/ANNUREV-BIOCHEM-060614-033910

Wells, S., Nornes, S., & Lardelli, M. (2011). Transgenic zebrafish recapitulating tbx16 gene early developmental expression. *PloS One*, *6*(6), e21559. https://doi.org/10.1371/journal.pone.0021559

Whitman, M., & Mercola, M. (2001). TGF- Superfamily Signaling and Left-Right Asymmetry. *Science Signaling*, *2001*(64), re1–re1. https://doi.org/10.1126/stke.2001.64.re1

Williams, D. W., Müller, F., Lavender, F. L., Orbán, L., & Maclean, N. (1996). High transgene activity in the yolk syncytial layer affects quantitative transient expression assays in zebrafish (Danio rerio) embryos. *Transgenic Research 1996 5:6*, *5*(6), 433–442. https://doi.org/10.1007/BF01980208

Williams, M. L. K., & Solnica-Krezel, L. (2020). Nodal and planar cell polarity signaling cooperate to regulate zebrafish convergence & extension gastrulation movements. *ELife*, *9*, 1–25. https://doi.org/10.7554/eLife.54445

Wilson, E. T., Cretekos, C. J., & Helde, K. A. (1995). Cell mixing during early epiboly in the zebrafish embryo. *Developmental Genetics*, *17*(1), 6–15. https://doi.org/10.1002/dvg.1020170103

Winklbauer, R., & Keller, R. E. (1996). Fibronectin, mesoderm migration, and gastrulation in Xenopus. *Developmental Biology*, *177*(2), 413–426. https://doi.org/10.1006/dbio.1996.0174

Witzel, S., Zimyanin, V., Carreira-Barbosa, F., Tada, M., & Heisenberg, C. P. (2006). Wnt11 controls cell contact persistence by local accumulation of Frizzled 7 at the plasma membrane. *Journal of Cell Biology*, *175*(5), 791–802. https://doi.org/10.1083/jcb.200606017

Wozniak, M. A., Modzelewska, K., Kwong, L., & Keely, P. J. (2004). Focal adhesion regulation of cell behavior. *Biochimica et Biophysica Acta (BBA) - Molecular Cell Research*, *1692*(2–3), 103–119. https://doi.org/10.1016/J.BBAMCR.2004.04.007

Xie, X., Aalipour, A., Gupta, S. V., & Melosh, N. A. (2015). Determining the Time Window for Dynamic Nanowire Cell Penetration Processes. *ACS Nano*, *9*(12), 11667–11677. https://doi.org/10.1021/ACSNANO.5B05498

Xie, Y., Su, N., Yang, J., Tan, Q., Huang, S., Jin, M., Ni, Z., Zhang, B., Zhang, D., Luo, F., Chen, H., Sun, X., Feng, J. Q., Qi, H., & Chen, L. (2020). FGF/FGFR signaling in health and disease. *Signal Transduction and Targeted Therapy*, *5*(1). https://doi.org/10.1038/s41392-020-00222-7

Xiong, F., Ma, W., Bénazéraf, B., Mahadevan, L., & Pourquié, O. (2020). Mechanical Coupling Coordinates the Co-elongation of Axial and Paraxial Tissues in Avian Embryos. *Developmental Cell*, *55*(3), 354-366.e5. https://doi.org/10.1016/j.devcel.2020.08.007

Yamada, K. M., & Sixt, M. (2019). Mechanisms of 3D cell migration. *Nature Reviews Molecular Cell Biology*, *20*(12), 738–752. https://doi.org/10.1038/s41580-019-0172-9

Yamashita, S., Miyagi, C., Carmany-Rampey, A., Shimizu, T., Fujii, R., Schier, A. F., & Hirano, T. (2002). Stat3 controls cell movements during zebrafish gastrulation. *Developmental Cell*, *2*(3), 363–375. https://doi.org/10.1016/S1534-5807(02)00126-0

Yamashita, S., Miyagi, C., Fukada, T., Kagara, N., Che, Y.-S., & Hirano, T. (2004). Zinc transporter LIVI controls epithelial-mesenchymal transition in zebrafish gastrula organizer. *Nature*, *429*(6989), 298–302. https://doi.org/10.1038/nature02545

Yamazaki, D., Oikawa, T., & Takenawa, T. (2007). Rac-WAVE-mediated actin reorganization is required for organization and maintenance of cell-cell adhesion. *Journal of Cell Science*, *120*(1), 86–100. https://doi.org/10.1242/jcs.03311

Yanagida, T., Nakase, M., Nishiyama, K., & Oosawa, F. (1984). Direct observation of motion of single F-actin filaments in the presence of myosin. *Nature 1984 307:5946*, *307*(5946), 58–60. https://doi.org/10.1038/307058a0

Yang, Y., & Mlodzik, M. (2015). Wnt-Frizzled/Planar Cell Polarity Signaling: Cellular Orientation by Facing the Wind (Wnt). *Annual Review of Cell and Developmental Biology*, *31*(1), 623–646. https://doi.org/10.1146/annurev-cellbio-100814-125315

Yao, M., Qiu, W., Liu, R., Efremov, A. K., Cong, P., Seddiki, R., Payre, M., Lim, C. T., Ladoux, B., Mège, R.-M., & Yan, J. (2014). Force-dependent conformational switch of α-catenin controls vinculin binding. *Nature Communications*, *5*(1), 4525. https://doi.org/10.1038/ncomms5525

Yap, A. S., & Kovacs, E. M. (2003). Direct cadherin-activated cell signaling. *Journal of Cell Biology*, *160*(1), 11–16. https://doi.org/10.1083/jcb.200208156

Yeh, Y.-C., Ling, J.-Y., Chen, W.-C., Lin, H.-H., & Tang, M.-J. (2017). Mechanotransduction of matrix stiffness in regulation of focal adhesion size and number: reciprocal regulation of caveolin-1 and β1 integrin. *Scientific Reports 2017 7:1*, *7*(1), 1–14. https://doi.org/10.1038/s41598-017-14932-6

Yin, C., Kiskowski, M., Pouille, P. A., Farge, E., & Solnica-Krezel, L. (2008). Cooperation of polarized cell intercalations drives convergence and extension of presomitic mesoderm during zebrafish gastrulation. *Journal of Cell Biology*, *180*(1), 221–232. https://doi.org/10.1083/jcb.200704150

Yokoi, H., Shimada, A., Carl, M., Takashima, S., Kobayashi, D., Narita, T., Jindo, T., Kimura, T., Kitagawa, T., Kage, T., Sawada, A., Naruse, K., Asakawa, S., Shimizu, N., Mitani, H., Shima, A., Tsutsumi, M., Hori, H., Wittbrodt, J., … Takeda, H. (2007). Mutant analyses reveal different functions of fgfr1 in medaka and zebrafish despite conserved ligand-receptor relationships. *Developmental Biology*, *304*(1), 326–337. https://doi.org/10.1016/j.ydbio.2006.12.043

Yonemura, S., Wada, Y., Watanabe, T., Nagafuchi, A., & Shibata, M. (2010a). α-Catenin as a tension transducer that induces adherens junction development. *Nature Cell Biology*, *12*(6), 533–542. https://doi.org/10.1038/ncb2055

Yonemura, S., Wada, Y., Watanabe, T., Nagafuchi, A., & Shibata, M. (2010b). alpha-Catenin as a tension transducer that induces adherens junction development. *Nature Cell Biology*, *12*(6), 533–542. https://doi.org/10.1038/ncb2055

Yoo, S. K., Deng, Q., Cavnar, P. J., Wu, Y. I., Hahn, K. M., & Huttenlocher, A. (2010). Differential Regulation of Protrusion and Polarity by PI(3)K during Neutrophil Motility in Live Zebrafish. *Developmental Cell*, *18*(2), 226–236. https://doi.org/10.1016/j.devcel.2009.11.015

Yoshida, K., & Inoue, K. (2001). Myosin II-dependent cylindrical protrusions induced by quinine in Dictyostelium: antagonizing effects of actin polymerization at the leading edge. *Journal of Cell Science*, *114*, 2155–2165. https://doi.org/10.1103/PhysRevLett.92.078101

Zegers, M. M., & Friedl, P. (2014). Rho GTPases in collective cell migration. *Small GTPases*, *5*(3), e983869. https://doi.org/10.4161/sgtp.28997

Zhang, J., Tang, L., Chen, Y., Duan, Z., Xiao, L., Li, W., Liu, X., & Shen, L. (2015). Upregulation of Abelson interactor protein 1 predicts tumor progression and poor outcome in epithelial ovarian cancer. *Human Pathology*, *46*(9), 1331–1340. https://doi.org/10.1016/j.humpath.2015.05.015

Zhang, L., Kendrick, C., Jülich, D., & Holley, S. A. (2008). Cell cycle progression is required for zebrafish somite morphogenesis but not segmentation clock function. *Development*, *135*(12), 2065–2070. https://doi.org/10.1242/dev.022673

Zhang, L., Zhou, H., Su, Y., Sun, Z., Zhang, H., Zhang, L., Zhang, Y., Ning, Y., Chen, Y.-G., & Meng, A. (2004). Zebrafish Dpr2 Inhibits Mesoderm Induction by Promoting Degradation of Nodal Receptors. *Science*, *306*(5693), 114–117. https://doi.org/10.1126/SCIENCE.1100569

Zhang, X., Ibrahimi, O. A., Olsen, S. K., Umemori, H., Mohammadi, M., & Ornitz, D. M. (2006). Receptor specificity of the fibroblast growth factor family: The complete mammalian FGF family. *Journal of Biological Chemistry*, *281*(23), 15694–15700. https://doi.org/10.1074/jbc.M601252200

Zhao, B., Tumaneng, K., & Guan, K.-L. (2011). The Hippo pathway in organ size control, tissue regeneration and stem cell self-renewal. *Nature Cell Biology 2011 13:8*, *13*(8), 877–883. https://doi.org/10.1038/ncb2303

Zigmond, S. H. (2004). Formin-induced nucleation of actin filaments This review comes from a themed issue on Cell structure and dynamics Edited by John A Cooper and Meg A Titus. *Current Opinion in Cell Biology*, *16*, 99–105. https://doi.org/10.1016/j.ceb.2003.10.019

Zihni, C., Mills, C., Matter, K., & Balda, M. S. (2016). Tight junctions: from simple barriers to multifunctional molecular gates. *Nature Reviews Molecular Cell Biology 2016 17:9*, *17*(9), 564–580. https://doi.org/10.1038/nrm.2016.80

Appendix

List of PhD publications

Polesskaya, A., Boutillon, A., Yang, S., Wang, Y., Romero, S., Molinie, N., Rocques, N., Fokin, A., Guérois, R., Bièche, I., Baoyu, C., David, N. B., & Gautreau, A. M. (2021). CYFIP2-containing WAVE complexes inhibit cell migration by a competition mechanism. *BioRxiv*. https://doi.org/doi.org/10.1101/2020.07.02.184655

Boutillon, A., Escot, S., & David, N. B. (2021). Deep and Spatially Controlled Volume Ablations using a Two-Photon Microscope in the Zebrafish Gastrula. *Journal of Visualized Experiments*, *173*, 1–16. https://doi.org/10.3791/62815

Souchaud, A., Boutillon, A., Charron, G., Asnacios, A., Noûs, C., David, N. B., Graner, F., & Gallet, F. (2021). Live 3D imaging and mapping of shear stresses within tissues using incompressible elastic beads. *BioRxiv*. https://doi.org/10.1242/dev.xxxxxx

Boutillon, A., Jahn, D., Gonzalez-Tirado, S., Starruss, J., Brusch, L., & David, N. B. (2021). Guidance by followers ensures long-range coordination of cell migration through α-Catenin mechanoperception. *BioRxiv*, 2021.04.26.441407. https://doi.org/https://doi.org/10.1101/2021.04.26.441407

Morizet, J., Ducourthial, G., Supatto, W., Boutillon, A., Legouis, R., Schanne-Klein, M.-C., Stringari, C., & Beaurepaire, E. (2019). High-speed polarization-resolved third-harmonic microscopy. *Optica*, *6*(3), 17–20.

Boutillon, A., Giger, F. A., & David, N. B. (2018). Analysis of in vivo cell migration in mosaic zebrafish embryos. In A. Gautreau (Ed.), *Methods in Molecular Biology* (Vol. 1749, pp. 213–226). Springer New York. https://doi.org/10.1007/978-1-4939-7701-7_16

CYFIP2-containing WAVE complexes inhibit cell migration by a competition mechanism

Anna Polesskaya[1], Arthur Boutillon[2, #], Sheng Yang[3, #], Yanan Wang[1], Stéphane Romero[1], Yijun Liu[3], Marc Lavielle[4], Sophie Vacher[5], Anne Schnitzler[5], Nicolas Molinie[1], Nathalie Rocques[1], Artem Fokin[1], Raphaël Guérois[6], Ivan Bièche[5], Baoyu Chen[3], Nicolas B. David[2], Alexis M. Gautreau[1]

co-second author

[1] CNRS UMR7654, Institut Polytechnique de Paris, 91120 Palaiseau, France.

[2] INSERM U1182, CNRS UMR7645, Institut Polytechnique de Paris, 91120 Palaiseau, France.

[3]Roy J. Carver Department of Biochemistry, Biophysics and Molecular Biology, Iowa State University, Ames, IA 50011, USA.

[4] INRIA Saclay & Center for Applied Mathematics (CMAP), Institut Polytechnique de Paris, 91120 Palaiseau, France.

[5] Pharmacogenomics Unit, Department of Genetics, Institut Curie, 26 rue d'Ulm, 75005 Paris, France.

[6] Institute for Integrative Biology of the Cell (I2BC), CEA, CNRS, University Paris-Saclay, CEA-Saclay, 91190 Gif-sur-Yvette, France.

Correspondence concerning mathematical modeling should be addressed to ML (Marc.Lavielle@inria.fr)

Correspondence concerning biomedical aspects and material requests should be addressed to the lead contact, AMG (alexis.gautreau@polytechnique.edu)

Running title: CYFIP2 inhibits cell migration

Keywords: Patient cohort, multiprotein complexes, Zebrafish embryo, Scar/WAVE, WAVE Regulatory Complex, Arp2/3.

Abbreviations: BIC, Bayesian Information Criteria; KD, knock-down; KO, knock-out; MFS, metastasis-free survival; RFS, Relapse-free survival.

ABSTRACT

Branched actin networks polymerized by the Arp2/3 complex are critical for cell migration. The WAVE complex is the major Arp2/3 activator at the leading edge of migrating cells. However, multiple distinct WAVE complexes can be assembled in a cell, due to the combinatorial complexity of paralogous subunits. When systematically analyzing the contribution of each WAVE complex subunit to the metastasis-free survival of breast cancer patients, we found that overexpression of the CYFIP2 subunit was surprisingly associated with good prognosis. Gain and loss of function experiments in transformed and untransformed mammary epithelial cells, as well as in prechordal plate cells in gastrulating zebrafish embryos, revealed that lamellipodium protrusion and cell migration were always inversely related to CYFIP2 levels. The role of CYFIP2 was systematically opposite to the role of the paralogous subunit CYFIP1 or of the NCKAP1 subunit, which determines levels of WAVE complexes. CYFIP2 showed no difference from CYFIP1 in assembling WAVE complexes or binding to active RAC1. CYFIP2-containing WAVE complexes, however, were less able to activate the Arp2/3 complex in response to RAC1 binding. CYFIP1- and CYFIP2-containing WAVE complexes thus compete for active RAC1 and produce different outcomes. Therefore, cell migration, lamellipodium protrusion and Arp2/3 activity are controlled by relative levels of CYFIP1 and CYFIP2.

INTRODUCTION

Vertebrate genomes are the result of two genome-wide duplications [1]. This explains why many protein families are encoded by up to four paralogous genes in the human genome, but by a single gene in invertebrates such as *Drosophila* or *C. elegans*. The availability of several paralogous genes in the human genome has permitted the emergence of new regulations or specialized functions of specific paralogs. In cancers, alteration of gene expression or mutation usually concerns a single specific member of the family, which has to be identified.

Ten to twenty percent of human proteins form stable multiprotein complexes [2]. These complexes are often referred to as molecular machines to emphasize that they perform elaborate functions through the coordination of their subunits [3]. When several subunits are encoded by paralogous genes, a combinatorial complexity arises. Different complexes, potentially displaying different regulations and functions, stem from the different assemblies of paralogous subunits. If a specific molecular machine is responsible for cancer progression, it is also critical to be able to identify it.

Cell migration is controlled by several multiprotein complexes [4]. The Arp2/3 complex generates branched actin networks, which power membrane protrusions. At the protrusive edge, WAVE complexes activate the Arp2/3 complex [5,6]. The WAVE-Arp2/3 pathway depends on the activity of the small GTPase RAC1, which is necessary and sufficient to generate lamellipodia [7]. The RAC1-WAVE-Arp2/3 pathway controls protrusion lifetime and migration persistence through numerous feedback and feedforward loops [8]. This pathway has been implicated in the migration and invasion of tumor cells in various model systems [4].

The combinatorial complexity of WAVE complexes is daunting. A WAVE complex is composed of 5 generic subunits, hereafter referred to as WAVE, ABI, BRK, NAP and CYFIP. Except BRK, all human subunits are encoded by paralogous genes, 3 for WAVE and ABI, and 2 for NAP and CYFIP [9]. There are as many as 3x3x2x2, *i.e.* 36, possible WAVE complexes, just by combining the different paralogous subunits. Furthermore, the *ABI1* gene has been shown to be alternatively spliced and the resulting isoforms do not possess the same ability to mediate macropinocytosis, which, like lamellipodium formation, depends on the ability of branched actin to drive protrusions [10]. In mouse embryonic fibroblasts, WAVE2 is critical for the formation of peripheral ruffles, whereas WAVE1 is critical for dorsal ruffles [11]. Thus, evidence already exists for functional specialization among WAVE complexes.

WAVE complex subunits have been mostly reported to be overexpressed in tumors [4]. In line with their function in promoting cell migration and invasion, their overexpression is generally associated with high grades and poor prognosis. High levels of WAVE subunits is of poor prognosis for patients in breast, ovary, lung and liver cancers [12–16]. The overexpression of WAVE3 in colorectal cancers, however, is associated with good prognosis [17]. Similar to the general trend, high expression of the NAP paralogs, NCKAP1 and NCKAP1L, has been associated with poor prognosis in breast cancer and leukemia, respectively [18,19]. High expression of ABI1 has also been associated with poor prognosis in breast and ovary cancers [20,21].

Whereas most studies, including cancer studies, focused on one subunit, we measured the expression levels of all the paralogous genes encoding subunits in a large cohort of breast cancer patients, in an attempt to tackle the complexity of the WAVE complex. This systematic endeavor allowed us to examine each of the 36 possible WAVE complexes for their possible association with metastasis-free survival (MFS). We found no evidence for the involvement of a specific WAVE complex assembly. The first order determinant of MFS was whether WAVE complexes contained the NCKAP1 subunit. The second order determinant was whether WAVE complexes contained the CYFIP2 subunit. Surprisingly, however, we found that high levels of *CYFIP2* were associated with good prognosis. This unexpected effect on MFS could be accounted for by the fact that CYFIP2-containing complexes specifically impair cell migration in a variety of cell systems. CYFIP2-containing WAVE complexes are less activated by RAC1 than CYFIP1-containing WAVE complexes, suggesting that they titrate out the major activator of the WAVE complex.

RESULTS

Systematic analysis of WAVE complex subunits in breast cancer

In a cohort of 527 breast cancer patients (Table S1), we measured by qRT-PCR the mRNA levels of the 11 genes encoding WAVE complex subunits. Expression values in tumors were normalized to the expression in healthy breast tissue. We found that the expression of several subunits is profoundly deregulated in breast cancer (Table 1). *CYFIP2*, *NCKAP1L* and *ABI3* were up-regulated in 37%, 22% and 12% of tumors, respectively. Cases of overexpression were in different subgroups of breast cancer patients. *NCKAP1L* is mostly overexpressed in the Hormone Receptor (HR)- ERBB2+ subgroup. *ABI3* is mostly overexpressed in the HR- ERBB2-, triple negative subgroup. *CYFIP2* is mostly overexpressed in the HR+ ERBB2- subgroup and in low-grade tumors of good prognosis (Table S1). *WASF3* and *WASF1* are down-regulated in 46% and 27% of the cohort. Underexpression of these WAVE subunits is also mostly displayed in the good prognosis HR+ ERBB2- subgroup. We then examined if fluctuations in subunit expression were associated with prognosis.

Since the outcome of patients is known in the cohort and given the role of the WAVE complex in tumor cell invasion, we were especially interested in the metastasis-free survival (MFS). MFS starts at the date of surgery and terminates at the date of the last news from the patient, of metastasis diagnostic, or of death. We applied to these right-censored data a classical Cox univariate model using the expression level of each subunit as the variable. We sorted the different subunit genes according to increasing p-values (Fig. S1). The first three genes were *NCKAP1*, *CYFIP2* and *NCKAP1L*. The levels of *NCKAP1* mRNA, within their natural fluctuations, were significantly associated with MFS (p=0.012, Fig. S1). Indeed, we previously reported that high levels of *NCKAP1* were associated with poor MFS [18]. Levels of *CYFIP2* and *NCKAP1L* also appeared significantly associated with MFS, but with a lower significance, p=0.138 and 0.288, respectively.

Our goal when measuring expression levels of all WAVE subunits in the cohort was to examine whether a particular combination of subunits would create a specific WAVE complex conferring invasive properties to tumor cells. This is why we chose to perform highly accurate measurements by qRT-PCR in our cohort of 527 patients, even if global analyses were already available in public databases containing a larger number of patients. To analyze the association of various WAVE assemblies with MFS, we needed to transform and normalize our variables, i.e. subunit levels. Using a monotonous function of the type $\log(x\text{-}c)$, levels of each subunit fitted a Gaussian distribution. Then we normalized transformed variables around 0 with a variance of 1, to allow a better comparison between different subunit levels. Transformation and normalization did not change the relative association of subunit levels with MFS, since, by univariate Cox analysis, the 3 most powerful subunits to predict MFS were still, first, *NCKAP1* with a p-value of 0.005, second, *CYFIP2* with a p-value of 0.059, just above the classical 5% significance level, but far above the third subunit, *NCKAP1L*, with a p-value of 0.397 (Fig. S1).

During these simple Cox analyses of the original subunit levels or of the transformed and normalized variables, we were struck by the fact that *NCKAP1* and *CYFIP2* had opposite coefficients for the association with MFS. Indeed, high levels of *NCKAP1* were associated with poor MFS, whereas high levels of *CYFIP2* were associated with good MFS (Fig.S1).

Using transformed and normalized variables, we were able to perform a multivariate Cox analysis to analyze the association of each of the 36 possible WAVE complexes with MFS (Fig.S1). We sorted the 36 WAVE complexes according to increasing p-values. The 18 best combinations all contained NCKAP1 as the NAP subunit, while the best 9 combinations also contained CYFIP2 as the CYFIP subunit, suggesting that NCKAP1 is the first order predictor, whereas CYFIP2 is the second order predictor in our cohort. The multivariate Cox analysis does not suggest a specific WAVE assembly that would be particularly associated with MFS, what seems to matter is whether the assembly contains NCKAP1 and/or CYFIP2. Computer simulations using random permutations of values confirmed that the prediction powers of NCKAP1 and CYFIP2 cannot be attributed to chance (Fig.S1).

We then evaluated further multivariate Cox models by adding up to 5 variables using NCKAP1, CYFIP2, WASF3 and ABI2 and BRK1 subunits in this order. The log-likelihood criterium increased when more subunits were introduced, but the log-likelihood always increases when further variables are added. Therefore, we compared the models using Bayesian Information Criteria (BIC). BIC introduces a penalty term for the number of variables used in the model to avoid overfitting. The model with 2 variables, NCKAP1 and CYFIP2, had the smallest BIC (Fig.S1) and thus appeared as the optimal model of MFS in our cohort. MFS over time can be accurately predicted from mRNA levels of *NCKAP1* and *CYFIP2*. In our optimal model, *NCKAP1* is a first order predictor with a p-value of 0.001, whereas *CYFIP2* is the second order predictor with a p-value of 0.012. Importantly, in this multivariate model, as in the initial univariate models, *NCKAP1* and *CYFIP2* have opposite coefficients, indicating that up-regulation of *NCKAP1*, but down-regulation of *CYFIP2*, are associated with poor prognosis. In the model, the higher the *CYFIP2* value, the better the MFS, for a given value of *NCKAP1*. To illustrate how the second order predictor *CYFIP2* modulates the MFS, we ran the model with expression levels found in patient tumors populating the outskirts of the distribution (Fig.1A). The extreme values of *NCKAP1* dominate the predicted MFS when *CYFIP2* values are

intermediate (Fig.1B). In contrast, extreme values of *CYFIP2* significantly oppose the effect of *NCKAP1*, when *NCKAP1* values are not extreme.

To validate the prediction of our statistical model that NCKAP1 and CYFIP2 control MFS, we used a public database of breast cancer patients, where the transcriptome of more than 3900 tumors, was analyzed by Affymetrix chips [22]. Given the large number of patients, more genes encoding WAVE complex subunits were significantly associated with relapse-free survival (RFS) than in our cohort containing slightly more than 500 patients. However, the two most strongly associated ones were *NCKAP1* and *CYFIP2*, as in our analyses. As our model predicted, high levels of NCKAP1 were associated with poor RFS, whereas high levels of CYFIP2 were associated with good RFS (Fig.1C). All these results together indicate that CYFIP2 should have a function at odds with the major function of WAVE complexes, that is to promote cell migration [4].

The WAVE complex subunit CYFIP2 inhibits the migration of mammary carcinoma cells

Since the expression of WAVE subunits CYFIP2 and NCKAP1 are associated with opposite prognoses in breast cancer patients, we sought to compare their function in mammary carcinoma cells. Moreover, we compared the two paralogous subunits CYFIP1 and CYFIP2 in two classical breast cancer cell lines, MCF7, which is HR+ ERBB2-, and MDA-MB-231, which is HR- ERBB2- (triple negative).

Depletion of the different subunits using RNAi had different impact on WAVE complex levels. Indeed, WAVE complexes are stable when fully assembled, providing an explanation as to why depletion of a subunit usually destabilizes the multiprotein complex it should be part of [9]. Depletion of NCKAP1 in MCF7 cells leads to a severe downregulation of WAVE complex subunits, including CYFIP1 and CYFIP2 (Fig.2A). This result shows a key role of NCKAP1 for the stability of CYFIP1- and CYFIP2-containing WAVE complexes in cells. Depletion of CYFIP1 leads to a significant destabilization of the WAVE complex, which can be appreciated on NCKAP1, WAVE2 and BRK1 levels. In contrast, depletion of CYFIP2 does not lead to a visible depletion of the same subunits. Since MCF7 cells have conserved their epithelial organisation, we assessed cell migration in a wound healing assay. CYFIP1 or NCKAP1 depleted cells failed to close the wound before 78-81h compared to 30 h for control cells (Fig. 2A and Movie S1). In sharp contrast, CYFIP2 depleted cells were not impaired in their ability to close the wound and were in fact significantly faster than controls (20 h vs. 30 h).

We then turned to MDA-MB-231 cells, which displayed the same overall pattern of subunit expression upon depletion of NCKAP1 or CYFIP1/2 as MCF7 cells (Fig.2B). Briefly, WAVE complexes were destabilized upon NCKAP1 or CYFIP1 depletion, but not upon CYFIP2 depletion. We thus decided to measure levels of CYFIP1 and 2 using purified CYFIP1- or CYFIP2-containing WAVE complexes as standards, serial dilutions and Western blots in their linear range (Fig.S2). We found that MDA-MB-231 express roughly 6-times more CYFIP1 than CYFIP2 (Fig.2C), providing a first level of explanation as to why CYFIP1 depletion affects more the stability of other subunits than CYFIP2. However, this was not the

only effect, since the depletion of each CYFIP protein resulted in approximately 50 % up-regulation of its remaining CYFIP paralog. These up-regulations of the paralogous CYFIP proteins were not observed at the mRNA level and might represent stabilization of CYFIP subunits with other WAVE complex subunits when the paralogous CYFIP protein is not expressed (Fig.S3).

We first evaluated in the Transwell assay the migration of MDA-MB-231 cells when CYFIP1, 2, or NCKAP1 were depleted using pools of siRNAs. Depletion of NCKAP1 and CYFIP1 significantly decreased the number of cells able to migrate through the filter, whereas the depletion of CYFIP2 had the converse effect (Fig.2D). The effect of transient siRNA-mediated depletions was confirmed using stable MDA-MB-231 lines expressing either a shRNA targeting NCKAP1 or CYFIP2 [5](Fig.S4). We then attempted to obtain stable MDA-MB-231 lines overexpressing NCKAP1 or CYFIP2. We obtained lines expressing GFP-tagged CYFIP2, but repeatedly failed in obtaining clones expressing NCKAP1 in parallel selection schemes. The overexpression of CYFIP2 slightly decreased cell migration in the Transwell assay, whereas CYFIP2 depletion increased it (Fig.S4). Loss- and gain-of function of CYFIP2 thus yield opposite phenotypes.

MDA-MB-231 cells are mesenchymal, unlike epithelial MCF7 cells. Nonetheless, in a wound healing assay, CYFIP2 depleted MDA-MB-231 closed the wound faster than controls, and MDA-MB-231 cells depleted of NCKAP1 and CYFIP1 were significantly delayed in doing so (Fig.S4), exactly as we had observed in MCF7 cells. We then turned to a more physiopathological assay for MDA-MB-231. We seeded isolated MDA-MB-231 cells in 3D gels of collagen type I. In these settings, mimicking invasion of the mesenchyme, differences in cell migration were more dramatic (Fig. 2E). NCKAP1 depleted cells hardly migrated at all, as evidenced by strongly decreased Mean Squared Displacement (MSD), mostly due to reduced speed. NCKAP1 depleted cells ended up entering into apoptosis during the first 24 h (Movie S2). CYFIP1 depleted cells were not significantly affected in their ability to migrate, even though they also appeared prone to die in these settings. CYFIP1 and NCKAP1 depleted cells formed significantly fewer protrusions than controls (Fig.2E). In contrast, CYFIP2 depleted cells often explored a significantly larger territory than controls. The increased MSD of CYFIP2 depleted cells could be accounted for by the dramatically increased migration persistence. The protrusive activity of CYFIP2 depleted cells was significantly increased compared to controls. Finally, CYFIP2 depleted cells had no issue of survival in 3D collagen, unlike cells depleted of NCKAP1 or CYFIP1.

In conclusion, in all the assays performed with the two breast cancer cell lines, the opposite roles of NCKAP1 and CYFIP2 were consistently observed and in line with their association with their prognostic roles in the metastasis-free survival of breast cancer patients.

CYFIP2 inhibits cell migration of untransformed cells

We wondered if the anti-migratory role of CYFIP2 was its normal function or rather associated with cell transformation. To address this question, we used the immortalized, but not transformed, MCF10A mammary cell line. MCF10A expressed approximately 6-fold more CYFIP1 than CYFIP2 (Fig.3A). CYFIP2 is thus less abundant than CYFIP1 in two cell lines, MCF10A and MDA-MB-231. As in MDA-MB-231, siRNA-mediated depletion of NCKAP1 and CYFIP1 from MCF10A cells significantly decreased protein levels of WAVE complex subunits, but not their mRNA levels (Fig.3B, Fig.S3), whereas CYFIP2 depletion did not affect the overall stability of WAVE complexes.

MCF10A cells are more epithelial than MDA-MB-231 cells. They establish cell-cell junctions and form epithelial islets. However, they are plastic epithelial cells. In 2D cultures, in their regular culture medium, which contains EGF, MCF10A cells display cell-cell junctions, but also frequently migrate as single cells. We depleted MCF10A cells with siRNA pools targeting either NCKAP1, CYFIP1 or CYFIP2. Cells depleted of NCKAP1 appeared as small and organized as a tight epithelium, whereas the cells depleted of CYFIP2 appeared larger with membrane protrusions, even if they remained associated with one another (Fig.3B, Movie S3). CYFIP1 depletion did not have a pronounced effect on cell morphology. We then recorded MCF10A cells to analyze cell migration. Trajectories corresponding to single cells were plotted (Fig.3C). NCKAP1 depleted single cells migrated much less than controls, an effect which was mostly due to decreased cell speed. In contrast, CYFIP2 depleted cells did not explore a wider territory than controls, nor did they migrate faster, but they significantly increased migration persistence. Importantly, same results were obtained with two single siRNA sequences for each gene (Fig.S5), indicating that these results were not due to off-targets. Such a phenotype, characterized by increased migration persistence of single MCF10A cells, was previously observed upon activation of RAC1 or upon depletion of the Arp2/3 inhibitory protein ARPIN [23].

To study differentiation of acini in Matrigel, we isolated *CYFIP2* knock-out (KO) clones using CRISPR-Cas9. From about 100 independent MCF10A clones, we selected two CYFIP2 negative clones, which turned out to be KO on both alleles due to insertions/deletions changing the ORF (Fig.S6A). As expected, *CYFIP2* KO clones displayed increased migration persistence (Fig.S6BC). The initial KO of CYFIP2 led to an increase of the level of WAVE complex subunits, as previously shown for siRNA assays, but this effect disappeared in long-term cultures (Fig.S6DE). The differentiation of *CYFIP2* KO clones was then assayed in Matrigel, where MCF10A cells develop acini structures. *CYFIP2* inactivation did not affect the morphogenetic program, nor cell polarity, but resulted in significantly larger 3D structures containing more cells than the control (Fig.3D). Similar results were previously obtained when ARPIN was inactivated [23]. CYFIP2 thus behaves like this well-established inhibitory protein of cell migration, ARPIN. This result on acini structures is consistent with the fact that the RAC1-WAVE-Arp2/3 pathway controls cell cycle progression [23].

To validate the anti-migratory function of CYFIP2 in a physiological system and to test whether this function is specific to breast cells or more general, we turned to the zebrafish embryo, and in particular to prechordal plate cells, which stereotypically migrate during

gastrulation [24,25]. Prechordal plate cells migrate from the fish organizer (shield) to the animal pole of the embryo by forming actin-rich protrusions. These RAC1 dependent protrusions are the 3D equivalents of 2D lamellipodia and are easily distinguished from thin, filopodia-like extensions [26,27]. We assessed the function of CYFIP1, CYFIP2 and NCKAP1 using both morpholino-mediated loss-of-function and mRNA over-expression.

We first analyzed prechordal plate cell trajectories, in embryos injected with morpholino and/or mRNA for CYFIP1, CYFIP2 and NCKAP1 (Fig.4A). Experiments were performed in a goosecoid:GFP transgenic line, allowing easy identification of prechordal plate cells. Nuclei were labelled by expression of a Histone2B–mCherry construct, the cells were tracked (Movie S5), and cell trajectories were plotted. Similar to what was observed using human cell lines, CYFIP2 depletion increased migration persistence as compared to injection of a control morpholino. This effect was rescued by co-injection of a morpholino-insensitive CYFIP2 mRNA, demonstrating the specificity of the phenotype. Consistently, overexpression of CYFIP2, i.e. injection of the same amount of mRNA as for the rescue but without the corresponding morpholino, decreased cell persistence. In contrast to CYFIP2, downregulation of CYFIP1 or NCKAP1 reduced cell persistence, both effects being rescued by the co-injection of the corresponding mRNAs.

We then used cell transplants to look for cell autonomous defects and analyzed cell dynamics and protrusivity. Few prechordal plate cells from a donor embryo injected with morpholino and/or mRNA were transplanted to the prechordal plate of an uninjected host embryo (Fig.4B). Actin-rich protrusions were highlighted by the enrichment of the LifeAct-mCherry marker (Fig.4B, Movie S6). CYFIP2 depletion doubled the number of protrusions compared to cells injected with a control morpholino (Fig.4B). This effect was rescued by a morpholino-insensitive CYFIP2 mRNA. Consistently, CYFIP2 overexpression decreased the number of protrusions, much like the depletion of NCKAP1 and CYFIP1. CYFIP2 depletion also significantly and specifically increased protrusion length (Fig.4B).

The results using zebrafish embryos are thus perfectly in line with those obtained in human breast cells and demonstrate that the unexpected anti-migratory function of CYFIP2 is a general and conserved function of this subunit, at least across vertebrates.

CYFIP2 rescues lamellipodium formation in *CYFIP1/2* double KO cells

To examine whether CYFIP2 was a functional subunit of the WAVE complex, we re-expressed CYFIP2 in B16-F1 *CYFIP1/2* double knock-out cells (DKO) [28]. GFP-CYFIP2 clearly rescued lamellipodium formation in DKO cells, like GFP-CYFIP1, even if CYFIP1 appeared to induce more prominent lamellipodia than CYFIP2 (Fig.5AB, movie S6). We also analyzed two point mutations of CYFIP2, R87C and I664M, that are recurring mutations found in patients affected by intellectual disability [29]. These two point mutations did not impair the ability of CYFIP2 to induce lamellipodia. On the opposite, the mutations seemed to induce more prominent lamellipodia (movie S7).

We quantitatively analyzed the effect of CYFIP2 and of its mutated derivatives on protrusions using line scans. The expression of CYFIP2 was unable to restore the full speed of

protrusions observed in parental B16-F1 cells or in CYFIP1-rescued DKO cells (Fig.5C). R87C and I664M mutations rendered CYFIP2 significantly more efficient at rescuing the protrusion rate, up to the level of parental or CYFIP1 reconstituted cells. We then analyzed the width of lamellipodia, using immunofluorescence of the ARPC2 subunit of the Arp2/3 complex and of cortactin, a protein that stabilizes the Arp2/3 at the branched junction between filaments [4]. In line with their faster protrusions, CYFIP1, R87C and I664M CYFIP2 induced lamellipodia deeper into the cell than wild type CYFIP2 (Fig.5DE). So CYFIP2 is a functional CYFIP protein, but less active than CYFIP1, and point mutations that induce developmental defects in patients alleviate this restrained activity of CYFIP2.

CYFIP2 containing WAVE complexes are poorly activated by active RAC1

CYFIP2 is 88 % identical to CYFIP1. So we replaced CYFIP1 with CYFIP2 in the molecular model of the WAVE complex derived from crystallography of a reconstitued complex containing a WAVE1 form lacking the central proline-rich region and a truncated ABI2 lacking the the disordered C-terminus [30]. We mapped on this model the WIRS binding site that allows the WAVE complex to interact with various transmembrane receptors [31]. None of these binding sites was affected by the substitutions in CYFIP2 (Fig.6A). Consistently, we observed by ultracentrifugation on sucrose gradients that CYFIP2 was incorporated into the native WAVE complex, which sediments at around 11 Swedbergs (Fig.6B)[32]. Two binding sites exist for active RAC1 at the surface of the WAVE complex: the so-called A site, which shares structural homology with the CYRI-B protein [33,34], and the D site [35]. None of the RAC1 binding sites was affected by substitutions in CYFIP2. To examine the binding to RAC1 and activation by RAC1, we reconstituted a WAVE complex with either CYFIP1 or CYFIP2 using a previously described procedure [36]. Both complexes interacted equally well with GTP-bound RAC1 (Fig.6C and D). In pyrene-actin polymerization assays, however, the CYFIP2-containing WAVE complex was poorly activated by RAC1 compared to the CYFIP1-containing WAVE complex (Fig.6E). These in vitro data are thus consistent with the observation that in cells CYFIP2 promotes lamellipodium formation, but not as well as CYFIP1.

DISCUSSION

Here we have systematically analyzed the expression levels of WAVE complex subunits in a cohort of breast cancer patients. *Ad hoc* statistical modeling, taking into account assembly rules among paralogous subunits, increased the statistical power of the analysis and revealed the unique role of the CYFIP2 subunit, whose overexpression is associated with good prognosis for metastasis-free survival. These findings were validated using an independent cohort of breast cancer patients available in public databases. *CYFIP2* had previously been implicated in pathologies, since it is mutated in children affected with intellectual disability and epileptic encephalopathy [37,38]. In zebrafish, CYFIP2 loss-of-function mutations result in defective axonal pathfinding in retinal ganglion cells [39]. This function of CYFIP2 is also not redundant with the one of the paralogous subunit, CYFIP1, which is involved in axon growth [40].

We have experimentally validated the prediction of our model, which implies a protective role of CYFIP2 overexpression in breast cancer. CYFIP2 is at odds with other subunits, since it is the first subunit of the WAVE complex that is ever reported to oppose cell migration. Indeed, we found that CYFIP2 opposes cell migration in a variety of cell systems, MCF10A, MDA-MB-231 and prechordal plate cells from the zebrafish embryo. In these experiments, CYFIP2 depletion enhances cell migration, whereas CYFIP2 overexpression decreases cell migration. We were struck by this anti-migratory role of CYFIP2, which to our knowledge was never reported before, even if depletion of different subunits of the WAVE complex did not always give the same phenotype [41–45].

In all cell systems we studied here, the main parameter that CYFIP2 controls is migration persistence, which relates to the persistence of lamellipodial protrusions [8]. In fact, the role of CYFIP2 is very similar to the Arp2/3 inhibitory protein Arpin that directly inhibits the Arp2/3 complex at the leading edge [46]. In neuronal growth cones, CYFIP2 was found to localize at the tip of filopodia, structures composed of linear actin and not of branched actin [40], in line with an inhibitory function of CYFIP2 on branched actin formation we suggest here.

CYFIP2 is highly related to CYFIP1, with 88 % identity. Both CYFIP proteins incorporate into WAVE complexes [47–49]. Accordingly, we found here that CYFIP2 depends on NCKAP1 for its stability, like CYFIP1 and that CYFIP2 is found into the same WAVE complex migrating at 11 Swedbergs as CYFIP1. Importantly, the residues of CYFIP1 that are involved in binding active RAC1 are all conserved in CYFIP2. However, we found that CYFIP2-containing WAVE complexes were less activatable by active RAC1 than CYFIP1-containing WAVE complexes. This property accounts for the observed phenotypes. Indeed, depletion of CYFIP2 can render available more active RAC1 to activate more CYFIP1-containing WAVE complexes, which are easily activatable (Fig.6F).

Another effect is expected to increase migration upon CYFIP2 depletion and to decrease it upon CYFIP1 depletion. In RNAi experiments, CYFIP1-depleted cells were found to overexpress CYFIP2, whereas CYFIP2-depleted cells were found to overexpress CYFIP1. This compensatory expression of the paralogous CYFIP was marginally observed at the mRNA level in some cases and more significantly at the protein level, suggesting that CYFIP proteins might be stabilized by the availability of partner subunits [9]. However, this compensatory expression of CYFIP1 is lost over time in the *CYFIP2* KO clones that we isolated from MCF10A cells, while enhanced migration persistence of *CYFIP2* KO clones is sustained, strongly suggesting that this effect has a minor contribution compared to the poor activation of CYFIP2-containing complexes by active RAC1.

This modulation of phenotypes based on subunit composition of complexes was previously described for the Arp2/3 complex [50]. The paralogous subunits ARPC1B and ARPC5L assemble Arp2/3 complexes, which are more activatable than the ones assembled around ARPC1A and ARPC5. The situation is perfectly analogous to the one described here for the WAVE complex assembled with CYFIP1 and CYFIP2 paralogous subunits. Vertebrate genomes encoding paralogous subunits for many stable multiprotein complexes thus offer numerous opportunities to fine tune cellular responses. The two examples of WAVE and Arp2/3 complexes illustrate that each cell of a vertebrate organism can regulate levels of cortical

branched actin, polymerized in response to signaling inputs, based on the expression of the paralogous genes that regulate the "activatability" of these molecular machines.

METHODS

Patient cohort for mRNA analysis

All patients (mean age 60.9 years, range 29-91 years) met the following criteria: primary unilateral nonmetastatic breast carcinoma for which complete clinical, histological and biological data were available; no radiotherapy or chemotherapy before surgery; and full follow-up at Institut Curie - Hospital René Huguenin. All patients before 2007 were informed that their tumor samples might be used for scientific purposes and had the opportunity to decline. Since 2007, patients treated in our institution have given their approval by signed informed consent. This study was approved by the local ethics committee (Breast Group of René Huguenin Hospital). Treatment (information available for 524 patients) consisted of modified radical mastectomy in 320 cases (61%) or breast-conserving surgery plus locoregional radiotherapy in 204 cases (39%). The patients had a physical examination and routine chest radiotherapy every 3 months for 2 years, then annually. Mammograms were done annually. Adjuvant therapy was administered to 416 patients, consisting of chemotherapy alone in 130 cases, hormone therapy alone in 178 cases and both treatments in 108 cases. During a median follow-up of 10.5 years (range 1 month to 36.3 years), 210 patients developed metastasis. Sixteen specimens of adjacent normal breast tissue from breast cancer patients or normal breast tissue from women undergoing cosmetic breast surgery were used as sources of normal RNA.

qRT-PCR

Specific mRNAs were quantified from the cycle number (Ct value) at which the increase in the fluorescence signal started to be detected by the laser detector of the ABI Prism 7900 sequence detection system (Perkin-Elmer Applied Biosystems, Foster City, CA) as previously described [52]. Specific transcripts were quantified using the following primers: WASF1-U (5'-CCTCTCATTTTGAAACAAGACCTCAG-3') and WASF1-L (5'-CTAAATGGCAAGGCAGAAAGTGAGT-3') for the *WASF1* gene (PCR product of 79 pb); WASF2-U (5'- AAAGCTGGGGACTTCTGGGTATC-3') and WASF2-L (5'-GTGAAGAAGCAGAGTCTGACTGTGGT-3') for the *WASF2* gene (PCR product of 122 pb); WASF3-U (5'- GAGTGATAAGCCACCGCCTCTG-3') and WASF3-L (5'-GCCCATCCTTCTTGTCATCTCTGTA-3') for the *WASF3* gene (PCR product of 62 pb); ABI1-U (5'-GGGGAACACTGGGACGGAAT-3') and ABI1-L (5'-GCTGTCCTGCCTGGACTATGCT-3') for the *ABI1* gene (PCR product of 124 pb); ABI2-U (5'-CCGTGGGCTCCACGTTCTTACT-3') and ABI2-L (5'-TCCTTCCTGAAAGGACAGCTCATCT-3') for the *ABI2* gene (PCR product of 90 pb); ABI3-U (5'-TGCTGCGGGTCGCTGACTA-3') and ABI3-L (5'-

GCGCCTTCCGCTTGTCTGT-3') for the *ABI3* gene (PCR product of 63 pb); BRK1-U (5'-AAAATCGCAGACTTTCTCAACTCGT-3') and BRK1-L (5'-TTCAAGGGCTGTCAATTTCTCGT-3') for the *BRK1* gene (PCR product of 84 pb); NCKAP1-U (5'-AGTGTACCCTTAGTGACCAGTTGCT-3') and NCKAP1-L (5'-TCAGGTTCCCCTTTCTTACCAGT-3') for the *NCKAP1* gene (PCR product of 106 pb); NCKAP1L-U (5'- GAAAAGTCCATGGAACCATCTCTCA-3') and NCKAP1L-L (5'-GTACTGGTCCTAAATGTTGCGTGCT-3') for the *NCKAP1L* gene (PCR product of 91 pb); CYFIP1-U (5'-CACGAGTACGGCTCTCCTGGTATC-3') and CYFIP1-L (5'-CCGCAGGTTCTGGAAGCACA-3') for the *CYFIP1* gene (PCR product of 102pb); CYFIP2-U (5'-CCCACGTCATGGAGGTGTACTCT-3') and CYFIP2-L (5'-TAATTGTAGCGTGTGGCTCTCTCA-3') for the *CYFIP2* gene (PCR product of 112pb); TBP-U (5'-TGCACAGGAGCCAAGAGTGAA-3') and TBP-L (5'-CACATCACAGCTCCCCACCA-3') for the *TBP* gene (PCR product of 132 bp), which was the reference gene used for normalization. Over and under-expression were defined as >3 and <0.33, respectively, the expression compared to the median expression of normal samples.

Public transcriptomics data on breast cancer [22] were interrogated using the kmplot website (http://kmplot.com) on June 26, 2019 using best cut-offs for JetSet determined best probes (*NCKAP1* 207738_s_at, *CYFIP2* 220999_s_at, [51].

Cell lines, transfection and establishment of stable clones

MCF10A cells were grown in DMEM/F12 medium supplemented with 5% horse serum, 20 ng/mL epidermal growth factor, 10 µg/mL insulin, 500 ng/mL hydrocortisone, and 100 ng/mL cholera toxin. MDA-MB-231 were grown in DMEM medium with 10% FBS. Medium and supplements were from Life Technologies and Sigma. Cells were incubated at 37°C in 5% CO_2. MCF10A and MDA-MB-231 were from the collection of breast cell lines organized by Thierry Dubois (Institut Curie, Paris).

Stable MCF10A cells expressing CYFIP2 were obtained by transfecting MCF10A cells, with the home-made plasmid MXS AAVS1L SA2A Puro bGHpA EF1Flag GFP CYFIP2 Sv40pA AAVS1R, or MXS AAVS1L SA2A Puro bGHpA EF1Flag GFP Blue Sv40pA AAVS1R as a control. Transfection was performed with Lipofectamine 2000 (Invitrogen). To obtain stable integration of the MXS plasmid at the AAVS1 site, cells were cotransfected with two TALEN plasmids inducing DNA double strand breaks at the AAVS1 locus (Addgene #59025 and 59026; [52]. Cells were selected with 1 µg/mL puromycine (Invivogen) and pooled. Stable MCF10A cells expressing shRNA were obtained by transfection with previously described pSUPER-Retro-Puro plasmids [5] and puromycin selection.

The stable 293 Flp-In cell line expressing Flag-HA-CYFIP1 were previously described [53]. An equivalent cell line expressing Flag-HA-CYFIP2 was obtained according to a published procedure[54].

MDA-MB-231 and MCF10A were depleted by siRNAs (OnTarget Smart Pools, Dharmacon), transfected at 20 nM final concentration using Lipofectamine RNAiMAX (Invitrogen), and re-

transfected 72h later, for the total of 6 days. This protocol was necessary due to an unusually long half-life of CYFIP2 protein (AP, unpublished observations).

The MCF10A CYFIP2 knockout cell line was generated with CRISPR/Cas9 system. The targeting sequence 5'-CAUUUGUCACGGGCAUUGCA-3' was used to induce the double strand break. For the negative control the non-targeting sequence 5'-AAAUGUGAGAUCAGAGUAAU-3' was used. Cells were transfected with crRNA:trackRNA duplex and the purified Cas9 protein by Lipofectamine CRISPRMAX™ Cas9 Transfection Reagent (all reagents from Thermofisher Scientific). The next day, cells were subjected to dilution at 0.8 cells/well in 96 well plates. Single clones were expanded and analyzed by CYFIP2 Western blot. 2 positive clones were identified. The PCR products amplified from genomic DNA containing the gRNA recognition site were then cloned (Zero Blunt PCR Cloning Kit, Thermofisher Scientific) and sequenced. A frameshift of +1 and a -1 in the 3rd exon of the CYFIP2 gene in both clones was confirmed by sequencing (see Fig. S6 for details).

Antibodies and Western blot

Cells were lysed in RIPA buffer and analyzed by Western blot. SDS-PAGE was performed using NuPAGE 4-12% Bis-Tris and 3-8% Tris-Acetate gels (Life Technologies). Nitrocellulose membranes were developed with horseradish peroxidase (HRP) coupled antibodies (Sigma) and SuperSignal West Femto chemiluminescent substrate (Thermo Fisher Scientific). Home-made rabbit polyclonal antibodies CYFIP1, ABI1, WAVE2 were previously described [32]. The mouse monoclonal antibody, 231H9, targeting BRK1 was previously described [55]. The antibodies targeting CYFIP-2 (Sigma SAB2701081), NCKAP1 (Bethyl A305-178A), cortactin (Millipore 4F11), ARPC2 (Millipore 07-227) and tubulin (Sigma T9026) were purchased. Quantification of wb was performed by densitometry, using the ImageJ software.

Sucrose gradient

For sucrose gradient analysis of WAVE subunits, Nitrogen cavitation (Parr instruments, 500 Psi for 20 min) followed by centrifugation (16,000 × g, 20 min) and ultracentrifugation (150,000 × g, 60 min) were used to prepare cytosolic extracts from cells trypsinized from two 15 cm dishes and resuspended in the XB buffer (20 mM HEPES, 100mM NaCl, 1mM MgCl2, 0.1 mM EDTA, 1mM DTT, pH 7.7). 200 µL of extract was loaded on the 11 mL 5–20% sucrose gradient in the XB buffer and subjected to ultracentrifugation for 17 h at 197,000 ×g in the swinging bucket rotor SW41 Ti (Beckman). 0.5 mL fractions were collected and concentrated by using trichloroacetic acid precipitation with insulin as a carrier. The samples were washed with acetone, dried and then resuspended in the 1x LDS loading buffer with 2.5% of β-ME for Western blot analysis.

Migration assays

Transwell migration assays were performed using FluoroBlok inserts with 8 µm holes (Corning, 351152), covered with 20 µg/ml fibronectin (Sigma, F1141). MDA-MB-231 cells

were plated in serum-free medium and allowed to migrate towards serum-containing medium for 16 h, incubated with 4 µg/ml calcein AM (Sigma, C1359) for 1 h, and images of fluorescent cells were acquired and quantified using ImageJ software.

2D migration was performed using 8 chamber Ibidi dishes (Biovalley 80826) covered with 20 µg/ml fibronectin. 3D migration was performed in 2 mg/ml collagen gel polymerized at 37°C (rat tail collagen type I, Corning 354263), with the cells sandwiched between the two layers of collagen. An inverted Axio Observer microscope (Zeiss) equipped with a Pecon Zeiss incubator XL multi S1 RED LS (Heating Unit XL S, Temp module, CO_2 module, Heating Insert PS and CO_2 cover), a definite focus module and a Hamamatsu camera C10600 Orca-R2 was used to perform videomicroscopy. Pictures were taken every 5 min for 24 h for 2D migration, and every 20 min for 48 h for 3D migration. Random migration of single cells and migration persistence, based on the angular shift between frames, was analyzed as previously described [46] using DiPer programs [56].

Rescue of DKO cells

B16-F1 mouse melanoma cells that are *CYFIP1/2* double KO were a kind gift of Klemens Rottner (Helmholtz-Zentrum für Infektionsforschung, Braunschweig). GFP-tagged human CYFIP1 or CYFIP2 (wild type or mutant) were transiently transfected into the DKO cells, and 48 h later, 10-minute videos (images taken every 10 seconds) were acquired using a confocal laser scanning microscope (TCS SP8, Leica) equipped with a high NA oil immersion objective (HC PL APO 63×/ 1.40, Leica), a white light laser (WLL, Leica) and controlled by the LasX software. Protrusion speed was measured using the Multi Kymograph tool in ImageJ software. For the LineScan analysis, images of fixed, stained cells were obtained, and analyzed as described in [46] and [23].

Zebrafish embryos, cell transplantation and imaging

Embryos were obtained by natural spawning of *Tg(-1.8gsc:GFP)ml1* adult fishes [57]. All animal studies were done in accordance with the guidelines issued by the Ministère de l'Education Nationale, de l'Enseignement Supérieur et de la Recherche and were approved by the Direction Départementale des Services Vétérinaires de l'Essonne and the Ethical Committee N°59.

Translation blocking morpholinos (Gene Tool LLC Philomath) were designed against zebrafish *CYFIP1* (AAAAACTATCCGCTTCGACTGTTCA) and *CYFIP2* (CGACACAGGTTCACTCACAAAACAG). The *NCKAP1* morpholino (CCGAGACATGGCTCAAACGACCGTC) was described in [58]. The control morpholino is a standard control (CCTCTTACCTCAGTTACAATTTATA). mRNAs were synthesized using pCS2+ plasmids containing the human genes described in [32] and the mMessage mMachine SP6 kit (Thermo Fischer).

For cell migration quantification, embryos were injected at the one-cell stage with 1.5 nl of a solution containing Histone2B-mCherry mRNA (30 ng/µl) and either control morpholino (0.1, 0.2 or 0.8mM), MoCYFIP1 (0.2mM), MoCYFIP2 (0.1mM) or MoNCKAP1 (0.8mM), with or

without mRNAs encoding either human CYFIP1 (10ng/µl), human CYFIP2 (10ng/µl) or human NCKAP1 (10ng/µl). Injected embryos were mounted in 0.2% agarose in embryo medium and imaged between 60% and 80% epiboly (6.5-8.5 hpf) under an upright TriM Scope II (La Vision Biotech) two photon microscope equipped with an environmental chamber (okolab) at 28°C using a 25x water immersion objective. Visualization of 3D movies and nuclei tracking were done using Imaris (Bitplane). Cell migration parameters were extracted using custom Matlab (Math Works) code and autocorrelation was computed using published Excel macros [56].

For protrusion analysis, embryos were injected in one cell at the four-cell stage with 1.5 nl of a solution containing Lifeact-mCherry mRNA (50 ng/µl) and either control morpholino (0.5 mM), MoCYFIP1 (0.2mM), MoCYFIP2 (0.1mM) or MoNCKAP1 (0.8mM), with or without mRNAs encoding either human CYFIP1 (10ng/µl), human CYFIP2 (10ng/µl) or human NCKAP1 (10ng/µl). Small cell groups were transplanted at shield stage (6 hpf) from the shield of an injected embryo to the shield of an untreated host. Embryos were then cultured in embryo medium [59] with 10 U/mL penicillin and 10 µg/mL streptomycin. Transplanted embryos were mounted in 0.2% agarose in embryo medium and imaged between 60% and 80% epiboly (6.5-8.5 hpf) under an inverted TCS SP8 confocal microscope equipped with environmental chamber (Leica) at 28°C using a HC PL APO 40x/1.10 W CS2 objective. Visualization of images was done on ImageJ, lamellipodia-like actin rich protrusions being quantified on the basis of morphological criteria as described in [26].

Reconstitution of WAVE complexes and in vitro assays

Recombinant WAVE complexes containing full-length human CYFIP1 or CYFIP2, full-length NCKAP1, full-length BRK1, ABI2 (1-158) and WAVE1 (1-230)-$(GGS)_6$-WCA (485-559), referred to as WRC230WCA were purified as previously described [35,36]. CYFIP1- and CYFIP2-containing WAVE complexes behaved similarly during expression and purification by various chromatographic steps. Other proteins, including the Arp2/3 complex, actin, WAVE1 WCA, Tev, GST-RAC1 (Q61L P29S, 1-188), and untagged RAC1 (Q61L P29S, 1-188) were purified as previously described [35].

GST pull-down experiments were performed as previously described [35]. Briefly, 200 pmol of GST-RAC1 and 200 pmol of WAVE complex were mixed with 20 µL of Glutathione Sepharose beads (GE Healthcare) in 1 mL of binding buffer (10 mM HEPES pH 7, 50 or 100 mM NaCl, 5% (w/v) glycerol, 2 mM $MgCl_2$, 1 mM DTT, and 0.05% Triton X100) at 4 °C for 30 min, followed by three washes using 1 mL of the binding buffer in each wash. Finally, the bound proteins were eluted with GST elution buffer (100 mM Tris-HCl pH 8.5, 30 mM reduced glutathione, and 2 mM $MgCl_2$) and examined on SDS-PAGE gels.

GST equilibrium pull-down assays were performed in the EPD buffer (10 mM HEPES pH 7, 50 mM NaCl, 5% (w/v) glycerol, 2 mM $MgCl_2$, and 1 mM DTT) as previous described (Chen et al., 2017). Essentially, each 100 µL of reaction contained 0.1 µM WRC230WCA, varying concentrations of GST-Rac1(Q61L P29S, 1-188), 30 µL of the Glutathione Sepharose beads, and 0.05% Triton X100. All protein samples and beads were first dialyzed or equilibrated in the EPD buffer prior to use. After gentle mixing at 4°C for 30 min, the beads were pelleted by a brief centrifugation, and the supernatant was immediately transferred to SDS loading buffer

and analyzed by Coomassie blue-stained SDS-PAGE gels. Total intensity of the CYFIP1/2 and NCKAP1 bands was quantified by ImageJ to determine the unbound WAVE complex. The derived fractional occupancy from several independent experiments was pooled and globally fitted to obtain the binding isotherms and the apparent dissociation constants K_D.

Actin polymerization assays were performed as previously described [35] with slight modifications. Each reaction (120 µL) contained 4 µM actin (5% pyrene labeled), 10 nM Arp2/3 complex, 100 nM WRC230WCA or WAVE1 WCA, and desired concentration of untagged RAC1 (Q61L P29S, 1-188) in NMEH20GD buffer (50 mM NaCl, 1 mM $MgCl_2$, 1 mM EGTA, 10 mM HEPES pH7.0, 20% (w/v) glycerol, and 1 mM DTT). Pyrene-actin fluorescence was recorded every 5 seconds at 22 °C using a 96-well flat-bottom black plate (Greiner Bio-One™) in a Spark plater reader (Tecan), with excitation at 365 nm and emission at 407 nm (15 nm bandwidth for both wavelengths).

Statistical analyses

Patient cohort. Relationships with mRNA levels and clinical parameters were identified using the χ^2 test. Statistical analyses using univariate and multivariate Cox proportional hazard models were performed with the R computing environment (R Development Core Team, 2017). Codes are available upon request.

Migration persistence. Exponential decay and plateau fit ($y = (1 - b) * e^{-\frac{t}{a}} + b$) was performed for all individual cells. Coefficients were then compared using one-way ANOVA. Statistical analysis was performed in R using linear mixed-effect models to take into account the resampling of the same statistical unit.

Significance. Differences were considered significant at confidence levels greater than 95% ($p < 0.05$). Four levels of statistical significance were distinguished: *P<0.05; **P<0.01; ***P<0.001; ****P<0.0001.

Acknowledgements

We thank Nelia Cordeiro for technical support, Theresia Stradal for sharing shRNA plasmids targeting NCKAP1 and CYFIP2, Klemens Rottner for the *CYFIP1/2* DKO cells, and Chuang Yu for his help with statistical tools. This work was supported by grants from the Agence Nationale de la Recherche (ANR-15-CE13-0016-01 for AMG and NBD), from the fondation ARC pour la Recherche sur le Cancer (PGA120140200831 for AMG and IB and DOC20170505494 to NM), from National Institute of Health (grant R35 GM128786) to BC, from Institut National du Cancer (INCA_6521 for AMG and IB, and INCA_11508 for AMG, IB and ML). We thank the Polytechnique Bioimaging Facility for assistance with live imaging on their equipment partly supported by Région Ile-de-France (interDIM) and Agence Nationale de la Recherche (ANR-11-EQPX-0029 Morphoscope2, ANR-10-INBS-04 France BioImaging)

Conflict of interest

The authors declare no conflict of interest

Author contributions

AP performed *in vitro* experiments of cell migration and wrote the manuscript. AB and NBD performed *in vivo* experiments in zebrafish embryos. ML performed statistical modeling. SV, AS and IB performed qRT-PCR measurements of WAVE complex expression. NM constructed the integrative plasmid used to overexpress CYFIP2. NR quantified CYFIP1/2 protein expression in cell lines. AF and YW isolated the CYFIP2 knockout clones and performed experiments with these clones. YW performed the sucrose gradient experiments. RG performed the structural comparison of CYFIP1/2 proteins. SR performed the confocal microscopy of B16-F1 cells and helped with the data analysis. SY, YL, and BC reconstituted CYFIP1/2 containing WAVE complexes and performed RAC1 binding and pyrene actin assays. AMG supervised the study and wrote the manuscript. All authors have commented on the manuscript and approved the submission.

REFERENCES

1. Dehal, P., and Boore, J.L. (2005). Two Rounds of Whole Genome Duplication in the Ancestral Vertebrate. PLoS Biology *3*, e314-9.

2. Ruepp, A., Waegele, B., Lechner, M., Brauner, B., Dunger-Kaltenbach, I., Fobo, G., Frishman, G., Montrone, C., and Mewes, H.W. (2010). CORUM: the comprehensive resource of mammalian protein complexes--2009. Nucleic Acids Research *38*, D497-501.

3. Alberts, B. (1998). The cell as a collection of protein machines: preparing the next generation of molecular biologists. Cell *92*, 291–294.

4. Molinie, N., and Gautreau, A. (2018). The Arp2/3 Regulatory System and Its Deregulation in Cancer. Physiological Reviews *98*, 215–238.

5. Steffen, A., Rottner, K., Ehinger, J., Innocenti, M., Scita, G., Wehland, J., and Stradal, T.E.B. (2004). Sra-1 and Nap1 link Rac to actin assembly driving lamellipodia formation. The EMBO Journal *23*, 749–759.

6. Lai, F.P.L., Szczodrak, M., Block, J., Faix, J., Breitsprecher, D., Mannherz, H.G., Stradal, T.E.B., Dunn, G.A., Small, J.V., and Rottner, K. (2008). Arp2/3 complex interactions and actin network turnover in lamellipodia. The EMBO Journal *27*, 982–992.

7. Steffen, A., Koestler, S.A., and Rottner, K. (2014). Requirements for and consequences of Rac-dependent protrusion. European Journal of Cell Biology *93*, 184–193.

8. Krause, M., and Gautreau, A. (2014). Steering cell migration: lamellipodium dynamics and the regulation of directional persistence. Nature Reviews Mol Cell Biol *15*, 577–590.

9. Derivery, E., and Gautreau, A. (2010). Generation of branched actin networks: assembly and regulation of the N-WASP and WAVE molecular machines. BioEssays : news and reviews in molecular, cellular and developmental biology *32*, 119–131.

10. Dubielecka, P.M., Cui, P., Xiong, X., Hossain, S., Heck, S., Angelov, L., and Kotula, L. (2010). Differential Regulation of Macropinocytosis by Abi1/Hssh3bp1 Isoforms. PLoS ONE *5*, e10430.

11. Suetsugu, S., Yamazaki, D., Kurisu, S., and Takenawa, T. (2003). Differential Roles of WAVE1 and WAVE2 in Dorsal and Peripheral Ruffle Formation for Fibroblast Cell Migration. Dev Cell *5*, 595–609.

12. Iwaya, K., Norio, K., and Mukai, K. (2007). Coexpression of Arp2 and WAVE2 predicts poor outcome in invasive breast carcinoma. Modern Pathology *20*, 339–343.

13. Zhang, J., Tang, L., Shen, L., Zhou, S., Duan, Z., Xiao, L., Cao, Y., Mu, X., Zha, L., and Wang, H. (2012). High level of WAVE1 expression is associated with tumor aggressiveness and unfavorable prognosis of epithelial ovarian cancer. Gynecologic oncology *127*, 223–230.

14. Semba, S., Iwaya, K., Matsubayashi, J., Serizawa, H., Kataba, H., Hirano, T., Kato, H., Matsuoka, T., and Mukai, K. (2006). Coexpression of actin-related protein 2 and Wiskott-Aldrich syndrome family verproline-homologous protein 2 in adenocarcinoma of the lung. Clinical cancer research : an official journal of the American Association for Cancer Research *12*, 2449–2454.

15. Yang, L.Y., Tao, Y.M., Ou, D.P., Wang, W., Chang, Z.G., and Wu, F. (2006). Increased Expression of Wiskott-Aldrich Syndrome Protein Family Verprolin-Homologous Protein 2 Correlated with Poor Prognosis of Hepatocellular Carcinoma. Clinical cancer research : an official journal of the American Association for Cancer Research *12*, 5673–5679.

16. Ji, Y., Li, B., Zhu, Z., Guo, X., He, W., Fan, Z., and Zhang, W. (2015). Overexpression of WAVE3 promotes tumor invasiveness and confers an unfavorable prognosis in human hepatocellular carcinoma. Biomedicine & pharmacotherapy = Biomédecine & pharmacothérapie *69*, 409–415.

17. Zhang, Y., Guan, X.-Y., Dong, B., Zhao, M., Wu, J.-H., Tian, X.-Y., and Hao, C.-Y. (2012). Expression of MMP-9 and WAVE3 in colorectal cancer and its relationship to clinicopathological features. Journal of Cancer Research and Clinical Oncology *138*, 2035–2044.

18. Lomakina, M.E., Lallemand, F., Vacher, S., Molinie, N., Dang, I., Cacheux, W., Chipysheva, T.A., Ermilova, V.D., Koning, L.D., Dubois, T., et al. (2016). Arpin downregulation in breast cancer is associated with poor prognosis. British journal of cancer *114*, 545–553.

19. Joshi, A.D., Hegde, G.V., Dickinson, J.D., Mittal, A.K., Lynch, J.C., Eudy, J.D., Armitage, J.O., Bierman, P.J., Bociek, R.G., Devetten, M.P., et al. (2007). ATM, CTLA4, MNDA, and HEM1 in High versus Low CD38-Expressing B-Cell Chronic Lymphocytic Leukemia. Clinical cancer research : an official journal of the American Association for Cancer Research *13*, 5295–5304.

20. Wang, C., Tran-Thanh, D., Moreno, J.C., Cawthorn, T.R., Jacks, L.M., Wang, D.-Y., McCready, D.R., and Done, S.J. (2010). Expression of Abl interactor 1 and its prognostic significance in breast cancer: a tissue-array-based investigation. Breast Cancer Research and Treatment *129*, 373–386.

21. Zhang, J., Tang, L., Chen, Y., Duan, Z., Xiao, L., Li, W., Liu, X., and Shen, L. (2015). Upregulation of Abelson interactor protein 1 predicts tumor progression and poor outcome in epithelial ovarian cancer. Human pathology *46*, 1331–1340.

22. Győrffy, B., Lanczky, A., Eklund, A.C., Denkert, C., Budczies, J., Li, Q., and Szallasi, Z. (2009). An online survival analysis tool to rapidly assess the effect of 22,277 genes on breast cancer prognosis using microarray data of 1,809 patients. Breast Cancer Research and Treatment *123*, 725–731.

23. Molinie, N., Rubtsova, S.N., Fokin, A., Visweshwaran, S.P., Rocques, N., Polesskaya, A., Schnitzler, A., Vacher, S., Denisov, E.V., Tashireva, L.A., et al. (2019). Cortical branched actin determines cell cycle progression. Cell Research *29*, 432–445.

24. Montero, J.-A., Kilian, B., Chan, J., Bayliss, P.E., and Heisenberg, C.-P. (2003). Phosphoinositide 3-kinase is required for process outgrowth and cell polarization of gastrulating mesendodermal cells. Current Biology *13*, 1279–1289.

25. Dumortier, J.G., Martin, S., Meyer, D., Rosa, F.M., and David, N.B. (2012). Collective mesendoderm migration relies on an intrinsic directionality signal transmitted through cell contacts. Proceedings of the National Academy of Sciences of the United States of America *109*, 16945–16950.

26. Diz-Muñoz, A., Krieg, M., Bergert, M., Ibarlucea-Benitez, I., Muller, D.J., Paluch, E., and Heisenberg, C.-P. (2010). Control of Directed Cell Migration In Vivo by Membrane-to-Cortex Attachment. PLoS Biology *8*, e1000544-12.

27. Petrie, R.J., Gavara, N., Chadwick, R.S., and Yamada, K.M. (2012). Nonpolarized signaling reveals two distinct modes of 3D cell migration. The Journal of Cell Biology *197*, 439–455.

28. Schaks, M., Singh, S.P., Kage, F., Thomason, P., Klünemann, T., Steffen, A., Blankenfeldt, W., Stradal, T.E., Insall, R.H., and Rottner, K. (2018). Distinct Interaction Sites of Rac GTPase with WAVE Regulatory Complex Have Non-redundant Functions in Vivo. Current Biology *28*, 3674-3684.e6.

29. Zweier, M., Begemann, A., McWalter, K., Cho, M.T., Abela, L., Banka, S., Behring, B., Berger, A., Brown, C.W., Carneiro, M., et al. (2019). Spatially clustering de novo variants in CYFIP2, encoding the cytoplasmic FMRP interacting protein 2, cause intellectual disability and seizures. Eur J Hum Genet *27*, 747–759.

30. Chen, Z., Borek, D., Padrick, S.B., Gomez, T.S., Metlagel, Z., Ismail, A.M., Umetani, J., Billadeau, D.D., Otwinowski, Z., and Rosen, M.K. (2010). Structure and control of the actin regulatory WAVE complex. Nature *468*, 533–538.

31. Chen, B., Brinkmann, K., Chen, Z., Pak, C.W., Liao, Y., Shi, S., Henry, L., Grishin, N.V., Bogdan, S., and Rosen, M.K. (2014). The WAVE regulatory complex links diverse receptors to the actin cytoskeleton. Cell *156*, 195–207.

32. Gautreau, A., Ho, H.H., Li, J., Steen, H., Gygi, S.P., and Kirschner, M.W. (2004). Purification and architecture of the ubiquitous Wave complex. Proceedings of the National Academy of Sciences of the United States of America *101*, 4379–4383.

33. Fort, L., Batista, J.M., Thomason, P.A., Spence, H.J., Whitelaw, J.A., Tweedy, L., Greaves, J., Martin, K.J., Anderson, K.I., Brown, P., et al. (2018). Fam49/CYRI interacts with Rac1 and locally suppresses protrusions. Nature Cell Biology *20*, 1159–1171.

34. Yelland, T., Le, A.H., Nikolaou, S., Insall, R., Machesky, L., and Ismail, S. (2021). Structural Basis of CYRI-B Direct Competition with Scar/WAVE Complex for Rac1. Structure *29*, 226-237.e4.

35. Chen, B., Chou, H.-T., Brautigam, C.A., Xing, W., Yang, S., Henry, L., Doolittle, L.K., Walz, T., and Rosen, M.K. (2017). Rac1 GTPase activates the WAVE regulatory complex through two distinct binding sites. eLife *6*, W529.

36. Chen, B., Padrick, S.B., Henry, L., and Rosen, M.K. (2014). Biochemical reconstitution of the WAVE regulatory complex. Methods in Enzymology *540*, 55–72.

37. Nakashima, M., Kato, M., Aoto, K., Shiina, M., Belal, H., Mukaida, S., Kumada, S., Sato, A., Zerem, A., Sagie, T.L., et al. (2018). De novo hotspot variants in CYFIP2 cause early-onset epileptic encephalopathy. Annals of neurology *83*, 794–806.

38. Zweier, M., Begemann, A., McWalter, K., Cho, M.T., Abela, L., Banka, S., Behring, B., Berger, A., Brown, C.W., Carneiro, M., et al. (2019). Spatially clustering de novo variants in CYFIP2, encoding the cytoplasmic FMRP interacting protein 2, cause intellectual disability and seizures. European journal of human genetics : EJHG, 1–13.

39. Pittman, A.J., Gaynes, J.A., and Chien, C.-B. (2010). nev (cyfip2) is required for retinal lamination and axon guidance in the zebrafish retinotectal system. Developmental Biology *344*, 784–794.

40. Cioni, J.-M., Wong, H.H.-W., Bressan, D., Kodama, L., Harris, W.A., and Holt, C.E. (2018). Axon-Axon Interactions Regulate Topographic Optic Tract Sorting via CYFIP2-Dependent WAVE Complex Function. Neuron *97*, 1078-1093.e6.

41. Blagg, S.L., Stewart, M., Sambles, C., and Insall, R.H. (2003). PIR121 Regulates Pseudopod Dynamics and SCAR Activity in Dictyostelium. Current Biology *13*, 1480–1487.

42. Ibarra, N., Blagg, S.L., Vazquez, F., and Insall, R.H. (2006). Nap1 Regulates Dictyostelium Cell Motility and Adhesion through SCAR-Dependent and -Independent Pathways. Current Biology *16*, 717–722.

43. Pollitt, A.Y., and Insall, R.H. (2008). Abi Mutants in Dictyostelium Reveal Specific Roles for the SCAR/WAVE Complex in Cytokinesis. Current Biology *18*, 203–210.

44. Litschko, C., Linkner, J., Brühmann, S., Stradal, T.E.B., Reinl, T., Jänsch, L., Rottner, K., and Faix, J. (2017). Differential functions of WAVE regulatory complex subunits in the regulation of actin-driven processes. European Journal of Cell Biology *96*, 715–727.

45. Korobova, F., and Svitkina, T. (2008). Arp2/3 complex is important for filopodia formation, growth cone motility, and neuritogenesis in neuronal cells. Molecular Biology of the Cell *19*, 1561–1574.

46. Dang, I., Gorelik, R., Sousa-Blin, C., Derivery, E., Guérin, C., Linkner, J., Nemethova, M., Dumortier, J.G., Giger, F.A., Chipysheva, T.A., et al. (2013). Inhibitory signalling to the Arp2/3 complex steers cell migration. Nature *503*, 281–284.

47. Stradal, T., Courtney, K.D., Rottner, K., Hahne, P., Small, J.V., and Pendergast, A.M. (2001). The Abl interactor proteins localize to sites of actin polymerization at the tips of lamellipodia and filopodia. Curr Biol *11*, 891–895.

48. Kumar, V., Kim, K., Joseph, C., Kourrich, S., Yoo, S.-H., Huang, H.C., Vitaterna, M.H., Villena, F.P.-M. de, Churchill, G., Bonci, A., et al. (2013). C57BL/6N mutation in cytoplasmic FMRP interacting protein 2 regulates cocaine response. Science *342*, 1508–1512.

49. Wan, C., Borgeson, B., Phanse, S., Tu, F., Drew, K., Clark, G., Xiong, X., Kagan, O., Kwan, J., Bezginov, A., et al. (2015). Panorama of ancient metazoan macromolecular complexes. Nature *525*, 339–344.

50. Abella, J.V.G., Galloni, C., Pernier, J., Barry, D.J., Kjær, S., Carlier, M.-F., and Way, M. (2016). Isoform diversity in the Arp2/3 complex determines actin filament dynamics. Nature Cell Biology *18*, 76–86.

51. Bieche, I., Parfait, B., Laurendeau, I., Girault, I., Vidaud, M., and Lidereau, R. (2001). Quantification of estrogen receptor alpha and beta expression in sporadic breast cancer. Oncogene *20*, 8109–8115.

52. González, F., Zhu, Z., Shi, Z.-D., Lelli, K., Verma, N., Li, Q.V., and Huangfu, D. (2014). An iCRISPR platform for rapid, multiplexable, and inducible genome editing in human pluripotent stem cells. Cell stem cell *15*, 215–226.

53. Derivery, E., Lombard, Be., Loew, D., and Gautreau, A. (2009). The Wave complex is intrinsically inactive. Cell Motility and the Cytoskeleton *66*, 777–790.

54. Derivery, E., and Gautreau, A. (2010). Assaying WAVE and WASH complex constitutive activities toward the Arp2/3 complex. Methods in Enzymology *484*, 677–695.

55. Derivery, E., Fink, J., Martin, D., Houdusse, A., Piel, M., Stradal, T.E., Louvard, D., and Gautreau, A. (2008). Free Brick1 is a trimeric precursor in the assembly of a functional wave complex. PLoS ONE *3*, e2462.

56. Gorelik, R., and Gautreau, A. (2014). Quantitative and unbiased analysis of directional persistence in cell migration. Nature Protocols *9*, 1931–1943.

57. Doitsidou, M., Reichman-Fried, M., Stebler, J., Köprunner, M., Dörries, J., Meyer, D., Esguerra, C.V., Leung, T., and Raz, E. (2002). Guidance of primordial germ cell migration by the chemokine SDF-1. Cell *111*, 647–659.

58. Biswas, S., Emond, M.R., and Jontes, J.D. (2010). Protocadherin-19 and N-cadherin interact to control cell movements during anterior neurulation. The Journal of Cell Biology *191*, 1029–1041.

59. Hans, S., Christison, J., Liu, D., and Westerfield, M. (2007). Fgf-dependent otic induction requires competence provided by Foxi1 and Dlx3b. BMC developmental biology *7*, 5.

Table 1: Tumours showing up- or down-regulation of WAVE complex subunits in breast cancer (> 3 or < 0.3)

Generic name	Gene name	All tumours		HR+ ERBB2-		HR+ ERBB2+		HR- ERBB2-		HR- ERBB2+	
		% down	% up	% down	% up	% down	% up	% down	% up	% down	% up
WAVE	***WASF1***	**27**	2	**37**	1	10	2	10	3	21	6
	WASF2	3	1	3	0	3	2	2	3	1	0
	WASF3	**46**	1	**56**	0	48	0	27	2	25	3
ABI	***ABI1***	0	1	0	0	0	2	0	3	0	1
	ABI2	3	0	1	0	2	0	7	0	3	0
	ABI3	1	**12**	1	5	0	17	0	**25**	3	17
BRK	***BRK1***	0	4	0	3	0	10	0	4	0	3
NAP	***NCKAP1***	0	2	0	1	0	2	0	6	0	4
	NCKAP1L	0	**22**	0	15	0	12	0	37	0	**39**
CYFIP	***CYFIP1***	0	4	0	1	0	12	0	6	0	7
	CYFIP2	1	**37**	1	**44**	0	36	0	30	1	17

Figures

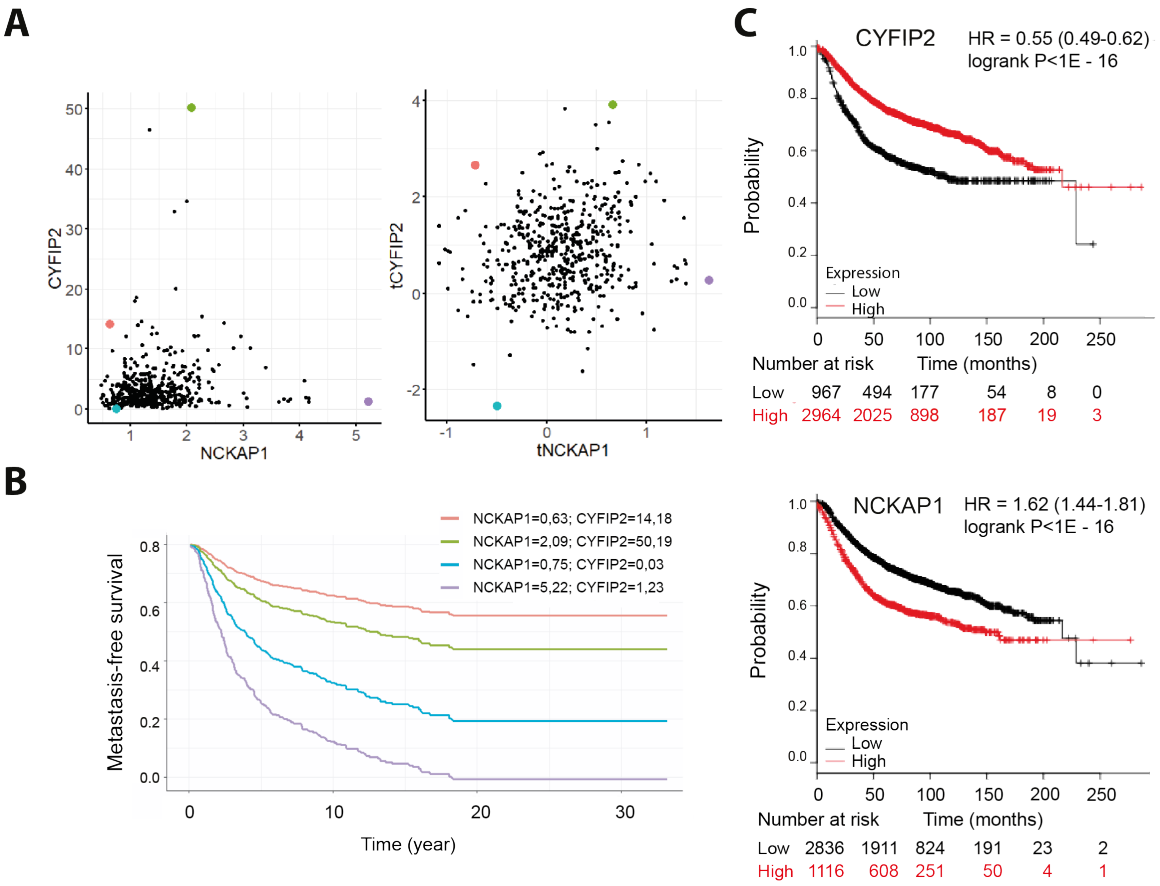

Fig.1, Polesskaya et al.

Figure 1. CYFIP2 overexpression is associated with good prognosis in breast cancer patients.

(A) Distribution of *NCKAP1* and *CYFIP2* mRNA levels in mammary carcinomas from a cohort of 527 breast cancer patients, before (left panel) or after transformation and normalization (right panel) **(B)** A multivariate Cox model predicting metastasis-free survival (MFS) based on *NCKAP1* and *CYFIP2* mRNA levels as the only two inputs was derived. The 4 highlighted tumors representing the different outskirts of gene expression in the cohort were chosen to run the model. The purple and turquoise patients developed metastases that were diagnosed after 922 and 1487 days, respectively. The red and green patients did not develop metastasis and survived for 4248 and 4146 days, respectively. Even though extreme *NCKAP1* values drive MFS in the red and purple patients, the extreme values of *CYFIP2* rule the outcome of the green and turquoise patients at intermediate values of *NCKAP1*. The model thus predicts that high levels of *NCKAP1* are associated with poor prognosis, whereas high levels of *CYFIP2* are associated with good prognosis. **(C)** Validation of the prediction using a public database, kmplot.com, containing more than 3900 breast cancer patients. Kaplan-Meier representations.

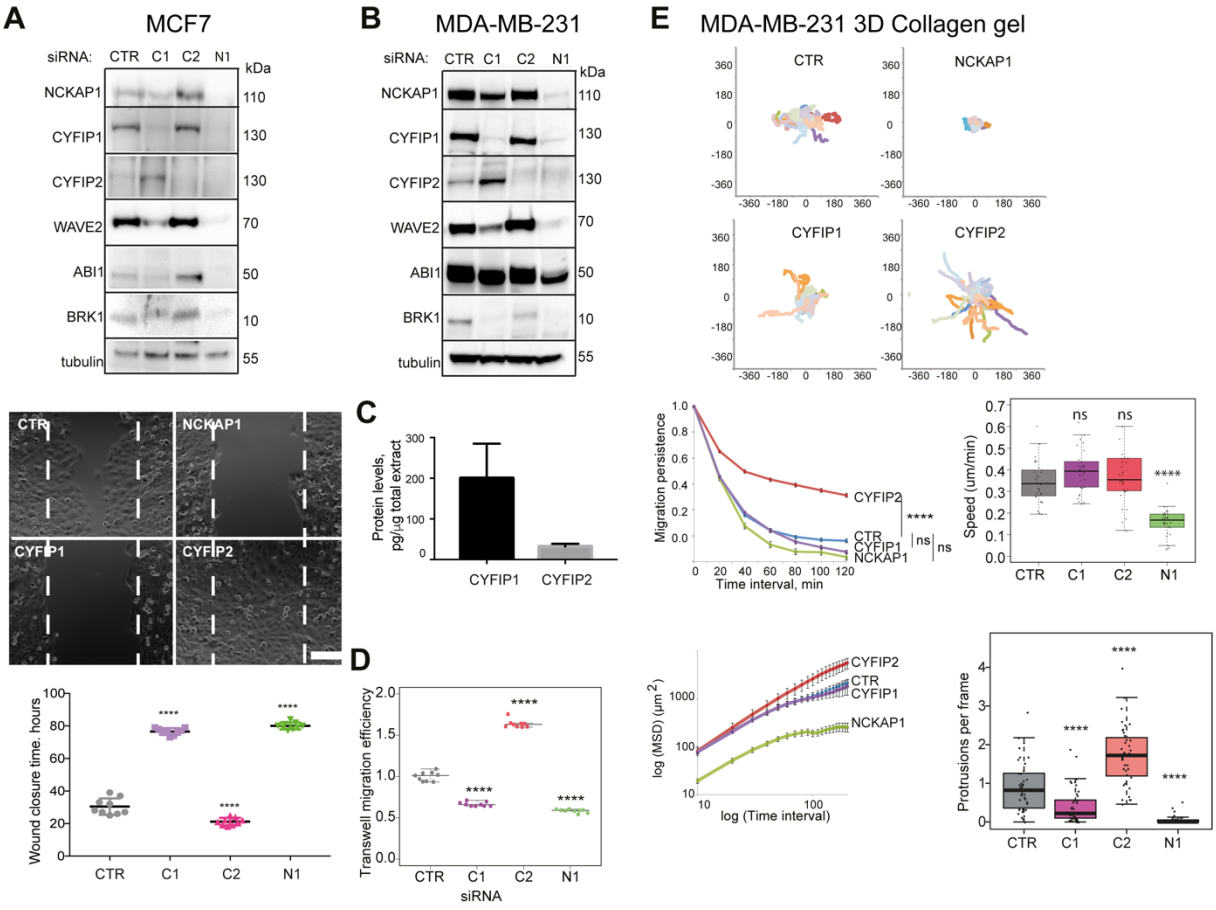

Fig.2, Polesskaya et al.

Figure 2. CYFIP2 inhibits the migration of human breast cancer cells. (**A**) MCF7 cells were transfected with pools of siRNAs targeting CYFIP1 (C1), CYFIP2 (C2), NCKAP1 (N1) or non-targeting ones (CTR). Western blots of WAVE complex subunits and tubulin as a loading control. Wound healing of MCF7 cells. Still images corresponding to the time, where the first wound is healed (CYFIP2). Quantification of nine technical repeats. Scale bar: 400 μm. (**B**) MDA-MB-231 cells were transfected with pools of siRNAs and analyzed by Western blots as above. (**C**) Levels of CYFIP1 and CYFIP2 proteins in MDA-MB-231. Mean ± SD of 3 biological repeats. (**D**) Quantification of Transwell migration efficiency of MDA-MB-231 cells, n=9. (**E**) Depleted MDA-MB-231 cells depleted of the indicated proteins were embedded in 3D collagen type I gels and recorded by videomicroscopy. Trajectories, migration persistence, Mean Square Displacement (MSD), and average number of protrusions per frame are plotted, n=30. *P<0.05; **P<0.01; ***P<0.001; ****P<0.0001.

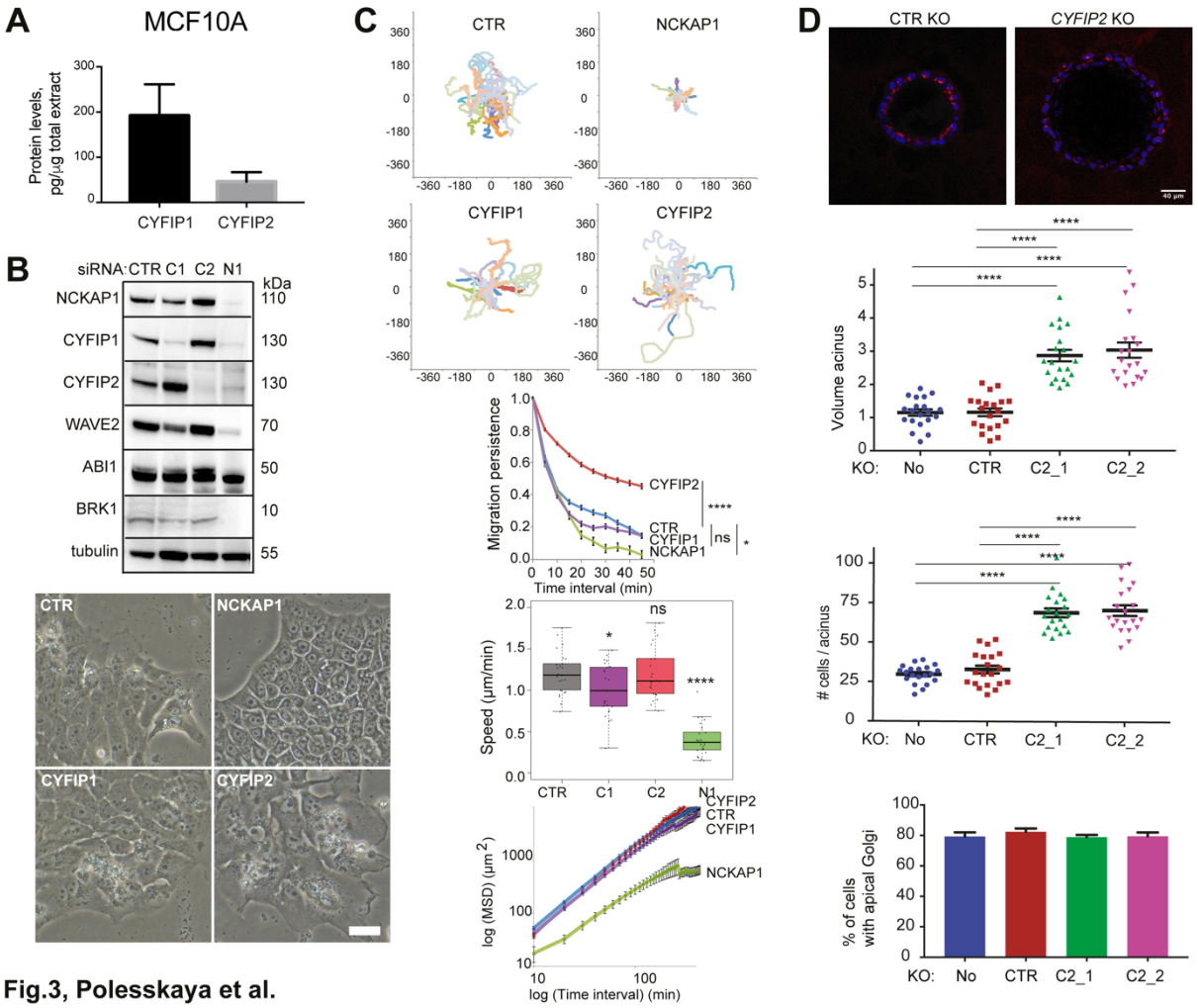

Fig.3, Polesskaya et al.

Figure 3. CYFIP2 inhibits the migration of normal breast epithelial cells and the growth of 3D acini. (**A**) Levels of CYFIP1 and CYFIP2 proteins in MDA-MB-231. Mean ± SD of 3 biological repeats. (**B**) MCF10A cells were transfected with pools of CYFIP1 (C1), CYFIP2 (C2), NCKAP1 (N1) or non-targeting siRNAs (CTR). WAVE complex subunits and tubulin as a loading control were analyzed by Western blot. Phase-contrast images of depleted cells. Scale bar: 50 µm. **(C)** Trajectories, migration persistence, speed, MSD extracted from random migration of single MCF10A cells. 2D migration, Fibronectin coating, n=25. (**D**) *CYFIP2* KO cells or parental MCF10A cells were differentiated at the surface of matrigel. Confocal microscopy of acini labeled with DAPI (blue) and the Golgi marker GM130 (red). Scale bar: 40 µm. Quantification of acinus volume and the number of cells per acinus, n=20. (**H**), Quantification of cells' polarity within acini, n=130. *P<0.05; ****P<0.0001.

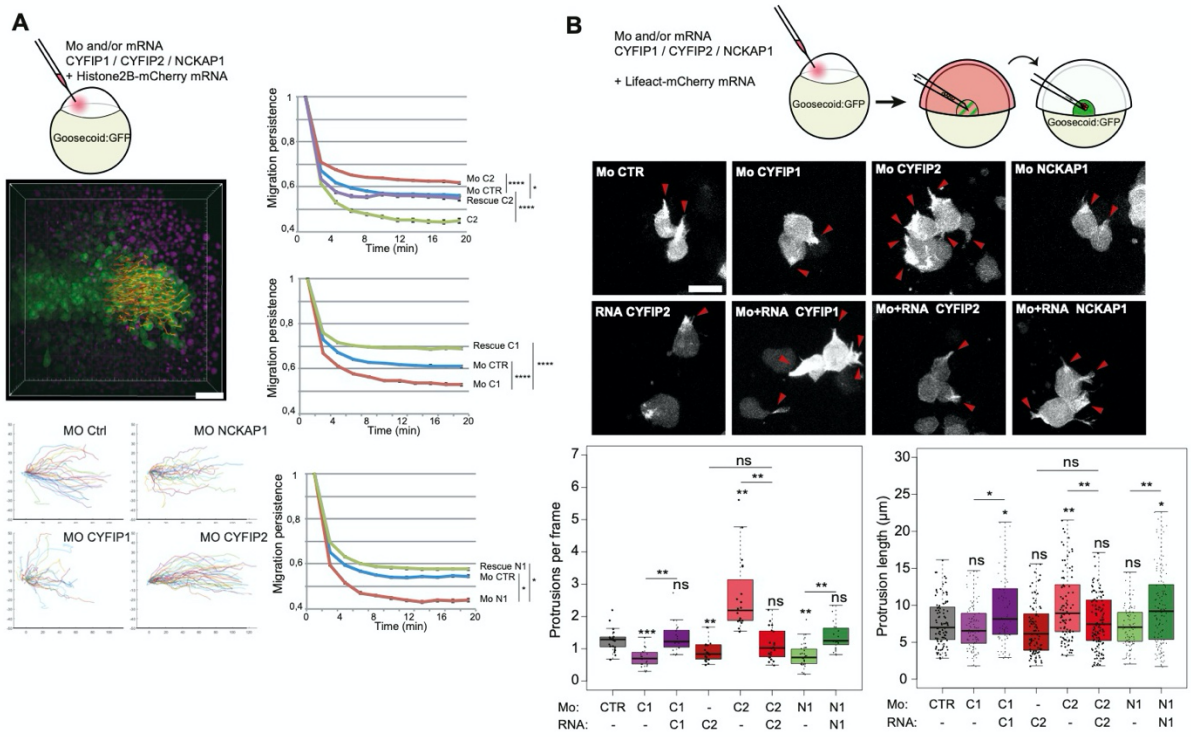

Figure 4. CYFIP2 inhibits migration persistence and actin rich protrusions in zebrafish embryos during gastrulation. (A) Scheme of the experimental design. Embryos were injected with Histone2B-mCherry mRNA and morpholinos (Mo) targeting a control sequence (CTR), CYFIP1 (C1), CYFIP2 (C2), NCKAP1 (N1), alone or in combination with mRNAs encoding the same proteins (rescue). Dorsal view of a volume acquisition of a Tg(Gsc:GFP) zebrafish embryo. Scale bar is 50 µm. Animal pole is located at the right. Notochord and prechordal plate cells express GFP (green) and nuclei express histone2B-mCherry (in magenta). Nuclei of prechordal plate cells are 3D-tracked over time (color coded) (Movie S5). Trajectories of 10 first time points (20 min) for 50 randomly selected cells for each condition, plotted at the same origin (axes in µm). Migration persistence of prechordal plate cells injected with the indicated MO and/or mRNA. (B) CYFIP2 inhibits actin rich protrusions in zebrafish embryos during gastrulation. Scheme of the experimental design. Donor embryos were injected with the actin filament marker LifeAct-mCherry mRNA and morpholinos (Mo) targeting a control sequence (CTR), CYFIP1 (C1), CYFIP2 (C2), NCKAP1 (N1), alone or in combination with mRNAs encoding the same proteins. Labeled prechordal plate cells from a donor embryo were transplanted into an uninjected embryo and recorded. Imaged of typical cells described in (A), red arrowheads indicate actin-rich protrusions. Scale bar: 20µm. Quantification of the average number of protrusions per frame, n=17 to 32 cells from 4 to 5 embryos per condition. Quantification of protrusion length, n=95 (randomly selected protrusions per condition). ANOVA on linear mixed model accounting for the sampling biases. ns P>0.05; * P<0.05; ** P<0.01; *** P<0.001. The p-values without a bar refer to comparisons with the control condition.

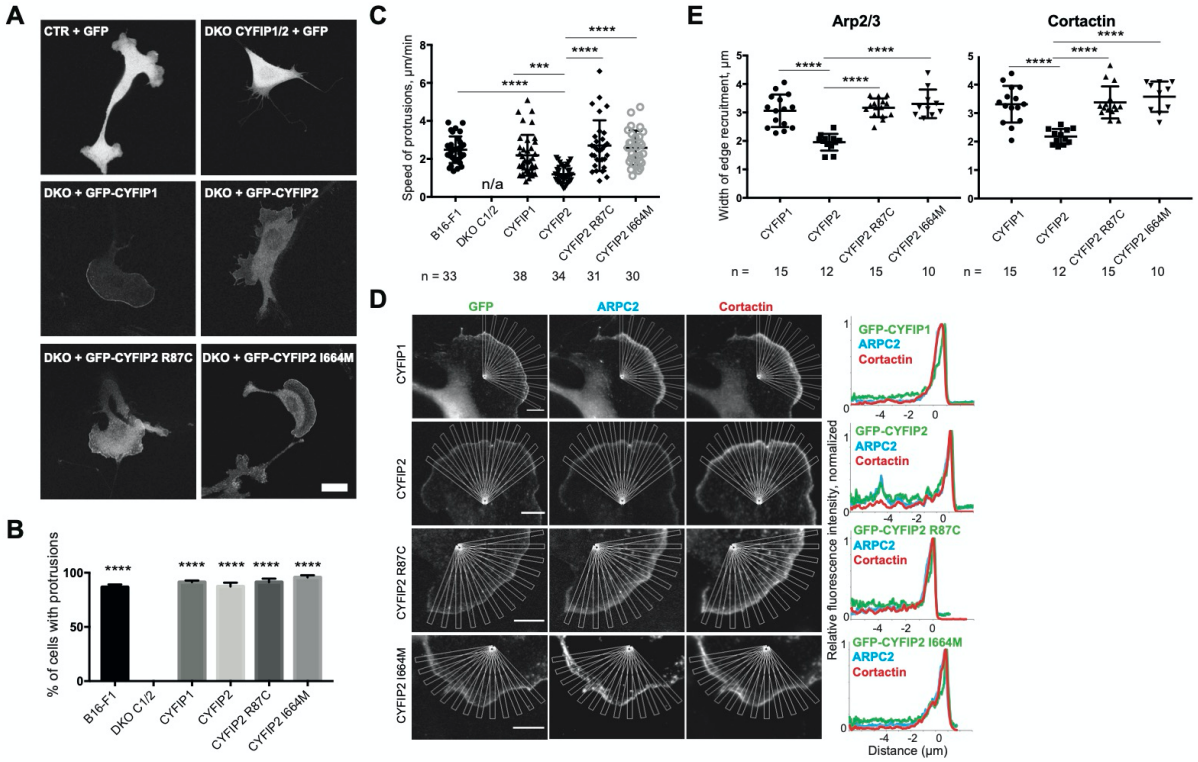

Fig.5, Polesskaya et al.

Figure 5. CYFIP2 rescues *CYFIP1/2* Double Knock-Out (DKO). GFP-tagged CYFIP1, CYFIP2, and two CYFIP2 mutants were expressed in B16-F1 control cells and in DKO cells. (A) Distribution of GFP fusion proteins and morphology of transfected cells. Scale bar: 20 µm. (B) Percentage of transfected cells forming protrusions, n=100, analysis by one-way ANOVA and Dunnett's multiple comparisons test. (C) Average speed of protrusions. Only the significant differences as determined by one-way ANOVA and Tukey's multiple comparisons test are indicated. (D) Recruitment of GFP-tagged CYFIP1, CYFIP2, and mutant CYFIP2 assessed by multiple radial line scans. Average profiles of the indicated markers upon registering line scans. Scale bars: 5µm. (E) Width of Arp2/3 and cortactin recruitment. ***P<0.001; ****P<0.0001.

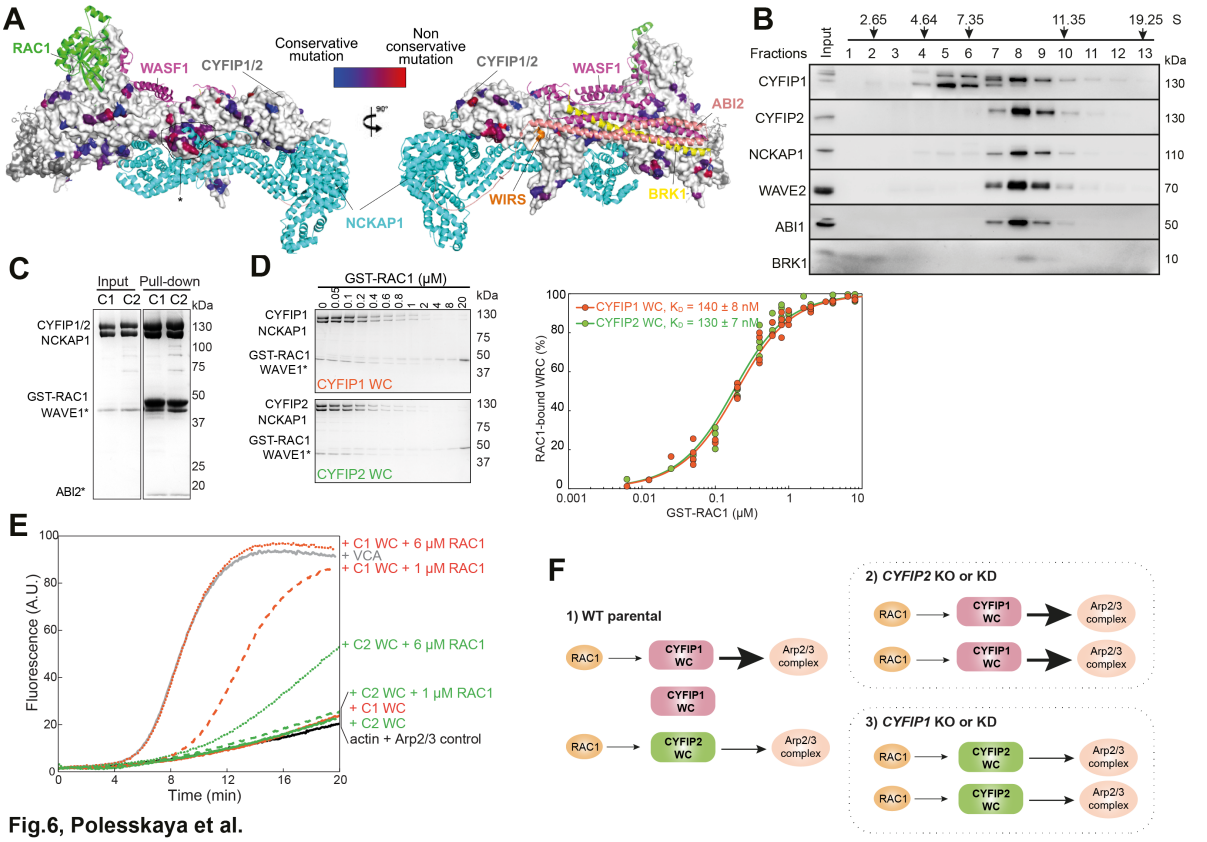

Fig.6, Polesskaya et al.

Figure 6. CYFIP2-containing WAVE complexes are less activatable by RAC1 than CYFIP1-containing WAVE complexes. (A) Structural models of CYFIP1 and CYFIP2. Sequence identity between CYFIP1 and CYFIP2 is 88% and non-conserved positions are colour-coded. The vast majority of non conserved residues fall outside of binding sites for known protein partners. WAVE complex subunits and WIRS peptide were obtained from PDB:4N78. RAC1 binding was modelled using the CYRI-B Rac1 complex as template (PDB:7AJK). (B) Ultracentrifugation of MCF10A lysate on a sucrose gradient. WAVE complex subunits are revealed by Western blots. The CYFIP1 antibody cross-reacts with a lower molecular weight band. (C) Coomassie-blue stained SDS-PAGE gels showing reconstitution of WAVE complexes containing CYFIP1 or CYFIP2 and pull-down with GTP-bound RAC1 (GST-RAC1 Q61L P29S). ABI2* and WAVE1* are not full length proteins (See Methods). (D) WAVE complexes containing supernatants upon pull-down with increasing amounts of GST-Rac1 Q61L P29S. Dissociation constants K_D and standard errors are derived from fitting of quantification of 4 independent experiments at various concentrations. (E) Pyrene-actin polymerization assay of CYFIP1- or CYFIP2-containing WAVE complexes. Conditions: 4 μM actin (5% pyrene-labeled), 10 nM Arp2/3 complex, 100 nM WAVE complexes (WC) or WAVE1 WCA, and indicated amounts of untagged Rac1 Q61L P29S. Results are representative of two independent experiments. (F) Model: CYFIP2-containing WAVE complexes activate less Arp2/3 upon RAC1 binding than CYFIP1-containing WAVE complexes. Upon depletion of CYFIP2, Arp2/3 activity increases, because more CYFIP1 containing complexes are activated by RAC1, leading to increased migration. On the opposite, upon depletion of CYFIP1, Arp2/3 activity decreases, despite compensatory increase in CYFIP2 levels, leading to reduced migration.

Table S1: Characteristics of the breast tumors relative to *CYFIP2* mRNA levels

	Number of patients (%)	**Number with metastases (%)**	***p-value*** [a]	***CYFIP2* mRNA normally expressed**	***CYFIP2* mRNA over expressed (> 3)**	***p-value*** [f]
Total	527 (100)	210 (39.8)		332 (63.0)	195 (37.0)	
Age						
<50	125 (23.7)	52 (41.6)	0.52 (NS)	82 (65.6)	43 (34.4)	0.49 (NS)
>50	402 (76.3)	158 (39.3)		250 (62.2)	152 (37.8)	
SBR histological grade [b,c]						
I	60 (11.7)	12 (20.0)	**0.0019**	34 (56.7)	26 (43.3)	**0.011**
II	241 (47.1)	100 (41.5)		141 (58.5)	100 (41.5)	
III	211 (41.2)	94 (44.5)		150 (71.1)	61 (28.9)	
Lymph node status [d]						
0	159 (30.5)	48 (30.2)	**<0.0000001**	96 (60.4)	63 (39.6)	0.66 (NS)
1-3	250 (47.9)	88 (35.2)		162 (64.8)	88 (35.2)	
>3	113 (21.6)	72 (63.7)		70 (61.9)	43 (38.1)	
Macroscopic tumor size [e]						
<25mm	248 (48.0)	77 (31.0)	**0.000015**	154 (62.1)	94 (37.9)	0.66 (NS)
>25mm	269 (52.0)	132 (49.1)		172 (63.9)	97 (36.1)	
ERα status						
Negative	181 (34.3)	76 (42.0)	0.10 (NS)	138 (76.2)	43 (23.8)	**0.0000052**
Positive	346 (65.7)	134 (38.7)		194 (56.1)	152 (43.9)	
PR status						
Negative	255 (48.4)	110 (43.1)	**0.025**	186 (72.9)	69 (27.1)	**0.0000047**
Positive	272 (51.6)	100 (36.8)		146 (53.7)	126 (46.3)	
ERBB2 status						
Negative	397 (75.3)	153 (38.5)	0.17 (NS)	235 (59.2)	162 (40.8)	**0.0016**
Positive	130 (24.7)	57 (43.8)		97 (74.6)	33 (25.4)	
Molecular subtypes						
HR- ERBB2-	102 (19.4)	38 (37.3)	0.054 (NS)	71 (69.6)	31 (30.4)	**0.00011**
HR- ERBB2+	72 (13.7)	36 (50.0)		60 (83.3)	12 (16.7)	
HR+ ERBB2-	295 (56.0)	115 (39.0)		164 (55.6)	131 (44.4)	
HR+ ERBB2+	58 (11.0)	21 (36.2)		37 (63.8)	21 (36.2)	

Supplemental figures

A

	Original values			Transformed and normalized values			
gene	coefficient	p-value	adjusted p-value	gene	coefficient	p-value	adjusted p-value
NCKAP1	0.27	0.012	0.132	*NCKAP1*	0.195	0.005	0.055
CYFIP2	-0.027	0.138	1	*CYFIP2*	-0.134	0.059	0.59
NCKAP1L	-0.051	0.288	1	*NCKAP1L*	-0.058	0.397	1
WASF2	-0.162	0.377	1	*WASF3*	-0.045	0.519	1
ABI3	-0.022	0.439	1	*ABI1*	0.042	0.546	1
WASF3	-0.066	0.573	1	*WASF2*	-0.041	0.561	1
ABI1	0.054	0.644	1	*ABI3*	-0.036	0.603	1
ABI2	-0.068	0.749	1	*BRK1*	0.035	0.609	1
CYFIP1	-0.01	0.866	1	*CYFIP1*	0.036	0.612	1
WASF1	0.009	0.930	1	*ABI2*	-0.034	0.624	1
BRK1	0.004	0.962	1	*WASF1*	-0.007	0.919	1

B

Subunit assembled					
NAP	CYFIP	ABI	WAVE	BRK	p-value
1	**2**	2	3	1	0,0023
1	**2**	2	2	1	0,0032
1	**2**	1	3	1	0,0036
1	**2**	3	3	1	0,0038
1	**2**	1	2	1	0,0044
1	**2**	3	2	1	0,0044
1	**2**	2	1	1	0,0050
1	**2**	1	1	1	0,0069
1	**2**	3	1	1	0,0076
1	1	2	2	1	0,0098
1	1	2	3	1	0,0115
1	1	2	1	1	0,0167
1	1	3	2	1	0,0220
1	1	1	2	1	0,0246
1	1	3	3	1	0,0352
1	1	1	3	1	0,0444
1	1	3	1	1	0,0470
1	1	1	1	1	0,0569
2	2	1	3	1	0,2212
2	2	1	2	1	0,2464
2	2	1	1	1	0,3183
2	2	3	3	1	0,3259
2	2	2	3	1	0,3649
2	2	3	2	1	0,3764
2	2	3	1	1	0,4103
2	2	2	2	1	0,4154
2	2	2	1	1	0,4287
2	1	1	2	1	0,5184
2	1	2	2	1	0,6576
2	1	2	3	1	0,6746
2	1	1	3	1	0,6847
2	1	3	2	1	0,7330
2	1	2	1	1	0,7767
2	1	3	3	1	0,7998
2	1	1	1	1	0,8247
2	1	3	1	1	0,8945

C

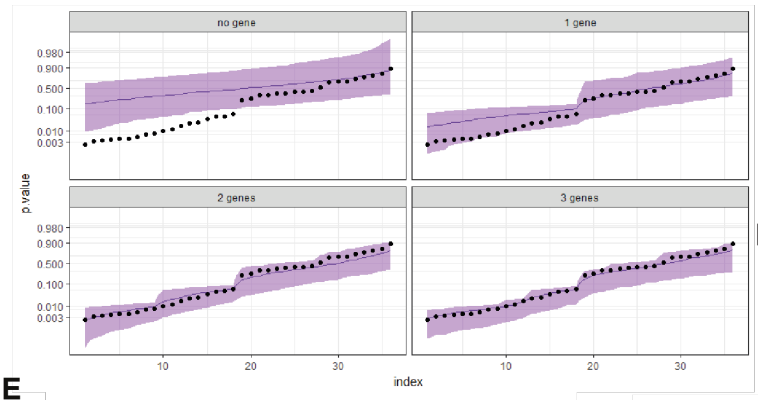

D

Genes	log.likelihood	BIC
-	-1234.7	2469.3
NCKAP1	-1230.7	2466.8
NCKAP1, CYFIP2	-1227.6	**2465.8**
NCKAP1, CYFIP2, WASF3	-1226.2	2468.4
NCKAP1, CYFIP2, WASF3, ABI2	-1225.4	2472.2
NCKAP1, CYFIP2, WASF3, ABI2, BRK1	-1224.9	2476.6

E

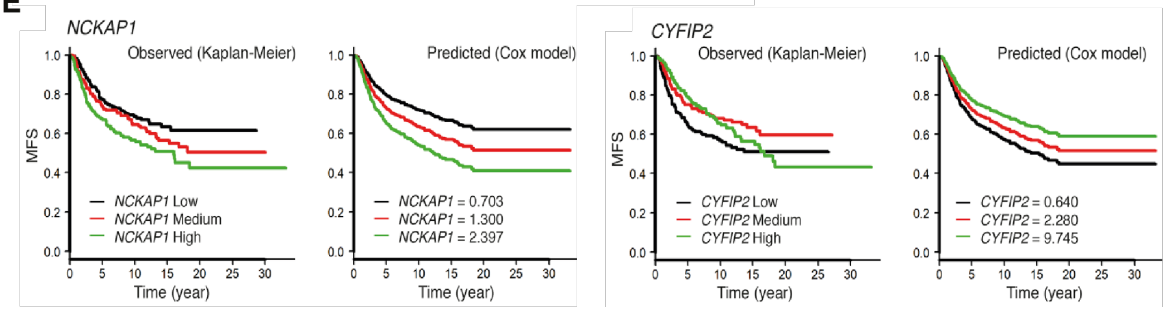

Figure S1. Statistical modeling of the association of WAVE complexes with metastasis-free survival (MFS). A Cox univariate analysis before and after transformation and normalization of mRNA levels of WAVE complex subunits. **B** Association of each WAVE assembly with MFS. **C** Random permutations. Experimental p values associated with the 36 WAVE assemblies (black dots) are compared with computed p-values corresponding to hypotheses (purple; 1000 simulations to derive the 90 % confidence interval): all subunits can be permuted (0 gene); all subunits except the most significant one, *NCKAP1*, can be permuted (1 gene); all subunits except the two most significant ones, *NCKAP1* and *CYFIP2*, can be permuted (2 genes); All subunits except the 3 most significant ones (3 genes) can be permuted. The small p-values obtained for the combination *NCKAP1* and *CYFIP2* are not obtained by chance, since computer simulations graphically illustrate the good agreement between what is observed and what is expected according to models when at least two of the most significant genes are fixed. **D** Comparison of the different models with Bayesian Information Criteria (BIC). The model with 2 fixed genes corresponds to the optimal statistical model, <hcih is used below and for Fig.1. **E** Kaplan-Meier of MFS as a function of NCKAP1 or CYFIP2 mRNA levels. Observed survival is modeled with the 2-variable Cox model.

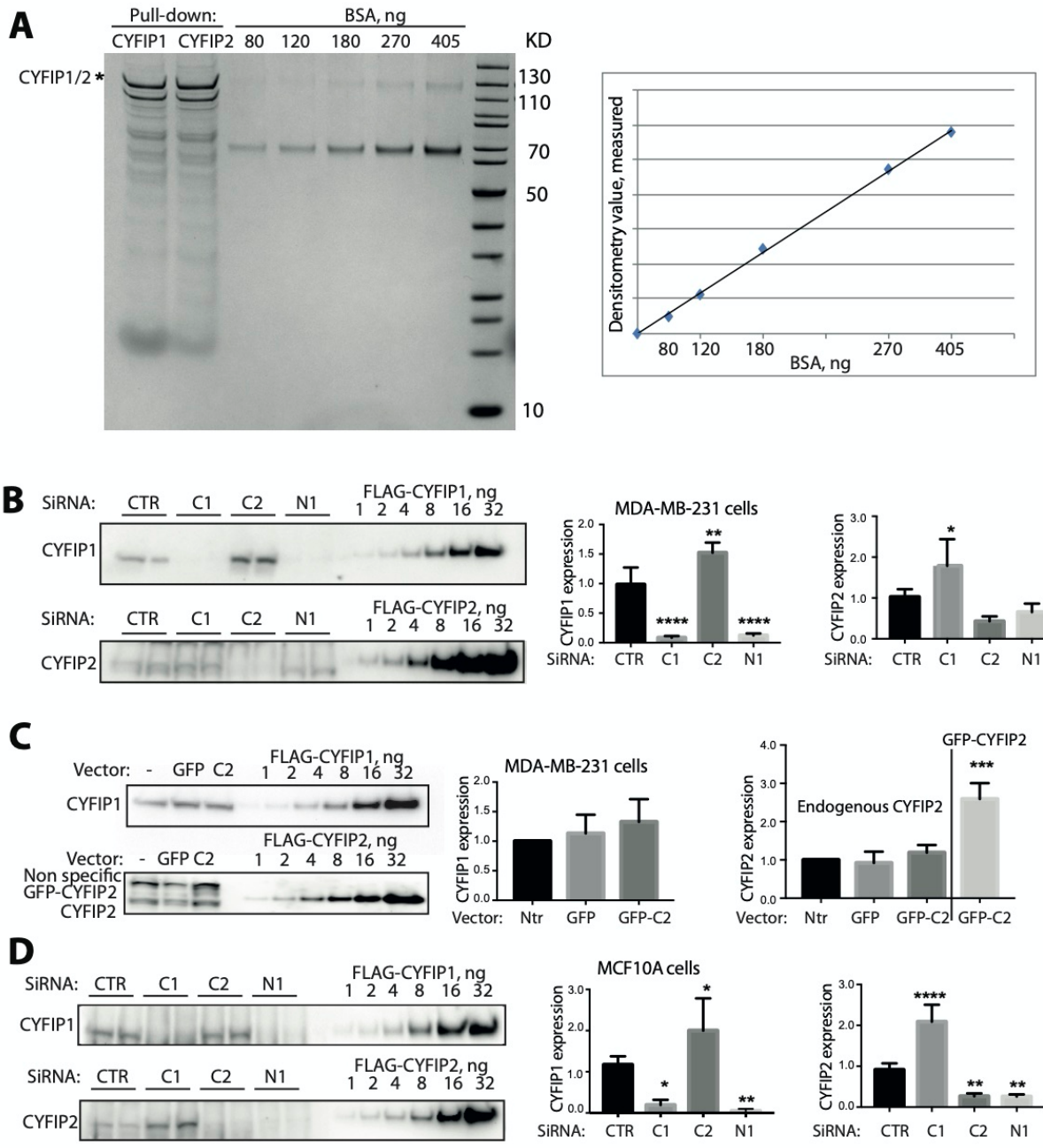

Figure S2. Quantification of CYFIP1/2 proteins in MDA-MB-231 and MCF10A cells. (A) Colloidal coomassie-stained gel with FLAG-tagged, purified CYFIP1/2-containing WAVE complexes, and BSA standard. We have purified tagged CYFIP1 or CYFIP2-containing WAVE complexes from stable 293 Flp-In cell lines. (B) Quantification of CYFIP1, CYFIP2 and NCKAP1 levels in MDA-MB-231 cells treated with siRNAs. Duplicate transfections of the siRNA smartpool were analyzed for each gene, the experiment was repeated twice (total n=4). (C) Quantification of CYFIP1, CYFIP2 and NCKAP1 levels in MDA-MB-231 stable cell lines expressing GFP or GFP-CYFIP2, n=3. (D) Quantification of CYFIP1, CYFIP2 and NCKAP1 levels in MCF10A cells treated with siRNAs. Duplicate transfections of the siRNA smartpool were analyzed for each gene, the experiment was repeated twice (total n=4). Mean ± SD. Shown are the statistically significant differences (one-way ANOVA). *P<0.05; **P<0.01; ***P<0.001; ****P<0.0001.

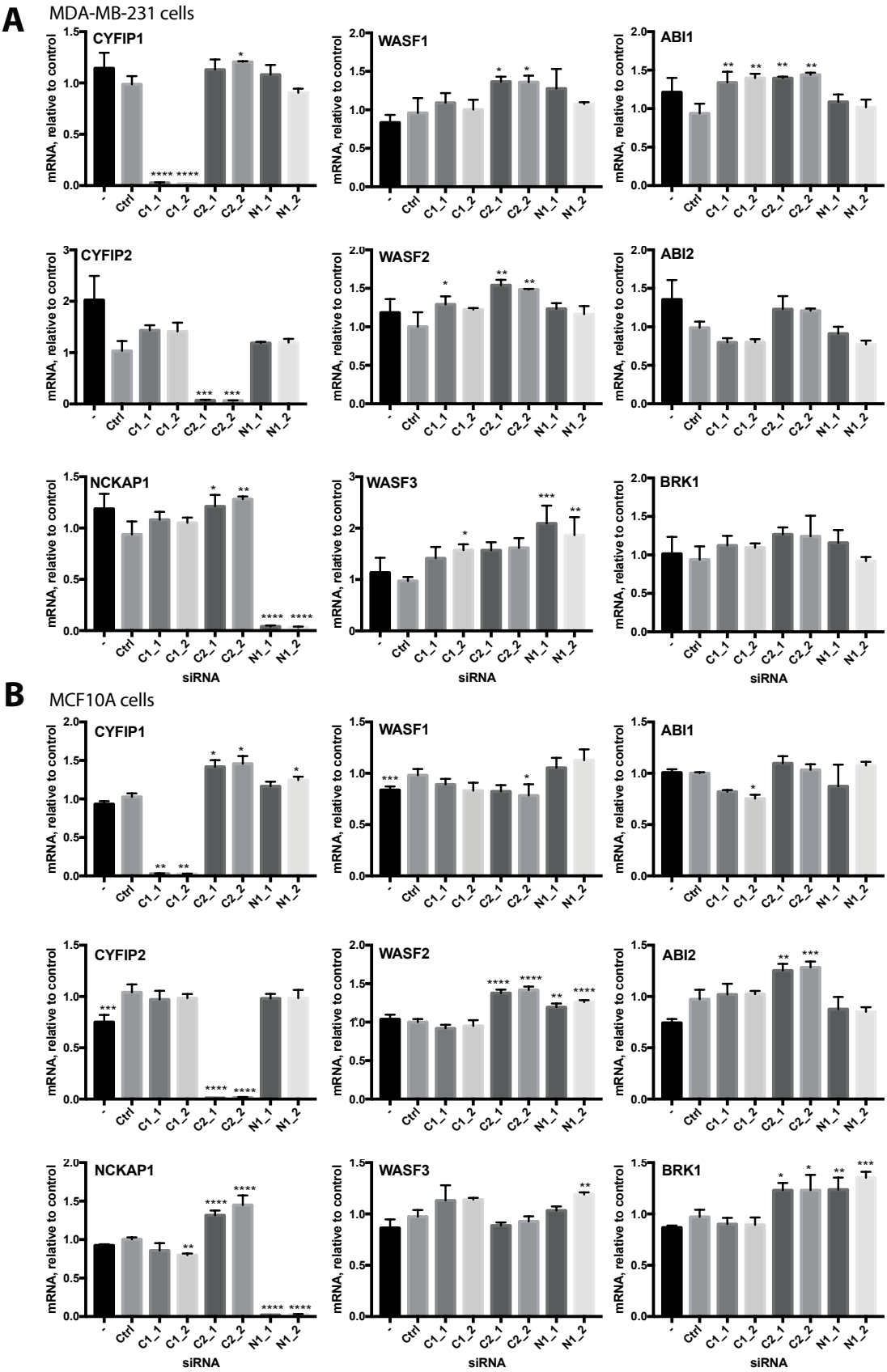

Figure S3. qRT-PCR analysis of mRNA levels of WAVE subunits in MDA-MB-231 and MCF10A cells transfected with two independent siRNAs targeting either CYFIP1 (C1),

CYFIP2 (C2), or NCKAP1 (N1). Mean ± SD of n=3 independent biological experiments, shown are the statistically significant differences (one-way ANOVA). *P<0.05; **P<0.01; ***P<0.001; ****P<0.0001.

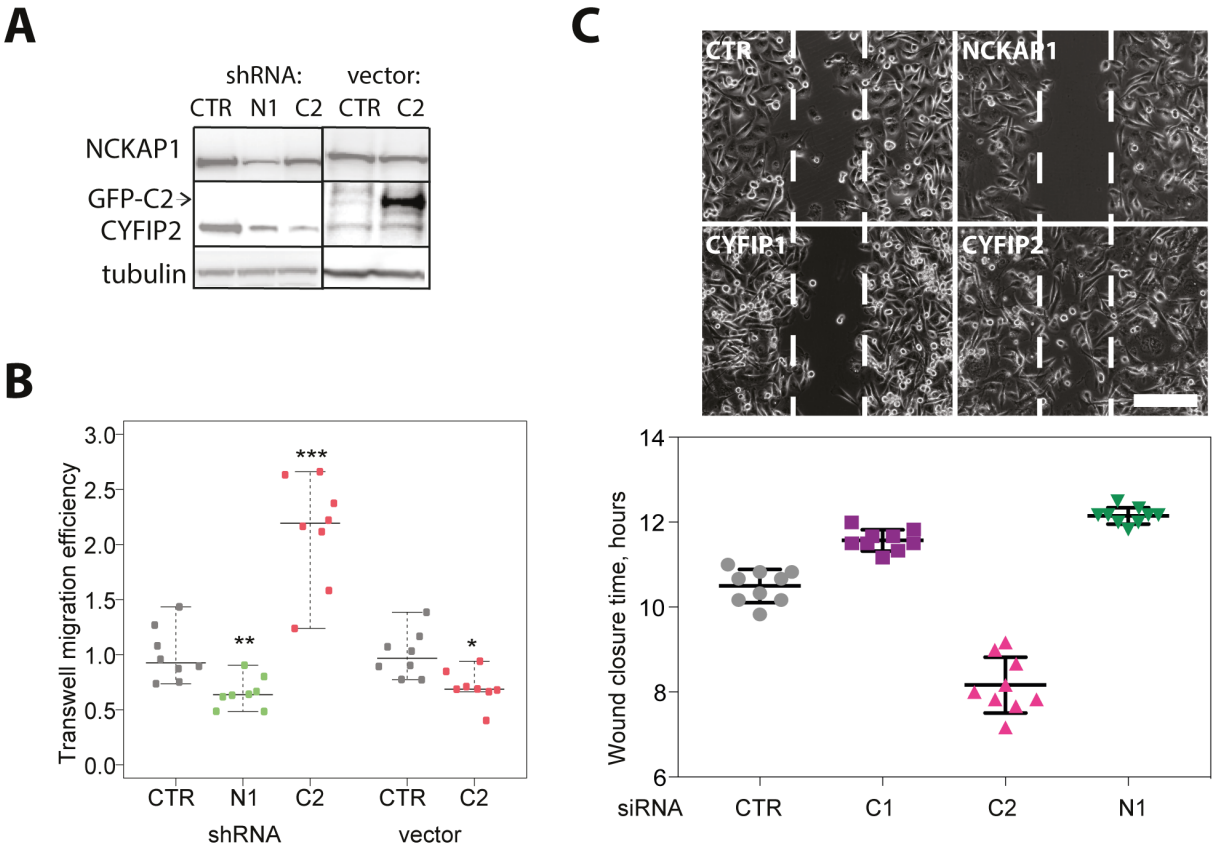

Figure S4. Wound healing and Transwell migration assays of MDA-MB-231 cells. (A) stable MDA-MB-231 cell lines expressing either the indicated shRNAs or overexpressing the GFP-CYFIP2 protein (GFP-C2) were analyzed by Western blots with NCKAP1 and CYFIP2 antibodies. (B) Quantification of Transwell migration efficiency of cells shown in (A), mean ± SD of n=9 (technical repeats), statistical analysis by one-way ANOVA. (C) Cells were transfected with indicated siRNAs targeting NCKAP1 (N1), CYFIP1 (C1), CYFIP2 (C2) or non-targeting controls (CTR) for 5 days, and plated on Ibidi dishes with inserts (Molinie & Gautreau, 2018). 24 h later, the inserts were removed, and wound healing was monitored by video microscopy as previously described. A picture was taken every 10 min for 18 h. Still images taken when the first wound is closed. Scale bar, 400 µm. Quantification of the closure time, mean ± SD of n=9 technical repeats, statistical analysis by one-way ANOVA.

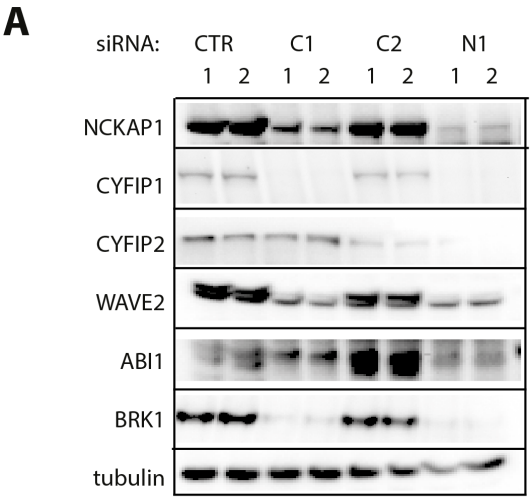

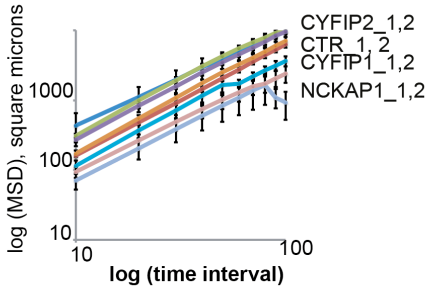

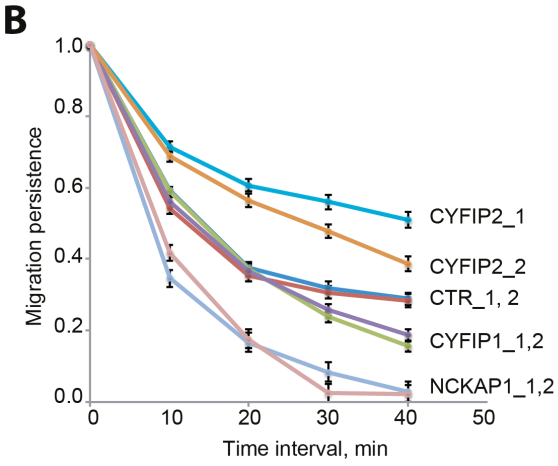

	comparison	p-value	
1	Ctr_1/C1_1	0.46	ns
2	Ctr_2/C1_1	0.82	ns
3	Ctr_1/C1_2	0.38	ns
4	Ctr_2/C1_2	0.71	ns
5	Ctr_1/C2_1	0.0012	**
6	Ctr_2/C2_1	0.00023	***
7	Ctr_1/C2_2	0.044	*
8	Ctr_2/C2_2	0.014	*
9	Ctr_1/N1_1	0.00020	***
10	Ctr_2/N1_1	0.00077	***
11	Ctr_1/N1_2	0.00049	***
12	Ctr_2/N1_2	0.0016	***

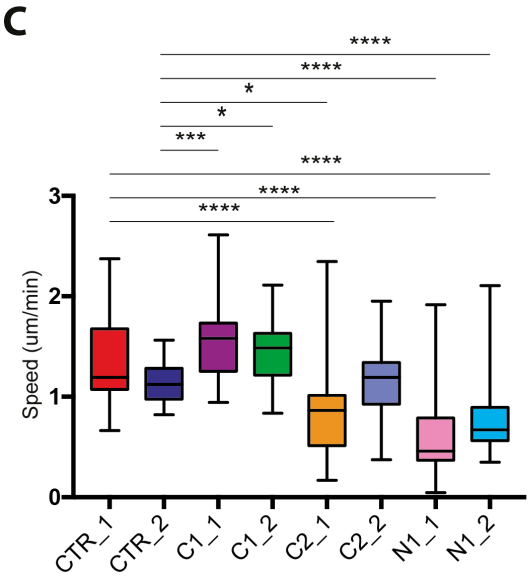

Figure S5. Two independent siRNAs targeting *CYFIP1*, *CYFIP2*, and *NCKAP1* were used to deplete the corresponding proteins from MCF10A cells. Depletion was evaluated by Western blot (A). From single cell trajectories of 2D random migration assays, migration persistence, speed and MSD were calculated and plotted (n=30 cells) (B-D). Statistical analysis was carried out by one-way ANOVA. In panel (C), only the significant differences are indicated.

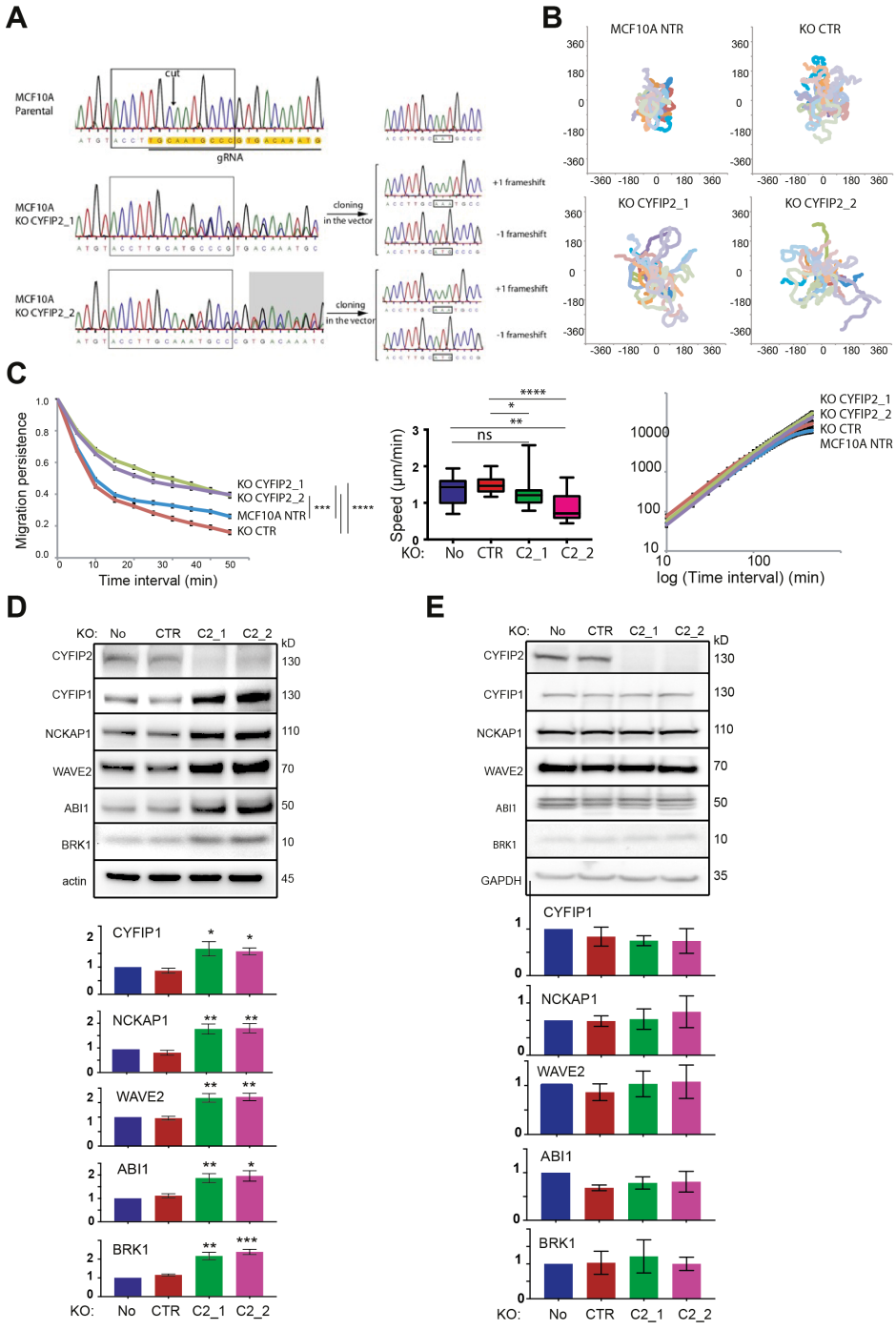

Figure S6. Characterization of CYFIP2 KO clones 1 and 2 in MCF10A cells. (**A**) The only two KO clones that were isolated appeared to have the same genetic alterations. Since they were truly independent, they were both analyzed in parallel in all subsequent assays. (**B**) Trajectories of CYFIP2 KO and control cells in 2D random migration assay, n=30. (**C**) Analysis of migration persistence, speed and MSD of cells shown in (**B**). (**D-E**) Expression of WAVE complex subunits and a quantification of three independent western blots in the above-shown cell lines immediately after selection (**D**) and after two months of culture (**E**).

Supplemental Reference

Molinie N & Gautreau A (2018) Directional Collective Migration in Wound Healing Assays. *Methods in molecular biology (Clifton, NJ)* 1749: 11–19

Legend to supplemental movies

Movie S1. CYFIP2 inhibits migration of MCF7 cells in a wound healing assay. Cells were transfected with indicated siRNAs targeting NCKAP1, CYFIP1, CYFIP2 or non-targeting controls (CTR) for 5 days, and plated on Ibidi dishes with inserts. 24 h later, inserts were removed, and wound healing was monitored by video microscopy. A picture was taken every 20 min. Scale bar: 400 μm.

Movie S2. CYFIP2 inhibits migration of MDA-MB-231 cells in 3D collagen gel. Cells transfected with the indicated siRNAs were recorded by phase contrast optics for 48 h with one frame every 20 min. Scale bar: 50 μm.

Movie S3. CYFIP2 inhibits migration of MCF10A cells. Cells transfected with the indicated siRNAs were recorded by phase contrast optics for 24 h with one frame every 5 min. For the calculation of migration parameters, only single cells were analyzed. Scale bar: 50 μm.

Movie S4. Four-dimensional tracking of prechordal plate nuclei. Nuclei of a Tg(gsc:GFP) embryo were labeled with Histone2B-mCherry (magenta). A Z-stack was acquired every 2 min. Nuclei of prechordal plate cells (identified by GFP expression and morphological criterion), not visible here, were 3D-tracked in time (white squares). Tracks are building up as cells are moving. Animal pole is to the right.

Movie S5. CYFIP2 inhibits actin rich protrusions in zebrafish embryos during gastrulation. Donor embryos were injected with the actin filament marker LifeAct-mCherry mRNA and morpholinos (Mo) targeting CYFIP1 (C1), CYFIP2 (C2), NCKAP1 (N1), alone or in combination with mRNAs encoding the same proteins. 1 frame per minute. Scale bar: 25 μm.

Movie S6. GFP-CYFIP2 restores lamellipodium protrusion and is recruited to the lamellipodial edge. B16-F1 mouse melanoma cells, control and CYFIP1/2 double knock-out (DKO) were transfected with the indicated GFP plasmids and green fluorescence was recorded every 10 s for 10 min.

Movie S7. R87C and I664M CYFIP2 restore lamellipodium protrusion and are recruited to the lamellipodial edge. CYFIP1/2 double knock-out (DKO) B16-F1 cells were transfected with the indicated GFP plasmids and green fluorescence was recorded every 10 s for 10 min.

jove

Deep and Spatially Controlled Volume Ablations using a Two-Photon Microscope in the Zebrafish Gastrula

Arthur Boutillon[1], **Sophie Escot**[1], **Nicolas B. David**[1]

[1] Laboratory for Optics and Biosciences, CNRS UMR7645, INSERM U1182, Institut Polytechnique de Paris

Corresponding Author

Nicolas B. David
nicolas.david@polytechnique.edu

Citation

Boutillon, A., Escot, S., David, N.B. Deep and Spatially Controlled Volume Ablations using a Two-Photon Microscope in the Zebrafish Gastrula. *J. Vis. Exp.* (173), e62815, doi:10.3791/62815 (2021).

Date Published

July 15, 2021

DOI

10.3791/62815

URL

jove.com/t/62815

Abstract

Morphogenesis involves many cell movements to organize cells into tissues and organs. For proper development, all these movements need to be tightly coordinated, and accumulating evidence suggests this is achieved, at least in part, through mechanical interactions. Testing this in the embryo requires direct physical perturbations. Laser ablations are an increasingly used option that allows relieving mechanical constraints or physically isolating two cell populations from each other. However, many ablations are performed with an ultraviolet (UV) laser, which offers limited axial resolution and tissue penetration. A method is described here to ablate deep, significant, and spatially well-defined volumes using a two-photon microscope. Ablations are demonstrated in a transgenic zebrafish line expressing the green fluorescent protein in the axial mesendoderm and used to sever the axial mesendoderm without affecting the overlying ectoderm or the underlying yolk cell. Cell behavior is monitored by live imaging before and after the ablation. The ablation protocol can be used at different developmental stages, on any cell type or tissue, at scales ranging from a few microns to more than a hundred microns.

Introduction

Cell-cell interactions play vital roles in development. Cells provide signals that their direct neighbors or cells further away can perceive, thereby influencing their fate and/or behavior. Many of these signals are chemical in nature. For instance, in the well-characterized induction events, one cell group produces diffusible molecules affecting the fate of another cell population[1]. Other signals, however, are mechanical; cells exert forces and constraints on their neighbors, which the neighbors perceive and respond to[2].

One way of studying the importance of these cell-cell interactions *in vivo* is to eliminate some cells and observe subsequent development. Unfortunately, available techniques to remove or destroy cells are limited. Cells can be removed surgically[3,4], using needles or small wires, but such treatments are invasive, not very precise, and usually performed under a stereomicroscope, preventing immediate

imaging under a microscope. Furthermore, targeting deep cells implies piercing a hole in overlying tissues, creating unwanted perturbations. Genetically encoded photosensitizers, such as KillerRed, have been used to induce cell death via light illumination[5]. Photosensitizers are chromophores that generate reactive oxygen species upon light irradiation. Their main limitation is that they require long light illuminations (around 15 min), which may be difficult to achieve if cells are moving, and that they induce cell death through apoptosis, which is not immediate.

Finally, laser ablations have been developed and widely used in the past 15 years[6,7,8,9,10,11,12]. A laser beam is focused on the targeted cell/tissue. It induces its ablation through heating, photoablation, or plasma-induced ablation; the involved process depends on the power density and exposure time[13]. Most ablation protocols use UV lasers for their high energy. However, UV light is both absorbed and scattered by biological tissues. Thus, targeting deep cells requires a high laser power, which then induces damages in more superficial, out-of-plane tissues. This limits the use of UV lasers to superficial structures and explains their relatively low axial resolution. Non-linear optics (so-called two-photon microscopy) uses non-linear properties of light to excite a fluorophore with two photons of approximately half-energy in the infrared domain. When applied to ablations, this has three main advantages. First, the infrared light is less scattered and less absorbed than UV light by biological tissues[14], allowing to reach deeper structures without increasing the required laser power. Second, the use of a femtosecond pulsed laser provides very high power densities, creating an ablation through plasma induction, which, contrary to heating, does not diffuse spatially[15]. Third, the power density inducing plasma formation is reached at the focal point only. Thanks to these properties, two-photon laser ablations can be used to precisely target deep cells without affecting the surrounding tissue environment.

Collective migrations are an excellent example of developmental processes in which cell-cell interactions are fundamental. Collective migrations are defined as cell migrations in which neighboring cells influence the behavior of one cell[16]. The nature of these interactions (chemical or mechanical) and how they affect cell migration can vary greatly and is often not entirely understood. The ability to remove cells and observe how this affects the others is critical in further unraveling these collective processes. A few years ago, we established — using surgical approaches — that the migration of the polster during zebrafish gastrulation is a collective migration[17]. The polster is a group of cells that constitutes the first internalizing cells on the dorsal side of the embryo[18]. These cells, labeled in green in the *Tg(gsc:GFP)* transgenic line, are located deep in the embryo, below several layers of epiblast cells. During gastrulation, this group leads the extension of the axial mesoderm, migrating from the embryonic organizer to the animal pole[19,20,21,22,23] (**Figure 1A**). We established that cells require contact with their neighbors to orient their migration in the direction of the animal pole. However, better understanding the cellular and molecular bases of this collective migration involves removing some cells to see how this influences the remaining ones. We, therefore, developed ablations of large and deep volumes using a two-photon microscopy setup. Here, we demonstrate the use of this protocol to sever the polster in its middle and observe the consequences on cell migration by tracking nuclei labeled with Histone2B-mCherry.

Protocol

All animal work was approved by the Ethical Committee N 59 and the Ministère de l'Education Nationale, de

l'Enseignement Supérieur et de la Recherche under the file number APAFIS#15859-2018051710341011v3. Some of the steps described below are specific to our equipment and software but could be easily adapted to different equipment.

1. Injection preparation

1. Prepare 75 mL of 1% agarose solution in Embryo Medium (EM).
2. Place the injecting mold in a 90 mm Petri dish and pour approximately 50 mL of agarose, enough for the mold to float. Let the agarose solidify and remove the injecting mold.
3. Prepare an agarose-coated dish by pouring 1 mL of agarose in a 30 mm Petri dish.
4. Prepare 4 µL of 30 ng/µL Histone2B-mCherry mRNA solution by diluting the stock solution in RNase-free water and keep on ice.
   NOTE: Take care to wear gloves while manipulating mRNA to avoid RNase-mediated degradation.
5. Pull an injection needle from a capillary using the micropipette puller.

2. Embryo preparation

1. Once fishes have laid eggs, collect, rinse, and harvest in a 90 mm Petri dish in EM. Place the embryos in a 28.5 °C incubator.
2. Wait 20 min for the first cell to become visible.
3. Transfer 30 embryos to the injection plate filled with EM. Squeeze embryos in the grooves using slightly blunt forceps and orient them with the animal pole up.
4. Using a microloader tip, fill an injection needle with 2 µL of mRNA solution. Insert the needle in the capillary holder placed in a micro-manipulator connected with polytetrafluoroethylene (PTFE) tubing to an air injector.
5. Under the stereomicroscope, carefully break the tip of the needle.
6. Inject the mRNA solution in the 1-cell stage embryos by inserting the needle in the cell.
   NOTE: The volume injected is approximately one-third of the cell volume.
7. Place back injected embryos in the 28.5 °C incubator.

3. Preparation of the two-photon microscope

NOTE: Two lasers are used in this protocol. One is used to image GFP (at 920 nm) and perform ablations (at 820 nm). It will be referred to as the green/ablation laser. The other is used at 1160 nm to image mCherry. It will be referred to as the red laser.

1. Set the green/ablation laser to 820 nm (ablation wavelength) and the red laser to 1160 nm (mCherry excitation).
2. Using movable mirrors on the optical path, align green/ablation and red laser beams both at the entry and exit of the scan head.
   NOTE: This increases the laser beam focus and minimizes focal volume for excitation and ablation.
3. Measure the maximum power of the green/ablation laser at 820 nm under the objective. To do so, place the power meter under the objective, close the black chamber, set green/ablation laser power to 100%, and open the shutters. Compute the percentage of laser power needed to reach 300 mW.

4. Set back the green/ablation laser to 920 nm (GFP excitation) and set the laser power to 7%. Set the red laser power to 15%.
5. Activate epi-PhotoMultiplier Tubes (PMT) detectors for green and red lines; set green and red line PMT sensitivity to 65.
6. Set the field of view to 400 x 400 µm, image resolution to 512 x 512 pixels, and scanning frequency to 800 Hz.
7. Select **3D Timelapse Imaging** mode. Then, create a folder and activate **Autosave** for data after each acquisition.
8. Assemble the heating chamber and set it to 28 °C. Wait at least 10 min for the chamber and the objective to warm.

4. Mounting the embryo

1. Under a fluorescence stereomicroscope, identify embryos at 70% epiboly that express GFP.
   NOTE: Select embryos with a bright signal in the axial mesoderm and no background fluorescence for better imaging quality.
2. Transfer three to four selected embryos in the agarose coated dish (step 1.3) using a plastic Pasteur pipette and carefully dechorionate them using fine forceps.
   NOTE: Dechorionated embryos are very delicate and will burst upon contact with air or plastic.
3. Pour 1 mL of 0.2% agarose in 1x penicillin-streptomycin EM in a small glass vial. Place the vial in a preheated 42 °C dry block heater.
   NOTE: The following steps must be performed quickly to allow embryo orientation before agarose sets.
4. Transfer a dechorionated embryo in the 0.2% agarose glass vial using a fire-polished glass pipette. Take care not to add too much EM in the agarose to avoid diluting it. Discard the remaining EM from the pipette and aspirate the embryo back along with enough agarose to cover the slide of the glass bottom dish before the embryo falls out of the pipette.
5. Blow the agarose and the embryo on the glass slide of the dish. Take care not to let the embryo touch the air or the plastic side of the dish. Next, fill the chamber around the glass slide with agarose.
6. Use an eyelash to orient the embryo so that the targeted region is at the top (**Figure 1B**).
   NOTE: When orienting embryos, take care to only touch the blastoderm, not the very fragile yolk. Agarose will set in around 1 min, depending on room temperature.
7. Wait ~5 min for the agarose to set completely, and then add a few drops of penicillin-streptomycin EM.

5. Locating the embryo and pre-ablation imaging

1. Place the glass bottom dish under the objective in the heated chamber. Immerse the objective in penicillin-streptomycin EM and close the heated chamber.
2. Move the slider to set the light path to oculars. Then, using oculars, fluorescent lamps, and stage control, find an embryo and set the focus to the surface of the embryo.
3. Turn the fluorescence lamp off, set the light path to PMTs, and close the black chamber.
   NOTE: Be careful to turn off all light sources in the black chamber as it might damage the PMTs.
4. Start live imaging and locate axial mesoderm. Adjust the green/ablation and red laser powers to have a good signal (i.e., between 1,000 and 20,000 photons per pixel for GFP expressing areas). Use the red channel to move

the stage to the very top of the embryo and set this position as Z = 0.

5. Choose a time-step of 1 min and a Z-step of 2 µm. A Z-course of 110 µm is sufficient to encompass the whole polster and is acquired in less than 1 min with these settings. Set the first slice 15 µm above the axial mesoderm (in the more superficial ectoderm).

   NOTE: The polster moves along a curved line so that the bottom slice of the Z-stack should be set 30 µm deeper than the polster deepest position to accommodate its movement during the time-lapse imaging (**Figure 1E**).

6. Record 10-15 min of pre-ablation movie.

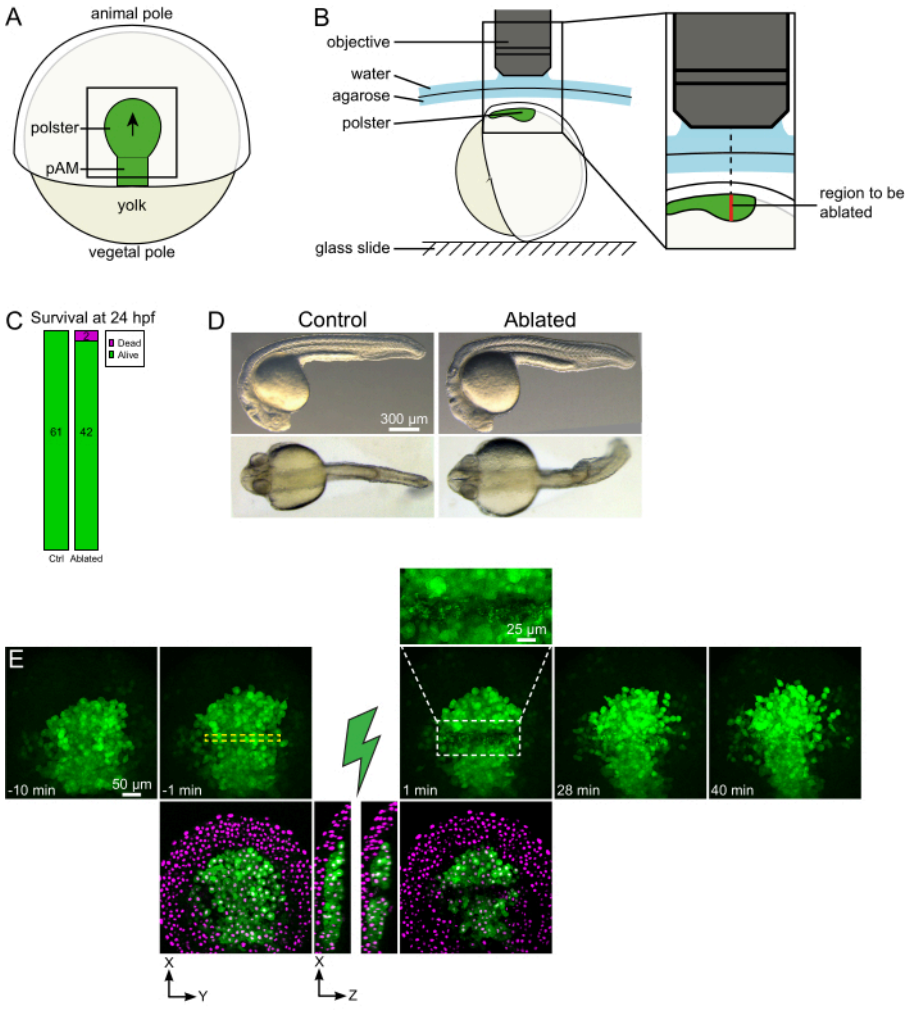

Figure 1: Successful outcome of laser ablations. (**A**) Scheme of a gastrulating embryo at 70% epiboly in dorsal view; pAM: posterior axial mesoderm; black arrow marks the direction of polster migration; black square indicates a typical field of view for ablations in the polster. (**B**) Scheme of embryo mounting for polster severing. Lateral view. The embryo is mounted such that the plane of the polster is perpendicular to the optical axis. (**C**) survival and (**D**) morphology of control and ablated embryos at 24 h post-fertilization. Scale bar is 300 µm. (**E**) Time sequence from laser ablation in the polster of a *Tg(gsc:GFP)* embryo expressing Histone2B-mCherry. Views with the green channel only are maximum projections. The close-up displays the ablated area containing cell debris. Views with green and red (displayed as magenta) channels are XY and XZ slices before and after ablation (the green lightning bolt represents ablation). XZ slices show that the overlying tissues (magenta nuclei without GFP expression) have not been affected by the ablation of underlying structures. The yellow dashed box corresponds to the ROI selected for laser ablation treatment. The scale bar is 50 µm in large views and 25 µm in the close-up. Please click here to view a larger version of this figure.

6. Target location and laser ablation

1. Locate the polster contour on live imaging and, using the Electro-Optic Modulator Region of Interest (EOM ROI) tool, draw a 20 pixel (15 µm) large rectangle that spans the width of the polster. Place this rectangle in the middle of the polster (**Figure 1E**).
2. Note the axial position of the highest and lowest planes containing polster cells. Ablations will be performed every 10 µm in between these two planes. Take care that the ROI does not overlap the yolk cell on any of these planes.
3. Place the stage at the lowest Z position of the interval. Ablations must be performed bottom-up as debris absorb light.
4. Set the green/ablation laser wavelength to 820 nm and set the **Power Percentage** to obtain an exit power of 300 mW (step 3.3).
5. Set the **Imaging Frequency** to 200 Hz.
6. Set green/ablation laser imaging EOM to 0 and select **ROI-Treat** mode.
7. Turn on the EOM and set the treatment to start immediately (after 0 frame).
8. Set the **Imaging Mode** to Timelapse and de-activate **Autosave**.
9. Set the **Time Step** to Fast mode.
10. Set the **Number of Treatment Frames** and **Number of Frames** to the value corresponding to the targeted depth (**Table 1**).

Depth (µm)	Treatment frames
-30	1
-35	1-2
-40	1-2
-45	2
-50	2-3
-55	3
-60	3-4
-65	4
-70	4
-75	4-5
-80	4-5
-85	5
-90	5
-95	5-6

-100	6
-105	6

Table 1: Suggested number of laser treatment frames as a function of targeted cell depth in the embryo (0 being the embryo's surface).

11. Start imaging. The acquisition is black as the shutter to PMT closes during EOM treatment.
12. Move up the stage to the next Z position of the list (step 6.2).
13. Repeat steps 6.10 to 6.12 until the top of the polster is reached.

7. Post-ablation verification and imaging

1. Set the green/ablation laser to 920 nm and 5% power. Set the green/ablation laser imaging EOM to 100 and select the **Fullfield** mode.
2. Set the **Imaging Frequency** to 800 Hz. Turn EOM off.
3. Go through the whole stack in live mode to check whether every plane has been ablated. If this is not the case, go back to step 6.2.
   NOTE: Ablation sometimes induces a vertical shift of neighboring tissues so that the Z-stack might have to be redefined.
4. Set the **Imaging Mode** to 3D Timelapse and re-activate **Autosave**. Record 40-60 min of post-ablation movie.
5. Check, in the post-ablation movie, whether the targeted cells were effectively ablated. Fluorescence recovery, or targeted cells occupying space and preventing follower cells from moving through, indicate that targeted cells were only photobleached and not ablated (**Figure 1E and Figure 2A**).

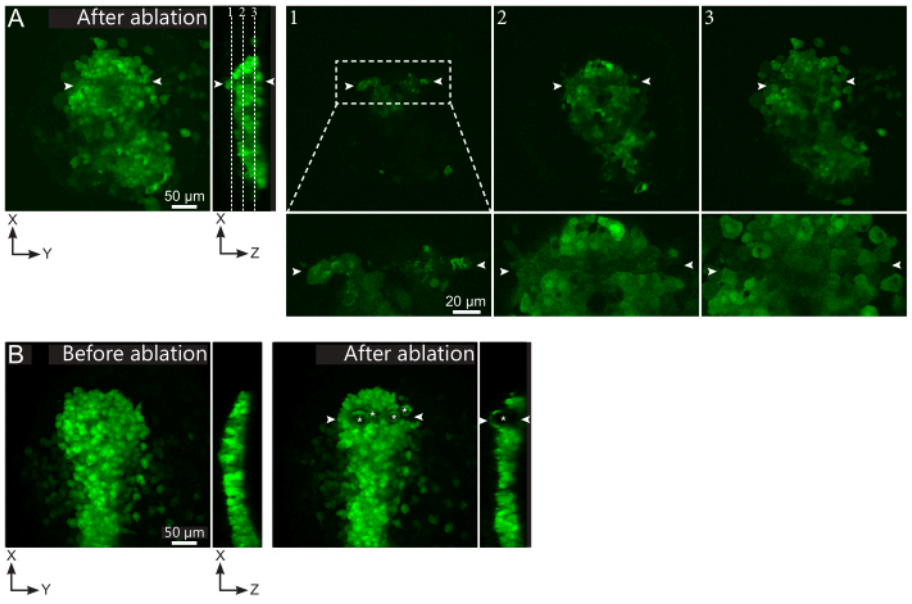

Figure 2: Negative results of laser ablations. (**A**) Typical examples of potential failures in laser ablation. Large XY views are maximum projections, XZ view is a reconstructed section. Laser treated area is located between the two white arrowheads. Three focal planes are highlighted in the reconstructed section and displayed on the right. They correspond to three different kinds of failures. Plane 1 shows that cells above the polster have been ablated. This can be identified by the presence of autofluorescent debris on this focal plane (see close-up) above the polster (see position of plane 1 on the reconstructed section). This likely results from an incorrect definition of the region to be ablated. Plane 2 shows cells that have been bleached but not ablated. They can be identified as the low fluorescence signal still reveals intact cell contours (see close-up). Plane 3 displays intact cells, which have hardly been bleached by laser treatment. This could result from an incorrect definition of the region to be ablated or from poor treatment. In the situations depicted in planes 2 and 3, it is possible to re-apply the ablation treatment to the non-ablated targeted cells. The scale bar is 50 µm in large views and 20 µm in close-ups. (**B**) A typical example of bubbles (marked by white asterisks) formed by cavitation because of a too intense laser treatment. Such bubbles are not limited to a Z-plane, sometimes even spanning the full height of the polster, deforming neighboring tissues. The scale bar is 50 µm. Please click here to view a larger version of this figure.

8. Data analysis

1. Open time-lapse series with the image analysis software and set correct pixel size.
2. In the **Spot** function, set the **Object Size** to 10 µm, as this is the average nucleus size during gastrulation. Then, run the **Spot** function to detect and track the nuclei.

NOTE: Detection may be slightly improved by considering the lower axial resolution, fitting a 12 µm long ellipsoidal shape along the Z-axis.

3. Use filters to remove false positives. In the *Tg(Gsc:GFP)* line, cells from the embryonic axis and some endodermal cells are labeled in green. Hence, filtering on green intensity allows a quick selection of these cells (**Figure 3A**).

4. Set the maximal distance between consecutive points to a value compatible with the speed of the cells.
   NOTE: Be careful to consider the time interval between two frames. Polster cells migrate at 2.8 ± 0.8 µm/min. Hence, allowing 4 µm of maximum displacement for a time step of 1 min removes most artefactual tracks.

5. Allowing gaps over one or two time points provides longer continuous tracks but may introduce tracking errors. If a nucleus is not detected correctly at a one-time point, consider re-running spot detection with different parameters/filters.

6. Visually check tracks and, if necessary, correct them.

7. Export the results as a .xlsx file. Process the file using published spreadsheet routines[24] (**Figure 3B**) and custom routines on data analysis software (available on request).

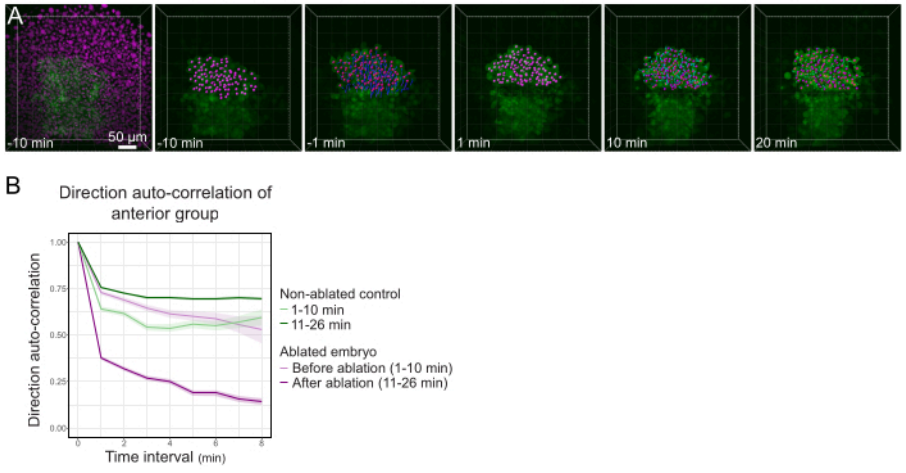

Figure 3: Isolation of the anterior half of the polster affects cell directionality. (**A**) 3D reconstructions a *Tg(gsc:GFP)* embryo expressing Histone2B-mCherry (displayed in magenta), before and after a laser ablation severing the polster in its middle. Nuclei belonging to the anterior half of the polster are marked with a magenta dot and tracked over time before and after ablation (see **Movie S1**). The scale bar is 50 µm. (**B**) As a measure of migration persistence, direction auto-correlation of cells belonging to the anterior part of the polster before and after ablation. Cells display a continuous motion before ablation, which drastically decreases after ablation, indicating loss of collective-oriented migration. Direction auto-correlation was also measured on cells forming the anterior half of the polster of a non-ablated embryo, as a control. The graph envelopes indicate standard error. Please click here to view a larger version of this figure.

Representative Results

To sever the polster in its middle, a *Tg(gsc:GFP)* embryo, injected with Histone2B-mCherry mRNAs was mounted at the 70% epiboly stage, as described in step 4. The polster was identified by GFP expression, and the embryo was mounted so that the plane of the polster is perpendicular to the optical axis (**Figure 1B**). Tilting the embryo away from this position will complicate the procedure. The light will have to go through more tissues to reach the ablation planes, and ablation planes will be tilted relative to embryonic axes. Having verified that all the cell nuclei are correctly labeled, a 10 min pre-ablation time-lapse was recorded to capture cell movements before ablation (**Figure 1E** and **Figure 3A**, **Movie S1**).

The polster was morphologically identified, and a rectangular area of 15 µm x 200 µm, located in its middle, was ablated on five focal planes to ensure severing on the whole depth of the polster (**Figure 1E**, **Movie S1**). Imaging was restarted right after ablation and used to monitor the efficiency of the procedure. If successful, the ablation will have eliminated all cellular structures and GFP and mCherry fluorescence so that the ablated volume should appear as a signal-free volume. However, some debris may be created. This debris is autofluorescent, both in the green and red channels, and usually displays irregular elongated shapes parallel to the direction of ablation (**Figure 1E**). A too intense treatment will form a large amount of debris that may act as an obstacle and perturb cell behavior. Stronger treatments will even induce cavitation, marked by the formation of bubbles in the tissue (**Figure 2B**). Cavitation is associated with a mechanical shock wave propagating in tissues and may induce damages out of the targeted volume[13,15]. Embryos with cavitation bubbles should be discarded, and treatment should be tuned down by performing fewer treatment frames.

Conversely, too little treatment may photobleach fluorophores without inducing plasma formation, hence without ablating (**Figure 2A**). Incomplete photobleaching can easily be spotted by the presence of dim fluorescence with a characteristic cellular shape (**Figure 2A**). Such embryos should be discarded or treated again performing more treatment frames. Complete photobleaching is more challenging to differentiate from successful ablation, as both would result in a signal-free volume. Photobleaching can, however, be identified retrospectively, as fluorescence will progressively recover in the course of the post-ablation imaging. This, however, implies that non-ablated embryos are imaged for at least half an hour, which is time-consuming. We, therefore, suggest adjusting the treatment intensity (by increasing the number of treatments) to induce the formation of few visible debris, which will not affect cell behavior but immediately confirm effective ablation. Finally, the absence of damage in cells surrounding the ablation volume should be checked on the first post-ablation images (**Figure 2A**). When laser treatment is tuned correctly (formation of few debris) damages in neighboring tissues are unlikely to result from the spatial spreading of the ablation, which is very well spatially defined, but rather result from inaccurate selection of the region to be ablated and/or tissue movements in the time between target selection and ablation. Embryos with affected neighboring tissues should be discarded.

After successful ablation, Z-stacks were captured every minute for 40 min, recording both the GFP cytoplasmic signal and the mCherry nuclear signal. Nuclei were then tracked, and their movement was used as a proxy for cell movement. Tracks corresponding to polster cells were identified on their

strong GFP signal (**Figure 3A**, Movie S1). The persistence of cell movement was measured by computing the cell direction auto-correlation[24]. Focusing on polster cells located in the anterior half of the polster revealed that severing the polster in its middle, thus separating these cells from the posterior part of the polster, decreased their direction autocorrelation (**Figure 3B**), demonstrating that proper migration of polster cells requires integrity of the whole polster, in line with its demonstrated collective migration[17].

After acquiring the post-ablation movie, embryos can be unmounted, carefully extracting them from the agarose using fine forceps, and incubated at 28.5 °C until they reach 24 h post-fertilization. Again, embryos should survive and should not present any apparent morphological defect (**Figure 1C,D**).

Movie S1: Successful laser ablation. Laser ablation in the middle of the polster of a *Tg(gsc:GFP)* embryo expressing Histone2B-mCherry. Nuclei from the anterior part of the polster are tracked over time and marked by magenta dots. Tracks are time color-coded (**Figure 3**). Empty frames correspond to laser ablation. Please click here to download this Movie.

Discussion

Here, we describe a protocol that uses non-linear optics to perform deep and spatially well-defined volume ablations. The most critical step of the protocol is to find treatment conditions that provide sufficient energy to allow ablations, but not too much energy, to avoid excessive debris or cavitation. The amount of delivered energy at the target site mainly depends on: (1) the laser exit power, (2) the quality of laser alignment, (3) the nature of the tissue through which the light passes to reach the ablation plane, (4) the depth of the ablation plane. Therefore, before each experiment, it is crucial to measure laser exit power, adjust it to a reference value (300 mW at 820 nm in our protocol), and ensure proper laser alignment. Under these assumptions, treatment conditions should be reproducible from one experimental day to another. We recommend performing extensive tests to define optimal parameters (laser power and number of treatment frames) for a specific sample type. These parameters can then be used in all similar experiments. In the example described here (severing of the polster during gastrulation), we have, for instance, established treatment conditions for ablations at different depths within the embryo (**Table 1**) and now rely on this chart when performing experiments. Of note, the 820 nm wavelength was chosen as it is, on our system, the wavelength providing the highest peak energies (due to laser and optics properties). Shorter or longer wavelengths could be used depending on system properties[6,11,12]. Depth of the targeted tissue being a critical parameter, embryo mounting is also a crucial step, as incorrect mounting may increase tissue thickness that light must pass through to reach the target volume.

One of the original features of the described protocol is to ablate an entire volume by performing successive ablations on different focal planes. Since ablations will generate debris that absorbs light, we identified that it is crucial to start ablation on the most profound plane and sequentially ablate from the deepest to the most superficial plane.

This protocol describes the ablation of deep and large volumes and the recording of neighboring tissue response within minutes after ablation to over an hour. One of the potential limitations of the protocol is the time required to perform ablation and restart imaging. Two factors limit this delay. The first one is the time needed to perform ablations on multiple focal planes. On our system, severing of the polster

is performed by a trained user in 2-3 min. This could be reduced by optimizing the software to automate the ablation on different planes. Still, total ablation time will equal the time required to scan the target region, times the number of repetitions on each focal plane, times the number of focal planes, which, in our conditions, is about 1 min. Considering cell migration speed, this means that some cells may enter or exit the targeted area during the ablation procedure. In our case, this did not prove to be an issue but could be if an absolute precision in cell targeting is required. The second limiting factor is that the same laser is used to perform ablation (at 820 nm) and excite green fluorophore (at 920 nm). The delay between the last ablation and the start of recording is thus defined by the time required to tune the laser from 820 nm to 920 nm, ranging from 30 s to 1 min.

In some cases, in particular, for smaller ablations (single-cell ablation, ablations of subcellular components such as cytoskeleton elements), recording the immediate response of the cell/tissue may be critical to infer its mechanical state[25,26,27]. In such cases, the limitation could be circumvented, either by imaging with another laser (here, for instance, recording only red signals with the 1160 nm laser or using a third laser line) or imaging green fluorophore at 820 nm. This is not the optimal wavelength for imaging (limited excitation of fluorophores, strong photo-toxic effects) but could be used over short periods to record immediate tissue response.

Few techniques are available to eliminate cells and see how this affects the rest of the embryo. The two main options are to remove cells physically or to destroy them, as in laser ablations. Compared to physical removal, cell destruction may release cytoplasmic content, which can influence neighboring cells. This was historically highlighted by the controversy and diverging results obtained by Wilhelm Roux and Hans Driesch regarding the mosaic or regulative development of the frog and sea urchin embryo[28]. More recently, differences have been observed in wound healing assays, depending on whether the wound is created by scratch (which destroys some cells) or removing an insert[29]. However, physically removing cells without damaging other tissues is only possible for cells at the very surface of the embryo and cells that are not too adherent to their neighbors, thus limiting the range of such approaches. Consequently, different strategies have been developed to destroy cells, laser ablations being the most employed. UV laser ablations have been and are increasingly used, in particular, to perform small, superficial ablations, and observe immediate tissue response.

We here described the use of infrared light to perform deeper and spatially well-defined ablations. The main limitation of this protocol is the requirement for an infrared pulsed laser and a two-photon imaging setup. However, such equipment is becoming more and more frequent on imaging platforms. In addition, the EOM used here to ablate one region in the image selectively could be replaced by a Fluorescence Recovery After Photobleaching (FRAP) module. Though less convenient, it could even be possible to perform the protocol without EOM nor FRAP modules by simply zooming on the targeted area[10]. Using a pulsed infrared laser brings two main advantages compared to most classical ablation protocols. First, thanks to the efficient penetration of infrared light in living tissues, deep focal planes can be reached with laser powers that do not induce out-of-focus damages. This allowed us to target cells as deep as 120 µm, out of reach with one-photon excitation protocols. Second, the use of non-linear optics ensures excellent axial resolution, permitting precisely controlled 3D ablations, even at depth in

the tissue. Combining these two advantages allows ablation of specifically defined, deep, and eventually large volumes.

We describe using a two-photon microscope to sever the polster, an experiment we and others recently performed[30]. With few adjustments, the proposed protocol could, however, be adapted to many different samples. We have, for instance, successfully used it to perform complete ablation of the polster, ablations within the lateral mesoderm during gastrulation, or ablations of individual Schwan cells during their migration on their associated axon, without affecting the axon. We, therefore, believe this protocol is a valuable and versatile tool, which should be helpful in many experimental systems to analyze the impact of some cells/tissues on the behavior and development of the neighboring structures.

Disclosures

The authors declare no competing interests.

Acknowledgments

We thank Emilie Menant for fish care, the Polytechnique Bioimaging Facility, in particular Pierre Mahou, for assistance with live imaging on their equipment partly supported by Région Ile-de-France (interDIM) and Agence Nationale de la Recherche (ANR-11-EQPX-0029 Morphoscope2, ANR-10-INBS-04 France BioImaging). This work was supported by the ANR grants 15-CE13-0016-1, 18-CE13-0024, 20-CE13-0016, and the European Union's Horizon 2020 research and innovation programme under the Marie Skłodowska-Curie grant agreement No 840201, the Ministère de l'Enseignement Supérieur et de la Recherche and the Centre National de la Recherche Scientifique.

References

1. Slack, J. M. W. Embryonic induction. *Mechanisms of Development.* **41** (2-3), 91-107 (1993).
2. Fernandez-Sanchez, M.-E., Brunet, T., Röper, J.-C., Farge, E. Mechanotransduction's impact on animal development, evolution, and tumorigenesis. *Annual Review of Cell and Developmental Biology.* **31**, 373-397 (2015).
3. Shih, J., Fraser, S. E. Characterizing the zebrafish organizer: microsurgical analysis at the early-shield stage. *Development.* **122** (4), 1313-1322 (1996).
4. Selleck, M. A. J. Culture and microsurgical manipulation of the early avian embryo. *Methods in Cell Biology.* **51** (51), 1-21 (1996).
5. Bulina, M.E. et al. A genetically encoded photosensitizer. *Nature Biotechnology.* **24** (1), 95-99 (2006).
6. Fang-Yen, C., Gabel, C. V., Samuel, A. D. T., Bargmann, C. I., Avery, L. Laser microsurgery in Caenorhabditis elegans. *Methods in Cell Biology.* **107**, 177-206 (2012).
7. Colombelli, J., Grill, S. W., Stelzer, E. H. K. Ultraviolet diffraction limited nanosurgery of live biological tissues. *Review of Scientific Instruments.* **75** (2), 472-478 (2004).
8. Smutny, M., Behrndt, M., Campinho, P., Ruprecht, V., Heisenberg, C.-P. UV laser ablation to measure cell and tissue-generated forces in the zebrafish embryo in vivo and ex vivo. *Methods in Molecular Biology (Clifton, N.J.).* **1189**, 219-235 (2015).
9. Behrndt, M. et al. Forces driving epithelial spreading in zebrafish gastrulation. *Science.* **338** (6104), 257-260 (2012).
10. Volpe, B. A., Fotino, T. H., Steiner, A. B. Confocal microscope-based laser ablation and regeneration assay

in zebrafish interneuromast cells. *Journal of Visualized Experiments: JoVE.* **2020** (159), 1-9 (2020).

11. Bonnet, I. et al. Mechanical state, material properties and continuous description of an epithelial tissue. *Journal of the Royal Society, Interface.* **9** (75), 2614-2623 (2012).
12. Rauzi, M., Lenne, P. F., Lecuit, T. Planar polarized actomyosin contractile flows control epithelial junction remodelling. *Nature.* **468** (7327), 1110-1115 (2010).
13. Niemz, M. H. *Laser-Tissue Interactions. Encyclopedia of Biomaterials and Biomedical Engineering, Second Edition - Four Volume Set.* Springer International Publishing. Cham (2019).
14. Smith, A. M., Mancini, M. C., Nie, S. Bioimaging: second window for in vivo imaging. *Nature Nanotechnology.* **4** (11), 710-711 (2009).
15. Rauzi, M., Lenne, P.-F. Cortical forces in cell shape changes and tissue morphogenesis. *Current Topics in Developmental Biology.* **95**, 93-144 (2011).
16. Theveneau, E., David, N. B. Migrations cellulaires collectives. *Medecine/Sciences.* **30** (8-9), 751-757 (2014).
17. Dumortier, J. G., Martin, S., Meyer, D., Rosa, F. M., David, N. B. Collective mesendoderm migration relies on an intrinsic directionality signal transmitted through cell contacts. *Proceedings of the National Academy of Sciences of the United States of America.* **109** (42), 16945-16950 (2012).
18. Solnica-Krezel, L., Stemple, D. L., Driever, W. Transparent things: cell fates and cell movements during early embryogenesis of zebrafish. *BioEssays.* **17** (11), 931-939 (1995).
19. Montero, J.-A., Kilian, B., Chan, J., Bayliss, P. E., Heisenberg, C.-P. Phosphoinositide 3-kinase is required for process outgrowth and cell polarization of gastrulating mesendodermal cells. *Current Biology.* **13** (15), 1279-1289 (2003).
20. Ulrich, F. et al. Slb/Wnt11 controls hypoblast cell migration and morphogenesis at the onset of zebrafish gastrulation. *Development.* **130** (22), 5375-5384 (2003).
21. Kai, M., Heisenberg, C.-P., Tada, M. Sphingosine-1-phosphate receptors regulate individual cell behaviours underlying the directed migration of prechordal plate progenitor cells during zebrafish gastrulation. *Development.* **135** (18), 3043-3051 (2008).
22. Smutny, M. et al. Friction forces position the neural anlage. *Nature Cell Biology.* **19** (4), 306-317 (2017).
23. Johansson, M., Giger, F. A., Fielding, T., Houart, C. Dkk1 controls cell-cell interaction through regulation of non-nuclear β-Catenin pools. *Developmental Cell.* **51** (6), 775-786.e3 (2019).
24. Gorelik, R., Gautreau, A. Quantitative and unbiased analysis of directional persistence in cell migration. *Nature Protocols.* **9** (8), 1931-1943 (2014).
25. Grill, S. W., Howard, J., Schäffer, E., Stelzer, E. H. K., Hyman, A. A. The distribution of active force generators controls mitotic spindle position. *Science (New York, N.Y.).* **301** (5632), 518-521 (2003).
26. Desprat, N., Supatto, W., Pouille, P.-A. A., Beaurepaire, E., Farge, E. Tissue deformation modulates twist expression to determine anterior midgut differentiation in Drosophila embryos. *Developmental Cell.* **15** (3), 470-477 (2008).

27. Farhadifar, R., Röper, J.-C., Aigouy, B., Eaton, S., Jülicher, F. The influence of cell mechanics, cell-cell interactions, and proliferation on epithelial packing. *Current Biology.* **17** (24), 2095-2104 (2007).

28. Willier, B. H., Oppenheimer, J. M. *Foundations of Experimental Embryology.* Englewood Cliffs: Prentice-Hall (1964).

29. Ashby, W. J., Zijlstra, A. Established and novel methods of interrogating two-dimensional cell migration. *Integrative Biology: Quantitative Biosciences from Nano to Macro.* **4** (11), 1338-1350 (2012).

30. Bosze, B. et al. Pcdh18a regulates endocytosis of E-cadherin during axial mesoderm development in zebrafish. *Histochemistry and Cell Biology.* 154 (5), 463-480 (2020).

© 2021. MANUSCRIPT SUBMITTED TO DEVELOPMENT (2021) 00, devxxxxxx. doi:10.1242/dev.xxxxxx

TECHNIQUES AND RESOURCES

Live 3D imaging and mapping of shear stresses within tissues using incompressible elastic beads

Alexandre Souchaud[1], Arthur Boutillon[2], Gaëlle Charron[1], Atef Asnacios[1], Camille Noûs[3], Nicolas B. David[2], François Graner[1] and François Gallet[1]

ABSTRACT

To investigate the role of mechanical constraints in morphogenesis and development, we develop a pipeline of techniques based on incompressible elastic sensors. These techniques combine the advantages of incompressible liquid droplets, which have been used as precise *in situ* shear stress sensors, and of elastic compressible beads, which are easier to tune and to use. Droplets of a polydimethylsiloxane (PDMS) mix, made fluorescent through specific covalent binding to a rhodamin dye, are produced by a microfluidics device. The elastomer rigidity after polymerization is adjusted to the tissue rigidity. Its mechanical properties are carefully calibrated in situ, for a sensor embedded in a cell aggregate submitted to uniaxial compression. The local shear stress tensor is retrieved from the sensor shape, accurately reconstructed through an active contour method. *In vitro*, within cell aggregates, and *in vivo*, in the prechordal plate of the Zebrafish embryo during gastrulation, our pipeline of techniques demonstrates its efficiency to directly measure the three dimensional shear stress repartition within a tissue, and its time evolution.

KEYWORDS: Mechanical stress, elastic gel, sensor, PDMS, cell aggregate, Zebrafish

INTRODUCTION

The cohesion and morphogenesis of living tissues require coordinated processes at the cellular scale, based on changes in cell number, size, shape, position and packing (Heisenberg and Bellaïche, 2013; Guirao et al., 2015). These rearrangements are possible because cells can generate and exert mechanical stresses on their surroundings, or conversely feel the stresses and transduce them into biological signals. The complete process is thus regulated under the dual control of genetics and mechanics, which mutually feedback on each other, and drive the growth and shape of tissues (Desprat et al., 2008). Hence, the impact of mechanics on tissue fate and organization is considerable, either for healthy organisms during embryo development (Krieg et al., 2008; Le Goff et al., 2013; Heisenberg and Bellaïche, 2013; Hiramatsu et al., 2013; Hamada, 2015; Herrera-Perez and Karen, 2018), or in pathological conditions (Wells, 2013; Delarue et al., 2014; Angeli and Stylianopoulos, 2016). Quantitative studies about the role of mechanical constraints in morphogenesis and development benefit from a precise and quantitative knowledge of the spatial distribution of mechanical stresses, from the subcellular scale to the tissue scale, and of its temporal evolution.

In the past decades numerous methods have been developed in order to achieve *in situ* stress measurements, using different and complementary techniques; for reviews see Sugimura et al. (2016); Campàs (2016); Roca-Cusachs et al. (2017); Gomez-Gonzalez et al. (2020). To summarize, these techniques can be classified into approximately four categories : (i) External contact manipulations, including micropipettes (Mitchison and Swann, 1954; Hochmuth, 2000; Von Dassow et al., 2010; Guevorkian et al., 2010), microplates (Desprat et al., 2005; Mitrossilis et al., 2009; Tinevez et al., 2009; Mgharbel et al., 2009), AFM indentation (Butt et al., 2005; Elkin et al., 2007; Xiong et al., 2009; Franze, 2011; Lau et al., 2015), traction force microscopy (TFM) (Nier et al., 2016) ; (ii) Manipulations using light, comprising laser ablation (Rauzi et al., 2008; Bonnet et al., 2012; Porazinski et al., 2015) and optical tweezers (Neuman and Nagy, 2008; Bambardekar et al., 2015) - and also by extent magnetic tweezers (Hosu et al., 2003; Tanase et al., 2007; Mazuel et al., 2015) ; (iii) Non-contact optical imaging, in which one can find birefringence (Nienhaus et al., 2009; Schluck and Aegerter, 2010) and stress inference (Chiou et al., 2012; Ishihara et al., 2013; Brodland et al., 2014; Roffay et al., 2021) ; and finally (iv) Embedded local sensors, from FRET at the molecular scale (Grashoff et al., 2010; Borghi et al., 2012) to microsensors at the cell scale (Campàs et al., 2014; Dolega et al., 2017; Mongera et al., 2018; Mohagheghian et al., 2018; Lee et al., 2019; Träber et al., 2019).

The latter technique based on microsensors is quantitative, barely perturbative, and suitable to monitor tissue stresses at the scale of a cell or a group of cells. Two main avenues have already been explored.

The pioneer article (Campàs et al., 2014) has used incompressible liquid droplets to measure the shear stress tensor, which is the most important stress component to understand how anisotropic forces govern tissue morphogenesis. Liquid microdroplets, made of fluorocarbon oil, have been injected in aggregates of mesenchymal cells, in living mandible explants. Coating the oil surface with a biocompatible surfactant enables the droplet insertion in the tissue. The mechanical stresses exerted by the surrounding cells modify the droplet shape, and the deviation from the average stress normal to the droplet surface can be calculated from its local curvature, according to Laplace's law. Direct and accurate

[1]Matière et Systèmes Complexes, UMR 7057 associée au CNRS et à l'Université de Paris, 10 rue Alice Domon et Léonie Duquet, 75013 Paris, France.
[2]Laboratory for Optics and Biosciences, Ecole Polytechnique, CNRS, INSERM, Institut Polytechnique de Paris, 91128 Palaiseau, France.
[3]Laboratory Cogitamus, France

Authors for correspondence: francois.gallet@u-paris.fr; francois.graner@u-paris.fr

Received xxx 2021

Development (2021) 00, devxxxxxx. doi:10.1242/dev.xxxxxx

measurements of the three-dimensional (3D) components and orientations of the shear stress tensor require a precise control and calibration of the liquid/tissue surface tension. The same group has refined the technique and successfully applied it to Zebrafish embryos (Mongera et al., 2018).

Other groups have favored elastic beads because they are easier to produce, tune, calibrate, manipulate, insert in tissues, and analyze. The stress exerted on a solid sensor by surrounding cells can be deduced from its deformation, provided that the elastic moduli are determined through an independent calibration. Inspired by Matrigel pressure sensors (Monnier et al., 2016), sensors have been prepared using polyacrylic acid (PAA) hydrogels (Dolega et al., 2017; Lee et al., 2019; Träber et al., 2019), whose Young modulus can be tuned from 60 to 4000 Pa (Lee et al., 2019), or alginate gels (Mohagheghian et al., 2018), and injected in cell aggregates or Zebrafish embryos. Water can flow in and out of an hydrogel, making it compressible. In principle this method yields access to the whole stress, that is, simultaneously the compression stress (including osmotic pressure contributions) and shear stress. The rest state for each sensor without stress can be determined at the end of the experiment by lysing the cells ; once the compression stress is determined, the shear stress can be estimated by substraction (Mohagheghian et al., 2018).

To combine the chemical and mechanical advantages of incompressible liquid droplets, namely fluorescence, functionalization, and accurate shear stress measurements, with the ease to tune and use compressible solid beads, we develop a pipeline of techniques based on incompressible solid beads of diameter comparable to the cell size. The material must exhibit a well-defined elastic behavior, with a Young modulus comparable to the one of the surrounding tissue (order of magnitude 10^3 Pa), in order to get a measurable deformation under physiological stresses, which expected order of magnitude is e.g. 10^2 Pa in zebrafish development (Mongera et al., 2018). Coating of the sensors surface is necessary to make them biocompatible and to make their insertion non-perturbative. To observe the sensor's deformation and get a precise 3D reconstruction of its shape, a stable fluorescent labelling is also needed.

Our choice fell on polydimethylsiloxane (PDMS), which is an elastic elastomer, with a Young modulus adjustable down to a few hundred Pa (Hobbie et al., 2008). Production of small droplets of PDMS polymerisable mixture, having a fixed diameter, can be easily controlled through a microfluidic device. We introduce a novel method to bind the elastomer to a fluorescent dye through covalent bonds, leading to a stable, homogeneous and high intensity fluorescence. Coating the PDMS with cell adhesion proteins is also possible in principle. The sensors can be embedded in the tissue in a non-perturbative way, and their deformation followed over minutes or hours. For 3D image analysis, we implement an active contour method algorithm to determine the shape of the deformed sensors. This method leads to direct and accurate measurements of the 3D components and orientations of the shear stress tensor.

The technique was successfully tested in two different systems, *in vitro* and *in vivo*. First, reconstituted cell aggregates were chosen as a tumor model, for which it is well known that mechanical constraints have a major influence on the organization and fate (Delarue et al., 2014; Northcott et al., 2018). Moreover, it is relatively easy to produce aggregates with embedded sensors, which makes it a privileged system to validate the method. Second, we investigated the distribution of mechanical constraints in the prechordal plate of the Zebrafish embryo during its development. Indeed, based on *in vitro* observation, it has been postulated that anisotropies and heterogeneities of mechanical stresses are present in the prechordal plate, and are of importance to guide its migration (Weber et al., 2012; Behrndt and Heisenberg, 2012). However, due to the lack of appropriate tools, the existence of such anisotropies could not be directly tested so far. The implantation of our mechanical sensors in this system could definitively help to decide between different models actually disputed.

In both cases, *in vitro* and *in vivo*, we report here results concerning the spatial repartition and temporal evolution of the shear stresses, providing clear demonstration of the usability and potential of these new sensors.

METHODS

The above requirements can be summarized as follows : the sensors must have a size comparable to the cell size, and be easily fabricated and manipulated in large quantities, with monodisperse radius ; they must be biocompatible and conveniently embedded in living tissues ; their rigidity has to be homogeneous and close to those of the tissues ; they can be fluorescently labelled in a homogeneous and stable way ; their 3D shape can be precisely reconstructed with minimal effort ; the effective shear modulus of the sensors can be reliably calibrated *in situ* ; the shear stress tensor can be decoupled from compression stress and directly derived from the 3D sensor's deformations by using linear elasticity ; shear stresses of order of 10^2 Pa can be measured with 10 Pa sensitivity. To satisfy simultaneously all these constraints, we introduce the following pipeline of techniques.

Microsensors fabrication

The microsensors were made out of a silicon elastomer similar to usual PDMS. The polymerizable mix preparation is first dispersed into liquid droplets of about 30 μm in size, thanks to a microfluidic circuit, and afterwards polymerized at $80 \pm 1°$C. Briefly, the main component of the elastomer is vinyl terminated polydimethylsiloxane, hereafter coined DMS. It is mixed with a polymeric hydrosilane (methylhydrosiloxane-dimethylsiloxane copolymer) that acts as a cross-linker via hydrosilylation of the vinyl ends of DMS (Fig. S1a). The ratio of cross-linker to DMS must be carefully controlled ($m_{cross} = 1.60 \times 10^{-2}\ m_{DMS}$) to achieve the desired shear modulus after polymerisation. The hydrosilylation reaction is initiated using Karstedt's catalyst ($m_{catal} = 4.286 \times 10^{-3}\ m_{DMS}$). A divinylic inhibitor (diallyl maleate) is also added ($m_{inhib} = 0.8571 \times 10^{-3}\ m_{DMS}$) to slow down the reaction kinetics. The as-prepared mixture needs to be stored at 4°C and should be used within a few days least the cross-linking reaction significantly moves forward.

Dispersing the polymerizable mix into spherical droplets of homogeneous size is obtained through a custom-made microfluidic circuit, by a classical flow focusing method (Haejune, 2007). The dispersed phase (polymer mix) meets the carrier phase (water) at a 4-channels crossing, and the resulting droplets suspension is collected at the output. The rectangular channel section is about $50 \times 20\ \mu m^2$. The injecting pressures of both phases is finely tuned and regulated by a Fluigent controller, in order to get a steady-state dripping instability and a constant droplet diameter. This diameter may be tuned between 20 and 40 μm. It is stable for a given droplet batch : the diameter distribution of droplets is quite monodisperse within a same production (Fig. 1).

Development (2021) 00, devxxxxxx. doi:10.1242/dev.xxxxxx

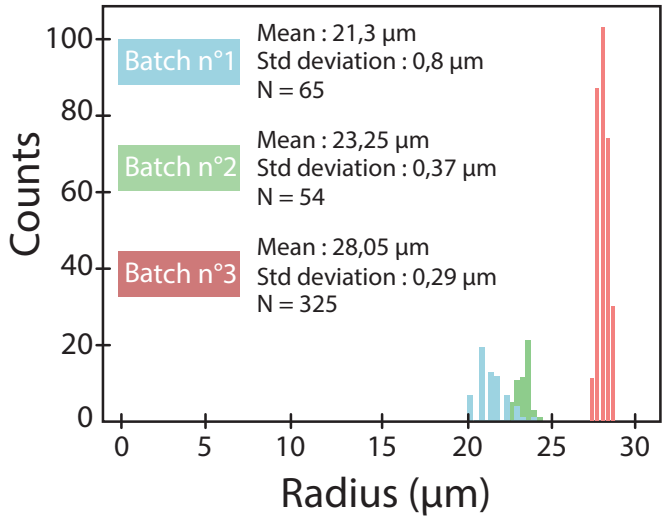

Fig. 1. Distribution of microsphere's radii for three different batches obtained with a microfluidic device

The droplets polymerization into spherical elastic beads is achieved by baking the suspension at $80^{\circ}\mathrm{C}$ during 3 h. The final gel is very soft. It sticks easily and irreversibly to any wall, including inert surfaces like teflon or silanized glass. Thus one must avoid the contact of the droplets with any solid surface during and after polymerization. To achieve this, the beaker containing the suspension is placed during baking on a turntable, rotating at about one turn per second. Since the gel is less dense than water, buoyancy makes the polymerized beads spontaneously concentrate at the center of the meniscus of the water free surface. Then, the concentrated suspension containing about 10^4 beads per mL can be collected with a micropipette, aliquoted in Eppendorf tubes and immediately stored in a freezer at $-20^{\circ}\mathrm{C}$. The beads remain stable for weeks at this temperature, and are thawed before immediate use.

Fluorescent labelling

In order to observe the sensors embedded in the tissue, a dye must be added to the elastomer. The objective is to get an homogeneous fluorescent signal, with high enough intensity, to be able to visualize the sensors with usual fluorescent microscopy techniques (confocal, spinning-disk and 2-photon microscopy) and to precisely reconstruct their 3D shape. Several hydrophobic dyes did not lead to satisfying labelling : either the dye could not be homogeneously dispersed in the polymer mix (fluorescein diacetate), or it was partially released in the water solution surrounding the beads, so that the fluorescent signal rapidly decreased with time (Nile Red and Cryptolyte™). We also attempted to label the elastomer with quantum dots (QDs) dispersed in the mixture. However, despite some specific coating to make them hydrophobic, QDs remained partially aggregated and the dispersion was not complete.

For efficient fluorescent labelling of the elastomer, two challenges needed to be overcome: the dye had to easily disperse into the polymerisable mix and, once dispersed and after curing, should not escape the meshwork of the gel and leak into the surroundings. Our strategy entailed attachment of the organic dye to the cross-linker via a parallel hydrosilylation reaction (Fig. S1b). The dye therefore needed to bear a vinyl terminal group. Isothiocyanate-bearing fluorophores can be conveniently modified through quantitative C-N bond formation. We selected Rhodamine B isothiocyanate because of its emission in the red and condensed it with allylamine to give a vinyl-terminated rhodamine B analogue (Fig. S1c). The compound was then added to DMS in a molar ratio of one fluorophore for 1,000 DMS strands (see Supplementary Files for details).

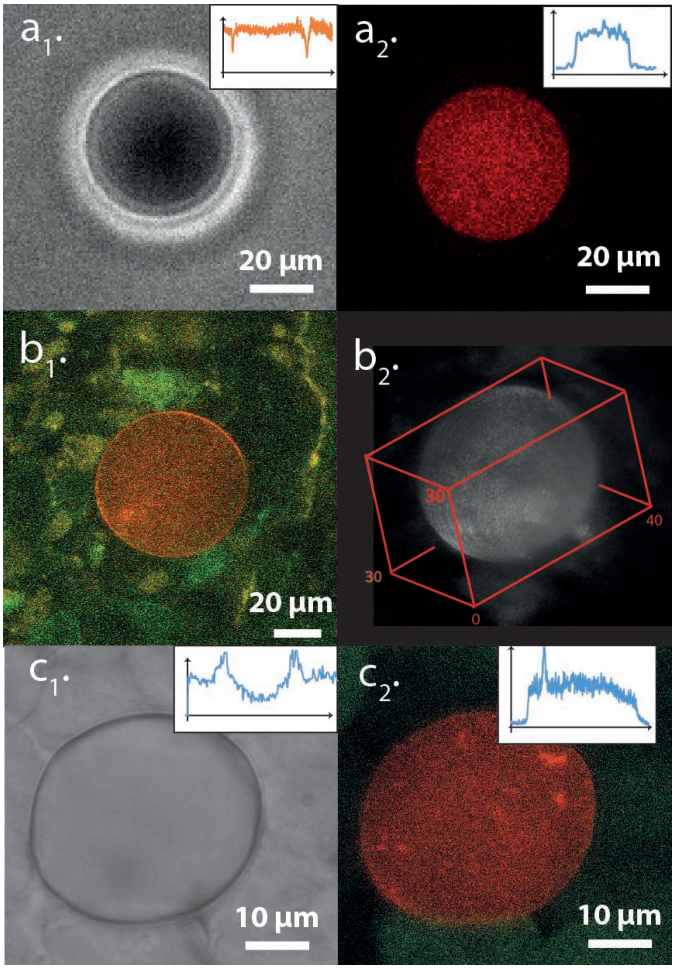

Fig. 2. Images of three sensors in different situations : (a) suspended in water ; (b) embedded in a CT26 reconstituted aggregate (green) ; (c) implanted in a zebrafish embryo (green). (a1) and (c1) are bright field images. (a2) is obtained with a spinning-disk, (b1) with a 2-photon and (c2) with a confocal microscope ; (b2) is a 3D reconstruction obtained with ImageJ software. The insets represent the intensity profile through the sensor's diameter

Figure 2 shows some examples of bright field and fluorescent images of single sensors (a) suspended in water ; (b) embedded in a CT26 reconstituted aggregate ; (c) implanted in a zebrafish embryo. Image (b2) is a 3D reconstruction obtained with ImageJ software, where the deformation from spherical shape is clearly visible. The fluorescent signal is homogeneous in the bead volume and the contrast is high enough to detect the sensor border (see section **Active contour method**). Moreover, we checked that the fluorescence in the elastomer remains stable over several

Development (2021) 00, devxxxxxx. doi:10.1242/dev.xxxxxx

days. Thus this labelling technique fulfills all the requirements for further quantitative image analysis.

Strain-stress relationship

When a bead is embedded in a tissue, it experiences mechanical forces exerted by its environment, which induce a deformation from its initial spherical shape, and makes it a sensor of local stresses. In the following we assume that the sensor is small enough, as compared to the length scale characterizing stress spatial variations, so that the stress tensor can be considered as homogeneous over the sensor's volume. Thus, stress variations at a scale smaller than the sensor cannot be detected. We also assume that the elastomer shows an ideally elastic behavior, and that its deformation remains small enough ($\lesssim 5\%$), so that linear elasticity applies. The local strain tensor $\bar{\bar{\varepsilon}}$ and stress tensor $\bar{\bar{\sigma}}$ are related through (Landau et al., 1986):

$$\bar{\bar{\varepsilon}} = \frac{1+\nu}{E}\bar{\bar{\sigma}}^d + \frac{1-2\nu}{E}\bar{\bar{\sigma}}^c \tag{1}$$

Here $\bar{\bar{\sigma}}^c = \frac{tr(\bar{\bar{\sigma}})}{3}\mathbb{1}$ represents the isotropic part of $\bar{\bar{\sigma}}$ (traction stress tensor, equivalent to a pressure) and $\bar{\bar{\sigma}}^d = \bar{\bar{\sigma}} - \bar{\bar{\sigma}}^c$ is the deviator, also known as shear stress tensor ; E is the Young modulus, and ν the Poisson's ratio.

The sensors are made out of a PDMS elastomer, which can be considered as incompressible in the range of physiological stresses (its compression modulus $K = \frac{E}{1-2\nu}$ is of the order of 10^6 Pa). This justifies the approximation $\nu \simeq \frac{1}{2}$, and thus Eq. 1 simplifies into : $\bar{\bar{\varepsilon}} = \frac{1+\nu}{E}\bar{\bar{\sigma}}^d$. Introducing the shear modulus $\mu = \frac{E}{2+2\nu} = \frac{E}{3}$, one gets:

$$\bar{\bar{\sigma}}^d = 2\mu\bar{\bar{\varepsilon}} \tag{2}$$

which we will use in the following.

Under external stresses, and assuming small deformations, the sensor's shape changes from a sphere of radius a to an ellipsoid of half-axes a_X, a_Y and a_Z. In the system of principal coordinates (X, Y, Z) of this ellipsoid, both the strain and stress tensors are diagonal, so that one can write :

$$\sigma^d_{XX} = 2\mu\varepsilon_{XX} = 2\mu\frac{(a_X - a)}{a} \tag{3}$$

$$\sigma^d_{XY} = 2\mu\varepsilon_{XY} = 0 \tag{4}$$

and similar relations for other stress components. Hence, provided that the shear modulus of the PDMS elastomer has been independently calibrated, the local shear stress tensor is fully determined by pointing the ellipsoid orientation and measuring the length of its half-axes.

Cell culture and preparation of aggregates

CT26 cells, stably transfected with Lifeact-GFP, were cultivated in T75 flasks at 37°C in 5% CO_2, in DMEM culture medium completed with 10% (v/v) Foetal Bovine Serum and 1% antibiotics (penicillin-streptomycin), and passed every 3 days. For the preparation of aggregates, confluent cells were detached by using 5 mL of buffer solution containing 0.05% trypsin. Incubation was limited to about 1 min, in order to form cell leaflets and avoid complete cell dispersion. In parallel, elastomer microsensors were functionalized by adding 1 mL of fibronectin solution in PBS (50 µg/mL) to 1 mL of freshly thawed bead suspension. The final suspension was left for incubation during 1 h at 37°C, and then directly added to ∼ 10 mL of detached cells suspension without further rinsing. Aggregates containing inserted beads were prepared in Petri dishes on which the cell and bead suspension was deposited, placed on an orbital agitator (∼ 50 rotations/min), and left to grow for at least 24 h in an incubator at 37°C. To get spherical aggregates, it is suitable to let them grow for at least 48 h. The diameter of the obtained aggregates lies between 100 and 500 µm. Within few exceptions, they contain at most one bead per aggregate.

Zebrafish preparation

Embryos were obtained by natural spawning of *Tg(-1.8 gsc:GFP)ml1* adult fishes (Doitsidou et al., 2002). All animal studies were approved by the Ethical Committee N°59 and the Ministère de l'Education Nationale, de l'Enseignement Supérieur et de la Recherche under the file number APAFIS#15859-2018051710341011v3.

Embryos were grown at 28.5°C until reaching shield stage (6 hours post fertilization). Embryos were then processed as explained in Boutillon et al. (2018). Using a large glass needle (35 µm opening) mounted on a pneumatic microinjector (Narishige IM-11-2) under a fluorescence-stereo microscope, a sensor was inserted in the shield of an embryo, which expresses GFP in the *Tg(-1.8 gsc:GFP)ml1* line. Transplanted embryos were then incubated at 28.5°C until reaching the desired stage between 60% and 85% of epiboly (6,5 to 8 hours post fertilization). Embryos were then selected for the presence of the sensor in the prechordal plate. Selected embryos were mounted in 0,2% agarose in embryo medium on the glass coverslip of a MatTek petri dish (Boutillon et al., 2018) and placed on an inverted TCS SP8 confocal microscope (Leica SP8) equipped with an environmental chamber (Life Imaging Services) at 28°C and a HC PL APO 40x/1.10 W CS2 objective (Leica). Imaging parameters were set to acquire the whole sensor (z-stack) in less than 15 seconds, to minimize displacement due to the migrating neighboring cells.

Image recording and analysis

Microscopy

To simultaneously image the tissue and the sensors embedded inside it, several techniques have been used:

(i) Frequently, sensors in suspension in water were imaged with a spinning-disk microscope (Andor Revolution CSU X1, mounted on an Olympus IX 81 inverted microscope equiped with a 40x water immersion objective), in order to check their sphericity, and the good quality of their fluorescence (intensity and homogeneity) (Fig. 2a).

(ii) 2-photon microscopy was used for the visualization of reconstituted cell aggregates. Experiments were carried out at the multiphoton facility of the ImagoSeine imaging platform (Institut Jacques Monod, Université de Paris). The aggregates were deposited in a Petri dish, in a chamber regulated at 37°C, and observed during a few hours under a 20x water immersion objective at the early stage of their adhesion to the bottom plate. For the rhodamin dye, the excitation laser was tuned at $\lambda = 840$ nm and the emitted light was collected through a dichroïc mirror at $\lambda \geq 585$ nm. Lifeact-GFP of CT26 cells was excited at $\lambda = 900$ nm and the fluorescence was collected at $\lambda \leq 585$ nm. Image stacks

were recorded along the optical axis every 0.5 µm, with a lateral resolution down to 0.1 µm/pixel (Fig. 2b).

(iii) A confocal microscope (Leica SP8) was used to image the prechordal plate of the Zebrafish embryos. The sample was maintained at $T = 28°$C. Image stacks (x40 water immersion objective) were recorded at regular time intervals (30 s to 1 min) at different stages of the epiboly, comprised between 60 and 85%. Since the prechordal plate is migrating at a velocity up to 2 µm/ min, the acquisition time for a whole stack must be smaller than 15 s to avoid drift in the images. Hence images were recorded every 2 µm. The excitation laser was tuned at $\lambda = 498$ and 550 nm and the emitted light was collected between $507 - 537$ nm and $569 - 673$ nm (Fig. 2c).

Active contour method

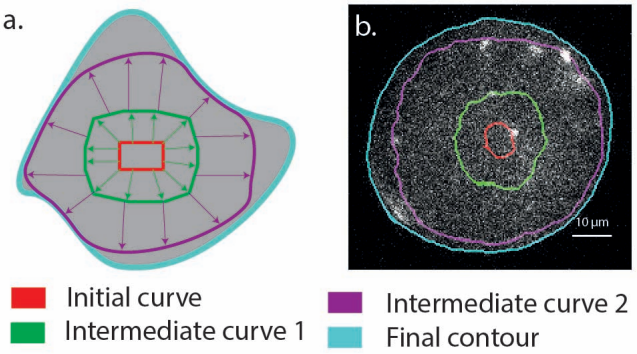

Fig. 3. Determination of the sensor's contour ; (a) Principle of the active contour method : the initial seed (red) progressively swells (green, purple), until it reaches the contour of the object (cyan), which minimizes its pseudo-energy (see text). (b) Example of contour determination for a sensor inserted in an aggregate (same color code as (a)).

A careful 3D reconstruction of the sensor's shape was required to retrieve the orientation and half-axes of the deformed beads with a good accuracy. Indeed, the usual built-in applications for 3D reconstructions, such as ImageJ plugins, do not lead to a reliable and accurate enough profile: the result depends on specific choices of parameters for the filters and for the intensity thresholds, which involve the subjective appreciation of the operator. Hence, we implemented an active contour method, as follows (Kass et al., 1988; Caselles et al., 1993; Marquez-Neila et al., 2014; Bendaoud, 2017) : the common principle of the different existing algorithms consists in considering a swelling (or shrinking) surface $\nu(s, n)$ at the n^{th} iterative stage, parametrized by its local coordinates $s = (s_1, s_2)$. A function $E(\nu)$ is associated to this surface and, like an energy, is built to reach a minimum when the surface $\nu(s, n)$ coïncides with the contour of the object. This pseudo-energy is the sum of three contributions:

$$E(\nu) = E_g(\nu) + E_s(\nu) + E_c(\nu) \tag{5}$$

The first term $E_g(\nu)$ is a gradient detection term :

$$E_g(\nu) = -\iint \|\vec{\nabla}(g_\sigma * I)\|^2 ds \tag{6}$$

It represents the norm of the intensity gradient, convoluted by a gaussian filter g_σ, and integrated over the surface ν. The minus sign ensures that $E_g(\nu)$ has a minimum when the intensity gradient on the surface ν is maximal.

The second term (surface energy) $E_s(\nu)$, is analogous to a Helfrich energy (Helfrich, 1973) :

$$E_s(\nu) = \iint \alpha ds + \iint \beta\kappa ds \tag{7}$$

where α is a surface tension, κ the local curvature of the surface ν, and β a curvature stiffness. This term limits the roughness of the final contour.

The last term (balloon energy) $E_b(\nu)$ is proportional to the volume V limited by ν, and forces the surface to swell or to shrink when iterating the process, according to the sign of the parameter δ :

$$E_b(\nu) = \delta \iiint dV \tag{8}$$

The details of the used python code can be found in (Souchaud, 2020) and on the Github platform (see **Data availability**). Starting from a seed located inside the contour to be detected, and taking $\delta < 0$, the volume delimited by ν enlarges at each step n of the algorithm, until $E(\nu)$ reaches a minimum, which defines the contour of the object. The principle of the method is illustrated in Figure 3a, and a example of contour determination for a micro-sensor is shown in Figure 3b. A movie (M1) showing the 3D reconstruction of a bead inserted in the prechordal plate of a Zebrafish embryo is available in supplementary files. Consequently, the final contour position only depends on the choice of δ and of two parameters α_1 and β_1 derived from α and β. In the algorithm, δ is an integer and must be equal to -1 to ensure convergence. We have checked that tuning α_1 and β_1 in a large range (variations up to 100%) changes the contour position by less than 0.2 µm. Thus the final accuracy Δ on the contour determination is not limited by the algorithm, but by the quality of the image. It is about 0.5 µm, over a sensor radius of about 15 µm.

Once the 3D contour of the sensor has been determined from the images, a renormalization factor $r = 0.935$ must be applied to the sensor's shape along the optical axis (z) direction. This factor takes into account a geometrical correction due to light refraction through the tissue/PDMS interface, which acts like a spherical diopter between two media of different optical indices ($1.35 < n_1 < 1.40$ for the living tissue ; $n_2 \simeq 1.44$ for PDMS). The factor r was calibrated *in situ*, by comparing the shape of hard non-deformable spherical sensors ($\mu \sim 2 \times 10^4$ Pa) to their reconstructed image. Calibrations were performed both in cell aggregates and in zebrafish embryos, leading to the same value $r = 0.935 \pm 0.02$, which was retained in the following.

With this active contour method, we estimate that we can detect a sensor deformation if the difference between two half axes is at least equal to threshold $\Delta = 0.5$ µm, which represents the accuracy of our measurements.

RESULTS

Sensors mechanical calibration

As shown in section **Strain-stress relationship**, determining *in situ* the local stress tensor requires to calibrate the sensors shear modulus μ. Its value was determined by two methods, first at the macroscopic scale with a commercial rheometer, and secondly *in situ* at the sensor's scale with a custom-made setup allowing uniaxial compression of aggregates.

Development (2021) 00, devxxxxxx. doi:10.1242/dev.xxxxxx

Macroscopic rheometry

A rheometer (ARES G2) was used to follow the evolution of the elastic moduli of the PDMS preparation during its gelification. The polymerizable mixture was introduced in either plate-plate or cone-plate geometry, and maintained at a constant temperature $T = 60^{\circ}\mathrm{C}$ or $T = 80^{\circ}\mathrm{C}$, whilst the storage and loss moduli G' and G'' were measured every 15 min, in the range $0.1\ \mathrm{Hz} < f < 10\ \mathrm{Hz}$. After a transient increase during about one hour, G' and G'' gradually tend towards a plateau, which final value is reached after ~ 12 h at $T = 60^{\circ}\mathrm{C}$, or ~ 3 h at $T = 80^{\circ}\mathrm{C}$.

At any given stage of gelification, G' was found independent of the excitation frequency f, and G'' increased approximately linearly with f, which corresponds to a Kelvin-Voigt behavior. Moreover, at the end of the gelification plateau, the ratio G'/G'' was found of the order of 10 at $f = 10$ Hz for a standard gel composition. Thus, when the PDMS gel is submitted to a static (or very slowly varying) stress, it may be considered as a purely elastic solid, and it is legitimate to confound its static shear modulus μ with its storage modulus G' extrapolated at $f = 0$ Hz.

The G' value, measured at the end of the polymerization plateau, was retained in the following as the value of the shear modulus for bulk PDMS μ_b. This value strongly depends on the mixture composition. It is close to 500 Pa for $m_{cross} = 0.0160\, m_{DMS}$, but reaches 1000 Pa for $m_{cross} = 0.0170\, m_{DMS}$. We noticed that the final value of μ_b depends also, but in a lesser extent, on the crosslinker and inhibitor concentrations, and on the gelification temperature.

The shear modulus μ_d, measured after the polymerization of a mix dispersed in water, appeared to be different from the bulk shear modulus μ_b. A small amount of polymerizing mixture was added to water and vigorously shaken for a few seconds to make a coarse emulsion. The suspension was left to buoy up at room temperature, during a timelapse τ, after which the suspension was centrifugated until complete droplets coalescence, and the supernatent was sampled and placed in the rheometer. The actual μ_d was always found smaller that the bulk μ_b measured for the same mix before emulsification. The ratio μ_d/μ_b reached a stable plateau value $\simeq 0.43$ when $\tau \gtrsim 24$ h. We interpreted this observation by assuming that a small amount of a mix component, likely the crosslinker, may diffuse out of the DMS emulsion droplets and dissolve in the surrounding water. As seen above, a small variation of the crosslinker concentration is enough to induce a significant change in the final mechanical properties of the gel. Since the microsensors are made from small droplets suspended in water before polymerization, this effect has to be considered for a proper calibration of their mechanical properties. In practice, we decided to measure μ_b with the rheometer for every batch of bulk mix polymer used to make microsensors, and then to apply a constant corrective factor in order to get an estimate of the final shear modulus μ_d of the spherical elastic sensors : $\mu_d = 0.43\ \mu_b$.

In situ calibration in aggregates

At the microsensor's length scale, one expects that capillary effects, due to the non-zero surface tension $\gamma_c \sim 10$ mN/m between the tissue and the PDMS sensor of radius $a \sim 15$ µm, might affect its global mechanical response (Style et al., 2017; Bico et al., 2018). Indeed, the contribution of the Laplace term $\frac{\gamma_c}{a} \sim 650$ Pa is comparable to the macroscopic shear modulus μ_d of the PDMS dispersion. This means that the relationship between the applied external stress and the deformation of the sensor involves both the shear stress modulus μ_d and the surface tension γ_c. For small deformations, it has been shown that one can take into account this elasto-capillary contribution by introducing an effective elastic constant μ_e (Carbonaro et al., 2020):

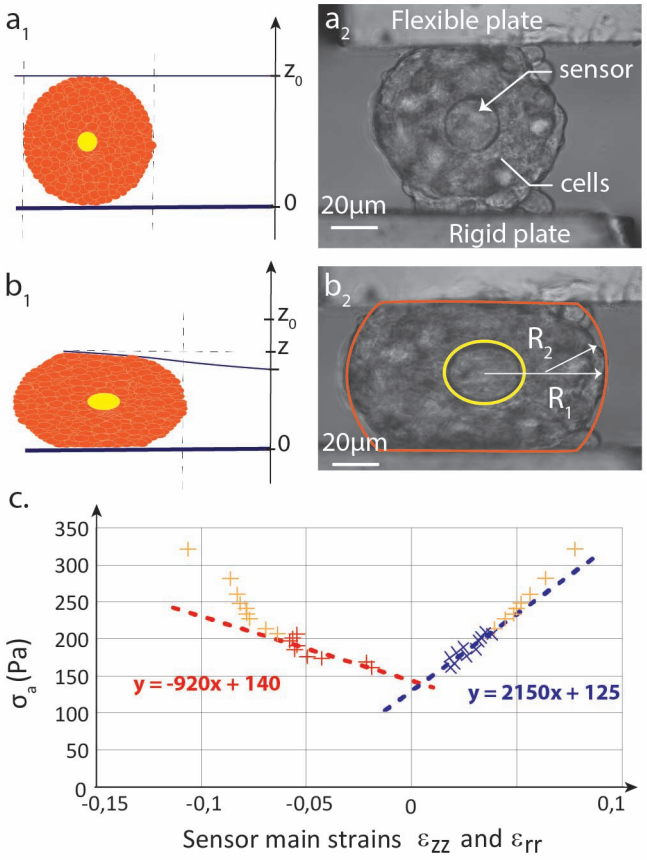

Fig. 4. In situ calibration of a sensor shear modulus. Principle (a1, b1) : a CT26 aggregate, initially spherical and containing a sensor at its center, is squeezed between two glass plates. The images (a2, b2) are analyzed to extract the sensor main strains ε_{zz} and ε_{rr}. (c) Variations of the average stress $\sigma_a(t)$ *vs* $\varepsilon_{zz}(t)$ (red crosses) and $\varepsilon_{rr}(t)$ (blue crosses) during the relaxation of a squeezed aggregate. Yellow points are recorded during the first ≈ 30 s of the relaxation. The shear modulus μ_e of the sensor can be extracted from the slopes of the straight lines (Eq.12 and **??**).

$$\bar{\bar{\sigma}}^d = 2\mu_e \bar{\bar{\varepsilon}} \tag{9}$$

with

$$\mu_e = \mu_d + K\frac{\gamma_c}{a} \tag{10}$$

K is a dimensionless constant of order unity. We thus performed an *in situ* calibration on a sensor embedded in a tissue, in order to directly measure μ_e.

For this calibration, we used a custom-made uniaxial rheometer, allowing to apply either a controlled force, or a controlled deformation to a cell aggregate (Desprat et al., 2005; 2006; Mitrossilis et al., 2010). To summarize, the cell aggregate may be squeezed between two glass plates, a rigid one and a flexible one acting like a cantilever. The plates are actuated by two piezoelectric stages. A feedback loop maintains the extremity of the flexible plate, on the aggregate side, at a fixed position, while its other extremity is free to relax with time. This allows to record the evolution of the force

$F(t)$ exerted on the aggregate, at constant aggregate's deformation. $F(t)$ is calculated from the flexible plate's deflection, knowing its rigidity $k = 81.2\ \mathrm{nN/\mu m}$.

Practically, we selected a CT26 aggregate of diameter comprised between 100 and 200 μm, containing a sensor localized close to the aggregate center, and we seized it between the two plates of the rheometer (Figure 4a). We then applied a step motion to the rigid plate to squeeze the aggregate, while the flexible plate extremity close to the aggregate is regulated at constant position. From this initial instant we recorded the relaxation of the flexible plate's deflection during 15 to 30 min, and thus the time evolution $F(t)$, while the aggregate deformation remained constant. Simultaneously, we imaged the shape of the sensor in its median plane (Figure 4b). Two or three successive squeezings and relaxations were operated on the same aggregate. From these relaxations we inferred at any time t the force $F(t)$ exerted on the aggregate, and the deformations $\varepsilon_{zz}(t)$ and $\varepsilon_{rr}(t)$ of the sensor, respectively in the compression direction and perpendicular to it.

As detailed in the appendix, we developed a model to establish the relationship between the sensor's deformation $\bar{\bar{\varepsilon}}$, and the average stress in the equatorial plane of the aggregate, defined as :

$$\sigma_a(t) = \frac{F(t)}{\pi R_1^2} \tag{11}$$

This model predicts :

$$\begin{aligned}\sigma_a &= -\frac{3\mu_e}{1+\frac{R_1}{2R_2}}\varepsilon_{zz} + \gamma_{ag}\left(\frac{1}{R_2}-\frac{1}{R_1}\right)\\ &= \frac{3\mu_e}{1+\frac{R_1}{2R_2}}2\varepsilon_{rr} + \gamma_{ag}\left(\frac{1}{R_2}-\frac{1}{R_1}\right)\end{aligned} \tag{12}$$

Here R_1 represents the equatorial radius of the aggregate, R_2 its curvature radius in the observation plane (Fig. 4b_1), and γ_{ag} is the surface tension between the aggregate and the culture medium (not to be confused with the sensor/aggregate surface tension γ_c). Eq. (12) is valid under the following approximations : (i) the aggregate is supposed spherical at rest and the z axis is a cylindrical symmetry axis at any time ; (ii) the sensor does not perturbate the stress distribution in the aggregate ; (iii) the sensor is approximately at the center of the aggregate ; (iv) the component $\sigma_{zz}(t)$ is assumed to be homogeneous in any plane perpendicular to the main compression axis.

Figure 4c shows an example of such a stress-strain relationship, measured during the relaxation of a squeezed aggregate. We experimentally check that $\sigma_a(t)$ linearly varies with $\varepsilon_{zz}(t)$ and with $\varepsilon_{rr}(t)$ during the relaxation, except for the yellow points which are recorded during the first ≈ 30 sec of the relaxation. Indeed, immediately after the step compression, the stress components quickly vary, due to different relaxation mechanisms in the aggregate. In this initial non-linear regime, it is likely that hypothesis (iii), namely in-plane spatial homogeneity of $\sigma_{zz}(t)$, is not valid. On the other hand, at longer time, the relaxation slows down and one expects that the homogeneity assumption becomes verified. In this regime, the experimental data meet the model prediction given by Eq. (12). Hence, from the linear fits shown in figure 4c, one can extract the values of the effective shear modulus $\mu_e = 790 \pm 160$ Pa and of the aggregate surface tension $\gamma_{ag} = 9 \pm 2\ \mathrm{mN/m}$ for this particular experiment. Note that we experimentally measure $\varepsilon_{zz} \simeq -2\varepsilon_{rr}$ at any time, which is consistent with the sensor's incompressibility and with the cylindrical symmetry assumptions.

Table 1. Comparison of the average value $\overline{\mu}_e$, measured *in situ*, and μ_d, measured for a coarse emulsion of the same gel. Experiments have been performed on two gels having slightly different compositions.

	$\overline{\mu}_e$ **(Pa)**	μ_d **(Pa)**
Gel 1	730 ± 250 $(N = 9)$	710 ± 150
Gel 2	320 ± 100 $(N = 3)$	410 ± 70

Two gels of slightly different compositions have been tested. Within our experimental accuracy, no significant difference can be detected between the value of $\overline{\mu}_e$, averaged over N assays in different aggregates, and the value of μ_d measured at the macroscopic scale for a coarse emulsion made out of the same gel (see Table 1). These results do not allow us to isolate the contribution of capillary effects in the effective shear modulus μ_e, according to Eq. 10. Either this contribution is smaller than expected, or the determination of μ_d and μ_e is not accurate enough to measure the difference between them. In the following, we will take μ_d as the reference value for the effective elastic shear modulus of the sensors.

From the uniaxial compression of aggregates we can also infer the surface tension γ_{ag} between the aggregate and the culture medium. The values range from 3 to 12 $\mathrm{mN/m}$ for different aggregates. Although the dispersion is important, the order of magnitude corresponds to the expected one.

Stress distribution in cell aggregates

13 aggregates, containing deformable sensors located at different positions, were imaged with a 2-photon microscope. We analysed the shape of 17 sensors. To compare the results, we define a dimensionless position $r = r_c/R_a$ as the ratio of the distance r_c from the aggregate center to the sensor center, over the distance R_a from the aggregate center to the aggregate edge in the direction of the sensor. This definition takes into account the fact that the aggregate might be not spherical but slightly ellipsoïdal.

The results are gathered in Fig. 5a. Each sensor is set at its reduced position r, and is represented by an ellipse showing its deformation projected in the (x, y) plane of the image. Since the actual deformations are small ($< 10\%$), they were artificially multiplied by a factor 4 on the scheme to be visible. The main components of the associated shear stress are represented as red bars of length proportional to the stress amplitude. In most cases, one of the main axes remains close to the Oz optical axis, which justifies the projection in the (x, y) plane.

By looking at the stress orientation and amplitude, one retrieves several pieces of information :

First, the in-plane main axes of the sensors are mostly aligned along the radial and orthoradial directions of the aggregate referential. Fig. 5b represents the distribution of angles between the radial direction and the sensor's longer axis direction (blue: sensors showing a difference in half axes larger than the estimated accuracy threshold 0.5 μm; red: other sensors). This distribution is non-uniform and indicates that the sensors are principally compressed in the orthoradial direction.

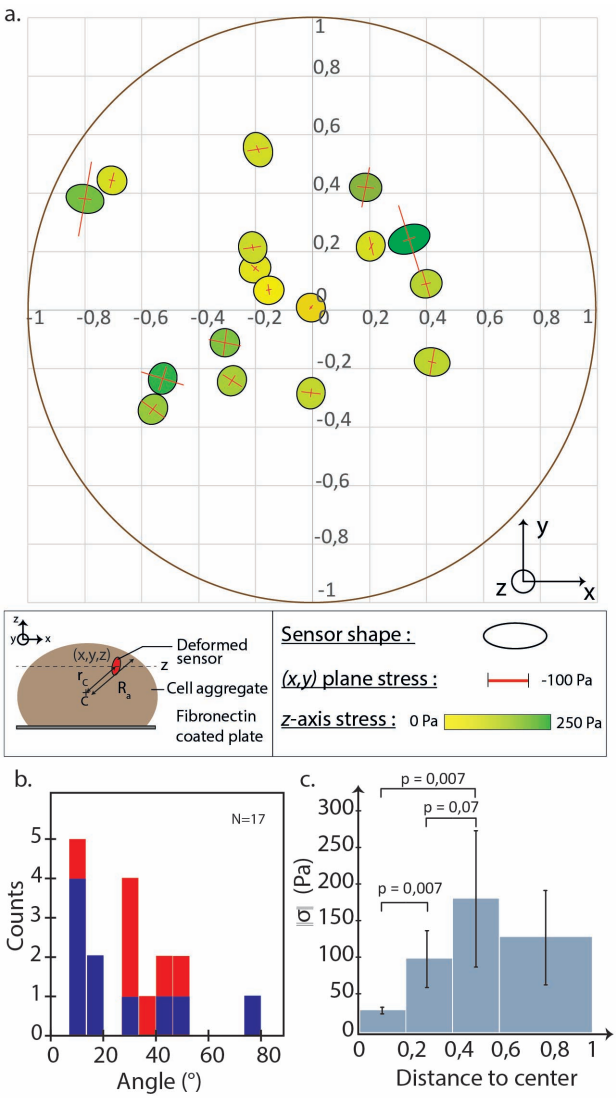

Fig. 5. (a) Stress distribution map in CT26 aggregates, from 17 sensors inserted in 13 different aggregates. Each sensor is set at its normalized position $r = r_c/R_a$. Its shape projected in the (x, y) plane is represented by an ellipse (the ellipticity is artificially multiplied by a factor 4 to make it more easily visible). The main shear stress components in the (x, y) plane are shown as red bars, while the projection of the stress in the z direction is represented by a color code. (b) Distribution of angles between the radial direction and the sensor longer axis direction (blue: sensors showing a difference in half axes larger than the estimated accuracy 0.5 µm ; red: other sensors). The sensors are principally compressed in the orthoradial direction. (c) Histogram of the shear stress amplitude $\|\sigma\|$ versus normalized distance to the center r.

Second, the component σ_{zz}, represented by a color code in Fig.5a, is always positive and ranges between 0 and 250 Pa (see **Discussion**).

Third, the stress amplitude $\|\sigma\|$ varies from the center to the edge of the aggregate. $\|\sigma\|$ is defined as the norm of the stress deviator:

$$\|\sigma\| = \left(\left(\sigma^d_{XX}\right)^2 + \left(\sigma^d_{YY}\right)^2 + \left(\sigma^d_{ZZ}\right)^2 \right)^{1/2} \qquad (13)$$

The histogram of $\|\sigma\|$ is represented in Fig. 5c versus the normalized distance r. Despite the uncertainty, we observe a significant trend for $\|\sigma\|$ to increase with r, and possibly to reach a maximum and decrease when approaching the edge of the aggregate.

In principle the evolution of this stress map can be followed in time. We were able to image the spreading of some aggregates deposited on the bottom plate of the Petri dish, during a few hours, by taking stacks every 15 min. In most cases, the axes orientations and half-lengths of the sensors remained stable with time, within experimental accuracy. Longer recordings would be necessary to see an evolution, and to follow the aggregate spreading process until its term.

Stress distribution in the prechordal plate of zebrafish embryos

In vivo, the spatial distribution of mechanical stresses, their inhomogeneities and their local anisotropy play a determinant role in the morphogenesis process, since they directly influence cell polarization and migration. For instance, it was established *in vitro* that Xenopus prechordal plate cells can be polarized by application of a mechanical stress of a few Pa (Weber et al., 2012). The prechordal plate (PPl) is a group of cells, that are the first ones to internalize on the dorsal side of the embryo, at the onset of gastrulation. During gastrulation, they migrate in direction of the animal pole, followed by notochord precursors (Kimmel et al., 1995; Solnica-Krezel et al., 1995). Based on this observation, it was proposed that migration of the PPl is guided *in vivo* by the existence of stress anisotropies within the tissue, used by cells as directional cues (Weber et al., 2012; Behrndt and Heisenberg, 2012). Our sensors, directly measuring the 3D stress anisotropy, and allowing to map the stress in the tissue, seemed particularly well suited for such an application. Also, the prechordal plate appeared as a good model to demonstrate their *in vivo* capabilities.

Spatial distribution

The prechordal plate and the notochord cells are labelled in the *Tg(gsc:GFP)* line, which was used in these experiments. Sensors were implanted in the PPl of seven different embryos. Some of them could be followed over time, by taking images every 30s or 60s. An overview of the full dataset is shown in supplementary files, table S1. We report here a selection of 12 measurements, at different stages of gastrulation, from 60 to 85% of epiboly. The common effective shear modulus of all the sensors was $\mu_d = 430$ Pa. To analyze the stress spatial distribution, the PPl was divided into 9 zones (front/middle/rear and left/center/right), as shown in figure 6e. For legibility, the projection of the shear stresses in the PPl (x, y) plane is drawn as an ellipse for each sensor, while the projection along the perpendicular axis z (confounded with the observation axis) is represented by a color code. In the PPl plane, x is the direction of the PPl progression and y the perpendicular one. All the stress components lie in a range comprised between $+60$ and -60 Pa, with approximately equal distribution between positive and negative values.

From figure 6e, no evident correlation emerges between the sensor location in one of the 9 zones of the PPl and the stress orientation and amplitude in the same zone. However, in Fig. 6f, the value of the shear stress amplitude $\|\sigma\|$, averaged over the left/center/right zones and over the different epiboly stages, is compared at the front ($N = 3$) and at the middle ($N = 7$) of the

Development (2021) 00, devxxxxxx. doi:10.1242/dev.xxxxxx

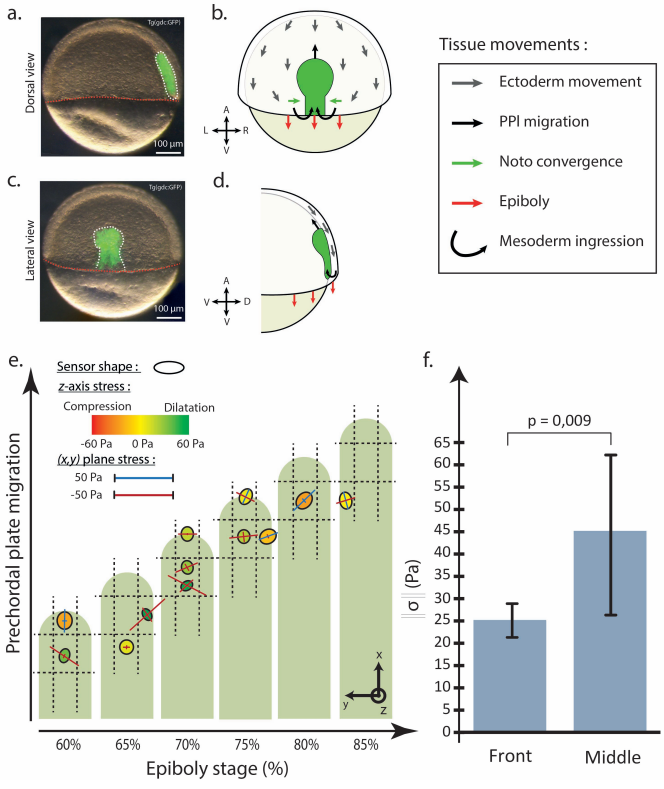

Fig. 6. Measurements of the shear stresses in the zebrafish prechordal plate (PPl) during epiboly. (a-d) : Ectoderm, prechordal plate (PPl) and notochord precursors (Noto) movements during gastrulation. (a,c) Bright fields and fluorescence images of a zebrafish Tg(gsc:GFP) embryo at 60% epiboly. Prechordal plate and notochord cells, expressing GFP in this transgenic line, are highlighted by the white dashed line. Red dashed line marks the margin of the embryo. (b,d) Schematics of corresponding pictures showing morphogenetic movements of the different tissues during gastrulation. Crossed arrows indicate animal-vegetal (A-V), left-right (L-R) and dorsal-ventral (D-V) embryonic axes of respective view. Panels a, b, c and d have been inspired by Smutny et al. (2017). (e) Mapping of shear stresses in the PPl at different epiboly stages (12 measurements on 7 different embryos). The projection on the (x, y) plane of the main shear stresses is drawn as an ellipse, while the projection along the normal axis z is represented by a color code. (f) Comparison of the shear stress amplitude $\|\sigma\|$, averaged at the front ($N = 3$) and in the middle ($N = 7$) of the PPl.

plate. The difference is significant and is a first indication that stress gradients exist in the PPl.

Time evolution

We were able to follow the evolution of the stress components for 7 sensors, during 15 to 30 min, at different stages of epiboly.They did not show any significant changes, except for one event which we describe now.

A sensor inserted in the PPl, and migrating with it, was imaged during 15 min, at the stage $70 - 75\%$ of epiboly. In Figure 7, the three main components σ_{XX}, σ_{YY}, and σ_{ZZ} are plotted versus time. Each principal axis (X, Y, Z) is color-labelled according to its nearest axis of the PPl referential: x (red), y (yellow) and z (blue).

In Fig. 7 one can follow the evolution of each shear stress component with time. The stress amplitude along the principal axis closest to the z axis (blue) changes from positive (extension) to negative (compression). In the same time, the stress along the axis

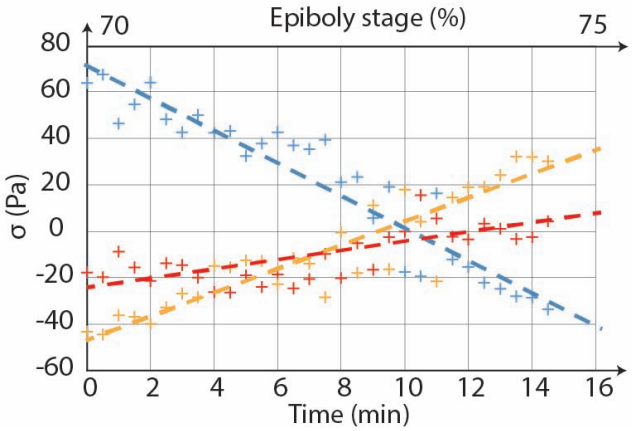

Fig. 7. Time evolution of the main components of the shear stress tensor, for a sensor located in the central zone of the PPl of a zebrafish embryo. Each principal axis (X, Y, Z) is color-labelled according to its nearest axis of the PPl referential. Within 15 minutes, the stress amplitude along the principal axis closest to the z axis (blue) changes from positive (extension) to negative (compression). In the same time, the stress along the axis closest to the y axis follows the opposite evolution (yellow), and so does, to a lesser extent, the component close to x axis (red). Dashed lines are guides for the eye.

closest to the y axis follows the opposite evolution (yellow), and so does, to a lesser extent, the component close to x axis (red). Their directions remain stable except for some small fluctuations. This event is a clear signature of a main change in the stress partition, which takes place within a few minutes at this stage of epiboly. The short duration of this event might explain why it has been observed only once, out of 7 assays. Of course, no general conclusion can be extracted from one single event, but its occurrence demonstrates that the technique enables to follow the time evolution of the shear stress tensor during the prechordal plate migration.

DISCUSSION

In both experiments, *in vitro* and *in vivo*, we have demonstrated that our pipeline of techniques, based on the use of PDMS elastic microsensors embedded in living tissues, can be used to locally determine the amplitudes and orientations of the shear stress components, to map them across the tissue, and to retrieve their temporal evolution.

In vitro, for freely spreading cell aggregates, the order of magnitude of the shear stress amplitude typically lies between 10 and 100 Pa, consistently with other measurements in similar systems (Lucio et al., 2017; Lee et al., 2019; Mohagheghian et al., 2018). Moreover, Fig. 5c shows that the deviator stress amplitude $\|\sigma\|$ increases from the aggregate center to its edge, and that the stress component along the orthoradial direction is larger than along the radial one. On the other hand, according to our observations, the optical axis Oz systematically coincides with one of the main shear stress axis, with a positive value of the shear (extension). A possible explanation would be that, besides the applied geometrical correction due to light refraction, light diffusion in the tissue may also affect the quality of the image, especially at large depth inside the tissue ($\gtrsim 100$ µm). If this is the case, the systematic elongation of the sensor in the z direction could be an artefact related to the imaging method. Fortunately, this does not affect our conclusions concerning the radial/orthoradial privileged orientations

Development (2021) 00, devxxxxxx. doi:10.1242/dev.xxxxxx

in the (x, y) plane, nor the variations of the stress amplitude with reduced distance r.

It is interesting to compare these results with those reported in (Lee et al., 2019) with hydrogel sensors embedded in spherical aggregates made of HS-5 fibroblasts. In this paper two components of the full stress tensor $\bar{\bar{\sigma}}$ were measured *vs* the distance to the aggregate center, respectively in the radial and orthoradial directions in the observation plane. Both their amplitudes are comprised between -400 and -1500 Pa. Their average value represents the isotropic part of the stress : it is negative and thus corresponds to a compression. The difference between the two components, which is the local shear stress, is of the order of ± 100 Pa, comparable to their measurements accuracy. This order of magnitude is similar to ours. Moreover, they observe that both stress components increase from the aggregate edge, to reach a maximum value, and then decrease again towards the aggregate center. Although the two experiments give access to different quantities (total shear in their case, shear stress in ours), the behaviors observed in both situations are consistent.

In vivo, in the prechordal plate of the Zebrafish embryo, we were able to measure both the amplitude and orientation of the main stress components at different stages of epiboly. The retrieved values are of the expected order of magnitude, 10^2 Pa, and the sensitivity is of order of 10^1 Pa. From our data we can highlight two emerging trends, which of course will have to be confirmed by further measurements. First, following the evolution of the main stress components with time have shown that some specific events may occur, which take place within a short time interval as compared to the gastrulation, and which denote important changes in the stress partition. Such events have to be systematically identified, to determine whether they occur at some particular stages of epiboly, and to learn about their specific role in the full migration process. Secondly, the total stress amplitude appears larger at the center of the PPl than at its front, which supports the hypothesis that stress gradients exist in the PPl and might play an active role in the PPl migration. A systematic survey of the stresses amplitude and orientation in the different PPl regions is needed to comfort this assumption. Another important issue, which was not investigated here, concerns the stress distribution in the direction orthogonal to the PPl plane. Indeed, one suspects that the friction of the PPl over the neurectoderm might play an important role in the migration process (Smutny et al., 2017). Thus, further investigations will also have to include the vertical position of the sensor inside the PPl as one of the relevant parameter of the problem.

To conclude, we have assembled a pipeline of techniques which meets all the requirements to quantitatively map in 3D + time the local shear stresses in living tissues, with a sensitivity of order of 10 Pa. In addition to other complementary techniques, it appears as a valuable tool to investigate the role of mechanical constraints in morphogenesis and development.

Acknowledgements

We acknowledge Alain Richert, Gaëtan Mary, Magid Badaoui, Alain Ponton and Sandra Lerouge for their assistance and advices in experimental handling, Hélène Delanoé-Ayari for critical reading of the manuscript, and Mathieu Roché and Julien Dervaux for fruitful discussions. We acknowledge the ImagoSeine facility, at Institut Jacques Monod, especially Xavier Baudin and Orestis Faklaris, and the Polytechnique Bioimaging Facility, for assistance with live imaging on their equipments.

Competing interests

The authors declare no competing interests

Contribution

A.S, F. Gr. and F. Ga. designed the experiments, with the help of G.C., A.A., A.B, N.D. ; A.S. carried out the experiments and data analysis, together with A.B. for the Zebrafish part under the supervision of N. D. ; G.C. supervised the chemistry of fluorescent labelling ; A.A. conducted the uniaxial rheometry ; F. Ga. did the appendix calculations ; C.N. inspired the scientific process and methodology ; F. Gr. and F. Ga. supervised the work ; A.S, F. Gr. and F. Ga. wrote the manuscript. All authors have read, corrected and approved the manuscript.

Funding

This work was made possible through a fellowship of the Ecole Doctorale EDPIF (AS), and a grant from the Domaine d'Intérêt Majeur program (complex systems) of the Ile-de-France region. Part of it was also supported by the labex «Who Am I?», labex ANR-11-LABX- 0071, and the Université de Paris, Idex ANR-18-IDEX-0001 funded by the French Government through its «Investments for the Future» program. The ImagoSeine facility is a member of the France BioImaging infrastructure and is supported by Agence Nationale de la Recherche (ANR-10-INSB-04). The Polytechnique Bioimaging Facility is partly supported by Région Ile-de-France (interDIM) and Agence Nationale de la Recherche (ANR-11-EQPX-0029 Morphoscope2, ANR-10-INBS-04 France BioImaging)

Data availability

The python code used for active contour detection is available here :
https://github.com/scikit-image/scikit-image/blob/main/skimage/segmentation/morphsnakes.py.
An example of contour determination can be found here :
https://github.com/Alex-code-lab/3D_contour_detection_and_fit_by_an_ellipsoid.

APPENDIX : EXPRESSION OF THE LOCAL STRESSES IN AN AGGREGATE SUBMITTED TO AN UNIAXIAL COMPRESSION

In this section we describe a model to calculate all the components of the stress tensor at any point of an aggregate submitted to an uniaxial compression, from which we derive the expression of the deformation of an elastic incompressible sensor embedded in the aggregate.

Notations

We assume that the aggregate, initially spherical, is squeezed between two plates applying on it a force $\vec{F} = -F\vec{e_z}$, and that the problem respects the cylindrical symmetry around axis Oz. The notations are explicited in Fig. 8. We use cylindrical coordinates $M(r, \phi, z)$, O is the aggregate center. $R(z)$ is the radius of the curve generating the aggregate cylindrical surface. The principal radii of curvature are:

$$\begin{aligned} R_\perp &= \frac{R}{\cos\theta} \\ R_\parallel &= -\frac{1}{\sin\theta}\frac{dR}{d\theta} \end{aligned} \tag{14}$$

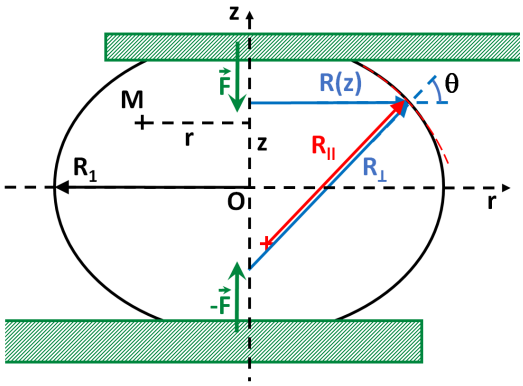

Fig. 8. Scheme of a squeezed aggregate, assumed to respect cylindrical symmetry around Oz. The current point M is identified by its coordinates (r, ϕ, z) where ϕ is the azimutal angle; $R(z)$ is the radius of the curve generating the aggregate cylindrical surface; $R_\perp$ and $R_\parallel$ are the principal curvature radii; R_1 is the equatorial value of $R(z)$; $\vec{F}$ is the force exerted by the plates on the aggregate.

with $\tan\theta = -\dfrac{dR}{dz}$.

In the particular case of a circular profile, which is a non-necessary but sufficient approximation for most situations, one has:

$$\begin{aligned} R_\parallel &= cst = R_2 \\ R(z) &= R_1 - R_2 + R_2\cos\theta \\ \frac{1}{R_\perp} &= \frac{\cos\theta}{R(z)} = \frac{1}{R_2} - \frac{1}{R(z)}\left(\frac{R_1}{R_2} - 1\right) \end{aligned} \tag{15}$$

where R_1 is the equatorial radius.

The local stress tensor is written as :

$$\bar{\bar{\sigma}} = \begin{pmatrix} \sigma_{rr} & \sigma_{r\phi} & \sigma_{rz} \\ \sigma_{r\phi} & \sigma_{\phi\phi} & \sigma_{\phi z} \\ \sigma_{rz} & \sigma_{\phi z} & \sigma_{zz} \end{pmatrix} \tag{16}$$

Mechanical equilibrium

In the absence of external volumic force, the mechanical equilibrium condition is written : $\vec{\mathrm{div}}(\bar{\bar{\sigma}}) = \vec{0}$, *i.e.* in cylindrical coordinates:

$$\begin{aligned} \frac{\partial\sigma_{rr}}{\partial r} + \frac{1}{r}\frac{\partial\sigma_{r\phi}}{\partial\phi} + \frac{1}{r}(\sigma_{rr} - \sigma_{\phi\phi}) + \frac{\partial\sigma_{rz}}{\partial z} &= 0 \\ \frac{\partial\sigma_{r\phi}}{\partial r} + \frac{2}{r}\sigma_{r\phi} + \frac{1}{r}\frac{\partial\sigma_{\phi\phi}}{\partial\phi} + \frac{\partial\sigma_{\phi z}}{\partial z} &= 0 \\ \frac{\partial\sigma_{rz}}{\partial r} + \frac{1}{r}\sigma_{rz} + \frac{1}{r}\frac{\partial\sigma_{\phi z}}{\partial\phi} + \frac{\partial\sigma_{zz}}{\partial z} &= 0 \end{aligned} \tag{17}$$

Due to the cylindrical symmetry, all the stress components are independent on the azimutal angle ϕ. Furthermore $\sigma_{r\phi} = \sigma_{z\phi} = 0$. Thus the above equations simplify into:

$$\begin{aligned} \frac{\partial\sigma_{rr}}{\partial r} + \frac{1}{r}(\sigma_{rr} - \sigma_{\phi\phi}) + \frac{\partial\sigma_{rz}}{\partial z} &= 0 \\ \frac{\partial\sigma_{rz}}{\partial r} + \frac{1}{r}\sigma_{rz} + \frac{\partial\sigma_{zz}}{\partial z} &= 0 \end{aligned} \tag{18}$$

We can also write the mechanical equilibrium condition at the aggregate surface, *i.e.* for $r = R(z)$. By equilibrating the local stresses at the boundary with the external pressure p_a outside the aggregate and the Laplace pressure, one finds in projection along the r and z axes at any point $M(R, z)$ of the surface:

$$\begin{aligned} \sigma_{rr} + \sigma_{zr}\tan\theta &= \sigma_{zz} + \frac{\sigma_{zr}}{\tan\theta} \\ &= -p_a - \gamma_{ag}\left(\frac{1}{R_\perp} + \frac{1}{R_\parallel}\right) \end{aligned} \tag{19}$$

We recall that γ_{ag} represents the surface tension between the aggregate and the external medium.

Finally, following Norotte et al. (2008), the global balance of forces exerted on the aggregate, in a plane perpendicular to Oz, at coordinate z, can be expressed as:

$$\int \sigma_{zz} 2\pi r dr + 2\pi\gamma_{ag} R(z)\cos\theta = -F - \pi R^2 p_a \tag{20}$$

Expression of $\bar{\bar{\sigma}}(r, z)$

We assume in the following that the expressions of the components $\sigma_{zz}(r, z)$, $\sigma_{rr}(r, z)$ and $\sigma_{\phi\phi}(r, z)$ can be approximated by a Taylor expansion to order r^2, according to :

$$\begin{aligned} \sigma_{zz}(r, z) &= -\sigma_0(z) + b_0(z)r^2 \\ \sigma_{rr}(r, z) &= -\sigma_1(z) + b_1(z)r^2 \\ \sigma_{\phi\phi}(r, z) &= -\sigma_2(z) + b_2(z)r^2 \end{aligned} \tag{21}$$

The functions $\sigma_i(z)$ and $b_i(z)$ $(i = 0, 1, 2)$ account for the z-dependence of the stress components. As shown below, they can be explicitly calculated from Eqs. (18) to (20). Note that $\sigma_i(z)$ is positive in case of a compression.

From equation (18) one derives the expression of σ_{rz} :

$$\sigma_{rz}(r, z) = \frac{r}{2}\sigma_0'(z) - \frac{r^3}{4}b_0'(z) \tag{22}$$

where the prime stands for the z-derivative.

Introducing the expression of σ_{rz} (Eq.(22)) in Eq. (18) yields:

$$\begin{aligned} 2b_1(z)r + \frac{\sigma_2(z) - \sigma_1(z)}{r} + (b_1(z) - b_2(z))r \\ + \frac{r}{2}\sigma_0''(z) - \frac{r^3}{4}b_0''(z) = 0 \end{aligned} \tag{23}$$

Since the components of $\bar{\bar{\sigma}}$ must not diverge in $r = 0$, necessarily $\sigma_2(z) = \sigma_1(z)$. There remains :

Development (2021) 00, devxxxxxx. doi:10.1242/dev.xxxxxx

$$3b_1(z) - b_2(z) + \frac{\sigma_0''(z)}{2} = \frac{r^2}{4} b_0''(z)$$

Because we limit the Taylor development to order r^2 for σ_{rr} and $\sigma_{\phi\phi}$, b_1 and b_2 do not depend on r. Consequently $b_0''(z) = 0$ and thus $b_0(z) = Az + B$, where A and B are two constants. Moreover, by z to $-z$ symmetry, σ_{zz} must be an even function of z, which implies $A = 0$. Therefore:

$$b_0(z) = B \tag{24}$$

Here B is a constant independent of z, but it may depend on time t if the stresses in the aggregate evolve with time.

At this stage an additional relation between $b_1(z)$ and $b_2(z)$ is required to close the equation system (18) to (20) and complete the calculation. In the following, we will assume for simplicity that the stress projection in any plane orthogonal to Oz is isotropic, which means $\sigma_{rr}(r,z) = \sigma_{\phi\phi}(r,z)$ and thus $b_1(z) = b_2(z)$. This most simple hypothesis can be partially justified by geometrical arguments, related to the incompressibility of the material, which we will not develop here. Other assumptions remain possible, but we have checked, after performing the whole calculation in different cases, that the result is not modified except for some minor numerical factors. Under this assumption, Eq. (23) simplifies into :

$$b_1(z) = b_2(z) = -\frac{\sigma_0''(z)}{4} \tag{25}$$

The integral of Eq. (20) may be calculated using Eq. (21), which leads to :

$$\sigma_0(z) = p_a + \frac{F}{\pi R^2(z)} + \frac{2\gamma_{ag}\cos\theta(z)}{R(z)} + \frac{1}{2}BR^2(z) \tag{26}$$

Eqs. (24), (25) and (26) are sufficient to calculate all the components of the stress tensor, at any point of a cylindrical aggregate of generator $R(z)$. For instance, one finds for $\sigma_{zz}(r,z)$:

$$\begin{aligned}\sigma_{zz}(r,z) = &- p_a - \frac{F}{\pi R^2(z)} - \frac{2\gamma_{ag}\cos\theta(z)}{R(z)} \\ &- \frac{1}{2}BR^2(z) + Br^2\end{aligned} \tag{27}$$

The only remaining free parameter in Eq. (27) is the constant B, the value of which will be discussed at the end of this section.

The other components $\sigma_{zr}(r,z)$ and $\sigma_{rr}(r,z) = \sigma_{\phi\phi}(r,z)$ can also be written after some long but straightforward calculations, using Eqs. (21), (22) and the boundary condition Eq. (19) to calculate $\sigma_1(z)$.

In the following, we only focus on the case of an aggregate with a circular profile, *i.e.* $R_{\|} = R_2 = cst$, and we write down the stress components in its equatorial plane $z = 0$. In this plane, $R_{\perp} = R_1$ and $\theta = 0$, which leads to :

$$\begin{aligned}\sigma_{zz}(r,0) = &- p_a - \frac{F}{\pi R_1^2} - \frac{2\gamma_{ag}}{R_1} \\ &+ \frac{1}{2}BR_1^2 - BR_1^2\left(1 - \frac{r^2}{R_1^2}\right)\end{aligned} \tag{28}$$

$$\begin{aligned}\sigma_{rr}(r,0) = \sigma_{\phi\phi}(r,0) = -p_a - \gamma_{ag}\left(\frac{1}{R_1} + \frac{1}{R_2}\right) ... \\ + \frac{R_1}{R_2}\left[\frac{F}{2\pi R_1^2} - \frac{\gamma_{ag}}{2}\left(\frac{1}{R_2} - \frac{1}{R_1}\right) - \frac{BR_1^2}{4}\right]\left(1 - \frac{r^2}{R_1^2}\right)\end{aligned} \tag{29}$$

$$\sigma_{rz}(r,0) = 0 \tag{30}$$

Deformation of a sensor embedded in the aggregate

We consider an elastic incompressible sensor, spherical at rest, embedded in the aggregate, of effective shear modulus μ_e. We assume that the mechanical properties of the sensor and of the aggregate are similar, and that the sensor diameter is small compared to the aggregate's one, so that the sensor inclusion does not perturbate the stress distribution in the aggregate. Due to incompressibility, only shear deformations of the sensor are admitted, and the the strain-stress tensors relationship reduces to (see Eq. (2)):

$$2\mu_e\bar{\bar{\varepsilon}} = \bar{\bar{\sigma}}^d = \bar{\bar{\sigma}} - \frac{1}{3}tr(\bar{\bar{\sigma}})\mathbf{I} \tag{31}$$

In the following, we assume that the sensor size is negligible with respect to the aggregate size. We also assume for simplicity that it is located in the equatorial plane $z = 0$, although the calculations could in principle be performed for any position in the aggregate. We introduce $\sigma_a = \dfrac{F}{\pi R_1^2}$ as the average stress exerted by the force F on the equatorial plane. Using Eqs. (28) and (29), one finds:

$$\begin{aligned}\sigma_a = &- \frac{3\mu_e\varepsilon_{zz}(r)}{1 + \dfrac{R_1}{2R_2}\left(1 - \dfrac{r^2}{R_1^2}\right)} + \gamma_{ag}\left(\frac{1}{R_2} - \frac{1}{R_1}\right) \\ &+ \frac{BR_1^2}{2}\left[\frac{2R_2 + (R_1 - 4R_2)\left(1 - \dfrac{r^2}{R_1^2}\right)}{2R_2 + R_1\left(1 - \dfrac{r^2}{R_1^2}\right)}\right]\end{aligned} \tag{32}$$

Equivalently, in Eq. (32) one can replace $-\varepsilon_{zz}$ by $+2\varepsilon_{rr}$, since incompressibility implies $\varepsilon_{rr} = \varepsilon_{\phi\phi} = -\dfrac{\varepsilon_{zz}}{2}$.

At the aggregate center ($r = 0,\ z = 0$), Eq. (32) simplifies into:

$$\begin{aligned}\sigma_a = &- \frac{3\mu_e\varepsilon_{zz}(r=0)}{1 + \dfrac{R_1}{2R_2}} + \gamma_{ag}\left(\frac{1}{R_2} - \frac{1}{R_1}\right) \\ &+ \frac{BR_1^2}{2}\left(\frac{R_1 - 2R_2}{R_1 + 2R_2}\right)\end{aligned} \tag{33}$$

At the aggregate edge ($r = R_1,\ z = 0$), one has :

$$\sigma_a = -3\mu_e\varepsilon_{zz}(r = R_1) + \gamma_{ag}\left(\frac{1}{R_2} - \frac{1}{R_1}\right) + \frac{BR_1^2}{2} \tag{34}$$

Development (2021) 00, devxxxxxx. doi:10.1242/dev.xxxxxx

Choice of the value of B

In this model, B has a homogeneous value over the volume of the sensor, but it may vary over time. Indeed, in the experiment one applies at $t = 0$ a step of displacement to the rigid plate, which imprints a constant deformation to the aggregate. Immediately after the step, the stress in the aggregate is inhomogeneous, but it rapidly evolves, within a few minutes, through different relaxation mechanisms, to become homogeneous again at the end of relaxation. $B(t)$ is therefore a function of time which must relax towards zero at infinite time. To interpret our data concerning $\sigma_a(\varepsilon)$, we discard the first moments of the relaxation, and we only consider the long time limit, for which we expect the stresses to be homogeneous again, allowing us to make the approximation $B = 0$. Within this assumption, Eq. (33) exactly reduces to Eq. (12) used in the main text. To comfort this assumption, we also performed the data analysis by taking a non-zero value for B, leading to parabolic variations for σ_{zz} as a function of r. Assuming for instance that σ_{zz} vanishes at the aggregate edge ($r = R_1,\ z = 0$), from Fig. (4c) one retrieves $\mu_e = 670$ Pa, instead of $\mu_e = 790$ Pa in the case $B = 0$. Considering all other sources of uncertainty, the results do not appear significantly different.

REFERENCES

S. Angeli and T. Stylianopoulos. Biphasic modeling of brain tumor biomechanics and response to radiation treatment. *Journal of Biomechanics*, 49 (6):1524–1531, 2016.

K. Bambardekar, R. Clément, O. Blanc, C. Chardès, and P.-F. Lenne. Direct laser manipulation reveals the mechanics of cell contacts in vivo. *Proceedings of the National Academy of Sciences*, 112(5):1416–1421, 2015.

M. Behrndt and C.-P. Heisenberg. Spurred by resistance: Mechanosensation in collective migration. *Developmental Cell*, 22(1):3–4, 2012.

M. Bendaoud. *Développement de méthodes d'extraction de contours sur des images à niveaux de gris*. PhD thesis, 2017.

J. Bico, Reyssat, and B. Roman. Elastocapillarity: When surface tension deforms elastic solids. *Annual Review of Fluid Mechanics*, 50(1):629–659, 2018.

I. Bonnet, P. Marcq, F. Bosveld, L. Fetler, Y. Bellaiche, and F. Graner. Mechanical state, material properties and continuous description of an epithelial tissue. *Journal of The Royal Society Interface*, 9(75):2614–2623, 2012.

N. Borghi, M. Sorokina, O. Shcherbakova, W. Weis, B. Pruitt, W. Nelson, and A. Dunn. E-cadherin is under constitutive actomyosin-generated tension that is increased at cell-cell contacts upon externally applied stretch. *Proceedings of the National Academy of Sciences*, 109(31):12568–12573, 2012.

A. Boutillon, F. A. Giger, and N. B. David. *Analysis of In Vivo Cell Migration in Mosaic Zebrafish Embryos*, pages 213–226. Springer New York, New York, NY, 2018.

G. Brodland, J. Veldhuis, S. Kim, M. Perrone, D. Mashburn, and M. S. Hutson. Cellfit: A cellular force-inference toolkit using curvilinear cell boundaries. *PLoS ONE*, 9(6):1–15, 2014.

H.-J. Butt, B. Cappella, and M. Kappl. Force measurements with the atomic force microscope: Technique, interpretation and applications. *Surface Science Reports*, 59(1-6):1–152, 2005.

O. Campàs. A toolbox to explore the mechanics of living embryonic tissues. *Seminars in Cell and Developmental Biology*, 55:119–130, 2016.

O. Campàs, T. Mammoto, S. Hasso, R. Sperling, D. O'Connell, A. Bischof, and D. Ingber. Quantifying cell-generated mechanical forces within living embryonic tissues. *Nature Methods*, 11(2):183–189, 2014.

A. Carbonaro, K.-N. Chagua-Encarnacion, C.-A. Charles, T. Phou, C. Ligoure, S. Mora, and D. Truzzolillo. Spinning elastic beads: a route for simultaneous measurements of the shear modulus and the interfacial energy of soft materials. *Soft Matter*, 16:8412–8421, 2020.

V. Caselles, F. Catte, B. Coll, and F. Dibos. A geometric model for edge detection. *Numerische Mathematik*, 66(1):1–31, 1993.

K. Chiou, L. Hufnagel, and B. Shraiman. Mechanical stress inference for two dimensional cell arrays. *PLoS Computational Biology*, 8(5):1–9, 2012.

M. Delarue, F. Montel, D. Vignjevic, J. Prost, J. Joanny, and G. Cappello. Compressive stress inhibits proliferation in tumor spheroids through a volume limitation. *Biophysical Journal*, 107:1821–1828, 2014.

N. Desprat, A. Richert, J. Simeon, and A. Asnacios. Creep function of a single living cell. *Biophysical Journal*, 88(3):2224–2233, 2005.

N. Desprat, A. Guiroy, and A. Asnacios. Microplates-based rheometer for a single living cell. *Reviex of scientifc intruments*, 77:055111, 2006.

N. Desprat, W. Supatto, P.-A. Pouille, E. Beaurepaire, and E. Farge. Tissue deformation modulates twist expression to determine anterior midgut differentiation in drosophila embryos. *Developmental Cell*, 15(3):470–477, 2008.

M. Doitsidou, M. Reichman-Fried, J. Stebler, M. Köprunner, J. Dorries, D. Meyer, C. Esguerra, T. Leung, and E. Raz. Guidance of primordial germ cell migration by the chemokine sdf-1. *Cell*, 11(5):647–659, 2002.

M. Dolega, M. Delarue, F. Ingremeau, J. Prost, A. Delon, and G. Cappello. Cell-like pressure sensors reveal increase of mechanical stress towards the core of multicellular spheroids under compression. *Nature Communications*, 8(4):14056, 2017.

B. Elkin, E. Azeloglu, K. Costa, and B. Morrison III. Mechanical heterogeneity of the rat hippocampus measured by atomic force microscope indentation. *Journal of Neurotrauma*, 24(5):812–822, 2007.

K. Franze. Atomic force microscopy and its contribution to understanding the development of the nervous system. *Current Opinion in Genetics and Development*, 21(5):530–537, 2011.

M. Gomez-Gonzalez, E. Latorre, M. Arroyo, and X. Trepat. Measuring mechanical stress in living tissues. *Nature Reviews Physics*, 2(6):300–317, 2020.

C. Grashoff, B. Hoffman, M. Brenner, R. Zhou, M. Parsons, M. Yang, and M. Schwartz. Measuring mechanical tension across vinculin reveals regulation of focal adhesion dynamics. *Nature*, 466(7303):263–266, 2010.

K. Guevorkian, M.-J. Colbert, M. Durth, S. Dufour, and F. Brochard-Wyart. Aspiration of biological viscoelastic drops. *Physical Review Letters*, 104 (21):218101, 2010.

B. Guirao, S. U. Rigaud, F. Bosveld, A. Bailles, J. Lopez-Gay, S. Ishihara, K. Sugimura, F. Graner, and Y. Bellaiche. Unified quantitative characterization of epithelial tissue development. *eLife*, 4:e08519, 2015.

K. Haejune. Controlled production of emulsion drops using an electric field in a flow-focusing microfluidic device. *Applied Physics Letters*, 91(13):211–218, 2007.

H. Hamada. Role of physical forces in embryonic development. *Seminars in Cell and Developmental Biology*, 47-48:88–91, 2015.

C. Heisenberg and Y. Bellaïche. Forces in tissue morphogenesis and patterning. *Cell*, 153:948–962, 2013.

W. Helfrich. Elastic properties of lipid bilayers : theory and possible experiments. *Z Naturforsch*, 28(11):693–703, 1973.

R. Herrera-Perez and K. Karen. Biophysical control of the cell rearrangements and cell shape changes that build epithelial tissues. *Current Opinion in Genetics and Development*, 51:88–95, 2018.

R. Hiramatsu, T. Matsuoka, C. Kimura-Yoshida, S.-W. Han, K. Mochida, T. Adachi, and I. Matsuo. External mechanical cues triggerthe establishment of the anterior-posterioraxis in early mouse embryos. *Developmental Cell*, 27(2):131–144, 2013.

E. K. Hobbie, S. Lin-Gibson, and S. Kumar. Non-brownian microrheology of a fluid-gel interface. *Physical Review Letters*, 100(7):076001, 2008.

R. Hochmuth. Micropipette aspiration of living cells. *Journal of Biomechanics*, 44(1):15–22, 2000.

B. G. Hosu, K. Jakab, P. Bánki, F. I. Tóth, and G. Forgacs. Magnetic tweezers for intracellular applications. *Review of Scientific Instruments*, 74(9): 4158–4163, 2003.

S. Ishihara, K. Sugimura, S. Cox, I. Bonnet, Y. Bellaïche, and F. Graner. Comparative study of non-invasive force and stress inference methods in tissue. *The European Physical Journal E*, 36(4):45, 2013.

M. Kass, A. Witkin, and D. Terzopoulos. Snakes : Active contour models. *International Journal of Computer Vision*, 1:321–331, 1988.

M. Krieg, Y. Arboleda-Estudillo, P.-H. Puech, J. Käfer, F. Graner, D. Müller, and C.-P. Heisenberg. Tensile forces govern germ-layer organization in zebrafish. *Nature Cell biology*, 10(4):429–436, 2008.

L. Landau, E. Lifshitz, A. Kosevich, and L. Pitaevskii. *Theory of Elasticity : course of theoretical physics*, volume 7. Elsevier, 1986.

K. Lau, H. Tao, H. Liu, J. Wen, K. Sturgeon, N. Sorfazlian, and S. Hopyan. Anisotropic stress orients remodelling of mammalian limb bud ectoderm. *Nature Cell Biology*, 17(5):569–579, 2015.

L. Le Goff, H. Rouault, and T. Lecuit. A global pattern of mechanical stress polarizes cell divisions and cell shape in the growing drosophila wing disc. *Development*, 140(19):4051–4059, 2013.

W. Lee, N. Kalashnikov, S. Mok, R. Halaoui, E. Kuzmin, A. Putnam, and C. Moraes. Dispersible hydrogel force sensors reveal patterns of solid mechanical stress in multicellular spheroid cultures. *Soft Matter*, 13(23): 4210–4213, 2019.

A. A. Lucio, A. Mongera, E. Shelton, R. Chen, A. M. Doyle, and O. Campas. Spatiotemporal variation of endogenous cell- generated stresses within 3D multicellular spheroids. *Scientific Reports*, 7:12022, 2017.

P. Marquez-Neila, L. Baumela, and L. Alvarez. A morphological approach to curvature-based evolution of curves and surfaces. *IEEE Transactions on Pattern Analysis and Machine Intelligence*, 36(1):2–17, 2014.

F. Mazuel, M. Reffay, V. Du, J.-C. Bacri, J.-P. Rieu, and C. Wilhelm. Magnetic flattening of stem-cell spheroids indicates a size-dependent elastocapillary transition. *Physical Review Letters*, 114(9):1416–1421, 2015.

A. Mgharbel, H. Delanoë-Ayari, and J. Rieu. Measuring accurately liquid and tissue surface tension with a compression plate tensiometer. *HFSP Journal*, 3(3):213–221, 2009.

J. Mitchison and M. Swann. The mechanical properties of the cell surface : I. the cell elastimeter. *Journal of Experimental Biology*, 31(3):443–460, 1954.

D. Mitrossilis, J. Fouchard, A. Guiroy, N. Desprat, N. Rodriguez, B. Fabry, and A. Asnacios. Single-cell response to stiffness exhibits muscle-like behavior. *Proceedings of the National Academy of Sciences*, 106(43):18243–18248, 2009.

D. Mitrossilis, J. Fouchard, D. Pereira, F. Postic, A. Richert, M. Saint-Jean, and A. Asnacios. Real-time single-cell response to stiffness. *Proceedings of the National Academy of Sciences*, 107(38):16518–16523, 2010.

E. Mohagheghian, J. Luo, J. Chen, G. Chaudhary, J. Chen, J. Sun, and N. Wang. Quantifying compressive forces between living cell layers and within tissues using elastic round microgels. *Nature Communications*, 9(1):1878, 2018.

A. Mongera, P. Rowghanian, H. Gustafson, E. Shelton, D. Kealhofer, E. K. Carn, and O. Campàs. A fluid-to-solid jamming transition underlies vertebrate body axis elongation. *Nature*, 561(7723):401–405, 2018.

S. Monnier, M. Delarue, B. Brunel, M. Dolega, A. Delon, and G. Cappello. Effect of an osmotic stress on multicellular aggregates. *Methods*, 94:114–119, 2016.

K. C. Neuman and A. Nagy. Single-molecule force spectroscopy: optical tweezers, magnetic tweezers and atomic force microscopy. *Nature Methods*, 5(6):491–505, 2008.

U. Nienhaus, T. Aegerter-Wilmsen, and C. M. Aegerter. Determination of mechanical stress distribution in drosophila wing discs using photoelasticity. *Mechanisms of Development*, 126(11):942 – 949, 2009.

V. Nier, S. Jain, C. T. Lim, S. Ishihara, B. Ladoux, and P. Marcq. Inference of internal stress in a cell monolayer. *Biophysical Journal*, 110(7):1625–1635, 2016.

C. Norotte, F. Marga, A. Neagu, I. Kosztin, and G. Forgacs. Experimental evaluation of apparent tissue surface tension based on the exact solution of the laplace equation. *Europhysics Letters*, 81(4):46003, 2008.

J. M. Northcott, I. S. Dean, J. K. Mouw, and V. M. Weaver. Feeling stress: The mechanics of cancer progression and aggression. *Frontiers in Cell and Developmental Biology*, 6:17, 2018.

S. Porazinski, H. Wang, Y. Asaoka, M. Behrndt, T. Miyamoto, H. Morita, and M. Furutani-Seiki. Yap is essential for tissue tension to ensure vertebrate 3d body shape. *Nature*, 521(7551):217–221, 2015.

M. Rauzi, P. Verant, T. Lecuit, and P.-F. Lenne. Nature and anisotropy of cortical forces orienting drosophila tissue morphogenesis. *Nature Cell Biology*, 10(12):1401–1410, 2008.

P. Roca-Cusachs, V. Conte, and X. Trepat. Quantifying forces in cell biology. *Nature Cell Biology*, 19(7):742–751, 2017.

C. Roffay, C.-J. Chan, B. Guirao, T. Hiiragi, and F. Graner. Inferring cell junction tension and pressure from cell geometry. *Develoment*, 148:1–16, 2021.

T. Schluck and C. M. Aegerter. Photo-elastic properties of the wing imaginal disc of drosophila. *Eur. Phys. J. E*, 33(2):111–115, 2010.

M. Smutny, Z. Akos, S. Grigolon, S. Shamipour, V. Ruprecht, D. Capek, M. Behrndt, E. Papusheva, M. Tada, B. Hof, T. Vicsek, G. Salbreux, and C.-P. Heisenberg. Friction forces position the neural anlage. *Nature Cell Biology*, 19(4):306, 2017.

A. Souchaud. *Cartographie des contraintes mécaniques in situ dans les tissus vivants*. PhD thesis, Université de Paris, 2020.

R. W. Style, A. Jagota, C.-Y. Hui, and E. R. Dufresne. Elastocapillarity: Surface tension and the mechanics of soft solids. *Annual Review of Condensed Matter Physics*, 8(1):99–118, 2017.

K. Sugimura, P.-F. Lenne, and F. Graner. Measuring forces and stresses in situ in living tissues. *Development*, 143(2):186–196, 2016.

M. Tanase, N. Biais, and M. Sheetz. Magnetic tweezers in cell biology. *Cell Mechanics*, 22(1):473–493, 2007.

J.-Y. Tinevez, U. Schulze, G. Salbreux, J. Roensch, J.-F. Joanny, and E. Paluch. Role of cortical tension in bleb growth. *Proceedings of the National Academy of Sciences*, 106(44):18581–18586, 2009.

N. Träber, K. Uhlmann, S. Girardo, G. Kesavan, K. Wagner, J. Friedrichs, and J. Guck. Polyacrylamide bead sensors for in vivo quantification of cell-scale stress in zebrafish development. *Scientific Reports*, 9(1):17031, 2019.

M. Von Dassow, J. A. Strother, and L. A. Davidson. Surprisingly simple mechanical behavior of a complex embryonic tissue. *PLoS ONE*, 5(12): 958–966, 2010.

G. Weber, M. Bjerke, and D. DeSimone. A mechanoresponsive cadherin-keratin complex directs polarized protrusive behavior and collective cell migration. *Developmental Cell*, 22(1):104–115, 2012.

R. Wells. Tissue mechanics and fibrosis. *Biochimica et Biophysica Acta : Molecular Basis of Disease*, 1832(7):884–890, 2013.

Y. Xiong, A. Lee, D. Suter, and G. Lee. Topography and nanomechanics of live neuronal growth cones analyzed by atomic force microscopy. *Biophysical Journal*, 96(12):5060–5072, 2009.

Guidance by followers ensures long-range coordination of cell migration through α-Catenin mechanoperception

Arthur Boutillon[1], Diego Jahn[2], Sebastián González-Tirado[2], Jörn Starruß[2], Lutz Brusch[2], Nicolas B. David[1]

[1] Laboratory for Optics and Biosciences, CNRS UMR7645, INSERM U1182, Institut Polytechnique de Paris, 91128 Palaiseau, France.

[2] Center for Information Services and High Performance Computing, Technische Universität Dresden, Dresden, Germany.

Abstract

Morphogenesis, wound healing and some cancer metastases depend upon migration of cell collectives that need to be guided to their destination as well as coordinated with other cell movements. During zebrafish gastrulation, extension of the embryonic axis is led by the mesendodermal polster that migrates towards the animal pole, followed by axial mesoderm that is undergoing convergence and extension. We here investigate how polster cells are guided towards the animal pole. Using a combination of precise laser ablations, advanced transplantations and functional as well as silico approaches, we establish that the directional information guiding polster cells is mechanical, and is provided by the anteriorward migration of the following cells. This information is detected by cell-cell contact through E-Cadherin/α-Catenin mechanotransduction and propagates from cell to cell over the whole tissue. Such guidance of migrating cells by followers ensures long-range coordination of movements and developmental robustness.

Introduction

Cell migration executes and orchestrates key events in development, homeostasis, and disease (Yamada and Sixt, 2019). Apart from a few examples of cells spreading through random migrations (Borrell and Marín, 2006; Pézeron et al., 2008), most cell migration events are precisely guided in vivo, with chemical or physical environmental cues orienting cell movement (Shellard and Mayor, 2020). The past decade has highlighted that many cells do not undertake migration on their own, but are rather influenced by neighbouring cells, in so-called collective migrations (Norden and Lecaudey, 2019; Scarpa and Mayor, 2016; Schumacher, 2019). This is relevant not only to epithelial cells that need to migrate while maintaining close contacts with their neighbours, but also to some mesenchymal cells. Though not bound to their neighbours, mesenchymal cells rely on interactions with surrounding cells to properly migrate. The best characterized instance is neural crest cells in Xenopus. In this system, cells undergo contact inhibition of locomotion (CIL), whereby contacting cells repolarize away from one another (Carmona-Fontaine et al., 2008; Scarpa et al., 2015). This provides outward polarity for cells in clusters and allows an efficient response to a chemoattractant. Concomitantly, group cohesion is provided by co-attraction, whereby neural crest cells express a chemoattractant to which they themselves respond (Carmona-Fontaine et al., 2011).

In addition to being directionally guided, many cell migrations need to be tightly coordinated with other cell movements. This is particularly true during development when many concomitant cell movements shape the forming embryo. Recent work has proposed mechanical interactions as a way to couple movements of different cell populations (Das et al., 2019; Xiong et al., 2020). However, the cellular bases for such interactions, and how long-range coordination can be achieved, remains poorly explored owing to the challenge of both properly imaging and quantifying cell migration in vivo, and of physically altering the cell's environment to probe the origin and the nature of guidance cues.

Here, we investigate these questions in zebrafish, analysing how the migration of the anterior axial mesendoderm is directed towards the animal pole. At the onset of gastrulation, the first cells to internalize on the dorsal side of the embryo are precursors of the polster (hereafter referred to as polster cells) (Kimmel et al., 1995; Solnica-Krezel et al., 1995). From the embryonic organiser, they migrate in a straight line towards the animal pole, leading the extension of the axis, and are followed by more posterior axial mesodermal cells, including posterior prechordal plate precursors and notochord precursors (Montero et al., 2005; Figure S1A). All these cells express the *Tg(gsc:GFP)* transgene, which also labels some endodermal cells (Figure S1A, Barone et al., 2017). Although different pathways have been implicated in the migration of polster cells (Blanco et al.,

2007; Kai et al., 2008; Montero et al., 2003, 2005; Shimizu et al., 2005; Yamashita et al., 2002, 2004), how polster cells are guided towards the animal pole remains unknown. In particular, loss-of-function of Wnt/PCP pathway components affects their migration directionality (Heisenberg et al., 2000; Ulrich et al., 2005), suggesting a potential instructive role of the Wnt/PCP pathway in cell guidance. However, ubiquitous optogenetic activation recently demonstrated unambiguously that the Wnt/PCP pathway plays only a permissive role in these cells (Čapek et al., 2019), reopening the question of how they are guided. A few years ago, we demonstrated that migration of polster cells is a collective process; cells require E-cadherin dependent contacts with their neighbours to perceive directional information and extend protrusions towards the animal pole (Dumortier et al., 2012). Yet the nature of the directional information transmitted at cell contacts and its origin have remained unknown.

In this study, we used complementary approaches, including precise 3D laser ablations and cell transplants, to map the directional information that guides polster cell migration. We identify follower cells as a source: it is their anteriorward movement that provides propagating mechanical information and orients the migration of polster cells. Cell autonomous inhibition of motility further revealed that mechanical information propagates from cell to cell, through their active migration. Looking for the molecular pathway enabling mechanosensation, we find that the mechanosensitive domain of α-Catenin is required for cell orientation. These results lead to a model of axis extension in which the anteriormost structure, the polster, is guided by more posterior, follower, cells. This mechanical 'guidance by followers' accounts for the long-range coordination of movements of the different cell populations forming the axis, and provides a basis for its developmental robustness.

Results

Polster cells do not exhibit Contact Inhibition of Locomotion nor co-attraction

Though they form a group, polster cells appear mesenchymal: all cells form protrusions (Dumortier et al., 2012) and gaps exist between cells (Smutny et al., 2017). Investigating the mechanisms ensuring their collective migration, we first sought to test if polster cells rely on similar processes as those driving neural crest cell migration, namely Contact Inhibition of Locomotion (CIL) and co-attraction.

We first tested CIL in polster cells by performing mixing assays (Carmona-Fontaine et al., 2008). Two groups of differently-labelled polster cells were transplanted next to each other at the animal pole of an early gastrula embryo, a region devoid of hypoblast cells that could otherwise

interfere with polster cells migration (Figure 1A, Movie S1). Interpenetration of the two groups was measured after 90 minutes as the normalized area of overlap between the two cell populations. The observed broad interpenetration argues against the existence of CIL, as illustrated by simulating the assay with cells displaying CIL or not (see Methods). Second, if CIL was occurring, cells would be expected to change direction upon contact with others (Carmona-Fontaine et al., 2008). We transplanted polster cells expressing H2B-mCherry at the animal pole of a host embryo, tracked their movements, and measured their change in direction upon collision with another polster cell (Figure 1B, Movie S1). As controls, we compared these changes to the natural tendency of these cells to change direction on their own, in absence of collision. We observed no difference in changes of direction with or without collision, arguing against a CIL behaviour.

To assess co-attraction, we transplanted single polster cells expressing Lifeact-mCherry in front of the polster and quantified their movement and protrusion orientations (Figure 1C, Movie S1). While isolated, cells displayed no clear preferred direction, and an almost random orientation of protrusions, suggesting the absence of strong co-attraction. We nevertheless noticed a small bias of movements and protrusions of isolated cells towards the polster, which could arise from a weak co-attraction or from the friction forces exerted by the ectoderm (Smutny et al., 2017). To discriminate between these possibilities, we transplanted two groups of differently-labelled polster cells at the animal pole, separated by some distance, and measured whether they attracted each other (Figure 1D, Movie S1) (Carmona-Fontaine et al., 2011). After 90 min, the distance between centroids had increased by 47±28 µm, arguing against any co-attraction. Furthermore, we observed that groups of cells at the animal pole spread as small clusters or isolated cells; they did not remain compact as would be expected in the case of co-attraction. We thus could not detect signs of CIL nor co-attraction in polster cells.

The directional information guiding the polster is not within the polster.

We therefore looked for other mechanisms that could guide polster cell collective migration. In previous work, we observed that isolated polster cells lack orientation cues, which are restored upon contact with a migrating polster, suggesting that directional cues are transmitted through cell-cell contacts (Dumortier et al., 2012). We sought to map the origin of this directional information. To do so, we developed large 3D ablations, to sever the polster at different positions and identify which regions are required for its oriented migration and where the directional information might come from. The use of non-linear optics provided sufficient axial resolution not to affect the yolk cell underneath, nor the ectoderm above (Figure S1B). Treated embryos could develop until at least 24 hours post fertilization (hpf) and presented only a slight delay compared to controls, suggesting that the laser treatment was not harmful (Figure S1C).

We first tested if the first row of polster cells acts as leaders to guide follower cells, a mechanism described in many instances of collective migration (Haeger et al., 2015; Vishwakarma et al., 2020). The front row of cells was ablated and the movement of posterior cells was quantified by tracking their H2B-mCherry-labelled nuclei (Movies S2 and S3). For each cell, we measured both instantaneous speed (Figure S2B), referred to as absolute speed, and its axial component, in the direction of the animal pole, referred to as axial speed (Figure 2B). Removal of front cells did not affect follower polster cells' absolute (Figure S2B) nor axial speed (Figure 2B). To confirm that front cells do not guide follower cells, we directly quantified cell protrusion orientation before and after ablation by transplanting a few polster cells expressing Lifeact-mCherry into the polster of an unlabelled host (Figure 2A). Providing scarce labelling, this allows precise quantification of cell protrusions and measurement of their orientation (Boutillon et al., 2018). Ablation of the front cell row had no significant effect on protrusion orientation of follower cells (Figure 2C), confirming that front cells are not required to guide them.

To identify the source of directional information, ablations were performed at different antero-posterior positions. First, to isolate the anterior half from the posterior part, middle polster cells were removed by a transversal ablation (Figure 2A, Movie S3). While the absolute speed of anterior cells was not affected by isolation (Figure S2B), their axial speed (animalward motion) decreased dramatically (Figure 2B). As a control for non-specific effects induced by laser ablation, we performed sagittal ablations, parallel to the direction of migration, separating the left and right anterior polster, but leaving each side in contact with the posterior polster (Figure 2A, Movie S3). Such an ablation did not significantly reduce axial speed (Figure 2B). Decrease of axial speed but not of absolute speed upon separation of the entire anterior half of the polster suggested that cells exhibited poorer orientation. We directly tested this by quantifying protrusion orientation of Lifeact-mCherry expressing cells transplanted in the polster before laser ablations. Whereas control sagittal ablations did not affect cell orientation, transversal ablations strongly disrupted protrusion orientation of cells in the isolated anterior polster (Figure 2C). Interestingly, cells in the posterior half were still oriented (Figure 2C) and their axial speed was higher than cells in the anterior part (Figure S2C) suggesting that the directional information guiding the migration is present in the posterior polster.

To test if the directional information is contained in the posterior polster, we performed similar ablation experiments, this time separating the entire polster from the following axial mesoderm (Figures 2A and S1D, Movie S3). Strikingly, this procedure abolished the animalward movement of polster cells, without affecting their absolute speed (Figures 2B and S2B). Consistent with this loss of direction, the orientation of protrusions was completely lost after ablation (Figure 2C). These experiments reveal that, contrary to what we previously proposed (Dumortier et al.,

2012), the directional information orienting polster cells is not contained within the polster itself, but rather seems to be provided by contact with the posterior axial mesoderm.

Contact with the following axial mesoderm is required for polster oriented migration

To directly test if the following axial mesoderm is the source of directional information, we performed more posterior laser ablations, leaving some axial mesoderm in contact with the polster (3.7±1 rows of cells) (Figures 2A and S1D, Movie S3). This largely restored polster migration compared to ablations separating the polster from the following mesoderm (Figure 2B). Consistent with this, cell orientation was also restored (Figure 2C) suggesting that contact between polster and axial mesoderm is necessary for proper orientation and migration of polster cells. This idea is further supported by the observation that, in ablations separating the polster from the following axial mesoderm, the axial mesoderm continued elongating, resulting in wound closure in 24±2 min (n=14 embryos). A few minutes after wound closure, polster migration resumed (Figure S2D) leading to normal development at 24 hpf (Figure S1C).

We sought to confirm these surprising results with a second, independent approach. Using large glass pipettes, we removed the endogenous polster from *Tg(gsc:GFP)* embryos (Figure 3A). In such embryos, axial mesoderm continues elongating. We then transplanted a group of polster cells, with H2B-mCherry labelled nuclei, ahead of the axial mesoderm (Figure 3B, Movie S4). While isolated, these cells spread isotropically, migrating without any preferred direction. In contrast, after contact with the axial mesoderm, polster cells migrated towards the animal pole (Figures 3C and 3D). Repeating this experiment with some Lifeact-mCherry-labelled cells among the transplanted polster cells, we observed that cell protrusion orientation was randomly distributed before contact but became oriented towards the animal pole once the transplanted group was contacted by the axial mesoderm (Figure 3E). In accordance with laser ablations, these observations demonstrate that the polster requires contact with the following axial mesoderm to orient its migration towards the animal pole.

Extension of the following axial mesoderm is required for polster migration orientation

Trying to identify the nature of the directional information, we wondered if polster cells simply required contact with the axial mesoderm, or if they required the animalward movement of the axis undergoing convergence-extension (Myers et al., 2002). To address this question, we examined the migration of a wild-type polster in front of a defective axis: we genetically slowed axis extension in embryos (see below) and replaced their polster with wild-type polster cells (Figure 4A). As a control, we performed polster replacements between wild-type embryos, and observed no

difference in speed of the polster or of the axial mesoderm compared to untreated embryos (Figure 4A). Inhibiting the non-canonical Wnt-PCP pathway affects axis extension (Čapek et al., 2019; Heisenberg et al., 2000; Ulrich et al., 2005). Consistently, expression of Dsh-DEP+, a dominant negative form of Dsh specifically blocking the PCP pathway (Tada and Smith, 2000), strongly slowed axial mesoderm extension (Figure 4A). Importantly, in Dsh-DEP+ expressing embryos, a transplanted, wild-type polster showed a similar reduction in speed (Figure 4A). A second genetic manipulation that dramatically slows down axial mesoderm extension is expression of Rac1 N17 (Figure 4A), a dominant negative form of the Rac1 small GTPase (DN-Rac1) (Tahinci and Symes, 2003). In DN-Rac1-expressing embryos, the animalward movement of a transplanted, wild-type polster was essentially abrogated (Figure 4A). These results demonstrate that the extension of axial mesoderm, not simply contact with it, is required for the migration of the polster.

Active migration of polster cells is required for axis elongation

That the axial mesoderm extends without polster cells, and that this extension is required for polster migration raised the possibility that the polster is simply passively pushed towards the animal pole by the independently-extending axis. To test whether active migration of polster cells is required, we used DN-Rac1 to inhibit their migration (Dumortier et al., 2012), and then transplanted a non-migrating polster into a wild-type embryo. A DN-Rac1-expressing polster replacing that of a wild-type embryo did not move towards the animal pole (Figure 4B) and blocked the elongation of the axial mesoderm. Active migration of polster cells is thus required for their movement towards the animal pole. Interestingly, however, we noticed that when replacing the polster by a small number of DN-Rac1 cells, these cells, while non-motile, were efficiently displaced towards the animal pole by the extending axis (Figures 4B and 4C), demonstrating that extension of the axis does generate pushing forces, though not sufficient to displace an entire polster.

Polster cells can be oriented by another migrating tissue

That axial cells exert pushing forces and that their animalward movement is required to orient polster cell migration suggest that the movement of the axial mesoderm provides mechanical information that orients the active migration of polster cells. We could not, however, rule out that axial cells provide a chemical cue transmitted only through cell-cell contacts. In this case, axis extension would be required to maintain contact and hence transmission of the chemical cue between the two tissues. To distinguish between mechanical and chemical signal, we first transplanted wild-type cells into a polster expressing DN-Rac1 (Figure 4C). Such a polster remains in contact with the axis, so any chemical signal should propagate normally. In such a context, wild-type cells formed protrusions at the same frequency as in a wild-type replaced polster (Figure 4C inlay).

Protrusion orientation, however, was randomized (Figure 4C). This result argues against a chemical signal transmitted from cell to cell.

If polster cells become oriented by the movement of more posterior cells, they may not specifically require interactions with axial mesoderm, but could be oriented by other migrating cells. To test this, we transplanted polster cells ahead of the lateral mesoderm (Figure 5A, Movie S5). Lateral mesoderm cells, visible in the *Tg(tbx16:GFP)* line (Figure 5A), internalize at the embryonic margin before migrating towards the animal pole (Solnica-Krezel et al., 1995). We quantified polster cell migration and orientation before and after contact with the lateral mesoderm. Before contact, polster cells moved and extended protrusions without a preferred orientation. Upon contact with the lateral mesoderm, they aligned both their migration and protrusions (Figures 5B and 5D) with the movement of the lateral mesoderm. This experiment shows that guidance of polster migration is not specific to posterior axial mesoderm, but can be triggered by another migrating tissue.

Polster cells are oriented by actively migrating neighbours

A mechanical signal orienting migration could arise from polster cells being pushed and displaced or from these cells sensing the active migration of their direct neighbours. To distinguish between these sources, we transplanted a few wild-type cells within a small group of DN-Rac1 expressing cells at the front of the polster. Transplanted cells are thus still displaced by the extension of the axis (the small DN-Rac1 cell cluster is displaced, see Figure 4B) but are only in contact with non-motile DN-Rac1 cells. In this context, the protrusions of wild-type cells without actively migrating neighbours were less oriented than those of wild-type cells in a similar small group of other wild-type cells (Figure 4D): polster cells thus require contact with motile neighbours to become oriented. This suggests that motile cells exert forces on their neighbours that serve as directional information.

Adherens junctions ensure cell-cell adhesion and can elicit mechanotransduction, and are therefore strong candidates to transmit and perceive forces. If true, cadherin should be required both within polster cells to perceive forces, and in neighbouring cells, to apply forces. We previously demonstrated, and here confirmed, that E-cadherin knock-down cell-autonomously leads to a loss of protrusion orientation (Dumortier et al., 2012), which is rescued by expression of E-cadherin-GFP (Figure S3A). We tested for an E-cadherin requirement in neighbouring cells by transplanting wild-type cells within a small E-cadherin knocked-down cell cluster. The absence of E-cadherin in neighbours led to a loss of orientation of wild-type cells (Figure 4D). Cadherins are thus required both within polster cells and in their migrating neighbours to orient cell protrusions, suggesting that cadherins transmit forces and their inherent directional information.

Polster cell orientation requires α-Catenin and Vinculin mediated mechanosensation

In some cells, however, Cadherins can influence cell migration without their cytoplasmic domain, in an adhesion and force independent process (Nguyen and Mège, 2016). We thus checked whether the cytoplasmic domain of E-cadherin is required for cell orientation. E-cadherin knocked-down cells, expressing a form of E-cadherin lacking the intracellular domain (E-cadherinΔcyto, Maître et al., 2012), were transplanted into a wild-type polster. Contrary to wild-type E-cadherin, expression of E-cadherinΔcyto did not rescue protrusion orientation (Figure S3A), consistent with a mechanotransducer role of E-cadherin.

Looking for downstream effectors of E-cadherin, Plakoglobin was an obvious candidate. In Xenopus polster cells (anterior axial mesendoderm), it is recruited to adherens junctions upon application of tension and is required for cell orientation in response to tension (Sonavane et al., 2017; Weber et al., 2012). In zebrafish, there are two paralogues of *plakoglobin* (*jupa* & *jupb*). Knocking down both with morpholinos led to cardiac oedema and embryonic death at 1 and 3 dpf, as previously described (Figure S3C) (Martin et al., 2009). However, the double knock-down did not affect protrusion orientation of polster cells (Figure S3B).

Another component of adherens junctions, α-Catenin, links E-cadherin to actin and can ensure mechanotransduction: under tension α-Catenin undergoes a conformational change, revealing the MI binding site for Vinculin and other proteins (Kobielak et al., 2004; Nieset et al., 1997; Pokutta et al., 2002; Yonemura et al., 2010). We thus tested whether α-Catenin mechanosensation is required for polster cell orientation. Knock-down of α-Catenin reduced protrusion orientation, which could be rescued by co-injection of α-Catenin mRNA, indicating that α-Catenin is required for polster cell orientation (Figure 6A, Movie S6). To determine if α-Catenin is required as a link between E-cadherin and the cytoskeleton or as a mechanosensor, we tried rescuing the knock-down with the α-CateninΔVBS construct, which still binds actin but lacks mechanosensation (Han et al., 2016; Huveneers et al., 2012; Twiss et al., 2012). As expected, this α-CateninΔVBS partially rescued developmental defects induced by α-Catenin knock-down (Han et al., 2016) (Figure S3D). Yet, it did not restore polster cell orientation (Figure 6B) suggesting that the mechanosensory function of α-Catenin is required to orient polster cells. To confirm this, we performed similar rescue experiments with the L344P form of α-Catenin, which bears a point mutation in the Vinculin binding site, preventing the tension-dependent recruitment of Vinculin (Seddiki et al., 2018). This tension-insensitive form did not rescue cell orientation (Figures 6B and S3D). As the Vinculin binding domain of α-Catenin appeared to be required for cell orientation, we directly tested the involvement of Vinculin, knocking down the two zebrafish paralogues (Figure 6A, Movie S6). Consistent with the α-Catenin results, Vinculin is required for proper cell orientation (Figure 6C). These results establish that polster cell orientation is driven by mechanotransduction mediated through E-cadherin, α-Catenin and Vinculin.

In silico simulations reveal the emergence of a robust collective behaviour

Overall, our results suggest that each polster cell is oriented by stresses exerted by actively migrating neighbours. To address which statiscal properties can emerge from such cell interactions and if this is sufficient to account for the observed collective migration of polster cells, we turned to an in silico approach and used the Cellular Potts Model (Graner and Glazier, 1992) in the modelling and simulation framework Morpheus (Starruß et al., 2014). Briefly, polster cells were given a Run and Tumble behaviour (see Methods and Figure S4) and a tendency to align with cells pulling on them (migrating towards them). Such a rule proved sufficient to induce the collective migration of polster cells, followed by animalward migrating axial mesodermal cells (Figure 7A, Movie S7). It also correctly reproduced experimental observations upon laser ablations (Movie S7). In particular, we could notice in simulations a slight backward movement of the cells at the posterior edge of the isolated group, and a tendency of the most anterior cells to migrate out of the group after ablations, two characteristics we could then identify in experimental data (Figure S5A). Of note, other simple rules, like correlating the movement of one cell to the movement of any of its neighbours, as observed in confluent epithelia (Poujade et al., 2007) for instance, could not reproduce experimental results (Movie S7).

We also mimicked experiments in which the speed of the axial mesoderm is reduced (presented in Figure 4A). Consistent with experimental observations, the speed of the simulated polster diminished, even though individual polster cell properties were unchanged (Figure 7B, Movie S7). This reduction of group speed stems from an emergent property of the interacting multicellular system: in simulations, we measured the orientation coherence of polster cells and found it to be linearly dependent on the speed of posterior cells (Figure S5B), so that when axis speed is reduced, polster cells maintain their individual speed, but are less oriented, leading to a reduction of the group speed. We directly tested this model prediction by measuring cell movement orientation in the experiments where axis extension was slowed and found the same striking correlation between axis speed and polster cell orientation (Figure S5B). Guidance by followers thus ensures axis integrity as an emergent property from cell-cell interactions.

Discussion

Precise guidance of migrating cells is required to achieve proper development and morphogenesis. In vitro, many chemical and physical cues can orient cell migration, but it is not clear how such cues can guide cells over long distances in the dynamic environment of the developing embryo. Here, focusing on the forming embryonic axis, we have shown that the polster, the anterior-most cell group, rather than being attracted to its destination by long-range signals, is guided by mechanical cues provided by the anteriorward movement of more posterior cells, creating a robust and self-organizing system. Interestingly, the idea that a mechanical information can propagate and coordinate movements of cells at a distance was recently proposed in two other systems (Das et al., 2019; Xiong et al., 2020). Yet, what generates the mechanical signal, how the mechanical information is perceived, and what cellular properties these signals regulate remained unknown. Here, we established that the mechanical signal is generated by the active migration of follower cells, that it is perceived through the E-cadherin – α-Catenin – Vinculin pathway, and that it controls cell orientation.

In vitro work in Xenopus established that migration of polster cells can be guided by pulling forces applied at the cell rear, leading to a model of collective migration in which more posterior cells would orient migration by acting as a drag (Behrndt and Heisenberg, 2012; Weber et al., 2012). Our observations that posterior cells can migrate without polster cells (Figure 3), that they can exert anteriorward forces sufficient to displace a group of non-motile cells (Figure 4B), and that orientation of polster cells requires the anteriorward movement of posterior cells (Figure 4A) demonstrate that, in zebrafish, posterior cells are not acting as a drag, but that it is their active migration which orients polster migration. How this active migration is perceived is, however, not obvious. One possibility is that it generates compressive forces perceived by polster cells. However, our finding that α-Catenin mechanosensing is required to orient cells rather points to cells perceiving tensile forces, as α-Catenin is opened under tension (Hoffman and Yap, 2015). Compression could then be detected as a source of shear stress: passive pushing of a cell attached to its neighbours would put adherens junctions under tension. Such friction forces have been identified between polster cells and the overlying ectoderm (Smutny et al., 2017), and shear stress induced by neighbours was recently implicated in the collective migration of endothelial cells (Patel et al., 2020). However, our observation that cells require their direct neighbours to be actively migrating and to express E-cadherin instead point to a third possibility. To migrate, cells emit anteriorward protrusions on which they pull to progress. These protrusions thus exert tensile forces on anterior neighbours, which could be used to orient them (Figure 7C), ensuring cell guidance by followers. In this case, protrusions would serve not only as grapples used to move forward (Lauffenburger and Horwitz, 1996) but also as a means to transmit directional information, a process reminiscent of Drosophila border cells

(Mishra et al., 2019). Simulations of such cell-cell interactions faithfully reproduced experimental observations, demonstrating that this mechanism is sufficient to account for the collective behaviour of polster cells.

How are cells oriented by their neighbours?

Our model suggests that cells perceive stresses exerted at their surface by neighbours and use them to orient actin rich protrusions. We identified the E-cadherin, α-Catenin, Vinculin pathway as the involved mechanosensor, in line with previous reports showing that stretch induces an α-Catenin change of conformation and Vinculin recruitment (Hoffman and Yap, 2015; Kim et al., 2015; Ladoux et al., 2015). In epithelial cells, this leads to reinforcement of adherens junctions (Jurado et al., 2016) and has been involved in controlling collective epithelial behaviours (Bazellières et al., 2015; Seddiki et al., 2018). How E-cadherin, α-Catenin and Vinculin control orientation of actin rich protrusions remains to be identified. One candidate is Merlin, as in collectively migrating epithelia, it transduces mechanosensation to coordinate Rac1 activity and lamellipodium formation (Das et al., 2015). Apart from Merlin, very little is known on how adherens junctions regulate cytoskeleton dynamics and cell migration (Vishwakarma et al., 2020) Nevertheless, there is accumulating evidence that mechanosensation at cell-cell contacts has a key role in coordinating many cell behaviours (Hirata et al., 2020; Vassilev et al., 2017; Vishwakarma et al., 2018). Unravelling the events downstream of α-Catenin and Vinculin is thus a very exciting avenue for future work, and the zebrafish polster appears as a convenient model system to progress on this line of inquiry.

What is driving axis elongation?

We demonstrated that orientation of polster cells, the cells that lead the formation of the embryonic axis, depends on the anteriorward movement of more posterior, following, cells. A question remains however: what is driving the movement of following cells? It was recently established that a group of cells, located just posterior to the polster, expresses *pcdh18a*, which, by modulating E-cadherin recycling, would transform them into a fast-migrating group (Bosze et al., 2020) which represents an attractive candidate to guide polster migration. If true, this, however, only shifts the question to how these cells are oriented towards the animal pole. One likely hypothesis is that these cells use the very same mechanism as the one we unveiled for the most anterior ones, relying on the active migration of following cells to orient their movement. In such an hypothesis, the system would be fuelled during early gastrulation by the continuous internalisation of cells at the margin (Giger and David, 2017; Krens et al., 2017) which serves as the symmetry breaking event. This

would provide a very simple, yet very robust, coupling of two key gastrulation movements, mesoderm internalization and axis elongation.

Coordination of movements

During development, and during gastrulation in particular, many different cell movements are taking place concomitantly. How the different cell populations coordinate their movements to ensure proper morphogenesis remains largely unknown. For axis elongation in fish, it is noticeable that mutants affecting extension of notochord precursors also affect progression of the anterior polster cells (Heisenberg et al., 2000; Topczewski et al., 2001). This co-occurrence could arise from these cells using similar pathways for their migration. Indeed, the Wnt/PCP pathway appears to be required both for the mediolateral intercalations driving posterior axis extension and for the directed migration of polster cells (Roszko et al., 2009). Alternatively, there may be mechanisms ensuring coordination of the two movements. Using transplants of entire polsters, we observed that progression of a wild-type polster is delayed when notochord progression is genetically delayed, revealing the existence of coordination mechanisms ensuring the integrity of the embryonic axis.

Achieving such coordination is not trivial. As illustrated by in silico simulations, systems in which cells have a directed motion towards the animal pole are very sensitive to any difference in speed between polster and more posterior cells (Figure 7B). Adjusting polster speed to axial speed would imply that axial cells instruct polster cells to slow down. On the opposite, guidance by followers spontaneously provides robustness to the system. The mechanical information that propagates through the tissue modulates cell orientation, and this is sufficient to modulate speed of the entire group. Guidance by followers, in which the cell-to-cell propagation of mechanical information orients cell polarity, is thus a very simple, yet very effective way of ensuring long-range coordination of cell movements and self-organized guidance. Such mechanical coordination is likely to control morphogenesis in other contexts, in embryonic development, organogenesis or cancer cell migration.

Acknowledgements

We thank S. Escot and F. Rosa for critically reading the manuscript; F. Graner and W. de Back for initial help with simulations, C. Wyart, J. de Rooij, E. Raz, R.M. Mège for fish lines and plasmids; Emilie Menant for fish care. We thank Pierre Mahou and the Polytechnique Bioimaging Facility for

assistance with live imaging on their equipment partly supported by Région Ile-de-France (interDIM) and Agence Nationale de la Recherche (ANR-11-EQPX-0029 Morphoscope2, ANR-10-INBS-04 France BioImaging). This work was supported by the ANR grants 15-CE13-0016-1, 18-CE13-0024, 20-CE13-0016. A.B. was supported by the Ministère de l'Enseignement Supérieur et de la Recherche, N.B.D. was supported by the Centre National de la Recherche Scientifique. L.B. acknowledges support by the BMBF through FitMultiCell grant 031L0159B. Model simulations for Bayesian parameter inference were performed on HPC resources granted by the ZIH at TU Dresden.

Author Contributions

AB and ND conceived experiments, which were performed by AB. DJ, SGT, JS, LB and ND developed the simulation model, performed the parameter estimation, ran simulations and wrote the corresponding methods section. AB and ND analysed data, wrote the manuscript. LB and ND secured funding.

Declaration of Interests

The authors declare no competing interests.

Figure Legends

Figure 1: Polster cells do not exhibit CIL nor CoA. (A) Group mixing assay: transplantation of two adjacent, differently labelled groups of polster cells (red and green). Simulated cells display migration characteristics similar to polster cells (see also Figure S4), with or without CIL behaviour. Overlap, highlighted in yellow, is measured at 90 min for experimental (n=11 embryos) and simulated data. (B) Collisions of polster cells transplanted at the animal pole. Change in direction (θ) is measured as the angle between the displacement vector before (red arrow) and after (other colours) a given time step, upon collision or not. Cumulative frequency of angle θ is displayed. Red: change in direction upon collision (n=82 cells); gray: 100 bootstrapped datasets of change in direction in absence of collision; black: combination of all 100 bootstrapped datasets. (C) Unique cells transplanted 58±25 µm ahead of the polster (n=19 cells). Cell trajectories and orientation of actin-rich protrusions (angle between the direction of the protrusion and the direction of the animal pole) are displayed before and after contact with the polster. Asterisks mark the initial position of the transplanted cell; white arrow indicates direction of the Animal Pole (AP) (D) Group attraction assay: transplantation of two

differently labelled groups of polster cells (n=7 embryos), initially 166±38 µm apart. White crosses mark group centroids; dashed lines mark the distance between centroids, which is plotted at 0 and 90 min. In this and following figures, ns: p.value ≥0.05; *: p<0.05; **: p<0.01; ***: $p<10^{-3}$; ****: $p<10^{-4}$.

Figure 2: Directional information is not contained in the polster. (A) Laser ablations at varying antero-posterior positions and/or orientations. Representative images of ablations, taken from experiments in which a few Lifeact-mCherry expressing cells were transplanted in the polster, to quantify protrusion orientation. Position of the ablation is indicated by a white dashed line on experimental images, and a red line on schematics; arrowheads mark actin rich protrusions; white arrow indicates direction of the Animal Pole (AP). (B) Axial speed of polster cells, tracked by H2B-mCherry labelling of their nucleus, n=8 to 10 embryos, 149±11 quantified cells per embryos. Gray bars indicate paired statistical tests on embryos before and after ablation. (C) Orientation of actin rich protrusions in Lifeact-mCherry labelled cells. Numbers of quantified cells were respectively 27 in 4 embryos; 24 in 4 embryos; 17 in 3 embryos; 34 in 5 embryos; and 24 in 3 embryos. (B-C) Schematics indicate the position of ablation; yellow and orange brackets indicate the region of the polster quantified after ablation.

Figure 3: Polster oriented migration requires contact with posterior axial mesoderm. (A) Removal of the polster revealed by in situ hybridization for *gsc* (red) and *tbxta* (blue) or fluorescence in the *Tg(gsc:GFP)* line. The blue arrow and thin white line mark the former polster position; red lines mark posterior axial mesoderm. (B) Transplantation of 59±51 polster cells, 106±43 µm ahead of the axis. The thin white line delineates transplanted cells; horizontal line marks the initial position of the rear of the transplanted group. (C) Trajectories, (D) axial speed (average of all transplanted cells in each embryo, n=6 embryos) and (E) actin rich protrusion orientations (n=15 Lifeact-mCherry labelled cells in 5 embryos) of transplanted cells. Gray bars indicate paired statistical tests.

Figure 4: Orientation of polster cells requires active migration of the following axial mesoderm. (A) Replacement of the polster by a wild-type (WT) polster, in control embryos or embryos in which axis extension is genetically slowed down. Axial speed of replaced polster cells (red boxes) and of the front of the following axial mesoderm (blue boxes) were measured. White line marks transplanted polster cells and red line marks following axial mesoderm. (B) Replacement of the polster by a WT polster or a DN-Rac1 expressing polster, of varying size. Lines mark the initial position of the polster front. Axial speed of polster cells is plotted as a function of polster size. Unmanipulated WT embryos have been quantified for comparison (blue circle). (C) Protrusion orientation of WT cells in WT (33

cells in 7 embryos) and DN-Rac1 (29 cells in 4 embryos) polsters. Inlay indicates the average number of protrusions per frame for each condition. (D) Protrusion orientation of WT cells transplanted among a small group of WT (25 cells in 6 embryos), DN-Rac1 (19 cells in 7 embryos) or Mo E-cadherin (11 cells in 6 embryos) cells labelled with H2B-mCerulean, in front of a WT polster. Inlay indicates the average number of protrusions per frame for each condition. White lines mark the endogenous polster of host embryos.

Figure 5: Lateral mesoderm can drive polster cell migration. (A) H2B-mCherry expressing polster cells (strong green, red nuclei) were transplanted ahead of the lateral mesoderm (*Tg(tbx16:GFP)*; faint green). A thin white line delineates polster cells; green line marks the lateral mesoderm anterior edge; horizontal line marks the position of the rear of the polster cell group upon contact with the lateral mesoderm. (B) Polster cell trajectories before and after contact with the lateral mesoderm of a typical experiment. (C) Axial speed (n=8 embryos) of transplanted polster cells before and after contact with the lateral mesoderm. (D) Protrusion orientation of Lifeact-mCherry expressing polster cells (red labelled actin) transplanted along with other polster cells expressing H2B-mCerulean (green with blue nuclei) in front of the lateral mesoderm, quantified before and after contact (22 red cells in 3 embryos).

Figure 6: α-Catenin mechanosensation and Vinculin are required for polster cell orientation. Actin rich protrusions of Lifeact-mCherry expressing cells transplanted in a WT polster. Arrowheads mark actin rich protrusions. Mo Ctrl: n=28 cells in 6 embryos for panel (B) and n=37 cells in 10 embryos for panel (C), Mo α-Catenin: n=25 cells in 6 embryos, rescue α-Catenin: n=22 cells in 4 embryos, rescue α-CateninΔVBS: n=34 cells in 8 embryos, rescue α-CateninL344P: n=30 cells in 8 embryos, Mo Vinculin a&b n=29 cells in 9 embryos, rescue Vinculin a&b n=24 cells in 6 embryos.

Figure 7: Guidance by followers. (A, B) Cellular Potts models testing different scenarios. (A) Polster cells are given a Run and Tumble behaviour, fitted to observations of isolated polster cells (see Figure S4). On their own, polster cells tend to disperse. When followed by axial mesoderm, they progress towards the animal pole, but mix with axial mesoderm. Adding mechanical sensitivity to neighbours migrating towards them (guidance by followers) is sufficient to account for the collective oriented migration of polster cells (and all experimental observations, see Movie S7). (B) If both polster cells and axial mesoderm are given oriented migrations towards the animal pole, differences in their speed will induce axis disruption. On the contrary, when polster cells are oriented by followers, polster speed spontaneously adjusts to axis speed. This stems from polster cell orientation being dependent on posterior cell speed (see Figure S5B). (C) Model of guidance of polster cells. Cells

perceive mechanical stimuli generated by the active migration of their neighbours, and orient their protrusive activity accordingly. This leads to propagation of the directional information through the entire group.

STAR Methods

Resource availability

Lead contact

Further information and requests for resources and reagents should be directed to and will be fulfilled by the lead contact, Nicolas David (Nicolas.david@polytechnique.edu)

Materials availability

This study did not generate new unique reagents.

Data and code availability

The Morpheus model generated during this study was deposited in the public model repository under MorpheusModelID:M0006 (https://identifiers.org/morpheus/M0006). Custom Matlab routines used to process cell tracks are available upon request.

Experimental model

Zebrafish embryos were obtained by natural spawning of AB, *Tg(tbx16:EGFP)* and *Tg(-1.8gsc:GFP)ml1* adult fishes (Doitsidou et al., 2002; Wells et al., 2011). All animal studies were approved by the Ethical Committee N°59 and the Ministère de l'Education Nationale, de l'Enseignement Supérieur et de la Recherche under the file number APAFIS#15859-2018051710341011v3.

Method details

In Situ Hybridization

Whole-mount colour and fluorescent In Situ Hybridization were performed following standard protocols (Hauptmann and Gerster, 1994) using *goosecoid*, *tbxta* and *ctslb* probes (Schulte-Merker et al., 1994; Stachel et al., 1993; Thisse et al., 1994).

Embryo injection

Translation blocking morpholinos (Gene Tool LLC Philomath) and concentration used were: Vinculin a (5□-CGTCTTGGTATGGAAAACTGGCATC-3') (0.3 mM), Vinculin b (5□-TGGAAAACCGGCATGATGATCGCTC-3') (0.3 mM), Jupa (Plakoglobin 1a) (5□-

GAGCCTCTCCCATGTGCATTTCCAT-3') (0.4 mM) (Martin et al., 2009), Jupb (Plakoglobin 1b) (5'-CCTCACTCATTTGCAGTGACATCAC-3') (0.1 mM), E-cadherin (5'-TAAATCGCAGCTCTTCCTTCCAACG-3') (0.3 mM) (Babb and Marrs, 2004), α-Catenin (5'-TAATGCTCGTCATGTTCCAAATTGC-3') (0.1 mM) (Han et al., 2016), Sox32 (5'-CAGGGAGCATCCGGTCGAGATACAT-3') (0.3 mM) (Dickmeis et al., 2001), and standard control (5'-CCTCTTACCTCAGTTACAATTTATA-3') (0.1 to 0.3 mM).

Capped sense mRNA were synthesized from pCS2+ constructs with mMessage mMachine SP6 kit (Thermo Fischer). Constructs and concentrations used were: Histone 2B mCherry (30 to 50 ng/µl), Histone2B-mCerulean (30 to 50 ng/µl), Lifeact-mCherry (30 to 50 ng/µl), Taram-A* (0.6ng/µl), DshDep^{+} (75 ng/µl), Rac1 N17 (2 or 10 nl/µl), DN-MLCK (100 ng/µl), Zf E-cadherin-GFP (60 ng/µl), Zf E-cadherin-Δcyto-GFP (60 ng/µl), Zf α-Catenin (30 ng/µl), Zf α-Catenin-ΔVBS (30 ng/µl) and Zf α-Catenin-L344P (30 ng/µl), Zf Vinculin a-GFP (25ng/µl), Zf Vinculin b-GFP (25ng/µl).

To label and/or affect the whole embryo, 5 nl were injected at the one-cell stage. For donor embryos for cell transplantation, 1.5 nl were injected in one cell at the four-cell stage.

Cell transplantation and microsurgery

Cell transplantations were performed as described in (Boutillon et al., 2018). Cells transplanted within the polster were taken from the shield of a *Tg(gsc:GFP)* donor and transplanted to the shield of a *Tg(gsc:GFP)* host at 6 hpf. Identity of transplanted cells was then assessed by their GFP expression. Cells transplanted out of the polster (animal pole, lateral side, ahead of the polster) were taken from donor embryos injected, in one cell out of four, with Tar* mRNA and Sox32 morpholino, so as to impose a polster identity (Dumortier et al., 2012). For single cell transplant, donor embryos were dissociated at shield stage in Ringer's without calcium solution prior to transplantation. Removal of the polster was performed in *Tg(gsc:GFP)* embryos, by aspiration with a large homemade glass pipette. The polster was identified on morphological criteria, confirmed by *in situ* hybridization against *ctslb*, a marker for polster identity, and *gsc*, a marker for prechordal plate (Figures 3A and S1).

Embryo imaging

Imaging of embryos for protrusion quantification was done on an inverted TCS SP8 confocal microscope (Leica) equipped with environmental chamber (Life Imaging Services) at 28°C using a HC PL APO 40x/1.10 W CS2 objective (Leica). Imaging of embryos for cell migration quantification was done under an upright TriM Scope II (La Vision Biotech) two-photon microscope equipped with an environmental chamber (okolab) at 28°C and a XLPLN25XWMP2 (Olympus) 25x water immersion objective or on the inverted TCS SP8 microscope (Leica) using a HCX PL Fluotar 10x/0.3 objective

(Leica). Injected embryos were mounted in 0.2% agarose in embryo medium between 60% and 70% epiboly (6.5-7.5 hpf). Embryos were imaged between 30 and 60 minutes, every one to three minutes.

Laser ablation

Laser ablation experiments were performed under the TriM Scope II microscope (La Vision Biotech) equipped with a femtosecond Mai Tai HP DeepSee laser (Spectra Physics) and an Insight DeepSee (Spectra Physics) laser. Embryos were imaged every minute for 10 to 15 minutes prior to ablation. GFP was excited by the Mai Tai laser set to 920 nm wavelength and mCherry by the Insight laser set to 1160nm. Ablations were performed with the Mai Tai laser at 820nm and exit power at 0.3 mW. Such an exit power allowed efficient ablation with very good axial confinement. The region to be ablated was defined as an XY ROI, and selectively illuminated using an EOM. To perform 3D ablations, laser treatment was performed on different focal planes, separated by 10 to 15 microns, starting with deeper planes. To compensate for the loss of energy in deeper planes, the number of treatment repeats was modulated with depth. Efficiency of the ablation was assessed by the absence of GFP fluorescence and the presence of cellular debris, and later confirmed by observation of locally modified cell behaviour. Embryos were imaged for 30 to 40 minutes following ablation. The polster was identified on morphological criteria and distance to the front, confirmed by *in situ* hybridization against *ctslb*, a marker for polster identity (Figure S1D).

Illustrations

Images were processed with FIJI. Figures were assembled with Adobe InDesign, movies with Adobe Premiere Pro.

Model simulations

To model cell motility and cell-cell interactions, we chose a Cellular Potts Model (CPM) since the CPM allows for arbitrary cell shapes, spatially resolved cell-cell contact interfaces and stochasticity in cell movement (Graner and Glazier, 1992). Multiple modelling and simulation frameworks for CPM exist including Chaste (Mirams et al., 2013; Pitt-Francis et al., 2009), CompuCell3D (Swat et al., 2012) and Morpheus (Starruß et al., 2014) which are free, open-source software. We have chosen Morpheus because of its user-friendly interface and its transparent separation of the solver code from the computational model description in the domain-specific language MorpheusML. The model description file was deposited in the public model repository

under MorpheusModelID:M0006 (https://identifiers.org/morpheus/M0006) which renders our multicellular simulations readily reproducible and extensible following the FAIR principles.

The simulations were performed on an elongated spatial domain with 500 x1500 grid nodes of a two-dimensional hexagonal lattice with periodic boundary conditions. Left- and right-flanking static obstacles left a central channel of 200 nodes width for the cells to migrate into. These obstacles were used to mimic lateral confinement by paraxial mesoderm. The spatial unit is chosen as 1µm per grid interval and the temporal unit as 1 min per time step. Monte Carlo step duration was chosen as 0.1 min to allow thousands of potential updates per lattice node during the simulated time span. Cell shape is controlled by a target area of experimentally measured 326 µm² (average of 360 experimental measures) and a target circumference taken from the isoareal circle. Both constraints enter the Hamiltonian with equal Lagrange multipliers of 1 (Graner and Glazier, 1992). Axial mesoderm cells (yellow in simulations) are given a directed motion targeted at the animal pole, the speed of which is modulated by varying the strength parameter of the Directed Motion plugin in Morpheus (Starruß et al., 2014). Unless specified, polster cells (green in simulations) are given a Run-and-Tumble motility with uniform reorientation probability of the target direction, a non-dimensional scaling factor "Run_duration_adjustment" of the Gamma-distributed probabilistic waiting times for reorientation events, i.e. Run_duration_adjustment * Γ(0.5,5 min) with a mean run time of Run_duration_adjustment*0.5*5 min, and a tunable Lagrange multiplier "motion_strength" that scales motion speed. The two parameter values for Run_duration_adjustment and motion_strength were estimated from experimental data of single cell trajectories (see below). In addition to the Run-and-Tumble motility, mechanical orientation of polster cells was simulated using the PyMapper plugin. At fixed time steps of 1 min, for each cell, neighbours are detected on 50 membrane points. For each neighbour, the angle between its velocity vector and the direction towards the considered cell is computed. If below a threshold "max_angle" (i.e. neighbour migrating towards the considered cell), the velocity vector of the neighbour is used as the new direction of the considered cell in the Directed Motion plugin. In case of several migrating neighbours, the direction vector is an average of their velocity vectors, weighed by the size of cell-cell contacts. In most simulations, 400 cells are initialized. An initial phase of 20 min without motility is used to equilibrate cell shapes and cell packing (not shown on the movies). Based on their antero-posterior position, cells are then given an identity, and the corresponding motility properties. Main parameters are summarized in Table S1.

For simulations with Contact Inhibition of Locomotion, identical parameters were used (Monte Carlo step duration, target area and circumference) and polster cells were given the same Run and Tumble behaviour. Instead of adding mechanical orientation, a CIL behaviour was added. Briefly, a membrane property is used to detect contact with neighbouring cells. The vector between

the cell center and the contact point is measured and the opposite vector is added to the current cell direction, with a tunable Lagrange multiplier "cil_strength". Simulations were performed on a square domain with 1000 x1000 grid nodes of a two-dimensional hexagonal lattice with periodic boundary conditions. Two groups of 40 cells were initialized, their centres 120 µm apart.

Parameter estimation

In order to fit the baseline cell motility parameters to experimentally observed single cell trajectory data, we define a distance function between the observed and simulated summary statistics.

$$d = \sum_i w_i^{MSD} * |MSD_i - msd_i| + \sum_{i<21min} w_i^{DAC} * |DAC_i - dac_i|$$

Here, MSD is the mean square displacement and DAC the direction autocorrelation function (Gorelik and Gautreau, 2014). Capital variables represent the experimental measurements, small letters represent the model observables. We calculate the sum of weighted (see below) differences between the ensemble (n~200) means of MSD and DAC at the time points $i \in$ {0min, 3min, 6min, 9min, 12min, 15min, 18min, 21min}. We optimize this distance function *d* employing the FitMultiCell software (https://fitmulticell.gitlab.io), which is a free, open-source Python tool embedding stochastic, multi-cellular Morpheus simulations in the highly parallel and unbiased Approximate Bayesian Computation – Sequential Monte Carlo (ABC-SMC) algorithm implemented by the computational framework pyABC (Klinger et al., 2018; Schälte and Hasenauer, 2020). FitMultiCell concurrently evaluates the model and distance measure *d* for trial parameter sets drawn from the evolving probability distribution across the search space, started from a uniform prior distribution. The distance measure *d* is then minimized over successive epochs by only accepting parameter sets with *d* below a gradually decreasing acceptance threshold ε. The pyABC meta-parameters for parameter sample number was set to 200 accepted trial parameter sets per epoch. The computations were run on the high performance computing cluster of ZIH at TU Dresden with 4 CPUs used per task, 2.5 GB/core. The approximate run time for 10 epochs was 20 hrs.

The weights w_i were chosen adaptively in pyABC to account for the different scales of MSD and DAC and two sets of optimization epochs were concatenated. First, a uniform prior distribution in the broad interval [0.01, 10] was chosen for each fit parameter and the adaptive-weight scheme of pyABC readjusted the w_i after each of 10 epochs. To avoid convergence problems for later epochs due to fluctuating weights, we used the posterior distributions of this first set of epochs as the prior for the second set of epochs, i.e. Run_duration_adjustment: [0.05, 4], motion_strength: [0.1, 2], advection_velocity: [0.05, 3]. The weights w_i of the second set of epochs were again adaptively

adjusted by pyABC but just initially and then kept fixed for the remaining 12 epochs. Convergence was judged by arriving at the plateau of the acceptance threshold ε in the ABC-SMC algorithm, see Figure S4. The following point estimate for the fitted model parameters and their confidence intervals were obtained (Figure S4A):

Run_duration_adjustment: 0.76, CI: [0.18, 1.95]

motion_strength: 0.50, CI: [0.28, 1.00]

advection_velocity: 1.42, CI: [0.24, 2.20]

The parameter advection_velocity was used to overlay a uniform translation onto all cells, capturing potential drag forces by the overlying ectoderm. Such common translation reproduces the experimentally observed baseline of 20% in DAC (Figure S4D).

Quantification and statistical analysis

Image analysis

Cell movements were quantified by tracking cell nuclei, labelled with H2B-mCherry, using IMARIS (Bitplane). Tracks were then processed using custom-made Matlab (Math Works) routines as described in (Dumortier et al., 2012). Axial mesoderm elongation was quantified by tracking migration of cells at its front. Actin-rich protrusions were quantified on Lifeact-mCherry expressing cells. Protrusion orientation was manually measured as the angle between protrusion axis and the animal-vegetal axis, using ImageJ (FIJI), as described in (Boutillon et al., 2018).

Statistical analysis

All statistical analyses were performed in R (R project). Cell migration absolute and axial speed were averaged over cells and embryos, and compared using Wilcoxon tests. When relevant, paired Wilcoxon tests were performed, as indicated on the corresponding boxplots. Protrusion angle distributions and frequency were compared using linear mixed models taking into account the fact that measurements are not independent (several measurements for each cell, several cells for each embryo).

To serve as controls for collision data (see Figure 1B), 100 bootstrapped datasets were generated by randomly picking, for 80 cells, one time-step where the cell moves freely (no collision) and measuring the angle between incident and efferent vectors (26±13 available times per cell). Each of these bootstrapped datasets, along with the combination of all, were compared to the angle of

deflection upon collision using a Kolmogorov-Smirnov test. Only one bootstrapped dataset is statistically different, which is less than expected by chance with an α risk of 5%.

Key Resources Table

REAGENT or RESOURCE	SOURCE	IDENTIFIER
Deposited data		
Raw images	This paper; Mendeley data	http://dx.doi.org/10.17632/7ckg3p8d7d.1
Experimental models: Organisms/strains		
Zebrafish AB Zebrafish *Tg(-1.8gsc:GFP)ml1*	Doitsidou et al., 2002	ZDB-ALT-051004-2
Zebrafish *Tg(tbx16:EGFP)*	Wells et al., 2011	ZDB-TGCONSTRCT-110722-1
Oligonucleotides		
Morpholino Vinculin a: CGTCTTGGTATGGAAAACTGGCATC	Gene Tools	This paper
Morpholino Vinculin b: TGGAAAACCGGCATGATGATCGCTC	Gene Tools	This paper
Morpholino Jupa (Plakoglobin 1a): GAGCCTCTCCCATGTGCATTTCCAT	Gene Tools	ZDB-MRPHLNO-091103-3
Morpholino Jupb (Plakoglobin 1b): CCTCACTCATTTGCAGTGACATCAC	Gene Tools	This paper
Morpholino E-Cadherin: TAAATCGCAGCTCTTCCTTCCAACG	Gene Tools	ZDB-MRPHLNO-050421-2
Morpholino α-Catenin: TAATGCTCGTCATGTTCCAAATTGC	Gene Tools	ZDB-MRPHLNO-120206-2
Morpholino Sox32: CAGGGAGCATCCGGTCGAGATACAT	Gene Tools	ZDB-MRPHLNO-051216-6
Morpholino standard control: CCTCTTACCTCAGTTACAATTTATA	Gene Tools	N/A
Software and algorithms		
ImageJ	Schneider et al., 2012	https://imagej.nih.gov/ij/
Matlab IMARIS	Math Works Bitplane	
R		https://www.r-project.org/
InDesign	Adobe	
Premiere Pro	Adobe	
Morpheus	Starruß et al., 2014	https://morpheus.gitlab.io/
Morpheus model	This paper	https://identifiers.org/morpheus/M0006

Supplemental Information

Table S1. Summary of model parameter values.

Model parameter	Symbol	Value	Unit	Reference
target cell area	A_0	326	µm²	experimental measurement
target cell circumference	C_0	$\sqrt{4\pi A_0}$	µm	free choice
polster cell, motion strength	λ_1	*0,5*	-	fitted to single cell data
polster cell, mean run time	T_1	*0,76*2,5*	min	fitted to single cell data
polster cell, advection velocity	v_1	*1,42*	$\frac{\mu m}{min}$	fitted to single cell data
maximum angle	α_{max}	$\pi/6$	-	fitted to collective behaviour

Figure S1: Situation of polster cells and laser ablations, related to Figure 2. (A) Scheme of a gastrulating embryo at 70% epiboly in dorsal view; lm: lateral mesoderm; black arrow marks the direction of polster migration. Close-ups on the forming embryonic axis in *Tg(gsc:GFP)* embryo where axis is labelled in green, along with some endodermal cells (white line delineates the polster; red lines mark the posterior axial mesoderm; arrowheads point to some endodermal cells), and in a fluorescent in situ hybridization (FISH) for different antero-posterior markers of the axis (sagittal and dorsal views). Polster precursors expressing *ctslb* and notochord precursors expressing *tbxta* appear in green, prechordal plate progenitors expressing *gsc* appear in red. (B) Representative *Tg(gsc:GFP)* embryo before and after laser ablation, here between the polster and the following mesoderm. Sagittal and dorsal views. Membranes are labelled in red by expression of mCherry-CAAX. Ablation is located between white arrowheads. YSL: yolk syncytial layer; EVL: enveloping layer. (C) Morphology and survival of control and ablated *Tg(gsc:GFP)* embryos at 24 hpf. The polster derivative, the hatching gland, is indicated by red arrowheads. (D) Fluorescent in situ hybridization for *ctslb* and *tbxta* on a representative embryo ablated at the interface between the polster and the posterior axial mesoderm. Position of the ablation is visible through red autofluorescent debris. Distance between the front of the polster and either the posterior edge of the *ctslb* domain, the position of ablations between the polster and following mesoderm, and of ablations within the following mesoderm.

Figure S2: Migration speed of polster cells after laser ablations, related to Figure 2. (A) 3D views of polster and axial mesoderm (green) migration, in a *Tg(gsc:GFP)* embryo expressing H2B-mCherry

(red). Nuclei belonging to the polster are highlighted in magenta and tracked over time (see Movie S2). AP: animal pole. (B) Absolute speed of polster cells in control and ablated embryos, corresponding to the axial speeds presented in Figure 2. (C) Axial speed of the anterior and posterior parts of the polster after ablation in its middle. (B-C) Schematics indicate the position of ablation; yellow and orange brackets indicate the region of the polster quantified after ablation. Gray bars indicate paired statistical tests on embryos before and after ablation. (D) Axial speed of polster cells in embryos ablated between the polster and the posterior mesoderm, as a function of time (n=6 embryos). The moment of the ablation and the average moment of wound healing are indicated.

Figure S3: E-cadherin is required for polster cell orientation while Plakoglobin is not, related to Figure 6. (A) Polster cells injected with Lifeact-mCherry RNAs and control morpholino (n=23cells in 6 embryos), E-cadherin morpholino (n=28 cells in 6 embryos), E-cadherin morpholino and E-cadherin mRNA (resc. E-cadherin: n=22 cells in 4 embryos), or E-cadherin morpholino and E-cadherinΔcyto (resc. E-cadherinΔcyto: n=34 cells in 8 embryos) mRNA were transplanted in a wild-type polster. Orientation of actin rich protrusions (arrowheads) were quantified. (B) Polster cells injected with Lifeact-mCherry RNAs and a control Morpholino (n=26 in 9 embryos) or Morpholinos targeting *jupa* and *jupb* (n=29 cells in 9 embryos) were transplanted in a wild-type polster. Orientation of protrusions were quantified. (C) Phenotypes at 24 and 72 hpf of control uninjected embryos (n=37) and embryos injected with *jupa* and *jupb* morpholinos (n=47). (D) Phenotypes at 24 hpf of embryos injected with a control morpholino or Mo α-Catenin, with or without mRNAs. (C-D) Number of analysed embryos are indicated above each bar.

Figure S4: Parameter estimation for Cellular Potts Model simulations, related to Figure 7. (A) Inference of model parameters from experimental data with ABC-SMC optimization using the FitMultiCell toolbox. Estimation results are shown as normalized two-parameter (top row) and one-parameter (bottom-row) kernel density estimates of the posterior parameter distributions. The red dot (top row) and red-dashed line (bottom row) represent the weighted median (for details see Methods, Parameter estimation). (B) Evolution of the acceptance threshold through optimization epochs. (C) Mean Square Displacement and (D) Differential Autocorrelation of experimental and simulated data with estimated parameters.

Figure S5: Comparison of simulated and experimental data, related to Figure 7. (A) Close-ups from simulated and experimental laser ablations, revealing two features we first noticed in simulations and then identified in experimental data: a backward movement of the cells at the posterior edge of the isolated group and a tendency of the most anterior cells to migrate out of the group. Both

features were quantified in experimental data. (B) Orientation of cell movements when speed of following cells (axis) varies. Experimental data are those presented in Figure 4A, and correspond to an unmanipulated polster (ctrl), or a wild-type poster transplanted in either a wild-type embryo, a Dsh-DEP+ injected embryo or a DN-Rac1 injected embryo. Simulations were performed with varying speed of axial cells, by modulating the Lagrange multiplier modulating their movement (Imposed Motion Strength). Distribution of orientations are plotted in the different situations as cumulative plots. The percentage of movements oriented towards the animal pole (<45%) is plotted as a function of the measured speed of the axis.

Movie S1: Polster cells do not exhibit CIL or CoA behaviour, related to Figure 1. Mixing assay: two differently labelled groups of polster cells were transplanted side by side at the animal pole of a host embryo. Their overlap (yellow) was measured after 90 min. Green is GFP, red is Lifeact-mCherry. Collision assay: example of a collision between polster cells transplanted at the animal pole of a host embryo. Nuclei, labelled with Histone2B-mCherry were tracked (white ellipsoid). Trajectories before and after contact are highlighted, respectively in cyan and yellow. One cell ahead of the polster: one polster cell, labelled with Lifeact-mCherry (red), was transplanted ahead of the polster (green). Two nearby groups: two differently labelled groups of polster cells were transplanted 160 µm apart, to see if they attract each other. Areas covered by each group are highlighted in green and red at times 0 and 90 min. Green is GFP, red is Lifeact-mCherry. Scale bar is 50 µm for all four movies.

Movie S2: Four-dimensional tracking of polster nuclei, related to Figure 2. Nuclei of a *Tg(gsc:GFP)* embryo were labelled with Histone2B-mCherry. Z-stacks were acquired every minute. Nuclei of polster cells, identified by GFP expression and morphological criteria, are highlighted in magenta and 3D-tracked in time. Animal pole is to the top. Scale bar is 50µm.

Movie S3: Laser ablations, related to Figure 2. Maximum projections of z-stacks acquired every minute in gastrulating *Tg(gsc:GFP)* embryos. Embryos were first imaged for 10 minutes. A laser ablation was then performed at the location indicated in each panel by the red bar on the movie and on the small schematic. Embryos were then imaged for 40 minutes. Animal pole is to the top. Scale bar is 50 µm.

Movie S4: Contact with posterior axial mesoderm drives polster cell migration, related to Figure 3. The polster of an unlabelled *Tg(gsc:GFP)* host was removed, while the following axial mesoderm was left intact (dim green). Polster cells from a *Tg(gsc:GFP)* donor (bright green), labelled with Histone2B-mCherry (red nuclei), were transplanted ahead of the axial mesoderm. Z-stacks were acquired every 2-minute, maximum projections are shown here. Before contact with the extending axial mesoderm,

transplanted polster cells do not display directional migration. After contact, the group of polster cells migrates in the same direction as the extending axial mesoderm. Animal pole is to the top. Scale bar is 50 µm.

Movie S5: Contact with the lateral mesoderm can orient polster cell migration, related to Figure 5. Polster cells from a *Tg(gsc:GFP)* donor (bright green), labelled with Histone2B-mCherry (red nuclei), were transplanted ahead of the lateral mesoderm of a *Tg(tbx16:GFP)* embryo (dim green). Z-stacks were acquired every 3-minute, maximum projections are shown here. Trajectories of representative cells are highlighted. Before contact with the lateral mesoderm, polster cells tend to spread (cyan tracks), while after contact they align with the lateral mesoderm (yellow tracks). Animal pole is to the top. Scale bar is 50 µm.

Movie S6: α-Catenin and Vinculin mediated mechanosensation is required for polster cell orientation, related to Figure 6. Polster cells injected with morpholino (Mo) or morpholino and mRNA (Resc.) and labelled with Lifeact-mCherry were transplanted in the polster of wild-type embryos and acquired in 3D over time. Maximum projections are shown. Time-interval between frames is, from left to right, top to bottom: 90 s, 60 s, 120 s, 60 s, 60 s, 120 s and 90 s. Animal pole (AP) is to the top. Scale bar is 20 µm.

Movie S7: Simulations of polster migration, related to Figure 7. Mechanical orientation (guidance by followers) can account for directed migration of the polster: movies of the three scenarios presented on Figure 7A. Simulations reproduce experimental observations: polster cells are given a Run and Tumble behaviour and mechanical sensitivity to neighbours migrating towards them (guidance by followers). When isolated cells, polster cells tend to disperse, an equivalent experimental condition (polster cells transplanted to the animal pole of a host embryo) is presented for comparison. Simulating laser ablations at the front does not affect polster migration, as observed (Figure 2 and Movie S3). Simulating laser ablation at the interface between polster and following mesoderm halts progression of the polster till wound healing, as observed (Figure 2 and Movie S3). Each cell responding to all its neighbours cannot account for experimental observations: a model in which each cell responds to any neighbour (migrating towards or away from it) can account for the directed migration of the polster (left movie) but cannot account for the behaviour of an isolated polster (center movie) or for the behaviour after laser ablation at the interface between the polster and the following mesoderm (right movie). Mechanical orientation (guidance by followers) provides robustness and coordination: movies of the three scenarios presented on Figure 7B. Coordination of the progression of the polster and of the following mesoderm can be achieved by giving both tissues a directed migration (left movie). However, such a system is very sensitive to differences in cell speed

(center movie). On the opposite, when polster cells are mechanically oriented, polster speed adjusts to the speed of the following mesoderm, ensuring axis continuity. This stems from polster cells being less oriented when followed by slow axial cells (see Figure S5B).

References

Babb, S.G., and Marrs, J.A. (2004). E-cadherin regulates cell movements and tissue formation in early zebrafish embryos. Dev. Dyn. *230*, 263–277, 10.1002/dvdy.20057.

Barone, V., Lang, M., Krens, S.F.G., Sikora, M., Guet, C., and Heisenberg, C. (2017). An Effective Feedback Loop between Cell-Cell Contact Duration and Morphogen Signaling Determines Cell Fate. Dev. Cell 198–211, 10.1016/j.devcel.2017.09.014.

Bazellières, E., Conte, V., Elosegui-Artola, A., Serra-Picamal, X., Bintanel-Morcillo, M., Roca-Cusachs, P., Muñoz, J.J., Sales-Pardo, M., Guimerà, R., and Trepat, X. (2015). Control of cell-cell forces and collective cell dynamics by the intercellular adhesome. Nat. Cell Biol. *17*, 409–420, 10.1038/ncb3135.

Behrndt, M., and Heisenberg, C.-P. (2012). Spurred by Resistance: Mechanosensation in Collective Migration. Dev. Cell *22*, 3–4, 10.1016/j.devcel.2011.12.018.

Blanco, M.J., Barrallo-Gimeno, A., Acloque, H., Reyes, A.E., Tada, M., Allende, M.L., Mayor, R., and Nieto, M.A. (2007). Snail1a and Snail1b cooperate in the anterior migration of the axial mesendoderm in the zebrafish embryo. Development *134*, 4073–4081, 10.1242/dev.006858.

Borrell, V., and Marín, O. (2006). Meninges control tangential migration of hem-derived Cajal-Retzius cells via CXCL12/CXCR4 signaling. Nat. Neurosci. *9*, 1284–1293, 10.1038/nn1764.

Bosze, B., Ono, Y., Mattes, B., Sinner, C., Gourain, V., Thumberger, T., Tlili, S., Wittbrodt, J., Saunders, T.E., Strähle, U., et al. (2020). Pcdh18a regulates endocytosis of E-cadherin during axial mesoderm development in zebrafish. Histochem. Cell Biol. 10.1007/s00418-020-01887-5.

Boutillon, A., Giger, F.A., and David, N.B. (2018). Analysis of In Vivo Cell Migration in Mosaic Zebrafish Embryos. Methods Mol. Biol. *1749*, 213–226, 10.1007/978-1-4939-7701-7_16.

Čapek, D., Smutny, M., Tichy, A.-M., Morri, M., Janovjak, H., and Heisenberg, C.-P. (2019). Light-activated Frizzled7 reveals a permissive role of non-canonical wnt signaling in mesendoderm cell migration. Elife *8*, 1–56, 10.7554/elife.42093.

Carmona-Fontaine, C., Matthews, H.K., Kuriyama, S., Moreno, M., Dunn, G.A., Parsons, M., Stern, C.D., and Mayor, R. (2008). Contact inhibition of locomotion in vivo controls neural crest directional migration. Nature *456*, 957–961, 10.1038/nature07441.

Carmona-Fontaine, C., Theveneau, E., Tzekou, A., Tada, M., Woods, M., Page, K.M., Parsons, M., Lambris, J.D., and Mayor, R. (2011). Complement fragment C3a controls mutual cell attraction during collective cell migration. Dev. Cell *21*, 1026–1037, 10.1016/j.devcel.2011.10.012.

Das, D., Jülich, D., Schwendinger-Schreck, J., Guillon, E., Lawton, A.K., Dray, N., Emonet, T., O'Hern, C.S., Shattuck, M.D., and Holley, S.A. (2019). Organization of Embryonic Morphogenesis via Mechanical Information. Dev. Cell *49*, 829-839.e5, 10.1016/j.devcel.2019.05.014.

Das, T., Safferling, K., Rausch, S., Grabe, N., Boehm, H., and Spatz, J.P. (2015). A molecular mechanotransduction pathway regulates collective migration of epithelial cells. Nat. Cell Biol. *17*, 276–287, 10.1038/ncb3115.

Dickmeis, T., Mourrain, P., Saint-Etienne, L., Fischer, N., Aanstad, P., Clark, M., Str??hle, U., Rosa, F.F.M.F., Strähle, U., and Rosa, F.F.M.F. (2001). A crucial component of the endoderm formation pathway, CASANOVA, is encoded by a novel sox-related gene. Genes Dev. *15*, 1487–1492, 10.1101/gad.196901.

Doitsidou, M., Reichman-Fried, M., Stebler, J., Köprunner, M., Dörries, J., Meyer, D., Esguerra, C. V, Leung, T., and Raz, E. (2002). Guidance of primordial germ cell migration by the chemokine SDF-1. Cell *111*, 647–659, doi.org/10.1016/S0092-8674(02)01135-2.

Dumortier, J.G., Martin, S., Meyer, D., Rosa, F.M., and David, N.B. (2012). Collective mesendoderm migration relies on an intrinsic directionality signal transmitted through cell contacts. Proc. Natl. Acad. Sci. U. S. A. *109*, 16945–16950, 10.1073/pnas.1205870109.

Giger, F.A., and David, N.B. (2017). Endodermal germ-layer formation through active actin-driven migration triggered by N-cadherin. Proc. Natl. Acad. Sci. *114*, 10143–10148, 10.1073/pnas.1708116114.

Glickman, N.S.S., Kimmel, C.B., Jones, M.A., and Adams, R.J. (2003). Shaping the zebrafish notochord. Development *130*, 873–887, 10.1242/dev.00314.

Gorelik, R., and Gautreau, A. (2014). Quantitative and unbiased analysis of directional persistence in cell migration. Nat. Protoc. *9*, 1931–1943, 10.1038/nprot.2014.131.

Graner, F., and Glazier, J.A. (1992). Simulation of biological cell sorting using a two-dimensional extended Potts model. Phys Rev Lett *69*, 2013–2016.

Haeger, A., Wolf, K., Zegers, M.M., and Friedl, P. (2015). Collective cell migration: guidance principles and hierarchies. Trends Cell Biol. *25*, 556–566, 10.1016/j.tcb.2015.06.003.

Han, M.K.L., Hoijman, E., Nöel, E., Garric, L., Bakkers, J., and de Rooij, J. (2016). αE-catenin-dependent mechanotransduction is essential for proper convergent extension in zebrafish. Biol. Open *5*, 1461–1472, 10.1242/bio.021378.

Hauptmann, G., and Gerster, T. (1994). Two-color whole-mount in situ hybridization to vertebrate and Drosophila embryos. Trends Genet. *10*, 266.

Heisenberg, C.-P., Tada, M., Rauch, G.-J.J., Saúde, L., Concha, M.L., Geisler, R., Stemple, D.L., Smith, J.C., Wilson, S.W., Saude, L., et al. (2000). Silberblick/Wnt11 mediates convergent extension movements during zebrafish gastrulation. Nature *405*, 76–81, 10.1038/35011068.

Hirata, H., Dobrokhotov, O., and Sokabe, M. (2020). Coordination between Cell Motility and Cell Cycle Progression in Keratinocyte Sheets via Cell-Cell Adhesion and Rac1. IScience *23*, 101729, 10.1016/j.isci.2020.101729.

Hoffman, B.D., and Yap, A.S. (2015). Towards a Dynamic Understanding of Cadherin-Based Mechanobiology. Trends Cell Biol. *25*, 803–814, 10.1016/j.tcb.2015.09.008.

Huveneers, S., Oldenburg, J., Spanjaard, E., van der Krogt, G., Grigoriev, I., Akhmanova, A., Rehmann, H., and de Rooij, J. (2012). Vinculin associates with endothelial VE-cadherin junctions to control force-dependent remodeling. J. Cell Biol. *196*, 641–652, 10.1083/jcb.201108120.

Jurado, J., de Navascués, J., and Gorfinkiel, N. (2016). α-Catenin stabilises Cadherin-Catenin complexes and modulates actomyosin dynamics to allow pulsatile apical contraction. J. Cell Sci. *129*, 4496–4508, 10.1242/jcs.193268.

Kai, M., Heisenberg, C.-P., and Tada, M. (2008). Sphingosine-1-phosphate receptors regulate individual cell behaviours underlying the directed migration of prechordal plate progenitor cells during zebrafish gastrulation. Development *135*, 3043–3051, 10.1242/dev.020396.

Kim, T.-J., Zheng, S., Sun, J., Muhamed, I., Wu, J., Lei, L., Kong, X., Leckband, D.E., and Wang, Y.

(2015). Dynamic visualization of α-catenin reveals rapid, reversible conformation switching between tension states. Curr. Biol. *25*, 218–224, 10.1016/j.cub.2014.11.017.

Kimmel, C.B., Ballard, W.W., Kimmel, S.R., Ullmann, B., and Schilling, T.F. (1995). Stages of embryonic development of the zebrafish. Dev. Dyn. *203*, 253–310, 10.1002/aja.1002030302.

Klinger, E., Rickert, D., and Hasenauer, J. (2018). pyABC: distributed, likelihood-free inference. Bioinformatics *34*, 3591–3593, 10.1093/bioinformatics/bty361.

Kobielak, A., Pasolli, H.A., and Fuchs, E. (2004). Mammalian formin-1 participates in adherens junctions and polymerization of linear actin cables. Nat. Cell Biol. *6*, 21–30, 10.1038/ncb1075.

Krens, S.F.G., Veldhuis, J.H., Barone, V., Čapek, D., Maître, J.-L., Brodland, G.W., and Heisenberg, C.-P. (2017). Interstitial fluid osmolarity modulates the action of differential tissue surface tension in progenitor cell segregation during gastrulation. Development *144*, 1798–1806, 10.1242/dev.144964.

Ladoux, B., Nelson, W.J., Yan, J., and Mège, R.M. (2015). The mechanotransduction machinery at work at adherens junctions. Integr. Biol. (Camb). *7*, 1109–1119, 10.1039/c5ib00070j.

Lauffenburger, D.A., and Horwitz, A.F. (1996). Cell migration: a physically integrated molecular process. Cell *84*, 359–369, 10.1016/s0092-8674(00)81280-5.

Lecuit, T., and Yap, A.S. (2015). E-cadherin junctions as active mechanical integrators in tissue dynamics. Nat. Cell Biol. *17*, 533–539, 10.1038/ncb3136.

Maître, J.-L., Berthoumieux, H., Krens, S.F.G., Salbreux, G., Jülicher, F., Paluch, E.K., and Heisenberg, C.-P. (2012). Adhesion Functions in Cell Sorting by Mechanically Coupling the Cortices of Adhering Cells. Science (80-.). *10*, 429–436, 10.1126/science.1225399.

Martin, E.D., Moriarty, M.A., Byrnes, L., and Grealy, M. (2009). Plakoglobin has both structural and signalling roles in zebrafish development. Dev. Biol. *327*, 83–96, 10.1016/j.ydbio.2008.11.036.

Mirams, G.R., Arthurs, C.J., Bernabeu, M.O., Bordas, R., Cooper, J., Corrias, A., Davit, Y., Dunn, S.-J., Fletcher, A.G., Harvey, D.G., et al. (2013). Chaste: an open source C++ library for computational physiology and biology. PLoS Comput. Biol. *9*, e1002970, 10.1371/journal.pcbi.1002970.

Mishra, A.K., Mondo, J.A., Campanale, J.P., and Montell, D.J. (2019). Coordination of protrusion dynamics within and between collectively migrating border cells by myosin II. Mol. Biol. Cell *30*, 2490–2502, 10.1091/mbc.E19-02-0124.

Montero, J.-A., Kilian, B., Chan, J., Bayliss, P.E., and Heisenberg, C.-P. (2003). Phosphoinositide 3-kinase is required for process outgrowth and cell polarization of gastrulating mesendodermal cells. Curr. Biol. *13*, 1279–1289, 10.1016/S0960-9822(03)00505-0.

Montero, J.-A., Carvalho, L., Wilsch-Bräuninger, M., Kilian, B., Mustafa, C., Heisenberg, C.-P., and Wilsch-Brauninger, M. (2005). Shield formation at the onset of zebrafish gastrulation. Development *132*, 1187–1198, 10.1242/dev.01667.

Myers, D.C., Sepich, D.S., and Solnica-Krezel, L. (2002). Convergence and extension in vertebrate gastrulae: cell movements according to or in search of identity? Trends Genet *18*, 447–455.

Nguyen, T., and Mège, R.M. (2016). N-Cadherin and Fibroblast Growth Factor Receptors crosstalk in the control of developmental and cancer cell migrations. Eur. J. Cell Biol. *95*, 415–426, 10.1016/j.ejcb.2016.05.002.

Nieset, J.E., Redfield, A.R., Jin, F., Knudsen, K.A., Johnson, K.R., and Wheelock, M.J. (1997). Characterization of the interactions of alpha-catenin with alpha-actinin and beta-catenin/plakoglobin. J. Cell Sci. *110 (Pt 8*, 1013–1022.

Norden, C., and Lecaudey, V. (2019). Collective cell migration: general themes and new paradigms. Curr. Opin. Genet. Dev. *57*, 54–60, 10.1016/j.gde.2019.06.013.

Patel, N.G., Nguyen, A., Xu, N., Ananthasekar, S., Alvarez, D.F., Stevens, T., and Tambe, D.T. (2020). Unleashing shear: Role of intercellular traction and cellular moments in collective cell migration. Biochem. Biophys. Res. Commun. *522*, 279–285, 10.1016/j.bbrc.2019.11.048.

Pézeron, G., Mourrain, P., Courty, S., Ghislain, J., Becker, T.S., Rosa, F.M., and David, N.B. (2008). Live analysis of endodermal layer formation identifies random walk as a novel gastrulation movement. Curr. Biol. *18*, 276–281, 10.1016/j.cub.2008.01.028.

Pitt-Francis, J., Pathmanathan, P., Bernabeu, M.O., Bordas, R., Cooper, J., Fletcher, A.G., Mirams, G.R., Murray, P., Osborne, J.M., Walter, A., et al. (2009). Chaste: A test-driven approach to software development for biological modelling. Comput. Phys. Commun. *180*, 2452–2471, 10.1016/j.cpc.2009.07.019.

Pokutta, S., Drees, F., Takai, Y., Nelson, W.J., and Weis, W.I. (2002). Biochemical and structural definition of the l-afadin- and actin-binding sites of alpha-catenin. J. Biol. Chem. *277*, 18868–18874, 10.1074/jbc.M201463200.

Poujade, M., Grasland-Mongrain, E., Hertzog, A., Jouanneau, J., Chavrier, P., Ladoux, B., Buguin, A., and Silberzan, P. (2007). Collective migration of an epithelial monolayer in response to a model wound.

Roszko, I., Sawada, A., and Solnica-Krezel, L. (2009). Regulation of convergence and extension movements during vertebrate gastrulation by the Wnt/PCP pathway. Semin. Cell Dev. Biol. *20*, 986–997, 10.1016/j.semcdb.2009.09.004.

Scarpa, E., and Mayor, R. (2016). Collective cell migration in development. J. Cell Biol. *212*, 143–155, 10.1083/jcb.201508047.

Scarpa, E., Szabó, A., Bibonne, A., Theveneau, E., Parsons, M., and Mayor, R. (2015). Cadherin Switch during EMT in Neural Crest Cells Leads to Contact Inhibition of Locomotion via Repolarization of Forces. Dev. Cell *34*, 421–434, 10.1016/j.devcel.2015.06.012.

Schälte, Y., and Hasenauer, J. (2020). Efficient exact inference for dynamical systems with noisy measurements using sequential approximate Bayesian computation. Bioinformatics *36*, i551–i559, 10.1093/bioinformatics/btaa397.

Schulte-Merker, S., van Eeden, F.J., Halpern, M.E., Kimmel, C.B., and Nüsslein-Volhard, C. (1994). no tail (ntl) is the zebrafish homologue of the mouse T (Brachyury) gene. Development *120*, 1009–1015.

Schumacher, L. (2019). Collective Cell Migration in Development. Adv. Exp. Med. Biol. *1146*, 105–116, 10.1007/978-3-030-17593-1_7.

Seddiki, R., Narayana, G.H.N.S., Strale, P.-O., Balcioglu, H.E., Peyret, G., Yao, M., Le, A.P., Teck Lim, C., Yan, J., Ladoux, B., et al. (2018). Force-dependent binding of vinculin to α-catenin regulates cell–cell contact stability and collective cell behavior. Mol. Biol. Cell *29*, 380–388, 10.1091/mbc.E17-04-0231.

Shellard, A., and Mayor, R. (2020). All Roads Lead to Directional Cell Migration. Trends Cell Biol. *30*, 852–868, 10.1016/j.tcb.2020.08.002.

Shimizu, T., Yabe, T., Muraoka, O., Yonemura, S., Aramaki, S., Hatta, K., Bae, Y.K., Nojima, H., and Hibi, M. (2005). E-cadherin is required for gastrulation cell movements in zebrafish. Mech. Dev. *122*, 747–763.

Smutny, M., Ákos, Z., Grigolon, S., Shamipour, S., Ruprecht, V., Čapek, D., Behrndt, M., Papusheva, E., Tada, M., Hof, B., et al. (2017). Friction forces position the neural anlage. Nat. Cell Biol. *19*, 306–317, 10.1038/ncb3492.

Solnica-Krezel, L., Stemple, D.L., and Driever, W. (1995). Transparent things: cell fates and cell movements during early embryogenesis of zebrafish. BioEssays *17*, 931–939, 10.1002/bies.950171106.

Sonavane, P.R., Wang, C., Dzamba, B., Weber, G.F., Periasamy, A., and DeSimone, D.W. (2017). Mechanical and signaling roles for keratin intermediate filaments in the assembly and morphogenesis of mesendoderm tissue at gastrulation. Development dev.155200, 10.1242/dev.155200.

Stachel, S.E., Grunwald, D.J., and Myers, P.Z. (1993). Lithium perturbation and goosecoid expression identify a dorsal specification pathway in the pregastrula zebrafish. Development *117*, 1261–1274.

Starruß, J., de Back, W., Brusch, L., and Deutsch, A. (2014). Morpheus: a user-friendly modeling environment for multiscale and multicellular systems biology. Bioinformatics *30*, 1331–1332, 10.1093/bioinformatics/btt772.

Swat, M.H., Thomas, G.L., Belmonte, J.M., Shirinifard, A., Hmeljak, D., and Glazier, J.A. (2012). Multi-scale modeling of tissues using CompuCell3D. Methods Cell Biol. *110*, 325–366, 10.1016/B978-0-12-388403-9.00013-8.

Tada, M., and Smith, J.C. (2000). Xwnt11 is a target of Xenopus Brachyury: regulation of gastrulation movements via Dishevelled, but not through the canonical Wnt pathway. Development *127*, 2227–2238.

Tahinci, E., and Symes, K. (2003). Distinct functions of Rho and Rac are required for convergent extension during Xenopus gastrulation. Dev. Biol. *259*, 318–335, 10.1016/S0012-1606(03)00206-9.

Thisse, C., Thisse, B., Halpern, M.E., and Postlethwait, J.H. (1994). goosecoid Expression in neurectoderm and mesendoderm is disrupted in zebrafish cyclops gastrulas. Dev. Biol. *164*, 420–429, 10.1006/dbio.1994.1212.

Topczewski, J., Sepich, D.S., Myers, D.C., Walker, C., Amores, A., Lele, Z., Hammerschmidt, M., Postlethwait, J., and Solnica-Krezel, L. (2001). The zebrafish glypican knypek controls cell polarity during gastrulation movements of convergent extension. Dev. Cell *1*, 251–264, 10.1016/s1534-5807(01)00005-3.

Twiss, F., Le Duc, Q., Van Der Horst, S., Tabdili, H., Van Der Krogt, G., Wang, N., Rehmann, H., Huveneers, S., Leckband, D.E., and De Rooij, J. (2012). Vinculin-dependent Cadherin mechanosensing regulates efficient epithelial barrier formation. Biol. Open *1*, 1128–1140, 10.1242/bio.20122428.

Ulrich, F., Krieg, M., Schotz, E.M., Link, V., Castanon, I., Schnabel, V., Taubenberger, A., Mueller, D., Puech, P.-H.P.-H., Heisenberg, C.-P., et al. (2005). Wnt11 functions in gastrulation by controlling cell cohesion through Rab5c and E-cadherin. Dev. Cell *9*, 555–564, 10.1016/j.devcel.2005.08.011.

Vassilev, V., Platek, A., Hiver, S., Enomoto, H., and Takeichi, M. (2017). Catenins Steer Cell Migration via Stabilization of Front-Rear Polarity. Dev. Cell *43*, 463-479.e5, 10.1016/j.devcel.2017.10.014.

Vishwakarma, M., Di Russo, J., Probst, D., Schwarz, U.S., Das, T., and Spatz, J.P. (2018). Mechanical interactions among followers determine the emergence of leaders in migrating epithelial cell collectives. Nat. Commun. *9*, 3469, 10.1038/s41467-018-05927-6.

Vishwakarma, M., Spatz, J.P., and Das, T. (2020). Mechanobiology of leader-follower dynamics in epithelial cell migration. Curr. Opin. Cell Biol. *66*, 97–103, 10.1016/j.ceb.2020.05.007.

Weber, G.F., Bjerke, M.A., and DeSimone, D.W. (2012). A mechanoresponsive cadherin-keratin complex directs polarized protrusive behavior and collective cell migration. Dev. Cell *22*, 104–115, 10.1016/j.devcel.2011.10.013.

Wells, S., Nornes, S., and Lardelli, M. (2011). Transgenic zebrafish recapitulating tbx16 gene early developmental expression. PLoS One *6*, e21559, 10.1371/journal.pone.0021559.

Xiong, F., Ma, W., Bénazéraf, B., Mahadevan, L., and Pourquié, O. (2020). Mechanical Coupling Coordinates the Co-elongation of Axial and Paraxial Tissues in Avian Embryos. Dev. Cell *55*, 354-366.e5, 10.1016/j.devcel.2020.08.007.

Yamada, K.M., and Sixt, M. (2019). Mechanisms of 3D cell migration. Nat. Rev. Mol. Cell Biol. *20*, 738–752, 10.1038/s41580-019-0172-9.

Yamashita, S., Miyagi, C., Carmany-Rampey, A., Shimizu, T., Fujii, R., Schier, A.F., and Hirano, T. (2002). Stat3 Controls Cell Movements during Zebrafish Gastrulation. Dev. Cell *2*, 363–375.

Yamashita, S., Miyagi, C., Fukada, T., Kagara, N., Che, Y.-S., and Hirano, T. (2004). Zinc transporter LIVI controls epithelial-mesenchymal transition in zebrafish gastrula organizer. Nature *429*, 298–302, 10.1038/nature02545.

Yonemura, S., Wada, Y., Watanabe, T., Nagafuchi, A., and Shibata, M. (2010). alpha-Catenin as a tension transducer that induces adherens junction development. Nat. Cell Biol. *12*, 533–542, 10.1038/ncb2055.

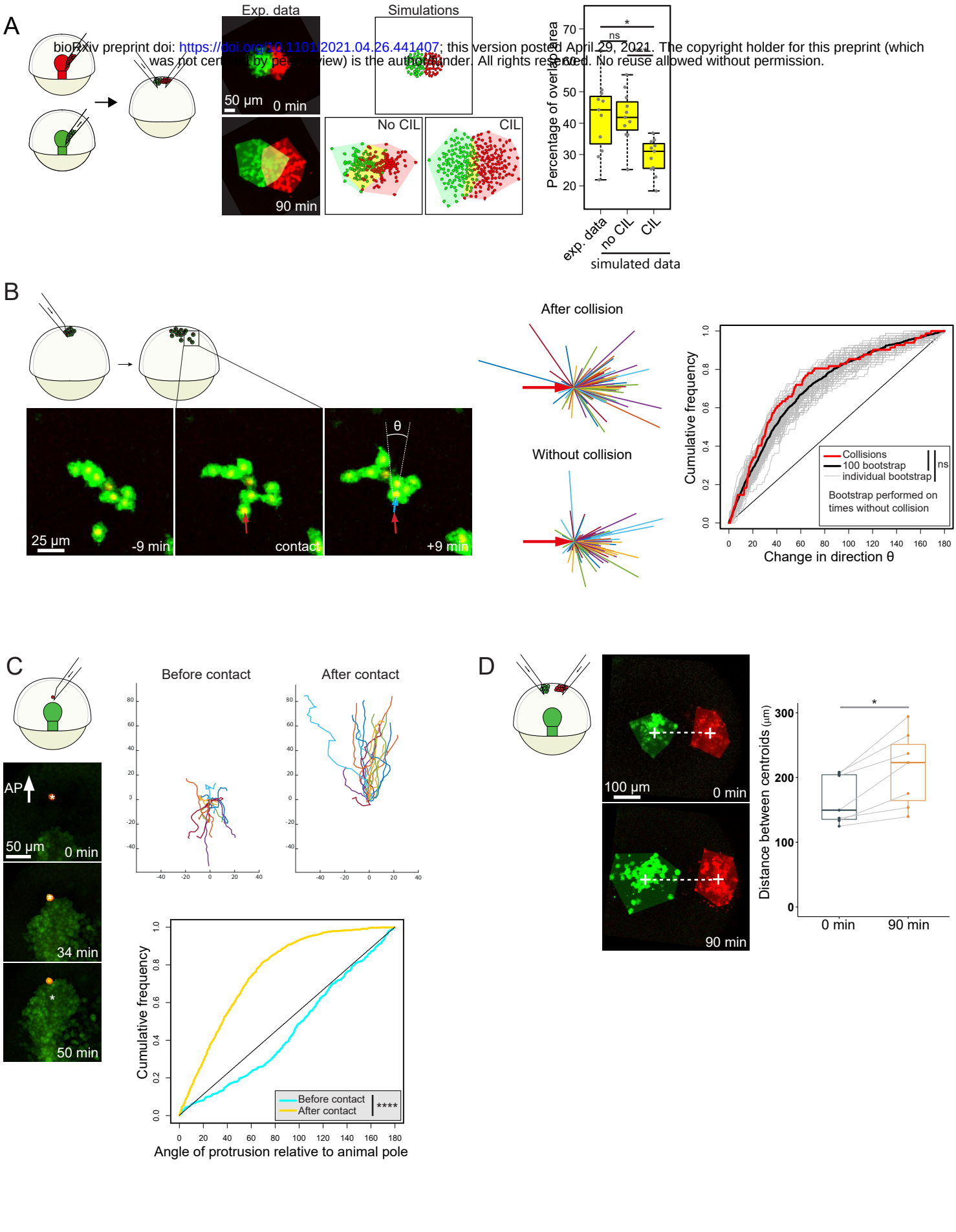

Figure 1

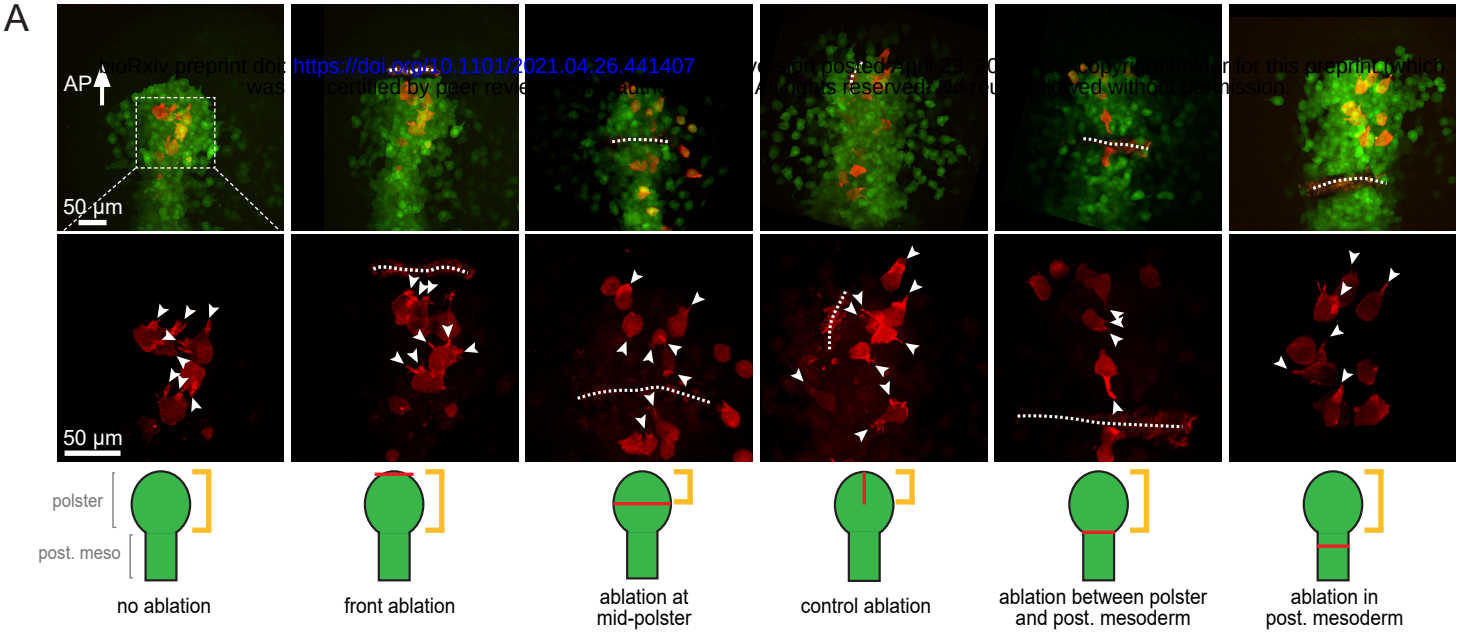

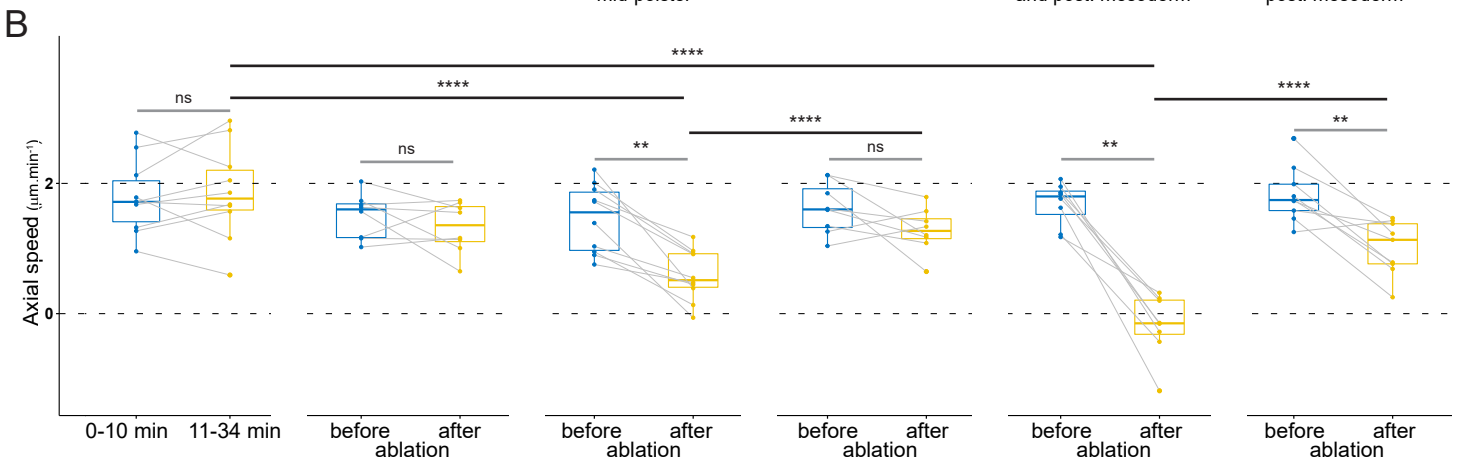

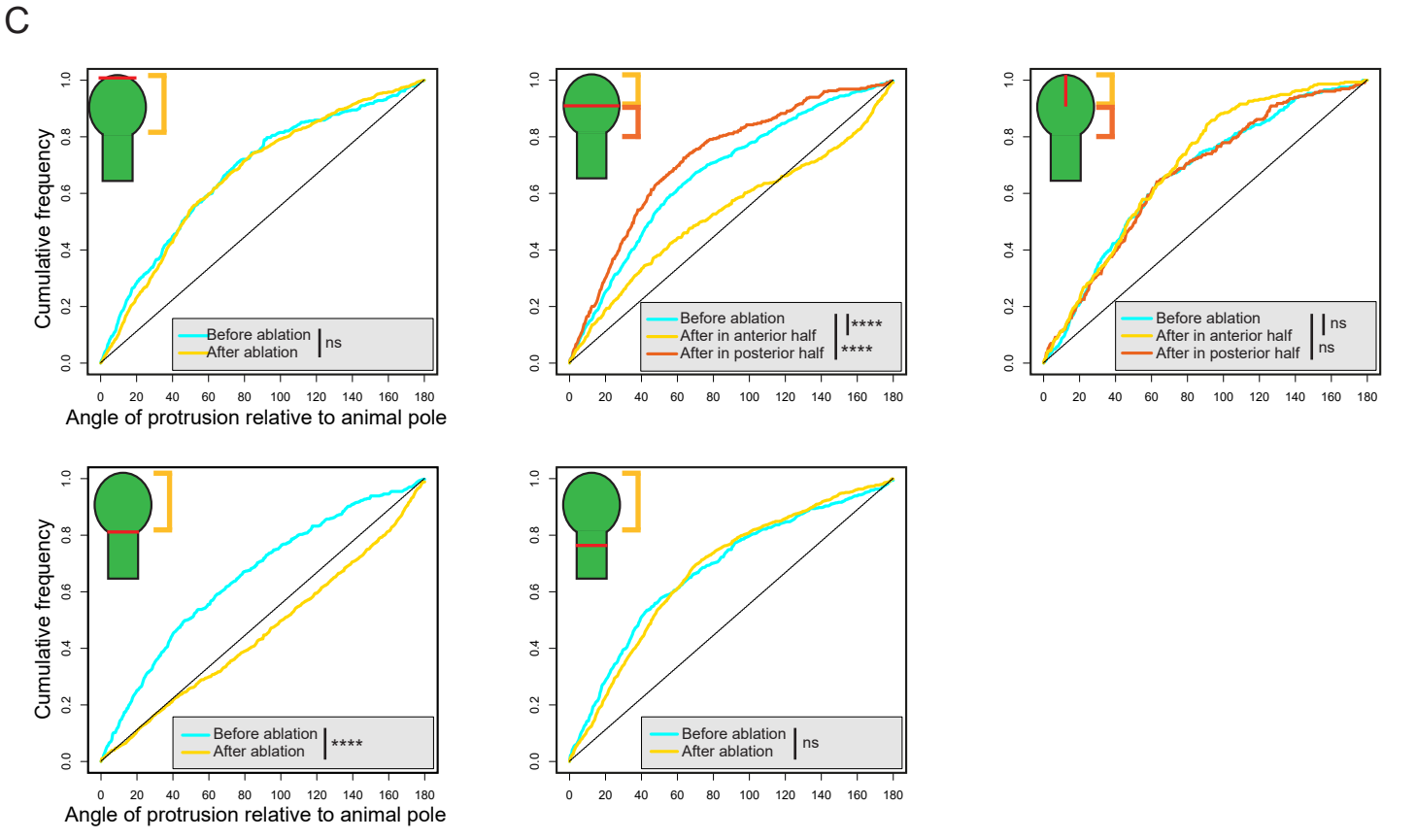

Figure 2

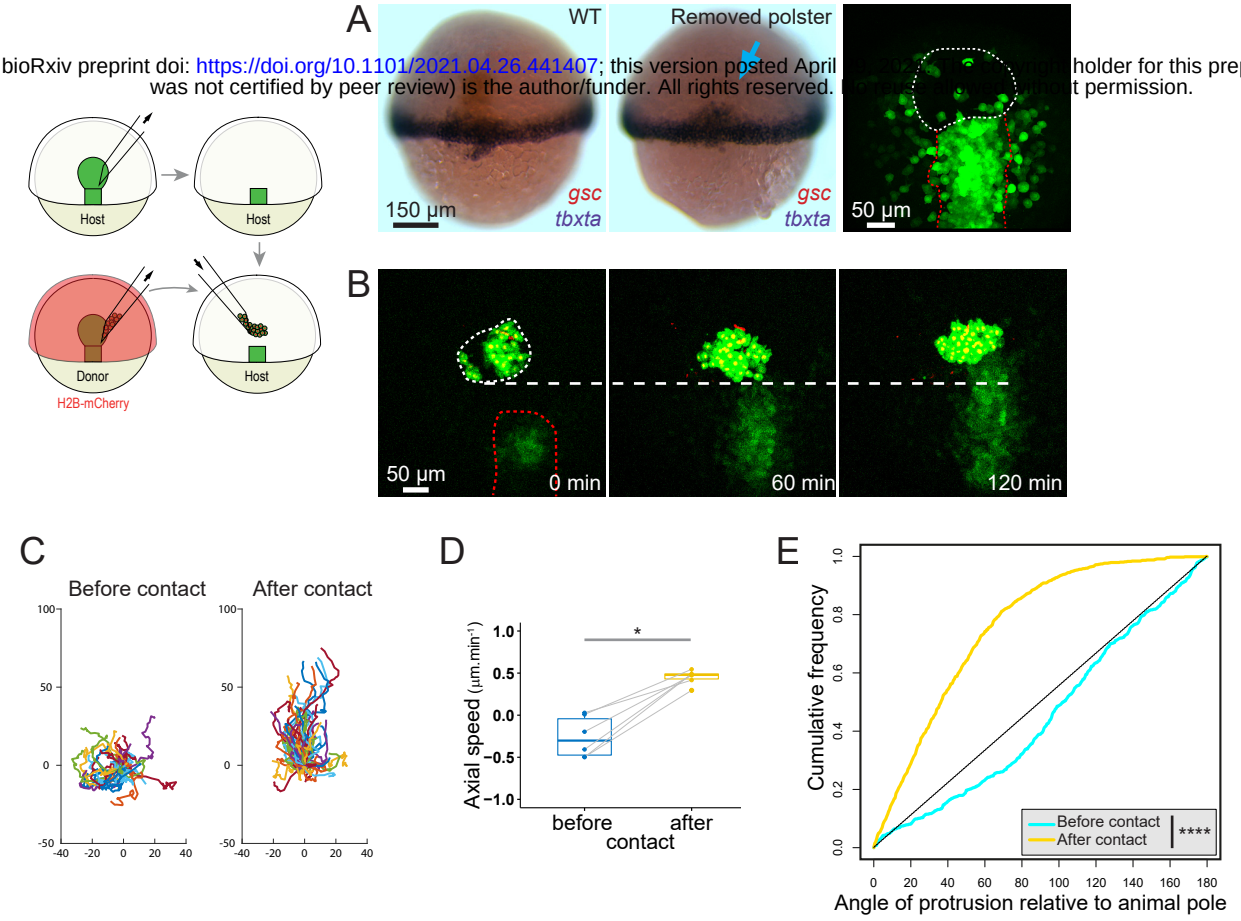

Figure 3

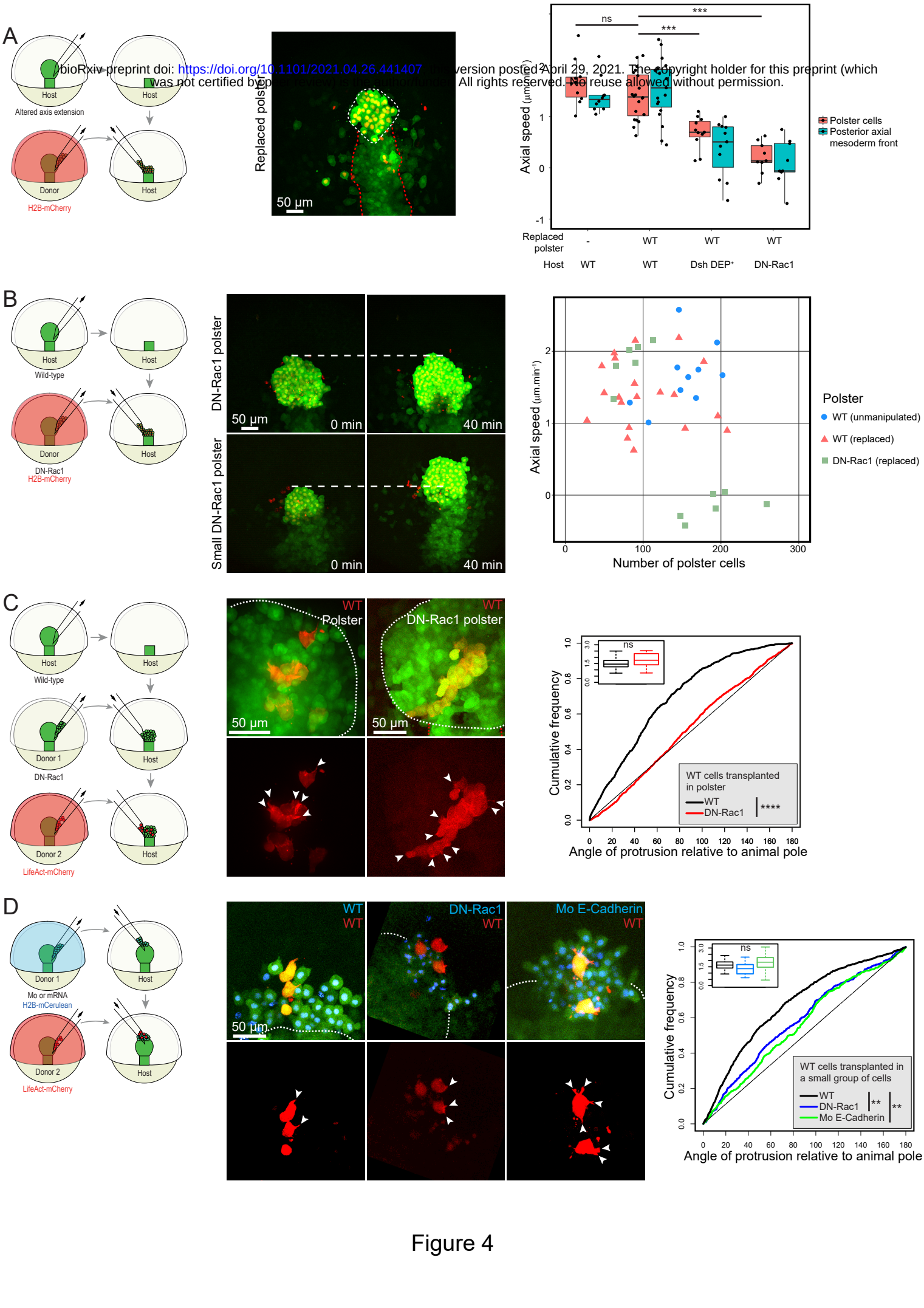

Figure 4

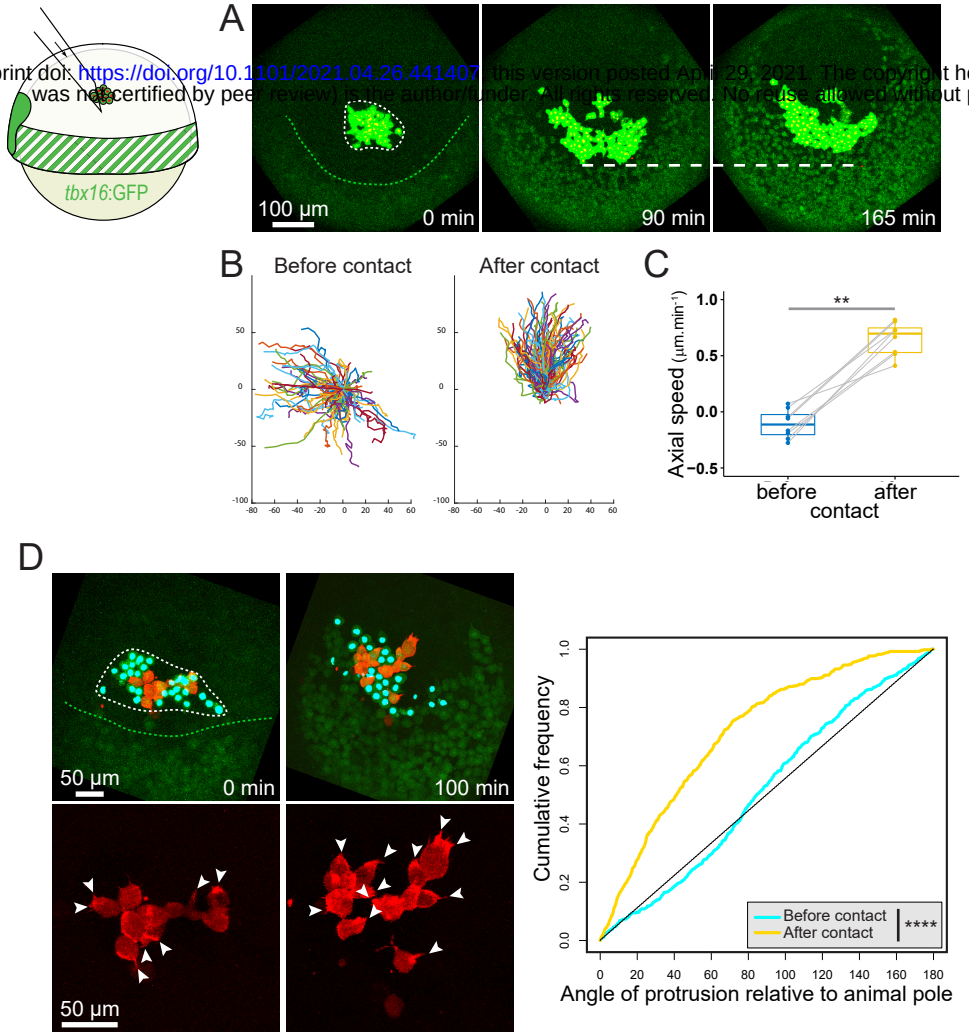

Figure 5

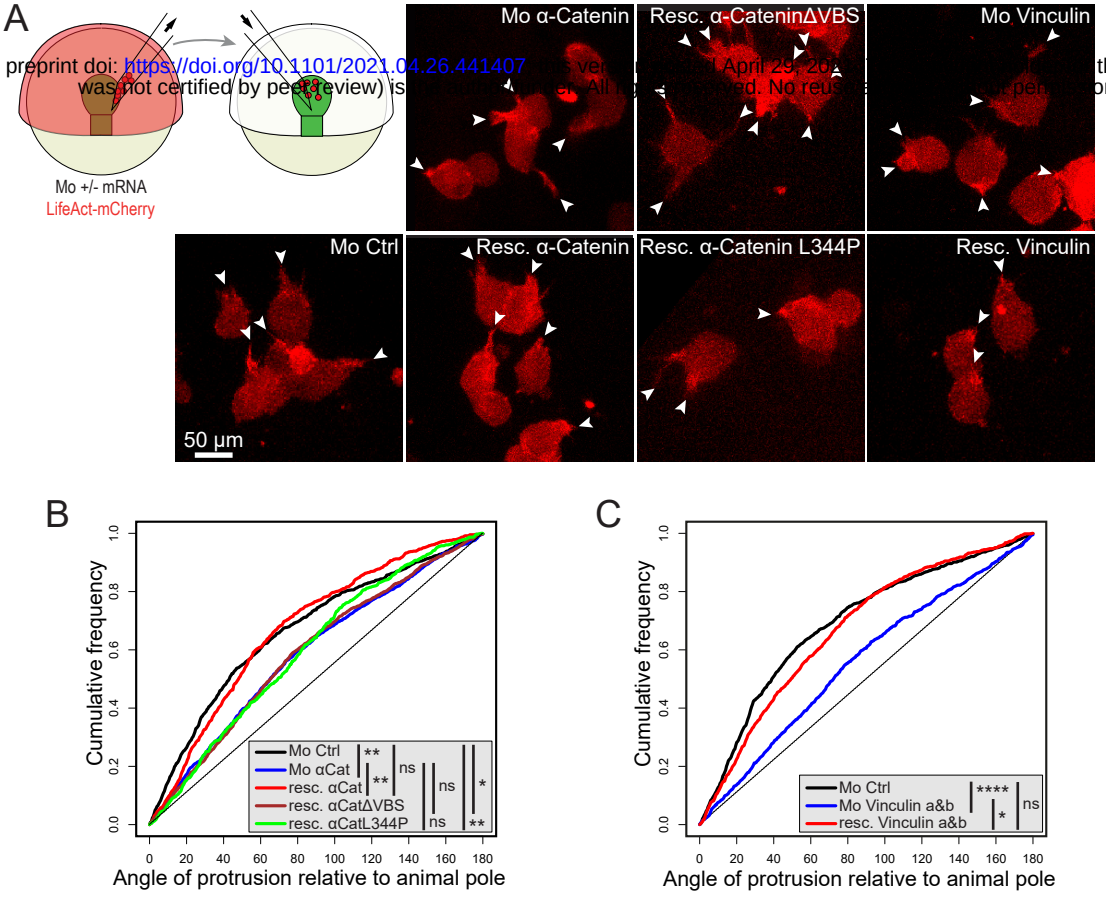

Figure 6

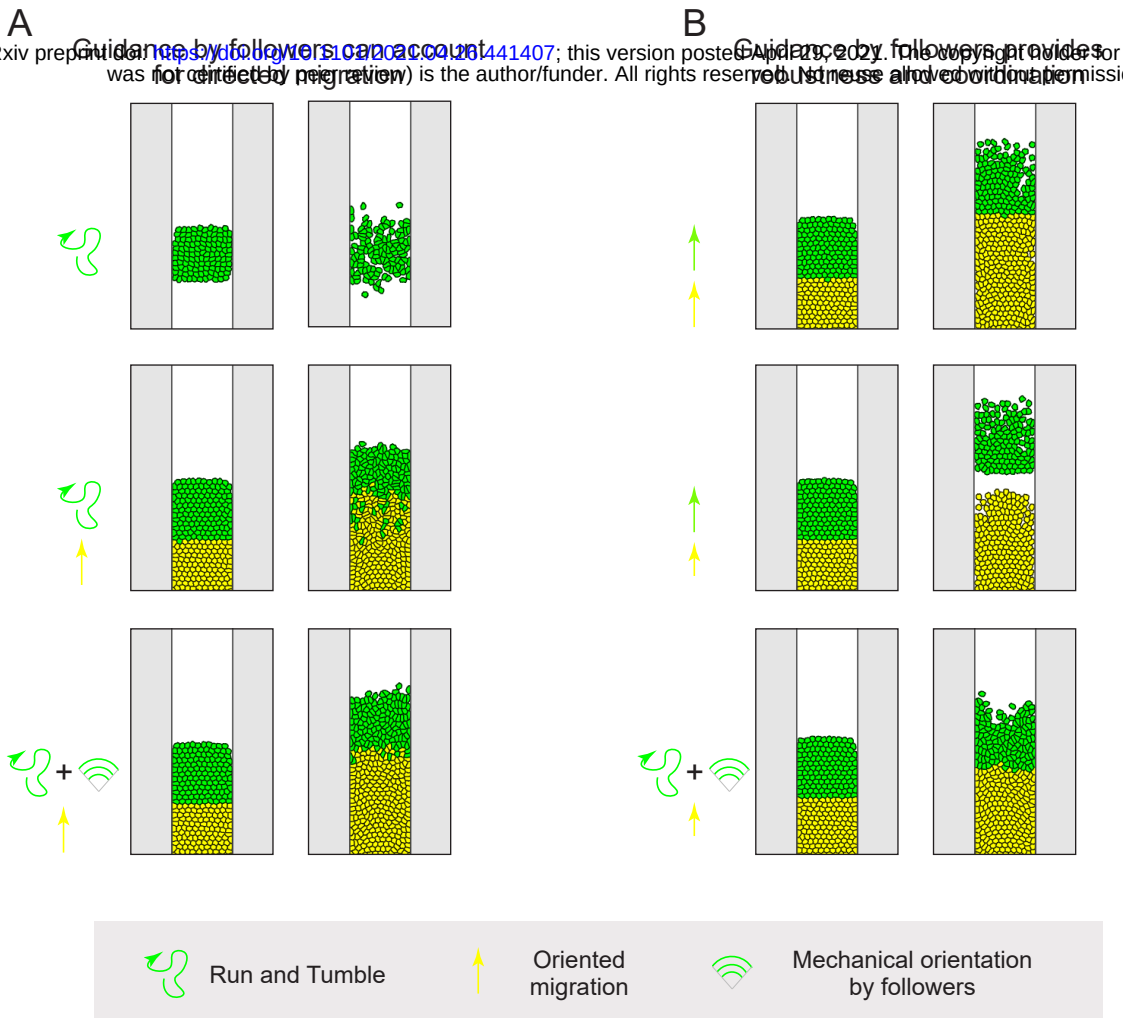

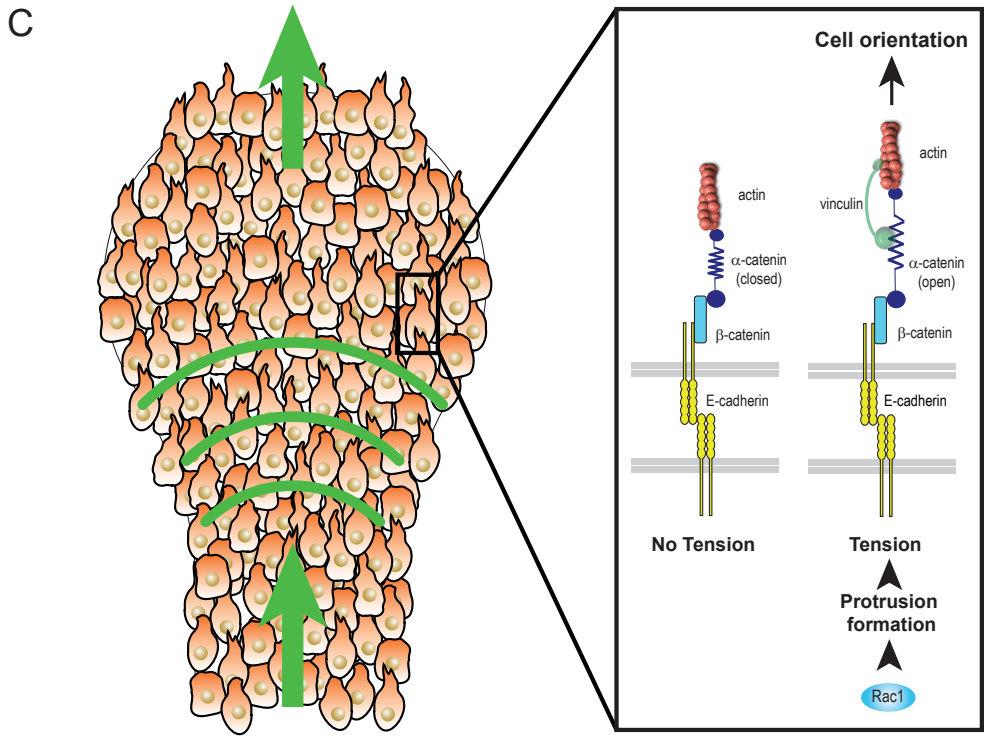

Figure 7

Letter Vol. 6, No. 3 / March 2019 / Optica 385

optica

High-speed polarization-resolved third-harmonic microscopy

Joséphine Morizet,[1] Guillaume Ducourthial,[1] Willy Supatto,[1] Arthur Boutillon,[1] Renaud Legouis,[2] Marie-Claire Schanne-Klein,[1] Chiara Stringari,[1,3] and Emmanuel Beaurepaire[1,4]

[1]Laboratoire d'Optique et Biosciences, Ecole polytechnique, CNRS, INSERM, 91128 Palaiseau, France
[2]Institute for Integrative Biology of the Cell (I2BC), CEA, CNRS, Univ. Paris-Sud, Université Paris-Saclay, 91198, Gif-sur-Yvette, France
[3]e-mail: chiara.stringari@polytechnique.edu
[4]e-mail: emmanuel.beaurepaire@polytechnique.edu

Received 29 August 2018; revised 29 January 2019; accepted 28 February 2019 (Doc. ID 344581); published 19 March 2019

Polarization-resolved third-harmonic generation (P-THG) is a sensitive probe of material anisotropy and molecular ordering. Despite its promises, this property has little been used in biological tissues due to the lack of measurement schemes compatible with dynamic samples. We report here on the development of a fast P-THG microscope where excitation polarization is switched between line scans using an electro-optic modulator, providing temporal resolution in the 10 ms range for the polarimetric measurement. We demonstrate novel applications enabled by this approach, associated with Fourier-based analysis: probing molecular order in deforming lipid structures undergoing phase transition; revealing crystallinity of flowing particles in the zebrafish embryo's inner ear; and detecting birefringence *in vivo*. These results establish that P-THG is ideally suited for probing lipid organization and mineralization in dynamic biological environments.

https://doi.org/10.1364/OPTICA.6.000385

Since its first demonstrations, third-harmonic generation (THG) microscopy [1] has emerged as an effective imaging modality for the label-free characterization of interfaces in cells and tissues, with applications ranging from cell and developmental biology to neuroscience [2–4]. The contrast mechanism of THG microscopy is somewhat peculiar. When the excitation field is focused by a high numerical aperture (NA) microscope objective, THG efficiency is dominated by the Gouy phase shift, which prevents phase matching between the fundamental and harmonic fields over the focal region in the case of isotropic normally dispersive media. The consequences for THG microscopy images are that no signal is generally obtained from homogeneous regions and optical heterogeneities at the micrometer or sub-micrometer scale are highlighted over a dark background. Lipid-water interfaces or cell-derived vesicles [3–5], for example, are readily visualized. This contrast permits label-free structural imaging of intact tissue with three-dimensional sectioning. THG imaging is also directly compatible with widely used multiphoton microscopy modalities such as fluorescence and second-harmonic generation, to which it can provide an informative morphological context [2,4–6].

A less used property of THG microscopy is its dependence on the driving field polarization when probing anisotropic media [Figs. 1(a)–1(b)]. One first remarkable characteristic is that no TH polarization is induced in an isotropic medium excited with a circular polarization, owing to $\chi^{(3)}$ tensor symmetries [7–9]; see Fig. 1(a). Therefore, the comparison of THG images obtained with linear (L-THG) and circular (C-THG) polarization provides a means to detect anisotropic media [8,10]. Furthermore, in birefringent media, THG signals can be obtained even from homogeneous regions if birefringence is strong enough to compensate the phase mismatch caused by the Gouy shift [8]. Moreover, THG from an anisotropic medium excited by a linearly polarized beam strongly depends on the angle between the driving polarization and the medium optical axes [Fig. 1(b)]. For example, at the surface of a multilamellar lipidic structure parallel to the propagation axis [Fig. 1(c)], the THG intensity variation as the incident polarization is rotated by 180° can be described as a single-peaked response in the form $I(\Phi) = A + B\cos(\Phi - \Phi_0)^2$, where B depends on molecular ordering, and Φ_0 depends on mean molecular orientation [11]. Inside a strongly birefringent medium such as a liquid crystal [Fig. 1(d)], this variation takes the double-peaked form $I(\Phi) = A + B\cos(\Phi - \Phi_0)^4 \sin(\Phi - \Phi_0)^2$, where Φ_0 depends on crystalline axes and on the type of phase matching involved [12].

The dependence of THG on incident polarization is therefore a probe of birefringence and molecular ordering. Despite its promises, this property has little been used for biological imaging beyond proofs of principle [8,10,11,13–15] up until now. The main reason is that probing the THG polarization dependence requires the recording of signals with several excitation polarization states while the sample is moving or deforming. We report here on the development of a fast polarization-resolved THG (P-THG) microscope where excitation polarization is switched within microseconds between every line scan using an electro-optic modulator [16,17], combined with a Fourier-based analysis method of the polarization data for identifying the different types of THG signals. We demonstrate three measurements enabled by

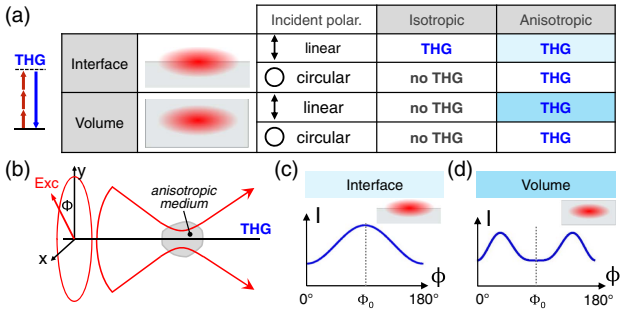

Fig. 1. Contrast mechanisms in P-THG microscopy. (a) Possibility of THG in isotropic and anisotropic materials depending on sample geometry and incident polarization. The red spot represents the beam focus. (b)–(d) Typical P-THG intensity profiles from (c) the interface or (d) the volume of an anisotropic material.

fast P-THG microscopy: (i) probing molecular order in deforming multilamellar lipid structures undergoing phase transition; (ii) revealing biomineralization of flowing particles in the highly dynamic environment of the zebrafish embryo's inner ear; and (iii) one-shot detection of birefringence from ordered lipids and biocrystals in live organisms.

We implemented our fast P-THG method [Fig. 2(a)] on a custom-built point-scanning multiphoton microscope integrating a femtosecond laser source (80 MHz, 1100 nm, 100 fs, Insight DS+, SpectraPhysics), galvanometric scanners (GSI Lumonics, USA), and a water immersion objective (25× , 1.05 NA, Olympus, Japan). Harmonic light detection was performed in transmission using a high-NA condenser (Olympus), filters (Semrock FF01-550/49 for SHG and FF01-377/50 for THG), photon-counting detectors (SensTech, UK), and lab-designed MHz-rate-counting electronics. Scanning, polarization control, and acquisition were synchronized using LabVIEW-written software and an I/O board (National Instruments, USA). Signal level was typically 20–80 photons/pixel with 5–10 µs/pixel and 40–150 mW excitation. Following previous works on fast polarization-resolved nonlinear imaging [16–18], we designed an alternative strategy consisting of scanning each line several times with different polarization states. This approach provides an interesting compromise between simplicity (hence robustness) and speed (temporal resolution in the millisecond range), and was not previously explored for THG imaging. The critical feature to implement was a polarization switching scheme operating in the sub-ms range [Fig. 2(b)] while maintaining good polarization purity at focus (Fig. S1). We achieved polarization state switching in less than 12 µs using an electro-optic modulator (EOM) driven by a high-voltage amplifier (350–150 and 302 RM, Conoptics, Connecticut, USA) and set between a half-wave plate (HWP1) and a quarter-wave plate (QWP1) [16] [Fig. 2(a)]. This configuration enables two polarization switching modalities, corresponding to rotating along either the equator or a meridian of the Poincaré sphere [Figs. 2(c) and 2(f)]. The first modality results in a linear polarization rotating in the plane transverse to the propagation axis [Figs. 2(c)–2(e)], and the second modality provides alternating linear and circular polarizations [Figs. 2(f)–2(h)]. Selecting one modality can be done by a 45° rotation of the QWP. We introduced an additional QWP (QWP2) at the entrance pupil of the objective in order to compensate for the polarization distortions caused by the microscope optics and the scanning system [Fig. 2(a)]. By iteratively adjusting the two QWPs' orientations for a series of voltage set points, we obtained an ellipticity $\sqrt{I_{\min}/I_{\max}}$ less than 0.08 for all incident linear polarizations [Figs. S1(a)–S1(b)] and >0.99 for circular polarizations [Fig. S1(c)]. We recorded all images over a 150 × 150 µm^2 region where artifactual angular shifts were less than 2° [Fig. S1(d)]. A second HWP (HWP2) was also inserted for convenient control of the polarization reference. X-P-Y acquisition was implemented by synchronizing galvanometer scanning and EOM voltage control, as shown in Fig. 2(b) and Visualization 1. A P-series of N images corresponding to N polarization states can then be reconstructed from the data [Fig. 2(b)]. The temporal resolution of the polarimetric analysis is here the time needed to record N lines, i.e., a few milliseconds: in the typical case of a line consisting of 400 pixels including scan flyback and with 5 µs pixel dwell time, it takes 8 ms to probe four polarization states or 36 ms to probe 18 polarization states. Figures 2(d)–2(h) illustrate the two acquisition modes described above. Here, THG and second-harmonic generation (SHG) polarization-resolved images of a starch granule are recorded simultaneously on two channels. Figures 2(c)–2(e) illustrate P-images where a linear polarization is rotated by 45° steps, and Figs. 2(f)–2(h) illustrate switching between circular and linear polarizations.

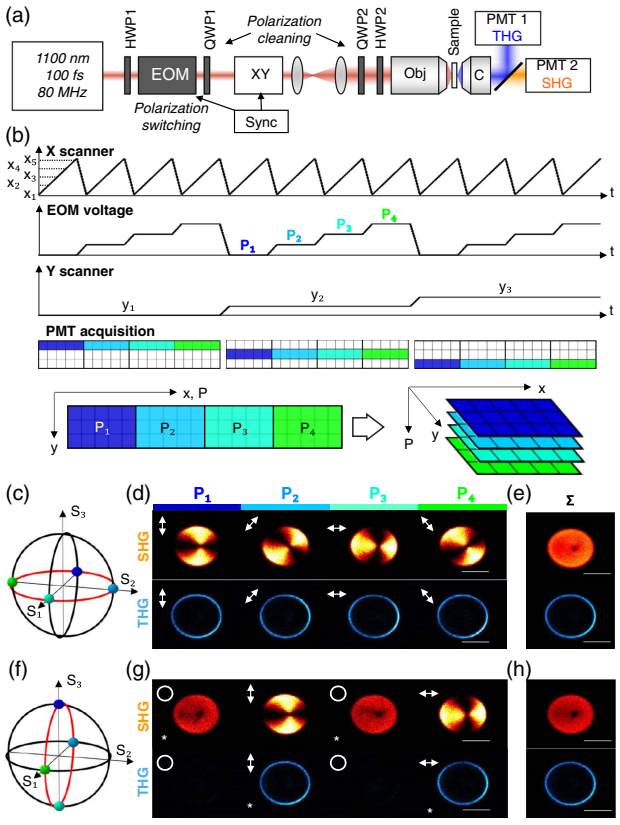

Fig. 2. EOM-based P-THG. (a) Experimental setup. (b) Sequence of scanning and EOM signals for XPY acquisition. (c)–(h) Simultaneous P-SHG and P-THG imaging of a starch granule while switching between linear polarization states (c)–(e) and horizontal/circular states (f)–(h). (e)–(h) Average of individual polarization images. (c)–(f) Polarization states shown on Poincaré sphere. Scale bar 10 µm.

We now discuss the possibilities offered by fast P-THG for probing dynamic processes. We recently reported that P-THG is sensitive to molecular order in lipid structures [11]. This capability comes from the fact that the third-order nonlinear susceptibility response of lipid molecules far from vibrational resonance is

dominated by the contribution of the aligned C-C bonds in the lipid tails. Multilamellar lipid vesicles (MLVs, or "lipid onions") are a good model of ordered molecular systems that can be probed using polarization-resolved nonlinear microscopy [11,18,19]. We recorded fast-P-THG images of 1,2-Dimyristoyl-sn-glycero-3-phosphorylcholine (DMPC, Avanti Polar Lipids, Alabama, USA) MLVs synthesized using the method described in [20] and Supplement 1 [Fig. 3(a) and Visualization 2]. Interestingly, since MLVs are birefringent, they produce THG through the two types of mechanisms discussed above: (i) heterogeneity-related THG is detected at the external lipid-solvent interface, and (ii) weaker THG signals resulting from birefringence-induced phase matching are recorded from the inner regions of the MLV. Signals recorded from the vesicle periphery and from inner regions therefore exhibit different polarization-resolved profiles [Fig. 3(a)]: the interface signal is maximized when the incident polarization is parallel to the C-C chains, i.e., perpendicular to the interface; in contrast, the birefringence-induced inner signals exhibit two maxima as the incident polarization is rotated by 180° [11,12]. To analyze such data, we developed a fit-free methodology relying on the calculation of the Fourier components of P-THG signals (FT-PTHG). As shown in Figs. 3(a)–3(b) and Fig. S2, interface signals are dominated by the first two Fourier components ($c_0 - c_1$), whereas birefringence-related signals are characterized by the additional presence of $c_2 - c_3$ components. FT-PTHG therefore provides a means to identify and analyze the two types of THG signals. We automatically calculated binary masks [Fig. 3(c)] selecting either interface- or birefringence-related THG by thresholding r-squared-based maps of the difference between raw data and reconstructions based on relevant Fourier orders (i.e., $c_0 + c_1$ for interface signals and $c_0 + c_2 + c_3$ for birefringence-related signals). We then extracted average lipid orientation at the pixel scale in both regions based on the phase of the first-order terms [Figs. 3(c) and S2].

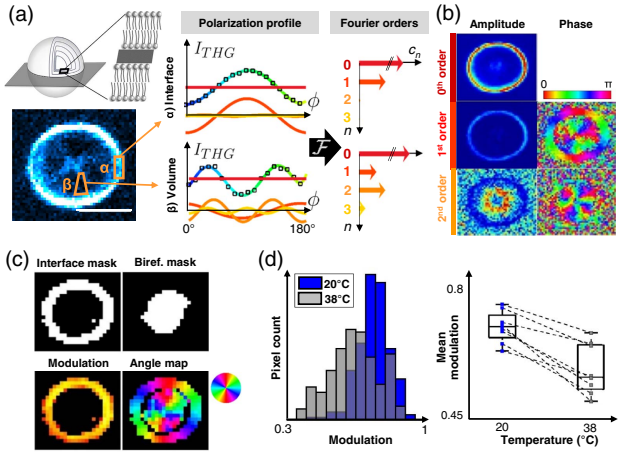

Fig. 3. Probing molecular order with Fourier analysis of P-THG data. (a) THG image of multilamellar lipid vesicle (MLV) from an 18-image P-THG sequence recorded with rotating linear polarizations. See Visualization 2. Scale bar 5 μm. Also shown are examples of polarization profiles and Fourier coefficients for interface and birefringence-related THG signals. (b) FT maps of the first three Fourier coefficients. (c) Masks, P-THG modulation, and molecular angle maps extracted from the data. (d) Decrease of the interface P-THG modulation amplitude measured in MLVs undergoing phase transition under heating. Left, pixel modulation histogram for a single vesicle. Right, pooled data from eight vesicles.

More importantly, we remind the reader that the modulation amplitude of interface P-THG signals $(I_{max} - I_{min})/I_{max} = 4c_1/(c_0 + 2c_1)$ is in MLVs a probe of molecular ordering [11]. We therefore used fast FT-PTHG to follow molecular disordering upon vesicle heating, and successfully monitored P-THG lipid order decrease in MLVs undergoing partial phase transition when heated from 20°C to 38°C [Fig. 3(d)]. Despite the fact that vesicles imaged at 38° exhibited deformations during imaging time at the sub-second scale, our acquisition scheme produced accurate modulation maps, revealing lipid disordering with sub-μm spatial resolution.

We then explored the possibility to detect biomineralization in a dynamic 3D environment using fast P-THG by analyzing the early stages of otolith formation in wild-type zebrafish embryos (see Supplement 1). The otolith is a mineralized structure involved in gravity sensing that grows under constrained biochemical conditions inside a cavity of the inner ear [Fig. 4(a)]. It is principally made of aragonite, a crystalline form of calcium carbonate. The initial stage of otolith growth is characterized by the transient presence in the cavity of precursor microparticles (or "spherules" [21]) of unknown nature, which move at speeds in the 1–50 μm/s range in a cilia-driven flow [21]. We found that both the forming otolith and these microparticles produce readily detectable THG signals in live embryos [Fig. 4(b), Visualization 3]. We then used fast P-THG to determine whether the microparticles are made of anisotropic material. We recorded P-THG images of flowing microparticles and, as a control, of 1 μm fluorescent polystyrene beads microinjected in the inner ear cavity. We analyzed the image series by extracting histograms of THG modulation amplitude for both types of objects [Figs. 4(c)–4(d), Fig. S3]. These data reveal without ambiguity that the endogenous microparticles are of crystalline nature (36 ± 16% P-THG modulation), unlike the isotropic polystyrene beads (18 ± 8% P-THG modulation). This experiment demonstrates the potential of P-THG for monitoring biomineralization *in vivo*. The findings reported here are particularly illustrative, as the microparticles exhibit rapid 3D motion, can form only in their native biological environment, and cannot be easily labeled.

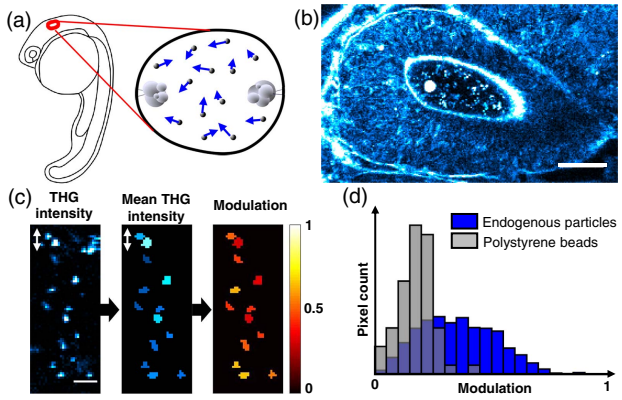

Fig. 4. *In vivo* detection of anisotropy of flowing microparticles in the zebrafish inner ear. (a) Schematic of the otic cavity in a 22 h post fertilization (hpf) zebrafish. (b) THG image of the cavity containing otolith precursor microparticles flowing at 1–50 μm/s. Scale bar 20 μm. See Visualization 3. (c) Extraction of the microparticles mean P-THG modulation. (d) Histogram of THG modulation for endogenous otolith microparticles (blue) and injected polystyrene beads (gray). The data identify that the microparticles are made of anisotropic material.

To demonstrate a final type of application of our method, we revisited an overlooked aspect of THG microscopy, which is that it provides a means to detect anisotropic materials by comparing images recorded with L-THG and C-THG incident polarization [8,10]. Our fast P-THG scheme provides a means to use this property in biologically relevant contexts by recording simultaneously the two images, in turn enabling ratiometric comparisons at the pixel scale. We implemented this idea by recording L-THG/C-THG image pairs in oil droplets, zebrafish otoliths *in vivo*, and MLVs [Figs. 5(a)–5(c)]. We used these data to derive an anisotropy parameter defined as C-THG/(L-THG+C-THG) [Figs. 5(d)–5(f)]. Oil droplets have isotropic molecular structure and produce no C-THG. We found that the growing larval otoliths exhibit strong P-THG modulation, like their precursor microparticles. Moreover, THG signals are obtained throughout the otolith with circular incident polarization, which is a signature of birefringence. Finally and as mentioned previously, MLVs exhibit both types of THG signals. As demonstrated in Figs. 5(g)–5(i), anisotropy parameter maps allow immediate identification of birefringence-related THG signals, with a threshold value around 17%. This provides a novel contrast strategy for label-free nonlinear microscopy. We applied this method to the detection of birefringent structures in live adult *C. elegans*. Intestinal cells of worms are densely packed with lipidic vesicles involved in metabolism. A fraction of these vesicles have been described as being birefringent, lysosome-related organelles [22]. THG observation of adult *C. elegans* worms provides detailed morphological images [23] where micrometer-sized vesicles in the intestine and epithelium are readily detected. We found that fast P-THG combined with anisotropy mapping identifies a fraction of these vesicles that do exhibit birefringence [Fig. 5(j)]. This contrast mechanism can therefore be exploited to identify structurally distinct intestinal stores *in vivo*.

In conclusion, we have described a methodology for fast polarization-resolved THG microcopy with millisecond temporal resolution on the polarimetric measurement. Our system can be used to perform a one-shot P-THG experiment where the incident polarization explores multiple states located along either the equator or a meridian of the Poincaré sphere, in turn probing either the molecular orientations or the $\chi^{(3)}$ tensor symmetries responsible for the P-THG response. We have shown that Fourier-based or ratiometric analyses of the polarization-resolved images obtained in this manner provide measurements uniquely suited for dynamically probing lipid molecular organization and/or biomineralization in biological environments such as unlabeled *C. elegans* worms and developing zebrafish embryos. These results establish a novel contrast modality for label-free nonlinear biomicroscopy.

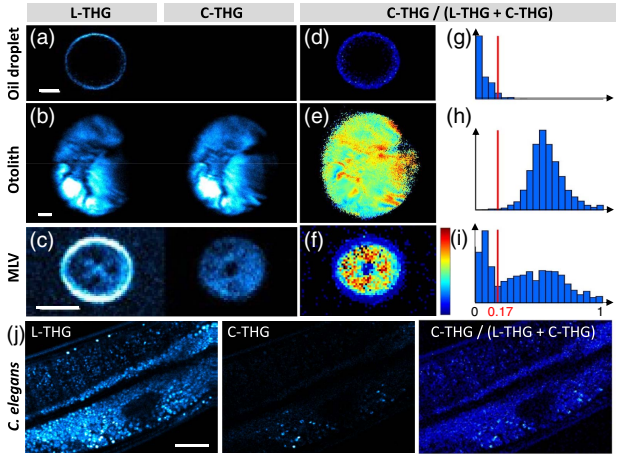

Fig. 5. Detection of birefringence with circular-linear polarization switching. (a)–(i) One-shot measurement of the anisotropy parameter C-THG/(L-THG+ C-THG) in an oil droplet (isotropic), a three-days zebrafish otolith (birefringent) and a MLV (both types of THG signals). Scale bars 5 μm. (j) Application: *in vivo* detection of birefringent granules in an adult *C. elegans* worm. Scale bar 20 μm.

Funding. Agence Nationale de la Recherche (ANR) (ANR-11-EQPX-0029, ANR-10-INBS-04, ANR-15-CE11-0012).

Acknowledgment. We thank Xavier Solinas for advice on electronics synchronization, Chrystel Faure for advice on MLV synthesis, Emilie Menant for zebrafish husbandry, Julien Vermot and Philippe Herbomel for discussion on zebrafish otolith formation, and Nicolas Olivier, Pierre Mahou, and Max Zimmerley for discussions on P-THG microscopy.

See Supplement 1 for supporting content.

REFERENCES

1. Y. Barad, H. Eisenberg, M. Horowitz, and Y. Silberberg, Appl. Phys. Lett. **70**, 922 (1997).
2. N. Olivier, M. A. Luengo-Oroz, L. Duloquin, E. Faure, T. Savy, I. Veilleux, X. Solinas, D. Débarre, P. Bourgine, A. Santos, N. Peyriéras, and E. Beaurepaire, Science **329**, 967 (2010).
3. M. J. Farrar, F. W. Wise, J. R. Fetcho, and C. B. Schaffer, Biophys. J. **100**, 1362 (2011).
4. B. Weigelin, G. J. Bakker, and P. Friedl, J. Cell Sci. **129**, 245 (2016).
5. D. Débarre, W. Supatto, A.-M. Pena, A. Fabre, T. Tordjmann, L. Combettes, M.-C. Schanne-Klein, and E. Beaurepaire, Nat. Methods **3**, 47 (2006).
6. N. Olivier, F. Aptel, K. Plamann, M.-C. Schanne-Klein, and E. Beaurepaire, Opt. Express **18**, 5028 (2010).
7. S. You, H. Tu, E. J. Chaney, Y. Sun, Y. Zhao, A. J. Bower, Y. Z. Liu, M. Marjanovic, S. Sinha, Y. Pu, and S. A. Boppart, Nat. Commun. **9**, 2125 (2018).
8. R. W. Boyd, *Nonlinear Optics* (2008).
9. D. Oron, E. Tal, and Y. Silberberg, Opt. Lett. **28**, 2315 (2003).
10. M. Samim, S. Krouglov, and V. Barzda, Phys. Rev. A **93**, 033839 (2016).
11. M. Zimmerley, P. Mahou, D. Débarre, M.-C. Schanne-Klein, and E. Beaurepaire, Phys. Rev. X **3**, 011002 (2013).
12. R. S. Pillai, M. Oh-e, H. Yokoyama, G. J. Brakenhoff, and M. Müller, Opt. Express **14**, 12976 (2006).
13. L. Kontenis, M. Samim, S. Krouglov, and V. Barzda, Opt. Express **25**, 13174 (2017).
14. G. Bautista, S. G. Pfisterer, M. J. Huttunen, S. Ranjan, K. Kanerva, E. Ikonen, and M. Kauranen, Biophys. J. **107**, 2230 (2014).
15. S. W. Chu, S. Y. Chen, G. W. Chern, T. H. Tsai, Y. C. Chen, B. L. Lin, and C. K. Sun, Biophys. J. **86**, 3914 (2004).
16. P. Stoller, K. M. Reiser, P. M. Celliers, and A. M. Rubenchik, Biophys. J. **82**, 3330 (2002).
17. E. L. Dewalt, S. Z. Sullivan, P. D. Schmitt, R. D. Muir, and G. J. Simpson, Anal. Chem. **86**, 8448 (2014).
18. M. Hofer, N. K. Balla, and S. Brasselet, Optica **4**, 795 (2017).
19. J. Cheng, S. Pautot, D. Weitz, and X. Xie, Proc. Natl. Acad. Sci. USA **100**, 9826 (2003).
20. A. D. Bangham, M. M. Standish, and J. C. Watkins, J. Mol. Biol. **13**, 238 (1965).
21. D. Wu, J. B. Freund, S. E. Fraser, and J. Vermot, Dev. Cell **20**, 271 (2011).
22. G. J. Hermann, L. K. Schroeder, C. A. Hieb, A. M. Kershner, B. M. Rabbitts, P. Fonarev, B. D. Grant, and J. R. Priess, Mol. Biol. Cell **16**, 3273 (2005).
23. G. J. Tserevelakis, E. V. Megalou, G. Filippidis, B. Petanidou, C. Fotakis, and N. Tavernarakis, PLoS One **9** e84431 (2014).

Chapter 16

Analysis of In Vivo Cell Migration in Mosaic Zebrafish Embryos

Arthur Boutillon, Florence A. Giger, and Nicolas B. David

Abstract

Being optically clear, the zebrafish embryo is a nice model system to analyze cell migration in vivo. This chapter describes a combination of injection and cell transplant procedures that allows creation of mosaic embryos, containing a few cells labeled differently from their neighbors. Rapid 5D confocal imaging of these embryos permits to simultaneously track and quantify the movement of large cell groups, as well as analyze the cellular or subcellular dynamics of transplanted cells during their migration. In addition, expression of a candidate gene can be modified in transplanted cells. Comparing behavior of these cells to control or neighboring cells allows determination of the role of the candidate gene in cell migration. We describe the procedure, focusing on one specific cell population during gastrulation, but it can easily be adapted to other cell populations and other migration events during early embryogenesis.

Key words Zebrafish, Live imaging, Cell migration, Cell transplantation, Mosaic embryos, Cell tracking

1 Introduction

Cell migration is key to build, shape, repair, and defend an organism. It has been extensively studied in vitro, providing invaluable knowledge on its cellular and molecular bases [1, 2]. It, however, clearly appeared in the past few years that a number of cells behave quite differently in vitro and in vivo [3, 4]. This likely stems from the more complex environment they encounter (3D extracellular matrix of varying stiffness, neighboring cells, guidance cues) leading, for instance, cells that would use only lamellipodia on a flat surface to use a wide array of cell processes (lamellipodia, pseudopodia of varying length and shapes, blebs, …) for their in vivo displacements [5]. Many cells, furthermore, display collective behaviors, their migration depending on interactions with neighboring cells [6, 7]. Understanding in vivo cell migration thus implies direct analysis of cells moving in their physiological environment.

Doing so obviously requires optically clear systems permitting cell observation without further manipulation or dissection. Cells also

Alexis Gautreau (ed.), *Cell Migration: Methods and Protocols*, Methods in Molecular Biology, vol. 1749,
https://doi.org/10.1007/978-1-4939-7701-7_16,

need to be labeled, usually through the expression of fluorescent proteins. This can be achieved using transgenic lines expressing reporter constructs in specific cell types. However, such a strategy often leads to the labeling of a whole cell population, when labeling sparse, isolated cells, is key to good imaging, in particular for analyzing cell contours, or membrane protrusions, which cannot be seen if neighboring cells are similarly labeled [8, 9]. Creating mosaic embryos, containing only one or few cells differing from surrounding cells, is thus crucial for precise analysis of their dynamics. Mosaic embryos, furthermore, permit to test consequences of activation/repression of genes/pathways on the migration of individual cells. Comparing the tracks and behavior of these cells with surrounding control cells under the same experimental conditions allows determination of the role of a particular gene in cell migration [10]. Here we describe a procedure, based on injections and cell transplants, to create mosaic zebrafish embryos during gastrulation and to image migrating cells.

Gastrulation is the developmental stage during which cells first migrate, to organize the embryo in different germ layers and set up the basis of the future body plan [11]. This involves a wide array of migration events, including random walks, directed migrations and collective movements. The fish embryo, being optically clear, offers direct access to these processes [12]. Among the diverse movements taking place during gastrulation, cells of the organizer (termed "shield" in zebrafish) internalize and migrate collectively toward the animal pole of the embryo, forming the prechordal plate [9, 13, 14]. We combine injections of RNAs encoding fluorescently tagged proteins, cell transplants and in vivo imaging, to analyze mechanisms of cell migration. We have successfully used this protocol to describe behavior of wild-type cells, dissect the pathways controlling their motility and orientation, as well as assess the importance of candidate genes in regulating cell migration in vivo [14–16]. The proposed protocol can be used to test the potential implication of any candidate gene in controlling cell migration in vivo. It can furthermore be easily adapted to analyze other cell types, or other developmental stages.

2 Material

2.1 RNA Injection

1. Stereomicroscope (Nikon, model SMZ18).
2. Glass capillaries (Internal Diameter = 0.58 mm, External Diameter = 1 mm).
3. Needle puller (KOPF Vertical pipette puller, model 720, David Kopf Instruments, Tujunga, CA, USA).
4. Injection mold (Fig. 1a, 3D model available as a .stl file on request; commercially available from adaptive science tools, model TU1).

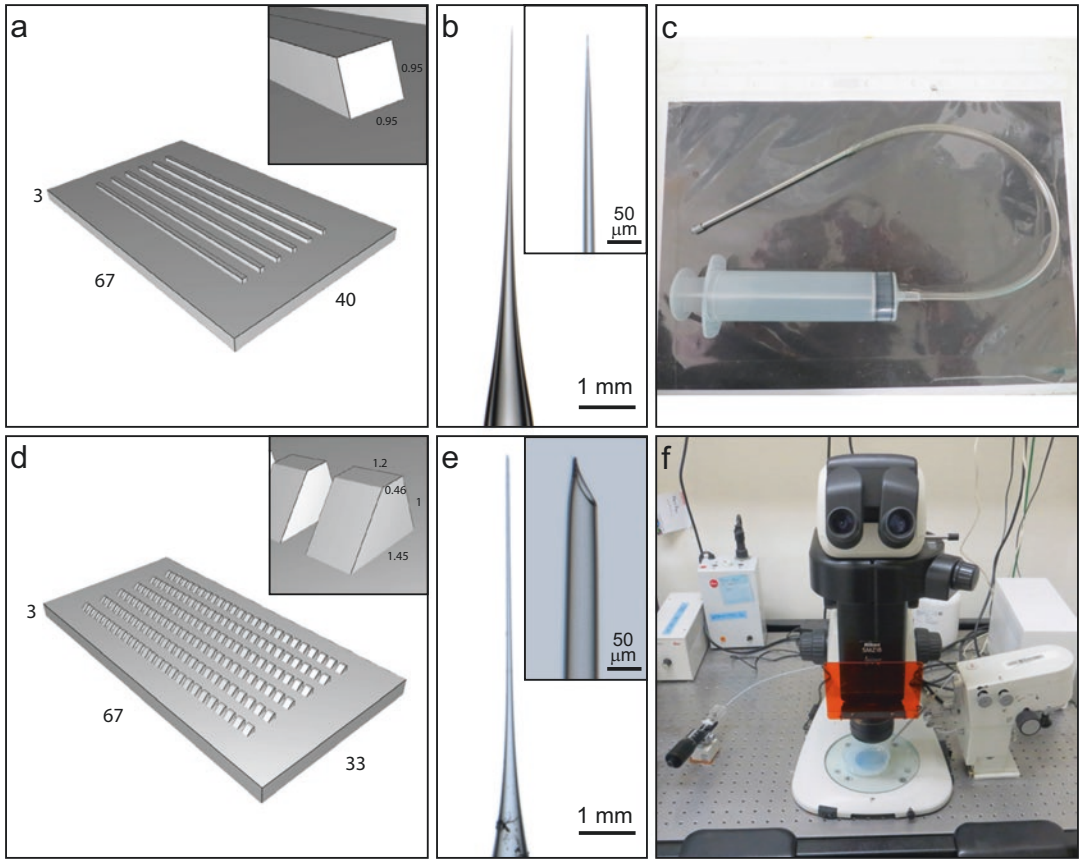

Fig. 1 Injection and transplant equipment. (**a**) 3D model of the injection mold used to prepare injection agarose plates. Dimensions are in mm. Model is available as a .stl file. (**b**) Typical injection needle. (**c**) Needle holder connected to a syringe, used to rinse transplant needles. (**d**) 3D model of the transplant mold used to prepare transplant agarose plates. Dimensions are in mm. Model is available as a .stl file. (**e**) Typical transplant needle. (**f**) General view of the transplant setup. Transplant needle is inserted in a needle holder, mounted on a mechanical micromanipulator. The needle is connected to a microinjector

5. Injector (Eppendorf, Transjector 5246).
6. Manipulator (Narishige, model M-152).
7. 20 µl microloader tips (Eppendorf) to load injection needles.
8. Plastic Pasteur pipettes for transferring embryos.
9. Embryo Medium (EM, Zebrafish book [17]): 15 mM NaCl, 0.5 mM KCl, 25 µM Na_2HPO_4, 45 µM KH_2PO_4, 1.3 mM $CaCl_2$, 1 mM $MgSO_4 \bullet 7H_2O$, 4 mM $NaHCO_3$, adjust to pH 7.2 with NaOH.
10. RNAs: mRNAs are prepared in vitro, using the mMessage mMachine kit (Ambion) to produce fully capped RNAs.
11. Sterile-filtered water (Sigma) for diluting RNAs.
12. Injection needle: needles should be long enough to reach the embryo within its chorion, without creating too large a hole in

the chorion. It however should be short enough to keep some rigidity, which is key to piercing the chorion and the embryo. Figure 1b shows a typical injection needle. To prepare a needle, mount a glass capillary (Internal Diameter 0.58 mm) on the needle puller. Adjust temperature and pulling strength (*see* **Note 1**). Test different settings until obtaining the desired needle shape (check needles under a dissection microscope). Once the puller is correctly set, prepare several dozen injection needles. Carefully store them in a petri dish, secured on a putty band and seal the dish with Parafilm to avoid dust.

13. Injection plate: melt 0.5 g of agarose in 50 ml EM in a microwave to prepare a 1% agarose gel. Pour it in a 90-mm petri dish. When the agarose is at 60 °C, gently place the injection mold so that it floats. Let the agarose solidify. Remove the mold with forceps, add some EM to prevent the gel from drying and store at 4 °C up to a month.

2.2 Shield to Shield Transplant

1. Fluorescent stereomicroscope (Nikon, model SMZ18).
2. Glass capillaries (Internal Diameter = 0.78 mm, External Diameter = 1 mm).
3. Microforge (Narishige, model MF900).
4. Microgrinder (Narishige, model EG-44).
5. Transplant mold (Fig. 1d, 3D model available as a .stl file on request; commercially available from adaptive science tools, model PT1).
6. Eyelash mounted on a stick.
7. Mechanical micromanipulator (Leica).
8. Microinjector (Narishige, model IM-9B).
9. Fine tweezers for dechorionation (Dumont Fine Science Tools).
10. 35 mm petri dishes.
11. Fire-polished glass Pasteur pipettes, to manipulate dechorionated embryos: approach the tip of the pipette close to the flame of a lighter until the glass slightly melts. Be careful not to melt it too much, otherwise the pipette opening may end up too small and embryos will be damaged when drawn into the pipette.
12. Penicillin/Streptomycin (Thermo Fisher Scientific): for transplanted embryos, use at 100 unit/ml Penicillin and 100 µg/ml streptomycin in EM.
13. Transplant needle: mount a glass capillary (Internal Diameter 0.78 mm) on the needle puller and pull the capillary. The stretched part of the needle should be around 1.5 cm (Fig. 1e). Test different settings until obtaining the desired shape and pull several dozen needles (*see* **Note 1**). Mount a needle on the microforge. Position the needle very close to the microforge's filament, at the point where its inside diameter is 25 µm. Briefly heat the

filament: upon dilatation, the filament touches the needle, the glass locally melts then breaks upon retraction of the filament. Using the microgrinder, grind the tip of the needle for one minute at maximum speed to form a 35° bevel (Fig. 1e; *see* **Note 2**). To remove glass residues, mount the needle on a needle holder connected to a syringe (Fig. 1c) and wash the tip by briefly aspiring 2% hydrofluoric acid (toxic and highly corrosive, manipulate under a chemical fume hood) over 5 mm. Repeat three times. Immediately rinse three times by aspiring acetone over 1 cm. Store the needles on a putty band in a Parafilm-sealed petri dish.

14. Transplant plate: melt 0.5 g of agarose in 50 ml EM in a microwave to prepare a 1% agarose gel. Pour it in a 90 mm petri dish. When the agarose is at 60 °C, gently place the injection mold so that it floats. Let the agarose solidify and remove the mold with forceps.
15. Transplant setup: around the fluorescent stereomicroscope, install the microinjector, connected to a needle holder mounted on the micromanipulator (Fig. 1f).

2.3 Mounting and Imaging

1. MatTek chamber (35 mm Dish, No. 1.5 Coverslip, 7 mm Glass Diameter, MatTek Corporation, Ashland, MA).
2. Microscopy: we use a Ti PFS (Nikon) inverted microscope equipped with a CSUX1-A1 (Yokogawa) spinning disc module, a 40× water immersion objective (plan Apo, N.A. = 1.15, Nikon), a Cobolt Calypso laser (491 nm, 100 mW), and a Cobolt Jive laser (561 nm, 100 mW) (Cobolt, 04-01 Series). The microscope is caged and heated using The Cube (Life Imaging Services) to maintain constant temperature and the sample is placed in a The Brick (life imaging Services) chamber to maintain constant hygrometry. Metamorph is used for acquisitions.

2.4 Software for Imaging and Picture Analyzing

1. Metamorph (Molecular Devices, LLC).
2. ImageJ.
3. XuvTool [18].
4. IMARIS (Bitplane).
5. Matlab (Mathworks).
6. R (R Foundation for Statistical Computing).

3 Methods

3.1 Embryo Injection

1. Warm the injection plate by placing it at 28 °C at least 30 min before injection.
2. Once fishes have laid, collect the embryos. Rinse them well to remove all the droppings and scales from the adults and har-

vest in EM in a 90-mm petri dish. Transfer 50 embryos in an empty injection plate and squeeze them gently inside the grooves using forceps, without piercing the chorion. Orient the embryos with the animal pole up. Fill the plate with EM.

3. Wear gloves while manipulating RNA to prevent contamination with RNAse, keep all solutions on ice. Prepare 4 µl of 50 ng/µl Histone2B-mCherry RNA solution by diluting the stock RNA solution in sterile-filtered water. This solution will be injected in embryos used as hosts in the transplant. Prepare 4 µl of 50 ng/µl Histone2B-mCherry RNA and 70 ng/µl LifeAct-GFP RNA. This will be injected in embryos used as cell donors in the transplant. To affect a particular pathway, it is possible to add other compounds to this solution, which will be present only in the transplanted cells. In particular, morpholinos or RNAs encoding dominant-negative or constitutively active forms of proteins can be used.
4. Using microloader tips, fill the injection needle with 2 µl of RNA solution. Insert the needle in a needle holder, mounted on a manipulator and connected to the injector. Under the stereomicroscope, delicately open the needle using forceps, either by scraping the tip or by breaking the very tip by pinching it. To test whether the needle is opened, apply pressure with the injector and check that a drop of RNA solution forms at the tip. Then put the tip of the needle into the EM to prevent it from drying.
5. To prepare host embryos, inject half of the embryos at the 1-cell stage, with the H2B-mCherry solution (Fig. 2a) (*see* **Note 3**). To do so, place an embryo close to the injection needle. Using the manipulator, pierce through the chorion and through the cell membrane so that the needle tip is inside the cell (Fig. 2b). Avoid piercing the yolk and injecting into the yolk. Inject 4 nl (*see* **Note 4**) and remove the needle. The embryo should stay in the agarose groove. Repeat for 25 embryos and put the plate at 28 °C. To prepare donor embryos, let embryos reach the 4-cell stage (1 hpf), and inject 2 nl of the H2B-mCherry and LifeAct-GFP solution into one of the four cells (Fig. 2c). Repeat for 25 embryos and put the plate at 28 °C.

3.2 Dechorionate

1. Coat a 35-mm plate with 1 ml of 1% agarose in EM. When the agarose has solidified, fill the plate with warmed EM (28 °C). Transfer embryos to be dechorionated with a plastic Pasteur pipette.
2. With two fine tweezers, carefully remove the chorion. This is done by pinching the chorion with one tweezers and delicately pulling on the scratch with the second tweezers (*see* **Note 5**). Repeat until the embryo is freed from the chorion. Tear the

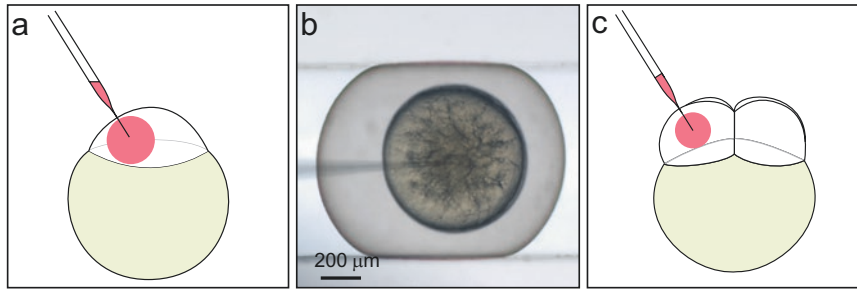

Fig. 2 Injection procedure. (**a**) Schematic of the injection procedure at the 1-cell stage. The injected volume on the schematic represents 4 nl. (**b**) 1-cell stage embryo maintained in an agarose groove. Injection needle is in the cell. (**c**) Schematic of the injection procedure at the 4-cell stage. The injected volume on the schematic represents 2 nl

chorion gently and progressively to avoid crushing the embryo. Dechorionated embryos are very fragile and will not survive contact with air or plastic: for further steps, use fire-polished glass pipettes and agarose-coated plates.

3. Clean the plate by removing torn chorions and damaged embryos with a glass pipette then carefully place the plate at 28 °C.

3.3 Shield to Shield Transplants

1. Fill a transplantation plate with Penicillin/Streptomycin EM and warm at 28 °C.
2. Wash the eyelash and transplant needle with 70% ethanol. For the transplant needle, mount it on a needle holder connected to a syringe and draw ethanol on 2 cm (Fig. 1c). Empty the needle and dry it by drawing air. Do not dry by blowing, as this may result in dust getting stuck in the needle.
3. When embryos have reached the shield stage (6 hpf), select donor and host embryos under a fluorescent stereo microscope. Pick embryos displaying bright and homogeneous fluorescence in the shield. Use the eyelash to manipulate and sort embryos. With a fire-polished glass pipette transfer selected embryos into the wells of the transplantation plate, aligning vertically and side by side hosts and donors. Rotate the embryos with the eyelash in order to place the shield up, slightly tilted toward the needle (Fig. 3a, b).
4. Install the transplant needle on the needle holder of the transplant setup (*see* **Note 6**). Under the fluorescent stereo microscope, orient correctly the bevel of the needle: if cells must be transplanted deep, turn the bevel downward; orient it upward to transplant cells superficially. Lower the needle into the EM and aspire EM over half of the stretched part of the needle (*see* **Note 7**).
5. Place a donor embryo in front of the needle and delicately insert the needle into the shield. Be careful not to pierce nor to be too

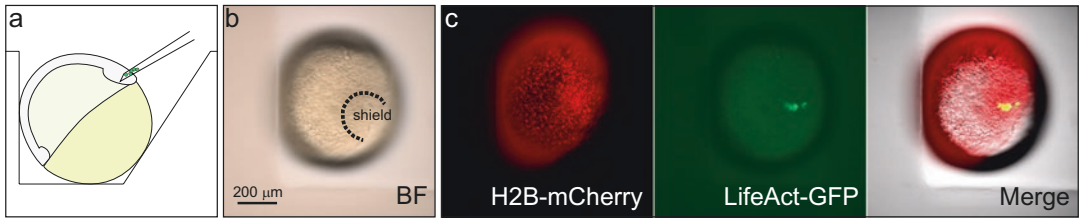

Fig. 3 Shield to shield transplant procedure. (**a**) Schematic of the transplant procedure. Embryos are maintained in individual wells, oriented with the shield up, slightly tilted toward the needle. The needle is used to draw cells from the shield of a donor embryo and inject them in the shield of a host embryo. (**b**) Bright field image of a host embryo in an agarose well. (**c**) This host embryo was injected at the 1-cell stage with RNAs encoding Histone2B-mCherry. All nuclei are thus labeled in red. A few cells expressing LifeAct-GFP were transplanted into the shield

close to the yolk. Gently draw up a few cells inside the needle (*see* **Note 8**). Using fluorescence, check that cells in the needle are labeled.

6. Place the corresponding host embryo in front of the needle and delicately insert the needle into the shield. Be careful not to approach the yolk too much. Gently blow the cells into the host, taking care not to add too much liquid with them. However, it may be necessary to keep expelling EM while moving the needle out of the embryo, in order for the cells not to stick to the needle. Be careful not to blow any air as this will damage the embryo. Use fluorescence to check that cells are now in the shield of the host embryo (Fig. 3c).
7. Repeat **steps 4** and **5** until all host embryos have been transplanted. Remove donor and damaged embryos. Carefully place the plate in a 28 °C incubator.
8. Clean transplant needle with water, as described in **step 2**.

3.4 Mounting Embryos

Embryos are mounted in a small volume of warm agarose, which cools and thus solidifies rapidly. Being fast is thus crucial: prepare workbench before mounting, so that all required equipment is at hand. Do not mount more than three embryos at a time.

1. Prepare 1 ml of 0.2% agarose in penicillin–streptomycin EM solution in a small glass vial and place it in a preheated 42 °C hot block.
2. Select 1–3 embryos and draw them in a fire-polished pipette. While the embryos are in the pipette, put the MatTek plate under the scope and focus on the bottom of the well.
3. Drop the embryos in the 0.2% agarose solution without adding too much EM. Discard the remaining EM and draw the embryos back into the pipette. Take care to draw enough agarose after the embryos in order to fill the well before the embryos fall out.

4. Blow a drop of agarose and the embryos into the MatTek well. Take care not to let the embryos touch air or the border of the well. Make sure the well is completely filled with agarose (*see* **Note 9**).
5. Depending on room temperature, the agarose will gel in about 1 min, during which embryos should be oriented using the eyelash. While orienting the embryo, be careful to touch it only on the blastoderm and not on the yolk, which is very fragile. Depending on the type of microscope used for imaging (upright or inverted), place the shield upward or downward, against the glass bottom. In the latter case, use fluorescence to spot transplanted cells and orient the embryo properly.
6. Wait a few minutes for the agarose to set completely, then add a drop of penicillin–streptomycin EM to prevent it from drying.

3.5 Imaging

1. Preheat the microscope cage at 28 °C at least 30 min before starting imaging.
2. Put the MatTek plate under the spinning-disc microscope and fill it with penicillin–streptomycin EM.
3. Set the hygrometry module to 80% relative humidity. In absence of hygrometry control, place a water-soaked tissue to keep constant moisture. This will prevent the EM from evaporating and the agarose from drying.
4. Using a 40× long range objective, spot an embryo and focus on labeled cells. Tune the laser power and exposure time to optimize image dynamics for both channels. Specified RNA doses should lead to bright GFP and mCherry signals, so that brief exposure times can be used (<100 ms; *see* **Note 10**). This limits photobleaching and toxicity, and allows for high frame rates, compatible with acquiring large z-stacks, at short time intervals (2 min). Using bright field, set the X and Y position, then the top and bottom of the z-stack, so that it encompasses the entire shield. Be careful to consider that the embryo is curved and that cells may therefore not migrate in a straight z plane. It may thus be useful to enlarge the z-stack in order to have the whole prechordal plate encompassed in the stack for the duration of the time lapse. To get a larger field of view, image several positions that will be stitched with the XuvTool software [18]. Neighboring stacks require a 5–10% overlap.
5. Repeat **step 4** for every embryo in the imaging plate then set the time interval to 2 min and z-step to 2 μm. Launch the time lapse for 2 h. Be careful that total acquisition time at each time step does not exceed 2 min.

3.6 Data Analysis

3.6.1 Quantification of Actin-Rich Protrusion Orientation

1. Load images in ImageJ using the Bioformat plugin (Fig. 4a).
2. Using the movement of labeled cells, determine the general direction of migration then rotate the movie using the "Rotate" function of ImageJ to set the direction angle to 0°.

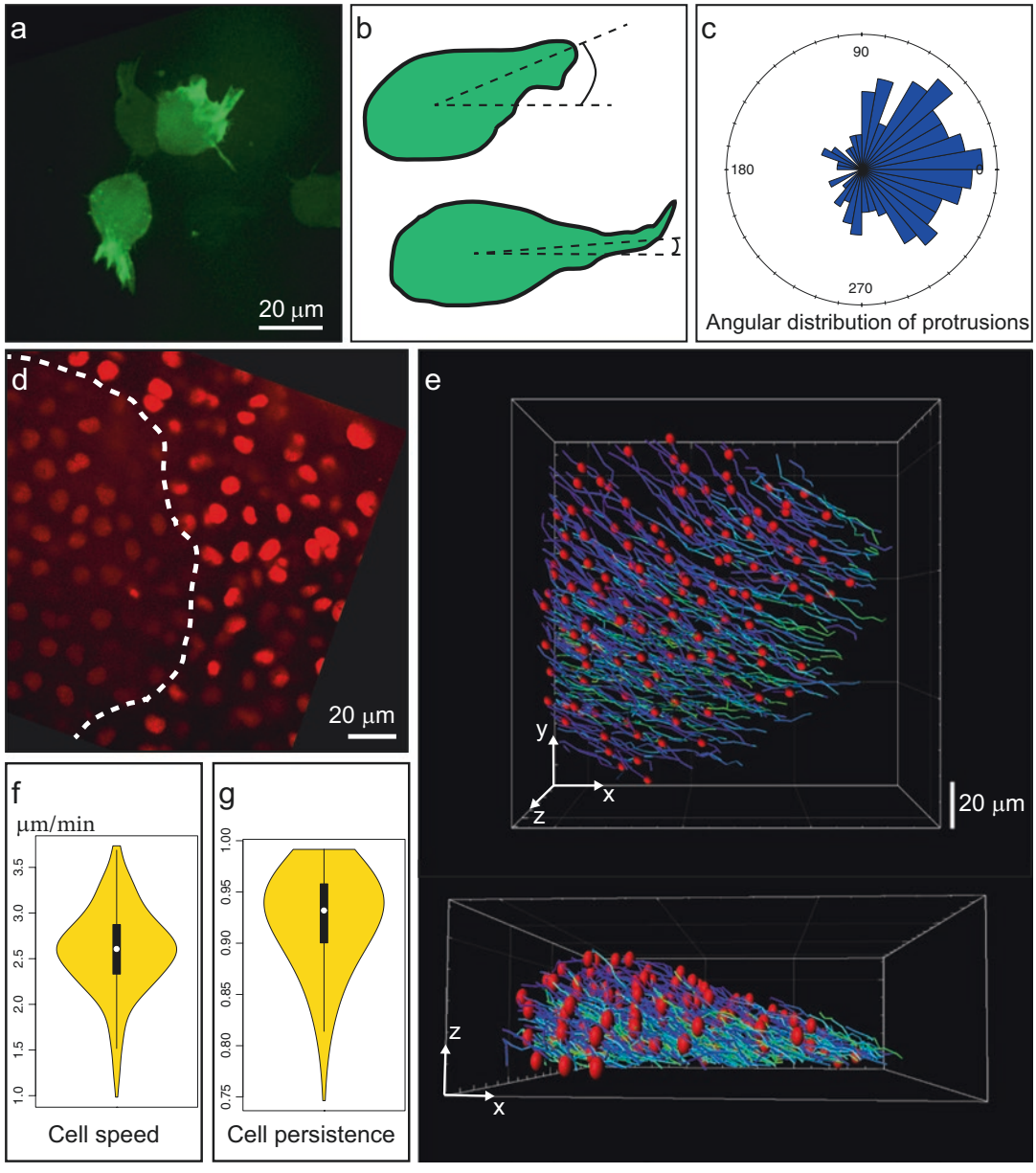

Fig. 4 Data analysis. (**a**) Transplanted cells expressing LifeAct-GFP. Large actin-rich protrusions are easily visible. (**b**) Measure of protrusion orientation. Image has been rotated so that the *x*-axis is aligned with migration movement. (**c**) Rose plot of the angular distribution of protrusions. (**d**) The host embryo expresses Histone2B-mCherry, labeling all nuclei in red. Dotted line delineates the limit between prechordal plate cells and ectodermal cells. (**e**) Tracks of prechordal plate cells, obtained in IMARIS. Upper part, *XY* view; lower part, *XZ* view. (**f**, **g**) Raw data from cell tracks are imported and processed in Matlab, to quantify migration properties. Here, distribution of average instant speed (**f**) of all tracked cells and distribution of cell persistence (**g**), calculated over five time steps

3. On the green channel, for each time step and each transplanted cell, look for actin-rich protrusions. We consider all protrusions exceeding 5 μm in length. If present, measure their 2D orientation using the "Angle" tool. Draw a straight line from the centroid of the cell toward the stem of the protrusion and measure the angle relative to the general direction of migration (Fig. 4b).
4. Use R and the circular package for data analysis and representation. If angles are measured over 0–180°, classic statistical tests can be used to compare two distributions, like the Kolmogorov-Smirnov test (ks.test). If angles are measured over 0–360°, circular statistical tests, like Watson's two sample test (watson.two.test), should be used. Data are best presented as a rose diagram (rose.diag) (Fig. 4c).

3.6.2 Cell Tracking

1. Open the time-lapse series with IMARIS. Set the pixel size, depending on the microscope and camera used for imaging (Fig. 4d).
2. Use the "Spot" function to locate and track nuclei. Set object size to 10 μm, which is the average nucleus size at this developmental stage. Due to lower axial resolution, nuclei may appear elongated in the axial dimension. It is therefore best to allow ellipsoidal shape, with 15 μm in the *Z* axis. Filter on spot quality to remove false positive. Filter on red intensity to discriminate between ectoderm cells and migrating prechordal plate cells, which, being deeper in the embryo, appear dimmer. Prechordal plate cells migrate at about 3 ± 0.8 μm/min [14], hence allow 9 μm as the maximal distance between consecutive time steps. Allowing gaps over one or two time points provides longer continuous tracks, without introducing too many track errors. Once automatic tracking is done, visually check tracks and manually correct them if necessary (Fig. 4e).
3. Export the results as a .csv file and process with MatLab. We use custom made Matlab routines to compute instant speed, persistence, coherence, orientation of movement, etc. for each cell. Routines are available on request (Fig. 4f, g).

4 Notes

1. Injections and transplants are technically demanding steps, which highly depend on needle quality. Pulling needles of the right shape (*see* Fig. 1b, e for reference) requires fine tuning of parameters but generally, to get short and sharp needles for injection, the temperature should be set low and the tension high. On the contrary, for long transplant needles, temperature should be high and tension low.

2. To ease penetration in embryos, which can be difficult at late developmental stages, it is possible to add a barb at the tip of transplant needles. Install a transplant needle on the microforge with the tip 50 μm above the filament. Heat the filament, lower the needle to briefly touch the filament and immediately pull back. By melting the very tip of the bevel, this will stretch a glass barb. If the barb is too long, break it with forceps (Fig. 1e, insert). Pay attention that this procedure may reduce the diameter of the needle opening.
3. Embryos meant to be hosts are injected at the 1-cell stage. Injected RNAs will diffuse in the cytoplasm, leading most cells to be labeled, but with varying intensities, depending on how much RNA they inherited. On the contrary, in donor embryos it is important that all labeled cells have inherited similar levels of RNAs, so that all transplanted cells are similar. Hence, donors are injected at the 4-cell stage, since the RNA will diffuse in a smaller volume and be distributed homogeneously into the daughter cells.
4. Some calibrate injection volume by injecting in an oil drop and measuring the diameter of the created droplet. Although theoretically precise, this technique implies that injection conditions are constant from one embryo to another. Experience proved this to be false, resistance to fluid flow in the needle varying largely from one embryo to another, due to differences in the position of the needle in the embryo, and partial, transient, clogging of the needle. To get reproducible injections, it is thus preferable to visually control the volume of injected liquid, which can be seen as a clearer droplet in the cytoplasm. By comparing the size of the droplet to the rest of the embryo, it is possible to have a good estimation of the injected volume (Fig. 2a, c). Phenol red may be added to the injection solution to better visualize the droplet.
5. While dechorionating, be very careful when first pinching the chorion, since this is when the embryo has the most chance to be crushed. In particular, for injected embryos, the chorion is pierced at the injection spot and embryos have a tendency to squeeze through this hole if chorion is brutally pinched.
6. Oil may be used instead of air in the transplant system. Being inelastic, oil provides a more reactive setup. Entirely fill the microinjector, the tubing and the needle with oil. Use the oil setup as described for the air setup. One drawback is that, to be efficient, the whole system must be purged of any air bubble, which may be difficult. Furthermore, needles filled with oil tend to get dirty and thus cannot be reused as many times as when used with air.
7. Be careful to have the right amount of liquid in your needle: enough to draw and blow cells without contact with air, but

not too much, otherwise the system will respond with a delay and sudden jolts. The interface between air and embryo medium must be kept in the stretched part of the needle.

8. Be careful not to draw up yolk in the needle, nor to draw up too much liquid after the cells, since injecting yolk or large volumes of liquid appear toxic to the host. Yolk can be seen as a transparent, nonfluorescent mass in the needle.
9. Once embryos have been deposited in the well, and before orienting them, briefly rinse the glass transfer pipette to avoid agarose solidifying into it. Otherwise, although not visible, agarose will partially clog the pipette and likely harm the next embryo that will be mounted.
10. Laser light and emitted fluorescent light are partially absorbed and diffracted by the sample, leading to signal attenuation when imaging deep. We use a custom Metamorph journal to compensate for this loss of signal. Exposure time is linearly increased while getting deeper in the sample, so that exposure time is doubled over the entire stack.

Acknowledgments

This work was supported by the grant PJA 20151203256 from Fondation ARC pour la Recherche sur le Cancer, and grant ANR-15-CE13-0016-02 from Agence Nationale de la Recherche.

References

1. Horwitz R, Webb D (2003) Cell migration. Curr Biol 13:R756–R759. https://doi.org/10.1016/B978-0-12-394447-4.20070-9
2. Vicente-Manzanares M, Horwitz AR (2011) Cell migration: an overview. Methods Mol Biol 769:1–24. https://doi.org/10.1007/978-1-61779-207-6_1
3. Lämmermann T, Sixt M (2009) Mechanical modes of "amoeboid" cell migration. Curr Opin Cell Biol 21:636–644. https://doi.org/10.1016/j.ceb.2009.05.003
4. te Boekhorst V, Preziosi L, Friedl P (2016) Plasticity of cell migration in vivo and in silico. Annu Rev Cell Dev Biol 3228361:1–28. https://doi.org/10.1146/annurev-cellbio-111315-125201
5. Ridley AJ (2011) Life at the leading edge. Cell 145:1012–1022. https://doi.org/10.1016/j.cell.2011.06.010
6. Haeger A, Wolf K, Zegers MM, Friedl P (2015) Collective cell migration: guidance principles and hierarchies. Trends Cell Biol 25:556–566. https://doi.org/10.1016/j.tcb.2015.06.003
7. Theveneau E, David NB (2014) Collective cell migrations. Med Sci (Paris) 30:751–757. https://doi.org/10.1051/medsci/20143008012
8. Row RH, Maître J-LL, Martin BL et al (2011) Completion of the epithelial to mesenchymal transition in zebrafish mesoderm requires Spadetail. Dev Biol 354:102–110. https://doi.org/10.1016/j.ydbio.2011.03.025
9. Montero J-A, Carvalho L, Wilsch-Bräuninger M et al (2005) Shield formation at the onset of zebrafish gastrulation. Development 132:1187–1198. https://doi.org/10.1242/dev.01667
10. Liang C-C, Park AY, Guan J-L (2007) In vitro scratch assay: a convenient and inexpensive method for analysis of cell migration in vitro. Nat Protoc 2:329–333. https://doi.org/10.1038/nprot.2007.30

11. Solnica-Krezel LL, Sepich DS (2012) Gastrulation: making and shaping germ layers. Annu Rev Cell Dev Biol 28:687–717. https://doi.org/10.1146/annurev-cellbio-092910-154043
12. Solnica-Krezel L, Stemple DL, Driever W (1995) Transparent things: cell fates and cell movements during early embryogenesis of zebrafish. BioEssays 17:931–939. https://doi.org/10.1002/bies.950171106
13. Kai M, Heisenberg C-P, Tada M (2008) Sphingosine-1-phosphate receptors regulate individual cell behaviours underlying the directed migration of prechordal plate progenitor cells during zebrafish gastrulation. Development 135:3043–3051. https://doi.org/10.1242/dev.020396
14. Dumortier JG, Martin S, Meyer D et al (2012) Collective mesendoderm migration relies on an intrinsic directionality signal transmitted through cell contacts. Proc Natl Acad Sci U S A 109:16945–16950. https://doi.org/10.1073/pnas.1205870109
15. Dumortier JG, David NB (2015) The TORC2 component, Sin1, controls migration of anterior mesendoderm during zebrafish gastrulation. PLoS One 10:e0118474. https://doi.org/10.1371/journal.pone.0118474
16. Dang I, Gorelik R, Sousa-Blin C et al (2013) Inhibitory signalling to the Arp2/3 complex steers cell migration. Nature 503:281–284. https://doi.org/10.1038/nature12611
17. Westerfield M (2000) The zebrafish book. A guide for the laboratory use of zebrafish (Danio rerio), 4th edn. University of Oregon, Eugene, OR
18. Emmenlauer M, Ronneberger O, Ponti A et al (2009) XuvTools: free, fast and reliable stitching of large 3D datasets. J Microsc 233:42–60. https://doi.org/10.1111/j.1365-2818.2008.03094.x

ECOLE DOCTORALE

Titre : Analyse des mécanismes de coordination des mouvements cellulaires dans le mésoderme axial durant la gastrulation du poisson zèbre *Danio rerio*.

Mots clés : migration collective, mécanosensation, imagerie live, microchirurgie laser, gastrulation, poisson zèbre.

Résumé : Le développement embryonnaire repose sur la migration de groupes de cellules au sein desquels l'orientation de chaque cellule dépend d'interactions avec ses voisines, un processus appelé migration cellulaire collective. Ces groupes doivent de plus coordonner leur migration avec d'autres mouvements cellulaires ayant lieu simultanément. Cette thèse s'intéresse à la coordination des mouvements cellulaire, au sein d'un groupe de cellules et entre différents tissus. Nous avons utilisé comme modèle l'extension, durant la gastrulation du poisson téléostéen Danio rerio, du mésoderme axial, composé du polster et du mésoderme axial postérieur, présentant des mouvements différents mais coordonnés. Nous avons développé des techniques d'ablation laser profonde en 3D ainsi que de transplantation cellulaire avancée, que nous avons combinées à des approches de génétique fonctionnelle et de simulation numérique. Nous avons montré que l'information de direction qui guide le polster provient du mouvement antérieur des cellules suiveuses. Les cellules du polster détectent des signaux mécaniques exercés par la migration des cellules suiveuses. Ce signal est perçu à travers les contacts cellule-cellule et la voie de signalisation de mécanotransduction passant par E-Cadhérine, α-Caténine et Vinculine. Les cellules détectant un tel signal s'alignent avec leurs suiveuses et le signal se propage à travers tout le tissu. Ce guidage de la migration par les suiveuses permet la coordination des mouvements sur de longues distances sans avoir besoin de gradient de chemoattractant préétabli. De plus, ce comportement assure la robustesse du développement, car il permet de maintenir un contact continu entre le polster et le mésoderme axial postérieur durant la gastrulation. Cette thèse contribue à une meilleure compréhension de la régulation des mouvements gastruléens dans le poisson-zèbre et a permis d'identifier un nouveau mécanisme par lequel la migration collective peut s'établir.

Title : Analysis of cell movement coordination mechanisms in the axial mesoderm during gastrulation of the zebrafish *Danio rerio***.**

Keywords : Collective migration, mechanosensation, live imaging, laser microsurgery, gastrulation, zebrafish.

Abstract : Embryonic development requires the migration of groups of cells in which guidance of each cell depends on interactions with its neighbours, a process deemed collective cell migration. These groups furthermore often needs to be coordinated with other cell movements taking place concomitantly. This PhD focused on coordination of cell movement in a group and between tissues. We used as a model the extension of the axial mesoderm during the gastrulation of the teleost fish Danio rerio. Axial mesoderm is indeed composed of two different tissues, the polster and the posterior axial mesoderm, with distinct but coordinated movements. We developed precise deep laser ablations, advanced transplantation techniques, and used functional genetic approaches as well as numerical simulations. We showed that the directional information guiding polster cells is provided by the anteriorward migration of the following cells. Polster cells detect, through cell-cell contact, a mechanical signal applied by migrating following cells via the E-Cadherin/α-Catenin/Vinculin mechanotransduction pathway. This signal ensures proper alignment of cell migration with followers and propagates from cell to cell over the whole tissue. Such guidance of migrating cells by followers allows long-range coordination of cell movements without the need for external chemoattraction. Furthermore, this behaviour ensures developmental robustness as it guarantees continuous contact between polster and posterior axial mesoderm during gastrulation. This PhD thus contributes to better understand how gastrulation movements are coordinated in zebrafish and identify a new mechanism by which collective cell migration is achieved.